



**HAL**  
open science

# Etude du potentiel des structure bio-imprimées en 3D comme nouvelles plateformes pour la production de protéines recombinantes

Laura Chastagnier

► **To cite this version:**

Laura Chastagnier. Etude du potentiel des structure bio-imprimées en 3D comme nouvelles plateformes pour la production de protéines recombinantes. Sciences agricoles. Université Claude Bernard - Lyon I, 2023. Français. NNT : 2023LYO10322 . tel-04780698

**HAL Id: tel-04780698**

**<https://theses.hal.science/tel-04780698v1>**

Submitted on 13 Nov 2024

**HAL** is a multi-disciplinary open access archive for the deposit and dissemination of scientific research documents, whether they are published or not. The documents may come from teaching and research institutions in France or abroad, or from public or private research centers.

L'archive ouverte pluridisciplinaire **HAL**, est destinée au dépôt et à la diffusion de documents scientifiques de niveau recherche, publiés ou non, émanant des établissements d'enseignement et de recherche français ou étrangers, des laboratoires publics ou privés.

# THESE de DOCTORAT DE L'UNIVERSITE CLAUDE BERNARD LYON 1

**Ecole Doctorale N° 205**  
**Ecole Doctorale Interdisciplinaire Sciences-Santé**

**Discipline** : Biotechnologies et Bioprocédés

Soutenue publiquement le 14/12/2023, par :

**Laura Chastagnier**

---

## **Exploring the potential of 3D bioprinted cellularized structures as an innovative platform for bioproduction of recombinant proteins**

---

Devant le jury composé de :

DAVID, Laurent	Professeur des Universités, UCBL	Président
GODIA, Francesc	Professeur des Universités, Université Autonome de Barcelone	Rapporteur
MALAQVIN, Laurent	Directeur de recherche, CNRS	Rapporteur
MARQUES, Alexandra	Chercheuse, Université du Minho Braga	Examinatrice
NIEMANN, Julia	Directrice R&D, Sartorius Stedim Biotech	Examinatrice
OLMOS, Eric	Professeur des Universités, Université de Lorraine	Examinateur
PETIOT, Emma	Chargée de Recherche, CNRS	Directrice de thèse



## ACKNOWLEDGEMENTS – REMERCIEMENTS

I will start by thanking the members of my jury, Pr. Godia and Dr. Malaquin for accepting to read my thesis and review my work. I also thank Pr. David, Dr. Niemann, Dr. Olmos and Dr. Marques for accepting to discuss and evaluate my work.

I also thank the members of the Sartorius team who funded and collaborated in this project: Magali Barbaroux, Julia Niemann, Oscar Reif, David Pollard and Lukas Raddatz. Thanks also to the whole Upstream Processing team from Göttingen for welcoming me and training me on the Ambr®250 system.

Tout au long de ma thèse, j'ai eu la chance de rencontrer et d'être supportée par beaucoup de belles personnes.

Emma, effectuer ma thèse sous ta supervision a été un plaisir immense et je t'en suis infiniment reconnaissante. Je te remercie pour tout ce que tu m'as apporté, ainsi que pour la confiance et la liberté que tu m'as offertes dans ce travail. Tu as cru en moi plus que je n'y croyais moi-même et tu m'as guidée sans relâche, avec patience et bienveillance, à travers cette aventure qui m'a fait grandir. Merci pour tout.

Je tiens également à remercier Christophe de m'avoir accueillie dans l'équipe 3d.Fab. Merci pour l'aide et les conseils que tu m'as apportés et surtout merci pour ta simplicité et ton humanité.

Je remercie sincèrement toutes les personnes qui ont contribué à ce travail,

Lucie, la reine de l'histologie et grimpeuse hors pair, merci pour ta gentillesse et pour les fous rires,

Céline, l'experte des cellules (et des poissons), merci d'avoir répandu la bonne humeur dans le labo

Elliott "the CHO's whisperer", mon fils préféré, merci pour ton aide et pour ton humour

Ilyes, ce fut un plaisir d'apprendre avec toi à dompter le spectromètre Raman,

Sarah, ma binôme de labo et de Krav Maga, merci pour ce magnifique King Julian et pour le reste

Edwin, merci de m'avoir initiée à la rhéologie, et merci pour ta patience et ta pédagogie,

Eric Olmos et Céline Loubière du LRGP pour les simulations CFD

Elisabeth Errazuriz-Cerda, pour les observations en microscopie électronique

Anne Baudouin, pour les analyses RMN

Je remercie aussi les postdocs, Alexandre, Mehdi, Carlos et Imen, pour les conseils et le partage de vos expériences, mais aussi pour les biscuits, les rires et les miaulements dans les couloirs.

Merci également à tous les membres de l'équipe Gembas/3d.Fab de l'ICBMS que je n'ai pas cités mais qui ont joué un rôle essentiel dans la réussite de cette thèse. Vous avez été une deuxième famille et je suis sincèrement reconnaissante pour l'atmosphère de bienveillance et de partage qui a fait de cette équipe le meilleur environnement pour apprendre et évoluer. Vous m'avez tous beaucoup appris et j'espère sincèrement que nos chemins se croiseront à nouveau dans le futur.

Merci à Meigge et Leslie pour tout ce que l'on a partagé au labo et en dehors, pour votre optimisme et pour cette belle amitié.

Je remercie chaleureusement Nicolas et Marjorie, mes frères d'armes dans la rédaction. Cette bataille finale a été difficile, mais nous nous sommes battus côte à côte et nous y sommes parvenus ensemble. Vous avez été d'un soutien précieux.

Je tiens également à exprimer ma sincère gratitude à toute la famille KMG Prométhée qui a grandement contribué à me garder forte et motivée, même lorsque le stress et les doutes semblaient insurmontables.

Evidemment, merci à tous mes amis, en particulier Karen, Alix, Matthieu et Romain d'avoir été là.

Enfin, je suis infiniment reconnaissante envers ma famille de m'avoir toujours encouragée, et sans qui je n'en serais pas là aujourd'hui. En particulier, merci à mes grands-parents de m'avoir inspiré la détermination et la persévérance qui m'ont permis d'accomplir ce travail.

Pour finir, je présente toute ma gratitude et mon amour à ma sœur Solène, que j'admire infiniment, et à mes parents qui, dès les premiers jours, n'ont jamais cessé de croire en moi alors que rien n'était gagné...

# TABLE OF CONTENTS

ACKNOWLEDGEMENTS – REMERCIEMENTS .....	3
Table of figures .....	10
Table of tables .....	13
Abbreviations .....	14
RESUMÉ FRANÇAIS .....	16
SUMMARY .....	18
INTRODUCTION.....	20
CHAPTER 1. BIBLIOGRAPHY.....	22
1.1. Cell culture-based production of biomolecules .....	22
1.1.1. History of animal-cell-based bioproduction.....	22
1.1.2. Industrial bioprocesses for animal cell-based production .....	23
1.1.3. A growing interest in single-use process equipment.....	28
1.1.4. Challenges in large-scale animal cell culture .....	29
1.1.5. Cell lines used for bioproduction .....	31
1.1.6. Proliferation, metabolism and productivity of HEK, CHO, MDCK, Vero cell lines 38	
1.1.7. Current strategies for the densification of cultures and optimization of bioproduction yields.....	42
1.2. 3D culture for bioproduction: which advantages?.....	47
1.2.1. Generalities on 3D cell culture.....	47
1.2.2. State of the art of 3D cell culture of bioproduction cell lines .....	51
1.3. Bioprinting, a proposed biomanufacturing tool for encapsulated cell culture .....	55
1.3.1. What is bioprinting and its advantages for large-scale 3D cultures?.....	55
1.3.2. Biomaterials used for microextrusion-based bioprinting.....	60
1.3.3. Gelatin .....	62
1.3.4. Alginate .....	65
1.3.5. Fibrinogen and fibrin.....	66

1.3.6.	Current challenges for the scale-up of large bioprinted tissues .....	68
1.4.	In situ transfection of 3D cell cultures.....	71
1.4.1.	Introduction – Context .....	73
1.4.2.	Principles of cell genetic engineering .....	74
1.4.3.	Standard transfection methods as a starting point for 3D transfection protocols 77	
1.4.4.	Methods of chemical in situ transfection .....	78
1.4.5.	Physical in situ & in vivo transfection .....	98
1.4.6.	Future applications for in situ transfection.....	101
1.4.7.	Conclusion.....	104
OBJECTIVES	.....	106
CHAPTER 2.	MATERIAL & METHODS .....	108
2.1.	Culture media and cell lines .....	108
2.1.1.	Culture media preparation.....	108
2.1.2.	Cell lines.....	110
2.1.3.	Cell lines amplification .....	112
2.2.	Small-scale 2D and bioprinting experiments for cell line characterization.....	115
2.2.1.	Bioink formulation .....	115
2.2.2.	3D Bioprinting.....	115
2.2.3.	Parameters screened for bioprinting & DOE Analysis .....	117
2.2.4.	Monitoring and characterization of cell proliferation in 2D and 3D bioprinted cultures	119
2.2.5.	Hydrogel characterization .....	129
2.3.	Scale up and bioreactor culture of bioprinted constructs .....	133
2.3.1.	3D printing of the construct’s culture chamber.....	133
2.3.2.	Liquid flow simulations with Computational Fluid Dynamic (CFD) .....	133
2.3.3.	Measurement of fluid residence time in the culture chamber .....	133
2.3.4.	Measurement of pressure drop in the culture chamber outlet pipe .....	134
2.3.5.	Bioreactor systems and settings .....	135

2.3.6.	Magnetic Resonance Imaging (MRI) macrostructural analysis .....	137
2.3.7.	Detection of IgG retained in hydrogel.....	138
2.4.	In situ cell transfection & transgene expression .....	139
2.4.1.	Production and extraction of plasmids extraction and validation .....	139
2.4.2.	Verification of plasmids integrity .....	142
2.4.3.	Synthesis of cationized gelatin .....	142
2.4.4.	Synthesis of cationized alginate .....	143
2.4.5.	NMR characterization of synthesized cationic materials .....	144
2.4.6.	Characterization of cationized gelatin rheology and imprimability.....	144
2.4.7.	Evaluation of cationized gelatin potential as transfecting agent in 2D .....	145
2.4.8.	Standard bioink formulation with naked plasmids.....	146
2.4.9.	Bioink formulation with additives and transforming agents .....	146
2.4.10.	Bioink formulation with cationic biomaterial components .....	147
2.4.11.	Evaluation of nucleic acid stability within the biomaterial .....	147
2.4.12.	DNA dosage in bioink and supernatants .....	147
2.4.13.	in situ Transfection .....	148
CHAPTER 3. DEVELOPMENT OF ANALYTICAL TOOLS TO STUDY SMALL-SCALE 3D CULTURES.....		149
3.1.	Hydrogel dissociation and cell counting .....	149
3.2.	Cell quantification on histological slides.....	156
3.3.	Analysis of cell growth thanks to calcein and spheroid sizes.....	159
3.4.	Cell metabolic activity as an indicator of cell proliferation .....	160
3.5.	Conclusion .....	162
CHAPTER 4. DESCRIPTION OF BIOPRODUCTION CELL LINES' BEHAVIOR IN 3D BIOPRINTED CULTURES .....		164
4.1.	Introduction .....	166
4.2.	Results and discussion .....	167
4.2.1.	Growth proliferation profiles of production cells in 3D hydrogel .....	167
4.2.2.	Metabolic activity of production cells in 3D environment .....	171



4.2.3.	3D distribution and organization of production cell lines.....	174
4.2.4.	Seeding density impact on 3D cell proliferation.....	179
4.2.5.	Modulation of the 3D environment and impact on production cell line proliferation.....	180
4.3.	Conclusion.....	187
4.4.	Acknowledgements .....	188
4.5.	Conclusion.....	189
CHAPTER 5. LARGE-SCALE 3D BIOPRINTED CULTURES DEVICES DEVELOPMENT .....		191
5.1.	Design and evolution of bioprinted constructs.....	194
5.2.	Design and evolution of "culture chambers.".....	195
5.2.1.	Multi-flow culture chamber conception .....	195
5.2.2.	Characterization of residence time in the "culture chamber" .....	197
5.2.3.	Improvements of the “culture chamber’s” designs.....	200
5.3.	Regulation bioreactor .....	204
5.3.1.	Standard cell culture stirred-tank bioreactors adaptations.....	204
5.3.2.	Optimized regulation of temperature, pH and dO <sub>2</sub> control .....	209
5.3.3.	Volume regulation in Ambr® 250ml .....	212
5.3.4.	Integration of new analytics in the bioreactor setup.....	215
5.4.	Conclusion.....	223
CHAPTER 6. BIOREACTOR CULTURE: A PLATFORM FOR ENHANCED 3D CELL CULTURE AND MONOCLONAL ANTIBODY PRODUCTION.....		225
6.1.	Cultivating large bioprinted constructs in bioreactors for densifying 3D cell cultures	225
6.2.	Bioproduction of monoclonal antibodies from 3D bioprinted cultures of CHO cells	228
6.2.1.	Establishment of a reference run: CHO cells’ suspension in Ambr®250.....	228
6.2.2.	Small-scale evaluation of SFM impact on cell growth and productivity .....	232
6.2.3.	Monoclonal antibody production from large bioprinted constructs in bioreactor...	242
6.3.	Conclusion.....	244

CHAPTER 7. IN SITU TRANSFECTION .....	246
7.1. Stability of transfecting plasmids in the bioink.....	246
7.1.1. DNA quantification on hydrogel consolidated samples .....	248
7.1.2. Optical characterization with fluorescent labelling and microscopy.....	249
7.2. Development and optimization of in-situ transfection methods .....	251
7.2.1. In situ transfection methods adapted from 2D protocols.....	251
7.2.2. Synthesis and qualification of cationic materials for the preparation of charged bioink as GAM for in-situ transfection .....	253
7.2.3. Evaluation of the different in situ transfection strategies .....	260
7.3. Conclusion.....	265
CHAPTER 8. GENERAL DISCUSSION .....	269
CONCLUSION .....	275
Valorization.....	277
Publications .....	277
Patents .....	277

## TABLE OF FIGURES

Figure 1.1 : Common bioreactor culture modes.....	26
Figure 1.2 : Principle of Raman scattering.....	27
Figure 1.3: Karyogram of HEK cells.....	34
Figure 1.4: Karyogram of CHO DG44 cells.....	36
Figure 1.5: Karyogram of Vero cells.....	38
Figure 1.6: Typical metabolic fluxes of mammalian bioproduction cell lines.....	39
Figure 1.7 : Classification and ambiguity of 2D, so-called 2.5D, and 3D culture systems.....	49
Figure 1.8. : Microscopic imaging on 3D cultures of primary ovarian follicles in GelMA.....	52
Figure 1.9: Cyst formation by MDCK cultivated in 3D collagen matrices.....	53
Figure 1.10: The different types of 3D bioprinting.....	57
Figure 1.11: The crucial constituents and applications of 3D bioprinting and main requirements for bioink properties.....	59
Figure 1.12: Mechanism of gelatine crosslinking by the action of transglutaminase.....	64
Figure 1.13: Complexation of alginate by calcium ions forming an “egg-box” configuration.....	66
Figure 1.14. : Fibrinogen polymerization by Thrombin to form fibrin fibers.....	67
Figure 1.15: Overview of the main methods and applications of in situ transfection.....	74
Figure 1.16: Basic transfection methodologies adapted for applications to in-vivo and in-situ transfection.....	77
Figure 1.17: Methodologies applied for in-situ and in-vivo transfection both chemically and physically mediated.....	92
Figure 1.18: Principle of in situ transfection in GAMs (Gene Activated Matrix).....	95
Figure 1.19: Prospects for implementing and using in situ 3D transfection strategies in biomedical, morphogenesis, and tissue engineering research.....	103
Figure 1.20: Graphical abstract presenting an overview of the main steps of the project.....	107
Figure 2.1. : Examples of 3D CAD model of bioprinted constructs.....	116
Figure 2.2: Micro-extrusion-based bioprinting protocol used for cellularized bioprinted constructs manufacturing.....	117
Figure 2.3: The two enzymatic reactions required for quantification of L-lactic acid.....	128
Figure 2.4: Procedure for hydrogel micro-porosity quantification.....	132
Figure 2.5: Schematic representation of the setup used for residence time determination in 3d printed culture chamber.....	134
Figure 2.6: Plasmids maps and qualification.....	141
Figure 2.7: Chemical reaction of 1,6-diaminohexane grafting to gelatin and alginate molecules.....	143

Figure 3.1: Comparison of dissociation protocols' efficiency.....	152
Figure 3.2: Analysis of cell viability, apoptosis, necrosis after dissociation with protocol B.....	154
Figure 3.3: Images of hek cells in bioprinted hydrogels acquired by transmission electron microscopy.....	158
Figure 3.4: Cell density measure in the same construct with three different protocols.....	158
Figure 3.5: Non-destructive monitoring of cell proliferation with calcein staining.....	160
Figure 3.6: Comparative evolution of cell density and lactate production.....	162
Figure 4.1: Proliferation and Metabolic profiles for 3D bioprinted cell line. Growth curve, specific rate of glucose consumption and lactate production.....	169
Figure 4.2: Evaluation of cell distribution and organization in 3D bioprinted constructs.....	177
Figure 4.3: Compared growth profile for seeded cell lines at 1 and 3 x 10 <sup>6</sup> cell/ml of bioink.....	179
Figure 4.4 : Biofabrication impact on HEK cell proliferation in 3D environment.....	183
Figure 5.1: Concept of the bioreactor system adapted to the culture of 3D bioprinted constructs.....	193
Figure 5.2: Geometry of the large-scale bioprinted Construct in CAD versus real construct picture...	194
Figure 5.3: Evolution of bioprinted construct design.....	195
Figure 5.4: 3D printed culture chamber design and CFD simulations.....	197
Figure 5.5: Measure of culture medium residence time in the culture chamber.....	199
Figure 5.6: Modifications of the chamber to improve the chamber's robustness, water-tightness and handling.....	201
Figure 5.7: Evolutions of the bioprinted construct's chamber (CAD).....	202
Figure 5.8: Evolution of the culture chamber's cap.....	203
Figure 5.9: Evolutions of the sealing joints.....	203
Figure 5.10: Comparative representation of the regulated stirred tanks.....	205
Figure 5.11: In-house developed bioreactor setup.....	207
Figure 5.12: Evolution of the modified Ambr®250 perfusion-cap.....	208
Figure 5.13 : Regulation of culture parameters for large bioprinted construct containing CHO cells cultured in adapted Ambr®250 setup.....	211
Figure 5.14: Evolution of bioreactor setup on Ambr®250 system for bioprinted constructs culture...	215
Figure 5.15: MRI imaging of bioprinted constructs with or without cells.....	217
Figure 5.16 : Establishment of a model for lactic acid monitoring with raman spectrometry .....	219
Figure 5.17: Bioreactor setups integrating Raman spectroscopy probes.....	221
Figure 5.18 : Detailed Pipe and Instrumentation Diagram of bioreactor setups integrating Raman spectroscopy probes.....	222
Figure 5.19: 3D printed chamber cap adapted to the insertion of a Rxn-20 contact-free Raman spectroscopy probe.....	223

Figure 5.20: Prospects for a proposed future bioreactor setup.....	224
Figure 6.1: Comparison of HEK-seeded large bioprinted constructs cultured 20 days in either static (incubator) or dynamic conditions (bioreactor). .....	226
Figure 6.2: Monitoring of cell proliferation and metabolites of CHO cells grown in suspension in Ambr®250 bioreactor.....	230
Figure 6.3: Kinetic parameters regarding cell proliferation, metabolism and mAb production in CHO cell suspension culture in Ambr®250.....	232
Figure 6.4: Reference suspension run and static bioprinted conditions evaluated.....	233
Figure 6.5: Characterization of HEK cell proliferation in large-scale bioprinted cultures.....	236
Figure 6.6: Characterization of CHO cells metabolism in bioprinted constructs.....	237
Figure 6.7: Antibody production from bioprinted cultures of CHO cells.....	239
Figure 6.8: Immunostaining (green) of mAb entrapped in the hydrogel in CHO cells bioprinted construct.....	240
Figure 6.9: Culture conditions and productivity of large bioprinted CHO cells culture in bioreactor.....	244
Figure 7.1: Fluorescent microscopy imaging of labelled pDNA retained in the hydrogel.....	250
Figure 7.2: Transfection efficiency in 2D cultures of HEK cells assessed via measurement of transgene expression.....	252
Figure 7.3: Cationic compounds qualification with H-NMR.....	256
Figure 7.4: Rheograms of non-consolidated bioinks.....	258
Figure 7.5: Estimation of the probability of plasmid-cell contact.....	261
Figure 7.6: GFP expression measured by flow cytometry of in situ transfected cells recovered by dissociation of the hydrogel.....	263
Figure 7.7: Evaluation of cationized gelatin as a GAM and in-situ transfecting reagent.....	264
Figure 8.1: Main advantages and limitations of the technology developed in the present work.....	276

## TABLE OF TABLES

Table 1.1 : Culture vessels used for animal cell culture at different scales and with various levels of physico-chemical regulation.....	parameter 25
Table 1.2: Advantages and limitation of single-use technologies for industrial bioproduction.....	29
Table 1.3: Example of some of the most represented cell lines used for bioproduction, their origin and applications.....	32
Table 1.4 : Commonly reported maximal values for different culture yields, in standard small and/or large scale cultures.....	41
Table 1.5 : Main characteristics of the selected bioproduction cell lines for our study.....	42
Table 1.6: Comparison of productivity and cell-specific productivity of production cell lines cultivated in adherent vs suspension conditions.....	46
Table 1.7: Comparison of 2D, 2.5D and 3D cultures.....	50
Table 1.8: Table summarizing the most relevant papers in the litterature in the field of in situ transfection of 3D cultures and tissues.....	81
Table 2.1: Detailed phases of the 4Cell® Xtra CHO media system reconstitution for 1 L of medium..	109
Table 2.2 : Characteristics, culture conditions and application of each cell lines.....	111
Table 2.3: Protocol for recovery of cells in 2D or suspension cultures during splitting for amplification.....	114
Table 2.4: DOE experiment design (parameters) and their associated growth rate when available....	118
Table 2.5: Detailed composition of the different mixes added to the culture supernatents to evaluate and compare the efficiency of CG to act as transfecting agent.....	146
Table 3.1: Dissociation protocols screened for their effect on cell recovery, viability and gel dissolution level.....	151
Table 3.2: pH and osmolality of dissociation solutions.....	155
Table 4.1: Comparison of growth and metabolic parameters in 2D cultures and 3D bioprinted constructs.....	170
Table 4.2: PLS models quality assessment.....	181
Table 4.3: Correlation matrix extracted from the DOE experiment.....	185
Table 5.1: Residence times (Rt) and their standard deviation measured in the culture chambers with homogenous flow configuration for two different flow rates.....	199
Table 5.2: Evolution of the dO2 control loop PID.....	212
Table 7.1: Evaluation of dsDNA stability in bioprinted constructs.....	247
Table 7.2: Mass balance of preparation reactions of cationized gelatin and alginate.....	254

## ABBREVIATIONS

<b>A</b>	GALA: Penetration peptide ( Glu-Ala-Leu-Ala repeats)
AM: Additive Manufacturing	GAM: Gene Activated Matrix
<b>B</b>	GAPDH: Glyceraldehyde-3-phosphate dehydrogenase
BHK: Baby Hamster Kidney cells	GATA 4: GATA nucleotide sequence binding protein 4
<b>C</b>	GelMA: Gelatin Methacrylate/methacryloyl
CA: Cationic Alginate	GET: GAG-binding Enhanced Transduction peptide
CAD: Computer-Aided Design	GMP: Good Manufacturing Practices
CFD: Computational Fluid Dynamic	GP135: dog podocalyxin
CG: Cationized Gelatin	GFP: Green Fluorescent Protein
CHO: Chinese Hamster Ovary cells	<b>H</b>
CT: Computed Tomography	HA: Hydroxyapatite
<b>D</b>	HALA: Penetration peptide made of His-Ala-Leu-Ala repeats
2D: 2- dimensional	HE: Hematoxylin-Eosin
2.5 D: 2.5- dimensional	HEK: Human Embryonic Kidney cells
3D: 3- dimensional	hUC-MSC: Human umbilical cord-derived mesenchymal stem cell
DAPI: 4',6-diamidino-2-phenylindole	HyA: Hyaluronic acid
D-GPT: D-glutamate-pyruvate transaminase	HPL: Human Platelet Lysate
DH: Diaminohexane	<b>I</b>
DHFR: dihydrofolate reductase	IgG: Immunoglobuline G
DMA: Dynamic Mechanical Analysis	IVC: Integral Viable Cells
DMEM: Dulbecco's Modified Eagle Medium	IVCC: Integral Viable Cell Concentration
DNA: Deoxyribonucleic acid	<b>K</b>
dO <sub>2</sub> : dissolved oxygen partial pressure	KALA: Penetration peptide Lys-Ala-Leu-Ala repeats (WEAKLAKALAKALAKHLAKALAKALKA)
DOE: Design Of Experiment	<b>L</b>
dPAMAM: Polyamidoamine dendrimer	LDH: Lactate Dehydrogenase
DSP: Downstream Processing	<b>M</b>
<b>E</b>	mAb: monoclonal antibody
ECM: Extracellular matrix	MDCK: Madin-Darby Canin Kidney cells
EDC: 1-ethyl-3-(3-dimethyl aminopropyl) carbodiimide hydrochloride salt	miRNA: micro RNA
EGFP: Enhanced Green Fluorescent Protein	MMP: Matrix metalloproteinase
ELISA: Enzyme-Linked Immunosorbent Assay	MRI: Magnetic Resonance Imaging
<b>F</b>	mRNA: Messenger RNA
sFB: static Fed-Batch	MSC: Mesenchymal Stem Cell
FDA: Food and Drugs Administration	MTX: Methotrexate
FMA: Feed Medium A	<b>N</b>
FMB: Feed Medium B	nHA: Nano-hydroxyapatite
<b>G</b>	NMR: Nuclear Magnetic Resonance
GAG: Glycosaminoglycan	

<b>O</b>	
OD: Optical Density	RDG: Arginylglycylaspartic acid
OPT: Optical Projection Tomography	RNA: Ribonucleic acid
<b>P</b>	RT: Room Temperature
pBMP-2: Plasmid carrying Bone Morphogenetic Protein 2 encoding gene	Rt: Residence time
PBS: Phosphate Buffered Saline (saline solution)	<b>S</b>
PCL: Polycaprolactone	SA: Standard Alginate
PDHK: Pyruvate dehydrogenase kinases	SAM: Stock and Adaptation Medium
PDH: Pyruvate dehydrogenase	SC: Semi-Continuous culture
pDNA: Plasmid DNA	SFM: Serum-Free Media
PEI: Polyethyleneimine	Standard Gelatin
PEI-Ac80: PEI with 80% of the primary and 20% of the secondary amines acetylated	siRNA : Small interfering RNA
PET: Polyethylene terephthalate	SP: Setpoint
PET: Positron Emission Tomography	SV40: Simian Virus 40
PGA: Poly(glycolic acid)	<b>T</b>
PI: Propidium Iodide	TAG / TG: transglutaminase
	TCD: Total Cell Concentration
PID: Proportional-Integral-Derivative	TEM: Transmission Electron Microscopy
P&ID: Pipe & Instrumentation Diagram	TMSP: 3-(Trimethylsilyl)propionic-2,2,3,3-d4 acid sodium salt
PLG : Poly(lactide-co-glycolide)	TPE: Thermoplastic elastomer
PLL: Poly-L-lysine	<b>U</b>
PLLA: Poly(L-lactic acid)	$\mu$ : Cell-specific growth rate
PLS: Partial Least Square	USP: Upstream processing
PM: Production Medium	<b>V</b>
PU: Polyurethane	VCD: Viable Cell Density
pVEGF: Plasmid carrying Vascular Endothelial Growth Factor encoding gene	<b>X</b>
<b>Q</b>	Xmax: Maximal cell density
Qgluc: cell-specific rate of glucose consumption	<b>Y</b>
Qlact: cell-specific rate of lactate production	Y <sub>lact/gluc</sub> : Molar ration of consumed glucose and produced lactate
QmAb: cell-specific rate of mAb production	
<b>R</b>	
RALA: Penetration peptide 30 amino acids Arg-Ala-Leu-Ala repeats (N-WEARLARALARALARHLARALARALRACEA-C)	



## RESUMÉ FRANÇAIS

Le marché des biopharmaceutiques a connu une croissance exponentielle et continue depuis la première production industrielle de biomolécules issues de lignées cellulaires animales à la fin des années 1960. Néanmoins, l'amélioration des procédés de bio-production se heurte à des défis persistants, notamment en ce qui concerne la densification des cultures et l'augmentation de la productivité. Les technologies existantes ont peine à la demande mondiale croissante et les cultures de cellules animales en suspension ou en monocouche dans les bioréacteurs traditionnels présentent un potentiel d'amélioration limité. Ce projet de thèse, issu d'une collaboration entre la plateforme académique 3D.Fab (ICBMS - Université Lyon 1) et l'entreprise Sartorius, a pour objectif de combiner l'expertise scientifique des deux parties pour proposer une stratégie innovante de production de protéines recombinantes. La bio-impression a été introduite comme outil de bio-fabrication novateur pour créer des cultures adhérentes de différentes lignées cellulaires de production en 3D avec des géométries complexes, contrôlées et reproductibles. L'objectif est d'explorer le potentiel des cultures adhérentes en 3D pour surmonter les limitations des procédés de production actuels. Notre travail a permis une meilleure compréhension des changements globaux des cinétiques cellulaires au sein des cultures en 3D et a décrit les avantages et les limitations de cette méthode de culture pour la bio-production. Nous avons démontré que les lignées cellulaires produisant des anticorps monoclonaux cultivées dans des structures 3D bio-imprimées présentaient une productivité spécifique plus élevée que notre culture de référence en bioréacteur en suspension, et une productivité spécifique équivalente aux valeurs rapportées dans la littérature pour les cultures optimisées en suspension alimentée (fed-batch). Ainsi, nous avons démontré le potentiel de cette technologie pour augmenter la productivité spécifique des cellules et soulevé des questions quant à sa capacité à surpasser la productivité spécifique maximale actuelle de 90 pg/cellule/jour. Nous avons ensuite pu réaliser des cultures bio-imprimées à plus large échelle en développant un système de bioréacteur personnalisé avec régulation des principaux paramètres de culture. Cependant, l'incapacité des cultures bio-imprimées à atteindre des densités cellulaires élevées entraîne une faible productivité volumique qui ne peut pas rivaliser avec les bioprocédés industriels actuels. Ensuite, nous avons démontré que la ressemblance de la culture cellulaire en 3D avec l'environnement *in vivo* peut déclencher des réponses physiologiques telles que l'alternance de cycles de croissance et d'apoptose, semblables à ceux observés dans les tissus *in vivo*. Finalement, des outils de transfection *in situ* ont été étudiés pour l'insertion progressive de matériel génétique dans les cellules cultivées en 3D. Cette technologie n'a pas permis d'atteindre des efficacités équivalentes à celles rapportées dans les

cultures en monocouche ou en suspension. Notre travail n'a pas pu surmonter cet obstacle, mais nous avons proposé des suggestions pour améliorer l'efficacité de la transfection in situ. Les résultats présentés dans ce travail nous ont amenés à conclure qu'avec les capacités techniques actuelles, cette technologie ne présente pas une alternative convaincante aux procédés industriels courants pour la production de protéines recombinantes. Néanmoins, sa similarité avec l'environnement in vivo et sa capacité à augmenter la productivité spécifique présentent un potentiel intéressant pour les traitements personnalisés ou thérapies de niche, telles que les traitements à base de cellules souches ou la production de vésicules extracellulaires.

## SUMMARY

The biopharmaceutical market has witnessed exponential growth and continuous evolution since the first industrial production of animal cell-based therapeutics in the late 1960s. Nevertheless, the quest for improved biomanufacturing processes faces persistent challenges, particularly in achieving high cell density and productivity. The existing technologies have struggled to meet the ever-increasing global demand for therapeutic agents and traditional bioreactor cultures of animal cells in suspension or as monolayers remain limited. This project originated from a collaborative effort between the academic platform 3D.Fab (ICBMS – Université Lyon 1) and the industrial company Sartorius. Our goal is to leverage the combined scientific expertise of both parties to introduce an innovative biomanufacturing strategy for producing recombinant proteins. We propose the application of bioprinting as a novel biofabrication tool to create complex, controlled, and reproducible 3D adherent cultures of various production cell lines. The objective is to explore the potential of 3D adherent cell cultures in addressing the limitations of current culture-based production. Our work has provided a deeper understanding of the global changes in cellular kinetics within 3D cultures and has described both the advantages and limitations of this culture method for bioproduction. We demonstrated that mAb-producing cell lines cultivated in such 3D bioprinted constructs exhibited higher specific productivity than our suspended bioreactor culture reference, and equivalent specific productivity compared to values reported in the literature for optimized fed-batch suspension cultures. Thus, we have demonstrated the potential of this technology to increase cell-specific productivity and raised questions about its potential to surpass the current maximum cell-specific productivity of 90 pg/cell/day. The 3D bioprinted culture of these production cell lines could be scaled up and cultivated in a custom bioreactor system with full control over key culture parameters. However, the inability of 3D cell culture to reach the high cell densities achieved in standard culture processes results in low volumetric productivity that cannot compete with current industrial bioprocesses. Our work has demonstrated that optimizing bioprinting parameters and hydrogel properties could enhance cell proliferation and increase the maximum cell density achievable. Nonetheless, while it is theoretically possible for cells to grow at very high cell density by colonizing 100% of the construct volume, it remains uncertain whether such a phenomenon is practically achievable. In fact, the greater resemblance of 3D cell culture to the *in vivo* environment may also trigger *in vivo*-like responses, such as cell-contact-induced apoptosis. Our research has indicated the presence of successive growth phases interspersed with stationary phases or even a reduction in cell density for some cell lines, which aligns with the growth-apoptosis cycles observed in tissues. Furthermore, existing *in situ* transfection tools have been studied for progressive insertion of

genetic material in cells grown in 3D cultures. Such technology has not yet achieved efficiencies equivalent to those reported in monolayer or suspension cultures. Our work has not been able to overcome this obstacle, but we have proposed suggestions for improving in situ transfection efficiency. The insight provided by this work led to the conclusion that, with current technical capabilities, this technology does not present a compelling alternative to standard large-scale industrial bioproduction processes for recombinant proteins. Nevertheless, its similarity to the in vivo environment, increased specific productivity, and the cell-protective effects of the hydrogel matrix against hydrodynamic stresses present intriguing potential for personalized or niche therapies, such as stem cell-based treatments or extracellular vesicle production.

# INTRODUCTION

The biopharmaceutical market has witnessed exponential growth and continuous evolution since the first industrial production of animal cell-based therapeutics in the late 1960s. Nevertheless, the quest for improved biomanufacturing processes faces persistent challenges, particularly in achieving high cell density and productivity. The existing technologies have struggled to meet the ever-increasing global demand for therapeutic agents. Although novel bioproduction strategies have emerged, traditional bioreactor cultures of animal cells in suspension or as monolayers remain the central approach. These methods have yet to significantly enhance maximal cell density and biomolecule productivity, which hinders progress.

This project originated from the collaborative effort between the academic platform 3D.Fab (ICBMS – Université Lyon 1) and the industrial company Sartorius. Its goal was to combine the scientific expertise of both parties to introduce an innovative biomanufacturing strategy for bioproduction. We propose the application of bioprinting as a novel biofabrication tool to create intricate, controlled, and reproducible 3D adherent cultures of various production cell lines. The objective is to explore the potential of 3D adherent cell cultures in addressing the limitations of suspension and monolayer cell culture-based bioproduction.

This project presents a multidisciplinary approach built on knowledge and techniques from diverse fields, including bioprocesses, bioproduction, bioprinting, cell biology, tissue engineering, and computational flow simulation. The utilization of 3D bioprinting was adapted from widely described know-hows in the tissue engineering fields. It enables the design and manufacturing of 3D cellularized constructs with a wide range of geometries and sizes. Traditional bioprocessing equipment used for intensive cell culture and therapeutic molecule production were adapted to suit this novel biomanufacturing model. Computational flow simulation was used to optimize the customized culture vessel and ensure uniform media flow throughout the 3D bioprinted construct.

In addition to these advancements, our work explores in situ transient transfection strategies to offer an alternative to the time-consuming process of developing stably transfected cell lines and to overcome the constraints of standard transient transfection in densified culture processes. The goal was to create a more flexible and time-efficient production platform for multiple recombinant protein production. In situ transient transfection is identified as a means to extend the transfection of proliferating cells throughout the entire culture process.

The techniques and technologies presented here are expected to facilitate the establishment of a unique small-scale production platform designed for the local and flexible manufacturing of multiple therapeutic recombinant proteins. The project also involves the development of specialized tools and methods to characterize these new bioprocesses, along with the implementation of sensors and customized culture systems.

# CHAPTER 1. BIBLIOGRAPHY

## 1.1. Cell culture-based production of biomolecules

### 1.1.1. *History of animal-cell-based bioproduction*

Animal cell-based bioproduction has significantly advanced in the last four decades [1,2]. It has become crucial for the biotechnology industry to obtain various products with therapeutic and diagnostic applications [3]. These products include viral vaccines, growth factors, monoclonal antibodies, and recombinant proteins [2–6]. They are used to prevent or treat a broad panel of diseases like cancer, viral infections, hereditary deficiencies, chronic and inflammatory illnesses [2].

The first industrial-scale vaccine production in animal cell cultures was carried out after Capstick et al. (1962) adapted BHK-21 (Baby Hamster Kidney) cells for growth in suspension. In 1965, the suspension-adapted BHK-21 cell line was used by Telling and Elsworth to produce an inactivated vaccine in a large-scale bioreactor (30L) in a serum-containing medium [7,8]. Cell culture-based production of viral vaccines has long become the preferred production method over animal-based and egg-based vaccines. It provides a more reproducible process, better availability, and higher product resemblance with the primary human isolate or human post-translational modifications. This results in higher therapeutic product efficiency and a lower risk of contamination or allergic reactions [9,10].

The first Food and Drug Administration (FDA) approval of recombinant protein production in mammalian cells (CHO) for therapeutic purposes was reported in 1987. It aimed to produce human recombinant tissue plasminogen activator [11,12]. It paved the way for the development of animal cell-based therapeutics bioproduction.

Since 2019, 70 to 80 % of newly approved therapeutic recombinant proteins have been produced in mammalian cells [2,5,13]. It is due to the ability of mammalian cells to produce high-value biomolecules, such as antibodies that require human-like glycosylation and complex post-translational modifications [14]. Since 2015, monoclonal antibodies (mAbs) have represented over 50% of new biopharmaceutical approvals. The demand for mAbs has been constantly rising, increasing mAbs sales from 50% of total biopharmaceutical sales in 2011 to 80% in 2021 [2].

In the last four years, the COVID-19 pandemic has demonstrated the necessity for fast innovation and development of therapeutics to reach high productivity during the healthcare crisis. It also reminded us of the substantial worldwide inequalities in medicines access [15,16]. While the right to health is considered a fundamental human right, therapeutic biomolecules

are produced by big pharmaceutical companies originating from high-income countries. Indeed, in 2021, the top-20 selling biopharmaceutical products were manufactured exclusively by large North American (BioNtech-Pfizer, Abbvie, Moderna, Johnson&Johnson, Regeneron, BMS, Eli Lilly, Amgen, Genentech, Alexion), European (Merck, Bayer, Roche, Janssen, Sanofi, Novartis) or Asian (Japanese) companies (Eisai, Ono, Takeda Pharmaceuticals) [2]. The high production costs and the need for specialized, large, and expensive infrastructures raise a barrier to developing smaller, localized therapeutics in lower-income countries [17].

Hence, since the first large-scale production of biopharmaceuticals in 1965, tremendous progress has been made in therapeutic molecule production from animal cells [3,18]. The fast evolution of the biopharmaceutical market led to the development of large and specialized production plants for the international distribution of therapeutics. While the demand for high-value and complex therapeutics increases continuously, the current processes face limitations due to the production's size, high cost and complexity [17]. These challenges are central concerns for biopharmaceutical companies. Reaching higher productivity commonly correlates to increasing bioproduction installations' size, costs and complexity. Such facts are responsible for aggregating bioproduction units in large multinational companies from high-income countries, thus widening the inequalities of access to medicine worldwide.

Therefore, the current limitations in the bioproduction of therapeutics raise two main matters:

- New innovative production processes enabling high production yields in smaller scale / simplified infrastructures would be strategic.
- Smaller, local, and less specific bioproduction platforms are needed to propose universal therapeutics manufacturing.

### 1.1.2. *Industrial bioprocesses for animal cell-based production*

Animal cells are fragile and sensitive to external physicochemical stress due to their thin membrane and large size (10-20  $\mu\text{m}$ ) [19,20]. Moreover, they have compelling requirements for good growth and production; they can only proliferate *in vitro* in tightly controlled environments. Therefore, multiple tools have been developed to culture animal cells at different scales and with various levels of culture parameters regulation (Table 1.1) [21]. At the lab scale, animal cells can be cultivated in Petri dishes. However, the preferred containers are usually T-flasks (25 to 175  $\text{cm}^2$ , Corning) for adherent cells or Erlenmeyer shake flasks (125 mL – 5L, Corning) for suspension cultures. These flasks are placed in an incubator, usually providing a controlled temperature and  $\text{CO}_2$ -enriched atmosphere for media buffering. However, there is



no precise pH regulation nor any oxygen monitoring. Shaking incubators are used for the culture of suspended cells in shaker flasks. Scaling up the cultures, multi-flasks are used to replace T-flasks and can provide culture surfaces up to 850 cm<sup>2</sup> (Thermo Scientific™). At the industrial scale, roller bottles and multi-surface systems can reach 25,280 cm<sup>2</sup> (Thermo Scientific™ Nunc™ Cell Factory™ Systems, Greiner Bio-One). Spinner flasks are often used for suspended cell culture, where a magnetic stirrer gently mixes the media. Finally, to perform large-scale bioproduction of therapeutics, bioreactors are the best choice. They exist from minimal (15 mL – Ambr<sup>®</sup>15 Sartorius) to very large (30,000 L – I-Series Solaris Biotech) culture volumes thus allowing easily process scale-up. They can be used for suspension (stirred tank, perfusion, etc.) or adherent (microcarriers, fixed-bed, etc.) cultures and provide tight monitoring and control of the whole culture process [22]. The main bioreactor culture types are presented in Figure 1.1.

Suspension cell culture bioreactors are regulated by a control system associated with a feedback loop from sensors inserted in the stirred tank. The homogeneity of the culture is ensured by motorized stirring. In recent years, advanced fixed-bed or packed-bed bioreactors like iCellis<sup>®</sup> 500 (Pall<sup>®</sup> Corporation), scale-X™ (Univercells<sup>®</sup>), and the Ascent<sup>®</sup> FBR System (Corning<sup>®</sup>) have become increasingly popular. These bioreactors use a vessel filled or packed with porous carrier fabric to support cell immobilization. The fixed/packed bed vessel is fed by continuous circulation of media pumped from a conditioning stirred tank [23]. They offer a surface area of up to 1000 m<sup>2</sup> (Ascent<sup>®</sup> FBR System – Corning<sup>®</sup>) for cell attachment and proliferation, with packed-vessel media working volumes from less than 1L to 25L [23–25]. Thus, launching the first iCellis<sup>®</sup> disposable fixed bed bioreactor (Pall<sup>®</sup> Corporation) equipment 13 years ago onto the bioproduction market [26–28] dramatically changed cell densification. Such systems allowed to reach adherent cell densities of up to 2.5 x 10<sup>8</sup> cells/mL [22]. They also proved their benefit for product recovery from the culture supernatant. They reduce the need for clarification steps and the downstream processes' cost and duration, thus minimizing the risks of damaging the final product. However, proliferation capacities are limited to anchorage surface availability and biocompatibility, while achieving uniform seeding and feeding of the cells remains challenging. It requires a thorough understanding and control of the fluidic path within the packed-bed cell support.

**Table 1.1 : Culture vessels used for animal cell culture at different scales and with various levels of physico-chemical parameter regulation.**

	T-Flask	Erlenmeyer shake flask	Multi-flask	Spinner flask	Roller bottle	Multi-surface system	Bioreactor
Type of culture	Adherent	Suspension	Adherent	Suspension	Adherent	Adherent	Suspension and Adherent
Surface or volume available	25 - 300 cm <sup>2</sup>	0.05 - 5 L	500 - 875 cm <sup>2</sup>	0.05 - 36 L	850 - 4250 cm <sup>2</sup>	1260 - 25,280 cm <sup>2</sup>	0.05 - 30,000 L
Example of equipment provider	Falcon® ; Corning® ; Nunc™ (EasYFlasks™)	Corning®	Thermo Scientific™ (Nunc™ TripleFlask™) Falcon® (Multi-Flask)	Corning® (Glass Spinner Flask)	Greiner Bio-One (CELLMASTER™) Corning®	Nunc™ (Cell Factory™ Systems)	Sartorius (Ambr®, Biostat®, Univessel®) Pall® (iCellis®500), Univercells (Scale-X™), Solaris™ Biotech (I-Series)

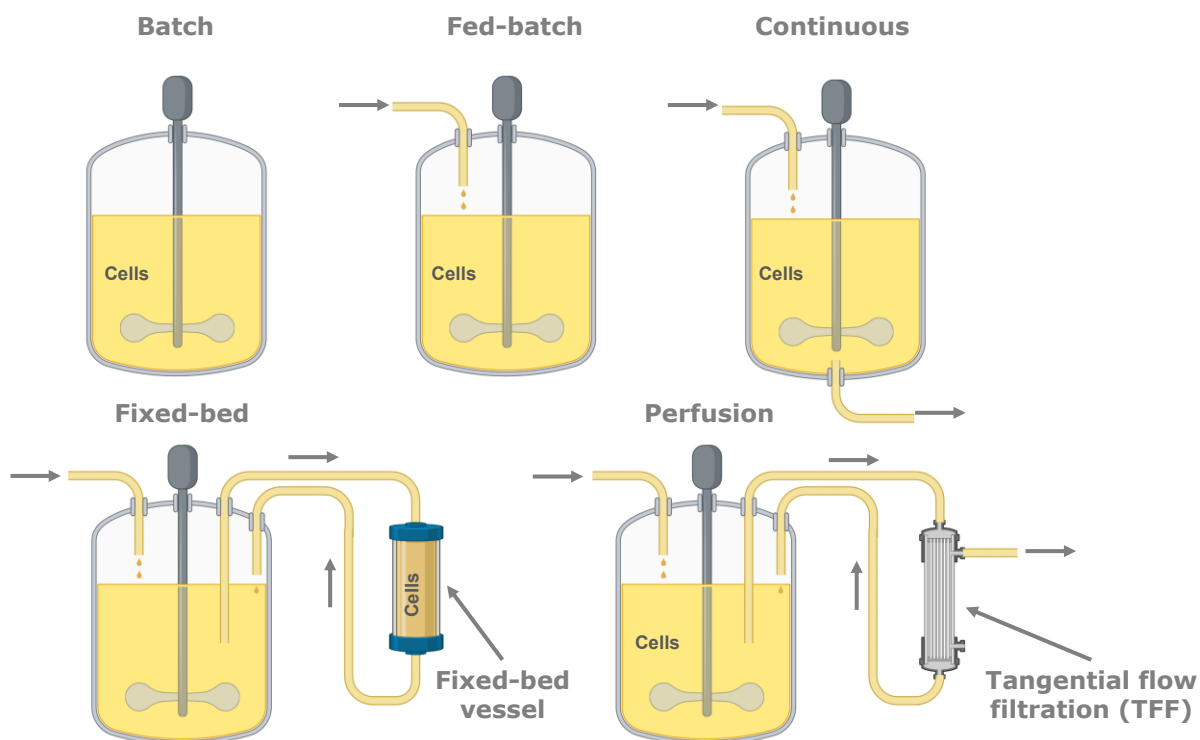


**Figure 1.1 : Common bioreactor culture modes:** In Batch, Fed-batch, Continuous, and Perfusion processes, cells are cultivated in suspension (or microcarrier) in the stirred tank. In Fixed-bed bioreactors, adherent cells are anchored on the fixed-bed. (Illustration created thanks to Biorender.com).

In bioreactor cultures, the cell environment is tightly controlled. Parameters such as temperature, pH and dissolved oxygen ( $\text{dO}_2$ ) are monitored thanks to sterile probes inserted in the tank [22,29,30]. The bioreactor system is connected to a controller that processes the recorded information from the online analytics. It thus responds to parameter deviation to maintain all parameters at their set point value by activating actuators (pumps, gas mass flow controller, stirrer, heater, etc...).

The evolution of biological parameters is mainly monitored in an off-line manner. Thus, the cell density and the substrates, metabolites, and product concentrations are observed along the culture thanks to a sterile discrete sampling of the culture supernatant. It limits the monitoring to a few time points and is a risk breach for culture sterility. In-line analytics are preferred as they provide continuous recording with reduced manipulation and lesser contamination risks. In the past decades, cell density was routinely monitored by measurement of optical density (O.D.) [31,32], capacitance [33,34] or Raman spectroscopy [35]. Among those technologies, spectroscopic technologies have the interesting feature of providing information about all suspended molecules in a single spectrum. Thus, Raman spectroscopy has raised interest in the

past decades as it can detect various molecules, including cell nutrients, secreted metabolites and bioproducts or intracellular molecules. It thus allows for their real-time quantification with a unique sensor [36,37]. This analytic technology is based on detecting shifts induced by inelastic scattering of molecules' vibrations after laser beam excitation [38,39] as illustrated in Figure 1.2. However, utilizing such technologies as online quantitative tools requires extensive qualification and calibration based on chemometric analysis.

Various Raman spectroscopy probes are available in the market and can be tailored to suit different applications. For instance, Endress-Hauser company offers a sealed immersion probe, the Rxn-40, designed for in situ Raman spectroscopy of liquid-phase samples. Additionally, they provide contact-free probes, like the Rxn-20, suitable for analyzing solids and semi-solids without direct contact with the material. Immersion probes, such as the Rxn-40, hold particular appeal for applications involving suspension and microcarrier cultures. In contrast, contact-free probes show great promise for applications in tissue engineering and 3D cell cultures. They enable non-destructive measurements from a distance, offer reproducible sampling, allow for precise "Focus" alignment, and facilitate volumetric analysis at the surface and in deeper layers of the sample.

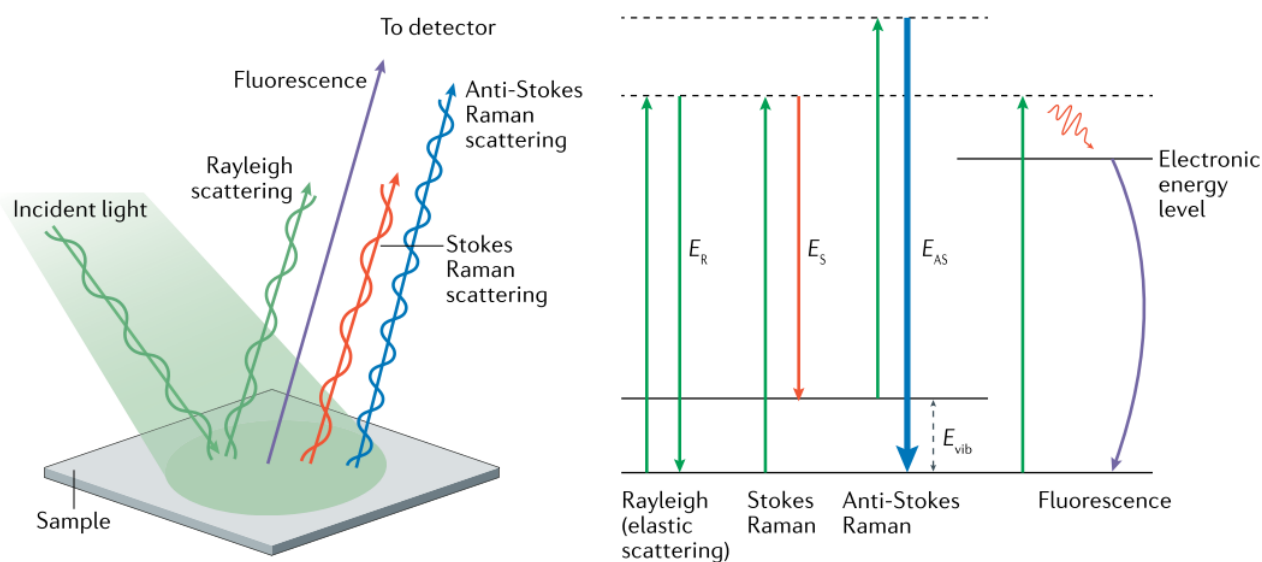


**Figure 1.2 : Principle of Raman scattering.** When light illuminates a sample, it can interact with the constituent molecules in numerous ways. Some light may be reflected from the surface through direct specular reflection or undergo elastic scattering (Rayleigh scattering), resulting in light emission from the sample of the same wavelength as the incident light. Suppose the energy of the illuminating photons matches an electronic energy level of the molecule. In that case, they can excite the molecule to this state, and de-excitation subsequently occurs

through the emission of a photon of a longer wavelength than the incident photon (fluorescence). Raman inelastic scattering can occur where incident photons induce a vibrational oscillation in the molecule specific to the chemical moiety. In the case of Stokes scattering, the molecule absorbs energy, and the wavelength of the emitted photon is less than that of the incidence photon. If the molecule is initially in a vibrationally excited state, it can de-excite vibrationally, transferring energy to the scattered photon (anti-Stokes scattering). All of these interactions can be measured and give information about the composition and environment of the molecules of interest in a sample.  $E_{AS}$ , the energy of anti-Stokes photon;  $E_R$ , the energy of Rayleigh scattered photon;  $E_S$ , the energy of Stokes photon;  $E_{vib}$ , the energy of molecular vibrational transition. **Credit: Mosca, S., Conti, C., Stone, N. et al. Spatially offset Raman spectroscopy. *Nat Rev Methods Primers* 1, 21 (2021). <https://doi-org/10.1038/s43586-021-00019-0> [38]**

### 1.1.3. A growing interest in single-use process equipment

Over the past 30 years, particularly within the last decade, there has been a growing interest in single-use manufacturing equipment [40,41]. Approximately 85% of the equipment used in pre-clinical bioprocessing is of the disposable type. Disposable kit includes various bioreactor kinds (such as wave-bioreactor pouches, stirred bags, stirred tanks, and perfusion units), sensors, and coupling/sampling/mixing devices [42,43]. Adopting single-use technologies also extends into downstream processing equipment [42]. Single-use bioreactors come in rigid and flexible forms (often bags), with plastic-based materials being the most commonly used. These materials undergo validation to ensure biocompatibility and minimize leachability concerns [42]. Nevertheless, significant concerns remain about leachables, extractables, and the binding of media components to these technologies [44,45]. Single-use bioreactors are available in volumes from a few millilitres, such as the Ambr®15 (Sartorius), to  $\sim 2 - 4 \text{ m}^3$  [40,43].

The main advantages and limitations of single-use bioreactors are summarized in Table 1.2. Typically, these systems are assembled with disposable sensors and have been pre-sterilized through gamma irradiation. After their use, they are discarded. Consequently, this technology significantly reduces the process duration. It eliminates most of the setup and sterilization procedures that are usually needed before the culture starts, while after production, the disassembling, cleaning, reassembling, and equipment validation steps are avoided [46]. Thus, these systems enable the rapid succession of batches, a quick process setup, reduced startup time, and high flexibility [44,47]. Additionally, cross-contamination risks from batch to batch are eliminated [44,46,47].

Counterintuitively, disposable biomanufacturing equipment was demonstrated to have reduced economic and environmental impact compared to reusable systems. This is due to the reduced consumption of water, cleaning buffers, chemicals, and electricity (heating) necessary for reusable systems' cleaning and sterilization [44,46]. They also provide simplified logistics and process planning [46].

Furthermore, the cost associated with equipment qualification before each batch and the validation of cleaning and sterilization procedures according to Good Manufacturing Practices (GMP) standards is a significant expense for biopharmaceutical companies, often ranking as the second-largest investment [46]. This cost is substantially reduced when using single-use systems, which are typically provided in a sterile, ready-to-use condition and are compliant with GMP standards. However, it's worth noting that in some instances, especially at large industrial scales (typically over 50 litres in volume), single-use equipment can become more expensive than reusable equipment and may exhibit reduced performance [46].

*Table 1.2: Advantages and limitation of single-use technologies for industrial bioproduction. Table adapted from Shukla A A and Gottschalk U 2013 Single-use disposable technologies for biopharmaceutical manufacturing Trends Biotechnol 31 147–54, doi: 10.1016/j.tibtech.2012.10.004*

Advantages	Limitations
Reduced capital costs for plant construction and commissioning	Leachable and extractible
Reduced risk for product cross-contamination between batches or in multi-products facility	Prior investment in fixed equipment
Rapid changeover and start-up	Scales limited to 2 – 4 m <sup>3</sup>
Lower utility cost due to reduced need for sterilization	A limited number of vendors
Reduced need for equipment qualification and cleaning validation	High cost of large-scale disposables
	Lack of universal standards for vendors
	Solid waste disposal

#### 1.1.4. Challenges in large-scale animal cell culture

In industrial bioproduction, bioreactors are the preferred production platforms. Nevertheless, industrial therapeutics manufacturing often implies scaling the cultures to huge volumes with high cell density. The culture of such large volumes faces a few challenges. One is maintaining culture media temperature, oxygenation, pH and global homogeneity in the overall process

based on heat and mass transfer principles [22,29,48–50]. In stirred tank bioreactors, it is achieved by stirring speed increase and by optimizing impeller geometry, oxygen bubbling rate and bubble size ( $K_La$ ). In scales over 10 L, the stirring is often turbulent to ensure gas, mass transfer and an efficient suspension of the cells or microcarrier in the large liquid volume. However, acceleration of stirring and bubbling also increases the risk of cell damage by hydrodynamic shear stress and surface tension [51–53]. The mechanical stress suffered by the suspended cells or microcarriers is generated by (i) turbulence due to media movement, (ii) collision between suspended cells/microcarriers or (iii) collision between a suspended cell/microcarrier and bioreactor wall or impeller [54–56]. Hydrodynamic stimuli have already been described to affect cell behaviours like growth, differentiation or production [57]. Hydrodynamic stress-induced DNA damage reduced the CHO cell culture's global and specific antibody production [58]. The mAbs galactosylation was affected by increased galactosylation.

One crucial step to optimize the cell cultures and bioproduction process consists of choosing the adequate stirring speed and direction (pumping up/down), the impeller model and diameter to provide good homogeneity and aeration while limiting cell damage [59,60]. Computational Fluid Dynamic (CFD) is often used to simulate the bioreactor's fluid path and velocity and predict possible bioreactor malfunctions such as insufficient mixing, cell accumulation/aggregation or hydrodynamic shear stress distribution [61,62].

Regarding aeration, even though the liquid culture media viscosity is equivalent to water, the high concentration of proteins and salt increases the surface tension [63,64]. It favours cell-to-bubble adhesion and foam formation, increasing the risk of cell damage. Surfactants such as Pluronic F-68 are now used to reduce foam formation and protect cells from hydrodynamic stress [52,65].

Finally, increasing the culture volume and cell density also increases the complexity and cost of downstream processing (DSP). It is mainly in the case of suspension cultures, where secreted products are collected with cell debris and released host-cell DNA and proteins.

**In conclusion, bioreactors are currently the most adequate system for controlling large-scale animal cell environments at industrial scales. The bioproduction scales and process complexity are constantly increasing to meet the growing demand for therapeutics and vaccines. Culture tanks are now reaching up to 30,000 L. Thus, new culture devices and methods must be developed. They should answer the need for culture densification and increased productivity while overcoming the limitations of current cell culture processes (i.e. oxygenation/cell damage/cell limited productivity).**

**Additionally, the rise of personalized medicine changed the bioproduction paradigm towards new production tools applied at smaller scales. Specialized productions now utilize smaller and more diverse device types. Single-use reactors have gained popularity as they serve as intermediate steps in the production chain and for screening process operating conditions. However, only a few methods are described for industrialized small-scale, personalized, controlled and reproducible production.**

#### *1.1.5. Cell lines used for bioproduction*

The cell culture system has emerged as a critical strategy for producing recombinant proteins and viral vaccines. Throughout bioproduction's evolution, clone selection, hybridization, and genetic engineering have transformed bioproduction cell lines from primary cells to immortalized and extensively optimized cell lines. *Table 1.3* provides an overview of bioproduction's most commonly employed cell lines.

We selected some of the most representative bioproduction cells used in the biopharmaceutical field for our study. They are listed below :

- HEK (Human Embryo Kidney) and CHO (Chinese Hamster Ovary) cells are highly engineered and optimized cell lines. They are the preferential cellular model for the bioproduction of recombinant proteins [66].
- MDCK (Mardin Darby Canine Kidney) and Vero (green monkey kidney) cells originate from primary cells and were only modified by spontaneous mutations. They are extensively used for viral vaccine production.



**Table 1.3: Example of some of the most represented cell lines used for bioproduction, their origin and applications**

Cell line	Origin	Immortalization and genetic modifications	Applications	Sources
<b>HEK293</b>	Human Embryo Kidney cells	Immortalized by transformation with adenovirus 5 functions	rProteins / Adenovirus (AdV) / Adeno-Associated Virus (AAV) / Lentivirus	[67,68]
<b>HEK293T</b>	Human Embryo Kidney cells	HEK293 transfected to express SV40 temperature-sensitive large T antigen	rProteins / Adenovirus (AdV) / Adeno-Associated Virus (AAV) / Lentivirus	[69]
<b>CHO</b>	Chinese Hamster Ovary cells	Spontaneous immortalization	rProteins / mAbs	[70]
<b>CHO DG44</b>	Chinese Hamster Ovary cells	CHO cells adapted to suspension <i>dhFr</i> gene depletion	rProteins / mAbs	[71,72]
<b>MDCK</b>	Epithelial cells from dog kidney	Spontaneous immortalization	Viral vaccines	[68,70,73]
<b>Vero</b>	Epithelial Kidney cells from green monkey	Spontaneous immortalization	Viral vaccines	[68,74]
<b>SF9</b>	Insect cells	Spontaneous immortalization	rProteins / VLPs	[67]
<b>BHK21</b>	Baby Hamster Kidney cells	Spontaneous immortalization	Factor VIII, Viral vaccines	[68,70]
<b>PER.C6</b>	Human retinal cells	Immortalization by transfection with an E1 minigene of adenovirus type 5	rProteins	[70,75]
<b>NSO / Sp2/0</b>	Myeloma cells mouse	Cancer cells or fusion with cancer cells	rProteins	[70]
<b>Hybridomas</b>	Hybridized murine cells	Fusion with cancer cells	Monoclonal antibodies	[76]
<b>MRC-5 / WI-38</b>	Human normal lung fibroblasts	Normal diploid cells	Viral vaccines	[68]
<b>DF-1 CEF</b>	Chicken embryo fibroblasts	Spontaneous immortalization	Viral vaccines	[68,77]

## **HEK cells**

The HEK immortalized cell line is extensively used in research for its abilities to be engineered or express recombinant proteins. Indeed, 90 % of transformed cells can easily be achieved thanks to transient transfection [78,79].

The cell line originated from a human embryo's kidney in 1973. The human embryonic kidney cell was transformed with human adenovirus 5 DNA [69]. A fast-growing variant was isolated and called HEK293. Genetic characterization of the HEK variant on microarray demonstrated that such cells express a wide range of genes specific to neuronal lineage [80]. It suggests HEK originated from an immature neuronal cell in the embryonic kidney. HEK cells also present abnormal karyotypes with more than 46 chromosomes. Genetic characterization highlighted a wide diversity of karyotypes within each clone, with some chromosomal alterations and pseudo triploidy [81]. Human adenovirus 5 DNA transformation resulted in the expression of the adenovirus E1A and E1B genes inducing replication and oncolytic effects. In addition the expression of these adenoviral genes provides interesting characteristics for rProtein and viral vector productions, with enhanced efficiency of adenovirus transduction, replication and transgene expression [66,69,82].

Later, the HEK293T cell line was created by stable transfection of HEK293 with genes encoding for the simian virus 40 (SV40) temperature-sensitive large T antigen [69]. The expression of the SV40 gene enhances protein expression yield by allowing episomal replication of plasmids containing the SV40 origin of replication. It enables the maintenance of transient gene expression in HEK293T across several generations. The SV40 large T antigen protein can bind to its specific origin of replication (ori), recruiting the DNA replication machinery, thus promoting plasmid DNA replication of plasmids [69,80].

HEK cells align with a broad range of tissue characteristics; they present both epithelial and mesenchymal characteristics [83], fibroblasts-like markers [84], genes specific to neuronal lineage [85] cancer stem cells [86], or adrenal gland [81]. This suggests that HEK kidney origin is uncertain and should not be used as a kidney cell model per se.

HEK cell line is FDA-approved for therapeutic molecules manufacturing. It has been used to produce recombinant proteins and viral vectors and was adapted to serum-free and suspension culture conditions. If some HEK can be adapted to suspension culture, the recommended mode of culture is adherent. Cells are cultured in monolayers, in T-flask or Petri dishes at the lab

scale. HEK can be cultivated on a larger scale in a microcarrier bioreactor or aggregate suspension. The size of bioreactors is usually limited to 500 L [87,88].

HEK variants are especially interesting for producing human recombinant proteins due to their ability to generate human glycosylation. Such human-like glycosylation is less immunogenic than the ones provided by the gold standard CHO non-human mammalian cell [89].

The counterpart is that HEK are more difficult to grow in large-scale serum-free culture. HEK present lower proliferation and production capacity than CHO cells. In fed-batch mode, they commonly reach  $\sim 3\text{-}5 \times 10^6$  cell/mL and 0.6 to 1 g/mL rProtein while CHO cells reach  $\sim 20 \times 10^6$  cell/mL and 4 to 10 g/L rProtein [90–92]. Additionally, HEK cells raise safety concerns due to their high susceptibility to infection and propagation of human viruses [89]. Their genetic variability (see Figure 1.3) makes it challenging to have reproducible and GMP-grade production [81,93].

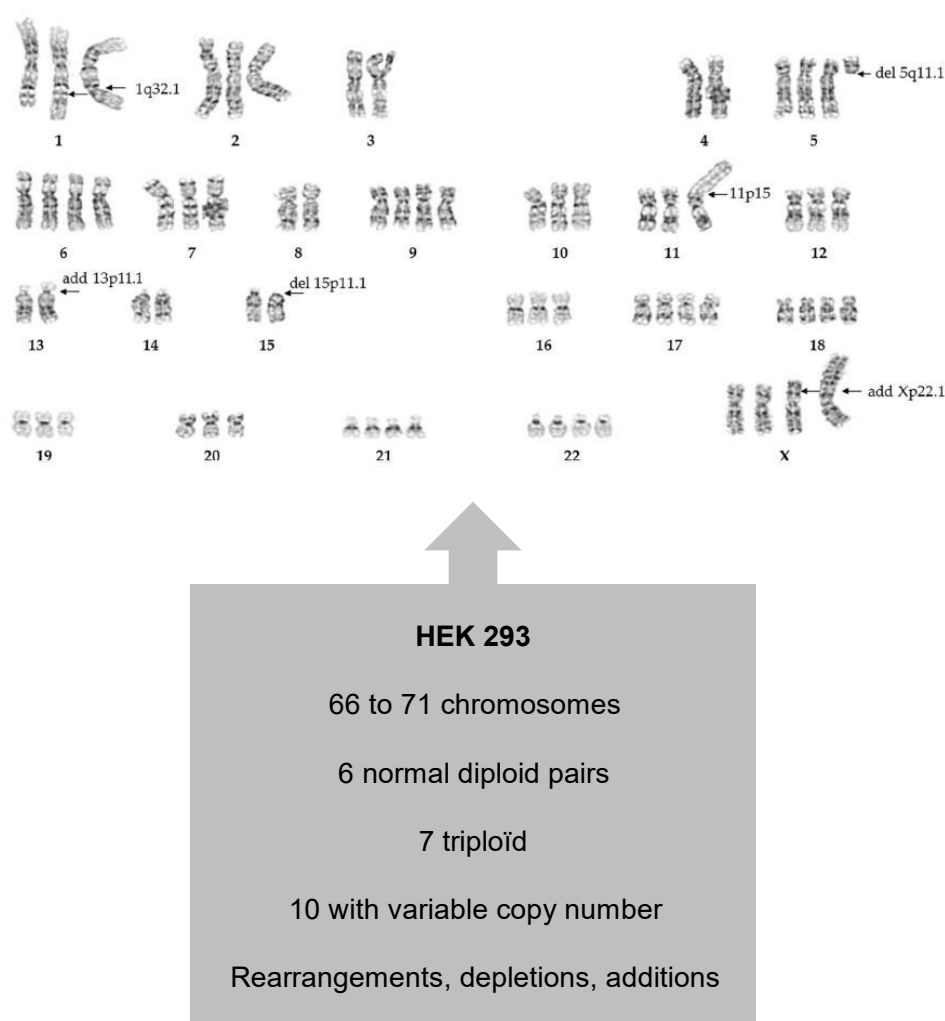


*Figure 1.3: Karyogram of HEK cells. Figure adapted from Binz R L, Tian E, Sadhukhan R, Zhou D, Hauer-Jensen M and Pathak R 2019 Identification of novel breakpoints for locus- and region-specific translocations*

## **CHO cells**

CHO cell line was extracted from Chinese Hamster Ovary in the early '60s [95]. A variant of the original CHO cell line, the CHO DG44, was established in the '80s by exposing the original CHO cell line to gamma irradiation [71,72]. Cell clones generated were screened to select ones deficient for dihydrofolate reductase (DHFR) [23], an enzyme that converts folate into tetrahydrofolate, a precursor for synthesis in nucleotide bases (purines and pyrimidines) [96]. Such mutation allows for easy selection of the clones subsequently transfected with the plasmids expressing *dhfr* and the gene of interest [66]. The selection is performed by cultivating cells in media lacking hypoxanthine and thymidine, the nucleoside precursors. High-producing clones are selected by the addition of Methotrexate (MTX) in the culture medium [97]. The MTX is a drug similar to folate, which can bind to the DHFR enzyme and inhibit the formation of tetrahydrofolate. In the presence of MTX, CHO cells with insufficient levels of DHFR cannot synthesize nucleotides and die. On the contrary, the cells with many copies of the cassette survive as they possess a high level of expression of the DHFR and gene of interest.

Due to the successive mutations and clonal selection, the CHO cell line has deviated from the original ovarian cells (see Figure 1.4). CHO cell lines have a fast growth rate and productivity in monolayer or suspension culture. It is due to the overexpression of proteins involved in DNA replication, transcription, translation, and control of apoptosis [98]. The protein expression of CHO DG44 has been compared to different Chinese hamster tissues. Proteomic analysis has shown significant differences between CHO DG44 cultivated in suspension and the native Chinese hamster ovarian tissue [98]. These proteome differences were equivalent to the differences measured between CHO DG44 and other hamster tissues (brain, heart, kidney, liver, lung and spleen). The CHO DG44 cell line cellular environment could explain such a difference in gene expression. They are cultivated in an agitated suspension culture with serum-free media, which differ significantly from the physiological conditions surrounding the native tissues.

CHO cell line has long been the main host for the industrial production of monoclonal antibodies. Indeed, in 2022, CHO cells were used to produce 89% of newly approved recombinant antibodies produced in mammalian cells [2]. They can undergo transient or stable transfection, but stable transfection is often preferred.

The cell line used in our study is the CHO DG44. The clone PTN1-CB-CC1/ LP16CLONE 38 was used as a clone of stably transfected CHO DG44 expressing a transgene encoding for a therapeutic human IgG1 whose target will be kept confidential. This cell line is widely

employed in the biopharmaceutical industry to establish stable cell lines producing therapeutic antibodies [2,66]. The cell line was adapted to suspension and serum-free culture and is mainly cultivated in suspension in stirred tank bioreactors for large-scale mAb manufacturing [99].

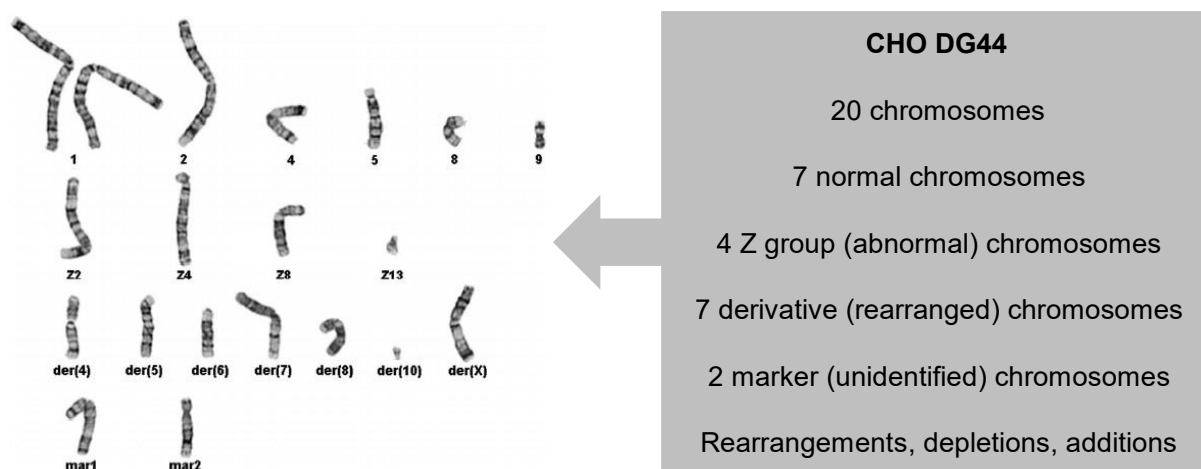


*Figure 1.4: Karyogram of CHO DG44 cells. Figure adapted from Derouazi M, Martinet D, Besuchet Schmutz N, Flaction R, Wicht M, Bertschinger M, Hacker D L, Beckmann J S and Wurm F M 2006 Genetic characterization of CHO production host DG44 and derivative recombinant cell lines Biochem Biophys Res Commun 340 1069–77, DOI 10.1016/j.bbrc.2005.12.111 [100]*

## MDCK cells

The Madin Darby Canine Kidney cells (MDCK) were isolated from an adult female cocker spaniel (dog) kidney in 1958 by S.H. Madin and N.B. Darby [101,102]. They were spontaneously immortalized through long-term culture. The parental MDCK cell line has a stable pseudo-diploid karyotype [103]. However, some sub-clones, such as MDCK I and MDCK II, isolated from the parental line present more genetic variability over long-term culture [103].

It was soon observed that MDCK had characteristic behaviour from renal tubule epithelial cells [104]. They were later confirmed to express markers from distal tubule epithelium [105,106].

MDCK cells are widely used in research as a model to study polarized epitheliums, tissue morphogenesis and kidney development or diseases. Their high sensitivity to viral infection makes it a good tool for analyzing infection mechanisms. The polarity of the MDCK monolayers makes it a perfect model for viral infection targeting polarized epithelia such as influenza and other coronaviruses [107,108], herpes simplex virus 1 [109,110], simian virus 5, Sendai virus and stomatitis virus [111,112]. Indeed, infection and release of virions from

polarized epithelia happen preferentially through either the apical or basolateral membrane [107,111–113]. This phenomenon is primarily attributed to the infection mechanism, which depends on N-acetylneuraminic sialic acid as a membrane receptor [112,114]. This mechanism is significantly enhanced through the apical membrane, mainly because of the elevated concentration of sialic acid [115,116]. On the contrary, sialic acid-independent infection can occur on both apical and basolateral membranes.

MDCK's sensitivity to infection makes it one of the most used cell lines for the industrial production of viral vaccines [117,118]. It is commonly used for the replication of influenza. To facilitate bioproduction, different cell variants have been developed to increase their sensitivity to infection and virus yield or even adapt to serum-free and suspension culture conditions [119–123]. However, adaptation to suspension conditions was very complex. The only success was reported in 2009 thanks to MDCK transfection with the human *siat7e* gene playing a role in cell adhesion [124]. Thus, the adherent cell form remains the primary cultured MDCK cell type at a large-scale. Its culture is performed on microcarriers in stirred tank bioreactors, with maximum working volumes of 1,000 – 2,000 L [73,125–129].

### **Vero cells**

The Vero cell line originated from an adult female African Green Monkey kidney epithelium [130,131]. It was established and registered to the Animal Cell Culture Collection (ACCC) in 1962 [102,131]. The Vero cell line became immortalized after spontaneous mutations. Genome profiling of this cell line highlighted various abnormalities in chromosome number and depletion in several genes (see Figure 1.5). It includes genes regulating the cell cycle or coding for interferon I [131]. Interferon I is a cytokine involved in the onset of a non-immune cell's antiviral state. Such a process induces the transcription of several genes, interfering with multiple stages of the viral replication cycle and signalling to immune cells [132,133]. The described mutations provide high susceptibility of Vero cells to different viruses and microorganisms. Their sensitivity is thus attributed to their incapacity to generate type I interferon as a response to viral infections [131].

Vero cells' vulnerability to viruses is a main workhorse for viral vaccine production. It has been widely used and optimized for virus production at industrial scale. For example, during the COVID pandemic, the Vero cell line presented the highest SARS-CoV-2 replication rate compared to other cell lines [134]. This cell type originated from kidney epithelium and is adherent and challenging to adapt to suspension culture. Such adaptation only succeeded recently in 2019 [124]. However, Vero cells are still extensively used in adherent cultures on microcarriers. Large-scale microcarrier cultures have been reported up to 6,000 L bioreactors.

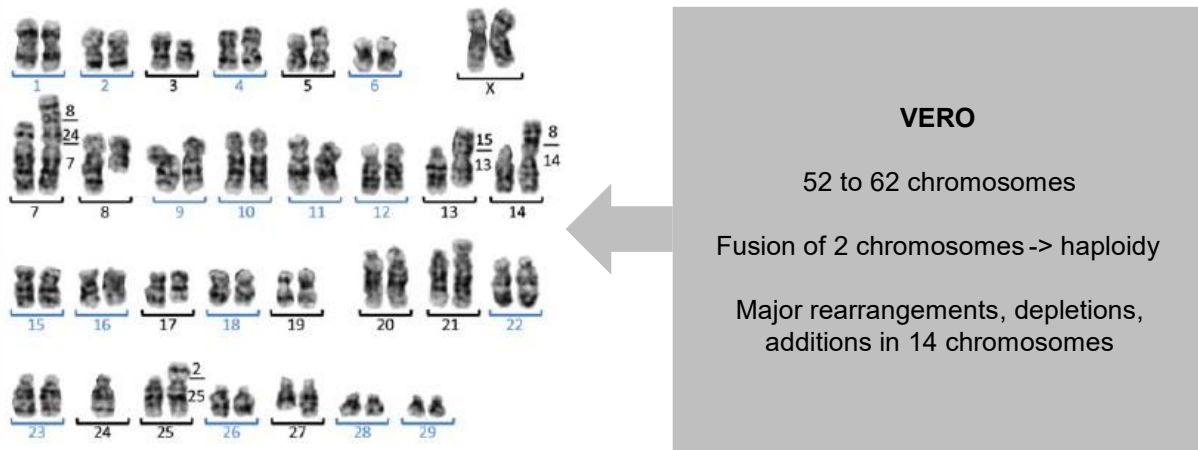


*Figure 1.5: Karyogram of Vero cells. Figure adapted from Naoki O, Arihiro K, Toshiyuki Y, Noriko H, Fumio K, Suyoshi S, Makoto K, Kentaro H and Hattori M 2014 The genome landscape of the African Green Monkey kidney-derived vero cell line DNA Research 21 673–83, DOI 10.1093/dnares/dsu029 [131]*

#### 1.1.6. Proliferation, metabolism and productivity of HEK, CHO, MDCK, Vero cell lines

The main bioproduction cell line's metabolism has been widely studied and described. The standard growth kinetic comprises an exponential growth phase of several days (~4-7 days) followed by a stationary phase (~2-3 days) and a death phase during which the culture is stopped. In industrial processes, they are known to enter the exponential growth phase soon after inoculation in the bioreactor [135].

During the exponential growth phase, mammalian cell lines tend to favour aerobic glycolysis, with at least 45% of ATP generated from glycolysis [135]. In this period, 75% of the pyruvate generated from glucose is converted to lactate [135] (see Figure 1.6\_A & C). It corresponds to the Warburg effect and is responsible for high glucose uptake and lactate secretion. This phenomenon has been reported in various fast-growing mammalian cell lines, including CHO [135,136], HEK [137,138] and MDCK [127,139,140]. The exponential growth phase is also characterized by fast glutamine consumption to fuel the TCA cycle [141,142]. The principal substrates of mammalian cell lines are Glucose, Glutamine, and Asparagine. To a lesser extent, their metabolization results in Lactate, Ammonia and Alanine accumulations of main metabolic wastes [135]. During the stationary phase, ATP is mainly produced by glucose oxidation in the TCA cycle, resulting in more efficient energy production and reduced accumulation of metabolic wastes [135,142] (see Figure 1.6\_B and C). The NADPH levels are maintained by glucose oxidation in the pentose phosphate pathway [142]. In the case of CHO cells, a metabolic shift can occur during the stationary and death phases, where glucose uptake is reduced, and

cells start consuming lactate as a substrate [135]. Such a shift from lactate production to its consumption is often observed in high-producing clones and has also been reported for other cells such as HEK [138] and Vero [143]. It is to be noticed that during their stationary phase, CHO cells have the highest mAb productivity [135].

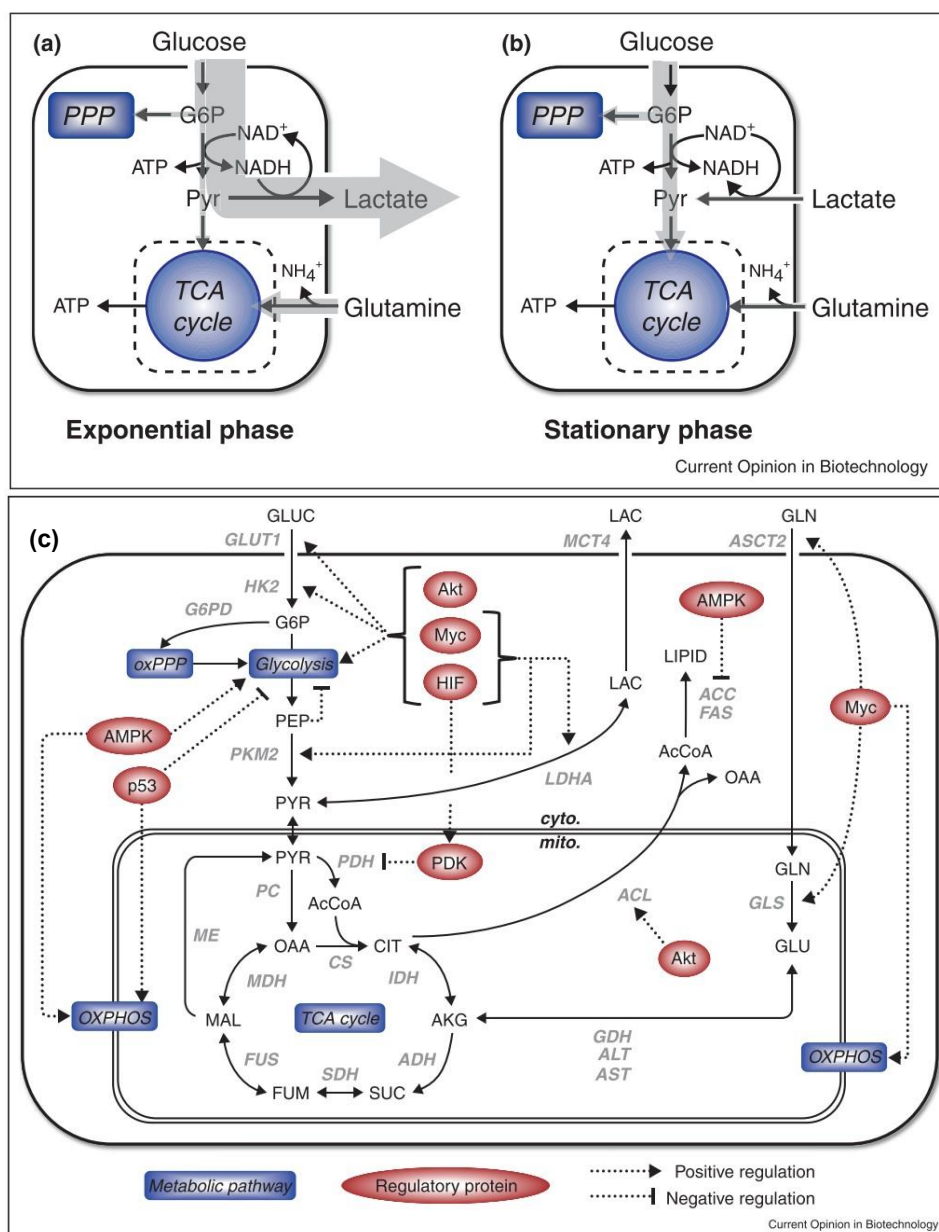


**Figure 1.6: Typical metabolic fluxes of mammalian bioproduction cell lines** (a) During exponential growth phase, the cells rely on aerobic glycolysis (Glucose) and Glutamine as main energy sources (b) During stationary phase, the energy is produced more efficiently by glucose oxidation in TCA cycle. (c) Major pathways of central carbon metabolism and key regulatory proteins that control enzyme expression and activation. Abbreviations of main metabolic pathways and intermediates: PPP: Pentose Phosphate Pathway, TCA: Tricarboxylic Acid cycle, OXPPOS: Oxidative phosphorylation, G6P: Glucose-6-Phosphate, Pyr: Pyruvate, GLUC: Glucose, LAC: Lactate, GLN: Glutamine, PEP: phosphoenolpyruvate, AcCoA: Acetyl-CoA, OAA: Oxaloacetic Acid, CIT: Citrate, AKG: Alpha-Ketoglutarate, SUC: Succinate, FUM: Fumarate, MAL: Malate, GLU: Glutamate. **Credit: Young J. 2013 Metabolic flux rewiring in mammalian cell cultures *Curr Opin Biotechnol* 24 1108–15, <https://doi.org/10.1016/j.copbio.2013.04.016> [142]**



These cell lines are commonly cultivated in batch or fed-batch cultures in stirred tank bioreactors. If all cell lines have been adapted to suspension, only CHO is almost exclusively grown in suspended cultures. Despite the growing interest in suspension cell processes, adherent cultures on microcarriers remain the preferred strategy for industrial bioproduction based on HEK, MDCK and Vero cells due to the challenges related to the adaptation to suspension condition. The maximal cell density and productivity achieved in such processes highly depend on the cell line, as presented in Table 1.4. The highest cell densities and productivities achieved in standard batch or fed-batch processes have been reported with CHO cell line (Table 1.4).

**Table 1.4 : Commonly reported maximal values for different culture yields, in standard small and/or large scale cultures. \*the value of 90 pg/cell/day in CHO cultures have been reported for cell clone enhanced by genetic engineering [144].**

	Batch/fed-batch cell density (10 <sup>6</sup> cell/mL)	Perfusion cell density (10 <sup>6</sup> cell/mL)	Growth rate (d <sup>-1</sup> )	rProtein titer (g/L)	Specific productivity rProt (pg/c/d)	Virus / baculovirus titer
<b>CHO</b>	<b>20 – 25</b> [99,145,146]	<b>132 - 214</b> [147]	<b>0.6 - 1.06</b> [99,148]	<b>3 - 10</b> [92,99,144,145,149]	<b>25 – 40</b> <b>(exceptionally 90*)</b> [99,144,145]	---
<b>HEK</b>	<b>1.5 – 5</b> [88,150,151]	<b>10 – 12</b> [152,153]	<b>0.62 - 0.84</b> [88,150]	<b>0.7 - 1.1</b> [91,151]	<b>4 – 22</b> [91]	---
<b>MDCK</b>	<b>2 - 5</b> [126–128,154]	<b>10 – 40</b> [155,156]	<b>0.69 – 0.96</b> [157]	---	---	<b>10<sup>9</sup> (TCID<sub>50</sub>/mL)</b> [126]
<b>Vero</b>	<b>2 - 3</b> [88,158,159].	<b>6 – 40</b> [160–162]	<b>0.46 - 1.25</b> [88,163,164]	---	---	<b>10<sup>10</sup> (TCID<sub>50</sub>/mL)</b> [165]

**In conclusion, HEK, CHO, MDCK and Vero cells are widely used in the bioproduction field for recombinant proteins and viral vaccines. All these cell types have been extensively studied and characterized in standard monolayer or suspension cultures. Their main characteristics are recapitulated in Table 1.5.**

*Table 1.5 : Main characteristics of the selected bioproduction cell lines for our study.*

Cell types	Generates human-like glycosylation patterns	Genetic stability	Easy to transfect	Sensitivity to infection	Used for large-scale rProteins production	Used in viral products large-scale manufacturing	High titers	Easy scale-up	Suitable for GMP production
HEK	✓	⊗	✓	✓	✓	✓	○	⊗	○
VERO	✓	○	○	✓	⊗	✓	✓	⊗	✓
MDCK	✓	○	○	✓	⊗	✓	○	⊗	✓
CHO	✓	✓	○	○	✓	⊗	✓	✓	✓

✓	High / Good	○	Medium/ Average	⊗	Low / Bad
---	-------------	---	-----------------	---	-----------

### 1.1.7. Current strategies for the densification of cultures and optimization of bioproduction yields

Three strategies coexist to increase production yields: (i) one consists in densifying the cultures by optimizing culture conditions to favor cell proliferation, (ii) the second is to increase cell-specific productivity, and (iii) improving product recovery.

The physicochemical environment is the primary actuator on cell viability and proliferation. Parameters routinely finetuned to optimize mammalian cell culture processes are the media temperature, pH, dissolved oxygen (dO<sub>2</sub>) concentrations and carbon resource. Optimization of media composition, feeding strategy and process parameters allowed an increase mAb productivity from 4 g/L to 10 g/L in CHO cell culture [92,149]. Design Of Experiment (DOE) is a valuable tool for such targets [166]. It allows for screening many parameters and studying their effect on various responses [167,168]. It is thus possible to identify the parameters significantly impacting our biological targets (cell growth, productivity etc..). Data treatment with mathematical regressions (Partial Least Square (PLS), Multilinear linear regression (MLR)) permits the establishment of descriptive/prediction models, later allowing an estimate of the optimal cultivation conditions (temperature, pH, dO<sub>2</sub>, glucose concentration, etc). Such

methodology has been widely employed in the bioprocessing field to optimize bioproductions [167,168].

### **Improving cell proliferation, production titers and product recovery**

Culture media composition is one of the first a major concern for large-scale cell culture improvement. Media supplementation with dedicated molecules such as amino acids, growth factors or lipids could play a strategic role in significantly improving growth and cell-specific production [169–172]. For example, it was reported that adding yeast hydrolysates or specific yeast peptones could enhance CHO maximal cell density by 70% and IgG production by 180% [173].

Numerous cell-specific media and supplements have been developed to answer the needs of each cell line and maximize their proliferation and production rates [88,174,175]. Also, to ensure GMP production, bioproduct integrity and eased product recovery, multiple media have been developed, including serum-free media (SFM), animal component-free media, protein-free media (for easier rProteins purification) and chemically defined media which entire formulation is known and controlled [169].

The choice of the bioreactor type and feeding strategy can also significantly impact cell proliferation and productivity. For example, it is known that fixed-bed perfused bioreactors can reach higher cell densities than standard fed-batch processes. Such systems allowed them to get adherent cell densities of  $2.5 \times 10^8$  cells/mL [24]. Nowadays, a broad interest is given to perfusion bioreactor cultures, which increase the maximal reachable cell density over  $10^8$  cells/mL, and volumetric production yields 10-fold higher than in standard fed-batch [176–178]. New biomanufacturing strategies are also emerging based on hybrid culture methods. Some examples are the association of successive perfusion and multiple fed-batch cultures for cell amplification and bioproduction process, respectively [99], or serial fed-batch cycles with complete media removal between each cycle [179]. Such strategies have increased process productivity by up to 217% with reduced media consumption [179].

However, increasing the final volumetric product titer is often limited as intensifying cell cultures is counterbalanced by an associated decrease in cell-specific productivity [180]. Therefore, complementary work must be done to increase cell-specific productivity in industrial processes.

### **Increasing cell-specific productivity**

Current processes face two main obstacles: (i) the production volume and associated complexity and cost, which keep increasing, and (ii) the limited specific productivity, which

tends to decrease in densified cell cultures. Therefore, finding ways to increase cell-specific productivity is a major leverage to improve bioproduction performances and reduce the bioproduction volumes. Multiple studies focus on protocols to maximize cell-specific productivity in the long-term basis. Thus, in 2004, the highest mAbs-specific productivity of ~90 pg/cell/day was reported by suspension culture of CHO cells in 10 L bioreactors [13]. Here, the culture was maintained for 20 days and reached  $10 \times 10^6$  cells/ml which is below the maximal cell densities reported nowadays (see Table 1.4). This process reached a final mAb titer of 4.7 g/L. Similar values (76 pg/cell/day) had been reported earlier, in 1991, with the production of chimeric antibodies by SP2/0 myeloma cells in continuous culture [181]. In the current intensified bioproduction processes, the highest specific productivities usually range from 25 to 40 pg/cell/day in most cases [99,182]. Some innovative biomanufacturing processes based on serial-fed batch cycles have raised the specific productivity of CHO cells to 50 – 60 pg/cel/day but remain 30 - 40% lower than the highest value reported 20 years ago [179].

To increase the specificity, some additives can be added to the media to inhibit cell autophagy or induce cell cycle arrest. Indeed, the antibody and rProteins secretion was proved to be increased during the stationary phase. The 3-methyl-adenine is an example of an autophagy inhibitor, which was reported to increase by 4-fold the specific productivity in CHO cell cultures [183]. Valeric, butyric and valproic acids, as well as 4-(2,5- dimethyl-1H-pyrrol-1-yl)-N-(2,5-dioxopyrrolidin-1-yl) benzamide, are examples of additives inducing cell cycle arrest by deacetylating and dephosphorylating histones. It then favour protein expression [99,184]. External stresses such as hyperosmolarity or pH variation were also proven to affect specific productivity [183,185,186].

Genetic engineering has optimised the cell lines in different ways [90]. Some examples are the enhancement of transcription factor synthesis for increased protein expression and cell metabolism performances [187]. Targeting cell metabolism was a parallel strategy for improving specific productivity. CHO cells were, for example, transfected with a vector carrying small inhibitory RNAs (siRNA) for lactate dehydrogenase (LDH), which converts pyruvate into lactate, and pyruvate dehydrogenase kinases (PDHKs), which is an inhibitor of pyruvate dehydrogenase (PDH) which converts pyruvate to acetyl-CoA. Such a strategy allowed to favour oxidative respiration over lactic fermentation and increased specific productivity by 75% [136,188]. Similarly, HEK engineering targeting genes involved in different cellular processes (proliferation, apoptosis, metabolism, glycosylation, secretion, and protein folding) increased cell-specific productivity from 4 to 22 pg/cell/day [90,91]. In 2013, CHO cell's genetic engineering allowed the production of an IgG hybridized with a signal peptide facilitating its extracellular secretion. It allowed to reach the highest specific

productivity of 90 pg/cell/day reported up to now [144]. Interestingly, some studies have reported productivity increased from 0.62 to 11-fold in CHO and MDCK cell lines cultivated in adherent conditions compared to suspension (see Table 1.6) [189–193].

**In conclusion, over the past 60 years, the scientific community has put much effort into constantly increasing production levels, mainly focusing on cell densification within bioproduction processes or targeting the increase in cell-specific productivity. However, current processes and methods still face limitations, especially in unlocking the specific productivity in high cell-density cultures. Much progress was made by optimizing cell culture physicochemical environment, nutrient feeding, media composition and supplementation or cell engineering. However, standard production processes are still far from the specific productivities reported 20 years ago in lower cell density cultures. There is, hence, a need for new culture systems and methods to answer the need for culture densification while maintaining high productivity and escaping the limitations of current cell culture processes.**

Table 1.6: Comparison of productivity and cell-specific productivity of production cell lines cultivated in adherent vs suspension conditions. The cell-specific productivity is noted “ $q_p$ ”.

Cell line	Type of culture	Product	Max prod suspension	Max prod adherent	Ratio prod adherent/ prod suspension	Max $q_p$ susp	Max $q_p$ adherent	Ratio $q_p$ adherent/ prod suspension	Reference
CHO	Monolayer vs suspended aggregates and single-cell suspension	rProtein	~10 - 15 ng/mL	~25 - 30 ng/mL	2	16 ng/10 <sup>5</sup> cells/h	11-12 ng/10 <sup>5</sup> cells/h	1.4	[189]
CHO	Microcarrier vs suspended aggregates and single-cell suspension	rProtein	27 mU/L	300 mU/L	11	20 mU/10 <sup>5</sup> cells	3.5 mU/10 <sup>5</sup> cells	5.7	[193]
CHO	Monolayer vs suspension	rProtein	10.3 mg/L	6.5 mg/L	0.62	~1 µg/10 <sup>6</sup> cells/d	~4 µg/10 <sup>6</sup> cells/d	4	[191]
CHO	Monolayer vs suspension	rProtein	~13-19 mg/L	~12-17 mg/L		2.82 mg/10 <sup>10</sup> cells/h	4.64 mg/10 <sup>10</sup> cells/h	1.64	[192]
MDCK	Microcarrier vs single-cell suspension	Virus	2.94 log10 HAU/100 µL	3.15 log10 HAU/100 µL	1.07	11,000 virions/cell	23,000 virions/cell	2.09	[190]

## 1.2. 3D culture for bioproduction: which advantages?

### 1.2.1. Generalities on 3D cell culture

*In vitro* cell culture allows the growth of cells in an artificial environment to study their characteristics and functions. Cell culture has been performed on planar 2D culture support for many years. Two-dimensional models have been used for cellular biology disease studies and drug testing. This mode of culture presents the advantage of being a very simplified model with a homogenous cell population and repartition, few uncontrolled parameters, and is easy to perform. However, it lacks accuracy in representing *in vivo* mechanisms. For example, 2D models help understand cell mechanisms but do not fully represent *in vivo* function. In cancerology, among all drugs selected during 2D testing, only 5 % are successful during pre-clinical trials *in vivo* [194,195]. In 2D culture, the cells usually present increased growth rates compared to *in vivo* conditions due to easy access to nutrients and growth factors and fast detachment and removal of dead cells from the support [196,197].

Another culture method called 2.5D consists of plating the cells on a thick layer of the matrix (extracellular matrix compounds, Matrigel, hydrogels) [198–200]. In these cultures, the support is not perfectly flat and offers *in vivo*-like adhesion sites. However, the cells with topographic structures are still growing on one surface. It provides a more *in vivo*-like support but doesn't allow realistic 3D structuration of the cells. 2.5D cultures have been demonstrated to provide more adequate cell responses and functions [198,199]. For example, cancer cells resistance to anticancer drug is increased in 2.5D cultures compared to 2D cultures [198].

For a few decades, 3D cell culture has raised attention as it better mimics the *in vivo* environment [196,201]. It is especially interesting in research to study tissues and organ functions, cell signalling, cell interactions, and disease modelling or drug testing. It allows the cells to grow and interact with their 3D surroundings and reproduce tissues and organ micro-structuration [202–205]. However, three-dimensional cultures are usually more complex to perform. It presents a higher number of uncontrolled parameters that possibly affect cell behaviour. Namely, cell-cell and cell-matrix interactions (integrin and cadherin adhesion) are involved in multiple cellular signaling pathways [19,206,207]. Cell behaviour and differentiation is also affected by the 3D support nature [208–210], porosity and micro-pattern [211] and mechanical properties [19,212]. The 3D cell-matrix or cell-cell interactions and the hindering of nutrients, waste or drug diffusion can strongly affect the expression of multiple genes, including genes associated with controlling cell proliferation, apoptosis, survival, or differentiation. Thus, it has been reported on cancer cells that the cell growth rate in 3D culture is reduced compared to planar cultures and is more representative of *in vivo* proliferation



[196,213,214]. As an example, DU145 cancer cells proliferation rates were decreased by 20 to 40% in 3D cultures compared to 2D condition [214].

On the contrary, cancer cells cultivated in 3D showed increased metabolic activity [215]. Thus, 3D cell cultures present gene expression profiles closer to native tissue, increasing resistance to anti-cancerous drugs in tumour models [196,201]. The shape, sensitivity to stimuli, gene expression, protein synthesis, and overall cell function of cells grown on 3D supports are commonly described as closer to the physiological state [195,213]. The reduced cell proliferation and metabolism in three-dimensional cultures are also responsible for the increased lifespan of the cultures [195].

The main differences between 2D, 2.5D and 3D cultures are presented in Figure 1.7 and Table 1.7.

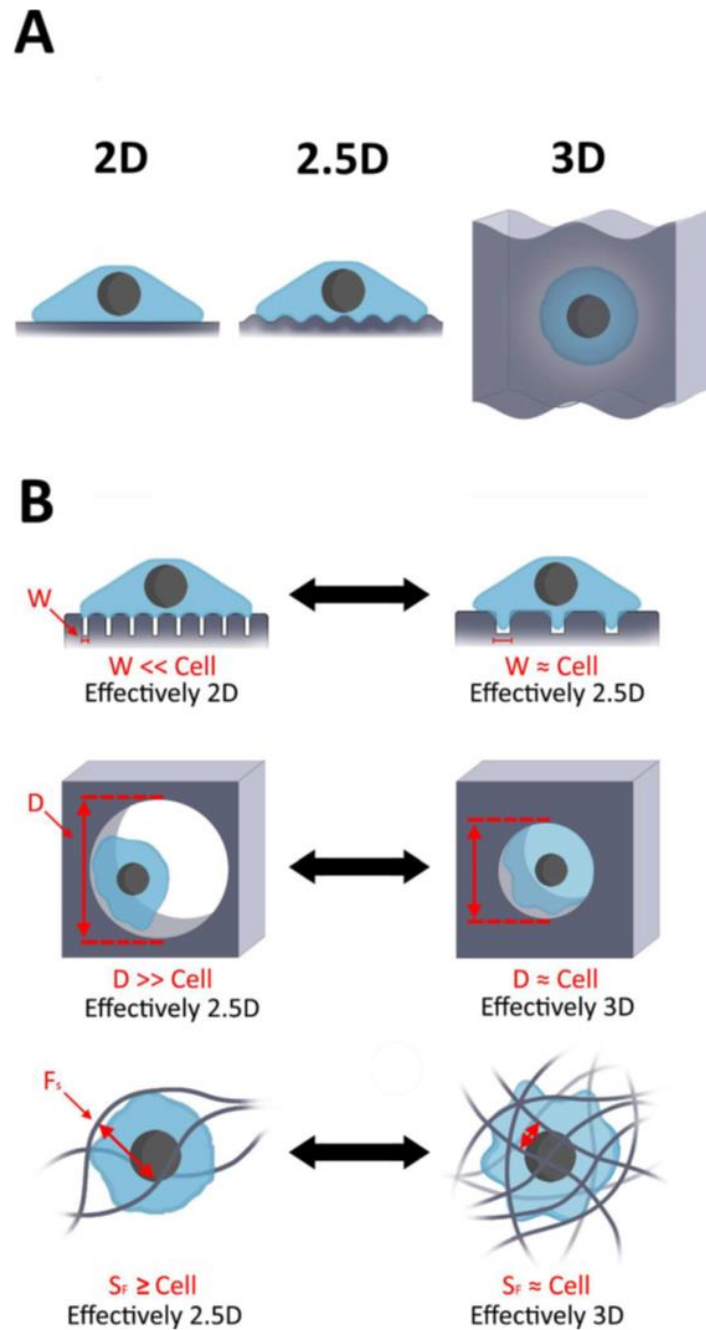


**Figure 1.7 : Classification and ambiguity of 2D, so-called 2.5D, and 3D culture systems.** (a) Common examples of 2D, 2.5D, and 3D culture systems. 2D culture systems are perceived by the cell as flat substrates; so-called 2.5D culture systems have topographical features that induce changes in the membrane curvature of the cell; 3D culture systems include those that completely and continuously encapsulate the cells to provide matrix contact on all sides. (b) Examples of cell culture systems with ambiguous dimensionality. Top panel micropillar systems could be classified as either 2D or 2.5D, depending on the size and spacing of the pillars concerning the basal cell membrane geometry ( $W$ ). Middle panel, encapsulation systems can be classified as either 2.5D or 3D depending on the material's pore size diameter ( $D$ ). Bottom panel, cell encapsulation within fibrous materials can be classified as 2.5D or 3D depending on the spacing between fibres ( $S_F$ ). **Credit: De La Zerda A, Kratochvil M J, Suhar N A and Heilshorn S C 2018 Review: Bioengineering strategies to probe T cell mechanobiology APL Bioeng 2 1–27 [199]**

Table 1.7: Comparison of 2D, 2.5D and 3D cultures

	2D	2.5D	3D
<b>Low cost</b>	✓	○	☒
<b>Easiness /simple protocols</b>	✓	○	☒
<b>Reproducibility</b>	✓	N.A.	○
<b>In-vivo representative morphology</b>	☒	○	✓
<b>Numerous and representative cell-junctions</b>	☒	○	✓
<b>Cell interaction with support material</b>	☒	✓	✓
<b>Complete differentiation</b>	○	✓	✓
<b>In-vivo representative proliferation</b>	☒	○	✓
<b>Tissue-like cell structuration</b>	☒	☒	✓
<b>gene expression and cell functions representative of in vivo</b>	☒	✓	✓
<b>Accurate response to stimuli</b>	☒	✓	✓
<b>Resistance to drugs</b>	☒	✓	✓
<b>N.A. Not Available</b>	✓ High / Good	○ Medium/Average	☒ Low/Bad

### 1.2.2. State of the art of 3D cell culture of bioproduction cell lines

Thus, cultivating primary cells in 3D conditions closer to *in vivo* modifies their phenotype. Interestingly, similar observations have been made for bioproduction cell lines despite these cells having undergone a long clonal selection process, spontaneous mutations, and, in some cases, heavy karyotype deviation and genetic engineering.

#### **CHO cells**

As mentioned previously, suspension cultures of CHO cells have been reported to present significant proteomic differences with native Chinese Hamster ovarian tissue [98]. Yet, CHO cell proteome has never been studied in 3D culture conditions. Less than five reports were found in the literature about 2.5D or 3D cultures of CHO cells [216,217]. Still, CHO cells have been reported to adhere and colonize bioprinted matrices composed of a mix of proteins and glycosaminoglycans (GAGs), containing 30% Hyaluronan [217]. Similar behaviour was observed for CHO aggregates ink-jetted on collagen type I scaffolds [218]. It was demonstrated that high-density CHO aggregate bioprinting could lead to the formation of intercellular junctions characterized by the expression of N-cadherin [219]. Such cellular junctions are encountered in native tissues and are essential to cell-cell communication. However, until now, no proteomic analysis has been carried out on CHO cells cultivated in conditions mimicking the native tissue, and it is not known if the gene expression profile differs from suspension or 2D CHO cultures.

Yet some studies report 3D printing of primary ovarian cells for ovary regeneration [220–222]. The 3D printing of ovarian follicles restored the reproductive endocrine function of sterile female mice by, enhancing the secretion of female hormones from bioprinted follicles [220]. Retrieving of the follicle cycle, maturation of oocytes and ovulation in 3D cultures of ovarian follicles in gelatin-methacryloyl (GelMA) scaffold has also been reported [222] (see Figure 1.8). Hence, this demonstrates that ovarian cells can be grown in 3D and conserve *in vivo*-like characteristics.

Such findings make one wonder if transitioning to an environment closer to *in-vivo* conditions would affect CHO cell physiology and its resemblance to ovarian, primary cells.

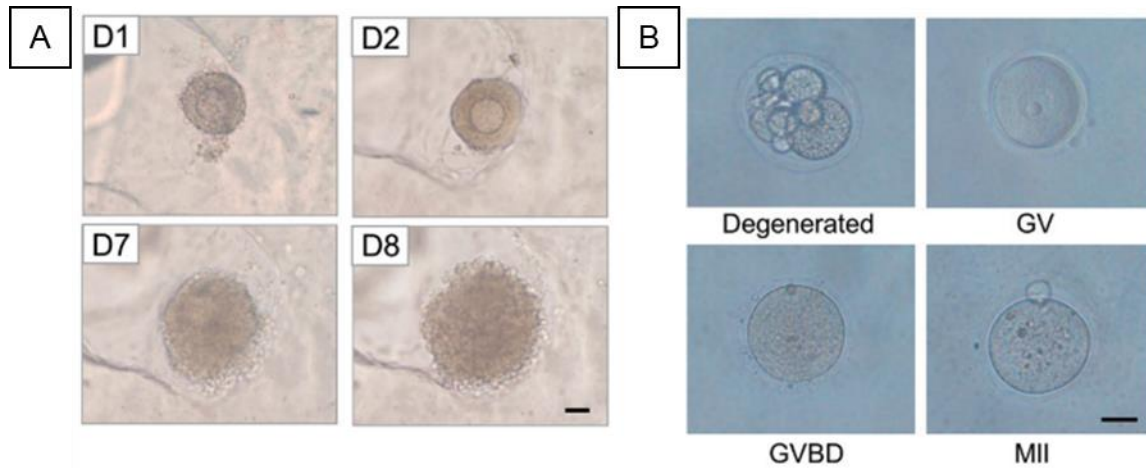


**Figure 1.8. : Microscopic imaging on 3D cultures of primary ovarian follicles in GelMA:** (A) Morphological observation of follicle growth and ovulation. (B) Representative images of oocytes of different stages. Scale bars = 50  $\mu\text{m}$ . GV: germinal vesicle; GVBD: germinal vesicle breakdown; MII: metaphase II. Credit: Wu T, Gao Y Y, Su J, Tang X N, Chen Q, Ma L W, Zhang J J, Wu J M and Wang S X 2022 *Three-dimensional bioprinting of artificial ovaries by an extrusion-based method using gelatin-methacryloyl bioink Climacteric 25 170–8*, DOI 10.1080/13697137.2021.1921726 [222]

### HEK cells

In 2D cultures, HEK cells present markers of a kidney developmental stage between the condensed mesenchyme and epithelial S-shaped body but no features of later differentiated steps like tubular segments, proximal tubules or collecting ducts [84,223]. Very few studies report 3D culture of HEK cells, and even fewer have tried to describe their metabolism, phenotypes and proliferation kinetics in such conditions. Yet, a few studies have confirmed the growth capacity of HEK cells in 3D conditions as cell aggregates [224], encapsulated in collagen microbeads [225] or in 3D hydrogel structures [226,227]. They even reported high cell concentrations and viability in the hydrogel matrix of gelatin, alginate and fibrinogen [226]. Interestingly, a more substantial biomolecule productivity in collagen microbeads was observed than in monolayers [225]. Interestingly, a report of HEK grown in small 3D aggregates demonstrated increased expression of markers associated with kidney progenitor cells, especially from glomeruli and proximal tubule, and exhibited some characteristics like embryonic stem cells [84,224].

### MDCK cells

In 1982, the culture of MDCK monolayers with collagen overlay allowed the detection of the formation of circular and polarized cell monolayers encircling a lumen [228]. This observation was confirmed as a characteristic behaviour of MDCK cells in 3D cultures in collagen or matrigel matrices where monolayers of polarized cells form hollow spheres (see Figure 1.9). These structures are called "cysts" and are the first step of kidney distal tubule formation in

MDCK 3D cultures [229–232]. Their polarization is often identified by the homogenous location of GP135 (dog podocalyxin) in the apical membrane of polarized MDCK [233–235]. MDCK are typically not motile but can become motile if cell-cell junctions are inhibited by scattering factors or antibodies anti-E-cadherin. Hepatocyte Growth Factor (HGF) is a scattering factor that allows morphogenesis by cyst branching, leading to tubule formation [234,236–238]. MDCK cells undergo epithelial-to-mesenchymal transition (EMT) during morphogenesis. In fact, during morphogenesis, acquiring partial mesenchymal phenotype allows the cells to gain motility and branching ability [230]. Some proteins involved in cellular adhesion to extracellular matrix (ECM), such as  $\alpha_3\beta_1$  integrin, are known to play a role in tubulogenesis [239].

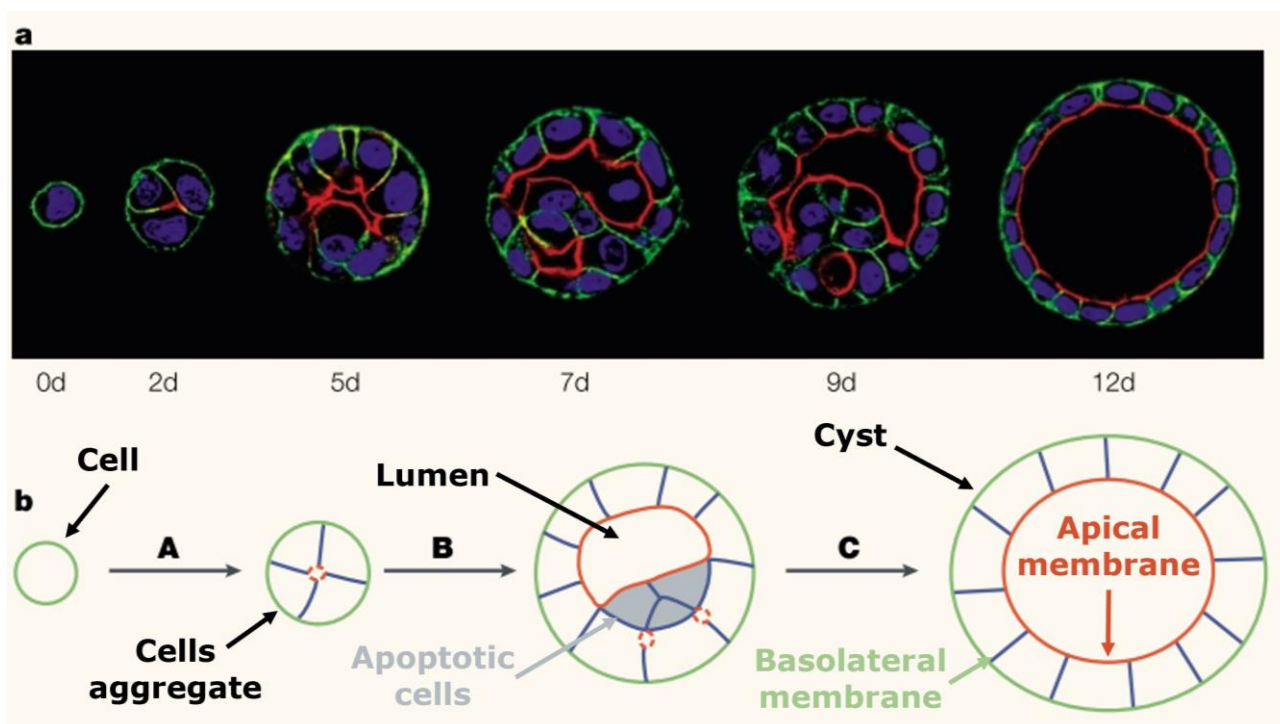


**Figure 1.9:** Cyst formation by MDCK cultivated in 3D collagen matrices. Illustration shows confocal sections with apical membrane (actin-red), basolateral membrane (p58 – green) and nuclei (DAPI – blue) stainings (a) and schematic representation (b) showing the steps of cyst formation in 3D culture of MDCK cells: A) formation of a cell aggregate, B) lumen formation after cells in the centre of aggregates undergo apoptosis C) mature cyst with a polarized structure formed of an apical membrane in the lumen and basolateral membrane in contact with the matrix. Adapted from: O'Brien LE, Zegers MM, Mostov KE. *Opinion: Building epithelial architecture: insights from three-dimensional culture models.* *Nat Rev Mol Cell Biol.* 2002 Jul;3(7):531-7. doi: 10.1038/nrm859. PMID: 12094219.

## Vero cells

Vero cells' 3D models have been used essentially for infectivity or cytotoxicity studies due to the sensitivity of the cells to viral infection [240] and toxins [241]. A 3D Vero cell culture application establishes a 3D model for studying parasite infection and propagation [242]. In this

case, the cells were homogenously suspended in a collagen I matrix. In 3D cultures, the parasite spreading behaviour differed significantly from 2D cultures and was more representative of *in vivo* infection. In other studies, Vero cells were seeded over collagen or gelatin scaffolds [240,241,243].

Interestingly, in these cases, Vero cells formed monolayers on the surface of the matrix and did not colonize the inner volume, resulting in 2.5D cultures [240,243]. Here, Vero cells presented elongated morphology with cytoplasmic extensions and micro-vesicles visible at the cells' surface, testifying biosynthetic activity [243]. Cells cultivated onto such scaffolds demonstrated prolonged cultivation times, with increased cell viability over 20 cultivation days and a further constant maximal viability over 56 days [240]. Regarding the Vero cell proteome, when seeded over gelatin scaffolds, cells synthesized large amounts of collagen IV in only 7 days [240]. The apical and basolateral membrane markers were detected, demonstrating that Vero grown in 2.5D onto collagen scaffolds were polarized, unlike standard 2D cultures. Until now, no study has described Vero cells' proliferation and metabolic kinetics in 3D cultures.

**In conclusion, the use of 3D cell cultures is now widespread and still getting more interest in regenerative medicine and tissue engineering due to their better representation of *in vivo* cell physiology and environment [244–246]. Their applications are wide: research in tissue regeneration for medical applications (implantation) [247–249], *in vitro* modelization of tissue functions for the study and understanding of cellular behaviours and interactions [250–252] as well as organs dysfunctions, degeneration, diseases, and infection [253–257], and *in vitro* modelization of pathologic tissues or organs for testing of therapeutics such as drug or gene therapies [255,258,259].**

**On the contrary, the 3D culture of bioproduction cells is still poorly described in the literature. The few reports available are often limited to defining their morphology and survival ability in 3D conditions. In some situations, tissue-specific behaviours such as morphogenesis or secretion of ECM components have been described. However, less than 10 studies have gone deeper to study the biomolecule or virus productivity in 3D production cell lines' cultures. Yet, these studies provide high perspectives for potential bioproduction applications of 3D cell cultures.**

**We should emphasize that actual culture methods used for bioproduction are far from the physiological environment in the cell's native tissue. But very little is known about the impact of the 3D biomechanical and environmental cues on cellular production capacities. Nevertheless, multiple studies suggest that mammalian cells, originally adherent, could**

have 1.5 to 3-fold higher specific productivities in adherent cultures than after adaptation to suspension [189–192,260].

Therefore, it would be interesting to evaluate how *in vitro* culture conditions closer to a physiological tissue-like environment can affect biomolecule productivity. Bioproduction cell lines' behaviour, metabolism, characteristics, and adaptability in 3D environments are little known. Still, it is expected that such behaviour will be significantly different and allow the recovery of the physiological state of such cells. According to the scarce literature found up to now, it is hypothesized that growing bioproduction cells in 3D could be beneficial for their bioproduction capacity and could leverage some of the roadblocks faced by the biopharmaceutical industry. 3D cell culture is a high potential intermediate production strategy in this context.

### 1.3. Bioprinting, a proposed biomanufacturing tool for encapsulated cell culture

The use of 3D cell cultures is now widespread and still getting more interest in regenerative medicine and tissue engineering due to their better representation of *in vivo* cell physiology and environment [244–246]. Their applications are wide: research in tissue regeneration for medical applications (implantation) [247–249], *in vitro* modelization of tissue functions for the study and understanding of cellular behaviors and interactions [250–252] as well as organs dysfunctions, degeneration, diseases, and infection [253–257], and *in vitro* modelization of pathologic tissues or organs for testing of therapeutics such as drug or gene therapies [255,258,259].

Bioprinting is currently mainly used for tissue engineering (bone, cartilage, skin, and other tissues/organs), regenerative medicine and tumour or tissue modelling for drug screening due to its ability to reproduce anatomically correct and patient-specific cell-laden structures [261]. Other applications are poorly developed, and the effect of bioprinting on production cell lines has yet never been described.

#### 1.3.1. *What is bioprinting and its advantages for large-scale 3D cultures?*

Multiple techniques exist to produce 3D cell cultures. At small scale, non-encapsulated, scaffold-free cell spheroids can be used [197]. However, when scaling up the size of the 3D cultures, a scaffold or an encapsulating material must be used. The most basic methods consist



of using a 3D scaffold over which the cells are seeded. The scaffolds are commonly constituted of fibrous materials with interconnected porosity, principally made of collagen and other ECM compounds [262–265]. They provide support within which the cells can adhere and proliferate. Many materials and techniques are available for such scaffold manufacturing. They must be chosen wisely, depending on the final application. Another method incorporates the cells in a jellified matrix (gels and hydrogels). Contrarily to the 3D scaffolds, the cells are not seeded over but mixed and encapsulated inside the material. It provides more homogeneous cell repartition. The cellularized gel matrices can be produced either by moulding or by bioprinting. If moulding is a more straightforward manufacturing method, it gives less freedom in achievable shapes and architectures.

Therefore, bioprinting, a more recent technology, has raised attention in recent decades due to its numerous advantages over molding. First is the high degree of freedom accessible for the construct's architecture. 3D bioprinting enables the production of a volume by superposition of successive layers. It is referred to as Additive Manufacturing (AM). The desired structure can be designed by Computer-Aided Design (CAD) software or from organ 3D scans (Computed Tomography / CT, Magnetic Resonance Imaging / MRI) [266]. The bioprinting process brings higher reproducibility and control of the 3D structure shape, macro-porosity and size with various patterning possibilities such as square pores, circular pores, gyroids or honeycombs.

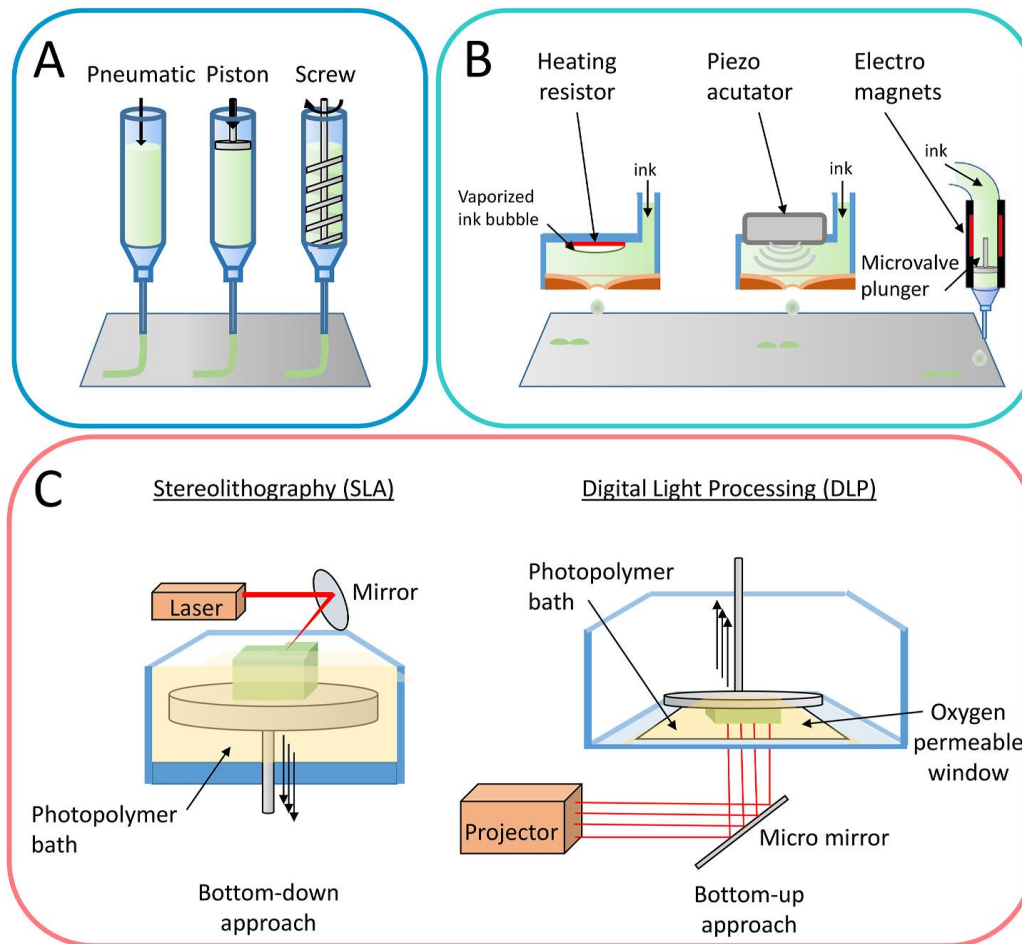


**Figure 1.10: The different types of 3D bioprinting.** (A) Three main types of mechanisms for extrusion printing: mechanical (piston or screw) or pneumatic (air pressure) dispensing systems. (B) Jetting mechanisms used for inkjet printing: heated vaporization, piezoelectric-based vibration or microvalve controlling. Inkjet printers use a sequential ejection of small droplets containing cells and hydrogel materials to construct tissues. (C) Two main types of light-assisted printing: stereolithography (laser) or digital light processing (projector). **Credit: Dufaud M, Solé L, Maumus M, Simon M, Perrier-Groult E, Subra G, Jorgensen C and Noël D 2022 3D bioprinting of articular cartilage: Recent advances and perspectives *Bioprinting* 28 [267]**

Numerous bioprinting technologies are available, each with its own distinct advantages and drawbacks, as illustrated in Figure 1.10 [268]. Micro-extrusion technology stands out as the most appropriate choice for producing large structures exceeding the size of cubic centimeters due to its ability to create substantial objects in a shorter timeframe with good shape fidelity and cell viability [267]. Nevertheless, it often sacrifices resolution compared to more precise techniques such as inkjet, laser-assisted printing, or stereolithography, which excel in small-scale and precise bioprinting applications. Micro-extrusion involves mechanically extruding the material using either a worm screw system or a piston actuated by a motor or pneumatic pressure. This bioprinting technique allows the printing a wide range of viscous materials (30 to  $6 \times 10^7$  mPa.s). It is also gentler for the cells, more flexible and usually less expensive than

the other bioprinting methods [269,270]. The layer-by-layer formation of a structure capable of supporting its weight requires specific rheology from the 3D-printed material [271–273]. Materials with elastic behavior and a known yield point are necessary for the material to be extruded as a filament through the nozzle and maintain the printed shape after extrusion [274]. Therefore, the materials must be wisely chosen based on their mechanical properties for 3D printing but also their biocompatibility, their effect on cell adhesion, proliferation and functions, their degradability and permeability to biomolecules, and their functionalization or bioactivity in specific applications (see Figure 1.11) [270]. These conditions result in a limited choice of biomaterials compared to other 3D culture methods.

**Microextrusion-based bioprinting is one of multiple techniques for producing large 3D cell cultures in the cm<sup>3</sup> range. This method provides homogenous cell repartition in the construct with a cell-friendly, low-cost, fast and reproducible manufacturing process and controlled construct geometry. The choice of 3D bioprinting compounds involve various aspects, including bioinks, bioprinting parameters, and post-bioprinting processing (Figure 1.11). These factors significantly influence the viability and functionality of cells, and subsequently impact their behavior in 3D cultures, such as proliferation, differentiation, and tissue formation.**

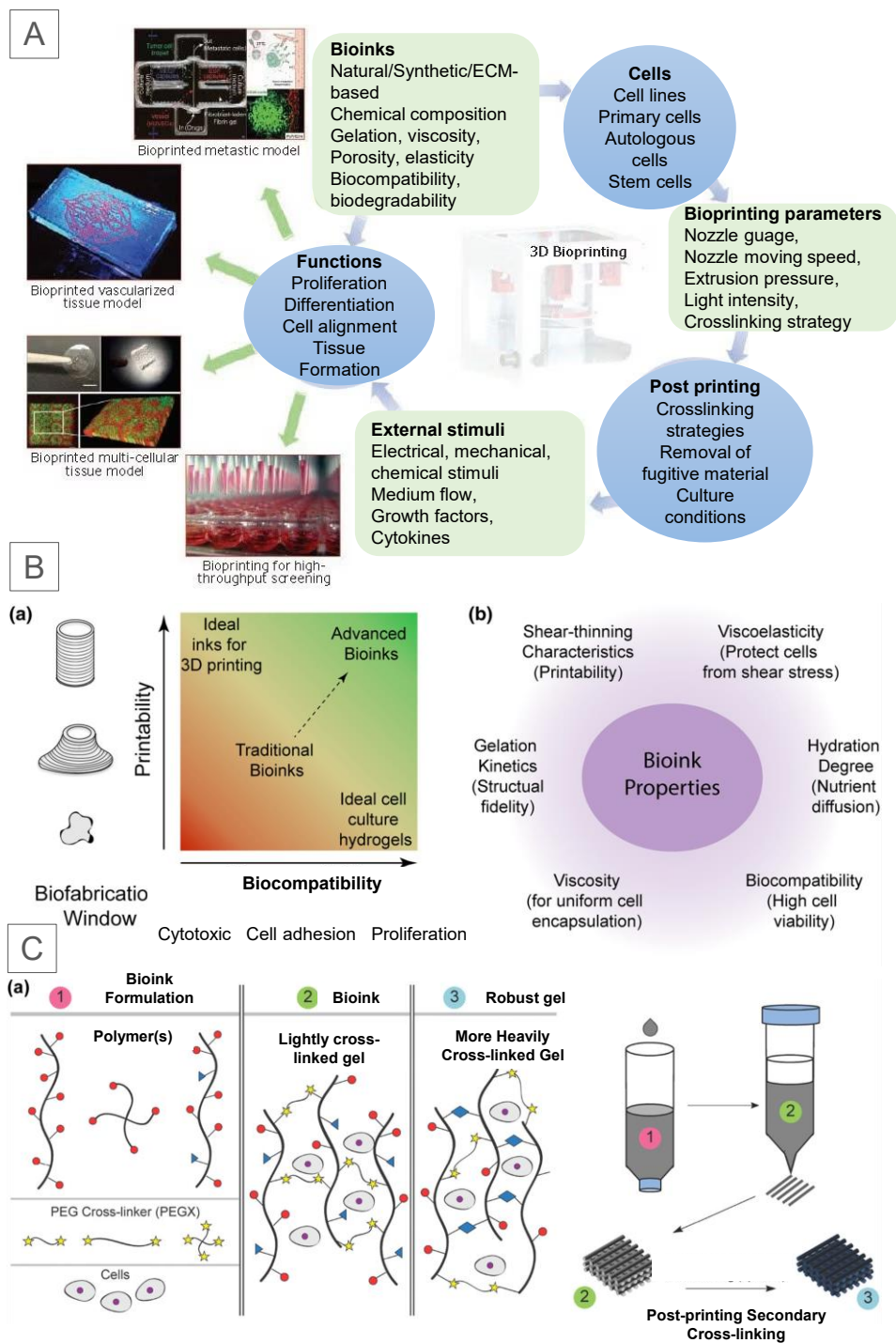


**Figure 1.11: The crucial constituents and applications of 3D bioprinting and main requirements for bioink properties.** (A) Bioinks, bioprinting parameters, and post-bioprinting processing are the main factors affecting cell viability and functionality. **Credit:** <https://www.sigmaaldrich.com/DE/de/technical-documents/technical-article/materials-science-and-engineering/3d-bioprinting/3d-bioprinting-tissue0>. (B) Bioink requirements with (a) Biofabrication window for rational design of bioinks requires compromise between printability and biocompatibility, (b) Ideal bioink characteristics require interplay between different materials properties.(C) Bioprinting process including, bioink formulation, bioprinting and consolidation. (B) and (C) **Credit:** Chimene D, Lennox K K, Kaunas R R and Gaharwar A K 2016 *Advanced Bioinks for 3D Printing: A Materials Science Perspective Ann Biomed Eng* 44 2090–102 [262]

### 1.3.2. *Biomaterials used for microextrusion-based bioprinting*

The bioprinting of mm<sup>3</sup> to cm<sup>3</sup> objects containing living cells requires specific bioinks properties [273]. Biomaterials must be chosen wisely to combine interesting properties for bioprinting, cell survival and proliferation. The best biomaterials can vary depending on the cell line and application. Numerous limitations are linked to the choice of biomaterial, including printability and resolution, resistance in time and degradability, ability to support cell proliferation, sterility or batch variability.

The bioink should allow for high-precision 3D printing at a centimeter scale with shape conservation during the printing process. It should also protect the cells from shear stress to ensure their survival during the passage of the printing nozzle. These criteria are dependent on bioink rheological properties and nozzle diameter [271].

Then, the bioink must also have optimal biocompatibility and mimic the natural cellular environment for cell adhesion to allow for cell survival and proliferation after printing. It should also exhibit biodegradability to support cell proliferation and complete colonization of the printed volume. Additionally, the components of the bioink should be capable of large-scale production with minimal variations across various supplier batches, and they should meet the criteria for medical-grade materials. These aspects are mainly dependent on the nature of the molecular network forming the biomaterial.

#### **Rheology**

The bioinks are characterized by rheological properties that will affect their printability and shape fidelity. Bioinks are usually described by their viscoelastic properties and yield stress [272]. The viscoelastic properties are characterized by the storage and loss modulus that respectively represent the energy stored (elastic behavior) or dissipated (viscous behavior) by the biomaterial during printing [272]. These are essential rheological parameters as they will affect the ability of bioink to flow in the nozzle during printing and to resist elastic deformation to maintain the printed shape. The yield stress represents the minimal stress necessary to induce bioink deformation and flow.

In extrusion-based bioprinting, shear-thinning is a crucial characteristic extensively investigated in bioinks. This property eases the process of extruding the biomaterial and supports the preservation of the 3D structure of the printed construct. Shear-thinning is characterized by a reduction of bioink viscosity, naming its ability to resist flowing under constraint when exposed to increasing shear stress during the extrusion phase [272]. This

property provides the bioink a cell-protective effect against shear stress [271,272]. Subsequently, after exiting the printing nozzle, the shear rate decreases, resulting in a concurrent elevation in viscosity essential for preserving the printed shape. Notably, a higher zero-shear viscosity is beneficial to prevent the collapse of the printed structure before the consolidation of the molecules network.

### **Bioink formulation**

Multiple biomaterials have been used for micro-extrusion-based bioprinting of live cells. These materials can be divided into two main categories: "synthetic" and "natural" (non-synthetic) compounds [270,273]. Synthetic materials characterized by well-defined properties are frequently better suited for bioprinting procedures, leading to enhanced reproducibility and controllable processes [273]. On the contrary, natural materials are predominantly ECM-based compounds and provide closer similarity with the physiological environment and superior properties for cell adhesion, proliferation, and interaction.

In 3D cell cultures, collagen is the main material used for scaffold manufacturing due to its similarity to in-vivo ECM. However, its mechanical properties do not allow the printing of pure collagen solutions at concentrations under 20 mg/mL [275,276]. Such concentrated collagen solutions are complex to prepare, and therefore, less concentrated collagen solutions associated with other compounds, such as Gelatin or Alginate, are often preferred for bioprinting applications [276–278]. These additional biocompatible compounds provide improved rheological properties for collagen-based bioink printability. Gelatin is a valuable substitute for collagen because it maintains a triple helix structure at temperatures below 30 °C [275]. Additionally, it offers essential RGD peptides for promoting cell adhesion and exhibits intriguing rheological properties suitable for bioprinting [273].

The most used natural materials for microextrusion-based bioprinting are commonly ECM-based compounds, Matrigel® (Corning®), collagen mixtures, Gelatin and methacrylate/methacrylamide/methacryloyl-gelatin (GelMA), fibrin, silk fibroin, cellulose-base materials, hyaluronic acid, chitosan, alginate, gellan gum and carrageenan [270]. Bioinks have been developed by mixing various compounds to optimize their printability and biocompatibility.

For example, a bio-ink formulated with a mixture of gelatin, alginate and fibrinogen has been developed by the team and patented [202,279,280]. This bioink will be used in the present work. Bioinks with similar formulations have also been reported in the literature [202,226]. These compounds were chosen for their respective properties, providing suitable rheology for

bioprinting and a biocompatible environment favourable to cell proliferation [202,279]. Additionally, these compounds exist in medical-grade materials and resist several weeks of culture. The main characteristics of these three bioink components will be presented in the following sections.

### 1.3.3. *Gelatin*

Gelatin is produced by denaturation and hydrolysis of collagen, usually from skin, bones, or tendons. In animals, collagen is the main structural component of connective tissues and represents up to 30% of total protein mass [281,282]. In mammal tissues, 28 types of collagens have been identified, the most abundant being collagen type I [281,283].

#### **Biochemical properties**

The hydrolysis of collagen to form gelatin results in a mixture of proteins and peptides forming a hydrogel with high water absorption [270]. The gelatin is extracted by boiling the tissues in water after the tissue's acidic (Type A gelatin) or alkaline (Type B gelatin) treatment. Type A gelatin has a mean of ~0.8 mmol/g of free carboxyl groups and an isoelectric point (pI) of 7.0-9.5 [284]. Conversely, type B has ~1.08 mmol/g of free carboxyl groups and a pI of 4.7-5.3. The gelatin conserves a composition similar to collagen, with a high proportion of glycine, proline and hydroxyproline [282]. Interestingly, gelatin has a less organized composition than collagen, decreasing its immunogenicity. Such characteristics could be valuable regarding the biocompatibility and implantability of bioink made of gelatin [285].

#### **Rheology**

Under 30°C, gelatin forms helicoidal structures and a 3D network, resulting in gelatin solution gelation [270]. Without gelatin crosslinking, this temperature-dependent gelation retains its reversibility, wherein heating the substance above 30°C disrupts the hydrogen bonds within the helical structures. Beyond 30°C, gelatin transforms into a fluid solution with viscosity determined by the gelatin concentration. Gelatin exhibits temperature-dependent rheological properties, making it challenging to 3D print as a pure solution. However, when combined with other biomaterials, it becomes a valuable component for creating adaptable bioinks [273]. Gelatin provides adjustable viscosity, yield stress and shear-thinning to the bioink, which are essential parameters for printability, shape fidelity and cell protection against shear stress [271–273].

## Post-printing treatment for consolidation of molecular network

Cellularized bioprinted constructs are commonly cultivated at 37°C. Thus, gelatin hydrogels can be crosslinked to conserve the 3D structure's shapes to form a covalently bound molecules network. The most common crosslinking method for gelatin hydrogel uses methacrylated gelatin (GelMA). GelMA contains methacrylamide and methacrylate groups; it is often referred to as “gelatin methacryloyl” but can also be encountered in the literature as “gelatin methacrylate” or “gelatin methacrylamide” [286]. It is synthesized by substitution of the reactive amine and hydroxyl groups of the amino acid residues with methacryloyl [286,287]. The GelMA hydrogel is consolidated by photopolymerization thanks to a photoinitiator such a 2-hydroxy-1-[4-(2-hydroxyethoxy) phenyl]-2-methyl-1-propanone, or lithium acylphosphinate salt (LAP) [286]. Light-induction will initiate a radical addition-type polymerization of methacryloyl molecules [288]. Although multiple studies have confirmed the biocompatibility of GelMA hydrogels [289–291], a concern remains for medical applications as unreacted methacrylate and photo-initiator are known to be cytotoxic [292].

Therefore, the use of native gelatin hydrogels is considered safer. More cell-friendly methods exist to consolidate gelatin networks without the need for the addition of methacrylate groups or photo-initiator. As an example, gelatin can be crosslinked enzymatically post-printing with transglutaminase (see Figure 1.12). Tissue transglutaminase, also known as type 2 transglutaminase (TG2), is a calcium-dependent enzyme able to create an isopeptide bond between the  $\epsilon$ -amino group of lysin residue and a  $\gamma$ -carbonyl group of a glutamine residue in proteins [293]. The formation of isopeptide bond releases ammonia. The transglutaminase-crosslinked Gelatin provided adequate support for cell adhesion [203,293,294]. Crosslinking of Gelatin with microbial transglutaminase was demonstrated to reduce the hydrogel swelling when placed in a liquid medium, and the reticulation was more effective on Gelatin purified



from salts [293]. Recently, the team patented a transglutaminase crosslinked formulation of our in-house bioink [295].

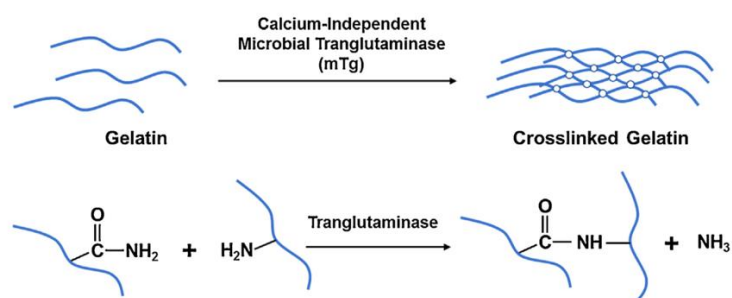


*Figure 1.12: Mechanism of gelatine crosslinking by the action of transglutaminase [296]*

### **Biocompatibility and cell proliferation**

Although denaturing collagen fibers form gelatin, specific sites are preserved, such as cell adhesion sites (RGD motif) or MMP-cleavable sites [297]. Collagen type I includes a structural matrix that supports cell adhesion and proliferation as it possesses multiple adhesion sites recognized by the cells. This adhesion process is mediated by integrins, a family of transmembrane proteins. They are the main actors of cell adhesion to collagen fibres, even though other cellular mechanisms can also intervene in this process [206,298,299]. Integrins can bind collagen-specific sites, laminin-specific sites, and RGD (Arginylglycylaspartic acid) peptide motifs also present in gelatin. Some signalling pathways involved in cell survival, control of transcription and proliferation, cell motility and cytoskeletal organization can be activated by integrin binding [206]. Therefore, gelatin is a biomaterial of choice in the formulation of a bioink.

### **Degradability**

Gelatin conserves some Matrix Metalloproteinases-cleavable sites present in collagen fibres [297]. Therefore, it is sensitive to enzymatic degradation, especially by collagenases and gelatinases such as MMP-2 and MMP-9, which are secreted by a wide range of cells, including primary cells such as fibroblasts, myofibroblasts, myocytes, neutrophils, macrophages, vascular smooth muscle cells, and endothelial cell [300,301], but also cell lines such as HEK [302], CHO [303] and MDCK [304,305]. Commercial Collagenase A solutions have already been reported to allow for the degradation of gelatin-based hydrogels [203,294].

**Hence, gelatin is widely used in extrusion-based bioprinting due to its favourable mechanical properties and biocompatibility. Its fast gelation at room temperature after printing, modulable viscosity, and shear-thinning behaviour make gelatin advantageous**

**for bioink printability, printed geometry conservation, and cell survival during bioprinting [306,307]. Also, it provides the appropriate yield stress necessary to ensure large object (>10cm<sup>3</sup>) printability [279].**

#### 1.3.4. *Alginate*

Alginate is a biomolecule widely used in microextrusion-based bioprinting due to its biocompatibility, low cost, printability, accessibility and controllable gelation [270]. It is a polysaccharide commonly extracted from brown algae (*Phaeophyceae*) [308]. Alginate is recovered by alkaline algae treatment, filtration, and precipitation. Afterwards, alginate is converted to alginic acid by HCl treatment. Some bacteria, such as *Azotobacter* and *Pseudomonas*, can also produce alginate in biofilms [309].

#### **Biochemical properties**

The alginate chemical structure and physical properties can vary depending on the algae species and batch lots. Its molecular mass ranges from 32,000 to 400,000 g/mol [308]. Alginate is formed of L-guluronate and D-mannuronate residues forming linear copolymers containing blocks of (1,4)-linked  $\beta$ -D-mannuronate (M) and  $\alpha$ -L-guluronate (G) residues, whose proportion varies depending on alginate source [308,310,311].

#### **Rheology**

Alginate is highly soluble in aqueous solutions, forming a viscous hydrogel. Alginate hydrogel's viscosity is affected by alginate's chemical structure and molecular weight and is inversely correlated to pH.

#### **Post-printing treatment for consolidation of molecular network**

Post-processing of the alginate hydrogels consists of hydrogel consolidation by chelation of the G blocks with divalent ions such as  $Mn^{2+}$ ,  $Co^{2+}$ ,  $Ni^{2+}$ ,  $Cu^{2+}$ ,  $Zn^{2+}$ ,  $Cd^{2+}$ ,  $Ca^{2+}$ ,  $Sr^{2+}$  and  $Ba^{2+}$ . Such reticulation allows the formation of an "egg box" configuration as represented in Figure 1.13 [310,312]. In bioengineering applications, Alginate is chelated with calcium ions from  $CaCl_2$  or  $CaCO_3$  solutions due to the low cytotoxicity of these solutions.

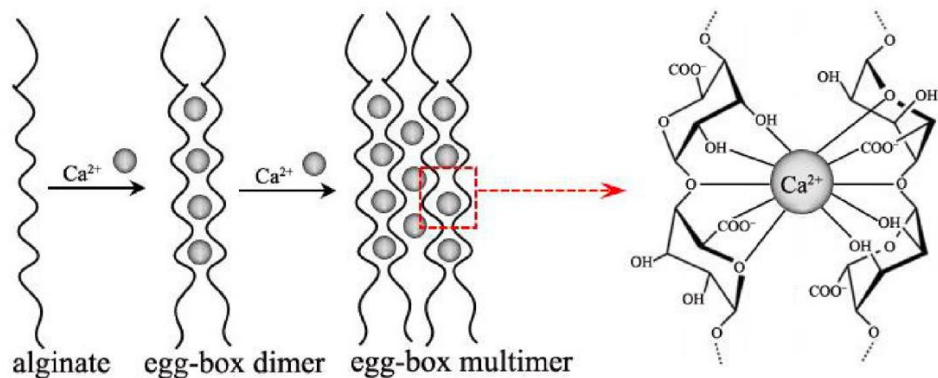


*Figure 1.13: Complexation of alginate by calcium ions forming an “egg-box” configuration. Credit: Zhang X, Wang X, Fan W, Liu Y, Wang Q and Weng L 2022 Fabrication, Property and Application of Calcium Alginate Fiber: A Review Polymers (Basel) 14 [313]*

### **Biocompatibility and cell proliferation**

Alginate is a biologically neutral component as it is not cytotoxicity nor immunogenic and does not present any adhesion site for cells [270,308]. Therefore, it is commonly formulated with other molecules offering cell adhesion sites like Gelatin, Collagen or Fibrinogen [314].

### **Degradation**

Alginate hydrogels are commonly degraded with sodium citrate treatments [315–317] or incubation in alginate lyase [318,319]. Sodium citrate buffer acts as chelating agents of the divalent ions involved in electrostatic interactions with alginate molecules, thus disrupting the hydrogel structure without altering the alginate molecules. On the other hand, Alginate lyase is an enzyme able to lyse the alginate polymers [320].

#### *1.3.5. Fibrinogen and fibrin*

Fibrinogen, or clotting factor I, is a glycoprotein in blood plasma involved in hemostasis and platelet aggregation. This protein is synthesized in the liver [321]. In humans, fibrinogen average concentration in blood plasma ranges from 2 to 5 mg/mL. The hemostatic process converts fibrinogen to insoluble fibrin by the Thrombin enzyme.

### **Biochemical properties**

Fibrinogen is a 340-kDa homodimeric glycoprotein composed of 6 chains (2A $\alpha$ , 2B $\beta$ , and 2 $\gamma$  polypeptide chains) linked by 29 disulfide bridges [321].

### **Rheology**

Fibrin is an elastic fibers that may provide hydrogel elasticity depending on the concentration. Yet, bioprinting of pure fibrinogen solutions is impossible due to its low viscosity and Newtonian behavior that prevents 3D printing and conservation of the shape [265,322]. Additionally, fibrinogen and fibrin do not have shear thinning properties to protect the cells from shear stress [273].

### Post-printing treatment for consolidation of molecular network

Fibrinogen can be crosslinked into fibrin by the action of Thrombin to form a hydrogel. Indeed, fibrinogen glycoprotein contains a cleavage site recognized by Thrombin; cleavage of the N-terminal fibrinopeptide converts fibrinogen to a fibrin monomer (see Figure 1.14). Multiple fibrin monomers assemble themselves to form fibrin fibres, also called protofibrils. It has been reported that the thrombin concentration affects the fibrin fibres' thickness. High Thrombin concentrations lead to thinner fibres with denser and more branched networks [321]. The fibrin fibers can also be crosslinked covalently with the FXIII factor, an enzyme from the transglutaminase family, or directly by tissue transglutaminase (TG2) [323].

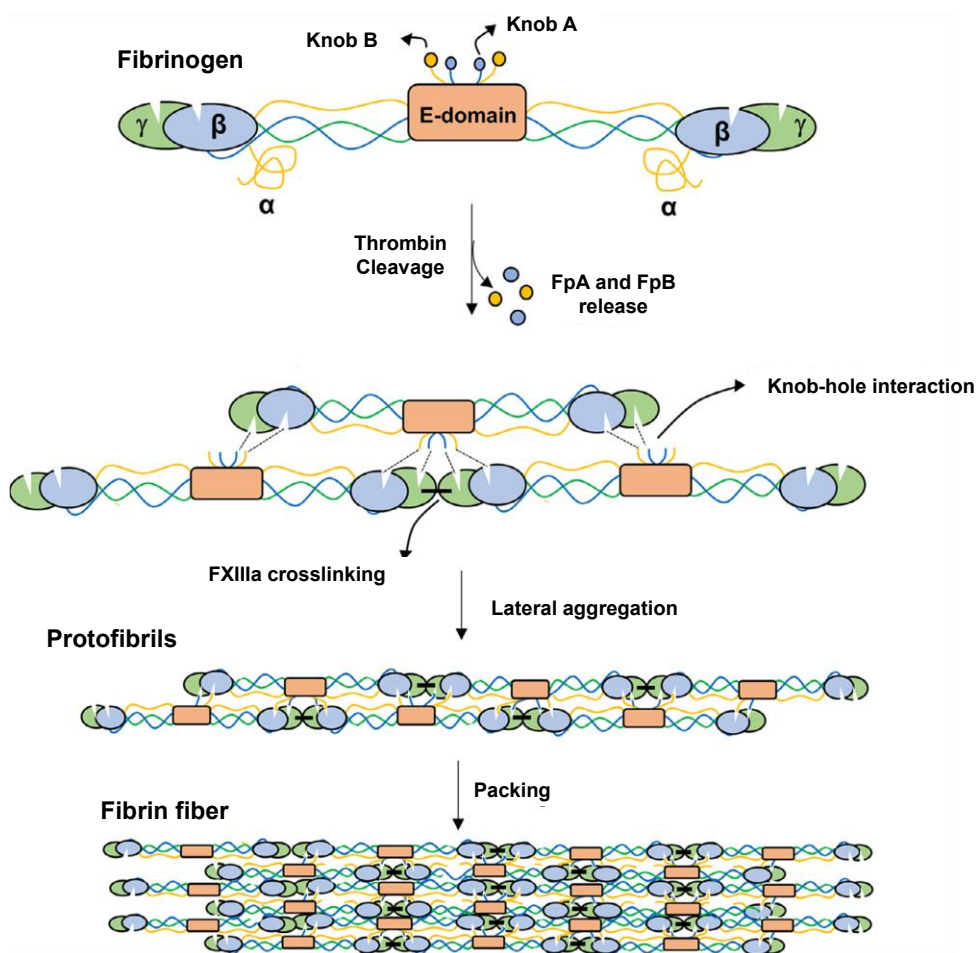


**Figure 1.14. : Fibrinogen polymerization by Thrombin to form fibrin fibers.** Fibrinogen is cleaved by thrombin, releasing fibrinopeptides (FpA & FpB) that allow the knob-hole interactions, forming protofibrils. Protofibrils interact through  $\alpha$  chains binding, leading to the packing and formation of fibrin fibers. **Credit: from de Melo B**

## **Biocompatibility and cell proliferation**

Fibrin is a component of ECM secreted within a tissue injury site to promote fibroblast proliferation and migration [324,325]. Thus, fibrinogen and fibrin provide great adhesion sites and an environment favourable to cell proliferation [203,294].

## **Degradation**

Fibrinolytic enzymes, such as some MMPs or plasmin, can degrade fibrin fibers [326–328]. Yet, fibrin hydrogel cohesion is weak, and its structural role in multiple-compound hydrogels is generally limited. Therefore, degrading the other compounds in these hydrogels' structure is usually enough to disrupt the objects [203,294]. Thus, in multi-compound hydrogels, fibrin is rarely targeted for gel degradation.

### *1.3.6. Current challenges for the scale-up of large bioprinted tissues*

When attempting to scale up bioprinting cultures, the viability and integrity of larger bioprinted cellular constructs, particularly those in the cubic centimeter (cm<sup>3</sup>) range, are compromised due to the restricted diffusion of culture medium and oxygen within the construct. Moreover, as the sizes exceed 1 cm<sup>3</sup>, finding suitable and sterile culture vessels becomes increasingly challenging, with limited options available in the commercial market. The lack of control over crucial culture parameters further hinders establishing an optimal cell environment.

To enhance the culture process for large 3D cultures, the following strategies should be considered:

1. Enhancing the diffusion of nutrients, oxygen, and cellular products within the 3D structure.
2. Developing specialized vessels designed for sterile culture to accommodate larger constructs.
3. Regulating environmental parameters to maintain optimal conditions tailored to the specific cell type and intended application.

## **Increasing molecules diffusion with adapted culture vessels**

When the scaffold separating the cells from the culture medium exceeds 300  $\mu\text{m}$  thickness, nutrient and oxygen transfer is restricted, leading to cell death [329]. Numerous studies have demonstrated the efficacy of dynamic culture systems in enhancing the renewal of culture medium, cell viability, and proliferation in 3D cellularized constructs. These systems promote the movement of culture medium, facilitating the transfer of nutrients and oxygen within the tissue and the removal of metabolic waste products. To induce fluid movements in 3D cultures, various strategies have been employed. One approach involves fixing a culture chamber at the bottom of a spinner flask [330]. However, the most commonly utilized techniques are specialized "bioreactors" designed for specific applications. The standard bioproduction bioreactors inspire these systems and have been developed in regenerative medicine for the engineering of 3D tissues [331–334].

In the existing literature, these systems have been successfully applied to 3D cellular constructs up to several cubic centimeters while maintaining culture sterility [279]. The most extensively reported methods are perfused bioreactors and rotative wall bioreactors (RWB). Rotative wall bioreactors consist of a cylindrical chamber containing a culture medium, with a tissue holder positioned within it. The chamber's wall can be rotated at a chosen rate, creating convective movements of the fluid inside [335]. In some variations of this bioreactor, the external wall remains fixed while the tissue holder rotates, allowing for the rotation of the tissue itself [336]. The positive impact of RWB on cell viability, tissue architecture, and preservation of tissue integrity has been demonstrated in various tissue types, including cartilage [336,337] and prostate [335].

On the other hand, perfusion bioreactors comprise a culture medium container that feeds a culture chamber [279]. Such system has already been implemented in our team with a culture chamber designed to fit the specific nature and shape of the tissue, and supplied with a culture medium through a pump [279]. In this work, the culture chamber and media reservoir were placed in an incubator to maintain the temperature to 37°C and media buffering with 5% CO<sub>2</sub>. Computational Fluid Dynamic (CFD) simulations were employed to model the fluid flow within the culture chamber and through the tissue, similar use of CFD have also been reported by other research teams [279,338–340]. This technique was used to increase the level of control over the structure, understanding and mastering media flow and diffusion in the construct to reach adequate perfusion flow rate and cell feeding [279]. In some cases, it was also applied to estimate the diffusion rate of dissolved gas and metabolites in the tissue scaffold [341,342].

Therefore, flow simulation and mass transfer studies can be performed to characterize the diffusion kinetics in the 3D constructs [279].

Hence, perfusion bioreactors enabled the controlled flow of culture medium through the construct, significantly enhancing the diffusion of nutrients and oxygen to the cells [279,343]. Numerous studies have shown the effectiveness of this technique in promoting cell proliferation and viability in different tissues, including dermis and connective tissue [279,344], hypodermis [345], liver [341], and lungs [346]. By improving mass transfer compared to static cultures, perfused conditions help preserve better cell morphology and function [347]. Some systems incorporate specific features, such as multiphase cultures with an air/liquid interface [338] or mechanical stimulations like shear stress [340], tensile forces [348], or vibrations [349]. However, the cultures are usually performed in incubators in conditions lacking monitoring and control capacity over the culture parameters.

### **Regulation cell environmental conditions**

Oxygen, pH, and temperature are critical parameters in cell culture, yet in most studies examined in this review, these culture parameters are not measured or regulated with precision. The bioreactors are commonly placed in incubators set at 37°C, 5% CO<sub>2</sub>, and 90% relative humidity. While the systems described in the literature lack complete control over these parameters, they demonstrate significant potential for automation and integration of online sensors.

In currently existing systems, the culture medium's pH and dissolved oxygen concentration are not precisely measured nor controlled. Only a few research teams have monitored the pH evolution [350,351] or the oxygen concentration in the gas supply during their processes [336,341,342,350]. Lovett et al. (2010) and Schmelzer et al. (2010) have even utilized a dO<sub>2</sub> probe to monitor the partial pressure of dissolved oxygen in the culture medium [342,350]. Nevertheless, despite the growing interest and advances in this field, none of these studies have precisely monitored and controlled pH, dO<sub>2</sub>, and temperature in the culture medium feeding. Yet, the similarity of these technologies with the highly controlled bioreactors used in the bioproduction field for suspension and microcarrier cell cultures offers great potential for increasing the level of control by automation and integration of analytics.

**Hence, custom bioreactor systems can be adapted to the culture of large bioprinted constructs and provide a sterile environment. Although the current technologies provide**

**limited capacity for monitoring and controlling the main culture parameters, they offer promising potential for improvement to overcome the limitations of large-scale bioprinted cultures.**

#### 1.4. In situ transfection of 3D cell cultures

In the field of 3D cell cultures, a new technology is gaining interest for transient cell engineering. Indeed, in situ transfection is a method allowing insertion of genetic material into cells growing in 3D culture conditions or even in live tissues [352]. This method is mainly used in regenerative medicine or gene therapy to induce the expression of target factors to enhance tissue maturation or disease treatment with gene silencing [353–355].

In the field of bioproduction, the use of in situ transient transfection could provide an alternative approach to the laborious task of generating stably transfected cell lines and to overcome the limitations of standard transient transfection in dense culture. In fact, in situ transient transfection is identified as a viable method to extend the transfection of rapidly dividing cells throughout the entire culture process.

The innovative methods and applications of in situ transfection have been the object of a literature review published in the journal *Biotechnology Advances* (DOI: 10.1016/j.biotechadv.2023.108211). This review is presented below. To facilitate the reading, the Material and Methods of the article was integrated to the Chapter 2 of this thesis. The abbreviations and references of the review were reported to the “Abbreviations” and “References” sections of the thesis. The numeration of the Figures was adapted on the model of the thesis format and the supplementary data were inserted as Figures in the article and in the manuscript.



# **In situ transient transfection of 3D cell cultures and tissues, a promising tool for tissue engineering and gene therapy.**

**Laura Chastagnier, Christophe Marquette, Emma Petiot\*.**

\*3d.FAB, univlyon, Université Lyon 1, CNRS, INSA, CPE-Lyon, ICBMS, UMR 5246, bat. Lederer, 5 rue Gaston Berger, 69100 Villeurbanne, France

## **ABSTRACT**

Various research fields use the transfection of mammalian cells with genetic material to induce the expression of a target transgene or gene silencing. It is a tool widely used in biological research, bioproduction, and therapy. Current transfection protocols are usually performed on 2D adherent cells or suspension cultures. The important rise of new gene therapies and regenerative medicine in the last decade raises the need for new tools to empower the *in situ* transfection of tissues and 3D cell cultures. This review will present novel *in situ* transfection methods based on a chemical or physical non-viral transfection of cells in tissues and 3D cultures, discuss the advantages and remaining gaps, and propose future developments and applications.

## **KEYWORDS**

In situ transfection, gene delivery, gene-activated matrices (GAMs), tissue engineering, gene therapy

#### 1.4.1. Introduction – Context

Since the 1970s, molecular biology and cell genetic engineering have been essential tools for several scientific fields. Genetic modification of mammalian cells was used to understand cell biology [356,357], to propose novel cell therapies [358] or production of therapeutics [359], and later to develop novel regenerative medicine strategies [360–363]. Mammalian cell genetic engineering involves transferring a gene of interest (transgene) into a target cell. The aim is to confer to cells new expression abilities and is named **cell transfection**. The first successful chemical-mediated introduction of genetic material in mammalian cells was performed in 1962 by Szybalska and Szybalski. They transfected a bone marrow cell line to express the Hypoxanthine Phosphoribosyl Transferase (HPT). This gene was initially extracted from an HPT-positive cell line [364,365]. From here, the work of Paul Berg's team in 1972 was a second major milestone. They produced the first recombinant DNA [366] which was successively used in 1973 by Cohen et al. to build a genetically modified bacteria [367] and then in 1980 by Gordon et al. to create the first mammalian cell transfection using recombinant DNA [357]. Several transformation methods were tested. This first genetic modification was chemically mediated, but during the early '80s, physical transfection methods were also reported on mammalian cells [368–372]. A decade later, DNA transfer using viral vectorization was deployed, leading to the current cell and gene therapy boom. Nowadays, for medical applications, nucleic acids (plasmid DNA or strand RNA) delivered by chemical or physical methods are preferred to viral vectors. Concerns regard safety purposes, while viral vectors are more likely to induce immunogenic reactions or mutagenicity. The use of viruses can also limit the cargo size of large genes [373,374].

In the last decade, the need and interest for new tools for the *in situ* transfection of tissues and 3D cell cultures were raised by the increasing number of applications of new gene therapies and tissue engineering strategies for regenerative medicine. Indeed, for both application fields, efficiently modifying cells within a biocompatible matrix could leverage their therapeutic efficiency and relevance. This review will present novel *in situ* transfection methods based on a chemical or physical non-viral transfection of cells in tissues and 3D cultures.

## METHODS AND APPLICATIONS OF *IN SITU* TRANSFECTION OF 3D CELL CULTURES AND TISSUES

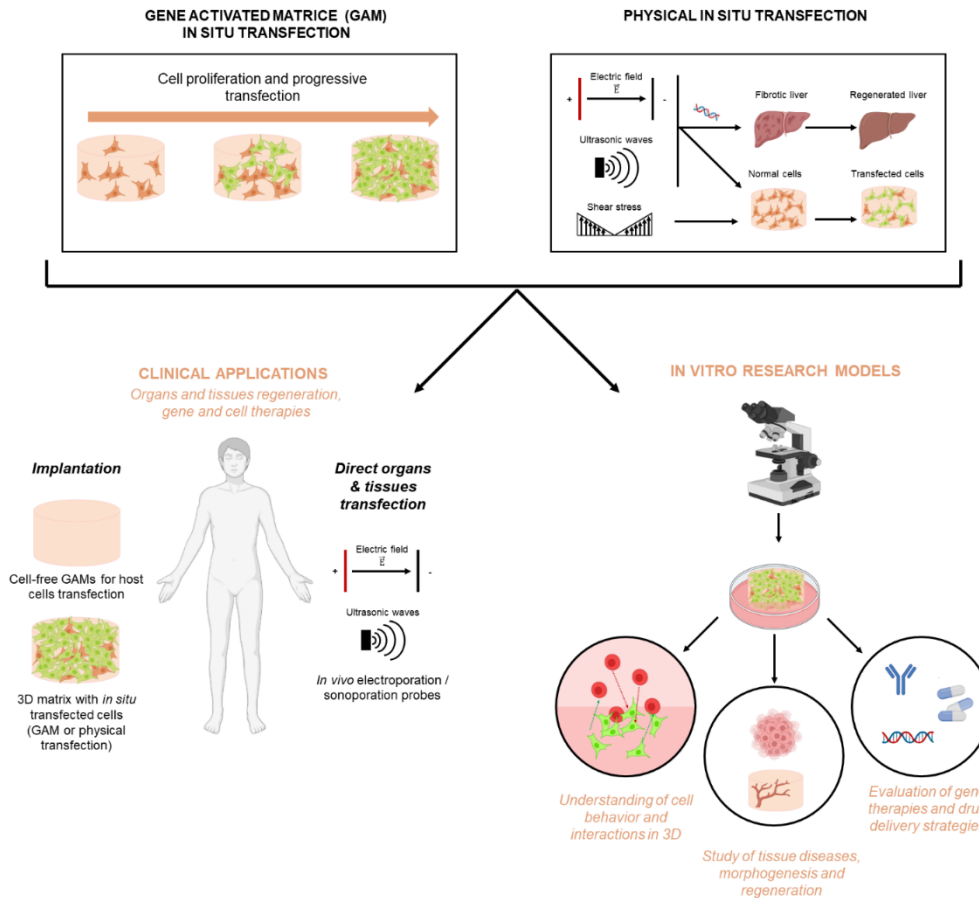


**Figure 1.15: Overview of the main methods and applications of *in situ* transfection.**

### 1.4.2. Principles of cell genetic engineering

The nucleic acids (plasmid DNA or stranded RNA) must overcome multiple biological barriers to reach efficient transgene integration and expression into the cells [369,375,376]. Indeed, it needs to cross the cell membrane and, in the case of DNA, get into the cell nucleus to be transcribed and further handled by cell machinery to be translated into proteins (Figure 1.16).

**Cellular uptake** is the first and foremost barrier to efficient transfection. Indeed, the negatively charged cell membrane repulses phosphate groups of nucleic acids (DNA and RNA). The probability of spontaneous uptake of a naked plasmid is very low. Nevertheless, Tsoncheva et al. (2005) could transfect up to 30% of cells by spontaneous uptake of naked DNA. It was achieved in 2D adherent or suspension cultures using a high DNA-to-cell ratio of 5 $\mu$ g plasmid DNA (pDNA) for 8 $\times 10^5$  cells/ml [377]. Since the '80s, transfection reagents have been

developed to facilitate plasmid entry into the cell [378–386]. Transfection reagents are complexing agents that can induce nucleic acid condensation, thus facilitating cell penetration by forming smaller complexes with positive charges or lipidic membranes [387]. The mechanisms described for the uptake of such complexes are either endocytosis [388–391] or fusion with the cell membrane in the case of some lipidic complexes [392]. However, the fusion mechanism is contested, suggesting that endocytosis is the primary mechanism for complexed-nucleic acid uptake [393,394]. Endocytosis of complexes formed of nucleic acids and cationic polymers, also called polyplexes, can happen through several mechanisms. They can be classified into either clathrin-dependent mechanisms [385,395] or clathrin-independent mechanisms, like micropinocytosis or caveolar internalization [385,396]. During endocytosis and micropinocytosis, polyplexes penetrate the membrane by entrapment into endosomes and macropinosomes.

Physical methods have been explored to disrupt cell membranes temporarily and favor naked nucleic acid uptake while avoiding using chemical reagents [397–399]. These methods use physical stress to create transient pores in cellular membranes [369]. Such a strategy proved efficient for both *in vivo* studies and *in vitro* 3D culture transfection. Transfection rates reaching 5% of tissue transfected were reported on *in vivo* applications using sonoporation [400]. In 3D *in vitro* cell cultures, efficiencies reaching 15% (electroporation) [401] to 31% (shear stress) [402] were reported. Nevertheless, physical stresses can damage tissue during the processes [403].

**Endosomal escape** is the next critical bottleneck for efficient transfection. Endosomes carrying complexes evolve into late endosomes and fuse with lysosomes. In the lysosomes, nucleic acids undergo enzymatic degradation in acidic conditions, leading to poor transfection efficiency. Caveolae-mediated endocytosis of polyplexes has demonstrated better transfections efficiencies than clathrin-dependent internalization. Indeed, the caveolae are directly transported to the Golgi apparatus by traveling along microtubules [385,386,404,405]. However, in other studies, Pelkmans et al. (2004) demonstrated that caveolae could be directed to early endosomes, leading to polyplexes degradation in lysosomes [406,407]. While endosomal escape mechanisms are not fully understood, several studies suggest that protonable polyplexes with buffering characteristics could have a protective effect against the endosome's pH gradients. This mechanism is the "proton sponge effect" [387,395]. The lysosome acidification is delayed by the buffering effect of the polyplexes and their capture of protons. The osmotic imbalance is then compensated by lysosome swelling and subsequent lysis [387,408]. Some other escape mechanisms discussed in the scientific community are based on

polyplex interaction with endosome membrane. A comprehensive review recently described these mechanisms [376].

Multiple hypothesis exists to explain lipoplexes endosomal escape. The main processes detailed in the literature are their direct fusion with endosome membrane, the membrane destabilization by detergent-like effect, or the flip-flop movements of the membrane induced by charge interaction between cationic lipids and negative phospholipid bilayer [395,409–411]. Fusion and flip-flop mechanisms induce the release of solely the plasmids into the cytoplasm. On the contrary, membrane destabilization can release intact lipoplexes from the endosomes.

After entering the cell, escaping from endosomes and the complexes, RNA molecules will be directly translated by the cell machinery. On the contrary, plasmid DNA (pDNA) still needs to reach the nucleus to be transcribed. Thus, an additional step is **DNA trafficking within the cell cytoplasm** to reach the nucleus while avoiding degradation by nucleases [412]. Lechardeur et al. have shown that encapsulated pDNA are protected from cytosolic nucleases [413]. DNA molecules larger than 1000 bp cannot freely travel thanks to diffusion within the cytoplasm due to cytoskeleton hindrance [414–416]. Some studies investigating intracellular trafficking of transfection complexes suggest that plasmids may be directed toward the nucleus by traveling along microtubules [405,416]. However, microtubules participate in lysosome motility [417–419]. Thus, the transportation of transfection complexes along microtubules can lead to the fusion and degradation of pDNA in lysosomes [420,421]. Unlike other methods, Cardarelli et al. (2016) showed that lipofectamine-DNA complexes could travel toward the nucleus by diffusion with Brownian movements. Consequently, this avoids transport along microtubules and lysosome entrapment [420]. Such lipofectamine-mediated transfection prevents 90% of lysosomal degradation of the lipoplexes when other lipoplexes (DOTAP/DOPC/DNA) were at 70% entrapped in lysosomes [415].

**Nuclear entry** of pDNA occurs mainly through nuclear pores [391]. However, some studies also suggest that endosomes could directly deliver pDNA to the nucleus, Golgi apparatus, or endoplasmic reticulum [404]. It is still unknown if pDNA release from the complexes occurs before entering the nucleus, during the endosomal escape, or after entering the nuclear compartment. Once inside the nucleus, **pDNA** can be handled by the cell machinery and undergo the transcription and translation processes similarly to host-cell genes.

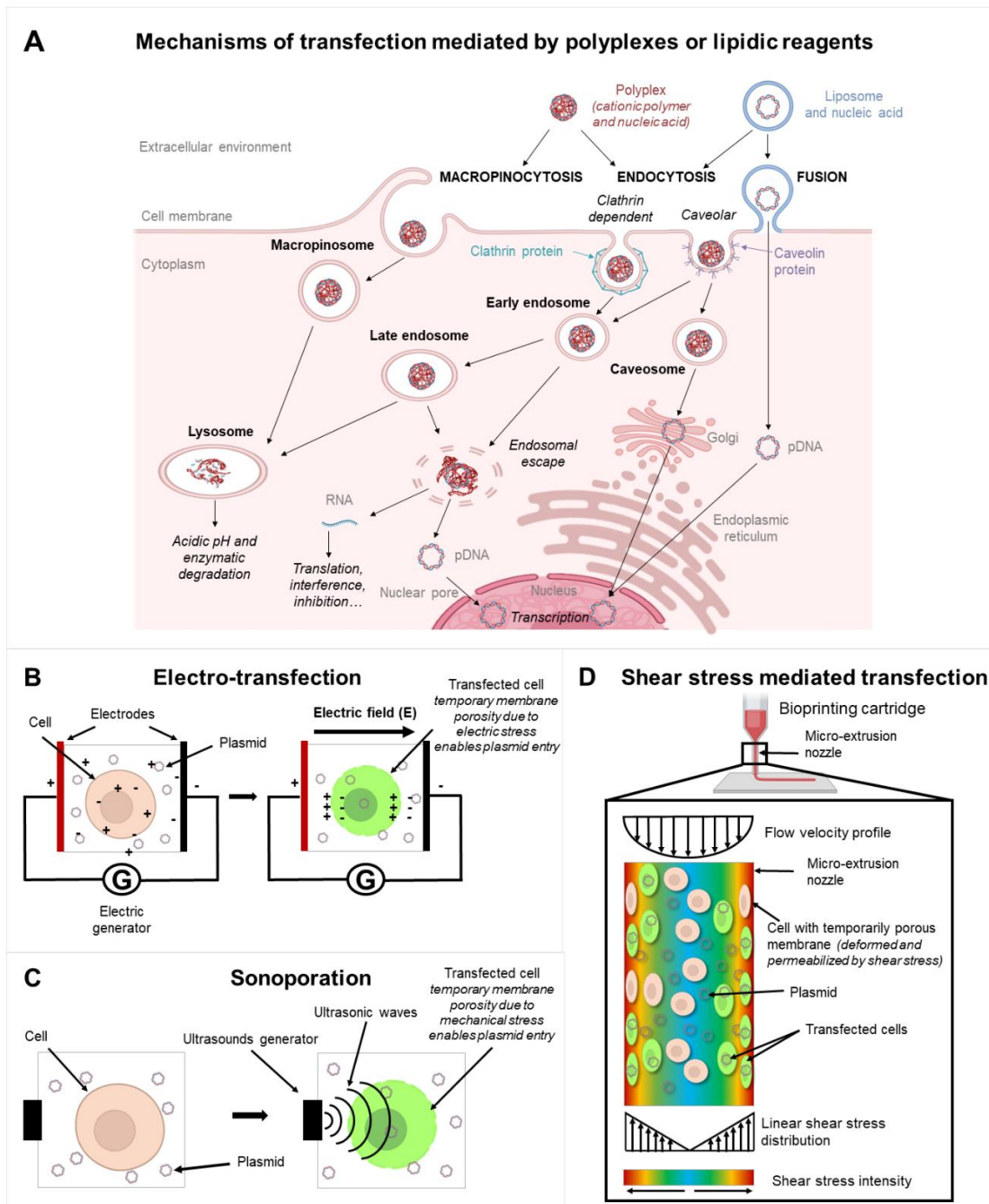


**Figure 1.16: Basic transfection methodologies adapted for applications to in-vivo and in-situ transfection.** The common routes for standard transfection complexes delivery to the nucleus with polyplexes or lipidic reagents (A) and the three main physical transfection methods (B, C & D): B- Electroporation, cell membrane charges are destabilized by an electric field, creating temporary disruption of the membrane. C) Sonoporation, cells are subjected to ultrasonic waves creating local stress and permeation of the membrane. D) Shear stress (microextrusion), cells are exposed to shear stress creating pores in the cell membrane.

### 1.4.3. Standard transfection methods as a starting point for 3D transfection protocols

The know-how developed for several years to transform mammalian cells is presently targeting the development of protocols for *in vivo* or 3D cellularized model transfection.

A large variety of transfection reagents have been evaluated since 1962. They have been mainly developed for 2D adherent or suspension cell cultures. Thus, the standard strategy is **direct transfection**, where nucleic acid complexes are directly added to 2D cultures supernatants to induce contact via diffusion in the liquid medium [384].

Such transfection protocols allow now to reach high transfection efficiencies. Even hard-to-transfect cells such as HUVECs were transfected with efficiencies up to 77% by Hunt et al. (2010) using the Effectene reagent [384]. For easy-to-transfect cell lines, such as HEK cells (Human Embryonic Kidney cells 293T), transfection efficiencies commonly exceed 90 % [422]. Most of the time, these transfection protocols were only effective in an optimized **serum-free culture medium** since nucleic acids are sensitive to degradation by serum nucleases [423]. Interactions with charged serum proteins negatively impact protocols based on cationic polymers or cationic-lipidic molecules. Nevertheless, few cationic-lipid-based reagents still show good transfection efficiencies with high transgene expression in the presence of serum [424]. Transgene expression usually happens 48 to 72 hours following contact with the transfection complexes.

The second type of protocol, **reverse transfection**, was developed to transfect 2D adherent cells on microarrays at the beginning of the 2000s [425–427]. It involves coating the culture plate with the plasmids by freeze-drying [428] or cationic polymer-DNA complexes deposition [429]. This technique enhanced and prolonged gene expression with maximal transgene expression after five days of culture, lasting up to 8 days. Standard direct transfection has a maximal expression after two days [429]. Spermine-pullulan [429], bovine serum [430], gelatin [431] and collagen [432] are examples of coating materials used for reverse transfection. **This technique was the premise of the 3D *in situ* transfection protocols.**

3D transfection tools are based on either **direct transfection** [433] or **reverse transfection** protocols. **Direct transfection** relies on a cell transfection step before cell seeding onto the 3D scaffolds or hydrogels. On the contrary, in reverse transfection, the 3D scaffolds or hydrogels carrying the transgenes allow for *in situ* and progressive tissue transfection. They were named **gene-activated matrices** (GAMs). Some physical transfection techniques were also adapted to 3D cultures. This review presents these different methods and their applications for *in situ* transfections (Table 1.8; Figure 1.17).

#### 1.4.4. *Methods of chemical in situ transfection*

The use of large 3D cell cultures is now widespread and still getting more interest in regenerative medicine and gene therapies. They are preferred over 2D cultures because they are

more representative of *in vivo* cell physiology and environment [244–246]. Such 3D cell structures are commonly used to produce engineered tissues. Their applications are wide: research in tissue regeneration for medical applications (implantation) [247–249], *in vitro* modelization of tissue functions for study and understanding of cellular behaviors and interactions [250–252] as well as organs dysfunctions, degeneration, diseases, and infection [253–257], and *in vitro* modelization of pathologic tissues or organs for testing of therapeutics such as drug or gene therapies [255,258,259].

With the rise of gene therapies, tissue engineering, and regenerative medicine since the end of the 90s, the interest in developing new transfection tools suitable for transforming 3D cell models and tissues has increased [434–437].

With a target of producing *in vitro* specialized tissue models, it has been of interest to either **express a transgene of interest** [363,438–445] **or to silence specific genes** [353,354].

However, when inserted *in vivo* or in a serum-containing culture medium, the nucleic acids are more vulnerable to serum nucleases. Consequently, **transfection only happens locally and briefly** [429]. In 3D culture conditions mimicking the physiological environment and *in vivo* applications, serum proteases can strongly limit cell transfection. When the plasmids or transfecting complexes are added to the culture medium or liquid environment in the case of chemical or physical transfection, the diffusion of DNA in the 3D cell structure is limited. The limitation of nucleic acid diffusion in the matrix or tissue leads to poor transfection efficiency and transfection occurring mainly on the superficial layers [446]. For such applications, *in situ* transfection, based on the principle of reverse transfection applied to 3D cell cultures, is highly interesting (Figure 1.18). Embedding plasmids in a hydrogel or a scaffold protects against enzymatic DNA degradation by nucleases and offers more stability to the plasmids in time [429,447]. Moreover, the nucleic acids are already embedded in the matrix and concentrated around the cells, ensuring better accessibility to transforming factors. Finally, the cells are progressively transfected when invading the support, thus allowing an extended transfection period [429,448] (Figure 1.18). This strategy gave primary cells and hard-to-transfect cell lines higher transfection efficiencies [428,449].

### **Innovative scaffolds and hydrogels for in situ gene delivery**

Many commercially available transfection agents are known for inducing cytotoxicity and reducing transfection efficiency in 3D cultures compared to 2D (Table 1.8) [450,451]. Therefore, developing new and less toxic complexing agents for transfection of 3D-engineered tissues has been an intense field of research and innovation. Among the most reported agents,



we find chitosan [452,453], chitosan-linked-polyethyleneimine (PEI) [450], alginate-grafted-PEI [454], cationized alginates [455], and other polyamide materials or extracellular matrix (ECM) compounds, with already validated transfection efficiency in 2D cultures.

These materials are now the base for formulating gene-activated matrices (GAMs). GAMs are 3D matrices complexing nucleic acids and enabling transfection during 3D culture. To obtain GAM, nucleic acids or complexes are formulated with the 3D matrix [448] or impregnated in the preformed 3D matrix [456–458]. Different mechanisms exist to stabilize nucleic acids in the GAM (Figure 1.18).

### **Gene-Activated Matrices (GAM) based on ECM compounds**

**Extracellular Matrix proteins are the most used biomolecules to create GAMs.** Collagen, one of the most represented molecules of the ECM, is extensively employed for scaffold biofabrication and 3D cell cultures. It is due to its properties of enhancement of cell adhesion and proliferation while mimicking the native cell environment. It is thus the material of choice for GAM conception for *in situ* transfection strategies. Other ECM molecules than collagen, like fibronectin or glycosaminoglycans (GAGs), were also proved to provide excellent support for cell adhesion, proliferation, and transfection thanks to their *in vivo*-like adhesion motives [459]. In the following described studies, 3D ECM-based scaffolds were soak-loaded with either naked plasmids, transfecting agents, polyplexes, and lipoplexes. Such practice questioned the homogeneity and reproducibility of the transfection complexes' repartition in the 3D matrix.

**Table 1.8: Table summarizing the most relevant papers in the literature in the field of *in situ* transfection of 3D cultures and tissues.** Involved cell type, applications, context, transfecting reagents, mechanism, main outcomes, efficiency, lasting of transgene and literature source are given. CG: cationized gelatine; GAG: Glycosaminoglycan; HA: Hydroxyapatite; HyA: Hyaluronic acid; nHA: Nanohydroxyapatite; PET: Polyethylene terephthalate; PGA: Poly(glycolic acid); PLG: Poly(lactide-co-glycolide); PU: Polyurethane

Cell type (tissue/organism)	Application	<i>in vitro</i> / <i>in vivo</i> (tissue)	Matrix	Cells seeded on the scaffold (S) / incorporated in the matrix (I)	Plasmid / RNA transfected	Transfection mechanism	Paper outcome	Transfection efficiency (% of transfected cells)	Lasting of gene expression / experiment	Reference
Chemical Transfection Extracellular matrix components as transfecting agents and Gene Activated Matrices										
Acellular (Bone / rat)	Bone regeneration	<i>in vivo</i>	Bovine tracheal collagen	NA	<b>Plasmid</b> Luciferase and B-Galactosidase encoding plasmids, bone morphogenetic protein-4 plasmid & a plasmid coding for a fragment of parathyroid hormone	Naked plasmid in collagen	Successful <i>in vivo</i> local transfection - accelerated repair of bone defect within 6 months (24 weeks)	N.A.	4 to 24 weeks	Fang et al., 1996 *
Osteoblast & Fibroblasts (Bone / dog)	Bone regeneration	<i>in vivo</i>	Bovine type I collagen	NA	<b>Plasmid</b> pNTb-gal plasmid (encoding a nuclear-targeted version of bacterial beta-galactosidase) & pMat-1 plasmid	Naked plasmid in collagen	successful <i>in vivo</i> local transfection - accelerated repair of 2 cm bone defect with bridge formation within 4 weeks and complete repair within 6 months	30–50% tissue cells expressing transgene after 3 weeks	> 6 weeks	Bonadio et al., 1999
MSC (bone marrow / rat)	Bone regeneration	<i>in vitro</i>	Collagen-PGA fibers	S	<b>Plasmid</b> pBacBH2 plasmid coding for hBMP-2	<b>Cationized Gelatin (CG)</b> -plasmid DNA complexes or dextran-plasmid complexes in collagen-PGA scaffold	Prolonged transgenes expression over 21 days and increased expression levels of 3 to 6-folds compared to 2D Successful transfection - Enhanced BMP2 expression after 2 days of both static and perfused <i>in vitro</i> cultures, with higher expression levels in perfused cultures. Highest BMP-2 and osteogenic genes expression, with faster tissue mineralization for <i>in vivo</i> implanted GAMs seeded with MSC cells.	N.A.	3 weeks	Hosseinkhani et al., 2006a
MSC (bone marrow / rat)	Bone regeneration	<i>in vitro</i> & <i>in vivo</i>	Collagen-PGA fibers	S	<b>Plasmid</b> pBacBH2 plasmid coding for hBMP-2	<b>Cationized Gelatin (CG)</b> plasmid DNA complexes in collagen-PGA scaffold	<i>In vitro</i> increased BMP-2 expression in 3D compared to 2D cultures with best condition obtained with PEI Ac80 <i>In vivo</i> accelerated bone regeneration by implantation of collagen-PGA scaffold activated with PEI-Ac80-DNA complexes.	N.A.	1-4 weeks	Hosseinkhani et al., 2006b *
MSC (bone marrow / rat)	Bone regeneration	<i>in vitro</i> & <i>in vivo</i>	Collagen-PGA fibers	S	<b>Plasmid</b> pBacBH2 (BMP-2)	<b>Acetylated PEI</b> (PEI-Ac80)-plasmid complexes in collagen-based scaffold	<i>In vivo</i> accelerated bone regeneration by implantation of collagen-PGA scaffold activated with PEI-Ac80-DNA complexes.	N.A.	3 weeks	Hosseinkhani et al., 2008

PL

Biotechnology Advances 68 (2023) :

Cell type (tissue/organism)	Application	<i>in vitro</i> / <i>in vivo</i> (tissue)	Matrix	Cells seeded on the scaffold (S) / incorporated in the matrix (I)	Plasmid / RNA transfected	Transfection mechanism	Paper outcome	Transfection efficiency (% of transfected cells)	Lasting of gene expression / experiment	Reference
HEK293T cells (N. A. / human) - N. A. (spinal cord / rat)	Spinal cord injury healing	<i>in vitro</i> & <i>in vivo</i>	<b>Fibronectin / Collagen I / Laminin I</b> coated PLG	S	<b>Plasmid</b> Plasmid encoding for firefly luciferase and b-galactosidase	<b>Lipoplexes</b> integrated to the ECM coating	<i>in vitro</i> : Best transfection obtained with fibronectin-coated scaffolds <i>in vivo</i> : <i>prolonged</i> transgene expression for up to 3 weeks after implantation	N.A.	3 weeks	De Laporte et al., 2009 *
MSC (bone marrow / rat)	Bone regeneration	<i>in vitro</i>	<b>Collagen, Collagen-GAG and Collagen-nHA</b> scaffolds	S	<b>Plasmid</b> GFP encoding plasmid and luciferase encoding plasmid	<b>PEI-pDNA</b> polyplexes combined to collagen-based scaffolds	Prolonged transgene expression over 3 weeks with best expression levels reached in collagen-nHA scaffolds	N.A.	3 weeks	Tierney et al., 2012
MSC (bone marrow / rat)	Bone regeneration	<i>in vitro</i>	<b>Collagen-nHA</b>	S	<b>Plasmid</b> pMaxGFP (GFP), pLuc (Gaussian luciferase) and pBMP2 (BMP2)	nHA-pDNA complexes in collagen-nHA scaffold	Successful transfection with BMP2 gene - Overexpression of osteogenic genes (osteocalcin) & increased calcium deposition indicative of MSC differentiation toward osteoblastic lineage.	N.A.	5 weeks	Curtin et al., 2012 *
MSC (bone marrow / human)	Bone regeneration	<i>in vitro</i>	<b>Collagen-nHA</b>	S	<b>Plasmid</b> GFP encoding plasmid, luciferase plasmid and ephrinB2 plasmid	PEI-pDNA polyplexes combined to collagen-nHA scaffold	Prolonged transgene expression 2 weeks and faster calcium deposition.	N.A.	2 weeks	Tierney et al., 2013
MSC (iliac crest bone marrow / human)	Bone regeneration	<i>in vitro</i> & <i>in vivo</i>	<b>Collagen-nHA</b>	S	<b>Plasmid</b> pGFP (GFP), pBMP2 (BMP 2), pVEGF (VEGF)	(PEI-pVEGF/PEI-pBMP2) or (nHA-pVEGF/nHA-pBMP2) or (PEI-pVEGF and nHA-pBMP2) in collagen-nHA scaffolds and (PEI-pGFP) or (nHA-pGFP) in collagen-nHA scaffolds	<i>In vitro</i> , osteogenesis and calcium deposition were significantly increased especially in (nHA-pVEGF/nHA-pBMP2) and (PEI-pVEGF and nHA-pBMP2) activated scaffolds. <i>In vivo</i> , the GAMS successfully transfected the host cells on the site of implantation. Fastest bone regeneration was achieved with dual nHA scaffolds which enhanced bone formation by 36-fold in 4 weeks	N.A.	4 weeks	Curtin et al., 2015
MSC (iliac crest bone marrow / human)	Research model for clinical gene delivery	<i>in vitro</i>	<b>Collagen-nHA</b>	S	<b>miRNA</b> miR-mimics and antagonists	nHA-miRNA complexes	RNA interferences achieved in 3D, reaching up to 88.4% interference after only 1 week without cytotoxicity	N.A.	1 week	Castano et al., 2015 *
MSC (bone marrow / rat)	Bone and cartilage repair	<i>in vitro</i>	<b>Collagen, Collagen-HA and collagen-HyA</b> scaffolds	S	<b>Plasmid</b> GFP encoding plasmid (pGFP) and Gaussia luciferase	<b>Chitosan-pDNA</b> nanoparticles on <b>collagen-based</b> scaffolds	Best transgene expression reached after 2 weeks with collagen scaffolds & prolonged expression for 4 weeks.	N.A.	4 weeks	Rafferty et al., 2015 *

(continued on next page)

Cell type (tissue/organism)	Application	<i>in vitro</i> / <i>in vivo</i> (tissue)	Matrix	Cells seeded on the scaffold (S) / incorporated in the matrix (I)	Plasmid / RNA transfected	Transfection mechanism	Paper outcome	Transfection efficiency (% of transfected cells)	Lasting of gene expression / experiment	Reference
					encoding plasmid (pGluc)					
MSC (iliac crest bone marrow / human)	Bone regeneration	<i>in vitro</i>	Collagen-nHA	S	miRNA nanomiR (miR-133a inhibiting complexes)	nHA-miRNA complexes in collagen-nHA scaffold	Successful inhibition of miRNA after 3 days and increase of osteogenesis markers up to 2 folds after 7 days, 80% increase in calcium deposition compared to non-transfected control (2 - 4 weeks) Increased calcium deposition with both BMP-2 and VEGF plasmid supplied in collagen-nHA scaffolds. <i>In vivo</i> , cell-free GAMS were colonized by host cells after implantation, plasmids were retained in the scaffold and host cells expressing the transgene were detected after only 7 days	N.A.	4 weeks	Menciá Castano et al., 2016
MSC (bone marrow / rat)	Bone regeneration	<i>in vitro</i> & <i>in vivo</i>	Collagen, Collagen-HA	S	Plasmid pGFP (GFP), pBMP-2 (BMP-2), pVEGF (VEGF)	Chitosan plasmid in collagen-based scaffold	Increased calcium deposition <i>in vitro</i> . Half reduced healing duration and bone regeneration <i>in vivo</i>	N.A.	4 weeks	Rafferty et al., 2017
MSC (bone marrow / rat)	Bone regeneration	<i>in vitro</i> & <i>in vivo</i>	Collagen-nHA	S	Plasmid pBMP-2/7 (multi-cistronic plasmid encoding both BMP-2 and BMP-7) and different plasmids coding for BMP-2	Cationic Chitosan-plasmid complexes in collagen-based scaffold	<i>In vitro</i> , 50% repression of the level of miRNA-133a in activated scaffolds leading to the 7-fold upregulation of osteogenic genes, faster mineralization & bone formation after 2 weeks. <i>In vivo</i> , successful delivery of miRNA to host cells leading to faster mineralization, bone regeneration and increased CD206+ macrophages recruitment. Significant upregulation of miRNA-16 levels in 3D scaffolds combined to LDH miRNA complexes after only 1 week while	N.A.	4 weeks	Rafferty et al., 2018
MSC (bone marrow / rat)	Bone regeneration	<i>in vitro</i> & <i>in vivo</i>	Collagen-nHA	S	miRNA antagoniR-133a	nHA-miRNA in collagen-nHA scaffold		N.A.	2-4 weeks	Castano et al., 2020
MSC (bone marrow / rat)	Bone regeneration	<i>in situ</i>	Collagen-nHA	S	Plasmid pLuc (Gaussia luciferase) siRNA & miRNA	MgAl-NO3 layered double hydroxide (LDH) - nucleic acids complexes in collagen-nHA scaffold		N.A.	1 week	Costard et al., 2020

(continued on next page)

Cell type (tissue/organism)	Application	<i>in vitro</i> / <i>in vivo</i> (tissue)	Matrix	Cells seeded on the scaffold (S) / incorporated in the matrix (I)	Plasmid / RNA transfected	Transfection mechanism	Paper outcome	Transfection efficiency (% of transfected cells)	Lasting of gene expression / experiment	Reference
<b>Scaffolds combined to penetration peptides</b>							delivery of siRNA targeting GAPDH mRNA did not show significant knockdown after a week.			
MSC (bone marrow / pig)	Bone and cartilage regeneration	<i>in vitro</i> & <i>in vivo</i>	Alginate-methylcellulose hydrogel	I	Plasmid pGFP (GFP), pLUC (Luciferase), pTomato (dtTomato), pBMP2 (BMP2), pTGF-β3 (TGF-β3) and pSOX9 (SOX9)	RALA peptide-plasmid complexes in the hydrogel	Successful and 2 weeks sustained transfection <i>in vitro</i> with a 10 fold higher expression in porous hydrogels containing more methylcellulose. <i>In vivo</i> implantation of the GAMS increased calcification and vascularization (pBMP2) or chondrogenesis (pTGF-βBMP and pTGF-βBMP-pSOX9)	N.A.	2 weeks	Gonzalez-Fernandez et al., 2019 *
MSC (bone marrow / rat)	Bone regeneration	<i>in vitro</i> & <i>in vivo</i>	Collagen, Collagen-HA, Collagen-GAG (chondroitin 6-sulfate), Collagen-HyA	S	Plasmid pGLuc (Gaussia Luciferase), pZsGreen1 (GFP), pBMP-2 (BMP-2), pVEGF (VEGF)	GET peptide-plasmid complexes in scaffold	<i>In vitro</i> , strong transgene expression after a week which is prolonged over 4 weeks. <i>In vivo</i> , transgene expression localized at the implantation site was measured up to 2 weeks. <i>In vitro</i> star-PLL-pDNA complexes activated scaffolds enhanced prolonged, non-toxic transgene expression during 4 weeks. <i>In vivo</i> , cell-free GAMS were colonized by host cells after implantation, plasmids were retained in the scaffold and host cells expressing the transgene were detected after only 1 week.	N.A.	4 weeks	Raftery et al., 2019
MSC (bone marrow / rat)	<i>In vivo</i> nanomedicine delivery for tissue regeneration	<i>in vitro</i> & <i>in vivo</i>	Collagen-GAG (chondroitin sulfate), Collagen-HyA, Collagen-HA or Collagen-nHA	S	Plasmid pGLuc (Gaussia Luciferase), pGFP (GFP)	Star-shaped poly (l-lysine) polypeptides - plasmid complexes in scaffold	Successful transfection in the 3D culture with siMMP-9 activated Col/GAG scaffolds leading to 40 to 60% (fibroblasts) or 30 to 50% (macrophages) MMP-9 gene downregulation with good cytocompatibility	N.A.	3 to 4 weeks	Walsh et al., 2019 *
Fibroblasts & THP-1 macrophages (N.A / human)	Healing of diabetic foot ulcers	<i>in vitro</i>	Collagen-GAG	S	siRNA siMMP-9 (MMP-9-targeting siRNA)	RALA peptide-siMMP-9 complexes in collagen-GAG scaffold	Successful transfection in 3D cultures. Highest transfection level was	N.A.	N.A.	Yan et al., 2020
MSC (bone marrow / rat)	Angiogenesis for bone repair	<i>in situ</i>	collagen-nanohydroxyapatite	S	Plasmid pGLuc (Gaussia luciferase) and pSDF-	different GET peptides combinations (N/P 6,		NA	2-3 weeks	Power et al., 2022 *

(continued on next page)

Cell type (tissue/organism)	Application	<i>in vitro</i> / <i>in vivo</i> (tissue)	Matrix	Cells seeded on the scaffold (S) / incorporated in the matrix (I)	Plasmid / RNA transfected	Transfection mechanism	Paper outcome	Transfection efficiency (% of transfected cells)	Lasting of gene expression / experiment	Reference
					1 $\alpha$ (stromal-derived factor 1 alpha)	<b>8, 11</b> complexed with plasmids in scaffold	achieved with the optimized GET <sup>®</sup> N/P 8 nanoparticles in coll-nHA scaffolds resulting in increased SDF 1 $\alpha$ protein production and enhanced angiogenic effect			
<b>Charged synthetic supports as complexing agents</b>										
Muscle cells (femoral muscle / mouse)	Treatment of cancer and congenital immunological diseases	<i>in vivo</i>	<b>Cationized Gelatin (CG)</b>	N.A.	<b>Plasmid</b> pSV-LacZ (LacZ, $\beta$ -galactosidase)	plasmid in <b>CG</b> -scaffold	Prolonged stabilization of plasmids within <i>in vivo</i> implanted hydrogels for 2-3 weeks depending on the hydrogel formulation. Longest stability achieved with Cationic Gelatin compared to plasmid injections (3 weeks versus 3 days respectively). Significant inhibition of TGF-hR expression and decreased of collagen content by <i>in vivo</i> injection of TGF-hR siRNA-CG complex. Arrest of renal interstitial fibrosis progression.	N.A.	1 to 2 weeks	Fukumaka et al., 2002 *
Kidney cells (kidney / mouse)	Treatment of renal fibrosis	<i>in vivo</i>	N.A.	N.A.	<b>Plasmid</b> pSUPER-TGF-hRII (expressing siRNA for Transforming Growth Factor-h Receptor)	<b>CG</b> -plasmid complexes	<i>In vivo</i> injection of cationized-gelatin-pDNA complexes led to maximal transfection after 60 h in the site of injection. Polyplexes travelled through sciatic and spinal nerves where increasing transgene expression was measured until day 6	N.A.	10 days	Kushibiki et al., 2006
Sensory neurons (subcutaneous / rat)	Nervous system regeneration	<i>in vivo</i>	N.A.	N.A.	<b>Plasmid</b> pdsRed2 N1 (dsRed2) and pEGFP (GFP)	<b>Cationized Gelatin</b> -plasmid complexes	Expression levels reached similar to 2D reverse transfection. Prolonged expression for 3 weeks. Improvement of polyplexes immobilization and repartition on the anionic nanofibers by the application of electric field during polyplexes adsorption. Best efficiency achieved with 1 V electric field.	47%	6 days	Thakor et al., 2007
MSC (bone marrow / rat)	Cartilage regeneration (chondrogenesis)	<i>in vitro</i>	PET non-woven fabric coated with <b>anionic gelatin (AG)</b> & <b>Pronectin</b>	S	<b>Plasmid</b> plasmid encoding for TGF $\beta$ -1	Cationic pullulan-spermine/DNA complex coated on <b>anionic gelatin</b>		N.A.	3 weeks	He et al., 2011 *
HEK-293 T (N.A. / human)	Research model for clinical gene delivery	<i>in vitro</i>	<b>Anionic Alginate-Polycaprolactone</b>	S	<b>Plasmid</b> pEGFP-C3 (GFP)	PEI-plasmid complexes adsorbed on <b>anionic alginate</b> fibers		N.A.	> 5 days	Hu and Ting, 2019

(continued on next page)

Cell type (tissue/organism)	Application	<i>in vitro</i> / <i>in vivo</i> (tissue)	Matrix	Cells seeded on the scaffold (S) / incorporated in the matrix (I)	Plasmid / RNA transfected	Transfection mechanism	Paper outcome	Transfection efficiency (% of transfected cells)	Lasting of gene expression / experiment	Reference
<b>Non-charged synthetic supports as GAMS</b>										
MSC (bone marrow / rat)	Research model for clinical gene delivery	<i>in vitro</i>	<b>PET non-woven fabric</b> coated with <b>Pronectin</b>	S	<b>Plasmid</b> pGL3 (firefly luciferase)	Cationic pullulan-plasmid complexes in <b>Pronectin</b> coating	Enhanced and prolonged gene expression level by 2 to 3-folds in dynamic cultures with agitation. Increased transgene expression on porous bioprinted scaffolds during the first week of culture	N.A.	1 week	Okazaki et al., 2007
MG-63 cells (bone osteosarcoma / human)	Bone regeneration	<i>in vitro</i> & <i>in vivo</i>	<b>Alginate</b>	I	<b>Plasmid</b> pcDNA3.1/rhBMP-2 (pBMP-2) (BMP-2)	naked plasmids in alginate (bioprinting)		46%	2 to 6 weeks	Loozen et al., 2013 *
<b>Physical Transfection</b>										
<b>Electroporation, sonoporation and electro-sonoporation</b>										
N.A. (liver / rat)	Delivery of therapeutic genes to the liver	<i>in vivo</i>	N.A.	NA	<b>Plasmid</b> pEGFP-C1 (eGFP)	<b>Electroporation</b> 8 pulses:50 V, 50 ms	<i>In vivo</i> transfection with GFP expression in rat liver. Transfection efficiency was improved by electric field increased up to 50 V. Identification of tissue damage and decreased transfection efficiency over 50 V.	N.A.	2 days	Suzuki et al., 1998 *
Chicken embryo	Research model	<i>in ovo</i>	N.A.	NA	<b>Plasmid</b> PmiwZ plasmid, clfgf (-) plasmid and clfgf (+) plasmid	<b>Electroporation</b> 6 pulses: 40 V, 60 ms	Transfection was achieved <i>in ovo</i> with good viability and maximal transgene expression at 8-24 h post transfection	N.A.	24-48 h	Sakamoto et al., 1998
N.A. (B16 melanoma tumor/ Mouse)	Cancer treatment	<i>in vivo</i>	N.A.	NA	<b>Plasmid</b> pGL3 (luciferase) and pTracer-CMV (GFP)	<b>Sonoporation (ultrasounds)</b> 400 SW	<i>in vivo</i> transfection achieved at a low efficiency rate with only 2.5% of the cellsexpressing the transgene. In the optimal sonoporation conditions, tumor volume was significantly reduced, showing the potential of combining sonoporation with therapeutic gene delivery for cancer treatment	2.5%	2 days	Miller et al., 1999
NIH 3 T3 fibroblasts, malignant melanoma Mewo, HeLa, Dunning prostate tumor R3327-AT1 cells (skin & prostate tumor /mouse & human)	Cancer treatment	<i>in vivo</i>	N.A.	NA	<b>Plasmid</b> pCMV-LacZ ( $\beta$ galactosidase)	<b>Sonoporation (ultrasounds)</b>	Successful <i>in vivo</i> transfection by sonication after intratumoral pDNA injections. Transgene expression was 10-fold higher when sonoporation was used compared to plasmid injection alone. The transfection was restricted to the injection	5%	1 - 3 days	Huber and Pfisterer, 2000

(continued on next page)

Cell type (tissue/organism)	Application	<i>in vitro</i> / <i>in vivo</i> (tissue)	Matrix	Cells seeded on the scaffold (S) / incorporated in the matrix (I)	Plasmid / RNA transfected	Transfection mechanism	Paper outcome	Transfection efficiency (% of transfected cells)	Lasting of gene expression / experiment	Reference
N.A. (muscle / rat)	Treatment of protein deficiencies-disorder	<i>in vivo</i>	N.A.	NA	<b>Plasmid</b> (MFP)-inducible hEPO expression plasmid, pGene/V5-hEPO, pSwitch	<b>Electroporation 8</b> pulses: 100 V, 50 ms	site (tumor) and did not reach the adjacent tissues <i>in vivo</i> transfection with inducible transgene expression thanks to a mifepristone (MFP)-inducible hEPO expression system. Transgene expression was maintained over 4 weeks and hematocrit levels increased from 47,2% to 53,8%. Successful transfection <i>in vivo</i> , 10-fold higher expression was reached when electroporation at 300 V/cm was used after plasmids injection compared to non-electroporated controls. Transfection with pmEPO plasmids led to erythropoietin expression <i>in vivo</i> up to 18 weeks. Significant tissue damage with necrotic areas was observed in electroporated muscles due to electric field exposure but were completely healed after 28 days. Successful <i>in vivo</i> transfection by electro-sonoporation. Electro-sonoporation demonstrated higher transfection efficiencies than electroporation or sonoporation alone with a 2-fold increased transgene expression and a reduced tissue damage. Transgene expression was maintained over 4 weeks. Successful <i>in vivo</i> transfection by sonoporation following plasmid injection in mice thigh muscle. Maximal	N.A.	4 weeks	Terada et al., 2001
11 N.A. (muscle / rat)	Delivery of therapeutic genes to skeletal muscles	<i>in vivo</i>	N.A.	NA	<b>Plasmid</b> pVR1255 (luciferase) p-mEPO (mouse erythropoietin) p-SEAP (human secreted embryonic alkaline phosphatase)	<b>Electroporation 8</b> pulses: 300 V/cm, 20 ms		N.A.	18 weeks	Hartikka et al., 2001 *
N.A. (muscle / mouse)	Delivery of therapeutic genes to skeletal muscles	<i>in vivo</i>	N.A.	NA	Plasmid pLuc and pActLuc (luciferase), pCAGGS-mIL-12 / pCAGGS-p35 / pCAGGS- p40 (mIL-12)	<b>Electro-sonoporation</b>		N.A.	4 weeks	Yamashita et al., 2002 *
N.A. (muscle / mouse)	Bone regeneration	<i>in vivo</i>	N.A.	NA	<b>Plasmid</b> pLuc (luciferase), phBMP-9 (hBMP-9)	<b>Sonoporation</b>		N.A.	4 weeks	Sheyn et al., 2006

(continued on next page)



Cell type (tissue/organism)	Application	<i>in vitro</i> / <i>in vivo</i> (tissue)	Matrix	Cells seeded on the scaffold (S) / incorporated in the matrix (I)	Plasmid / RNA transfected	Transfection mechanism	Paper outcome	Transfection efficiency (% of transfected cells)	Lasting of gene expression / experiment	Reference
HCT 116 cells (colorectal carcinoma / human) - LPB cells (sarcoma / mouse)	Cancer treatment	<i>in vitro</i>	N.A.	Spheroids	<b>Plasmid</b> pEGFP-C1 (eGFP)	<b>Electroporation</b> 10 pulses: 0.3 kV/cm, 5 ms, 1 Hz	transgene expression was reached after 2 weeks and sustained over more than 4 weeks. Transfection with phBMP9 significantly increased osteocalcin expression and ectopic bone formation. Low transfection efficiency achieved with electroporation. Only few cells were expressing the transgene with the highest rate achieved with a 0.3 kV/cm electric field. The transfected area were restricted to the surface of the spheroids. Above 0.3 kV/cm, cell viability decreased drastically. Successful <i>in vivo</i> electroporation of postnatal ferrets cerebral cortex which did not disturb the normal neuronal development. Transfection occurred in the entire thickness of the cortex in 2 days and lasted over 5 weeks	N.A.	1 day	Wasungu et al., 2009
N.A. (cerebral cortex / ferret)	Research model: delivery of genetic material to cerebral cortex	<i>in vivo</i>	N.A.	NA	<b>Plasmid</b> pCAG-EGFP (eGFP), pCAG-DsRed (RFP), pCAG-EGFP-CAG-Cdk5-DN and pCAG-Cdk5T33	<b>Electroporation</b>	Optimal <i>in vitro</i> transfection with plasmid concentration of 90 µg/ml of matrix allowing to reach a 5,8% cells transfected after 24 h. Successful <i>in vivo</i> transfection with dissolving microneedle injection of pDNA followed by electroporation.	N.A.	5 weeks	Borrell, 2010
CHO cells (ovary / Hamster)	Research model for therapeutic gene delivery	<i>in vitro</i>	<b>Collagen</b>	S	<b>Plasmid</b> pEGFP-N1 (eGFP)	<b>Electroporation</b> 8 pulses: 320 V, 5 ms, 1 Hz, 0.8 kV/cm	Expression of transgene was increased when electroporation was used and transgene expression was measured over 2 weeks. <i>In vivo</i> transfection of subcutaneous melanoma with	5.8%	1 day	Haberl and Pavlin, 2010
B16F10 melanoma cells (skin / mouse)	Cancer treatment	<i>in vivo</i>	N.A.	NA	<b>Plasmid</b> p2CMVmlL12 (mIL-12) and pCMV.Gluc (Gaussia luciferase)	<b>Electroporation</b> 8 pulses: 70 V/0.5 cm, 50 ms <b>and dissolving microneedles</b>		N.A.	2 weeks	Lee et al., 2011 *

(continued on next page)

Cell type (tissue/organism)	Application	<i>in vitro</i> / <i>in vivo</i> (tissue)	Matrix	Cells seeded on the scaffold (S) / incorporated in the matrix (I)	Plasmid / RNA transfected	Transfection mechanism	Paper outcome	Transfection efficiency (% of transfected cells)	Lasting of gene expression / experiment	Reference
HCT116 (human colorectal carcinoma)	Cancer treatment	<i>in vitro</i>	N.A.	Spheroids	Plasmid pEGFP-C1 (eGFP)	Electroporation (10 pulses of 500 V/cm, 5 ns, 1 Hz)	interleukin-12 plasmid inhibited tumor growth and prolonged mice survival. Low transfection efficiency with transgene expression detected at 1% of the cells in spheroids only with electric fields of 400 and 500 V/cm. High cell mortality and transfection restricted to the spheroids' surface. <i>in vitro</i> , Spheroids composed of only HaCaT cells showed low transfection efficiency with transfected cells only located to the surface or at the plasmids' injection site. Mixing HaCaT cells with B16-F10 cells and optimizing EP parameters (voltage and pulse duration) increased the transfection efficiency. <i>In vivo</i> intratumoral transfection demonstrate lower efficiency than for <i>in vitro</i> models.	1%	1 day	Chopin et al., 2012
HaCaT keratinocytes (skin / human) - melanoma B16-F10 cells (skin / mouse) - melanoma SKMEL-5 cells (skin / human)	Cancer treatment	<i>in vitro</i> & <i>in vivo</i>	N.A.	Spheroids	Plasmid phiL-15 (interleukin 15) and pEGFP-N1 (GFP)	Electroporation 10 pulses: 0.3 kV/cm, 5 ms, 1 Hz	<i>in vivo</i> intratumoral transfection demonstrate lower efficiency than for <i>in vitro</i> models. Successful <i>in vivo</i> transfection of periodontal ligament with detection of recombinant BMP-4 expression 1 week after electroporation. Cells expressing the transgene were also detected on adjacent tissues. Maximal expression at day 3 and detected up to 2 weeks post-transfection. Successful transfection using direct sonoporation on peritoneal tissues. The transfection was mainly restricted to the superficial layers in contact with the ultrasounds probe and had	N.A.	1-2 days	Marrero and Heller, 2012
N.A. (periodontal ligament/rat)	Alveolar bone regeneration	<i>in vivo</i>	N.A.	NA	Plasmid pCAGGS BMP4 (BMP-4), pCAGGS-GFP (GFP) and pCAGGS-lacZ ( $\beta$ -galactosidase)	Electroporation 16 pulses: 50 V, 50 ms width, 75 ms interval	Successful transfection using direct sonoporation on peritoneal tissues. The transfection was mainly restricted to the superficial layers in contact with the ultrasounds probe and had	N.A.	2 weeks	Tsuchiya et al., 2017
N.A. (peritoneum / mouse)	Treatment of peritoneal diseases	<i>in vivo</i>	N.A.	NA	Plasmid pCMV-luciferase (luciferase), pZsGreen1-N1 (GFP),	Sonoporation (ultrasounds) frequency: 2.04 MHz; duty: 50%; burst rate: 10 Hz; intensity: 4.0 W/cm <sup>2</sup>	Successful transfection using direct sonoporation on peritoneal tissues. The transfection was mainly restricted to the superficial layers in contact with the ultrasounds probe and had	N.A.	N.A.	Nishimura et al., 2019

(continued on next page)

Cell type (tissue/organism)	Application	<i>in vitro</i> / <i>in vivo</i> (tissue)	Matrix	Cells seeded on the scaffold (S) / incorporated in the matrix (I)	Plasmid / RNA transfected	Transfection mechanism	Paper outcome	Transfection efficiency (% of transfected cells)	Lasting of gene expression / experiment	Reference
HeLa & HEK293 cells (N.A. / human)	Research model for therapeutic gene delivery	<i>in vitro</i>	Peptide hydrogel matrix (PepGel)	I	<b>Plasmid</b> pAcGFP1-C1 (GFP) and pSpCas9(LJBB)-2A-GFP (PX458) (Crispr/Cas9 GFP)	<b>Electroporation</b> 3 pulses: 500 V, 3 ms, 1 Hz	few cytotoxicity. The efficiency of transfection was 10-fold higher in the visceral peritoneum compared to the parietal peritoneum, showing that the efficiency of this method is site specific. First report of 3D printed electroporation chamber for stable transfection of 3D bioprinted cell culture to deliver CRISPR/Cas9 plasmid. The use of the electro-chamber on bioprinted 3D cultures successfully transfected 15% of the cells concerning 87% cell viability. Successful <i>in vivo</i> transfection with 10-fold increase in transgene expression after electroporation compared to plasmid injection alone.	15%	2 days	Zhu et al., 2019 *
N.A. (skin / guinea pig)	Delivery of therapeutic genes to the skin	<i>in vivo</i>	N.A.	NA	<b>Plasmid</b> plasmid encoding firefly luciferase tagged with a DDK	<b>Electroporation</b> 8 pulses: 200 V, 150 ms	Monopolar gene electrotransfer allowed for lasting transgene expression over 21 days. Transfection occurred in all epidermis thickness and even reached deeper tissues without notable damage.	N.A.	3 weeks	Butylsheva et al., 2021 *
<b>Shear stress</b>										
Aortic endothelial cells (aorte / porc)	Aortic tissue regeneration	<i>in vitro</i> & <i>in vivo</i>	Collagen Fibrin	S	<b>Plasmid</b> pmaxGFP (GFP) and pIRES-VEGF-GFP (VEFF & GFP)	<b>Bioprinting (inkjet)</b>	Successful transfection of aortic endothelial cells while they are inkjet printed with plasmids. <i>In vitro</i> , transfection efficiency reached up to 14% with prolonged transgene expression for 1.5 weeks. High cells viability of 90% was conserved after printing. <i>in vivo</i> , aortic endothelial cells expressing the transgene were detected after 1 week.	14%	10 days	Xu et al., 2009

(continued on next page)

Cell type (tissue/organism)	Application	<i>in vitro</i> / <i>in vivo</i> (tissue)	Matrix	Cells seeded on the scaffold (S) / incorporated in the matrix (I)	Plasmid / RNA transfected	Transfection mechanism	Paper outcome	Transfection efficiency (% of transfected cells)	Lasting of gene expression / experiment	Reference
CHO-S cells (ovary / Hamster)	Gene delivery to 3D <i>in vitro</i> tissue models	<i>in vitro</i>	Collagen	S	Plasmid fibrillar GFP fused plasmid	Bioprinting (inkjet)	Successful transfection of cells during inkjet bioprinting reaching up to 31% efficiency after 1 day with 89% viability after printing Successful reprogramming of fibroblasts into neural lineage by shear-stress-mediated transfection during bioprinting. Bioprinted fibroblast cultures differentiated into neural tissue in 2 weeks. In optimal shear-stress conditions (190 Pa) transfection yielded at 16% while conserving 65% viability.	31%	24 h	Cui et al., 2010 *
Fibroblasts (dermis / human)	Neural tissue regeneration and cell reprogramming	<i>in vitro</i>	Waterborne Polyurethane (wPU)	I	Plasmid FoxD3 coding plasmid and GFP plasmid	Bioprinting (micro-extrusion)	Successful transfection of hUC-MSC during 3D bioprinting. The highest transfection efficiency was achieved with the lowest molecular weight polyurethane (PU1). <i>In vitro</i> , transgene expression in PU1 bioprinted structures reached similar levels than 2D control transfected with commercial reagent PolyFect. After implantation, hUC-MSC bioprinted in PU1 containing GATA4 coding plasmid led to complete regeneration of heart defects in zebrafish	16% to 30%	2 weeks	Ho and Hsu, 2018 *
hUC-MSC (umbilical cord / human)	Cardiac repair	<i>in vitro</i> & <i>in vivo</i>	Polyurethane (PU)	I	Plasmid GATA binding protein 4 (GATA4) coding plasmid	Bioprinting (microextrusion)	Successful transfection of hUC-MSC during 3D bioprinting. The highest transfection efficiency was achieved with the lowest molecular weight polyurethane (PU1). <i>In vitro</i> , transgene expression in PU1 bioprinted structures reached similar levels than 2D control transfected with commercial reagent PolyFect. After implantation, hUC-MSC bioprinted in PU1 containing GATA4 coding plasmid led to complete regeneration of heart defects in zebrafish	N.A.	2 weeks to 1 month	Huang et al., 2020

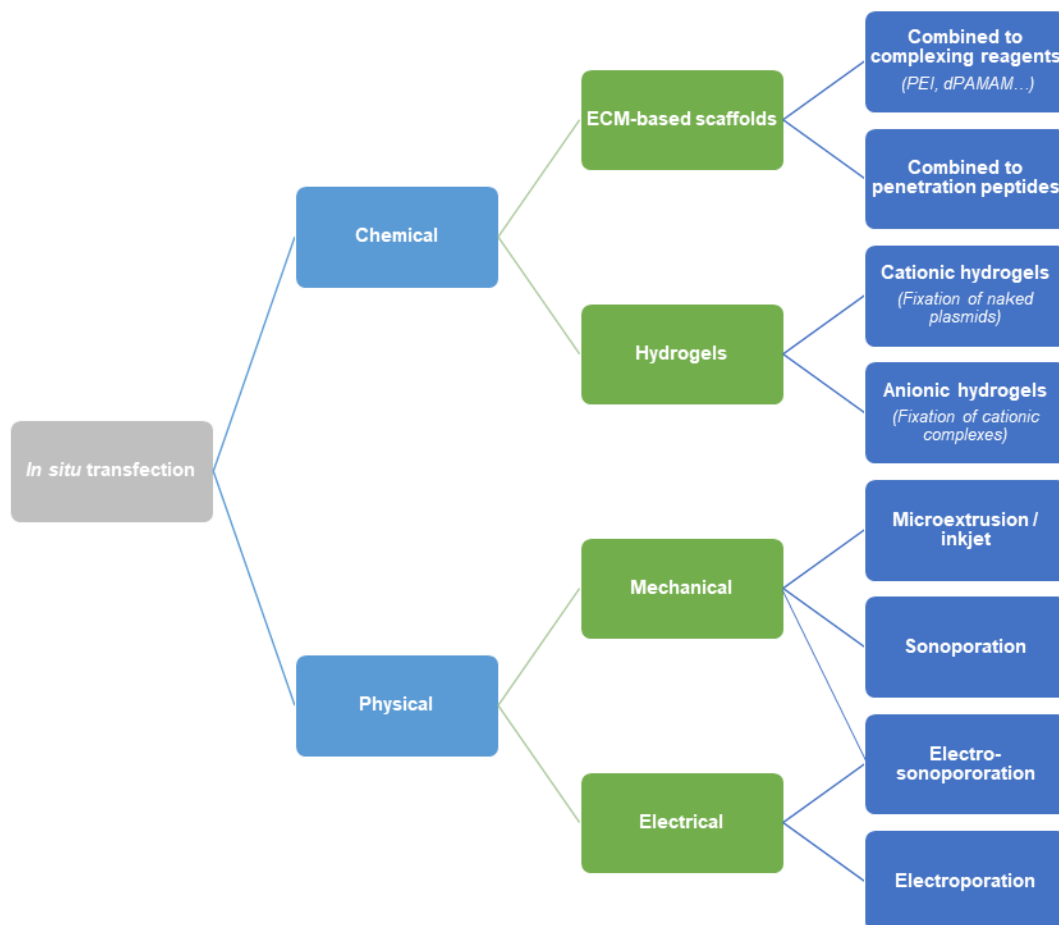


**Figure 1.17:** Methodologies applied for *in-situ* and *in-vivo* transfection both chemically and physically mediated.

**Collagen-based scaffolds'** interaction with nucleic acid was enhanced thanks to their association with various cationic polymers and particles [460,461]. Collagen was impregnated with complexes formed with **PEI** [461], **acetylated PEI (PEI-Ac80)** [440], **dextran-spermine cationic polysaccharide** [462], **modified cyclodextrin nanoparticles** [463], **polyamidoamine dendrimer (dPAMAM)** [456,464], **cationized gelatin** [465], or **chitosan** [466].

**Chitosan** demonstrated interesting properties for *in situ* transfection when combined with **collagen-based scaffolds** [437,444,466]. Chitosan is a natural cationic polysaccharide derived from chitin [467]. It was proved to have lower cytotoxicity than PEI, poly-L-lysine (PLL), or Lipofectamine [451,452,468,469] achieving viabilities of 60-90 % compared to viabilities > 40% with Lipofectamine in HEK cells [452]. Chitosan-DNA complexes favor cellular uptake and protect plasmids from DNase I degradation [451,466] . They demonstrated good transfection efficiency in 2D and *in vivo* [470,471]. Using **collagen-based scaffolds** soaked with **chitosan-plasmid complexes** proved its efficiency *in vitro*, with transfection sustained for up to 4 weeks [466]. Complexes' charge, diameter, and zeta potential have to be

wisely chosen as they impact transfection efficiency [453,466]. Chitosan molecular weight and deacetylation degree strongly affect these parameters [453].

**Collagen sponges** have also been formulated with **nano-hydroxyapatite (nHA)** particles [457,463,472–475]. The role of **nHA** was to offer better support for cell adhesion and proliferation, inducing improved cells to polyplexes contacts [472]. Additionally, pDNA complexation by nHA was already demonstrated in 2D cultures [476]. It was mainly used in bone tissue engineering to transfect MSC or pre-osteoblast cells [461,473,477,478]. In these cases, nHA particles were demonstrated to have a leveraged activity on the transfection efficiency. Indeed, 20% to 88% of interference on the GAPDH reporter gene was measured over 7 days on 3D collagen-nHA scaffold cultures containing micro-RNA (miRNA) nanomiR-mimics and nanoantagomiRs [478]. Nevertheless, cytotoxic effects were demonstrated for nHA particles diameters higher than 70 nm, both in 2D [479] and 3D cultures [457,478].

**Collagen-based scaffolds** were then associated with **lipidic transfection reagents**. Two commercial lipidic reagents, 3DFect, and 3DFectIN, were explicitly designed for *in vitro* 3D transfections [480]. These reagents can complex pDNA or small interfering RNA (siRNA) to form lipoplexes later incorporated into hydrogel formulations or loaded on scaffolds. Several 3D cultured cell lines reported efficient transfection on collagen-based scaffolds with these two lipidic reagents. All cell lines expressed transgenic alkaline phosphatase above 75 pg/ $\mu$ L, while expression was sustained over 5 days [480].

**Gene-Activated Matrices combined with penetration peptides** is a novel strategy incorporating **synthesized penetration peptides** in **collagen-based** scaffolds. Such penetration peptides have also been reported for *in situ* transfection in other matrices, such as alginate-methylcellulose hydrogels [481]. They are highly promising as they allow the GAM formulation with biocompatible and non-cytotoxic materials while avoiding chemicals. Such penetration peptides are small peptides of less than 30 amino acids, rich in arginine groups [482]. The arginine residues confer a positive charge to the peptides, favoring interactions with negatively charged nucleic acids and cell membranes. Penetration peptides can cross the cell membrane by different mechanisms to travel through the cytoplasm and enter the nucleus [483]. The interaction of arginine groups with cell membranes enhances the internalization mechanism by micropinocytosis. Direct translocation through the cell membrane is also possible [484,485]. This ability is not altered when binding with small molecules such as pDNA or siRNA

[482,483,486,487]. Since 2019, literature has reported three types of penetration peptides evaluated for *in vitro* transfection of 3D cultures: star-shaped polypeptides [488], GAG-binding Enhanced Transduction peptides (GET peptide) [482,489], and RALA peptide (Arg-Ala-Leu-Ala repeats) [458]. It is worth mentioning that the RALA peptide was developed and optimized based on previously synthesized penetration peptides GALA (Glu-Ala-Leu-Ala repeats) and KALA (Lys-Ala-Leu-Ala repeats) [490,491]. In this peptide sequence, the presence of cationic hydrophilic arginine and hydrophobic leucine residues gives an amphipathic character to the peptide. These allow penetrating and fusogenic properties [492]. This peptide was used to form RALA-siMMP-9 complexes incorporated within a collagen/GAG scaffold. It was evaluated *in vitro* as a potential matrix-metalloproteinase 9 (MMP-9) downregulating treatment for diabetic ulcer healing [458]. This scaffold demonstrated good cytocompatibility and an efficient MMP-9 downregulation of 40-60 % in 3D cultures [458]. Other penetration peptides, such as HALA (His-Ala-Leu-Ala repeats), have been optimized to increase transfection efficiency in 2D. They could be good candidates for *in situ* transfection of 3D cultures [375,491].

**Numerous applications of collagen-based GAMs for *in vivo* transfection** have also been reported. First *in-vivo* and *in situ* transfections using GAMs were performed with collagen scaffolds containing plasmids to repair bone defects [493,494]. In these conditions, pDNA entrapped in collagen sponges allowed efficient transfection *in vivo* after implantation (30 to 50 % of transfected cells) [493,494]. Bone and cartilage repair as well as enhancement of angiogenesis are the most reported applications for *in vivo* transfection with GAMs. In this purpose, collagen matrices were used for *in vivo* transfection associated with naked plasmids [493,494], dPAMAM-plasmid complexes [464] or even with penetration peptides-nucleic acids complexes. An interesting example of *in vivo* application of GAM incorporating penetration peptides used **GET/pBMP2/pVEGF** complexes coding for Bone Morphogenetic Protein 2 (BMP 2) and Vascular Endothelial Growth Factor (VEGF). This GAM demonstrated efficient *in vivo* transfection leading to faster regeneration of large bone defects within four weeks [482]. Other examples of efficient *in vivo* transfection used collagen-based GAMs combined with RALA or star-shaped poly(L-lysine) penetration peptides [481,488]. Then, broadening to ECM biomolecules, De Laporte et al. (2009) screened different **ECM proteins to coat poly(lactide-co-glycolide (PLG) scaffolds for plasmid delivery *in vivo*** to treat spinal cord injury [459]. Lipoplexes made of transfast® reagent and pDNA coding for luciferase were efficiently delivered to cells thanks to surface coating with collagen I, fibronectin, or laminin [459]. The highest transfection efficiency was obtained with fibronectin-coated scaffolds with 10- or 100-times increased luciferase activity (RLU/mg protein) than in collagen-or laminin-coated

scaffolds. Other studies evaluating the DNA-PEI complexes uptake by cells growing on collagen or fibronectin-coated surfaces in 2D cultures confirmed such results [460,495].

In every *in vivo* transfection procedure, prolonged transgene expression was detected for at least 3 to 6 weeks, depending on the specificities of the scaffold.

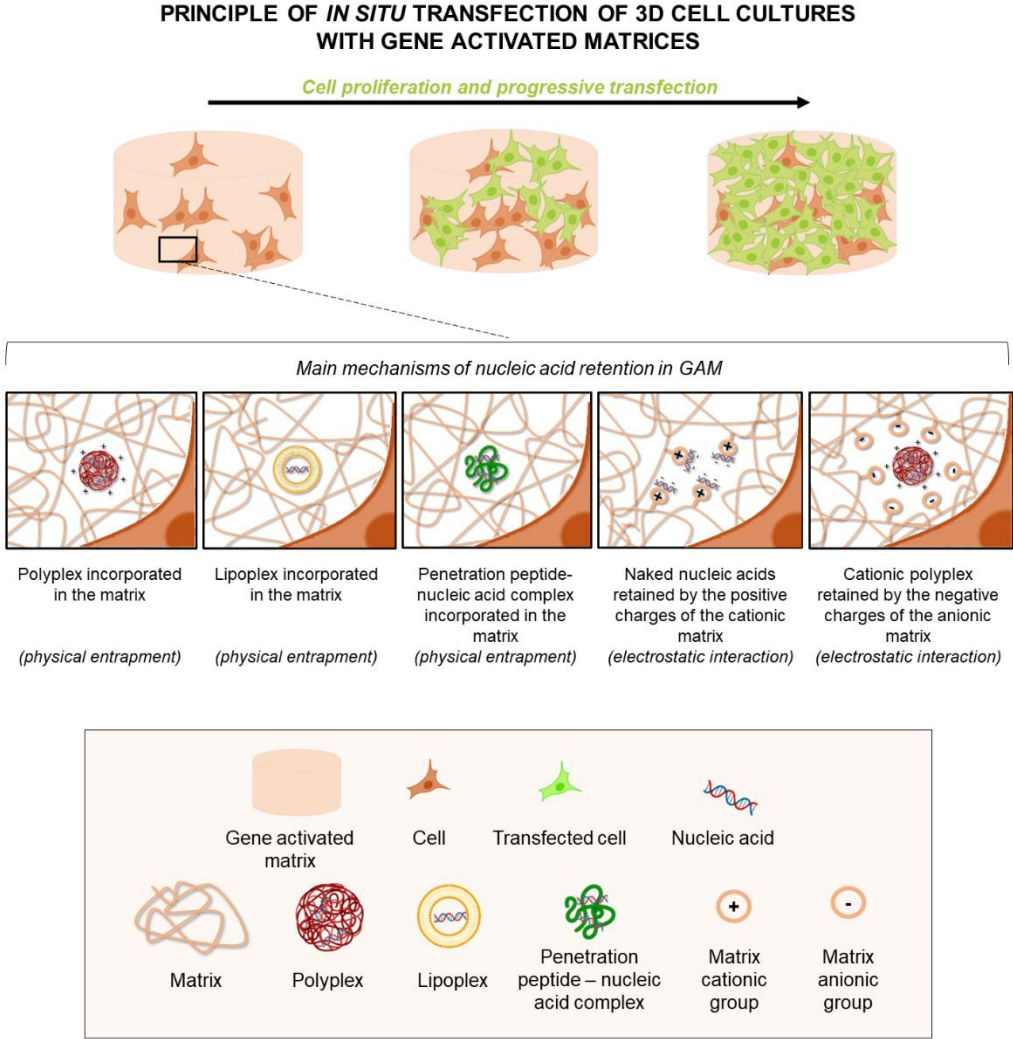


**Figure 1.18: Principle of *in situ* transfection in GAMs (Gene Activated Matrix).** The cells get progressively transfected while growing in the matrix in which they are encapsulated. The figure presents several options to immobilize nucleic acids: stabilizing polyplexes, lipoplexes, or complexes formed with penetrating peptides within the matrix and the direct immobilization of nucleic acid or polyplexes thanks to electrostatic bonds with the charged biomatrix carrying either cationic or anionic groups.



## Charged synthetic GAM as complexing agents

Another type of GAM was developed for *in situ* transfection to prevent the use of complexing agents impregnated or formulated in the matrix. Modified hydrogels were prepared to present cationic charges, thus allowing the hydrogel to act as a condensing agent itself. Few studies demonstrated that cationic hydrogels and scaffolds could retain nucleic acids [455,496].

**Cationic scaffolds** formulated from **cationized gelatin (CG)** were used for *in vivo* transfection [447,448,496]. **Cationized gelatin (CG)** is produced by **covalent bonding** between the carboxyl group of gelatin and a primary amine to form an amide bond. The activation of gelatin carboxyl groups can be performed with 1-ethyl-3-(3-dimethyl aminopropyl) carbodiimide hydrochloride salt (EDC) and a successive hybridization with an amino group, such as ethylenediamine [448,496–498], putrescine, spermidine or spermine [498]. Consequently, the amino groups provide positive charges to the scaffold, forming electrostatic bonds with negatively charged phosphate groups from nucleic acids. The physicochemical environment of the interaction between DNA and **cationized gelatin (CG)** was proved to impact the complexation of the pDNA significantly. The formation of CG-pDNA complexes in either 5% glucose or phosphate-buffered saline solution (PBS) strongly influenced the particle's zeta potential and the transgene expression [496]. Indeed, CG-pDNA polyplexes formed in 5% glucose had ten times higher zeta potential, leading to a 5-fold increase of transgene expression compared to complexes formed in PBS [496].

In 2002, proof-of-concept studies demonstrated the stabilization of plasmid encapsulated in **cationized gelatin (CG)** over seven days post-implantation *in vivo* [448,496]. Then, the pDNA was progressively released during the hydrogel degradation. Plasmid content in CG hydrogels decreased over time, stabilizing at 40% after 20 days. This nucleic acid's release rate was demonstrated to depend on CG hydrogel water content and its crosslinking degree. Indeed, DNA release was faster when crosslinking with a reduced amount of glutaraldehyde, thus inducing an increased hydrogel water content. Other examples of successful *in vivo* **implantation of gene-activated cationic gelatin** leading to local cell transfection in mice and rats can be found in the literature [448,496,498]. In 2011, cationized gelatin transfected rabbit chondrocytes in **3D *in vitro* cultures** [497]. Here, the authors modified the surface of an electrospun poly(L-lactic acid) (PLLA) scaffold nanofibers with cationized gelatin. They

demonstrated that rabbit articular chondrocytes' viability, proliferation, and differentiation increased compared to non-modified PLLA nanofibers.

Similarly to cationized scaffolds, **anionic scaffolds** were used to bind nucleic acid-cationic polymer complexes to perform **3D cell culture transfection *in vitro***. In 2011, a study presented negatively charged gelatin to bind luciferase coding plasmid DNA complexed with cationic polymers [447]. The gelatin was prepared by covalent bonding with succinic anhydride. It was first **evaluated on 2D cultures** by reverse transfection on anionic gelatin-coated plates with the tracking of luciferase activity. The plasmid-pullulan/spermin cationic complexes bound to negatively charged gelatin exhibited a 10-fold increase in luciferase activity compared to the conventional transfection method in the presence of serum. **In 3D cultures** the negatively charged scaffold acted as immobilization support for cationic complexes. Luciferase expression levels equivalent to those measured in 2D reverse transfection were also measured in 3D PET and collagen scaffolds coated with anionic gelatin and pullulan/spermine-pDNA complexes, demonstrating the applicability of this method for *in situ* transfection [447]. The enhanced transfection efficiency was suggested to be due (i) to a better immobilization of cationic complexes by electrostatic interactions with negatively charged matrix and (ii) to a facilitated release of plasmids thanks to the destabilization of electrostatic interactions between the plasmid and cationic complexes by anionic groups of gelatins.

Based on the same principle, co-electrospun scaffolds of polycaprolactone (PCL) coated with **anionic alginate** were used to immobilize PEI-pDNA complexes [499]. Cationic polyplexes were here forced to interact with the anionic alginate under a direct current electric field. These scaffolds supported cell proliferation and were used for *in situ* gene delivery to HEK cells.

**Various innovative scaffolds can be used for chemical *in situ* gene delivery. Even though GAMs are up-and-coming tools for *in situ* transfection and have shown promising results, the transfection efficiency in 3D cultures and tissues is still way lower than what can be reached in 2D or suspension cultures. Indeed, in conventional 2D transfection protocols, transfection efficiencies are usually considered satisfactory when getting over 60 to 70% of transfected cells and can easily reach more than 90% with negligible cytotoxicity. On the contrary, for 3D cultures and tissues *in situ* transfection, the transfection efficiency rarely exceeds 20%, which is already considered a high transfection rate. Papers reporting over 30% of cells transfected *in situ* are less than a dozen, and none reached 60% transfection. Thus, favoring cell adhesion and proliferation on the scaffolds might increase transfection efficiency. Here, synthesized cationic scaffolds are identified as a real**

advantage. They are characterized by an increased cationic amino groups content which offers better cell adhesion and increased proliferation, as well as improved stabilization of naked plasmids by electrostatic interactions [500–504]. However, it is essential to note that the zeta potential of cationic polymers must be optimized as zeta potentials under 10 mV or over 17 mV can respectively reduce cell adhesion and cause cytotoxicity [453,501,503]. *In vitro*, it is well known that cell growth in 3D macroscopic structures is limited. Such limitation is mainly due to poor diffusion of nutrients and oxygen in the 3D scaffold and poor elimination of metabolic waste. Little cell growth could prevent *in situ* transfection in 3D cultures. Optimized addition of growth and signaling factors have been tentatively used to enhance cell proliferation in 3D cultures. The use of bioprocess and perfusion bioreactors has also been a promising strategy. Thus, many custom culture systems have been developed to culture 3D cellularized scaffolds, aiming to either increase the dynamic diffusion of nutrients and oxygen in the scaffolds or provide optimized culture parameters (temperature, pH, oxygen) [505,506]. Such tools would be interesting for cells cultured on GAMs as increased cell proliferation would surely lead to increased and sustained transfection, with cells getting in contact with the plasmids as they spread and colonize the matrix.

#### 1.4.5. *Physical in situ & in vivo transfection*

Physical transfection methods have been used since the mid-‘80s to generate mechanical, electrical, thermic, or magnetic stresses on the cell membrane and induce the formation of transient pores [369,507], favoring naked nucleic acid uptake [397–399]. Electroporation (electric field) or sonoporation (ultrasonic waves) are the two most common physical transfection methods for unspecific gene transfer in large cell amounts (mass transfection). Physical transfection techniques for medical applications present the advantage of avoiding the introduction of chemical reagents into the body. Thus, the first *in vivo* transfection trials using such an approach were reported at the end of the ‘90s [400,508–512]. Ten years later, the first physical transfusions were applied to 3D cell culture models [513,514].

#### **Electroporation, sonoporation, and electro-sonoporation**

Transfection by **electroporation**, also called electro-transfection, consists in exposing the cells to an electric field and creating transient pores in the cell membrane. The electric field perturbs negatively charged membrane tension [515]. The membrane is then destabilized

with local and temporary disruption. Two hypotheses co-exist to explain DNA uptake during electroporation. First, pDNA entry occurs through the cell's permeated membrane via an electrophoresis phenomenon which is favored due to nucleic acids charge. Second, the endocytosis pathway is electro-stimulated [516]. **Sonoporation** uses ultrasonic pulses to create microbubbles pulsating near cells and mechanically increasing membrane permeability. Thus, small molecules such as nucleic acids can enter the cell membrane [517,518]. **Electro-sonoporation** combines **electroporation and sonoporation while cells are simultaneously subjected to ultrasounds and an electric field** [519].

In the last 20 years, numerous works have presented electroporation and sonoporation for *in vivo* applications [400,508–512,520–524]. Nevertheless, only a few have reported physical transfection of 3D macroscopic cell cultures *in vitro* [401,513,514,525–527]. *In vivo*, electroporation was assessed on multiple tissues such as muscles [508], liver [511], or skin [512]. *In vivo*, tissue transfection by electroporation achieved very low transfection efficiency, reaching less than 6% of cells transfected [446,527]. Additionally, concomitant tissue damage, inflammation, and necrosis by exposition to a voltage above 50 V with 16 rectangular pulses of 50 ms width and 75 ms interval were observed by histological staining of tissue sections [508,528,529]. The damages can also be evaluated by measurement of tissue thinning and fibrosis, testifying of tissue degradation, and scarring [529]. In this case, it was reducing the frequency of electric pulses from 150 kHz to 100 kHz, which allowed to decrease damages by half. Electric pulse duration was identified as another key parameter to be optimized to avoid tissue damage and maximize the transfection rate. Indeed, shorter pulses demonstrated less cytotoxicity and reduced transfection efficiency [527]. Higher electro-transfection efficiencies reaching **up to 15% of the cells transfected with high viability (85%)** were achieved *in vitro* with a 3D printed system for electroporation of 3D cell cultures [401]. The matrix comprised a commercial peptide hydrogel (PGmatrix from PepGel company) in which the cells and plasmids were embedded. The 3D printed chamber allowed micro-perfusion of the tissue. Four flat electroporation electrodes could be inserted into the chamber to generate multidirectional electric frequency scanning. A multidirectional electric field was shown to favor transfection by efficiently permeating the cell membrane.

Higher *in vivo* transfection efficiency was achieved by **electro-sonoporation** [403]. This comparative study evaluated electroporation, sonoporation, or electro-sonoporation for *in vivo* mice muscle transfection with luciferase coding plasmid. In the optimal transfection conditions, electro-sonoporation showed better results than electroporation alone, with more than a 2-fold increase in luciferase activity after 3 days, or sonoporation alone, which did not allow to transfect mice muscles (no luciferase activity detected). Tissue damage due to electric pulses

was evaluated by Hematoxylin-Eosin staining of muscle sections and significantly reduced in the case of electro-sonoporation. However, some superficial tissue damages caused by the electric pulses were still visible and could be problematic for medical applications. A novel *in vivo* transfection strategy was developed in 2011 to reduce the tissue damage caused by physical transfection. This method uses a **degradable micro-needle filled with pDNA and an electroporation electrode** [530]. This technique demonstrated promising results in mice with local subcutaneous transfection leading to interleukin-12 expression and tumor regression, with minimal damage to the tissue (micron scale holes).

### **Shear stress**

Several studies describing the impact of **shear stress** on cell physiology demonstrated that it could generate transient cell membrane permeability, enabling plasmid uptake [402,531–533] and enhancing endocytosis pathways [534]. Recently, one proof of concept allows transferring such behavior to 3D cell culture through bioprinting [402]. However, the physical and mechanical stresses suffered by the cells are also resulting in lower cell viability.

Exploiting the effect of shear stress on membranes, efficient cell transfection during inkjet bioprinting of CHO cells, reaching **31.5% of cells expressing transgene with low apoptosis (3.5%)**, was reported in 2010 [402]. Only three years later, even higher transfection efficiencies were reported by micro-extrusion with **alginate hydrogels** for transfection of mesenchymal stem cells with naked BMP-2 encoding plasmids [436]. Micro-extrusion-based bioprinting induces shear stress thanks to flow rate, nozzle geometry, and hydrogel mechanical properties [532,535]. This process allowed up to **46% of transfected cells** [436]. Later, in 2018, micro-extrusion-based 3D printing was used to transfect fibroblasts [533]. Fibroblasts were successfully transfected during the bioprinting process with naked Fox3D plasmids, coding for the genes Sox2, Sox10, Oct4, and Nanog. The fibroblasts were then further reprogrammed into neural crest-associated cells. In this case, the micro-extruded matrix was a **polyurethane hydrogel (PU)**. An optimal shear stress of 190 Pa was identified, generating transfection efficiency and cell viability of 15.6% and 65%, respectively. Based on the same principle, in 2020, human umbilical cord-derived mesenchymal stem cells (hUC-MSCs) were transfected by micro-extrusion in PU hydrogels containing naked GATA binding protein 4 (GATA4) plasmids [536].

**This literature review supports that physical transfection methods allow local transfection *in vivo* and *in vitro* on 3D cell cultures. The procedures are commonly close to standard**

transfection protocols applied to suspension cultures. These procedures present the advantage of avoiding chemical use. However, they are generally responsible for significant cell/tissue damage from exposure to physical/mechanical stresses. These damages can be limited when optimizing the procedure's parameters like frequency/duration of electrical pulses, field voltage for electroporation, ultrasounds frequency/flow rate for sonoporation, nozzle geometry/hydrogel mechanical properties for micro-extrusion [532,535].

Physical transfection methods have several drawbacks regarding *in vitro* 3D cultures or *in vivo* applications. First, the transfection efficiency is commonly very low (< 15%) and localized. Current tools target the superficial scaffold layers, with very few to no cells transfected in deeper layers. Then, when trying to reduce the cell damage by adjusting the protocol parameters, the transfection efficiencies are also reduced.

#### 1.4.6. Future applications for *in situ* transfection

*In situ* transfection studies reviewed in the literature have mainly targeted gene therapy applications in regenerative medicine. These studies applied primarily for *in vivo* or *in vitro* transfection of engineered tissues with signaling factors for growth, differentiation, or angiogenesis [442,443,445]. They used *in situ* transfection for the evaluation of treatment for diseases or cancers thanks to the expression of proteins of interest or gene silencing [353–355]. However, *in situ* transfection shows excellent potential for other application fields, such as studying tissue morphogenesis or cellular physiology in 3D.

Among the different methods proposed in the literature, gene-activated matrices seem the most promising approach for future applications of *in situ* transfections. It offers the localizable, progressive, and continuous transfection of cells in 3D macroscopic tissues (Figure 1.19). These advantages are precious in the case of sizeable 3D cell cultures > cm<sup>3</sup> or *in vivo* cell transfection.

First, it could support research and development for tissue engineering and regenerative medicine. Indeed, the comprehension of cell growth and spreading in 3D matrices are still minimal. They are commonly evaluated at the end of the culture, thanks to destructive histology slicing. No other non-destructive monitoring tools for depth detection within 3D structures are available. We believe that gene-activated matrices could support the understanding of tissue morphogenesis. Indeed, cell transfection occurs in the activated matrix while cells are spreading, allowing for progressive gene release and transfection [448,494] (Figure 1.19).

GAM could be applied as a research tool to study and monitor cell proliferation in their 3D environment if cells are transfected with genes coding for reporter proteins such as fluorescent or luminescent proteins. While cells colonize and spread within their matrix, their progressive transfection and detection would allow cell proliferation and organization monitoring. Also, while the 3D matrix retains both cells and DNA segregated in a single location, this strategy allows for very localized transfection. Such very local transfection can enable the creation of complex structures which bring together different types of cells (transfected/untransfected) to study their biological interactions. It is particularly true for GAM matrices that could be 3D precisely localized thanks to 3D bioprinting. We could also imagine producing GAM with multiple targeted genes for local expression of biochemical cues for cell organization. Such a strategy would allow scientists to screen the effect of numerous factors in a 3D culture and accelerate tissue engineering research strategies.

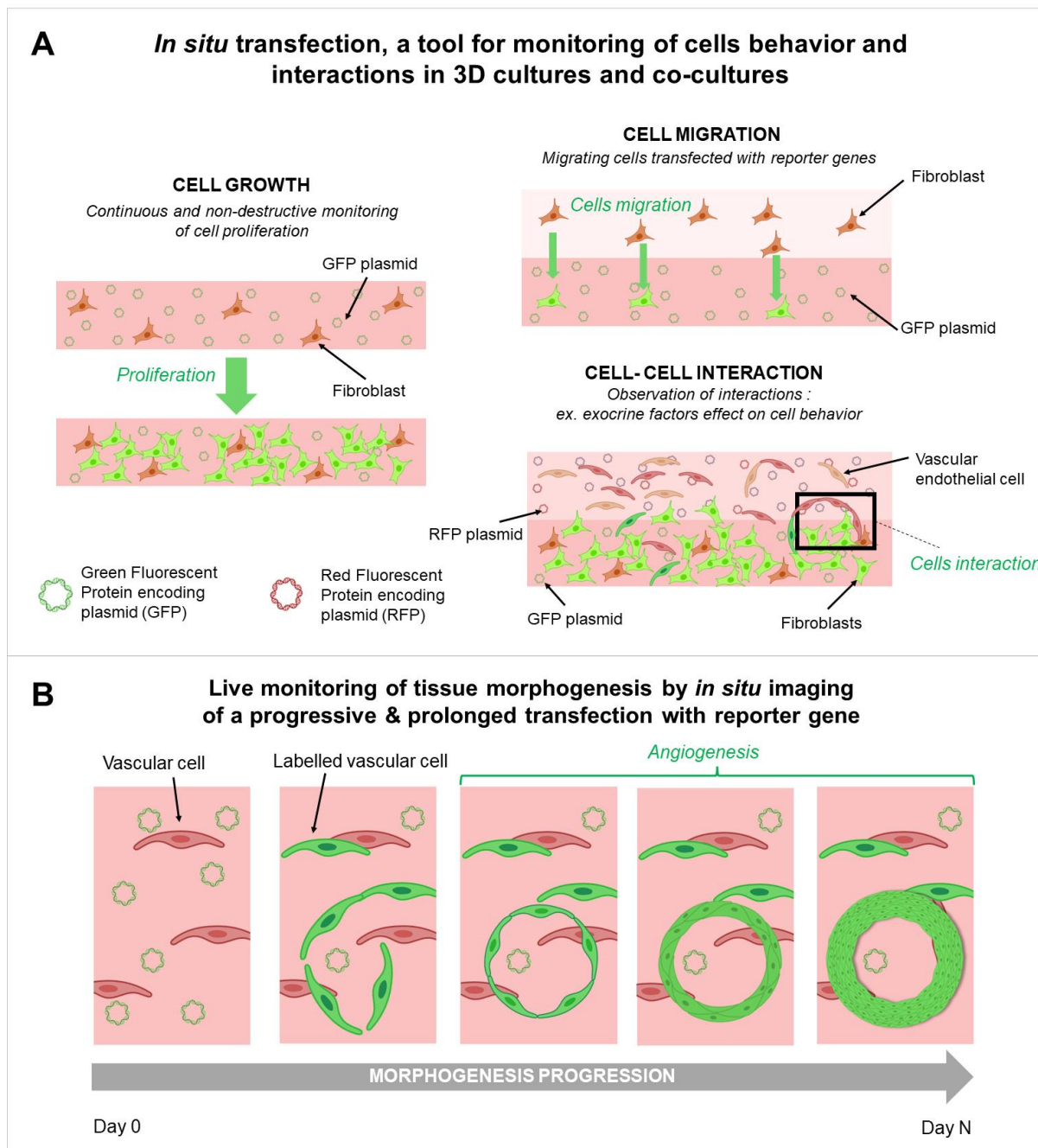


**Figure 1.19: Prospects for implementing and using *in situ* 3D transfection strategies in biomedical, morphogenesis, and tissue engineering research.** A- Application to understanding cell proliferation, cell migration, and cell-to-cell communication B- Application to the *in situ* tissue morphogenesis and cell organization monitoring.

Second, such tools aim at extending the duration of cell transfection. Such a strategy has direct applications for protein expression and fundamental research allowing for more extended experiments (> 48h transfection), but it is also valuable for biopharmaceutical industries.

Recently, *in vivo*, transfection to produce therapeutic molecules within patient host cells has gained substantial interest. The most recent proof of concept is the production of anti-covid vaccines based on intramuscular injection of lipoplexes of messenger RNA (mRNA) coding for the viral spike protein of SARS-CoV-2. Such a breakthrough in vaccine application paved the way for other viral antigen introduction for their expression by the body [537–540]. Similarly,



considering the therapeutic field of monoclonal antibody-mediated treatments, Andrews *et al.* (2017) provided a proof-of-concept of a therapeutic approach using *in vivo* electroporation transfection. In this approach, *in vivo* transfected mice expressed L and H antibody chains of anti-Influenza and anti-Ebola monoclonal antibodies. Mice then demonstrated significantly high survival rates compared to control groups after exposition to the viruses, with up to 90% (anti-Influenza) and 95% (anti-Ebola) survival [541]. The main limitation to such therapeutic approaches remains the nucleic acid stability within the body and their short-expression period [540]. Here, the GAMs could enable prolonged DNA/RNA stability *in vivo* for a more durable and progressive transgene expression and attenuated immunogenic reactions.

**This review describes how *in situ* 3D cultures and tissue transfection presents great promise for gene therapies and regenerative medicine. However, we still lack some understanding of the phenomenon underlying cell transfection in 3D configuration, especially in the presence of GAMs. Additionally, available analytical tools lack the precision to evaluate transfection efficiency. Indeed, in standard 2D or suspension protocols, transfection efficiency is commonly assessed by measuring the percentage of transfected cells in the whole population thanks to microscopy or cytometry tools. In 3D cell structures and tissues, evaluating the number of transfected cells is often complicated, especially in a non-destructive way. Most *in situ* transfection studies do not provide quantitative data on the percentage of transfected cells (see Table 1.8). The transfection efficiency is mainly evaluated by measuring the transgene's expression level by comparison with control levels. In the case of tissue repair applications, transfection efficiency was assessed thanks to qualitative aspects of the tissue compared to non-transfected protocol. It is thus challenging to compare the protocol's efficiency presented in the different published studies where the *in situ* transfection protocols, transgene, cell type, and cell density can differ. To further investigate the efficacy of the reported *in situ* methods, strategic work of the scientific community has to be done to develop better analytical tools enabling standardized, reproducible, and comparable evaluations of 3D cell culture transfection.**

#### 1.4.7. Conclusion

1.  
In the frame of gene therapy and regenerative medicine, three-dimensional cell culture models are preferred over two-dimensional models as they better represent cell behaviors and interactions observed *in vivo* [244]. Consequently, to provide relevant models, the transfection

of cells in 3D cellularized structures is of high interest since it can enable a local, progressive, and continuous modification of the cells while colonizing the 3D system. It offers interest for local therapies as the host cells will be transfected with the therapeutic gene of interest. *In situ*, transfection would be a valuable method for progressive gene delivery in 3D cell cultures for tissue engineering. Still, it could also be a useful analytical tool for analyzing cell spreading in 3D structures. Finally, *in situ*, transfection offers great perspectives in biopharmaceutical fields for new bioproduction methods *in vivo* or personalized biomolecule production in 3D cell cultures. Using Gene-Activated Matrices seems particularly promising among the different *in situ* transfection methods. However, the transfection efficiencies in 3D and *in vivo* are still far from what can be achieved in 2D cultures. Critical optimization work must still be carried out to increase the efficiency of such protocols and the GAMs formulation. The following strategic and missing step will describe the mechanisms of nucleic acid uptakes, protection, and transport during 3D *in situ* transfection.

## OBJECTIVES

This project introduces an innovative bioproduction strategy based on 3D bioprinted cell cultures, with the aim of evaluating their potential for recombinant protein production and their capacity to overcome current biomanufacturing challenges. The project has four primary objectives:

- 1) Contextualization: To identify the context, state of the art, and challenges relevant to this project.
- 2) 3D Bioprinted Cultures: To develop, describe, and optimize 3D bioprinted cultures with various production cell lines.
- 3) Bioreactor Setup: To develop a dedicated bioreactor setup for scaling up bioprinted cultures and recombinant protein production.
- 4) In Situ Transfection: To establish an efficient in situ transfection protocol.

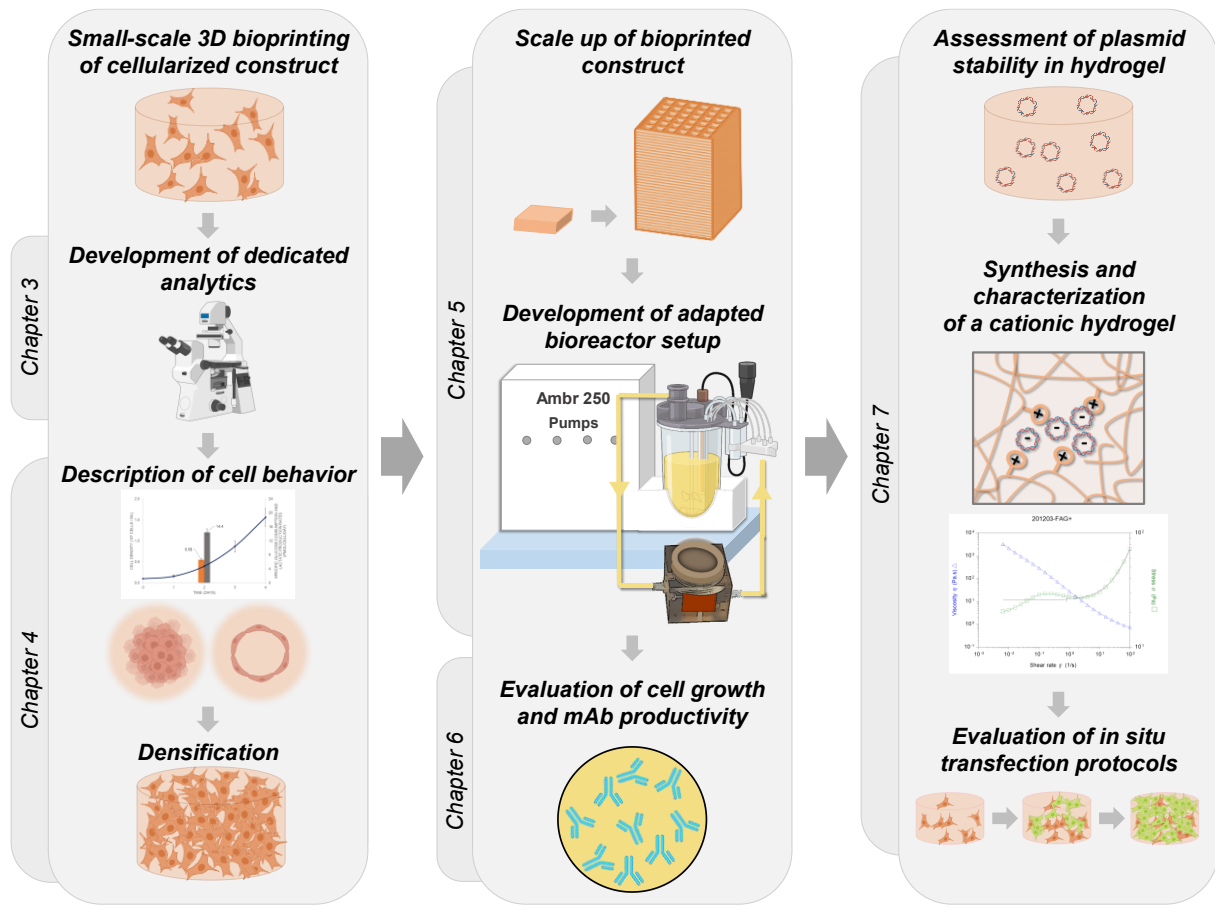
The contextualization and state of the art were presented in the bibliography (Chapter 1), covering the evolution and advances in biopharmaceutical production, 3D cell culture / bioprinting, and in situ transfection. This chapter aims to provide insight into the current limitations of biomanufacturing that this project seeks to address and the key advantages of 3D bioprinting and in situ transfection.

The project's primary technical focus is on establishing and characterizing a 3D bioprinted culture model with various bioproduction cell lines. This development requires specialized analytical tools and will be conducted at a small scale to screen cultivation conditions. This will be detailed in the first two results chapters (Chapter 3 & 4).

Subsequently, to assess the potential of 3D bioprinted cultures for "large-scale" production, we aim to scale up the cultures and transition to an "industrial-like" process condition. This will involve customizing two traditional bioreactor systems and developing a novel setup suited for the culture of 3D bioprinted constructs. We will also investigate the capacity for recombinant protein production using this technology (Chapters 5 and 6).

Finally, the last chapter of results (Chapter 7) will focus on the exploration of in situ transfection potential for prolonged insertion of genetic material in cells entrapped in the bioprinted constructs.

The project will conclude with a general discussion of the results and proposals for future investigations and advancements in the developed technology.



**Universal bioproduction platform for flexible manufacturing of multiple rProteins**

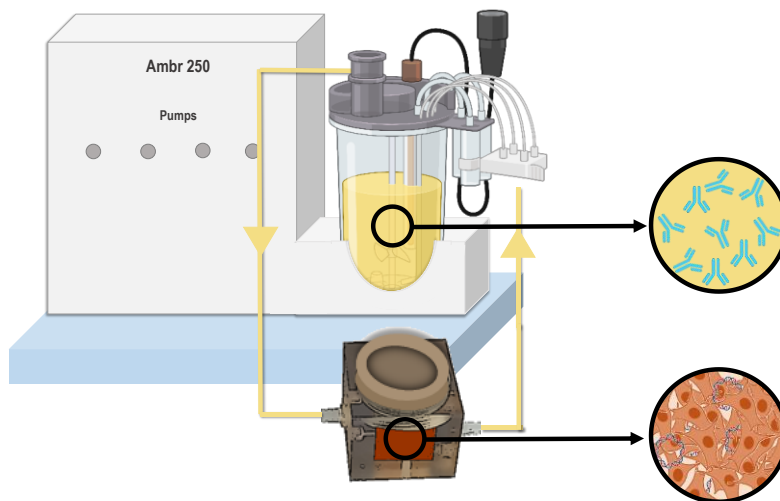


Figure 1.20: Graphical Abstract presenting an overview of the main steps of the project

## CHAPTER 2. MATERIAL & METHODS

### 2.1. Culture media and cell lines

#### 2.1.1. *Culture media preparation*

Dulbecco's Modified Eagle Medium (DMEM) already supplemented with glucose at a concentration of 4.5 g/L, GlutaMAX™ and pyruvate (31966-021, Gibco, Thermo Fisher Scientific, United States) was further supplemented with 10% FBS (A3160802, Gibco) and used as the standard medium for amplification of adherent mammalian cell cultures in 2D and in 3D bioprinted constructs. This medium will be designated as DMEM(+) to highlight the presence of calcium ions, in opposition to DMEM(-) which will be used to label a DMEM medium depleted from calcium ions. DMEM(-) was prepared with calcium-free DMEM supplemented with 10% FBS, 250 U/mL Penicillin/Streptomycin (15140122, GIBCO) and 5 µg/mL Amphotericin B (15290026, GIBCO) and was used for the preparation of bioinks.

CHO cells were amplified in 4Cell® Xtra CHO Stock and Adaptation Medium (SAM) (CQP3FA1114, Sartorius) serum-free medium. The 4Cell® Xtra CHO Production Medium (PM) (CQP3FA2115, Sartorius) was used for bioreactor cultures of CHO cells. Bioreactor cultures were regularly fed with 4Cell® Xtra CHO Feed Medium A (FMA) (CQP3FA3120, Sartorius) and 4Cell® Xtra CHO Feed Medium B (FMB) (CQP3FA4119, Sartorius). All 4Cell® Xtra CHO media were purchased in powder form. The media reconstitution protocol is detailed in Table 2.1.

The powdered media were quickly reconstituted in a demineralized water volume equivalent to 75 - 97% of the final volume. SAM and PM were supplemented with 6 mM GlutaMAX™ (35050061, Gibco). After media reconstitution pH was adjusted by measuring with pHmeter (HI 2221 Calibration Check pH/ORP meter ; Hanna Instruments). Finally, the media volume was adjusted to desired volume with a volumetric flask before sterile filtration on a 0.22 µm sterile PES membrane (Stericup Quick Release-GP, S2GPU05RE, Merck-millipore). All media were stored at 4 °C, protected from light. Sterility of filtered media was tested by incubating 2mL of media in a multiwell plate at 37°C for 2 days followed by microscopic observation for potential contamination detection. For sterility testing, FMA and FMB media were diluted in PM at 4% v/v and 0.4% v/v to avoid precipitation of concentrated feed solutions.

**Table 2.1: Detailed phases of the 4Cell® Xtra CHO media system reconstitution for 1 L of medium.** The expected osmolality of culture media (SAM and PM) are indicated for non-diluted media. The expected osmolality of feed media (FMA and FMB) are indicated for media solutions diluted to 1/5.

Medium	Mass of medium powder (g)	1st stirring duration (min)	2M NaOH Addition (mL)	5M NaOH Addition (mL)	2nd stirring duration (min)	Mass of buffering agent NaHCO <sub>3</sub> (g)	3rd stirring duration (min)	pH adjusted with	Targetted pH range	Expected osmolality (mOsmol/kg)	GlutaMAX™ Supplementation (mM)
SAM	20.0	60	3.0	0	30	1.8	15	2M NaOH	6.90 - 7.30	270 - 330	6
PM	22.3	60	0	6.2	30	1.8	15	2M NaOH	6.90 - 7.35	275 - 330	6
FMA	154.1	60	0	15.7	30	0	0	2M NaOH	6.50 - 6.80	208 - 268	0
FMB	94.6	60	0	160	30	0	0	5M NaOH	11.00 - 11.40	218 - 266	0

### 2.1.2. Cell lines

The experiments used four production cell lines: HEK, CHO, MDCK and Vero. The HEK cells were kindly provided by Dr. C. Maise-Paradisi (INRA-UCBL-EPHE "Viral Infections and Comparative Pathology," Lyon, France) and MDCK cells were provided by the academic laboratory VirPath (Centre International de Recherche en Infectiologie U1111 INSERM - UMR 5308 CNRS - ENS Lyon - UCBL1). The CHO DG44 (PTN1-CB-CC1; Cellca-Sartorius), VERO (CCL-81™; ATCC®) were acquired from manufacturers.

The HEK cells are a HEK293T adherent clone. The CHO cells are a CHO-DG44 host. It is a dihydrofolate reductase (DHFR)-deficient line co-transfected with an exogenous *dhfr* gene and a transgene coding for a recombinant protein of interest [100]. It is widely used for recombinant protein production due to the easy selection of high-producing clones with methotrexate (MTX) [100,542]. The clone PTN1-CB-CC1/ LP16CLONE 38 was used in the present project as a clone of stably transfected CHO DG44 expressing a transgene encoding for a therapeutic human IgG1. The IgG1 target will be kept confidential.

Cell lines characteristics and culture conditions are presented in Table 2.2.

**Table 2.2 : Characteristics, culture conditions and application of each cell lines**

	Species of origin	Species classification	Tissue of origin	Type of cell	Recommended culture mode	Temperature (°C)	CO <sub>2</sub> (%)	Humidity (%)	Agitated	Agitation Speed (rpm) – orbital diameter (mm)	Culture medium	Characteristics
<b>HEK</b>	Human	Mammalian	Kidney (Embryo)	Fibro-blastic, Endothelial, Epithelial or Neuronal	Adherent	37	5	80	No	N.A.	DMEM (+)	Immortalized Expresses SV40 large T antigen
<b>VERO</b>	Monkey (African green monkey)	Mammalian	Kidney (Adult)	Epithelial	Adherent	37	5	80	No	N.A.	DMEM (+)	Immortalized Sensitive to viral infection
<b>MDCK</b>	Dog (Cocker Spaniel)	Mammalian	Kidney tubule (Adult)	Epithelial	Adherent	37	5	80	No	N.A.	DMEM (+)	Immortalized Sensitive to viral infection
<b>CHO</b>	Chinese hamster	Mammalian	Ovary (Adult)	Fibroblastic	Suspension	37	7.5	80	Yes	130 - 25	DMEM (+) SAM PM FMA FMB	Immortalized DHFR-deficient Expresses human IgG1



### 2.1.3. *Cell lines amplification*

#### **Adherent cultures**

CHO DG44, HEK, MDCK, and VERO were always amplified in 2D cultures in previously described DMEM(+) medium. CHO DG44 sub-culture was performed by two means ; similarly to the other cell lines in 2D cultures for 3D bioprinting qualification (Chapter 4) and in suspension cultures with specific serum-free media for larger scale culture and experiments aiming to compare bioproduction in 3D with standard bioreactor processes (Chapter 6).

The cells were cultivated in T75 flasks (Corning) in an incubator with 5% CO<sub>2</sub>, 80% humidity, and 37°C. All cells were split twice a week. All cell types were tested mycoplasma-free. Sub-culture protocols used for adherent cell lines are presented in Table 2.3. The supernatant was discarded (HEK, MDCK, VERO) or collected to harvest suspended cells (CHO), as detailed in Table 2.3. Flask bottoms were gently rinsed with PBS (phosphate buffer saline, 14190169, Thermofisher Scientific) before adding Trypsin. The MDCK cell line being particularly tough to detach from the flasks, so a 1-hour incubation in PBS at 37°C was required before adding trypsin. Trypsin (15400054, Thermofisher scientific) was added to the flasks at a concentration of 0.5 g/L (1X) for all adherent cell lines except for HEK for which a 0.25 g/L (0.5X) concentration was used due to the sensitivity of this line to enzymatic damages. Cells were incubated with Trypsin at 37°C for 2 min (HEK, VERO, CHO) or 5 min (MDCK), and then a volume of DMEM(+) was added for Trypsin inactivation by serum proteases. The cell suspension was recovered in a 50 mL sterile tube and centrifugated according to conditions detailed in Table 2.3, to eliminate the Trypsin-containing supernatant. Cells were resuspended in 10 mL of fresh DMEM(+). Then viable cell density (VCD) was evaluated on a Malassez Hemocytometer with Trypan blue (15250061, Gibco) exclusion method. Targeted cell seeding concentration was adjusted by sampling the appropriate volume of cell suspension to add in a T-75 flask with an adapted volume of fresh media.

#### **Suspension cultures**

CHO cells were amplified in suspension with SAM serum-free medium prepared as described in section 2.1.1. Working cell banks were thawed in 10 mL fresh Stock & Adaptation Medium supplemented with 15 nM methotrexate (MTX) (M8407, Sigma-Aldrich) at 4°C and centrifuged at 190g for 3 min. Cell pellets were resuspended in 10 mL pre-warmed SAM supplemented with 15 nM methotrexate at 37°C. Viable cell density (VCD) was evaluated by cell counting on a Malassez Hemocytometer with Trypan blue (15250061, Gibco) exclusion method. Cells were seeded at a concentration of  $0.2 \times 10^6$  cell/mL in 250mL shake flasks

(431144, Corning) with 50mL working volumes or in 500 mL shake flasks (431145, Corning) with 150mL working volumes.

Cultures were grown in shaker incubator at 37°C with 7.5% CO<sub>2</sub> and agitated at 130 rpm with 25 mm orbital shaking. The medium was supplemented with 15 nM MTX for high-producing-clone selection for the first 3 splittings. Methotrexate was then removed from the medium until the end of the culture. Cells splitting was performed two-times a week, VCD was determined as previously described and an appropriate volume of cell suspension was used to inoculate a new flask at a concentration of 0.2x10<sup>6</sup> cells/mL. If the cell volume to use for inoculation was over 1/3 of working volume, cell suspension was centrifugated and concentrated in fresh medium before inoculation. CHO cells were used at the fifth passage for bioreactor experiments. Cells were used at the fourth or sixth passage for small-scale experiments

**Table 2.3: Protocol for recovery of cells in 2D or suspension cultures during splitting for amplification**

	Type of culture	Type of flask	Suspended cells harvest from supernatant	Incubation in PBS at 37°C <i>Yes/No - duration (hr)</i>	Trypsinization <i>Volume (mL) - concentration (g/L) - time (min)</i>	Volume of media for Trypsin inactivation (mL)	Centrifugation <i>Time (min) - speed (g)</i>	Cell seeding density	Volume of fresh media (mL per T75 or 500 mL SF)
<b>HEK</b>	2D	T-flask	No	No	2.5 - 0.25 - 2	5	5 - 300	12,000 cells/cm <sup>2</sup>	10
<b>VERO</b>	2D	T-flask	No	No	2.5 - 0.5 - 2	5	5 - 300	30,000 cells/cm <sup>2</sup>	8
<b>MDCK</b>	2D	T-flask	No	Yes - 1 hr	5 - 0.5 - 5	10	5 - 300	5,000 cells/cm <sup>2</sup>	8
<b>CHO</b>	2D	T-flask	Yes	No	2.5 - 0.5 - 2	5	3 - 190	200,000 cells/mL	12
<b>CHO</b>	Suspension	Shake Flask	Yes	No	N.A	N.A	3 - 190	200,000 cells/mL	100

## 2.2.Small-scale 2D and bioprinting experiments for cell line characterization

### 2.2.1. *Bioink formulation*

#### **Formulation of stock bioink components**

Stock solutions were prepared the day before bioprinting for better component dissolution and kept in an incubator at 37°C. Fibrinogen stock solution was prepared by dissolving 8% w/v Fibrinogen from bovine plasma (F8630-1G, Merck) in DMEM (-) medium. Alginate stock solution was prepared by dissolving 4% w/v Alginate (Alginic acid sodium salt with very low viscosity, A18565.36, Alfa Aesar) with DMEM(-), vigorous agitation after addition of the medium allowed to prevent formation of large aggregated alginate powder blocks which are difficult to dissolve. Gelatin stock solution was prepared by dissolving 20%w/v Gelatin from porcine skin (Sigma Aldrich, G1890) in DMEM (-) medium.

#### **Standard bioink formulation**

Targeted cell concentration was adjusted by pelleting the appropriate volume of cells at 300g (HEK, MDCK, VERO) or 190g (CHO) for 5 min. The pellet was resuspended in the appropriate volume of Fibrinogen solution. The proper volumes of Alginate and Gelatin solutions were further added to reach a final concentration in the bioink of 2%<sub>w/v</sub> Fibrinogen, 2%<sub>w/v</sub> Alginate, and 5%<sub>w/v</sub> Gelatin (Formulation A) or 2%<sub>w/v</sub> Fibrinogen, 1%<sub>w/v</sub> Alginate, and 10%<sub>w/v</sub> Gelatin (Formulation B). The cells and the three components of the bioink were mixed and homogenised by carefully pipetting with a viscous-liquid pipet. The bioink was then incubated for 10 min at 37°C before being poured into a sterile printing syringe. The bioink was then incubated for 30 min at 21°C (Formulation A) or at 28°C (Formulation B) before cellularized structures 3D bioprinting.

### 2.2.2. *3D Bioprinting*

#### **3D modelling of bioprinted structures geometry**

The bioprinted structures were designed by Computer Aided Design (CAD) using 3D modelling software TSIM (Advanced Solutions, Inc). The small-scale construct was drawn as parallelepipedal geometry of 0.2 cm<sup>3</sup> volume of bioink (1x1x0.2 cm), with or without porosity. The large-scale constructs geometries were designed with defined trajectories to guide the 3D printing process's path. They were shaped as meshed parallelepipedal volumes to create macro-porous structures, with a one-layer perimeter to ensure the structure maintain and cohesion. The design of large construct geometry and porosity has been the object of multiple optimizations that will be further detailed in Chapter 5.

Examples of biprinted constructs' CAD models are presented in Figure 2.1.

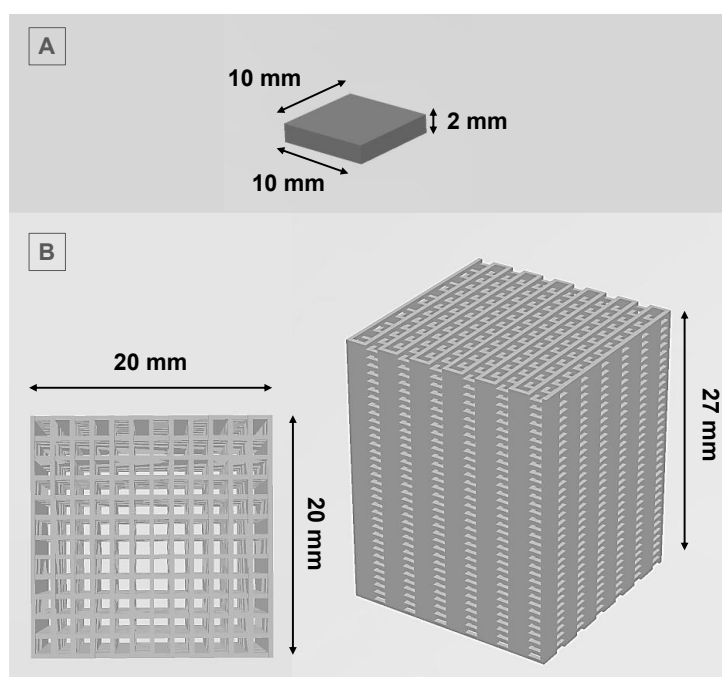


*Figure 2.1. : Examples of 3D CAD model of biprinted constructs at (A) small-scale (0.2 cm<sup>3</sup>) and (B) large-scale (10.8 cm<sup>3</sup>)*

### **Bioprinting procedure**

Thanks to a heating syringe holder, bioprinting was performed at 21°C for formulation A, corresponding to the ambient thermoregulated atmosphere, or 28°C for formulation B. The bioink structures were bioprinted by pneumatic micro-extrusion using a BioAssemblyBot 3D printer (Advanced Solutions, Inc). Pneumatic pressures ranging from 20 to 50 psi resulted in the formation of a smooth, continuous filament. The printing speed was set at 8 mm/s, and the acceleration of the printing nozzle was set at 300 mm/s<sup>2</sup>.

### **Hydrogel consolidation**

The biprinted constructs were consolidated with solutions of different compositions. All solutions contained CaCl<sub>2</sub> (C5670-500G, Merck) from 0.026 %w/v to 3 %w/v and transglutaminase (TAG) (ACTIVA WM, Ajinomoto) from 0.04 %w/v to 4 %w/v. Some solutions were supplemented with 10 U/mL thrombin (Thrombin from bovine plasma, t4648-10KU, Merck). The solutions were prepared in demineralised water, or DMEM medium (equivalent to 0.026 %v/w CaCl<sub>2</sub>), and sterilized by filtration. The composition of each solution used is reported in Table 2.4. The consolidation process was carried out at 37°C, 21°C, or 4°C

for 15 min or 60 min (Table 2.4). The cellularized structures were then rinsed twice with 0.9% NaCl sterile solution (Versol, PharmaService).

The complete procedure for bioprinting process is schematically presented in Figure 2.2.

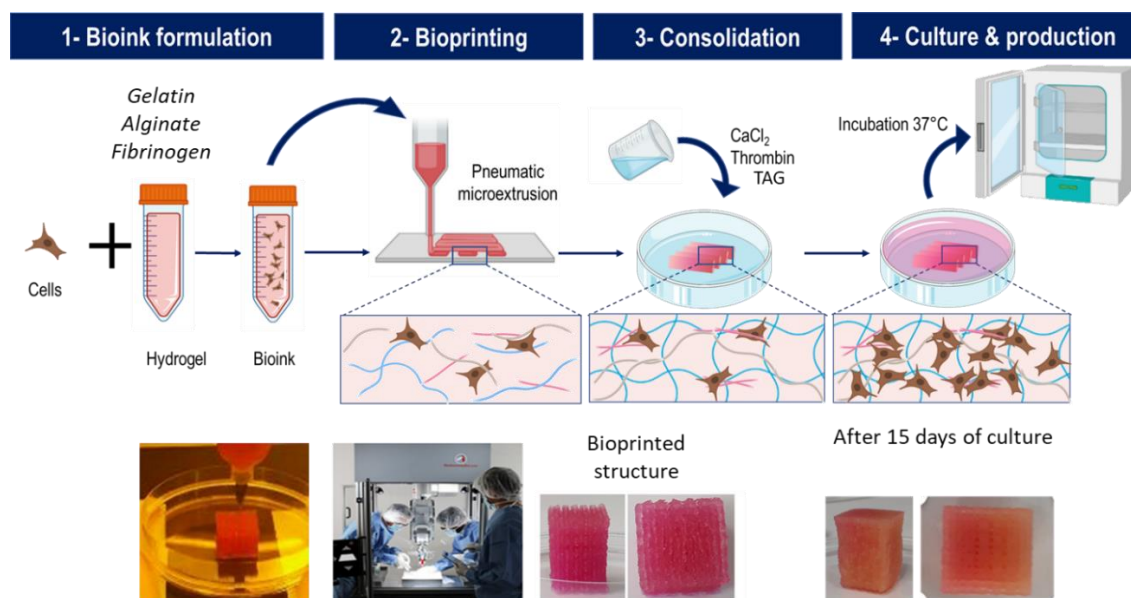


**Figure 2.2: Micro-extrusion-based bioprinting protocol for cellularized bioprinted constructs manufacturing**

### 2.2.3. Parameters screened for bioprinting & DOE Analysis

A Design Of Experiment (DOE) was realized to study the impact of bioprinting parameters on cell growth and metabolism. It includes the bioink formulation and several reticulation and micro-extrusion process parameters. The parameters matrix was designed using a fractional plan with central points on MODDE13® software (Sartorius). The data extracted from proliferation, metabolism and hydrogel properties studies were analyzed on the same software with Poly Least Square analysis to establish predictive models and identify optimized conditions. The different conditions tested are presented in Table 2.4. The quality of predictive PLS model fitting was evaluated on three variables. First, the regression coefficient  $R^2$  represents the variation of the response explained by the model. The second indicator  $Q^2$ , is the predictive ability of the model, also known as model predictive power. It represents the ability to generalize to new, unseen data. According to the recommendation of MODDE13® software user guide, a  $Q^2$  tends to underestimate the model; it should be over 0.1 to have a significant model and a  $Q^2$  over 0.5 with  $(R^2 - Q^2) < 0.3$  indicates a good model [543]. The last indicator is reproducibility, representing the response variation in replicates of the same condition compared to the total response variation. This parameter is expected to be superior to 0.5.

The different conditions tested are presented in Table 2.4.

**Table 2.4: DOE experiment design (parameters) and their associated growth rate when available. SUPPLEMENTARY 1 from our submitted paper presented in Chapter 4 (no DOI).**

Exp number	Bioprinting parameters			Crosslinking parameters						Proliferation
	Bioink Formulation	Macro-porosity ( $\mu\text{m}$ )	Filament diameter ( $\mu\text{m}$ )	Temperature ( $^{\circ}\text{C}$ )	Time (min)	Transglutaminase (%w/v)	Thrombine (U/mL)	CaCl2 (%w/v)	DMEM (%)	Growth rate (day-1)
1	A	400	400	21	60	0.04	0	3.000	0	N.A
2	A	0	400	37	15	0.04	0	0.030	0	N.A
3	A	0	200	21	60	4	0	0.030	0	N.A
4	A	400	200	37	60	0.04	10	0.030	0	N.A
5	A	400	200	37	15	4	0	3.000	0	N.A
6	A	0	400	37	60	4	10	3.000	0	N.A
7	A	0	200	21	15	0.04	10	3.000	0	N.A
8	A	400	400	21	15	4	10	0.030	0	N.A
9	A	400	800	37	15	4	10	3.000	0	N.A
10	A	400	800	37	15	1	10	3.000	0	N.A
11	A	400	800	37	60	0.40	10	3.000	0	N.A
12	A	400	800	37	60	4	10	0.026	100	N.A
13	A	400	800	37	15	1	10	0.026	100	N.A
14	A	400	800	37	60	0.40	10	0.026	100	N.A
15	A	0	400	37	60	4	10	1.400	0	-0.01
16	A	0	400	37	60	0.40	10	1.400	0	0.01
17	A	0	400	37	60	4	10	0.026	100	0.04
18	A	0	400	37	60	0.40	10	0.026	100	0.03
19	A	0	400	37	60	4	10	0.026	0	0.05
20	A	0	400	37	60	0.40	10	0.026	0	0.05
21	A	0	400	37	60	0.40	10	1.400	0	0.08
22	B	0	400	37	60	0.40	10	1.400	0	0.09
23	A	0	400	21	60	0.40	10	1.400	0	0.13
24	B	0	400	21	60	0.40	10	1.400	0	0.04
25	A	0	400	4	60	0.40	10	1.400	0	0.05
26	B	0	400	4	60	0.40	10	1.400	0	0.11
27	B	0	800	37	60	0.04	10	0.026	0	N.A
28	B	0	800	37	15	4	0	3.000	0	0.00
29	B	0	800	37	60	4	0	0.026	100	0.03
30	B	0	800	37	15	0.04	10	0.026	100	N.A
31	B	0	800	37	15	0.04	10	3.000	100	0.11
32	B	0	800	37	60	4	10	3.000	100	-0.06
33	B	0	800	37	37.5	2.02	5	1.513	50	0.02
34	B	0	800	37	60	4	0	0.026	0	0.04
35	B	0	800	37	15	4	10	0.026	0	0.01
36	B	0	800	37	15	0.04	0	3.000	0	N.A
37	B	0	800	37	60	4	0	3.000	100	0.11
38	B	0	800	4	60	0.77	7.5	2.500	100	0.07
39	B	0	800	21	37.5	2.02	5	1.513	50	0.11
40	B	0	800	4	60	0.77	7.5	1.300	10	0.09

#### 2.2.4. *Monitoring and characterization of cell proliferation in 2D and 3D bioprinted cultures*

Standard cultivation protocol of 3D bioprinted constructs was performed in 12-well plates at 37°C in 5% CO<sub>2</sub> incubator within 2 ml of DMEM(+). Culture medium was renewed three times a week, every two to three days. Before every medium renewal, old supernatants were recovered and stored at -20°C for further analysis of metabolites.

##### **Evaluation of cell proliferation from 2D cell cultures**

Each cell line was seeded in 12 well plates at a concentration of  $0.03 \times 10^6$  cell/cm<sup>2</sup> with 1 mL of DMEM(+) medium per well, resulting in a  $0.1 \times 10^6$  cell/mL concentration. The cells from three wells were trypsinized every day for four days for a discrete assessment of cell number in triplicates. Trypsinization and cell counting were performed as described for cell amplification in section 2.2.1.

##### **Cell harvest from bioprinted constructs with hydrogel dissociation: protocol optimization**

Cell proliferation trends were described by cell counting after bioprinted construct dissociation. For the first experiments characterizing the cell behavior in 3D of the four cell lines, presented in Chapter 4 section 4.2.1., cells were harvested by dissociation with 3% collagenase A in PBS (14190169, Thermofisher scientific). A 3% w/v collagenase A (10103586001, Merck) (4.5 U/mL) was prepared in PBS 1X (Gibco) solution and warmed at 37°C in a water bath. The tissues were rinsed once with 2mL PBS, then weighted before being immersed in the collagenase solution (0.5 mL for a 0.2 cm<sup>3</sup> tissue). Cellularized structures were then incubated at 37°C in a water bath with vigorous agitation every 10 to 20 minutes until complete dissociation (~40 min – 1h for a 0.2 cm<sup>3</sup> tissue). The tubes were centrifugated, and the cell pellets were resuspended in 1mL PBS. Tubes were weighted to estimate the exact suspension volume before cell counting on Malassez Hemocytometer with Trypan blue exclusion. For the following experiments, presented in Chapter 4 section 4.2.5, the dissociation protocol was improved by screening multiple dissociation procedures and selecting the one leading to the best cell recovery, reducing hydrogel debris and higher cell viability. Various protocols were evaluated in Chapter 3 section 3.1:

##### *GentleMACS*

The tissues were rinsed once with PBS 1X (Gibco), then weighted before being immersed in 5 mL PBS in a gentleMACS™ Dissociator tube. The tube was placed in the gentleMACS™ Dissociator (Miltenyi Biotec), and the program Lung\_02 was used 3 times simultaneously. The cell mixture was recovered from the spinning tube which was rinsed twice with 5 mL PBS. The



PBS used for rinsing the spinning tube was retrieved in the same tube as the cell mixture. The tubes were centrifugated and the cell pellets were resuspended in 1mL PBS, tubes were weighted to estimate the exact suspension volume before cell counting.

#### *Collagenase A 3% in calcium-free DMEM*

A collagénase A 3% w/v solution (4.5 U/mL) was prepared in calcium-free DMEM supplemented with 10% FBS. The tissue dissociation process was then carried out as described previously in section 2.4.1.

#### *Collagenase dispase*

A collagenase/dispaseR (COLLDISP-RO Roche) 1mg/mL (Collagenase: 0.1U/mL, Dispase: 0.8U/mL) in PBS was heated at 37°C in a water bath. The tissues were rinsed once with PBS 1X (Gibco), then weighted before being immersed in the collagenase/dispase solution (1 mL for a 0.2 cm<sup>3</sup> tissue) and incubated at 37°C in a water bath with vigorous agitation every 10 to 20 minutes, during 2h. The tubes were then incubated overnight at 4°C. The tubes were centrifugated, and the cell pellets were resuspended in 1mL PBS; tubes were weighted to estimate the exact suspension volume before cell counting.

#### *Human Platelet Lysate (HPL)*

HPL was pre-heated at 37°C in a water bath. The tissues were rinsed once with PBS 1X (Gibco), then weighted before being immersed in 1.5 mL of HPL and incubated à 37°C in a water bath until complete dissociation. The tubes were centrifugated, and the cell pellets were resuspended in 1mL PBS; tubes were weighted to estimate the exact suspension volume before cell counting.

#### *Pepsin*

A Pepsin solution (Pepsin/HCl cleaning solution, Mettler Toledo, 51350100) was used at pH 1,82 and with a pH adjusted to 8,5 with NaOH. The tissues were rinsed once with PBS 1X (Gibco), then weighted before being immersed in the Pepsin solution (1 mL for a 0.2 cm<sup>3</sup> tissue) and incubated at 37°C in a water bath with vigorous agitation every 10 to 20 minutes.

#### *TrypLE™*

TrypLE™ Express 1X solution (TrypLE™ Express Enzyme (1X), no phenol red, 12604013, Gibco™) was heated at 37°C in a water bath. The tissues were rinsed once with PBS 1X (Gibco), then weighted before being immersed in the TrypLE solution (1 mL for a 0.2 cm<sup>3</sup> tissue) and incubated at 37°C in a water bath with vigorous agitation every 10 to 20 minutes.

#### *Trypsin-EDTA*

Trypsin-EDTA 1X (Trypsin: 0.25 g/L, 0.0105mM ; EDTA 4Na 2H<sub>2</sub>O : 0.038 g/L, 0.09130226 mM) (Gibco™, Trypsin-EDTA (0.5%), no phenol red, 15400054) was heated at 37°C in a water bath. The tissues were rinsed once with 2mL PBS 1X (Gibco), then weighted before being immersed in the trypsin solution (1 mL for a 0.2 cm<sup>3</sup> tissue) and incubated at 37°C in a waterbath with vigorous agitation every 10 to 20 minutes.

#### *EDTA*

A EDTA (EthyleneDiamine Tetraacetic Acid, tetrasodium – dihydrate– MW : 416.2 g/mol - CALBIOCHEM - 34103) 50 mM solution was prepared by dissolving 0.4162g in 10 mL PBS 1X (Gibco), pH was then adjusted to 7 with HCl (pH 7.15) and the volume was completed to 20 mL with PBS. The solution was heated at 37°C in a waterbath. The tissues were rinsed once with PBS 1X (Gibco), then weighted before being immersed in the EDTA solution (0.5 mL for a 0.2 cm<sup>3</sup> tissue) and incubated at 37°C in a waterbath with vigorous agitation every 10 to 20 minutes.

#### *Sodium citrate*

Multiple solutions of varying sodium citrate concentration were evaluated for bioprinted constructs dissociation. The solutions were prepared with 55mM or 100 mM sodium citrate (Sodium citrate monobasic anhydrous – MW: 214.11 g/mol - Sigma – 71497) in deionized water or in PBS.

The sodium citrate 55 mM and 100 mM solutions were prepared by dissolving 0,235g and 0.428g respectively of sodium citrate, in 10 mL of deionized water or PBS. pH was then adjusted to 7 by addition of 2M NaOH, and the volume was completed to 20 mL. The solutions were heated at 37°C in a water bath. The tissues were rinsed once with PBS, then weighted before being immersed in the sodium citrate solutions (1 mL for a 0.2 cm<sup>3</sup> tissue) and incubated at 37°C in a water bath with vigorous agitation every 10 to 20 minutes.

#### *EDTA / sodium citrate*

A solution was prepared by mixing 2 mL EDTA and 2 mL sodium citrate 100 mM solution and pre-heated at 37°C. The tissues were rinsed once with PBS, weighed before being immersed in 1.5 mL of this solution, and incubated à 37°C in a water bath.

#### *Alginate lyase / EDTA / sodium citrate*

A solution was prepared by mixing 0.5 mL of Alginate lyase (5 U/mL) solution, 0,5 mL EDTA and 0.5 mL sodium citrate 100 mM, and pre-heated at 37°C. The tissues were rinsed once with

PBS, weighed before being immersed in 1.5 mL of this solution, and incubated à 37°C in a water bath.

*Alginate lyase followed by collagenase A*

A solution of Alginate lyase 5 U/mL was prepared by dissolving 0.5 mg/mL of Alginate lyase (A1603-100MG, Sigma Aldrich) in PBS 1X (Gibco). A collagenase A (10103586001, Merck) 3% w/v in PBS 1X (Gibco) solution (4.5 U/mL) was prepared. Both solutions were heated at 37°C in a water bath. The tissues were rinsed once with PBS 1X (Gibco), then weighted before being immersed in the Alginate lyase solution (0.5 mL for a 0.2 cm<sup>3</sup> tissue) and incubated 15 min at 37°C in a water bath. After 15 min, the tissues were still in one piece but seemed fragile. The tubes were then centrifugated to remove de Alginate lyase solution, and the tissue was rinsed with 1 mL PBS before being centrifugated again to remove the PBS. The tissue was then immersed in the collagenase solution (0.5 mL for a 0.2 cm<sup>3</sup> tissue) and incubated at 37°C in a water bath until complete dissociation. The tubes were centrifugated, and the cell pellets were resuspended in 1mL PBS; tubes were weighted to estimate the exact suspension volume before cell counting.

*Alginate lyase / Collagenase A*

A collagenase A (10103586001, Merck) 3% w/v (4.5 U/mL) in PBS 1X (Gibco) solution was prepared. A collagenase A / Alginate lyase solution was prepared by dissolving 0.5mg/mL of Alginate lyase (A1603-100MG, Sigma Aldrich) in 3% collagenase solution (Alginate lyase 5 U/mL; Collagenase 4.5 U/mL). The collagenase A / Alginate lyase was heated at 37°C in a waterbath. The tissues were rinsed once with PBS 1X (Gibco), then weighted before being immersed in the collagenase/alginate lyase solution (0.5 mL for a 0.2 cm<sup>3</sup> tissue) and incubated at 37°C in a waterbath with vigorous agitation every 10 to 20 minutes, until complete dissociation. The tubes were centrifugated and the cell pellets were resuspended in 1mL PBS, tubes were weighted to estimate the exact suspension volume before cell counting.

*Sodium citrate followed by Alginate lyase / Collagenase A*

The tissues were rinsed once with PBS 1X (Gibco), then weighted before being immersed in 1mL of 100mM sodium citrate solution (section 6.9) pre-heated at 37°C, and incubated 15 minutes at 37°C in a waterbath. The tubes were then centrifugated to remove de sodium citrate solution and the tissue was rinsed with 1 mL PBS before being centrifugated again to remove the PBS. The tissue was then immersed in 0.5 mL of a solution containing 0.5 mg/mL Alginate lyase and 3 %w/v Collagenase A in demineralized water and incubated at 37°C in a waterbath until complete dissociation (~35 min).

Later, an alternative method allowed the elimination of the first centrifugation step and, thus, reduced cell loss and experiment duration. For this protocol, the alginate lyase/Collagenase A solution was prepared with the respective concentrations of 1 mg/mL and 6 %w/v (designated as “2X” Alginate lyase/collagenase A solution). The weighted tissues were immersed in 100 mM sodium citrate solution (0.5 mL for a 0.2 cm<sup>3</sup> construct) and incubated for 5 min at 37°C. Then, an equal volume of alginate lyase/Collagenase A (2X) solution was added, without removal of sodium citrate, to reach a final concentration of 50 mM sodium citrate / 0.5 mg/mL alginate lyase / 3%w/v Collagenase A. Tubes were further and incubated at 37°C in a water bath until complete dissociation (~10-15 min). The tubes were centrifuged and the cell pellets were resuspended in 1mL PBS, tubes were weighted to estimate the exact suspension volume before cell counting.

### **Evaluation of cell viability after dissociation**

After dissociation and counting on hemocytometer, the cell suspension was centrifuged and the cell pellet was resuspended in FACS Buffer at a minimal concentration of 1 x 10<sup>6</sup> cell/mL. A BD Pharmingen™ FITC Annexin V Apoptosis Detection Kit I (556547, BD Biosciences) was used to stain apoptotic and necrotic cells. Apoptosis is a programmed cell death process which involves, during its early stage, the translocation of a phospholipid called phosphatidylserine (PS) from the intracellular compartment to the outer layer of the plasma membrane. Annexin V, a protein specifically binding to PS, can be conjugated with fluorochromes such as FITC. It labels Annexin V a highly sensitive probe for flow cytometric analysis, enabling the identification of cells undergoing apoptosis. Propidium iodide (PI), a fluorescent dye, is employed to stain DNA. PI selectively stains the DNA of cells that have lost plasma membrane integrity, such as those in the late stages of apoptosis or necrotic cells. Viable or early apoptotic cells, which still possess intact membranes, do not allow the entry of PI. The detection of PI fluorescence occurs in the orange range of the spectrum, utilizing a 562-588 nm band pass filter. PI is detected with a 562-588 nm band pass filter.

A volume of 2μL of FITC Annexin and 2μL of PI were added per 0.1 x 10<sup>6</sup> cells. The tubes were homogenized and incubated in the dark for 30 min at 4°C. The cells were then rinsed twice with FACS Buffer (centrifugation 1200 rpm, 5 min), resuspended in 300 μL of FACS Buffer and analyzed by flow cytometry. The data were analysed with Cyflogic software, which allowed the identification of four different populations: live cells (no staining), early apoptotic cells (Annexin staining), late apoptotic cells (Annexin and PI staining) and necrotic cells (PI staining).

## Osmolality measurement

The osmolality of different dissociation and reticulation solutions was measured with OsmoTouch 1 Osmometer (Astori Tecnica). This device is designed to assess the cryoscopic point variation and determine the osmolality of liquid samples. Freezing point depression osmometers use the relationship between the number of moles of solute in a solution and the change in freezing point [544]. The approximate number of moles of solute can be determined by comparing the freezing point of a solution to that of a pure solvent.

The device was calibrated by evaluating the osmolarity of several calibration standard solutions, namely 100 mOsm/kg (STD2101, Astori Tecnica), 900 mOsm/kg (STD2109, Astori Tecnica), 2,000 mOsm/kg (STD2120, Astori Tecnica), 2,500 mOsm/kg (STD2125, Astori Tecnica), 3,000 mOsm/kg (STD2130, Astori Tecnica), and a verification solution of 323 mOsm/kg (63225/OSM, Astori Tecnica). The measure of sample osmolality was assessed by filling the sample in a plastic tube and placing the tube in the assigned location into the osmometer. The measure-head of the osmometer, composed of a thermistor to measure the temperature, was plunged into the sample. The program initiated the sample freezing to measure the cryoscopic point after supercooling, thanks to a cooling unit composed of a bath with Peltier cells controlled by the device's software. The osmolality is then automatically calculated by the OsmoTouch 1 Osmometer.

## Determination of cell growth kinetics in 2D and 3D cultures

Growth curves were obtained by dissociating triplicated constructs every 2 to 3 days (3 times a week). The data were used to calculate the cells' global or maximal growth rate along the culture. First, the Integral Viable Cell Concentration (IVCC) was calculated with the trapezoidal rule method as the area under the curve of the viable cell concentration (cells/mL) represented as a function of time (days). The Integral Viable Cell number (IVC) was calculated with the same method as the area under the curve of the total viable cell number (cells) represented as a function of time (days). IVCC and IVC were calculated with the following formulas:

$$IVCC = \int_{t_0}^t X dt = \sum_{i=0}^{i=(n-1)} \frac{(X_i + X_{i+1}) \cdot (t_{i+1} - t_i)}{2}$$

$$IVC = \int_{t_0}^t x dt = \sum_{i=0}^{i=(n-1)} \frac{(x_i + x_{i+1}) \cdot (t_{i+1} - t_i)}{2}$$

Where,

$n$  is the number of points on the growth curve,

$X$  is the cell concentration measured per milliliter of hydrogel for 3D cultures or milliliter of supernatant for 2D cultures (cell/mL) at a time  $t$  (days),

$x$  is the total cell number (cells) measured in the whole bioprinted construct at a time  $t$ ,

$t_0$  is the starting time of the studied period (days).

During non-exponential growth phases, the growth rate is not constant, it is then possible to estimate a global growth rate with the following equation :

$$\mu = \frac{\Delta X}{\Delta t \cdot X_{av}} = \frac{X_t - X_0}{IVCC}$$

Where,

$\Delta$  represents a variation of parameter over the studied period,

$\mu$  is the growth rate (day<sup>-1</sup>),  $X$  is the cell concentration measured per milliliter of hydrogel for 3D cultures or milliliter of supernatant for 2D cultures (cell/mL) at a time  $t$  (days),

$X_0$  is the cell concentration (cell/mL) measured at time  $t_0$ ,

$X_{av}$  is the average cell concentration during  $\Delta t$  (cell/mL),

$t_0$  is the starting time of the studied period (days).

During exponential growth phase, the growth rate is constant and maximal. It can be calculated as the slope of the Napierian logarithm of cell concentration represented as a function of time:  $\ln(X) = f(t)$ . The maximal growth rate ( $\mu_{max}$ ) is thus given by the following equation :

$$\mu_{max} = \frac{\Delta \ln(X)}{\Delta t} = \frac{\ln(X_t) - \ln(X_0)}{(t - t_0)}$$

The error on the cell concentration measurement was estimated by calculating the standard deviation between triplicate at each point. The mean error is of 64% The error on growth rate calculation was calculated by propagation of relative errors:

$$\delta\mu = \sqrt{\left(\frac{\delta X_0}{X_0}\right)^2 + \left(\frac{\delta X_t}{X_t}\right)^2} \cdot \mu$$

Where  $\delta$  represents the error.

### **Cell 3D organization**

Cell 3D organization was observed through histology analysis. For histological staining, samples were fixed using paraformaldehyde for one night at 4°C. They were then dehydrated in a gradient of increasing ethanol concentrations and embedded in paraffin. Samples were cut into 5  $\mu\text{m}$  thick sections. Before histological staining, sections were deparaffinized and rehydrated by successive incubations in Toluene and ethanol solutions of decreasing concentration.

#### *Live cells staining*

Calcein green staining (Invitrogen, Thermo Fisher Scientific, C1430) was used to observe the live cell network in the 3D structure. The Calcein-AM is a non-fluorescent molecule formed of calcein, covalently bond to acetoxymethyl ester (AM) [545]. This molecule can cross the cell membrane and enter the cytoplasm. In live cells, esterase enzymes are active and hydrolyse the acetoxymethyl ester bond to calcein [545]. The calcein molecule freed from the acetomethyl group emits green fluorescence. Detection of green fluorescence from cells incubated in calcein-AM is thus indicative of living cells.

The bioprinted constructs were incubated for 30 minutes at 37°C with 2  $\mu\text{M}$  Calcein AM (Invitrogen, Thermo Fisher Scientific, C1430) before being observed under a fluorescence microscope (Nikon Eclipse Ts2R). In some experiments, DAPI (4',6-Diamidino-2-Phenylindole, Dilactate) (D3571, Invitrogen) was used to simultaneously staining dead cells. Indeed, DAPI is a DNA intercalant which can cross permeated membranes of dead cells and is often used to dye cell nuclei.

#### *Observation of cell morphology and repartition with histological staining*

For histological staining, samples were rinsed in PBS and fixed using paraformaldehyde solution (Antigenfix ; DiaPath ; P0014) overnight at 4°C. They were then rinsed in PBS, followed by dehydration in a gradient of increasing ethanol concentrations from 30% to 70% and stored at 4°C in 70% ethanol until paraffine embedding. For paraffine embedding, the samples were first incubated in 90% ethanol at 35°C followed by successive incubations in two 100% ethanol baths at 55°C. The samples were then transferred successively to two

Methylcyclohexane baths at 55°C. Each incubation lasted for 10-15 min. Then, the samples were incubated in paraffine for 28 min at 60°C for paraffine impregnation. It was followed by a second incubation in fresh paraffine at 60°C for 5 min in the mould to form the paraffine block. Samples were sliced into 5 µm thin sections. For Hematoxylin-Eosin (HE) or DAPI (4',6-Diamidino-2-Phenylindole, Dilactate; Invitrogen D3571) staining, sections were deparaffinized and rehydrated by successive incubation in Toluene followed by decreasing gradients of ethanol from 100% to 70% and finally PBS. The Hematoxylin Eosin Fast Quick kit (Diapath 010263) was used to stain the sections. The slides were dipped in toning solution and then immersed for 5 min in Hematoxylin solution. Then, the slides were rinsed with water until wastewater was clear and dipped again in toning solution and then in 30% ethanol. Then, the slides were immersed for 30 seconds in Eosin. Sections were finally dehydrated in ethanol gradient increasing from 70% to 100% and mounted using Biomount DPX (Biognost BM500). For DAPI staining, the slides were deparaffined and rehydrated with the same protocol. The sections were then covered with 0.3 µM DAPI solution for 15 min in the dark, rinsed twice with PBS and mounted using Fluoromount™ (Sigma Aldrich, F4680). Image acquisition was performed on light and fluorescent microscope (Nikon Eclipse Ts2R).

### **Monitoring of cell central carbon metabolism in 2D and 3D cultures**

Spent media were recovered in triplicate three times a week at 2 to 3 days intervals and were stored at -20°C. These samples were used to quantify the lactic acid secreted by cell metabolism and evaluate glucose consumption.

The lactic acid concentration was quantified using the L-Lactic Acid Assay from Megazyme (L-Lactic Acid (L-Lactate) Assay Kit, K-LATE, Megazyme) for auto-analyzer procedures. The assay was performed according to the manufacturer's instructions. Each sample was deposited in triplicate in the 96-well plate. The plates were incubated at 25°C in the dark for 10 min before measurement of the absorbance at 340 nm with a spectrophotometer (TECAN infinite For highly concentrated samples, dilutions were performed in deionized water, and a commercial fresh medium was used as a negative control.

The L-Lactate assay kit principle is based on two enzymatic reactions, as illustrated in Figure 2.3. In the first reaction, L-lactate is oxidized to pyruvate by the enzymatic action of L-lactate dehydrogenase (L-LDH) using NAD<sup>+</sup> as a cofactor (equation (1)). However, it should be noted that the conversion of lactate to pyruvate is reversible. To prevent the occurrence of the reverse reaction and enable the total conversion of lactate and NAD<sup>+</sup> to pyruvate and NADH/H<sup>+</sup>, a



second enzymatic reaction was used to consume the pyruvate produced by the first reaction. This reaction involves the conversion of pyruvate (in excess of D-glutamate) to D-alanine and 2-oxoglutarate, catalyzed by the enzyme D-glutamate-pyruvate transaminase (D-GPT) (2). Since the first reaction involves a stoichiometric conversion of lactate and NAD<sup>+</sup> to pyruvate and NADH/H<sup>+</sup>, NADH's molar concentration is equal to lactate's initial molar concentration. Consequently, the absorbance of NADH can be measured at its maximum absorbance wavelength of 340 nm using a spectrophotometer. The absorbance value is directly proportional to the concentration of NADH within a specified concentration range of 0 to 0.30 g/L, as specified by the manufacturer and validated through measurements obtained from a calibration curve with lactate concentrations ranging from 0 to 0.5 g/L. The use of a standard solution of known concentration of lactate allows for the determination of the initial lactate concentration in the samples.

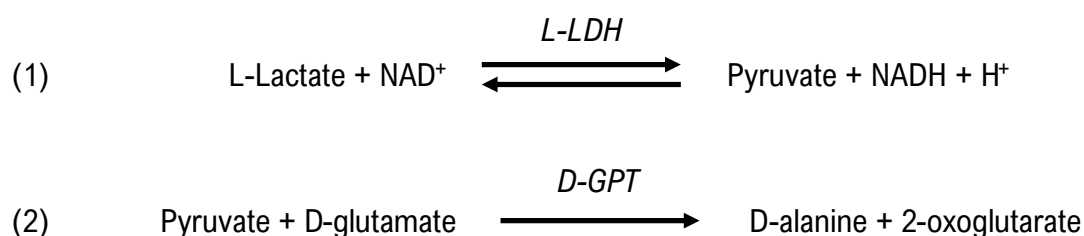


**Figure 2.3:** The two enzymatic reactions required for quantification of L-lactic acid. L-LDH: L-lactate dehydrogenase ; D-GPT: D-glutamate-pyruvate transaminase.

The glucose concentration was measured by NMR analysis of the culture supernatants. The analysis used a Bruker Avance III spectrometer with a 500MHz 1H resonance frequency and a BBFO probe. A single pulse sequence was used for the acquisitions. Before the acquisitions, the supernatant samples were lyophilized and the dry mass was dissolved in Deuterium Oxide (D215F; Eurisotop). Quantifying glucose was possible by adding, as an internal reference, 3-(Trimethylsilyl)propionic-2,2,3,3-d4 acid sodium salt (TMSP) at a concentration of 1,285 g/L in the sample. The characteristic pic of TMSP at 0 ppm was used as a reference for glucose quantification.

The discrete production of lactate and consumption of glucose measured in supernatant before medium renewal were summed to assess total lactate production and glucose consumption over the culture. The error on cumulated productions and consumptions were calculated with the propagation of relative errors as previously described for the growth rate.

## Determination of global cell-specific metabolic kinetics in 2D and 3D cultures

To further characterize cell metabolism, the average cell-specific lactate production or glucose consumption rate, respectively  $q_{\text{lact}}$  and  $q_{\text{gluc}}$ , were calculated as the slope of the graph of the cumulative metabolite production or uptake (in mmol) as a function of IVC over the whole culture. The following equation gives this:

$$M_t - M_0 = q_M \int_{t_0}^t x \, dt \leftrightarrow q_M = \frac{M_t - M_0}{\int_{t_0}^t x \, dt}$$
$$q_M = \frac{M_t - M_0}{\text{IVC}}$$

Where,

$M_t$  and  $M_0$  represent the total production (mmol) of the studied metabolite (lactate or glucose) at a time  $t$  or  $t_0$ , respectively,

$q_M$  is the specific production rate of the studied metabolite. In case of molecule consumption (substrate), the calculated  $q_M$  was inferior to zero (consumption = negative production), therefore we used the value of  $(-1) \times q_M$  to indicate a positive consumption rate.

The glucose-to-lactate conversion yield ( $Y_{\text{lact/gluc}}$ ) representing the number of moles of lactate produced per glucose consumed, was calculated with the following equation:

$$Y_{\text{lact/gluc}} = \frac{q_{\text{lact}}}{q_{\text{gluc}}}$$

This ratio was indicative of the efficiency of cell metabolism as a  $Y_{\text{lact/gluc}} < 1$  indicates an oxidative (respiratory) metabolism and  $Y_{\text{lact/gluc}} > 1$  is characteristic of a fermentative metabolism.

### 2.2.5. Hydrogel characterization

#### Dynamic Mechanical Analysis (DMA)

The viscoelastic behavior of consolidated hydrogels were evaluated at days 1 and 10 of culture after bioprinting on  $0.2\text{cm}^3$  constructs. It was characterized by frequency sweep experiments in dynamic mechanical analysis (DMA) in compression mode. These experiments were conducted with a rotational rheometer (DHR2, TA Instruments, Guyancourt, France) with a DMA mode (torque = 0 N) and a parallel plate geometry (8 mm). Thanks to a Peltier plate, the samples were maintained at  $37^\circ\text{C}$  during the acquisitions. A preliminary study defined the linear viscoelastic domain, corresponding to the displacement range where the material properties are assumed to be constant. This domain is determined using oscillatory compression experiments with

constant frequency and varying displacement. Then, dynamic compression tests were performed with a frequency range of 0.1–10 Hz (i.e. 0.628–62.8 rad/s) at a constant displacement within the linear viscoelastic regime. In these dynamic compression tests, bioink undergoes a periodical mechanical strain  $\varepsilon$  of minimal amplitude  $\varepsilon_0$  ( $< 1\%$ ) and of angular frequency  $\omega$  following the equation (1):

$$\varepsilon = \varepsilon_0 \sin(\omega t) \quad \text{Equation (1)}$$

In the case of the generalized Maxwell model, the storage  $E'(\omega)$  part of the complex modulus is expressed by the equations (2):

$$E'(\omega) = E_0 \left[ 1 + \sum_{\alpha=1}^m \frac{\beta_{\alpha} \omega^2 \tau_{\alpha}^2}{1 + \omega^2 \tau_{\alpha}^2} \right] \quad \text{Equation (2)}$$

$$\eta = E_0 \sum_{\alpha=1}^m \beta_{\alpha} \tau_{\alpha} \quad \text{Equation (3)}$$

where  $E_0$  is Young's modulus of the isolated spring. The relaxation times,  $\tau_{\alpha}$ , and the dimensionless reference parameters  $\beta_{\alpha}$  stand for the contribution of each branch to the global modulus. The overall viscosity  $\eta$  can be defined as Equation 3. The time-constant values were regularly distributed between the reciprocals of the highest (62.8 rad/s) and the lowest (0.628 rad/s) angular frequencies of the experimental dynamic modulus. The chosen number of modes was sufficiently high to obtain accurate fitting, but not too large to avoid inconsistent results (e.g., negative values of  $\beta_{\alpha}$ ). Practically speaking, this led to three-time constants ( $m = 2$ ), regularly spaced on a logarithmic scale between  $5 \times 10^{-2}$  s and  $5 \times 10^{-1}$  s.

Identification was achieved by solving the following minimization problem described by equation (3):

$$f_{\text{obj}}(E_0, \beta_1 \dots \beta_m) = \sum_i^k \left[ \frac{(E'_i - E_i^{\text{mes}})^2}{E_i^{\text{mes}}} \right] \quad (3)$$

where  $E_i^{\text{mes}}$  is the storage modulus obtained from the measured data and  $E'_i$  is the one computed with viscoelastic parameters.  $k$  is the number of measurements acquired during the frequency sweep compression test. The optimization procedure was performed by using the Microsoft Excel Solver (version 2016) with the Generalized Reduced Gradient (GRG) nonlinear solving method.

The measured Young's Modulus was used to compare the elastic behavior of different hydrogel formulations and consolidations.

## **Transmission Electron Microscopy (TEM)**

TEM imaging was performed at the “Centre d'Imagerie Quantitative Lyon-Est” (CIQLE) for the ultrastructural study. Before image acquisition, bioprinted constructs were fixed with 2% glutaraldehyde (Electron Microscopy Sciences EMS) in PBS at 4°C for 15 min. They were then stored at 4°C with 2% glutaraldehyde (EMS) in 0.1 M sodium cacodylate (pH 7.4) for 1 to 7 days before preparation for TEM imaging. After washing three times in 0.2 M sodium cacodylate buffer, printed pieces were post-fixed with 1% aqueous osmium tetroxide (EMS) at room temperature for 1 hour. Samples were then dehydrated in an ethanol gradient at room temperature and embedded in Epon epoxy resin. After polymerization, ultrathin sections (100 nm) were cut on a UC7 (Leica) ultramicrotome and collected on 200 mesh grids. Sections were stained with uranyl acetate and lead citrate before observations on a Jeol 1400JEM (Tokyo, Japan) transmission electron microscope equipped with an Orius 1000 camera and Digital Micrograph. TEM images were analyzed on ImageJ for determination of the hydrogel microporosity.

## **Image analysis**

Image analysis acquired on calcein-stained constructs, DAPI-stained histological slices and TEM imaging of the hydrogel microstructure were analyzed on ImageJ software. The images were converted to 8-bit binary images. To measure the percent of void (porosity) a threshold was set to a binary value of 140-150 (TEM), corresponding to the light zones in the images (see Figure 2.4). To estimate the percent of surface occupied by the cells, the threshold was manually adjusted for DAPI and calcein, depending on the initial image intensities, and in a range of 24-32 for calcein images and 40-70 for DAPI images.

The percent of the surface with binary values over the threshold was measured and estimated to correspond to the percent of micro-porosity (TEM) or the percent of surface colonized by the cells (calcein/DAPI). The values were used to compare the microstructure of different hydrogels or evaluate cell proliferation (calcein) and distribution (DAPI). It is important to note that TEM image analysis provides only comparative information about global microporosity. Indeed, the quantification of micro-pore's average diameter was not accessible due to the irregular porosity shape. Thus, quality of the microporosity, either interconnected channels opened to the external environment or to enclosed void spaces in the hydrogel was not described.

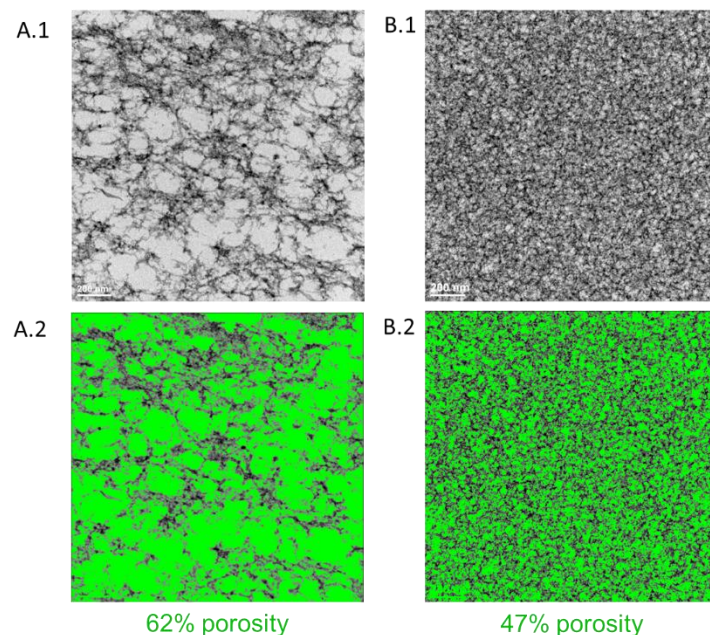


**Figure 2.4: Procedure for hydrogel micro-porosity quantification.** Example of image analysis on TEM images. A.1 and B.1 show the TEM imaging of two different hydrogels microstructures. A.2 and B.2 show the threshold setting to evaluate the percent of void surface (in green). **SUPPLEMENTARY 4 extracted from our submitted paper presented in Chapter 4.**

### Parameters screened for bioprinting with Design of Experiment (DOE)

A Design Of Experiment (DOE) was realized to study the impact of bioprinting parameters on cell growth and metabolism. It includes the bioink formulation and several reticulation and micro-extrusion process parameters. The parameters matrix was designed using a fractional plan with central points on MODDE13® software (Sartorius). The data extracted from proliferation, metabolism and hydrogel properties studies were analyzed on the same software with Poly Least Square analysis to establish predictive models and identify optimized conditions. The different conditions tested are presented in Table 2.4. The quality of predictive PLS model fitting was evaluated on three variables. First, the regression coefficient  $R^2$  represents the variation of the response explained by the model. The second indicator  $Q^2$ , is the predictive ability of the model, also known as model predictive power. It represents the ability to generalize to new, unseen data. According to the recommendation of MODDE13® software user guide, a  $Q^2$  tends to underestimate the model, it should be over 0.1 to have a significant model and a  $Q^2$  over 0.5 with  $(R^2 - Q^2) < 0.3$  indicates a good model [543]. The last indicator is reproducibility, representing the response variation in replicates of the same condition compared to the total response variation. This parameter is expected to be superior to 0.5.

## 2.3. Scale up and bioreactor culture of bioprinted constructs

### 2.3.1. 3D printing of the construct's culture chamber

A culture chamber was designed by Computer Assisted Design (CAD) using 3D modelling software Autodesk® Fusion 360™ to fit the bioprinted construct geometry. This vessel was designed to allow for media flow circulation inside the chamber through connection with perfusion tubings. The position of media flow entry and exit were chosen according to flow simulations that will be presented in the next paragraph section.

The vessel was printed in acrylate-based material (VeroClear® ; Stratasys) using the Object 30 Pro inkjet printer (Stratasys). As part of the printing procedure, the material was photopolymerized by exposition to UV. Support and un-polymerized material were removed by scraping, rinsing with high-pressured water and overnight washing in by immersion in 70% ethanol bath or 0.2M NaOH according to the manufacturer's recommendations. After washing, the printed chamber was rinsed in demineralized water.

The design and washing procedure of the 3D printed chamber have evolved along the duration of this Ph.D and the different geometries and procedures will be detailed in Chapter 5.

### 2.3.2. Liquid flow simulations with Computational Fluid Dynamic (CFD)

Fluid dynamic simulations were performed by the « Laboratoire Réactions et Génie des Procédés » (LRGP \_ Pr. Eric Olmos) using ANSYS Fluent solver. Generated data was treated with CFD Post software (ANSYS Inc., version 16.1). Fluid properties were assimilated to those of water at 37 °C (density  $\rho = 993 \text{ kg.m}^{-3}$  and dynamic viscosity  $\mu = 6.92 \times 10^{-4} \text{ Pa.s}^{-1}$ ). The simulations were performed for a parallelepipedal construct of 2x2x2.7 cm size with 12x12 square-shaped pores of 1.2 mm side. CFD was used to identify homogenous and heterogenous flow path conditions according to the location of fluid entry and exit on the culture chamber.

### 2.3.3. Measurement of fluid residence time in the culture chamber

Residence time was determined according to Dirac method. It was measured in the 3D printed culture chamber containing an acellular 3D printed hydrogel structure. The hydrogel structure geometry was that of a parallelepipedal construct of 2x2x2.7 cm size with 12x12 square-shaped pores of 1.2 mm side. The culture chamber containing the tissue was continuously perfused with demineralized water. Just after exiting the chamber, water was recovered in a becker. The fluid contained in the becker was drained at the same flow rate than water perfusion to keep a constant volume (20 mL) and maintained homogenous by magnetic agitation. A conductivity probe was immersed in the liquid contained in the becker. A standard range of NaCl solutions

at concentrations of 0.0 ; 0.10 ; 0.15 and 0.20 M NaCl was measured with the conductivity probe to generate a standard curve.

At a time  $t_0$ , a solution of 0.2 M NaCl was injected at the entry of the chamber while maintaining continuous perfusion with deionized water. At the same time, a timer was started to record the elapsed time. Evolution of conductivity was continuously measured in the flow exiting the chamber until the conductivity reached a peak and then decreased and stabilized back at 0 mS/cm. The residence time (Rt) was calculated with the following equation:

$$Rt = \frac{\int C(t) \cdot t \, dt}{\int C(t) \, dt}$$

Where  $C(t)$  represents the concentration of NaCl measured at a time  $t$ . The integrals were calculated as the area under the curve of  $C(t)$  as a function of time and  $(C(t).t)$  as a function of time with the trapezoidal rule presented previously.

Multiple flow rates and entry/exit location were evaluated.

The setup used for the experiment is presented in Figure 2.5.

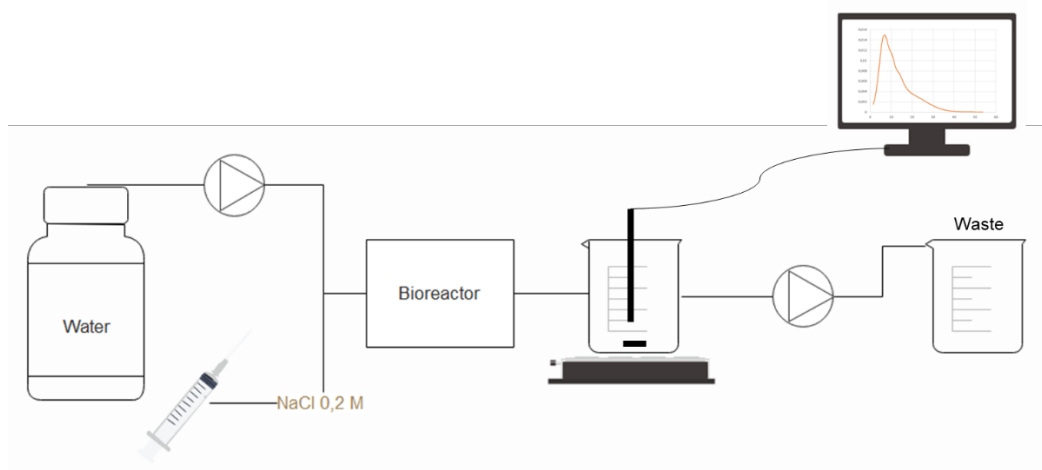


**Figure 2.5: Schematic representation of the setup used for residence time determination in 3D printed culture chamber.**

#### 2.3.4. Measurement of pressure drop in the culture chamber outlet pipe

Two diameters of tubing were used for the outlet flow of the perfused culture chamber. The regular pressure drop,  $\Delta P$  (Pa), was calculated for 1 meter of tubing with Hagen-Poiseuille equation:

$$\Delta P = \frac{128 \eta \cdot L \cdot Q}{\pi D^4}$$

Where,

$\eta$  is the dynamic viscosity of the fluid (Pa.s)

$L$  is the pipe length (m)

$Q$  is the injection flow rate (m<sup>3</sup>/s)

$D$  is the tubing diameter (m)

The equation of Hagen-Poiseuille is applicable only for laminar flows which can be characterized by calculating the Reynolds number (Re) as follows:

$$Re = \frac{\rho \cdot v \cdot D}{\eta}$$

where  $\rho$  is the fluid density (kg/m<sup>3</sup>), and  $v$  is the mean velocity of flow (m/s).

In our case, we used tubing with diameters  $D = 2$  and 4 mm and maximal flow rate of 10 mL/min. Hence, the average velocity were respectively  $v = 5.30$  and 1.32 mm/s. The fluid density and dynamic viscosity were considered equal to those of water with  $\rho = 1000$  kg/m<sup>3</sup>,  $\eta = 0.89$  mPa.s.

In these conditions, the Reynolds number was always inferior to 120 and 60 respectively which testifies of a laminar flow.

Hence, the equation Hagen-Poiseuille was applied to calculate the pressure drops in our experiments for diameters 2 and 4 mm and a maximal flow rate of 10 ml/min of media.

### 2.3.5. *Bioreactor systems and settings*

#### **In-house customed system**

The first developed bioreactor setup was performed using a customed Cytosys controller (Ipratech, Belgium) to control and regulate culture parameters (pH, dO<sub>2</sub>, temperature). The controller comprised three peristaltic pumps, a gas injecting port connected to air, CO<sub>2</sub> and nitrogen feedings. The control system also included connecting ports for a heating jacket, a stirrer motor as well as dissolved oxygen (dO<sub>2</sub>), pH and temperature probes. A DASbox® 250mL tank (Eppendorf, Hambourg, Allemagne) was used as culture medium container and culture parameters were monitored inside the tank using a temperature probe (DASGIP DASbox Platinum RTD Temperature Sensor ; Eppendorf) and probes for online assessment of pH (EasyFermPlus PHI K8 120 ; 238633-1513 ; Hamilton Company) and dO<sub>2</sub> (OxyFermFDA 120 ; 237450 ; Hamilton Company).

Temperature of the medium was maintained at 37°C with a heating jacket. Injections of air and nitrogen were used to regulate the dissolved oxygen concentration. An injection of gaseous CO<sub>2</sub>



or NaOH 0.2M solution were used as pH actuators. The pH probe was calibrated using a 2 points calibration with pH 4 and pH 7 buffer solutions.

The secretion of lactic acid in the culture medium was monitored by daily sampling of culture supernatant and subsequent lactate quantification with enzymatic assay kit (K-LATE, Megazyme) as described in section 2.2.4. A complementary method was developed for online-monitoring of metabolites with a Rxn2 Raman analyser (Kaiser) and a Raman spectroscopy probe (Rxn-40 ; Kaiser) placed in the DASbox® tank.

The bioreactor culture system composed of the DASbox®, probes and tubing, as well as the printed perfused vessel were sterilized by autoclaving 20 min at 121°C.

The culture medium was sterile-introduced in the DASbox® one day before the start of the bioreactor culture and dO<sub>2</sub> probe calibration was performed in the media regulated at 37°C, by overnight injection of air until reaching saturation.

HEK and CHO cells were used to bioprinting large constructs up to 10.8 cm<sup>3</sup> cultivated in bioreactors (see Figure 2.1). The bioink preparation and bioprinting processes were conducted according to the procedures described in sections 2.2.1 and 2.2.2. To reduce the total duration of the process, the diameter of the printing needle was increased from 400µm to 800µm.

After consolidation, the bioprinted cellular construct was introduced in the culture vessel under laminar flow. The vessel was sterile-closed and connected to the perfusion tubing for media circulation. A peristaltic pump of the controller was used to create the perfusion flow by pumping the regulated media from the DASbox® through the bioprinted tissue at 10mL/min.

### **Transfer to commercial Ambr®250 system**

The previously developed setup was transferred to a the commercial Ambr®250 HT demonstration unit kindly provided by Sartorius. The single-use Ambr®250 vessel was used as container for culture medium and allowed pH, dO<sub>2</sub> and temperature regulation.

The culture steps and settings were executed through the Ambr® Runtime control software, thanks to a program scripted with the Ambr® Definition software.

The 3D printed culture chamber and tubing were sterilized by autoclaving 20 min at 121°C. The Ambr®250 pumps were sterilized with a 6% hydrogen peroxide (H<sub>2</sub>O<sub>2</sub>) solution (516813-500ML, Merck), according to manufacturer recommendations and following the Cleaning in place (CIP) and Sanitization in place (SIP) procedures. Bioreactors were filled with production medium (PM) the day before inoculation. Temperature and Dissolved oxygen (DO) regulations

were started shortly after bioreactor filling and pH regulation was started the day of inoculation. In this system, pure O<sub>2</sub> gasing was used instead of air gasing to improve the dO<sub>2</sub> regulation.

This bioreactor setup was used to study bioprinted CHO cell cultures and production of monoclonal antibodies (mAb). A CHO suspension culture was used as reference for comparison of cell proliferation and mAb production with the bioprinted cultures.

The adaptation of the bioreactor setup and regulation settings for the culture of large bioprinted construct has been the object of numerous optimizations that will be presented in detail in Chapter 5.

### **Reference suspension bioreactor culture**

A reference bioreactor run was performed with CHO cells grown in suspension fed-batch mode, in Ambr®250 system. The cells were amplified in suspension cultures as described in section 2.1.3, and inoculated in the stirred tank at a concentration of  $0.3 \times 10^6$  cell/mL. Prior to bioreactor inoculation, the system was sterilized and prepared as previously described by following the Cleaning in place (CIP) and Sanitization in place (SIP) procedures and filling the stirred tank with production medium (PM) the day before inoculation. The start of temperature, dissolved oxygen (dO<sub>2</sub>) and pH regulations were carried out as previously described for bioprinted constructs cultures. Here also, O<sub>2</sub> gasing was used instead of air gasing to improve the dO<sub>2</sub> regulation.

#### *2.3.6. Magnetic Resonance Imaging (MRI) macrostructural analysis*

At the end of the culture, the cellularized structure was fixated by incubation in Antigenfix (DiaPath, P0014) overnight at 4°C. The construct was then rinsed and kept in ethanol 70% before MRI analysis to study the 3D macrostructure of the construct.

The MRI protocol was performed utilizing a seven Tesla Bruker BioSpec MR system (Bruker Biospin GbmH, Germany) equipped with a 400 mT/m maximal amplitude gradient set. The system was controlled using a Bruker workstation connected to ParaVision5.1 software for data acquisition and post-processing. In order to obtain in vitro MR images, a transmit-receive radio-frequency body coil with an outer diameter of 112 mm and an inner diameter of 72 mm was utilized.

The sample was then positioned inside the transmit-receive body coil, which was placed at the center of the 7T MRI system. For the acquisition of high-resolution 3D MR images of the

printed bio-tissue, a tridimensional T2-weighted MR sequence based on the Rapid Acquisition with Relaxation Enhanced (RARE) method was employed in the transversal orientation. The acquisition parameters were as follows: Echo Time (TE) of 35.8 ms, Repetition Time (TR) of 600 ms, bandwidth of 75 kHz, RARE accelerator factor of 8, and a number of averages of 2. A total of 256 slices with a slice thickness of 273  $\mu\text{m}$  were acquired within a 3.50 x 3.50 x 3.50  $\text{cm}^3$  field of view. The in-plane matrix size was 256 x 256 x 128, which was interpolated to 256 x 256 x 256 pixels, resulting in a final in-plane isotropic resolution of 137 x 137 x 137  $\mu\text{m}$ . The total acquisition time for this process was 1 hour, 1 minute, and 26 seconds.

A 3D image of the structure was modelled from the DICOM files using 3DSlicer software.

### 2.3.7. *Detection of IgG retained in hydrogel*

#### **Monoclonal antibody quantification in supernatant**

Quantification of IgG1 production in CHO cell cultures was performed by ELISA assay. A dark 96 plate (C8 LOCKWELL FLUORO BLACK MAXISORP, 446471, Thermo Scientific) was coated with a 100  $\mu\text{g}/\text{mL}$  protein A (RPA-100 (Ultra pure r Protein A, RC7278, RepliGen) in 0.1M carbonate buffer pH 9 solution (potassium carbonate, PROLABO, 26 726.297), overnight at 4°C. The plate was then rinsed 3 times with PBS and saturated for 1h with 3% BSA (Sigma Aldrich, A2153 – 10g) in PBS referred to as “PBSA” solution at 37°C. After saturation of the support, the plate was rinsed as previously described, then diluted samples and standard range were deposited in the wells. The standard range was prepared by successive dilutions of a 7.21 g/L human IgG1 stock solution in PBSA to achieve a concentration range between 0 to 1000 ng/mL. The plate was incubated with the samples for 2h at 37°C. Then the plate was rinsed again and incubated 2h at 37°C with secondary antibody solution prepared by 1/10<sup>5</sup> dilution in PBSA of Alkaline phosphatase conjugated affiniPure Goat Anti Human IgG (Jackson Immunoresearch, 109-055-003). After rinsing of the plate, the chemoluminescent substrate solution (11685627001, Sigma Aldrich) diluted at a 1% v/v in 0.1 M Tris-HCl, 0.1 M NaCl, pH 9.5 buffer was added in each well and incubated 10 min in the dark. Luminescence was measured with a Berthold which 10s exposure per well.

This method was cross-validated by quantifying the IgG1 of a sample set with HPLC (Dionex UltiMate 3000 HPLC system; Thermo Scientific) on a Yarra 3  $\mu\text{m}$  SEC 3000 column (Phenomenex). The HPLC assessment of mAb concentration was kindly performed by Moritz Speckenbach from Sartorius Stedim Biotech GmbH (Goettingen, Germany).

#### **Detection of IgG retained in the hydrogel**

Immunohistochemistry was used on CHO bioprinted construct histological slices to observe the presence of IgG retained in the hydrogel. The slices were deparaffined and rehydrated as previously described. Then sample unmasking was performed by incubating the slides for 30 min à 37°C in 800 U/mL Hyaluronidase in PBS solution, in a humid chamber to avoid sample drying. The slides were then rinsed 3 times for 5 min in PBS and saturated with 5% w/v BSA solution (BSA standard fraction V, Euromedex 04-100-812-C) for 1h at RT to bloc unspecific affinity sites. Finally, a FITC-conjugated secondary antibody solution at a 1/100 dilution was deposited on the slides to cover the sample slides. The samples were incubated with the secondary antibody for 2h at 37°C in a humid chamber. Then, the slides were rinsed 3 times in deionized water and mounted using Fluoromount™ (Sigma Aldrich, F4680). Imaging was performed with a fluorescent microscope (Nikon Eclipse Ts2R).

Then hydrogels were dissociated after the 14 days of culture with the optimized dissociation protocol described in section 2.2.4 with Sodium citrate 100mM followed by 0.5 mg/mL Alginate lyase – 3% Collagenase A. After complete dissociation of the hydrogel, the solution was centrifuged to remove the cells. We analyzed the recovered supernatant, including the enzymatic cocktail from the dissociation solution and dissolved hydrogel, for mAb quantification using the ELISA assay described in above.

## 2.4. In situ cell transfection & transgene expression

### 2.4.1. *Production and extraction of plasmids extraction and validation*

To easily evaluate the feasibility of *in situ* transfection inside the bioprinted construct, we decided to used fluorescent marker genes. Two plasmids were evaluated in this study, the first one pEGFP-C1 encoded for the enhanced Green Fluorescent Protein (eGFP or GFP) while the second encoded for the mCherry (red fluorescent) protein (pEGFP-C1 or pmCherry-C1 – 4.7 kpb). Both plasmids presented the SV40 promoter (see Figure 2.6). Plasmids stock preparation were performed by replicating and extracting the plasmids from producing *E.coli* strains. Bacteria were cultured overnight (15 to 24h) in a Luria Broth medium (Sigma – L3022-1KG). Bacteria were recovered by centrifugation 15 min at 3220 g. Plasmids were extracted using the Qiagen Plasmid Maxi Kit (10) ref : 12162) and resuspended in sterile deionized water and stored at -20°C prior use. Plasmid concentration and purity were determined by absorbance measurements at 230, 260 and 280 nm with a Nanodrop (Thermofischer Scientific, USA).

When looking at the ratio of absorbances measured at 260 nm and 280 nm ( $A_{260}/A_{280}$ ), a value of 1.8 or more is considered to indicate the absence of RNA contamination in the sample.

The A260/A230 ratio is used to evaluate the presence of other contaminants such as proteins. It is usually comprised in a range of 2.0 – 2.2 and values under 2.0 may indicate the presence of a contaminant. For all the plasmid extractions performed in this work, the A260/A280 and A260/A230 were always over 1.8 and 2.2 respectively which confirmed that the extracted plasmids had high purity.

Then the plasmids were linearized by digestion with a restriction enzyme (BamHI) and migrated by electrophoresis on an agar gel with a DNA ladder as molecular-weight size marker (1 kb Plus DNA Ladder, BioLabs Inc.). A loading dye was used for visual tracking of DNA migration during electrophoresis. The migration was conducted by application of an electric field with maximal intensity and power. A 50V tension was applied for 10 min followed by 100V for 50 min. The gel was then recovered, immersed in Ethidium bromide (DNA intercalant) for 20 min and rinsed 3 times with demineralized water and DNA was revealed under UV exposure. The revealed gels only presented one line at the 4.7 kb location (see Figure 2.6) confirming the correct size of both plasmids and the absence of RNA or DNA contaminants.

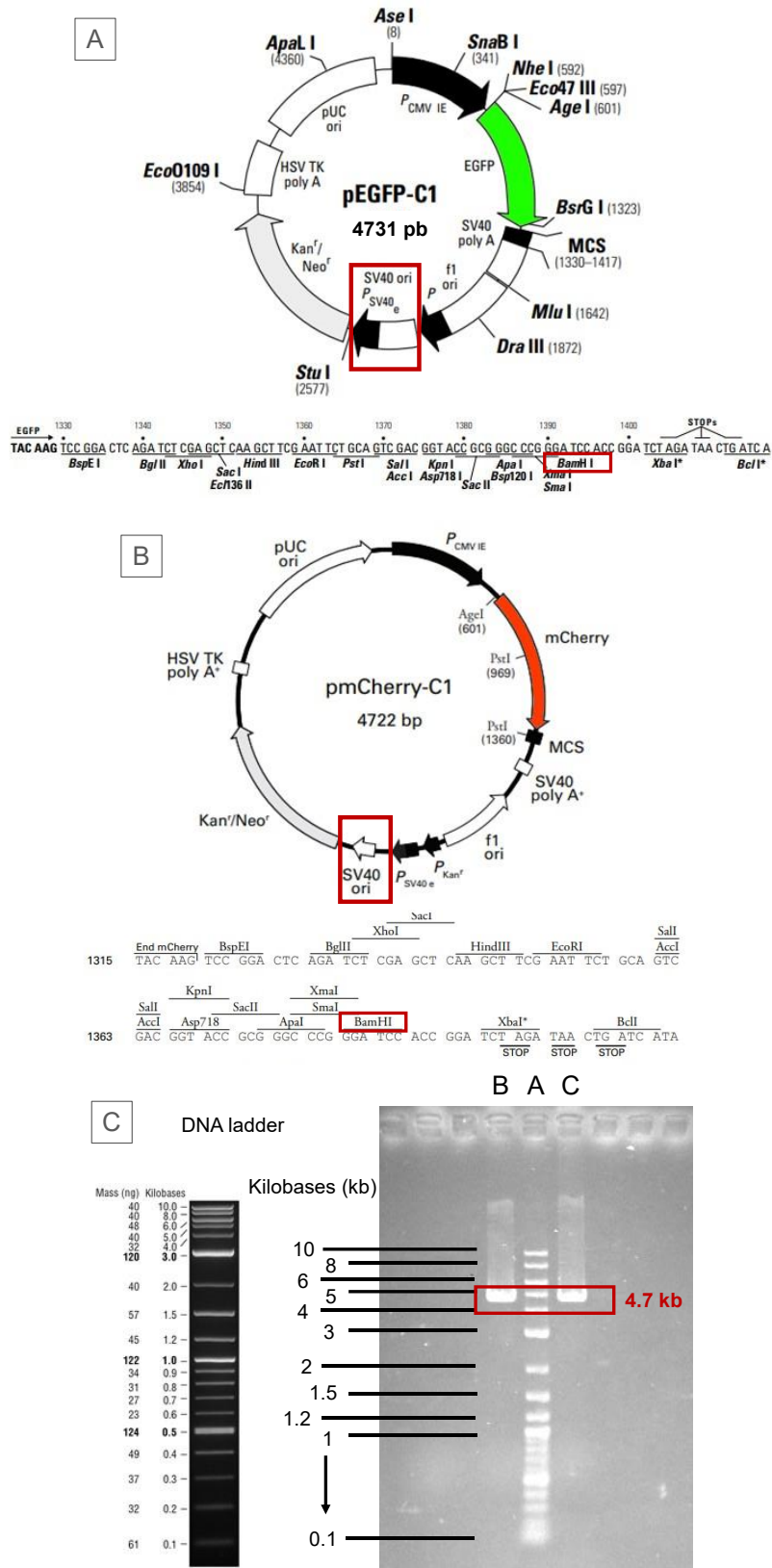


**Figure 2.6: Plasmids maps and qualification.** Genes mapping of (A) the plasmid pEGFP-C1, image extracted and adapted from “Addgene.org” (plasmid discontinued from provider) and (B) the plasmid pmCherry-C1, image extracted and adapted from provider website “Takarabio.com”. (C) DNA revelation with BET after electrophoresis on agar gel with: (A) the DNA ladder (molecular weight marker from 0.1 to 10 kb), (B) the sample from pEGFP-C1 extraction and (C) is the sample from pmCherry-C1 extraction

#### 2.4.2. Verification of plasmids integrity

Plasmids were digested with restriction enzyme BamHI, and deposited on a gel of polyacrylamide. A molecular weight ladder was used as to determine the size of the plasmids. They were migrated by electrophoresis by application of an electric field with maximal intensity and power. A 50V tension was applied for 10 min followed by 100V for 50 min. The gel was then recovered, immersed in Ethidium bromide (DNA intercalant) for 20 min and rinsed 3 times with demineralized water and DNA was revealed under UV exposure.

#### 2.4.3. Synthesis of cationized gelatin

Cationic gelatin (CG) was synthesized based on literature protocols [546,547]. Cationic gelatin (CG) was prepared by dissolving gelatin (Sigma Aldrich – G1890-500G) in a pH 5.8 phosphate buffer at a concentration of 40 g/L. After complete dissolution at 37°C, diaminohexane (Fluka – 33000) was added for a final concentration of 1.16 M. After complete dissolution, the pH was adjusted to pH 5 by addition of highly concentrated HCl (37%). After pH adjustment, EDC (Ethyl-3-(3-dimethylaminopropyl) Carbodiimide) (Sigma Aldrich – E7750) was added to the solution to a final concentration of 0.116 M. The reaction is presented in Figure 2.7.

The vessel was then covered with plastic film to avoid evaporation and the solution was incubated 18h to 24h at room temperature with agitation. The solution was then placed in dialysis pouches with extrusion size 500 –1000 Dalton (Interchim – Float-A-lyser – G235063) and dialysed 48h at room temperature against deionized water. The dialysate was then recovered, lyophilized during 72h and the lyophilized powder was stocked at -80°C. Stock solution of cationized gelatin for bioink formulation was prepared by dissolving 20% w/v of the lyophilized powder in DMEM (-) medium.

The theoretical recovered mass of synthesized product was calculated based on the standard gelatin the “Product information sheet” (Gelatin Type A, G1890, Sigma). According to the manufacturer, the gelatin type A possesses an average number of free carboxylic groups of 78-80 mmol/100g of gelatin. If ideally, every free carboxylic group were grafted and bond with different diaminohexane molecules, then the recovered cationic gelatin mass should be calculated as follow:

$$m_{CG\_th} = m_{G\_init} + \frac{m_{G\_init} * n_{free\ carb} * MW_{DH}}{100 * 1000}$$

Where,

$m_{CG\_th}$  is the theoretical maximal recovery mass of cationized gelatin (CG) in grams,

$m_{G\_init}$  is the mass of standard gelatin used for the synthesis ,

$n_{free\ carb}$  is the average number of free carboxylic groups for 100g of gelatin

$MW_{DH}$  is the molecular weight of 1,6-diaminohexane (116.21 g/mol).

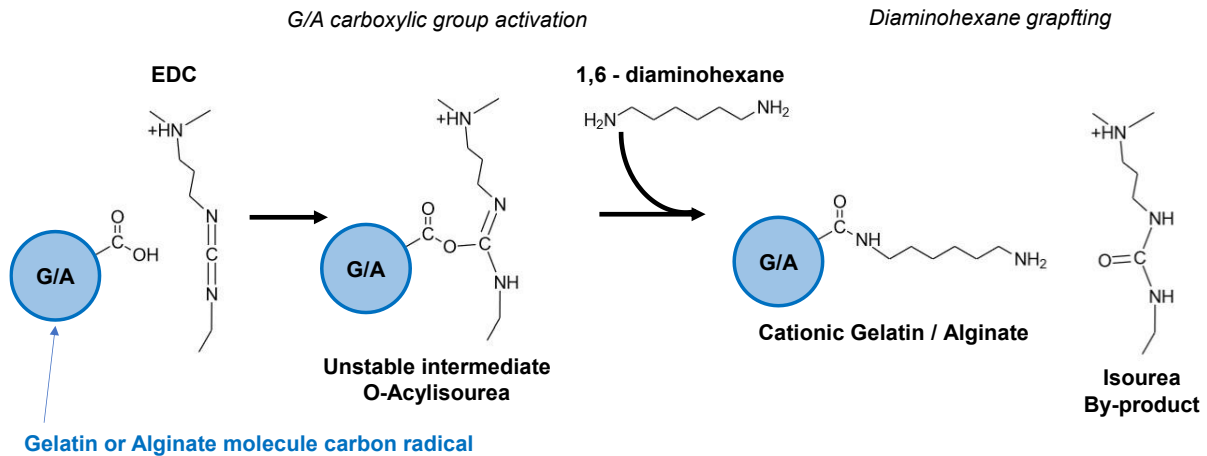


**Figure 2.7:** Chemical reaction of 1,6-diaminohexane grafting to gelatin and alginate molecules. EDC: 1-Ethyl-3-(3-dimethylaminopropyl)carbodiimide. The molecules were generated on ChemDraw online: <https://chemdrawdirect.perkinelmer.cloud/js/sample/index.html>

#### 2.4.4. Synthesis of cationized alginate

Cationic alginate (CA) was synthesized based on a literature protocol [548]. Alginate powder (Alfa Aesar - A18565) was dissolved at a concentration of 10 g/L in a 2-[N-Morpholino] ethanesulfonic acid (MES) 0.1M and NaCl à 0.5M (pH 4.5) buffer. EDC (Ethyl-3-(3-dimethylaminopropyl) Carbodiimide) (Sigma Aldrich – E7750) was added to the solution for a final concentration of 50 g/L. Diaminohexane (Fluka – 33000) was then added for a final concentration of 30 g/L. The reaction is presented in Figure 2.7.

The preparation vessel is covered to avoid evaporation and the solution was incubated 2h at room temperature under agitation. The solution was then placed in dialysis bags with exclusion size 3500 –5000 Dalton (Interchim – Float-A-lyser – G235065) and dialysed 24h at room temperature with deionized water. The dialysate was then recovered, lyophilized during 72h and the lyophilized powder was stocked at  $-80^{\circ}C$ . Stock solution of cationized alginate (CA) for bioink formulation was prepared by dissolving 4%w/v of the lyophilized powder in DMEM (-) medium.

The theoretical recovered mass of synthesized product was calculated based on the knowledge that one monomer of standard alginate possesses one free carboxylic group and the average molecular weight of an alginate monomer is ~ 176 g/mol. If hypothesing that every monomer



provides a carboxylic group that each bind with a different diaminohexane molecule, the maximal expected product mass should be calculated with the following equation:

$$m_{CA_{th}} = m_{A_{init}} + \frac{m_{A_{init}} * MW_{DH}}{MW_A}$$

Where,

$m_{CA_{th}}$  is the theoretical maximal recovery mass of cationized alginate in grams,

$m_{A_{init}}$  is the mass of standard alginate used for the synthesis,

$MW_A$  is the average molecular weight of an alginate monomer (~176 g/mol),

$MW_{DH}$  is the molecular weight of 1,6-diaminohexane (116.21 g/mol).

#### 2.4.5. *NMR characterization of synthesized cationic materials*

Cationized materials were analyzed by proton Nuclear Magnetic Resonance (H-NMR) to evaluate the success of diaminohexane grafting on the gelatin and alginate molecules. Before the acquisitions, at least 50 mg of the lyophilised samples were dissolved in 800 $\mu$ L of Deuterium Oxide (D215F; Eurisotop) and incubated overnight at 4°C before being placed in an NMR tube. Standard gelatin and alginate, pure 1,6-diaminohexane, pure EDC and MES buffer powder (used for CA synthesis only) were prepared in D<sub>2</sub>O and were used as reference spectra. The acquisitions were performed with a Bruker Avance III spectrometer with a 500MHz 1H resonance frequency and a BBFO probe. Single pulse sequence was used for the acquisitions.

#### 2.4.6. *Characterization of cationized gelatin rheology and imprimability*

The rheology of bioink prepared with cationic gelatin based on formulation A ratios was characterized with a stress controlled rotational rheometer (DHR2, TA Instruments, Guyancourt, France) and a 25 mm parallel plate. The samples were maintained at 21°C during the acquisitions thanks to a Peltier plate, this temperature corresponds to the printing conditions. The rheology of bioink prepared with cationic gelatin was compared with the one of standard bioink. The yield stress of the biomaterial was measurement with a logarithmic flow sweep procedure with shear stress range from 1.0 x 10<sup>-3</sup> s<sup>-1</sup> to 100 s<sup>-1</sup> and then decrease from 100 s<sup>-1</sup> to 1.0x10<sup>-3</sup> s<sup>-1</sup>. The evolution of viscosity and shear stress were observed on the acquired rheograms. The yield stress and rate index were calculated with the the constitutive equation of the Herschel-Bulkley model after the yield stress was reached:

$$\tau = \tau_0 + k\dot{\gamma}^n \quad \text{if } \tau \geq \tau_0$$

Where,

$\tau$  represents the shear stress,

$\tau_0$  is the yield stress,

$k$  is the consistency index (Pa.s<sup>n</sup>)

$\dot{\gamma}$  is the shear rate (s<sup>-1</sup>),

$n$  is the flow index.

The yield stress defines the solid part of the fluid and the flow index its capacity of shear-thinning when flowing.

#### 2.4.7. *Evaluation of cationized gelatin potential as transfecting agent in 2D*

HEK cells were seeded in 24 well plates at a cell density of 30 000 cells/cm<sup>2</sup> one day prior to transfection. A volume of 1 mL DMEM(+) per well was used for cell culture. To prepare the transfection complexes, 500  $\mu$ L of cationized gelatin liquified at 37°C were mixed with 7.2  $\mu$ L of a 1.4  $\mu$ g/ $\mu$ L pEGFP-C1 plasmids stock solution to reach a concentration of 20  $\mu$ g/mL of plasmids in cationic gelatin (CG). The mix was vortexed to homogenize the formulation and incubated for 30 min at 37°C in a waterbath. A 100 $\mu$ L of this mix was then added to the 1 mL of culture supernatant in each culture well. Plates were placed in an incubator at 37°C for cell culture. Comparative conditions were prepared according to the same protocol except the cationized gelatin was replaced by standard gelatin (SG) or DMEM(-) medium (without gelatin) to mix with the plasmids. Negative controls were prepared with standard and cationized gelatin without plasmid addition. A standard PEI transfection protocol was used as positive control. For this, 473  $\mu$ L of DMEM(-) were mixed with 20  $\mu$ L of 1mg/mL Polyethylenimine (PEI) solution (Polyethylenimine, Linear, MW 25000, Transfection Grade, 23966-1, Polysciences Inc.) and 7.2  $\mu$ L of 1.4  $\mu$ g/ $\mu$ L plasmid solution to reach a final 20 $\mu$ g/mL concentration. The mix then processed through the same steps previously described. The composition of the different mixes is summarized in Table 2.5. Cell transfection was assessed by fluorescence microscope observations 3 days after addition of the complexes in supernatant. The efficiency of transfection was estimated by image analysis with ImageJ software by measuring the fraction of green fluorescent surface area on total area.

**Table 2.5: Detailed composition of the different mixes added to the culture supernatants to evaluate and compare the efficiency of CG to act as transfecting agent. Conditions 1, 2 and 3 are the tested mixes whose transfection efficiencies were compared. Positive refers to the positive control and Negative 1 and 2 are two negative controls for cell transfection. CG refers to Cationic Gelatin and SG to Standard Gelatin.**

	CG solution ( $\mu\text{L}$ )	SG solution ( $\mu\text{L}$ )	DMEM(-) ( $\mu\text{L}$ )	PEI solution ( $\mu\text{L}$ )	Plasmid final concentration ( $\mu\text{g}/\text{mL}$ )
Condition 1	500	0	0	0	20
Condition 2	0	500	0	0	20
Condition 3	0	0	500	0	20
Negative 1	500	0	0	0	0
Negative 2	0	500	0	0	0
Positive	0	0	473	20	20

#### 2.4.8. Standard bioink formulation with naked plasmids

Plasmids were added to the gelatin 20% solution and incubated either overnight or 10 min, at 37°C before the preparation of the cellularized biomaterial. The concentration of the plasmid in the gelatin stock solution was adjusted to obtain the desired final concentration in the formulated bioink. Then, the bioink was prepared as previously described in section 2.2.2.

#### 2.4.9. Bioink formulation with additives and transforming agents

Transfection reagents are molecules that are enhancing the potential of nucleic acids (DNA or RNA) to penetrate in the targeted cells. As an example, the plasmids were complexed with two commercial transfection reagent (PEI or Lipofectamine 3000) according to the supplier recommendations. PEI (Polysciences Inc - 23966-1)-DNA complexes were prepared by mixing DNA with PEI at w/w ratios 2:1 (PEI [ $\mu\text{g}$ ] : plasmid [ $\mu\text{g}$ ]) in DMEM(-) medium. Lipofectamine3000 (InvitroGen - L3000-001) - DNA complexes were prepared by mixing DNA with Lipofectamin and P3000 at w/v ratios 1:1:1 (Lipofectamine [ $\mu\text{L}$ ] : P3000 [ $\mu\text{L}$ ] : plasmid [ $\mu\text{g}$ ]) in serum-free DMEM(-) medium. For the in situ transfection experiments, bioink formulation A was chosen. The complexed plasmids were added to the gelatin 20% solution and incubated either overnight or 10 min, at 37°C before the preparation of the cellularized biomaterial. The plasmid concentration within gelatin was adjusted according to the final concentration expected in the formulated biomaterial where gelatin solution represents 25% v/v of bioink volume.

#### 2.4.10. *Bioink formulation with cationic biomaterial components*

For the *in situ* transfection experiments with cationized components, bioink formulation A was chosen and adapted by replacing standard gelatin by its cationic equivalent.

Cationized gelatin-based bioink was prepared by adding plasmids at concentrations ranging from 40 µg/mL to 80 µg/mL in the cationic gelatin to reach final concentrations from 10µg/mL to 20 µg/mL in the biomaterial where gelatin solution represents 25%v/v of bioink volume. Plasmids were added to the cationic gelatin 20%w/v solution and incubated 30 min, at 37°C before the preparation of the bioink. Negative controls were prepared with standard biomaterial formulation and cationic biomaterial, both prepared without addition of plasmids. A comparative condition was also prepared with standard bioink containing naked plasmid (see below 2.2.1). Transfection efficiency was further monitored by fluorescence microscopy observations or dissociation of the tissues and flow cytometry on the recovered cells.

#### 2.4.11. *Evaluation of nucleic acid stability within the biomaterial*

DNA stability was evaluated thanks to labelling with nucleic acid intercalating dye, DAPI, which is fluorescent at 450-490nm. the plasmids solution (1.5 µg/µL) was mixed and incubated with a 11 mM DAPI solution or a 2.5 mM Sytox orange solution at a 1 : 1 volume ratio. This step aimed to fluorescently label the plasmids with intercalant reagents. The mixture was then added in the hydrogel at a 1 : 1 volume ratio corresponding to a 0.375 µg/µL plasmid concentration in bioink. Biomaterial was then consolidated according to several protocols listed in section that will be detailed in Chapter 7. DNA fluorescence was monitored over 15 days by fluorescent microscopy, to confirm its stability within the biomaterial.

#### 2.4.12. *DNA dosage in bioink and supernatants*

In order to quantify the remaining plasmids in the bioink or released in the supernatant, a protocol was developed utilizing the Qubit® dsDNA BR Assay Kit. This kit employs a fluorescent dye specifically designed to stain double-stranded DNA. The Qubit fluorometer automatically detects and quantifies fluorescence within a DNA concentration range of 0.2 ng/µL to 2000 ng/µL. To confirm the linearity in the range of our measurements, a standard curve was prepared using 12 points ranging from 0.001 µg/mL to 200 µg/mL of plasmids in dH<sub>2</sub>O. To assess the stability of DNA in the bioink, plasmids were introduced into the bioink at a concentration of 4µg/mL. The constructs were then consolidated for 1 hour using a solution of 3% CaCl<sub>2</sub>, 4% transglutaminase and 10 U/mL Thrombin. Subsequently they were cultured for 7 days at a temperature of 37°C. Then, the constructs were dissociated in a 3% solution of

Collagenase A. The resulting dissociation supernatant was collected for DNA quantification. Additionally, the culture supernatant obtained on day 5 was also collected to measure the released plasmids. Controls were established using dissociated hydrogel without plasmids, non-consolidated bioink with either 0 or 4 µg/mL plasmids (dissolved 1/5 in PBS), and a 3% Collagenase A solution with either 0 or 10 µg/mL plasmids.

#### 2.4.13. *in situ* Transfection

Bioinks were prepared as previously described. Multiple conditions were tested where plasmids were added directly to standard bioinks as naked plasmids or were complexed to transfectin agents PEI or Lipofectamine 3000 prior to mixing with the bioink components. Naked plasmids were also added to cationic bioinks prepared with cationized gelatin. Each time, 300 µL of bioink was deposited with a pipet into 24 well plates or 200 µL in 48 well plates to create a thin layer of hydrogel (< 2 mm) on the bottom of the plates. Reticulation solution was added on top of the hydrogels and left 5 min at room temperature before a 55 min incubation at 37°C. The molded constructs were then rinsed 3 times with 0.9% NaCl solution. The cultures were performed in an incubator at 37°C with DMEM(+) medium.

The transfection of cells was monitored by regular fluorescent microscopy observations.

## CHAPTER 3. DEVELOPMENT OF ANALYTICAL TOOLS TO STUDY SMALL-SCALE 3D CULTURES

In the last 10 years, the rising interest in tissue engineering has led to fast advances in 3D cell cultures and bioprinting. Such advancements have been achieved by incorporating technologies and methodologies from various disciplines to overcome existing barriers. Nonetheless, important challenges continue to hinder the development of these fields. One obstacle is the lack of appropriate analytical tools for precise cell study within 3D structures. While numerous analytical tools are available for characterizing cell cultures in standard modes, such as 2D monolayer culture and cell suspensions, most of these techniques are not directly applicable to 3D cell culture.

A major barrier in this project was the precise quantification of cell proliferation within 3D bioprinted constructs. To address this issue, work was made to adapt existing standard analytical tools for traditional cell culture modes or tissue biopsy analysis, making them applicable to 3D cell cultures.

### 3.1. Hydrogel dissociation and cell counting

The cells are directly recovered and quantified from supernatant samples in standard suspension cultures. In 2D cultures, adherent cells are detached from the anchorage surface by actions of proteases, mainly Trysin, or mechanical scaping. However, cell recovery from the 3D bioprinted cultures is more complex as the cells are encapsulated inside the hydrogel matrix. The standard cell recovery techniques could not be directly used in such case. Therefore, in 3D bioprinted constructs, direct cell quantification could only be performed after dissociation of the hydrogel. Thus, the cell extraction protocols from hydrogels or extracellular matrix had to be developed concomitantly to the cell growth evaluation presented in Chapter 4, Figure 4.1. This work is presented here as a preliminary work but was integrated as Supplementary Table S1 & S2 of the Publication presented in Chapter 4.

The initial dissociation protocol used for this study is from my previous work on 3D bioprinted dermis dissociation I developed during my master's internship. This work has been published in the publication and patented [203,549].

The protocol was carried out on hydrogel constructs prepared with Formulation A (2% Fibrinogen, 2% Alginate and 5% Gelatin) and consolidated with 3%<sub>w/v</sub> CaCl<sub>2</sub>, 4%<sub>w/v</sub> transglutaminase and 10 U/mL Thrombin. The protocol consisted of a first 5 min incubation in

trypsin to detach the cells from the matrix. Then, construct rinsing and a follow-up incubation in 3% Collagenase A solution was used to hydrolyze the gelatin of the hydrogel. The procedure lasted 3 to 4 hours and resulted in incomplete hydrogel dissociation. The presence of hydrogel debris from 10 to 100  $\mu\text{m}$ -scale was observed (see Figure 3.1). Additionally, even if almost 100% of the cells could be recovered, the viability was very low (22%). The viability loss was associated with both a sensitivity of HEK cells to trypsin and the duration of the dissolution process, leading to cell exposure to deprived nutrient conditions.

Therefore, dissociation protocol optimization was engaged to reduce its duration and increase its overall efficiency. Protocol efficiency was evaluated on cell recovery, viability, and hydrogel complete dissolution. The chosen dissociation protocols were screened among enzymatic, chemical, or mechanical procedures. The mechanical dissociation was performed with a gentleMACS equipment. For the enzymatic dissociations, we screened Collagenase A, Collagenase/Dispase, Trypsin, TrypLE, Alginate lyase, Pepsin and Human Platelet Lysate (HPL) while chemical processes included EDTA, Sodium citrate. Each was chosen for its ability to degrade one of the hydrogel matrix's compounds or to detach the cells from the matrix.

Thus, Collagenase can degrade collagen fibres, while Dispase is a protease that cleaves fibronectin and collagen IV [550]. Pepsin is also a protease and can solubilize a wide range of proteins, including collagen [551]. Trypsin, TrypLE, a Trypsin-like protease [552], and EDTA are used to degrade cell-anchorage and cell-cell tight-junctions' proteins such as integrins or cadherins [553,554]. In fact, Trypsin is an endopeptidase able to hydrolyze peptide bonds enzymatically, EDTA is a chemical with a similar effect and is often used as a Trypsin substitute. Alginate lyase hydrolyzes the Alginate polymers by cleaving the beta-1,4 glycosidic bond between two adjacent sugar residues via a beta-elimination mechanism [555,556]. Sodium citrate and EDTA are chelating agents able to recover the calcium ions involved in electrostatic bonds, which alginate disrupts the alginate molecules network [317,557]. Human Platelet Lysate can supplement culture media as a substitute for FBS with a Good-Manufacturing Practice grade (GMP) [558]. It contains Matrix Metalloproteinases (MMP) 2 and 9 (gelatinase) [559] which are enzymes able to degrade the compounds of extracellular matrix, especially gelatin [560]. The results of the dissociation protocols are presented in Table 3.1.

**Table 3.1: Dissociation protocols screened for their effect on cell recovery, viability and gel dissolution level.** Cell concentration hydrogel loading was standardized to  $1 \times 10^6$  cells/mL. Protocol dissociation screening were tested right after their preparation and consolidation. Cell number and viability were determined by counting the recovered cells on Malassez slide with Trypan Blue exclusion method.

PROTOCOL	CELL VIABILITY (%) (Trypan blue)	CELL TOTAL RECOVERY (%)	ESTIMATED GEL DISSOCIATION (%)
3% Collagenase A in PBS (4.5 U/mL)	22	100	85
3% Collagenase A in DMEM (w/o FBS) (4.5 U/mL)	25	100	85
Collagenase/Dispase (0.1U/mL ; 0.8U/mL)	16	100	65
Trypsin 1X	NA	0	0
TrypLE 1X	NA	0	0
Pepsin 0.5%	NA	0	0
Mechanical (3 x GentleMACS lungs_01 )	NA	< 5%	50
EDTA 50 mM	NA	NA	0
Sodium citrate 55 mM and 100 mM	NA	NA	15
Human Platelet Lysate	NA	NA	70
Alginate lyase + EDTA + sodium citrate	NA	NA	15
EDTA + sodium citrate	NA	NA	15
Alginate lyase (5U/mL) followed by Collagenase A 3%	45	74	90
Alginate lyase (5U/mL) + Collagenase A 3%	34	30	87
Na <sup>2+</sup> -citrate followed by Alginate lyase/CollA	35	85	100

First, the protocols based on actions of solely Trypsin, TrypLE, EDTA and Pepsin did not permit the dissociation of the hydrogel as expected. Consequently, the cells could not be recovered. On the contrary, the protocols using sodium citrate solution either as a single component or combined with EDTA and Alginate lyase solutions allowed to weaken the hydrogel. It resulted in the fractionation of the construct in large pieces over the mm size. Yet, even after over 3h of incubation at 37°C, the construct did not dissociate further.

The mechanical gel dissociation with tissue dissociator gentleMACS, allowed for the breaking of the hydrogel into small pieces of the mm size or smaller debris. Yet, the cells could not be efficiently recovered with a yield below 5% and 100% cell death.

Finally, all the protocols demonstrating cell recovery and hydrogel dissociation over 50% contained Collagenase A. It demonstrates the importance of degrading the crosslinked gelatin from the hydrogel. The collagenase concentration was also proved to be of importance. Indeed, the Collagenase/Dispase solution displayed lower efficiency for hydrogel dissociation than the other collagenase-based protocols. It is mainly due to the lesser collagenase concentration and subsequent activity of 0.1 U/mL compared to 4.5 U/mL in the other collagenase solutions. Such incomplete dissociation was observed in protocols run with only collagenase or collagenase-



Dispase digestion resulting in numerous 10 to 100  $\mu\text{m}$ -scale hydrogel debris as shown in Figure 3.1.

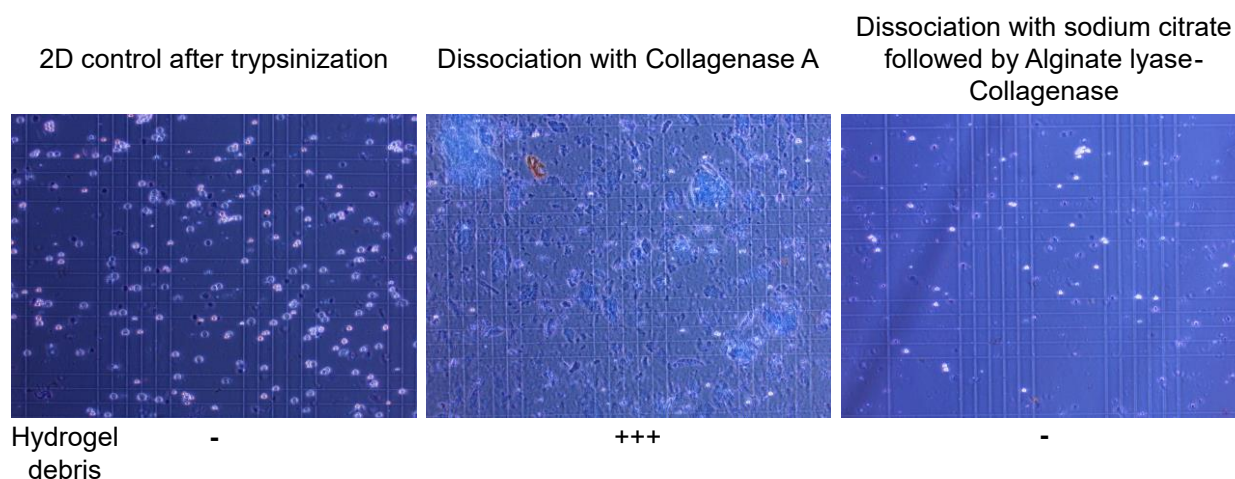


**Figure 3.1: Comparison of dissociation protocols' efficiency.** Cell solution recovered after trypsinization (2D control) or dissociation of hydrogel constructs with two different protocols. Protocol run with Collagenase only (2<sup>nd</sup> image) resulted in the presence of hydrogel debris visible as darker blue pieces in the picture.

Total cell recovery was estimated to be 100%, even though some cells were still encapsulated in the hydrogel debris. This is probably because hydrogel debris is stained by Trypan blue, and those in the 10 to 20  $\mu\text{m}$  range are very difficult to distinguish from dead cells. Therefore, some debris may be counted as dead cells, resulting in an inexact estimation of total cell density.

Among the protocols allowing hydrogel dissolution, several sequences were screened to reach the highest recovery. Collagenase/Alginate lyase solution resulted in poor 30% cell recovery with 34% viability despite an efficient hydrogel dissociation. However, incubation in an Alginate lyase solution and subsequent incubation in a Collagenase A solution led to 2.5-fold higher recovery (74% with 45% viability). Similarly, a preliminary incubation in sodium citrate solution before the incubation in Collagenase/Alginate lyase led to an even improved cell recovery, up to 85%, while reaching ~35% viability. Again, this last condition resulted in the complete hydrogel dissociation.

Consequently, the two best protocols for cell extraction from the 3D bioprinted matrix were :

- A- A 15 min incubation in Alginate lyase (5U/mL) solution followed by incubation in Collagenase A 3% solution until complete hydrogel dissociation (30min to 1h)
- B- A 5 min incubation in 55 mM sodium citrate solution followed by incubation in an Alginate lyase (5U/mL) / Collagenase A 3% solution prepared in PBS until complete dissociation (~ 30min).

**The two selected protocols were estimated to result in similar yields with a 90-100% dissociation of the hydrogel, 74-85% cell recovery, and 35-45% viability (see Table 3.1). Both protocols target the two main structural compounds of the hydrogel, alginate and gelatin. This allowed us to reduce the total dissociation process from 3 - 4h to less than 1h.**

Protocol B was chosen among the two for subsequent experiments. Indeed, it allowed a 100% dissociation of the hydrogel, which is advantageous for cell counting as it reduces the risk of mistaking and counting hydrogel debris for dead cells.

In the bioproduction field, there is a notable interest in two aspects: the recovery of live cells as the end product and the conduction of cell characterization studies throughout the cultivation process. Consequently, obtaining a pure cell solution free from any hydrogel remnants is advantageous when analyzing cells using sophisticated techniques such as flow cytometry assays. This capability facilitates the examination of samples through flow cytometry without any hindrance caused by the buildup of hydrogel debris within the capillaries, thereby improving the overall effectiveness of the analysis.

To go deeper into the description of the effect of dissociation protocols, and verify if it would be possible to recover live cells as a final product, the collected cells were analyzed in cytometry to evaluate the ratio of viable, apoptotic and necrotic cells after dissociation. The cells were stained with Annexin V-FITC and Propidium Iodide (PI), markers for apoptosis onset and necrosis, as described in Chapter 2.

The results showed that over 90% of the cells were apoptotic, with more than 50% in early apoptosis and 40% in late apoptosis (See Figure 3.2). Only 5.5 % of cells were viable, and less than 2% were necrotic.

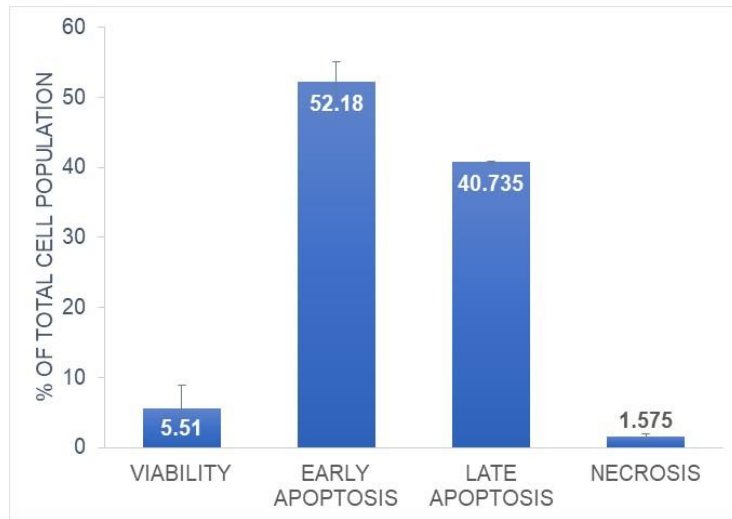


***Figure 3.2: Analysis of cell viability, apoptosis, necrosis after dissociation with protocol B***

Hence, we were able to reduce the protocol duration, but it was not sufficient to reach high cell viability. Among the two protocols with the highest viabilities (protocols 1 & 2 presented above), the viability was lower in the protocol using the sodium citrate phosphate buffer (55mM sodium citrate in PBS). It is known that the physiological osmolality is comprised in a range of 280 – 330 mOsm/kg. Therefore, we decided to evaluate the osmolality of different sodium citrate solutions presented in Table 3.2.

**Table 3.2: pH and osmolality of dissociation solutions.** Orange values indicate hyper-osmotic or hypotonic conditions (extracted from Supplementary 3 from our submitted research paper presented in Chapter 4)

Solution preparation					
Solvent	Sodium citrate (mM)	Alginate lyase (mg/mL)	pH adjustment to ~7 with NaOH	final pH	Osmolality (mOsmol/kg)
H <sub>2</sub> O	25	0	Yes	6.86	79
H <sub>2</sub> O	55	0	Yes	6.72	172
H <sub>2</sub> O	100	0	Yes	6.4	309
PBS	25	0	Yes	7.28	346
PBS	55	0	Yes	7.37	423
PBS	100	0	Yes	7.42	533
0.9% NaCl	25	0	Yes	7.58	351
0.9% NaCl	55	0	Yes	7.53	430
0.9% NaCl	100	0	Yes	7.43	539
H <sub>2</sub> O	55	0.5	Yes	6.73	211
H <sub>2</sub> O	100	0.5	Yes	6.67	327

The results showed that the 55 mM sodium citrate solution prepared in PBS was slightly hyper-osmotic (423 mOsm/kg), which could explain the high cell apoptosis. It has been reported that renal cells could survive hyper-osmolality up to 500 mOsmol/kg but would become apoptotic and die over this value [561]. Hypotonic solutions (< 280mOsmol) can also promote cell apoptosis [562,563]. In our case, it consists of all the solutions prepared in H<sub>2</sub>O with citrate concentration below 100mM. Still, the solutions with osmolality in the physiological range (iso-osmolality) were 100 mM sodium citrate in dH<sub>2</sub>O and 25 mM sodium citrate in PBS or 0.9% NaCl solution. All sodium citrate solutions had their pH adjusted and comprised in a range of 6.4 - 7.6.

**The solution adjusted to a 100 mM sodium citrate in dH<sub>2</sub>O was chosen for the optimized dissociation protocol.**

It is essential to emphasize that the number of cells lost during dissociation remains uncertain. This evaluation is not straightforward and requires a calibrated reference method for accuracy. As a result, the osmolality of the solution may not be the sole factor influencing cell viability. Additionally, the impact of shear stress during the homogenization of cells in the bioink, bioprinting, and the consolidation of hydrogel on cell viability is also undetermined and challenging to assess. Both of these factors could potentially affect the viability of cells recovered immediately after dissociation on day zero. Indeed, it is a complex task to determine whether the dead cells observed after dissociation were already nonviable within the construct or if they perished during the dissociation process.

### 3.2. Cell quantification on histological slides

Another parameter of interest when qualifying a cellularized structure is the overall cell density within the construct and the cell repartition in 3D. This parameter was evaluated thanks to standard histology analysis transposed to our cellularized bioprinted structure. Thus, samples were first dehydrated and paraffin-embedded. They were then sliced into a 5  $\mu$ m thick sections. Then, after paraffin removal, cell nuclei were stained with DAPI. It allowed to describe the cell density by counting the number of nuclei from DAPI-stained histological sections with particle analysis on ImageJ. This procedure allowed to determine the repartition of cells over one slice of the samples.

It would thus be necessary to slice the integrality of the object to describe and quantify the overall cells on the histological section with a realistic representation of the whole construct. In the case of the largest object bioprinted obtained in this project (10.8 cm<sup>3</sup> construct), and considering the dehydration shrinkage factor of ~ 50% during histological treatment, it would

be necessary to slice 200 sections. Such protocols represent tremendous work and still result in a single sample point.

To still estimate the cell density in the samples, we applied a hypothesis for its calculation. First, the slice is representative of the overall volume of the sample. Calculation can use the cell nuclei mean as representative of the reconstituted volume. Hence, to estimate the cell density, the surface occupied by the hydrogel was calculated in each picture by surface analysis in ImageJ and divided by the shrinkage factor of 0.5 to convert the measured surface to its original dimension.

Second, HEK cells diameter and nuclei diameter are over  $5\mu\text{m}$  as shown in Figure 3.3. Indeed, image analysis on multiple HEK cells images acquired from Transmission Electron Microscopy showed an average cell diameter of  $13.5 \pm 2.0 \mu\text{m}$  and an average nucleus diameter of  $9.4 \pm 0.9 \mu\text{m}$  ( $n=5$ ).

Two different cell quantifications methods were applied, in the first method (Method 1), the number of nuclei counted on histological slices were considered to be representative of constructs sections of  $5\mu\text{m}$ , corresponding to the thickness of the histological section. However, considering that HEK cells diameter is  $13\mu\text{m}$ , the number of cells per image from  $5\mu\text{m}$  section will overestimate the cell density as one cell nuclei can be counted in two or more different sections and the cell will occupy a larger volume than that observed on the section. Thus, we also used a second method (Method 2), in which we estimated the cell count measured on histological sections to be representative of a  $13 \mu\text{m}$  thick section, corresponding to the diameter of an HEK cell. The second method had the advantage to reduce the risk of overestimating the cell density. The cell density calculated from these methods were compared to results obtained with dissociation as shown in Figure 3.4.

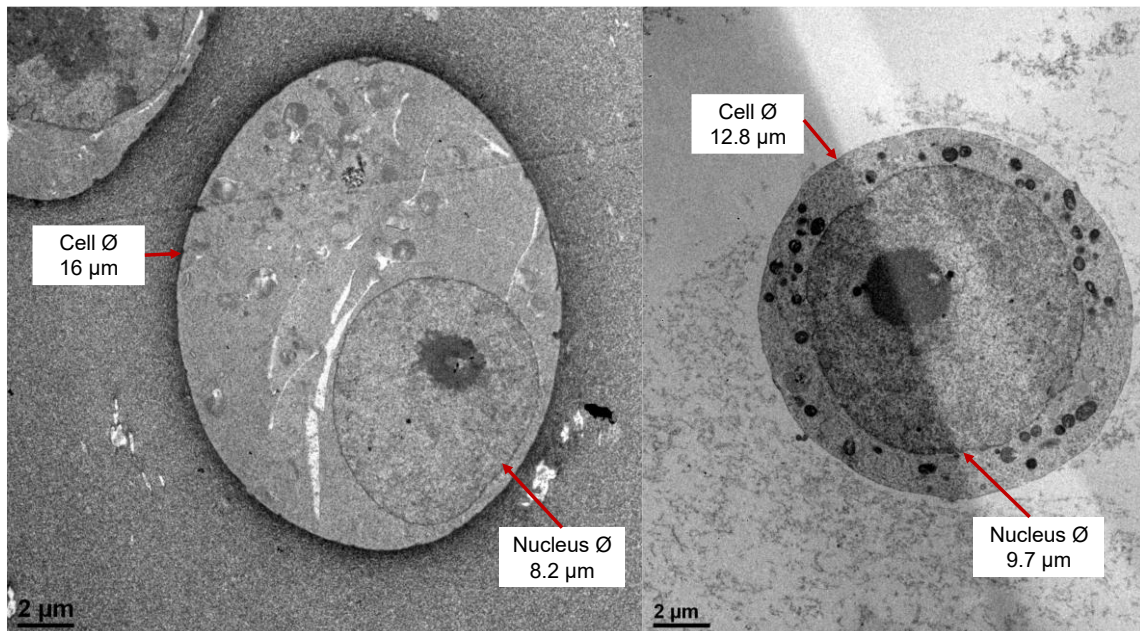


**Figure 3.3: Images of HEK cells in bioprinted hydrogels acquired by Transmission Electron Microscopy.**

Comparison between, estimated cell density from nuclein counting and construct dissociation was significantly different. Cell concentration measured after dissociation were very low compared to the concentration estimated by image analysis (see Figure 3.4). This ascertainment proves that all the analytical methods available or developed to assess cell concentration in 3D cultures have bias and have limited precision. Cell loss is expected concerning construct dissociation due to exposure to several steps and straingent dissolution condition. While nuclei counting from construct slices represents only a very local cell concentration and is heterogeneous on the whole construct.

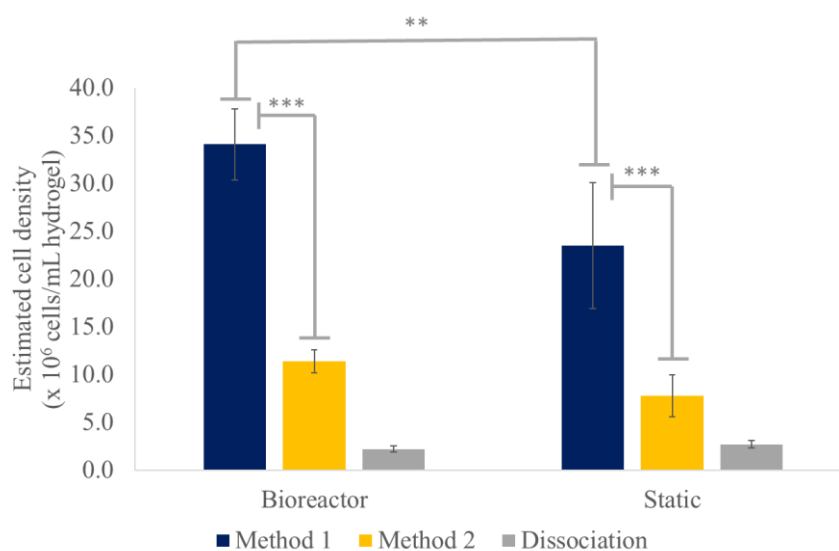


**Figure 3.4: Cell density measure in the same construct with three different protocols : Method 1 is based on image analysis (particle counting) of DAPI-stained nuclei on histological slides estimated to represent a 5μm thick**

*section, Method 2 used the same process and evaluated the image to be representative of a 13  $\mu\text{m}$  thick section, finally, dissociation was used to assess cell number by direct counting after cell recovery.*

### 3.3. Analysis of cell growth thanks to calcein and spheroid sizes

All of the previous analytical methods presented and developed for monitoring cell proliferation in bioprinted construct are destructive. With this in mind, our objective was to establish a non-destructive procedure for continuously assessing cell viability and proliferation over a 20-day culture period. We employed the calcein staining technique described in Chapter 2 to label live cells within the bioprinted constructs. Using fluorescent microscopy to observe calcein-stained cells, we identified the formation of cell aggregates, referred to as "spheroids," in HEK and MDCK cultures. In contrast, CHO and Vero cells did not exhibit noticeable large aggregates visible through calcein staining. Image analysis using ImageJ software allowed us to track the size of spheroids formed by HEK and MDCK cells.

When comparing the changes in spheroid diameters with the alterations in cell density measured through dissociation, we observed a similar trend in MDCK cell cultures. However, in the case of HEK cell cultures, no apparent similarity was evident, as depicted in Figure 3.5. Consequently, microscopic imaging of MDCK cell cultures for spheroid size analysis could serve as an additional method for monitoring cell proliferation. Nevertheless, it's worth noting that after approximately 13 days, the cells began to spread out in layers, and spheroids were no longer visible. Therefore, this method is most suitable for tracking cell proliferation during the initial days of culture. Additionally, it's important to acknowledge that this analytical method may not apply to all cell lines due to variations in their proliferative behavior. While spheroid measurements can offer qualitative insights into MDCK cell proliferation, they do not precisely quantify cell numbers.



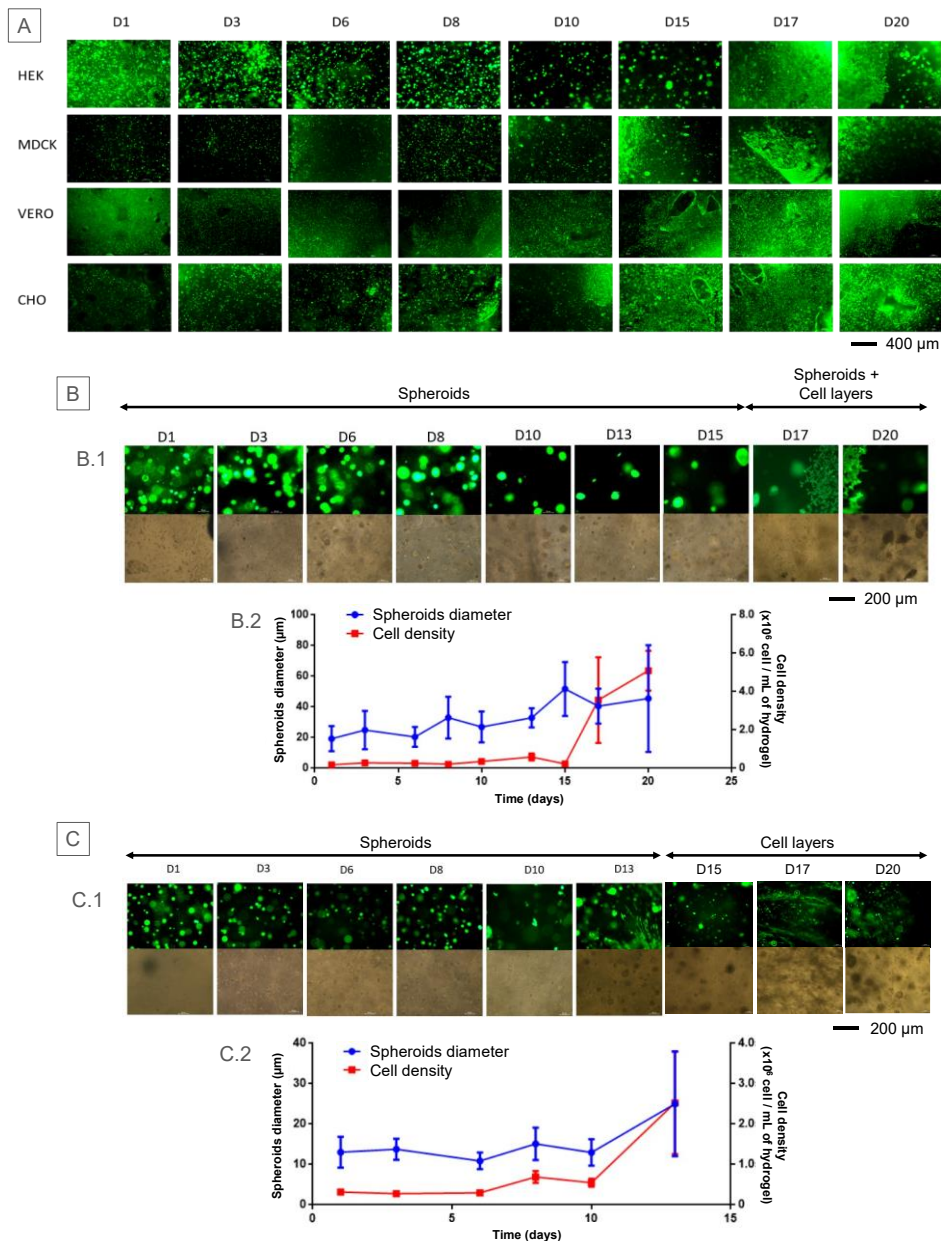


**Figure 3.5: Non-destructive monitoring of cell proliferation with calcein staining** (A) Example of cell viability monitoring with fluorescent microscopy of calcein-stained cell lines (scale bar is 400  $\mu\text{m}$ ). (B) shows the growth behavior of HEK (B.1) and MDCK (C.1) cells forming spheroids (scale bars are 200  $\mu\text{m}$ ), and (C) presents the evolution of average measured spheroids diameters and cell density of HEK (B.2) and MDCK (C.2) cells.

### 3.4. Cell metabolic activity as an indicator of cell proliferation

Lactate is a waste by-product of cell metabolism. It is mainly produced in anaerobic conditions but fast-growing cell lines are known to release high lactate levels even in the presence of oxygen [135,136,142]. We selected lactate as a non-destructive indicator of cell proliferation. By monitoring cell metabolic activity through lactate measurement, we observed a direct correlation between lactate production and the state of cell proliferation.

During the initial 3 to 15 days of culture, the bioprinted cell line underwent a lag phase with a low proliferation rate. This phase corresponded to a constant, linear evolution of lactate

production, indicating a steady production rate. As the cells entered a more rapid proliferative phase, an acceleration in lactate production became evident. This transition is illustrated in Figure 3.6 by changes in the lactate production slope, as indicated by red arrows. Notably, this shift coincided with the onset of faster growth for all kidney cell lines (HEK, MDCK, Vero).

Conversely, CHO cells exhibited an accelerated lactate production five days before the initiation of rapid cell proliferation. In all cases, faster cell proliferation was linked to an increased lactate production rate compared to the lag phase. Consequently, lactate was selected as the preferred non-invasive technique for monitoring cell proliferative status.

However, while the evolution of lactate concentration offers insights into cell proliferation and identifying the end of the lag phase, it does not provide a quantitative analysis of cell density. Furthermore, aside from the cell proliferation rate, other environmental factors can influence cell metabolism. Additionally, certain cell lines, like CHO cells, are known to have the capability to consume lactate in suspension cultures in cases of substrate depletion.

Therefore, although the lactate assay is a valuable non-invasive tool for assessing cell proliferation, it is crucial to recognize that other variables may influence it. As a result, it should be used as a supplementary tool alongside dissociation or image analysis of cell constructs rather than as the sole analytical method. Nonetheless, it offers a straightforward way of comparing cell behavior under different culture conditions.

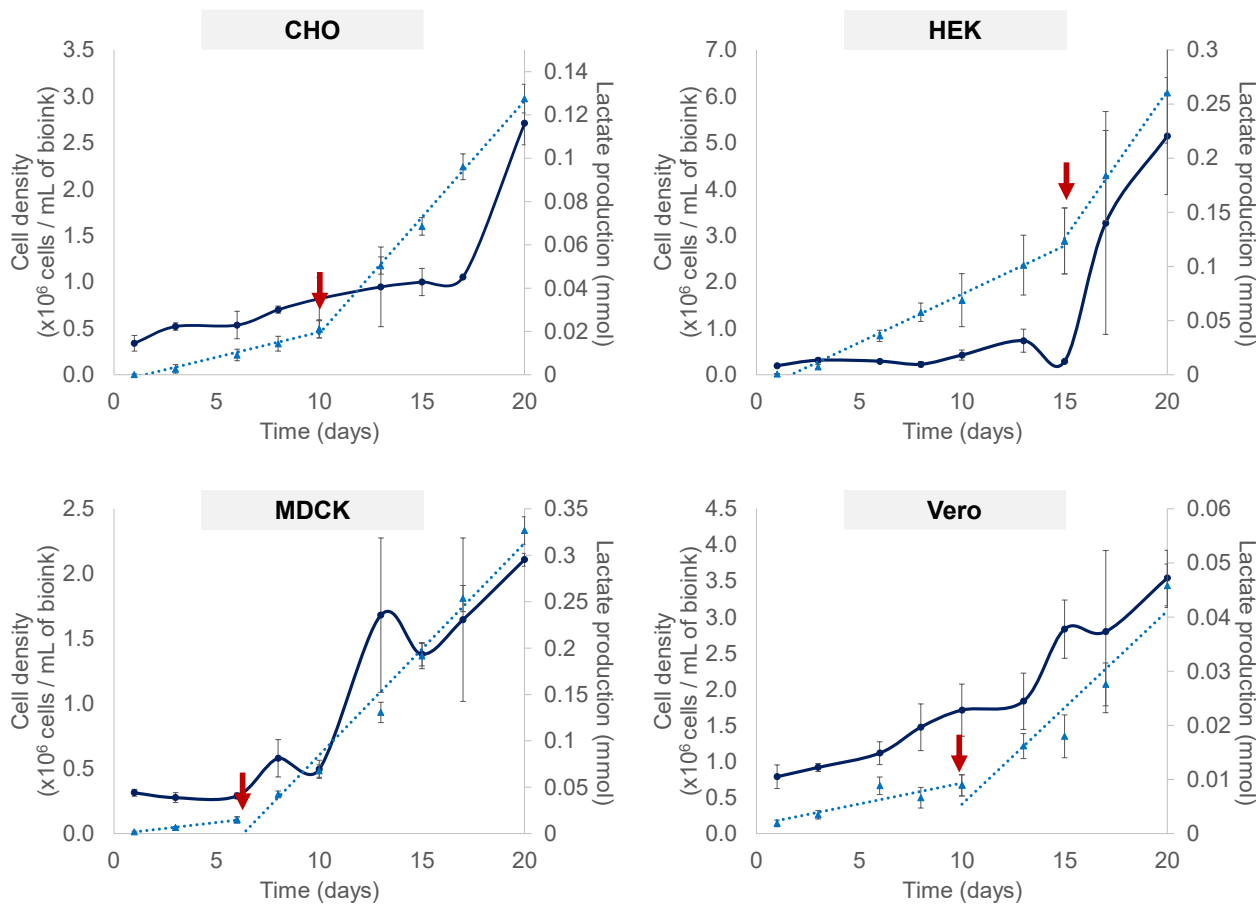


**Figure 3.6: Comparative evolution of cell density and lactate production.** Trends are presented for the four cell lines over 20 days of culture in bioprinted constructs. Cell density is represented by a dark blue curve and lactate production by a light blue dot line. The red arrows indicate a change in lactate production rate identified by a slope change.

### 3.5. Conclusion

In summary, this chapter introduced a range of analytical tools developed and utilized in this project to examine cell behavior within 3D bioprinted constructs. The comprehensive quantification of cells throughout the entire construct volume was exclusively feasible through cell dissociation. We established an optimized protocol to reduce sample processing time and maintain physiological osmolality. However, accurately assessing the total cell loss during the dissociation process and distinguishing between cells that perished during dissociation and those that were already nonviable and trapped within the hydrogel posed challenges in precisely determining cell density and viability within the constructs. Furthermore, despite efforts to improve the viability of recovered cells, a significant mortality rate persisted, with as few as 5% of cells remaining viable, while over 50% were in early apoptosis, and the remainder were in late apoptosis or necrosis. Therefore, combining dissociation with other analytical techniques such as image analysis of histological slides and live cell imaging and monitoring lactate production is advantageous. Although each method has its limitations, cross-validating the

results obtained from these diverse techniques enables the confirmation of cell proliferation trends. Lastly, non-destructive methods like the lactate assay from supernatant samples can be scaled up for larger-scale bioreactor cultures without culture interruption.

## CHAPTER 4. DESCRIPTION OF BIOPRODUCTION CELL LINES' BEHAVIOR IN 3D BIOPRINTED CULTURES

The project's initial phase aimed to confirm the capability of four mammalian bioproduction cell lines to survive and proliferate within 3D bioprinted structures. Each cell line was seeded in a bioink comprising Fibrinogen, Alginate, and Gelatin and further bioprinted. Cell survival was continually monitored during the culture by staining live cells with calcein and conducting microscopic observations. Additionally, the constructs were dissociated three times a week to assess cell proliferation. The outcomes revealed that all mammalian cell lines survived and exhibited significant proliferation within the bioprinted constructs, sustaining growth over a 20-day culture period. These results and further investigations into the physiological characteristics of these cells within bioprinted constructs have been the subject of a research article recently submitted to the journal *Biofabrication*.

The Material and Methods section of the article was incorporated into Chapter 2 of this thesis. The thesis's respective "Abbreviations" and "References" sections included abbreviations and references from this scientific article. The numbering of figures was adjusted to adhere to the thesis format guidelines, and supplementary data were integrated as figures within the article and the manuscript.

# **Production cell lines 3D bioprinting : Evaluation of a novel bioproduction support.**

Laura Chastagnier<sup>1</sup>, Lucie Essayan<sup>1</sup>, Celine Thomann<sup>1</sup>, Julia Niemann<sup>3</sup>, Elisabeth Errazuriz-Cerda<sup>4</sup>, Manon Laithier<sup>1;2</sup>, Anne Baudouin<sup>2</sup>, Christophe Marquette<sup>1</sup>, Emma Petiot<sup>1</sup>

<sup>1</sup> 3d.FAB, Univ Lyon, Université Lyon1, CNRS, INSA, CPE-Lyon, ICBMS, UMR 5246, 43, Bd du 11 novembre, 69100 Villeurbanne cedex, France

<sup>2</sup> Centre Commun de RMN, CNRS, Université Lyon 1, CPE-Lyon, Bâtiment Lederer, 1 Rue Victor Grignard, 69100 Villeurbanne, France

<sup>3</sup> Sartorius Stedim Biotech GmbH, August Spindler Strasse 11 Goettingen, D-37079 Germany

<sup>4</sup> Centre d'Imagerie Quantitative Lyon-Est (CIQLE), Université Claude Bernard Lyon 1, Lyon, France

## **ABSTRACT**

Three-dimensional cell culture is a powerful tool for medical and research applications to recapitulate *in vivo*-like environments. In the last decade, bioprinting technologies have gained increasing interest in generating homogenous or complex 3D cell cultures. However, even though researchers have already reported physiological changes occurring in 3D cultures, the precise proliferative and metabolic modifications and the parameters impacting cell physiology are not yet fully understood. In this work, we aim to provide a better understanding of the growth and metabolic changes occurring in 3D bioprinted constructs. The proliferation and central carbon metabolism of four mammalian cell lines (HEK, MDCK, Vero, CHO) were characterized in 3D bioprinted cultures. Then, a Design Of Experiment (DOE) was used to screen multiple factors associated to bioprinting parameters and hydrogel properties, and evaluate their effect on cell physiology. We demonstrated that immortalized bioproduction cell lines could recover some characteristics from their original tissues when cultivated in 3D bioprinted constructs. These cells showed reduced growth rates, increased metabolic activity and specific 3D organization. Multiple parameters affecting cell metabolism and proliferation in 3D bioprinted constructs were identified.

## **KEYWORDS**

**Bioprinting, bioproduction, 3D culture, metabolism, design of experiment**

## 4.1.Introduction

Biopharmaceutical manufacturing from animal cell lines has been widely used and developed since the late '80s [13,564]. It allows the production of macromolecules with correct post-translational modifications and good productivity at large scale [565]. These animal cells have been selected and adapted to maximize bioproduction yields for decades. They are essentially immortalized, highly selected or mutated, and present non-physiological behaviors [80,146]. Their growth, death and metabolic kinetics were extensively described with precise Flux Balance Analysis (FBA) [139,566–569] vast databases now do exist that describe their biological kinetics. This deep understanding of the production cell line behaviors was mandatory to optimize biopharmaceutical production processes.

To answer the growing demand for therapeutics and vaccines [99,177,570], bioproduction using cell lines had also to be intensified. One such strategy was to densify the cultures to reach higher cell concentrations, thus increasing final product titers. These densification strategies consisted of increasing adhesion support specific surfaces. Nowadays, adherent cells are mainly cultured on microcarriers or in fixed-bed reactors to enable scale-up in industrial-scale bioreactors. These strategies, where proliferation capacities are limited to adhesion surface availabilities, strongly impede very large-scale culture, limiting bioproduction volumes to a maximum of 6000 L [571].

To cope with this issue, broad interest has been given in recent decades to suspension cell lines, which often reach higher cell densities than adherent cultures [572]. These suspension cell lines, which originated from adherent cells, were progressively adapted to suspension culture by clone selection in unfavorable conditions for adhesion [573]. However, these cell lines' successive selections and adaptations to non-physiological and intensified cultures have caused their significant deviation from original *in-vivo* characteristics [98]. It is now clearly shown in several productions that increasing cell density has decreased their secreting capacity and cell-specific productivity of recombinant protein or viral products [574–577].

Our hypothesis is that growing production cells adherently but in a 3D environment could alleviate the current limitations observed for production capacity. Indeed, a few studies have confirmed the growth capacity of different production cells in 3D conditions [224–227], even reporting high cell concentrations and viability [226], and interestingly, in some cases, also substantially increased productivity of recombinant protein or viral products [240–242,578,579].

This study investigates the growth capacity and physiology of four well-known qualified production cells, HEK, MDCK, CHO and Vero cells, in a novel 3D bioproduction environment. Cell lines were selected among the most used in the biopharmaceutical field. As example, CHO cells are the leading cell platform for monoclonal antibody production (89% of approved mammalian-cell-based products are from CHO cells [2]). In contrast, the HEK cell platform is extensively used to produce recombinant proteins and viral vectors [78]. We aim to pave the way for novel bioproduction processes by describing the amplification phase for potential bioproduction in 3D hydrogel support. We chose to use hydrogel 3D bioprinting, which is a central tool for 3D biofabrication since the last decade [580]. Part of the success of bioprinting comes from the ability to allow for homogenous cell distribution [581], complex and controlled three-dimensional architectures [202] and scalable and reproducible manufacturing [581].

In the present study, the behavior of the 4 production cells was first scrutinized to evaluate their proliferative and metabolic kinetics and their 3D distribution and organization in 3D bioprinted hydrogels. In the second step, we intended to identify the biofabrication parameters which could affect these cells' proliferative kinetics.

## 4.2. Results and discussion

We aim to study the growth and physiological behavior of production cell lines cultivated in 3D environments compared to 2D cultures. The selected 3D environment was a biocompatible and proliferative biomaterial, structured in 3D enabled through bioprinting. It allows the cells to grow in adherence inside a volume. The selected hydrogel is a proprietary bioink formulation composed of 2% w/v Fibrinogen, 2% w/v Alginate, and 5% w/v Gelatin [279,280]. Small-scale (10×10×2 mm) bioprinted cellularized structures were used. The hydrogel was seeded with 1.0 x 10<sup>6</sup> cells/mL of hydrogel. After biofabrication, the constructs were consolidated for 1h at 37°C in a solution of 3% w/v CaCl<sub>2</sub>, 4% w/v transglutaminase, and 10 U/mL of thrombin. The constructs were then grown in a serum-containing culture medium for 20 days of culture, with medium refreshment 3 times a week.

### 4.2.1. *Growth proliferation profiles of production cells in 3D hydrogel*

First, over 20 days of culture, discrete live cell staining demonstrated the ability of all production cells to survive and proliferate within the 3D hydrogel structures (Chapter 3, Figure 3.5). Then, their growth capabilities were evaluated in 3D by cell counting, which was enabled by an optimized hydrogel dissociation protocol, allowing us to recover up to ~85 % of the cells seeded in the hydrogel (Chapter 3, Table 3.1). We thus monitored the growth profile and



estimate the maximal specific growth rates in 3D constructs for each cell type. Subsequently, the observed behaviors were compared to the ones in 2D culture.

In the 3D environment, we observed unconventional growth profiles with no exponential growth phase. In contrast, 2D culture present exponential growth as soon as the second culture day for all cell lines (Figure 4.1). In 3D, the four cell lines showed a long lag phase of at least 6 days followed by a linear growth phase. However, even after 20 days, no growth phase arrest was observed in any of the cell cultures. Regarding proliferation rate, the specific growth rate ( $\mu$ ) was decreased by 2 to 9-fold in 3D cultures compared to 2D cultures for every cell line studied (Figure 4.1\_C). Each cell line profile will be further discussed separately.

### **CHO cells**

Only one growth phase was identified in CHO cell cultures, starting after a 17-days lag phase. The lag phase was characterised with a growth rate close to zero and cell density maintained under  $1.0 \times 10^6$  cell/mL. Later, during the linear growth phase,  $\mu$  was  $0.29 \text{ day}^{-1}$  and the highest cell density reached  $2.7 \times 10^6$  cell/mL of hydrogel. The growth rate during this proliferative phase was decreased more than 3-fold compared to growth rate measured in 2D and reference growth rate reported for such cells [193] (see Figure 4.1\_C & Table 4.1).

### **HEK cells**

HEK 3D cultures presented two linear growth phases after a lag phase of 8 days. During the lag phase, the cell density was maintained at  $\sim 0.3 \times 10^6$  cells/mL of hydrogel. The two linear growth phases, starting at 8 and 15 days, respectively, were characterised by growth rates at least 2 times lower than observed in 2D and compared to the growth rate reported for HEK cells in literature [88] (see Figure 4.1\_C & Table 4.1). The first growth rate lasted for 5 days and was followed by a light decrease in cell density from  $0.7$  to  $0.3 \times 10^6$  cell/mL. The second growth phase was maintained for 5 days until culture arrest. The highest cell density was achieved in HEK bioprinted cultures after 20 days of culture was  $5.0 \times 10^6$  cell/mL of hydrogel, corresponding to  $0.5 \times 10^6$  cell/mL of media.

### **MDCK cells**

MDCK cells presented similar profiles to HEK with a lag phase lasting only 6 days, followed by two growth phases (Figure 4.1\_B). The cell density was maintained under  $0.3 \times 10^6$  cells/mL of hydrogel during the lag phase. A maximal growth rate of  $0.33 \text{ day}^{-1}$  was reached during the first growth phase, while a higher cell density of  $\sim 2.0 \times 10^6$  cell/mL of bioink was achieved during the second growth phase. This growth rate represents a 3-fold decrease compared to 2D conditions and growth rates reported in the literature for adherent MDCK cells [582].

## GROWTH KINETICS IN 2D AND 3D CULTURES

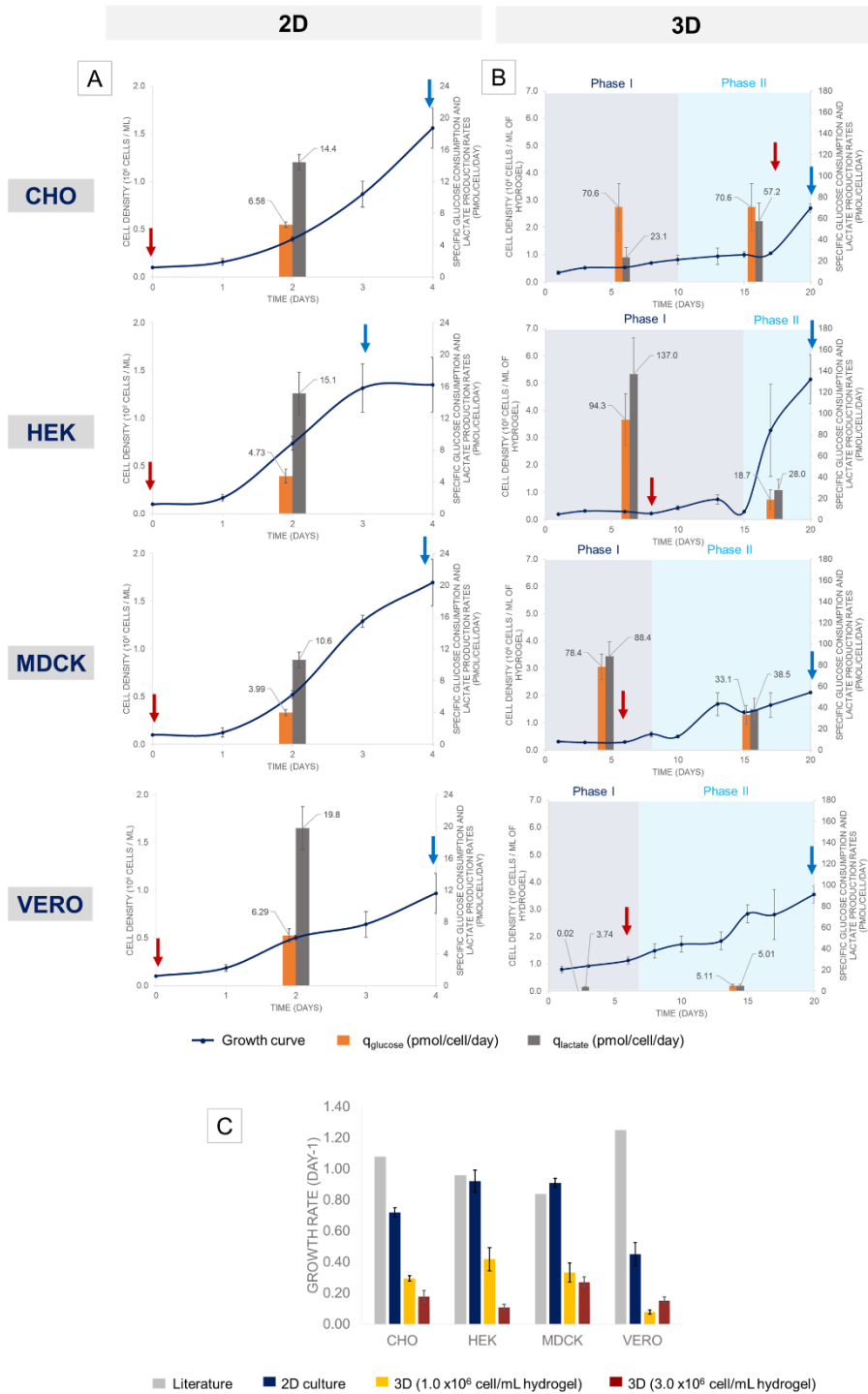


**FIGURE 4.1: Proliferation and Metabolic profiles for 3D bioprinted cell line.** Growth curve (dark blue line) and specific rate of glucose consumption (orange bar) and lactate production (grey bar) of HEK, MDCK, CHO and Vero in 2D (A) and in 3D bioprinted constructs seeded with  $1.0 \times 10^6$  cell/mL of bioink ( $n = 2$  or  $3$ ) (B). The red arrows indicate the end of the lag phase, and the blue arrows indicate de peak of maximal cell density. In (B) the two metabolic phases are identified by two different background colors. (C) presents a comparison of growth rates in 2D (dark blue) and 3D constructs seeded with  $1.0 \times 10^6$  cell/mL of bioink (yellow) or  $3.0 \times 10^6$  cell/mL of bioink (red) ( $n = 2$  or  $3$ ).

**Table 4.1: Comparison of growth and metabolic parameters in 2D cultures and 3D bioprinted constructs seeded with  $1.0 \times 10^6$  cell/mL of bioink. Several parameters are presented: Growth rate, specific metabolic rates of glucose consumption and lactate production, and average lactate to glucose molar ratio.**

		2D	3D - Phase I	3D - Phase II	Reference	Source
CHO	$\mu$ (d <sup>-1</sup> )	0.72 ± 0.03	0.29 ± 0.02		0.96	Chevalot et al. 1994 [193]
	$q_{\text{gluc}}$ (pmol/cell/day)	6.58 ± 0.91	70.6 ± 22.13		4.82	Ahn et al. 2011 [52]
	$q_{\text{lact}}$ (pmol/cell/day)	14.4 ± 1.95	23.1 ± 9.27	57.2 ± 17.26	7.19	
	$Y_{\text{lact/gluc}}$	2.19	0.33	0.81	NA	NA
HEK	$\mu$ (d <sup>-1</sup> )	0.92 ± 0.07	0.42 ± 0.07		0.84	Yang et al. 2019 [44]
	$q_{\text{gluc}}$ (pmol/cell/day)	4.73 ± 0.85	94.3 ± 24.22	18.7 ± 9.24	3.34	Henry et al. 2011 [583]
	$q_{\text{lact}}$ (pmol/cell/day)	15.1 ± 2.66	137 ± 34.24	28 ± 10.13	5.04	
	$Y_{\text{lact/gluc}}$	3.19	1.45	1.50	NA	NA
MDCK	$\mu$ (d <sup>-1</sup> )	0.91 ± 0.03	0.33 ± 0.06		1.08	Bock et al. [582]
	$q_{\text{gluc}}$ (pmol/cell/day)	3.99 ± 0.36	78.4 ± 12.19	33.1 ± 8.72	3.72	
	$q_{\text{lact}}$ (pmol/cell/day)	10.6 ± 0.98	88.4 ± 13.60	38.5 ± 10.08	3.38	
	$Y_{\text{lact/gluc}}$	2.66	1.13	1.16	NA	NA
VERO	$\mu$ (d <sup>-1</sup> )	0.45 ± 0.08	0.08 ± 0.01		0.46 to 1.25	Petiot et al. 2010 Arifin et al. 2010 [163,164]
	$q_{\text{gluc}}$ (pmol/cell/day)	6.29 ± 0.85	0.02 ± 0.00	5.11 ± 1.19	8.40 to 11.52	Petiot et al. 2010 [164]
	$q_{\text{lact}}$ (pmol/cell/day)	19.8 ± 2.70	3.74 ± 0.48	5.01 ± 1.17	9.12 to 18.24	
	$Y_{\text{lact/gluc}}$	3.15	187.00	0.98	NA	NA

## **VERO cells**

Vero cells grown in 3D environment were characterized by a lag phase lasting for 6 days followed by a very slow linear growth maintained for the rest of the culture. During this phase, the growth rate was only 0.08 day<sup>-1</sup> which is 5 to 15-folds lower than observed in 2D cultures and shown in literature references [163,164], respectively. Vero cells reached a maximal cell density of  $3.5 \times 10^6$  cell/mL of hydrogel.

In standard 2D cultures, production cell lines are characterized by high proliferation rates with doubling times down to 12-24h, which is advantageous for intensifying bioproduction processes [170,573]. As can be seen from the data, the cultivation of such cell lines in 3D environment is characterized by a substantial delay of cell proliferation and significant decrease of growth rate and maximal cell density.

Indeed, the maximal cell density reached in 3D cultures ranged from 2.0 to  $5.0 \times 10^6$  cells/mL of hydrogel, representing 0.2 to  $0.5 \times 10^6$  cells/mL of culture media. These final concentrations are very low compared to the values reported in standard 2D cultures and fed-batch culture reported in literature. They are commonly ranging from  $7.0 \times 10^6$  to  $25 \times 10^6$  cells/mL depending on the cell lines [145,153,584].

### *4.2.2. Metabolic activity of production cells in 3D environment*

To further describe the behavior of these four cell lines in 3D culture conditions, their central carbon metabolism was evaluated by measurement of glycolysis activity through the assessment of glucose and L-lactic acid consumption and production rates, respectively. A comparison of the metabolic state in 3D culture and traditional 2D culture was performed.

The total lactate production and glucose consumption were linearly correlated to the integral cell number for all cell lines. The specific rates of lactate production and glucose consumption were calculated as the slope of the graph showing the total metabolite production or uptake as a function of the IVC over the whole culture. A “break” in the graph line, corresponding to a change in the slope’s value, was systematically observed for all cell lines and with both metabolites. This was the expression of a modification in the cell-specific metabolic rates. For all cell lines, the change in specific rates occurred simultaneously for lactate and glucose. Therefore, all cell lines cultivated in 3D conditions presented two distinct metabolic phases that

are shown in Figure 4.1\_B with different background colors. Each metabolic phase had constant specific metabolic rates.

The metabolism shift was not always associated with the proliferation status change described previously. When comparing cell metabolism in 2D and 3D cultures, all cell lines except for Vero demonstrated a 2 to 10-fold increase of both the specific glucose consumption and lactic acid production rates compared to 2D cultures. On the contrary, the glucose-to-lactate conversion yield ( $Y_{\text{lact/gluc}}$ ) was always 2 to 3-fold higher in 2D cultures than in 3D bioprinted structures, demonstrating a clear difference in metabolism and cell physiological state while grown in 3D (see Table 4.1).

### **CHO cells**

During the first metabolic phase (Phase I) CHO cells presented a 1.6-fold increase in specific lactate production rate and a 10-fold increase in glucose consumption rate compared to 2D cultures (see Figure 4.1\_A & B). During the second metabolic phase, the glucose consumption rate remained constant, but the lactate production rate was increased by 2-fold, remaining 4-fold higher than in 2D conditions and literature reports [585]. In both metabolic phases, 3D CHO cell cultures presented a glucose to lactate conversion yield ( $Y_{\text{lact/gluc}}$ ) under 1 (see Table 4.1), representative of metabolism mainly oxidative.

### **HEK cells**

In HEK cells 3D cultures, the specific glucose consumption rate was increased by 20-fold and specific lactate production by 9-fold during Phase I, compared to 2D cultures. Both metabolic rates decreased 5-fold during the second phase but remained superior to those measured in 2D cultures and reported in the literature [583]. During both metabolic phases, HEK cells bioprinted cultures presented a metabolism with a  $Y_{\text{lact/gluc}} > 1$ . It commonly demonstrates that glucose consumption is mainly directed to lactic fermentation or that other carbon sources participate to its accumulation. The  $Y_{\text{lact/gluc}}$  conversion yield in 2D culture is even higher, exceeding the maximal aerobic glycolysis conversion rate of 2. This confirms here that other carbon sources contribute to pyruvate and lactate production, like amino acids.

### **MDCK cells**

Comparing MDCK cells grown in 3D conditions to 2D cultures highlighted a 20-fold increase in specific glucose consumption rate and an 8-fold increase in specific lactate production during Phase I. A decrease of 2-fold in both metabolic rates characterized the second metabolic phase. Yet, these rates remained superior to those measured in 2D cultures and those reported in the

literature [582]. Like HEK cells, MDCK also presented a lactate-to-glucose ratio ( $Y_{\text{lact/gluc}}$ ) over 1, characteristic of a more fermentative metabolism.

### **VERO cells**

Vero cells were the only cell lines that presented equivalent or even reduced metabolic activity in 3D environments compared to 2D cultures. During the first metabolic phase, the specific glucose consumption was close to zero, and specific lactate production was reduced by 5-fold compared to 2D conditions. During the second metabolic phase, the specific glucose consumption was equivalent to that measured in 2D cultures and reported in the literature. In contrast, specific lactate productivity was decreased by 4-fold compared to standard cultures [164]. Vero cells had a more oxidative metabolism during Phase II ( $Y_{\text{lact/gluc}} < 1$ ). At the same time, the first metabolic phase (correlating with the lag phase) was characterized by a very high  $Y_{\text{lact/gluc}}$  ratio, indicating a probable preferential use of other carbon sources than glucose.

In classical cell culture processes (2D and suspension processes), the metabolism of such fast-growing cell lines is often deregulated and turned toward aerobic glycolysis, indicated by fast glucose consumption and lactate accumulation, associated with reduced oxidative respiration rates [14, 29, 30]. Such metabolic deregulation is characterized by inefficient carbon source utilization preferentially directed toward lactate production. The abnormal lactate production in aerobic conditions was first reported in cancer cells [586,587] and was also detected in diseased, injured or inflamed tissues [588,589]. Hence, bioproduction processes use cell lines significantly derived from their original form and which present non-physiologic kinetics optimised for high cell density processes. Until now, the overall metabolic changes occurring when changing the culture condition from 2D to 3D are still poorly described and quantified. Our work provided insight into the metabolic changes occurring when culturing such production cell lines in 3D environments. The increase of global metabolic activity in 3D cultures has already been reported in 3D cancer cell models [215] and is closer to the in vivo characteristics of tissue metabolism. Additionally, the  $Y_{\text{lact/gluc}}$  was at least divided by 2 for all cell lines during their growth. The decreased lactate-to-glucose molar ratio indicates a reduced lactic fermentation compared to 2D cultures. This finding agrees with increased mitochondrial respiration in 3D cultures reported for other cells [590].

One possible explanation for this increased efficiency within 3D culture is the presence of diffusion gradients within the 3D hydrogel, leading to cell feeding regulation and a better metabolism balance. However, further metabolic flow analysis would be necessary to fully understand the differences in metabolic pathways between 2D and 3D cultures for each cell line.

#### 4.2.3. 3D distribution and organization of production cell lines

Cell morphology and 3D organization is another clue to observe cells physiology. Thus, after having characterized production cells growth and metabolism in 3D, their repartition and 3D organization was observed in 3D hydrogel structures, thanks to live cells staining and histological analysis. Cells selected originate from either kidney (HEK, MDCK, Vero) or ovary tissues (CHO), consequently we will compare their organization with their tissue of origin.

##### **CHO cells**

Live cells monitoring of 3D bioprinted CHO cells indicated that the first 10 days were characterized by cells organized in single-cell or very small aggregates (Chapter 3, Figure 3.5). Interestingly, after these 10 days period the cells started spreading into the shape of cell layers on the surface of the 3D structures. In 2D cultures, CHO cells were able to return to adherent phenotype due to adhesion-favorable culture conditions in the presence of serum.

Histological sections of 3D bioprinted CHO cultures stained with Hematoxylin-Eosin (HE) demonstrated the presence of large irregular cell aggregates (100  $\mu\text{m}$  in diameter) after 20 days of culture (Figure 4.2\_a.1). It is known that CHO cells are originated from a fibroblastic cell from the ovary of a Chinese hamster [591]. Interestingly, the structures observed in the bioprinted hydrogel presented strong similarities with the organization of ovary interstitial tissue (see Figure 4.2\_b.1). Finally, cell nuclei staining with DAPI on histological sections enabled to demonstrate a homogenous CHO repartition inside the 3D constructs (see Figure 4.2\_c.1).

##### **HEK cells**

During the first 15 days of their growth in 3D, corresponding to their lag phase, HEK proliferated only as spherical or ovoid cells aggregates (Chapter 3, Figure 3.5). After this period, the cells started spreading as cells monolayers on the surface of the construct. The HEK cells growing at the surface presented irregular shapes and could aggregate, forming multilayers also observed in 2D HEK cells cultures. Histological sections stained with Hematoxylin-Eosin (HE) confirmed the presence of circular, large and dense cell aggregates (100  $\mu\text{m}$  in diameter) after 20 days (Figure 4.2\_a.2).

HEK cells' ability to proliferate in 3D cultures as large aggregates has already been reported [226]. HEK cells were even demonstrated to colonize up to 90% of a hydrogel matrix composed of Gelatin, Alginate and Fibrinogen [226]. Again, the structure obtained in the 3D hydrogel

were found to be like the original kidney glomeruli organization shown in kidney histological sections (see Figure 4.2\_b.2).

These cells originated from the human embryonic kidney, but their exact nature is unknown. It has been reported in literature that HEK cells grown in 2D express some genes specific to different types of cells and tissues such as genes specific to neuronal lineage [85] or cancer stem cells [86], suggesting that their kidney origin is uncertain. However, an increased expression of markers of kidney progenitor cells, especially from glomeruli and proximal tubule, has been reported in HEK grown in 3D aggregates [84,224]. Yet, despite presenting similar cell organisation than kidney glomeruli, the HEK cells structuration in 3D cultures also resembles tumoral organization. This is consistent with the known oncogenic potential of HEK-immortalized cell line [93,592]. In addition, cancer-like cell characteristics could also present advantageous properties for viral vector manufacturing, especially to produce oncolytic viruses that preferentially infect and replicate in cancer cells and tumoral environments [593,594]. Additional studies of specific cancer or kidney cell markers would allow us to explore these hypotheses.

Cell nuclei staining with DAPI on histological sections highlighted the preferential location of the HEK cells on the periphery of the hydrogel (Figure 4.2\_c.2). Image analysis of DAPI histological slides shows a non-homogeneous repartition of the HEK nuclei in the hydrogel. 2-fold more cells accumulate in the first 1.75 mm depth of the hydrogel than in its centre (Figure 4.2\_C & D). This indicates a growth limitation in the deeper part of the hydrogel.

### **MDCK cells**

The first 10 days of MDCK cells 3D culture were characterized by cells growing as single cells or small aggregates (Chapter 3, Figure 3.5). After 10 days, the cells started proliferating as monolayer on the surface of the construct with elongated morphology like those observed in MDCK 2D cultures. In contrast to HEK cells, the renal origin of MDCK cell is well established. Indeed, MDCK cell line is originated from the tubules of a dog's kidney [595]. Their epithelial origin explains their homogenous distribution in monolayer in 2D cultures. Interestingly, HE's staining of histological sections demonstrated the apparition of cellular structures forming a circular monolayer of cells encircling a lumen, characteristic of cyst formation (Figure 4.2\_a.3). This structure, typical of kidney tubules, was already reported in MDCK cultures in type-I Collagen and Matrigel 3D hydrogels [596]. Still, it is the first time that this behavior is observed in a hydrogel made of Alginate, Gelatin and Fibrinogen. MDCK cysts are the first step of distal tubule formation and kidney tubule morphogenesis [229–232] (see kidney tubule histological section in Figure 4.2\_b.3). Similarly, to HEK cells, MDCK nuclei staining showed that the cell



density was 4-fold higher in the first 1.75 mm depth of the construct than in the center, demonstrating a gradient of proliferation (Figure 4.2\_c.3).

### **VERO cells**

Live cell staining showed that Vero cells organized as single cells until 10 days of growth, after which they started proliferating as cell layers on the surface of the constructs, like their behavior in 2D cultures. Histological analysis with HE and DAPI staining showed that Vero epithelial cells mainly proliferated as cell layers on the surface of the hydrogel, with very few cells surviving inside the structure (Figure 4.2\_a.4 & c.4). This finding is consistent with other studies reporting that Vero cells seeded over Collagen or Gelatin scaffolds formed monolayers on the surface of the matrix with elongated morphology [240,241,243]. The Vero cell line originates from the kidney of an African Green monkey and are known to be epithelial. It may explain their inability to grow inside the hydrogel matrix (see an example of kidney epithelium in Figure 4.2\_c.4). Additionally, in normal conditions, Vero cells do not secrete Matrix-Metalloproteinases (MMPs) [597], contrarily to CHO [303,598], HEK [302] and MDCK cells [304]. The secretion of MMPs, especially collagenases (MMP-1, MMP-8 and MMP-13) and gelatinases (MMP-2 and MMP-9), allows for the degradation of multiple extracellular matrix compounds, especially collagen and gelatin [560,599]. These proteinases are known to play a role in cell migration during wound healing, angiogenesis, and tumor invasion in cancer by degrading the extracellular matrix and, consequently, enabling cell migration [600–602]. Therefore, the ability to secrete MMPs may play an important role in cells' ability to colonize the hydrogel as they would need to degrade the biomaterial to be able to spread in the volume. Interestingly, it was reported that infection with influenza virus could enhance MMP-9 production in Vero and MMP-2 [305]. It suggests that infected Vero cells might be able to degrade the biomaterial and more efficiently colonize a hydrogel matrix, consequently reaching higher cell density in 3D cultures. Therefore, Vero 3D cell culture in a hydrogel matrix should be evaluated under infection and could offer interesting potential for viruses and viral particles production.

Hence, live cell staining and histology confirmed the viability and spreading of all cell lines in 3D environment after a 20-day culture (see Figure 4.2 and Figure 3.5). The study of cell distribution and 3D organization showed different behavior for all cell lines. Interestingly, the interaction with a 3D hydrogel mimicking *in-vivo* extracellular matrix provides cues for each cell line to interact and organize differently. Indeed, each of the 4 production cell lines organized differently, despite some (HEK, MDCK, Vero) having the same tissue of origin.

MORPHOLOGY AND VIABILITY OF CELL LINES IN 2D AND 3D CULTURES

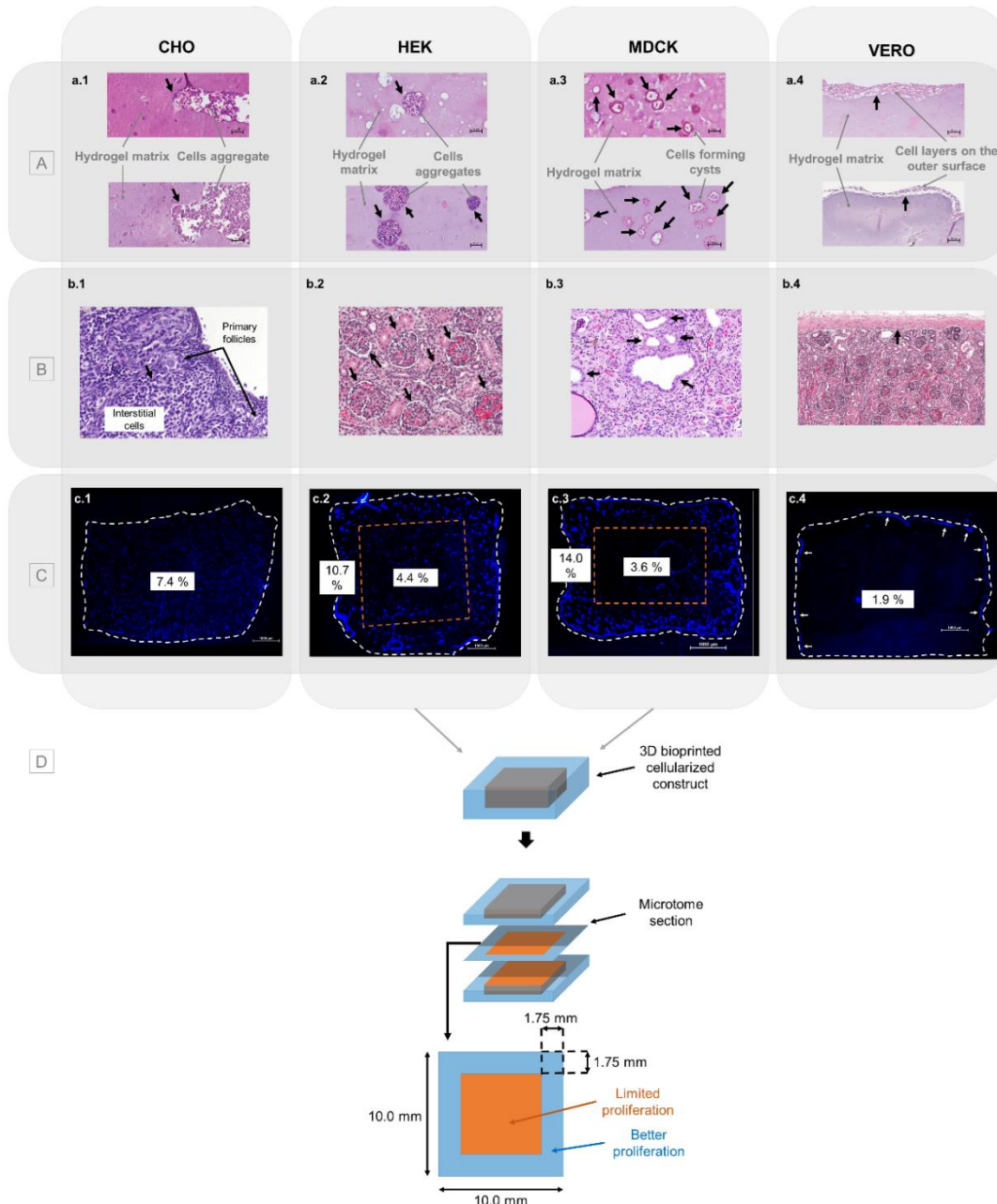


**FIGURE 4.2: Evaluation of cell distribution and organization in 3D bioprinted constructs.** Hematoxylin-Eosin staining on histological sections of (A) bioprinted constructs at day 20: (a.1) CHO, (a.2) HEK, (a.3) MDCK and (a.4) Vero, compared to (B) literature tissue histological sections : (b.1) Ovarian sections from female rat (black arrows indicate interstitial tissue), picture was extracted from Alchalabi et al. 2016 [603], (b.2) Human Kidney glomeruli (indicated by black arrows) at 19 weeks gestation, picture extracted from Ernst et al. 2019 [604], (b.3) Human kidney tubules (hyperplasia) indicated by black arrows, picture extracted from Seely et al. 2017 [605], and (b.4) Nephrogenic zone of human kidney at 35 weeks of gestation (epithelium indicated with black arrows), picture extracted from Ernst et al. 2019 [604]. (C) Repartition of cell in the constructs thanks to DAPI staining of nuclei on histological slices : (c.1) CHO, (c.2) HEK, (c.3) MDCK and (c.4) Vero. Numbers specify the surface occupied by the cells (analyzed on ImageJ). The white dot line delimits the external surface of the construct. The growth limit in HEK (c.2) and MDCK (c.3) the orange dot line identifies constructs and is schematized in (D). For Vero cells (c.4), the cell sheets at the surface are indicated by the white arrows.

This observation probably results from the fact that they originate from different tissues within the same organ and from different mammalian species. Additionally, bioproduction cell lines are immortalized cell lines that have undergone decades of cell line development with multiple clonal selection, spontaneous mutations, or even genetic engineering for some which caused significant phenotypic deviations [93,98,591]. Yet, when cultures in 3D conditions, those cells could reproduce 3D tissue-like architecture, recapitulating their original organization (i.e. cyst, epithelial layer, glomerula etc..).

This is not surprising since 3D cell culture has long been proven to provide culture conditions closer to *in-vivo* environments [196,201]. It enables cells to grow, interact with their 3D surroundings and reproduce tissues and organ micro-structuration [195,196]. Thus, cells grown in 3D conditions were reported to present functions, including gene expression profiles, growth rates [196], metabolic activity [215], response to drugs and stimuli [196,201], protein synthesis and increased lifespan of the cultures [195], which are closer to *in-vivo* behavior. This is mainly due to the interaction with the extracellular matrix and other cells through integrin and cadherin bonding, which are involved in multiple cellular signaling pathways [206,207]. The pattern of the anchorage surface also affects cell morphology and spreading [211]. The 3D matrix mechanical properties can also affect cell morphology, proliferation, apoptosis, invasiveness, or even gene expression. These are involved in reprogramming numerous cell types, including HEK and MDCK [208–210] mainly by creating cytoskeletal tension [212]. A particularly remarkable structuration was the formation of cysts by MDCK cells, which originated from distal tubules. Cysts are polarized spherical structures with an apical membrane in contact with the lumen and a basolateral membrane in contact with the extracellular matrix [229–232]. It was reported on multiple occasions that MDCK cells can even undergo the next steps of tubule morphogenesis and branching in presence of Hepatocyte Growth Factor (HGF) [234,236–238]. It was also demonstrated that  $\alpha_3\beta_1$  integrin, which is involved in cell adhesion to extracellular matrix (ECM), plays a role in tubulogenesis [239].

Additionally, the cell regionalization was observed thanks to cell nuclei staining with DAPI on histological sections. It again highlighted different behaviour depending on the cell types. The preferential location of HEK and MDCK cells in the first 1.75 mm depth of their construct (Figure 4.2\_C & D) with fewer cells in the center are consistent with the literature reporting limited cell proliferation in 3D cultures. It is commonly described as due to inefficient diffusion of nutrients and oxygen in the 3D matrix [329,606]. On the contrary, their ability to switch from lactate production to lactate consumption could explain the homogenous repartition of CHO cells within the overall 3D construct. This metabolic shift prevents lactate accumulation and carbon source deprivation [568,607].

#### 4.2.4. Seeding density impact on 3D cell proliferation

As in 2D or suspension cell culture processes, reduced growth rate, lag phase and low cell densities can result from a critical low cell seeding density [608–610]. In the case of biofabrication thanks by bioprinting, it is well known that the micro-extrusion process can strongly affect cell recovery post-printing [271]. Thus, in our bioprinting condition, cell recovery post-printing was evaluated.

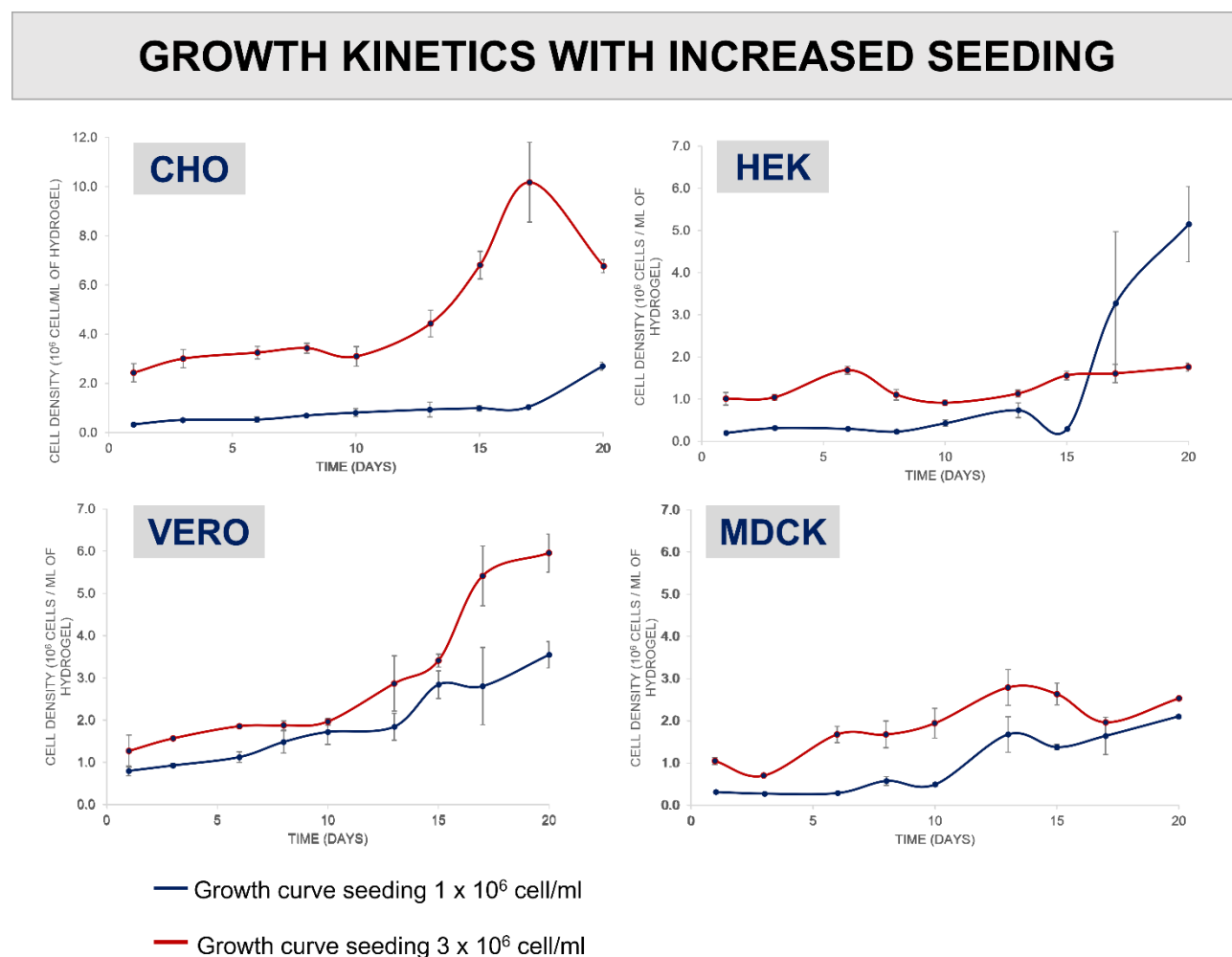


**Figure 4.3:** Compared growth profile for seeded cell lines at  $1$  and  $3 \times 10^6$  cell/ml of bioink. (SUPPLEMENTARY 6)

The cell loss was high for HEK, MDCK, and CHO, reaching up to 65-80% of seeded cells. On the contrary, Vero bioprinted cells presented a much higher cell recovery with only 20% loss. To cope with this recovery issue, seeding densities for all cells were increased 3-times and the growth follow-up for 20 days.

In all cases, the lag phase observed previously was either decreased or disappeared completely (See Figure 4.3). The maximal cell densities achieved were also significantly increased for

Vero and MDCK cells (2-fold) and CHO cells (5-fold) as shown in Figure 4.3. Moreover, exponential growth was detected for CHO (see Figure 4.3). This led to a maximal cell density of  $10.0 \times 10^6$  cells/mL. Still, the maximal cell densities achieved in 3D remains very low compared to those achieved in standard fed-batch processes. For example, CHO cell commonly reaches up to  $25 \times 10^6$  cell/mL in fed-batch [145]. In the case of HEK cells, a more erratic growth profile was observed. A short growth was observed from day 2 followed by a stabilization of the cell density close to  $1\text{-}1.5 \times 10^6$  cell/ml hydrogel. Notably, increasing the cell densities induced no modifications of 3D cell organization.

In conclusion, 3D culture in hydrogel was shown to clearly affect the proliferation, metabolism, and organization of the 4 different production cell lines. Still, even if increasing the hydrogel seeding fastened the 3D cell growth onset, it did not significantly affect the growth rates in any of the bioprinted cultures (see Figure 4.1\_C).

#### 4.2.5. *Modulation of the 3D environment and impact on production cell line proliferation*

In 3D cultures, cell physiology is affected by various cues, including cell-cell and cell-matrix interactions, mechanical properties, micro-porosity, and the associated molecules' diffusion kinetics [611–613]. All these cues play a role in reconstituting a more physiological environment and enhancing or limiting the cell's proliferation. Moreover, when 3D cultures are obtained through bioprinting, several process parameters are known to affect the final biomaterial properties and the cell recovery after biofabrication.

In this second part of the study, we aimed to identify the biofabrication parameters affecting cell proliferation trends and cell spreading into the hydrogel. Since HEK cells were having the longest lag phase (10 days), these cells were used as a model to decipher the impact of multiple parameters such as the hydrogel formulation, its consolidation process, and the bioprinting nozzle diameter.

First, the hydrogel microstructural and mechanical properties were modulated by modifying the biofabrication parameters. Eight biofabrication parameters were screened in a DOE : bioink formulation, bioink filament diameter, and hydrogel consolidation parameters (temperature, duration, concentrations of transglutaminase /  $\text{CaCl}_2$  / thrombin / DMEM). They are known to affect biomaterial mechanical properties, hydrogel composition and its rheological properties, and shear stress applied to cells. The forty conditions, with 233 samples, constituting the DOE screening, are listed in Chapter 2, Table 2.4. The data were analyzed with Partial Least Square

(PLS) regression to establish predictive models for hydrogel properties and cell proliferation. The  $R^2$ ,  $Q^2$  and reproducibility obtained for each model are presented in Table 4.2. Only the regression coefficient  $R^2 > 0.5$  models were considered acceptable. Young modulus and microporosity measurements assessed the hydrogel mechanical and microstructure properties. Microporosity was qualified at a sub-cellular level thanks to transmission electronic microscopy (TEM), and young modulus by Dynamic Mechanical Analysis (DMA) protocols.

**Table 4.2: PLS models quality assessment.** Regression coefficients ( $R^2$ ,  $Q^2$ ) and reproducibility of the predictive models established with DOE experiment.

		$R^2$	$Q^2$	Reproducibility
<b>Hydrogel microstructure</b>	<b>DMA day 0 (kPa)</b>	0.61	0.51	0.66
	<b>DMA day 10 (kPa)</b>	0.70	0.55	0.84
	<b>Microporosity day 1</b>	0.70	0.62	0.88
	<b>Microporosity day 10</b>	0.52	0.45	0.56
<b>Cell proliferation</b>	<b>Xmax day 10 (cell/g)</b>	0.30	0.03	0.29
	<b>Xmax day 10 (total cell)</b>	0.41	0.05	0.68
	<b><math>\mu_{max}</math> (d<sup>-1</sup>)</b>	0.17	0.07	0.41
	<b>Calcein day 10 (%)</b>	0.10	-0.09	0.32

After printing (day 1), the observed average Young Modulus varied from  $0.31 \pm 0.24$  kPa in the less elastic hydrogels to  $29.5 \pm 7.1$  kPa in most elastic hydrogels. These values increased after 10 days of culture, ranging from  $8.5 \pm 2.1$  kPa to  $60.7 \pm 12.0$  kPa. It should be noted that a few hydrogel samples were too smooth and fragile to be measured ( $<0.01$  kPa). Young's Modulus measurements evolved differently depending on their consolidation conditions. Hence, in the PLS model, the parameters most impacting the hydrogel mechanical properties were the temperature, the transglutaminase and  $\text{CaCl}_2$  concentration, and the consolidation duration. Thus, increasing consolidation parameters can increase the initial Young Modulus by 2-log, demonstrating their substantial impact on the cell's 3D environment.

The hydrogel microstructures and microporosity were evaluated to complement such mechanical observations at Day 1 and 10. The density and strength of the molecules network create the hydrogel's microstructure responsible for its mechanical characteristics. It was confirmed by the regression observed between DMA and microporosity at Day 10, which showed an inversely proportional correlation between hydrogel's Young's Modulus and

microporosity ( $R^2 = -0.67$ ). Thus, increasing hydrogel microporosity decreases the hydrogel elasticity.

Average porosities measured ranged from  $44 \pm 5 \%$  to  $84 \pm 3 \%$  (day1) and from  $41 \pm 6 \%$  to  $74 \pm 4\%$  (day 10). The PLS prediction model highlighted that the transglutaminase,  $\text{CaCl}_2$  concentrations and the consolidation duration impact the hydrogel structure the most (Figure 4.4\_A). Among them, transglutaminase concentration is the most decisive factor. Transglutaminase cross-links the Gelatin [293] and Fibrinogen molecules [323]. Therefore, increasing transglutaminase concentration enhances the consolidation of both protein networks to form denser structures. Similarly, the duration of this enzyme activity or its optimal temperature affects microporosity and mechanical properties.

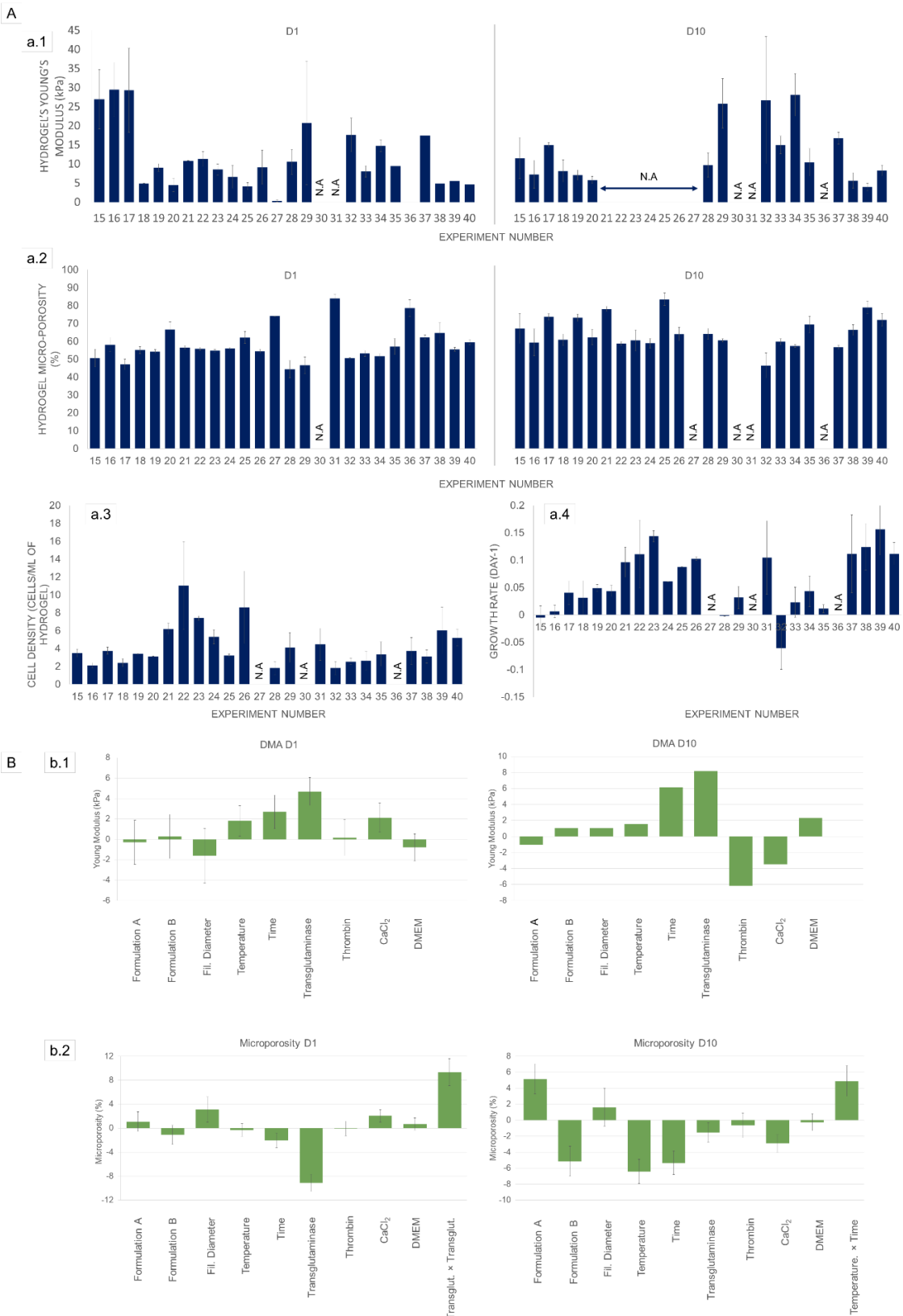


**FIGURE 4.4 : Biofabrication impact on HEK cell proliferation in 3D environment.** (a.1 & a.2) Distribution of condition's hydrogel mechanical properties (day 1 & 10 :  $n > 2$ ), (a.3 & a.4) of micro-porosity (day 1 & 10:  $n > 3$ ), (a.5) cell density achieved at Day 10 and of (a.6) associated growth rates ( $n = 2$ ). Associated impact of bio fabrication factor's (b.1\_DMA measures ; b.2\_Microporosity).



The optimal temperature for free transglutaminase activity is 40°C [614]. Thus, after 10 days of culture, the constructs at 37°C or for a longer time showed significantly lower microporosities than those cross-linked at 21°C or below and for a short time.

Then, we investigate if modification of hydrogel microstructure and mechanical properties could impact HEK 3D cell growth kinetics. Cell proliferation was measured by two approaches: construct dissociation and further cell counting, or the assessment of the percent of surface occupied by the live stained cells by image analysis. The predictive cell density and growth rate models had poor fitting ( $R^2 < 0.5$ ) (see Table 4.2). These models were not considered acceptable. The lack of fit is probably due to the low reproducibility observed between samples with high standard variation and low precision levels of these analytics. They are based on data extracted from dissociations or image analysis, and their respective precision were of 39% and 60%. Indeed, image analysis of 3D constructs cellularization is subjected to variability as the cell distribution was observed as heterogeneous (as described in section 3.3). Similarly, hydrogel dissolution and counting involve several steps affecting total cell recovery.

However, while no robust predictive models were fitting, we still observed significant differences between DOE conditions in both maximal cell densities and growth rates achieved. The best conditions had an extended growth phase up to 10-day cultures, thus maintaining growth rates of 0.11 to 0.13 d<sup>-1</sup>. Indeed, such growth rates were observed for only 3-days in the initial and non-optimized protocols. Additionally, the most optimal condition of the DOE had reduced cell mortality after the bioprinting process with only 25% cell loss against of 67 % in initial condition. Thus, a cell density of 10 x 10<sup>6</sup> cell/mL of hydrogel was achieved, a value 15-fold superior to the cell concentration reached in the initial condition. Such results were obtained with bioprinted constructs of either formulation A or B, printed with a 400µm nozzle and consolidated for 60 min in a solution of 0.4%<sub>w/v</sub> transglutaminase, 1.4%<sub>w/v</sub> CaCl<sub>2</sub> and 10 U/mL thrombin. Interestingly, we were able to identify a positive correlation between the hydrogel microporosity measured and both the growth rate ( $R^2=0.6$ ), and the space occupied by live cells ( $R^2=0.8$ ) (see DOE correlation matrix in Table 4.3). These results suggest that molecules diffusion (nutrients, oxygen) within the hydrogel or reduced space for cell anchorage and growth can strongly limit cell aggregate sizes. Further studies would be needed to precisely describe diffusion kinetics in the different hydrogels and relate such characteristics with hydrogel microporosity and cell growth.

**Table 4.3: Correlation matrix extracted from the DOE experiment, showing the correlation between factors and responses. Form. :** Formulation of the bioink ; **Diam Ø :** diameter of the printing nozzle; **TAG :** Transglutaminase concentration; **Thr. :** Thrombine concentration; **DMA:** Young's modulus, **Calcein :** measured fluorescent surface (live cells) in the bioprinted construct; **Xmax :** maximal cell concentration ;  $\mu$  specific growth rate between D1 and D10; **Micro. :** Microporosity calculated on TEM images. (SUPPLEMENTARY 7)

	Form(B)	Diam Ø (µm)	Temperature (°C)	Time (min)	TAG (%w/v)	Thr (U/mL)	CaCl2 (%w/v)	DMEM (%)	DMA D0 (kPa)	DMA D10 (kPa)	Calcein D10 (%)	Calcein D6 (%)	Xmax D10 (cell/g)	Xmax D10 (total cells)	lactate mmol	$\mu$ (day <sup>-1</sup> )	Micro D0 (%)	Micro D10 (no cell) (%)
<b>Form(B)</b>	1	0.55	-0.29	-0.25	-0.04	-0.56	0.29	0.12	-0.29	0.06	0.20	-0.10	-0.08	0.06	0.45	0.07	0.18	--
<b>Diam Ø (µm)</b>	0.55	1	0.01	-0.57	0.09	-0.50	0.37	0.32	-0.20	0.05	0.30	-0.03	-0.25	-0.08	0.40	-0.07	0.24	--
<b>Temperature (°C)</b>	-0.29	0.01	1	-0.21	0.32	-0.02	-0.19	0.10	0.26	0.18	-0.08	-0.15	-0.28	-0.42	-0.57	-0.44	-0.04	--
<b>Time (min)</b>	-0.25	-0.57	-0.21	1	0.01	0.21	-0.35	-0.04	0.10	0.21	0.11	0.24	0.20	-0.03	-0.02	0.15	-0.31	--
<b>TAG (%w/v)</b>	-0.04	0.09	0.32	0.01	1	-0.26	-0.12	0.16	0.40	0.59	0.45	0.37	-0.09	-0.24	0.01	-0.25	-0.57	-0.61
<b>Thr (U/mL)</b>	-0.56	-0.50	-0.02	0.21	-0.26	1	-0.26	-0.10	0.05	-0.30	-0.54	-0.03	0.13	0.10	-0.37	-0.01	-0.04	--
<b>CaCl2 (%w/v)</b>	0.29	0.37	-0.19	-0.35	-0.12	-0.26	1	-0.15	0.18	0.04	0.10	-0.06	0.09	0.31	0.12	0.14	0.29	-0.57
<b>DMEM (%)</b>	0.12	0.32	0.10	-0.04	0.16	-0.10	-0.15	1	-0.18	0.04	0.13	-0.01	-0.16	-0.03	0.05	-0.01	-0.10	-0.11
<b>DMA D0 (kPa)</b>	-0.29	-0.20	0.26	0.10	0.40	0.05	0.18	-0.18	1	0.44	0.14	0.38	0.11	-0.13	-0.20	-0.10	-0.47	-0.67
<b>DMA D10 (kPa)</b>	0.06	0.05	0.18	0.21	0.59	-0.30	0.04	0.04	0.44	1	0.44	0.30	0.14	-0.15	-0.02	-0.11	-0.55	-0.43
<b>Calcein D10 (%)</b>	0.20	0.30	-0.08	0.11	0.45	-0.54	0.10	0.13	0.14	0.44	1	0.41	0.22	0.05	0.45	0.21	-0.43	0.80
<b>Calcein D6 (%)</b>	-0.10	-0.03	-0.15	0.24	0.37	-0.03	-0.06	-0.01	0.38	0.30	0.41	1	0.36	0.05	0.31	0.12	-0.58	0.48
<b>Xmax D10 (cell/g)</b>	-0.08	-0.25	-0.28	0.20	-0.09	0.13	0.09	-0.16	0.11	0.14	0.22	0.36	1	0.70	0.16	0.70	-0.20	-0.05
<b>Xmax D10 (total cells)</b>	0.06	-0.08	-0.42	-0.03	-0.24	0.10	0.31	-0.03	-0.13	-0.15	0.05	0.05	0.70	1	0.33	0.71	0.12	0.52
<b>lactate mmol</b>	0.45	0.40	-0.57	-0.02	0.01	-0.37	0.12	0.05	-0.20	-0.02	0.45	0.31	0.16	0.33	1	0.37	-0.07	0.31
<b><math>\mu</math> (day<sup>-1</sup>)</b>	0.07	-0.07	-0.44	0.15	-0.25	-0.01	0.14	-0.01	-0.10	-0.11	0.21	0.12	0.70	0.71	0.37	1	0.07	0.60
<b>Micro D0 (%)</b>	0.18	0.24	-0.04	-0.31	-0.57	-0.04	0.29	-0.10	-0.47	-0.55	-0.43	-0.58	-0.20	0.12	-0.07	0.07	1	0.62
<b>Micro D10 (no cell) (%)</b>	--	--	--	--	-0.61	--	-0.57	-0.11	-0.67	-0.43	0.80	0.48	-0.05	0.52	0.31	0.60	0.62	1

Until now, production cell proliferation, metabolic kinetics and organization in 3D have never been described precisely in the literature, even though HEK [224–227], CHO [216,217], MDCK [229–232] and Vero cells [240–242] have all already been cultured in 3D. Our study confirmed the ability of such cell lines to proliferate in 3D culture conditions. We observed for all the cells a particular growth profile, presenting a long period of slow-to-no-growth, followed by a reduced proliferation rate associated with efficient oxidative metabolism. Thus, our observations provide new insight into the 3D cell physiology of these cells.

It is commonly accepted that 3D cell cultures have decreased proliferation rates, closer to *in vivo* kinetics, than standard 2D *in vitro* culture. Such a decrease in growth rate in 3D culture has already been reported for both cancerous and primary cell lines [590,615,616]. In some of these studies, authors described cells blocked in the G1 phase of their cell cycle. This phenomenon is mainly explained by the inhibition of proliferation by cell-cell contact in the case of cells growing in spheroids or aggregates. The cell-matrix or 3D cell-cell interactions in 3D involve multiple signaling pathways and gene expression, including genes associated with controlling cell proliferation, apoptosis, survival, or differentiation [195]. In our case, the 3D environment also substantially impacted the recovery of the cell's physiological organization. A similar conclusion was reported in cancer cells cultivated in 3D, which provided better modelling of *in vivo* tumors [215]. Thus, HEK and CHO demonstrated both epithelial and non-epithelial structuration by forming cell monolayers at the surface of constructs and large cellular aggregates in the hydrogel. Vero and MDCK cells presented epithelial organization by creating cell sheets at the surface of the constructs. MDCK also formed cysts, a structure characteristic of their kidney tubule origin.

Finally, the effect of the 3D environment and the associated biofabrication tool on cell behavior was evaluated in a DOE with a fractional factorial plan. Parameters impacting both hydrogel properties and cell proliferation were identified. The hydrogel consolidation process has the most impact on mechanical and microstructural properties. Still, the microstructure is a strategic feature of the biofabricated support as it can strongly enhance or limit cell proliferation. The accessibility of nutrients and O<sub>2</sub>, and metabolic waste removal mainly depend on the 3D construct thickness and the matrix's nature and microstructure. All these factors strongly impact the diffusion rate of molecules [329,606]. As an example, it was demonstrated that nutrient diffusion was limited to 300 µm depth in static cultures of liver tissue slices and in normal tissues [329,606]. In some other work, mathematical models have estimated the maximal hydrogel thickness for efficient oxygen diffusion in different ECM-based matrices from 1 mm in low diffusion matrices (basement matrix /Matrigel) to 3.2 mm in collagen I matrices [617].

Finally, based on the literature review [240–242,578,579], our results allow to hypothesise that such novel 3D cultivation format could positively impact cellular productivity compared to standard adherent or suspension culture. For example, the cell structuration and polarization in 3D cultures is known to be favorable to infection by viruses and result in higher viral product titers [578]. Then, the metabolic cell efficiency and increased metabolic activity observed in our 3D culture could be associated with enhanced biomolecule production. Indeed, in bioproduction processes, high lactate production was associated with a drop in production yields, and numerous strategies have targeted lactic fermentation reduction to increase biomolecule production [136]. Moreover, deviation from physiological conditions was demonstrated to decrease cell-specific productivity. Indeed, increased cell-specific productivity has already been reported in adherent cell cultures compared to suspension [191,260]. Such bioprinted 3D cultures of production cell lines are now about to be evaluated for their production capacities of recombinant proteins and viral products.

### 4.3. Conclusion

Bioproduction cell lines have been used for decades to produce therapeutic biomolecules and viral products. Their proliferative and metabolic kinetics have been widely described in standard 2D and suspension cultures. The recent challenges in intensifying cell cultures to increase cell density raise the need for new techniques. For this purpose, 3D cultures of cells embedded in a matrix could provide interesting perspectives as the cells could densely colonize a volume. Bioprinting is the sole biofabrication tool which would ultimately allow for the reproducible, controllable, and sizable generation of 3D cellularized constructs. In the 3D constructs, cells are not limited to a surface and are more efficiently protected from hydrodynamic shear stress caused by media stirring or gas bubbles.

This work offers insight into physiological changes during 3D cell cultures and the factors influencing cell behavior. We demonstrated that even highly selected, mutated, and deviated non-primary cell lines could recover physiological characteristics closer to *in vivo* conditions. Such cell lines were proved to proliferate in 3D biofabricated culture conditions. The biofabrication protocols and the ultimate biomaterial microporosity can modulate cell growth and spread into the structure. We also reported increased metabolic activity and reduced fermentative behavior in our 3D construct.

Therefore, in addition to the high potential of 3D bioprinted cell cultures for medical applications such as regenerative medicine or tissue modelling for drug testing, we identified another prospect for bioproduction applications here.

#### 4.4. Acknowledgements

The Sartorius company funded this work. We sincerely thank the persons from Sartorius who were invested and contributed to the project, Magali Barbaroux, David Pollard and Oscar Reif. We also acknowledge the Centre Commun de RMN (CCRMN) from Université Lyon 1, for the NMR acquisitions and the CIQLE from Université Lyon 1 for the transmission electronic microscopy imaging.

## 4.5. Conclusion

This chapter discussed the differences between 2D and 3D cell cultures regarding cell proliferation, metabolic activity, and organization. In 2D cultures, cell lines have high proliferation rates and metabolic deregulation, while 3D cultures have a delay in cell proliferation and reach lower cell density. The metabolic changes in 3D cultures result in increased cell-specific metabolic rates, reduced lactate production and increased mitochondrial respiration. The presence of diffusion gradients in the 3D hydrogel has also been identified as a limiting factor for cell proliferation. Nutrient and oxygen diffusion influence the regionalization of cells within the 3D construct. Comparison of different hydrogel conditions with the design of experiments showed that hydrogel microporosity significantly impacted cell proliferation. Live cell staining and histology confirmed the viability and spreading of the four mammalian cell lines in 3D environments, with each cell line presenting a different 3D organization specific to their tissue of origin. 3D cell culture provides conditions closer to in-vivo environments, allowing cells to interact with their surroundings and reproduce tissue-like structures. We propose that the mechanical properties of the 3D matrix and cell adhesion molecules play a role in cell morphology and behavior.

As a future application of such a novel 3D cultivation format, we believe it could improve cellular productivity compared to standard adherent or suspension cultures. The metabolic efficiency and activity in 3D cultures may lead to higher biomolecule production. Indeed, strategies to reduce lactic fermentation have already been used to increase biomolecule production [136]. Moreover, in literature, the adherent cell cultures have already been described to significantly increase specific productivity by 1.5 to 3-folds compared to less physiological culture conditions in suspension [189–192,260].

More specifically, in the case of CHO and HEK 3D cell culture, they were proved to proliferate at high cell density in hydrogel matrices with CHO cells reaching a peak cell density at  $1.0 \times 10^8$  cell/mL after 25 days in alginate–poly-L-lysine microcapsules [618] and HEK cells colonizing about ~90% of the 3D Gelatin-Alginate-Fibrinogen hydrogel volume [226]. In the later case, the hydrogel was composed of 10% Gelatin, 1% Alginate and 2% Fibrinogen which is equivalent to our Formulation A. However the bioink was only consolidated with 100 mM ( $\sim 1.1$  %<sub>w(g)/v(mL)</sub>) CaCl<sub>2</sub> and 20 U/mL Thrombin. However, in our cultures, bioprinted constructs tended to degrade after 3 to 5 days when transglutaminase concentration in consolidation solution was  $\leq 0.04$  %<sub>w/v</sub>. Additionally, both studies achieved such results with very thin constructs of 200 - 900  $\mu\text{m}$  thickness [226,618].

Regarding their production of recombinant proteins in 3D culture, encapsulated CHO cells in alginate–poly-L-lysine–alginate microcapsules released recombinant antibodies even after implantation *in vivo* [618] and HEK cells demonstrated a 4 to 67- fold increased cell-specific protein productivity when encapsulated in collagen microbeads compared to 2D cell cultures [225]. Still, Their slower proliferation in 3D resulted in lower global production yield.

In another bioproduction field, 3D cultures of Vero and MDCK cells provide exciting potential for virus production. The structuration and polarization of cells in 3D cultures can enhance viral infection and increase viral product titers. For example, Vero scaffold-free spheroids were more vulnerable to infection and had faster virus production rates than 2D cultures [578]. Similar observations were reported on Vero 3D cultures in collagen or gelatin scaffolds. They showed increased sensitivity to virus infection [240] compared to monolayer cultures. Interestingly, the cells' sensitivity to viral infection did not decrease after 55 days of culture [240]. The Vero cells polarization in 3D or 2.5D conditions could explain here their increased sensitivity to viral infection [240].

However, the production process should respect some requirements to produce therapeutic products for medical applications. It includes a reproducible and controlled culture process that respects the cGMP guidelines. The production scale should also be increased for sufficient product manufacturing for patient treatment.

**Thus, the following chapters will present a scale-up of the bioprinted construct and the development of an automated, controlled and reproducible culture process.**

## CHAPTER 5. LARGE-SCALE 3D BIOPRINTED CULTURES DEVICES DEVELOPMENT

After studying and optimizing the behavior of the cell lines in 3D at a small scale, we evaluated the feasibility of bioprinted cultures scale-up. For this, we significantly increased the scale of our models by a factor of 20 to 50. We focused on 3D bioprinted structures, each approximately 10 cm<sup>3</sup> in size. Our goal was to create and cultivate these structures for a minimum of one week in order to compare their growth kinetics and behaviors at various scales.

This scale-up presented several key challenges:

1. The maximal size of bioprinted construct is limited and few structures over the cm<sup>3</sup> are reported due to technical capacity (bioink, bioprinter etc).
2. In thicker constructs, the diffusion of culture media is hindered and results in restricted access to nutrients and oxygen, improper removal and subsequent accumulation of metabolic waste at the center of the construct.
3. There is currently no standardized existing vessel designed for culturing large, tissue-like structures in vitro with regulated culture parameters.
4. Maintaining control over the cellular environment, particularly regarding factors like culture medium's pH, cell access to a carbon source (feeding), and oxygen levels (dissolved oxygen, or dO<sub>2</sub>), is challenging.

To address these challenges, we built upon the field of tissue engineering for selecting and designing our bioreactor models. Bioreactor culture vessels have gained significance for cultivating sizable tissue-like structures due to their ability to provide a controlled and regulated environment for larger-scale cultures. For thicker constructs exceeding 2 mm in width, we recognized the need to enhance dynamic flow to ensure an homogeneous media diffusion throughout the construct. Dynamic liquid flow provided by such bioreactors as already been proved to enhance media diffusion within 3D structures [334,619]. The criteria identified for satisfactory bioreactor system are listed below:

- Maintain long-term sterility and watertightness
- Maintain favourable growth conditions (physico chemical environment)
- Allow for homogeneous and controlled feeding of the cells (flow distribution)
- Allow for monitoring (discrete sampling / continuous monitoring)
- Ease the bioprinted construct installation and chamber sealing



A novel device was developed as none of the commercial culture devices could satisfy all our criteria. It was designed as a dedicated bioreactor system to generate a controlled media flow throughout the bioprinted construct. The concept of this equipment was based on the setting of fixed-bed bioreactors illustrated in Chapter 1 Figure 1.1. The main difference being the cells growing within the whole hydrogel volume instead of the surface of a packed support. A standard stirred tank bioreactor with a working capacity of 250 mL and integrated sensors to regulate the parameters of the culture medium was used. The regulation was performed by a control system applying actuators in response to the feedback loop. The stirred-tank was used as a media reservoir to feed the bioprinted construct placed in an individual and personalized vessel, designated as "culture chamber" and located outside of the stirred tank (see Figure 5.1). Therefore, the culture chamber was continuously perfused with a controlled culture media flow maintained under controlled physicochemical conditions (including pH, pO<sub>2</sub>, and temperature). This bioreactor setup was designed for conducting 3D construct cultures for up to 20 days.

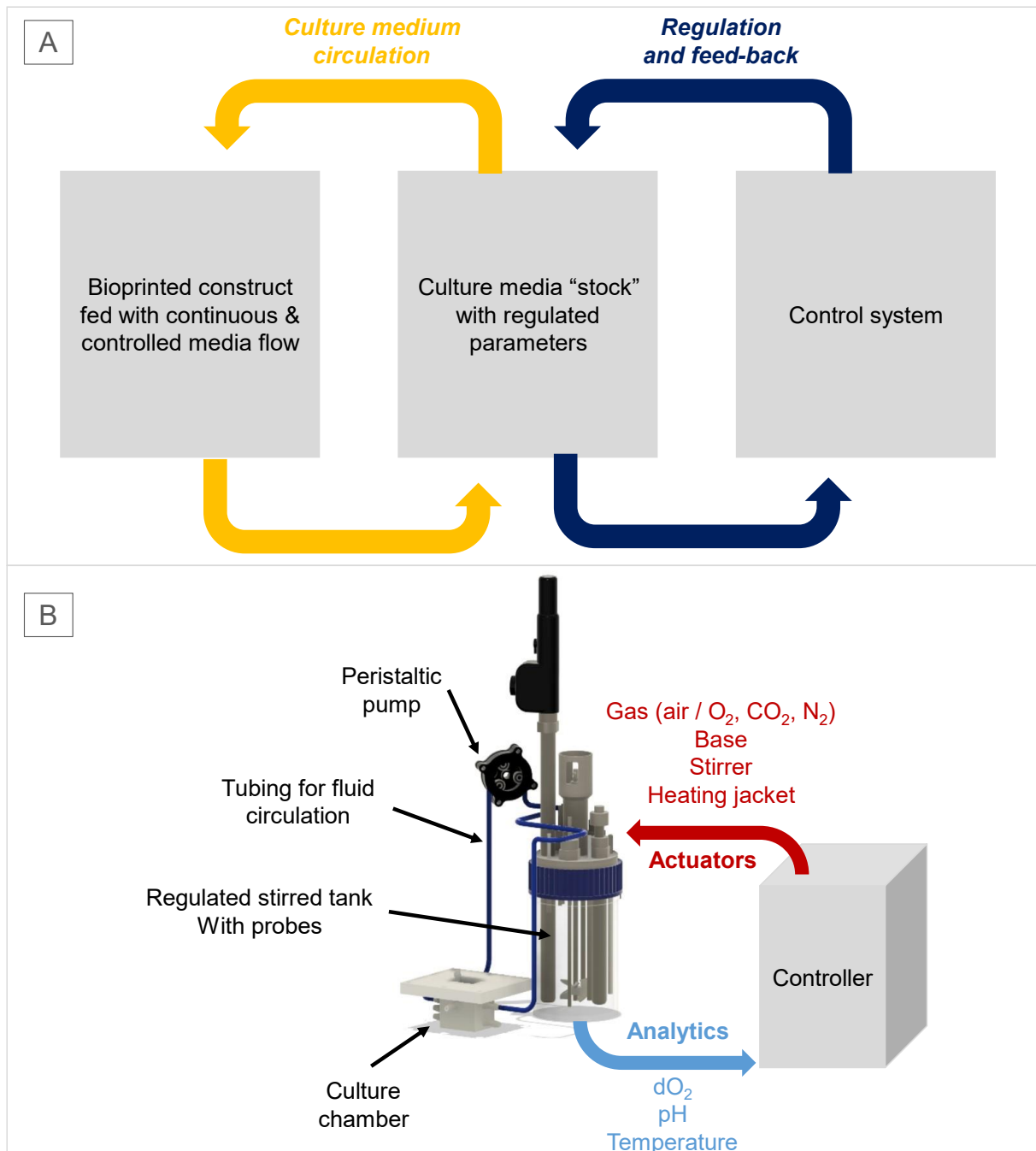


**Figure 5.1: Concept of the bioreactor system adapted to the culture of 3D bioprinted constructs.** (A) Conceptual scaled-up culture system for large bioprinted constructs. It includes a control system used to regulate the culture media's physico-chemical state and a continuous dynamic flow of culture medium through the bioprinted Construct (B) Schematic representation of the regulated culture system comprising an in-house personalized "culture chamber", an Eppendorf DASbox® stirred tank and a Cytosys® (Ipratech) controller.

Numerous parameters had to be studied and optimized to develop such a culture process. These parameters concerned the construct size and geometry (3D printing, porosity, cell survival), the design of the culture chamber (material, flow control, robustness, etc...) and finally, the optimization of the bioreactor system (setup, regulations, analytics).

## 5.1. Design and evolution of bioprinted constructs

To evaluate the feasibility of the scale-up of bioprinted cultures, the construct size was increased by 20 to 50. A cuboid geometry including internal porosity was elected for its easiness to be modelled and printed. Such geometry can remain stable on each of its sides. This characteristic makes it easier to manipulate than most other shapes, such as cylinders, spheres or more complex geometries. It consequently reduces the risk of contamination during construct handling. The construct's cuboid shape also facilitated the design of the associated culture chamber, with flat surfaces and reduced material consumption (few support materials and thin walls).

Hence, the bioprinted construct was scaled up from  $0.2 \text{ cm}^3$  ( $1 \times 1 \times 0.2 \text{ cm}$ ) to  $10.8 \text{ cm}^3$  ( $2 \times 2 \times 2.7 \text{ cm}$ ) and designed as a rectangular cuboid. For constructs exceeding 2 mm thickness, we recognized the need for dynamic nutrient flow to ensure homogenous media diffusion throughout the construct. As a result, the construct's geometry incorporate macroporosity within the structure, maintaining a maximum hydrogel thickness of  $800 \mu\text{m}$  throughout the entire construct and facilitating fluid path and media diffusion. Therefore, the bioprinted constructs were printed as  $2 \times 2 \times 2.7 \text{ cm}$  (x, y, z) rectangle cuboid with porosity parallel to the Z direction (2.7 cm side). The initial design had  $12 \times 12$  pores with square sections of 0.8 mm side (Figure 5.2). Such geometry corresponded to a total construct volume of  $10.8 \text{ cm}^3$  (total scale-up factor of  $\sim 50$ ) comprising  $\sim 8.3 \text{ cm}^3$  of hydrogel (hydrogel volume scale-up factor  $\sim 40$ ) and  $\sim 2.5 \text{ cm}^3$  of void (porosity).

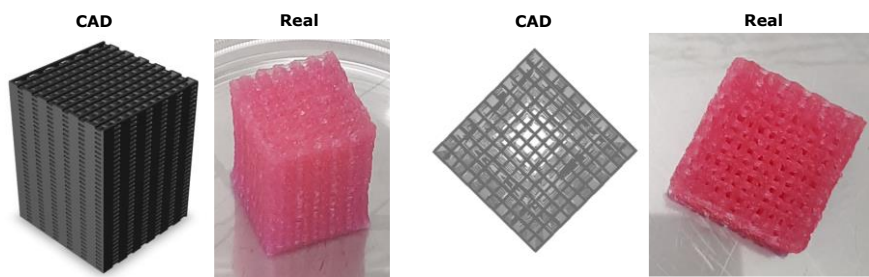


**Figure 5.2: Geometry of the large-scale bioprinted Construct in CAD versus real construct picture**

As depicted in Figure 5.2, the construct structure of  $10.8 \text{ cm}^3$  could be successfully printed with a conserved overall shape and self-supporting structure. Nevertheless, due to hydrogel shear-thinning properties, the hydrogel filament underwent swelling after exiting the printing nozzle. The fidelity of printing shape with CAD-designed shape was complex to achieve. Indeed, construct height was increased, and pore size decreased drastically (see Figure 5.2). Thus, in a

subsequent experiment presented in paragraph 5.2.2, pore size reduction hindered the flow path, causing inefficient feeding of the embedded cells, and overpressure in the culture chamber associated to media leaks.

Several modifications were operated; the gradual reduction of the pores' numbers to increase their size, and reduction of construct length (Z direction) to go from a  $2 \times 2 \times 2.7$  cm cuboid to a  $2 \times 2 \times 2$  cm cube (see Figure 5.3). These modifications allowed for improved liquid flow circulation inside the culture chamber. The final geometry was  $8 \text{ cm}^3$  of total volume (total scale-up factor 40) with a total hydrogel volume of  $\sim 3.9 \text{ cm}^3$  (hydrogel volume scale-up factor  $\sim 20$ ).

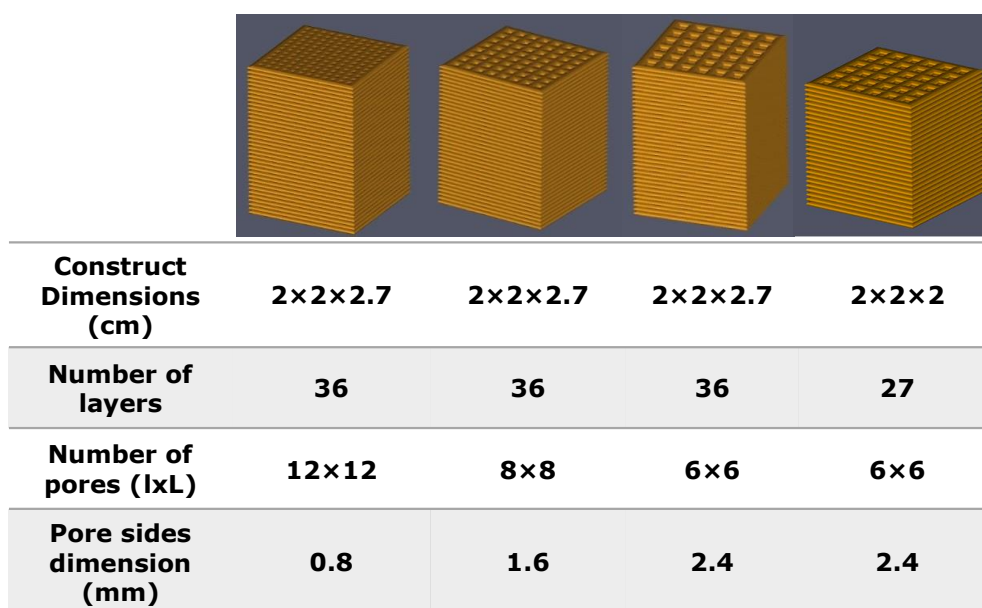


*Figure 5.3: Evolution of bioprinted construct design*

## 5.2.Design and evolution of "culture chambers."

### 5.2.1. *Multi-flow culture chamber conception*

Customizing the culture chambers to accommodate the specific shapes of the bioprinted constructs was essential. This is why 3D printing of the culture chambers proved to be a valuable strategy. It offered the flexibility to adjust the shape to match each unique 3D design and allowed for iterative improvements to the chamber design. Therefore, both the bioprinted constructs and the 3D culture chambers were initially designed using CAD (Computer-Aided Design) software and then 3D printed. However, during the implementation of this concept, we encountered several challenges.

The culture chambers were 3D printed by inkjetting with Veroclear®, a polyacrylate-based resin. This material was validated from previous work in the lab to possess satisfactory biocompatibility (contact and leachable), printability (resolution, fidelity, easy connection process), impermeability (no leaks) and sterilizability (resistance to multiple autoclave cycle), transparency (visualization of construct, media level, bubbles, etc) and low roughness (cleaning quality). A work is currently performed in the team to develop new manufacturing methods based on Arburg Plastic Freeforming printer (Freeformer) with polycarbonate material (Makrolon®) used for commercial manufacturing of sensors and bioreactor parts [620].

For biomolecules production in bioreactors, homogenous mixing and access to nutrients is essential. Therefore, we wanted to generate an homogenous flow inside the bioreactor culture chamber. However, as cell behavior in large bioprinted constructs is not well known, we still wished to keep the possibility of generating different flow profiles to either generate heterogeneity in the flow distribution or be able to have localized feeding. Therefore, we opted for a multi-entry culture chamber enabling for generation of multiple flow configurations.

The culture chamber was designed after computational fluid dynamic (CFD) simulations. This work was performed in collaboration with the Laboratoire Réactions et Génie des Procédés (Céline Loubière & Eric Olmos : Nancy, France). It was designed with 7 different entry/exit ports to be able to generate different flow configurations in a single "culture chamber" (Figure 5.4). Figure 5.4\_C demonstrate that thanks to selected flow path (entry and exit), it was possible to generate homogenous or heterogenous nutritive flow path inside the bioprinted construct.

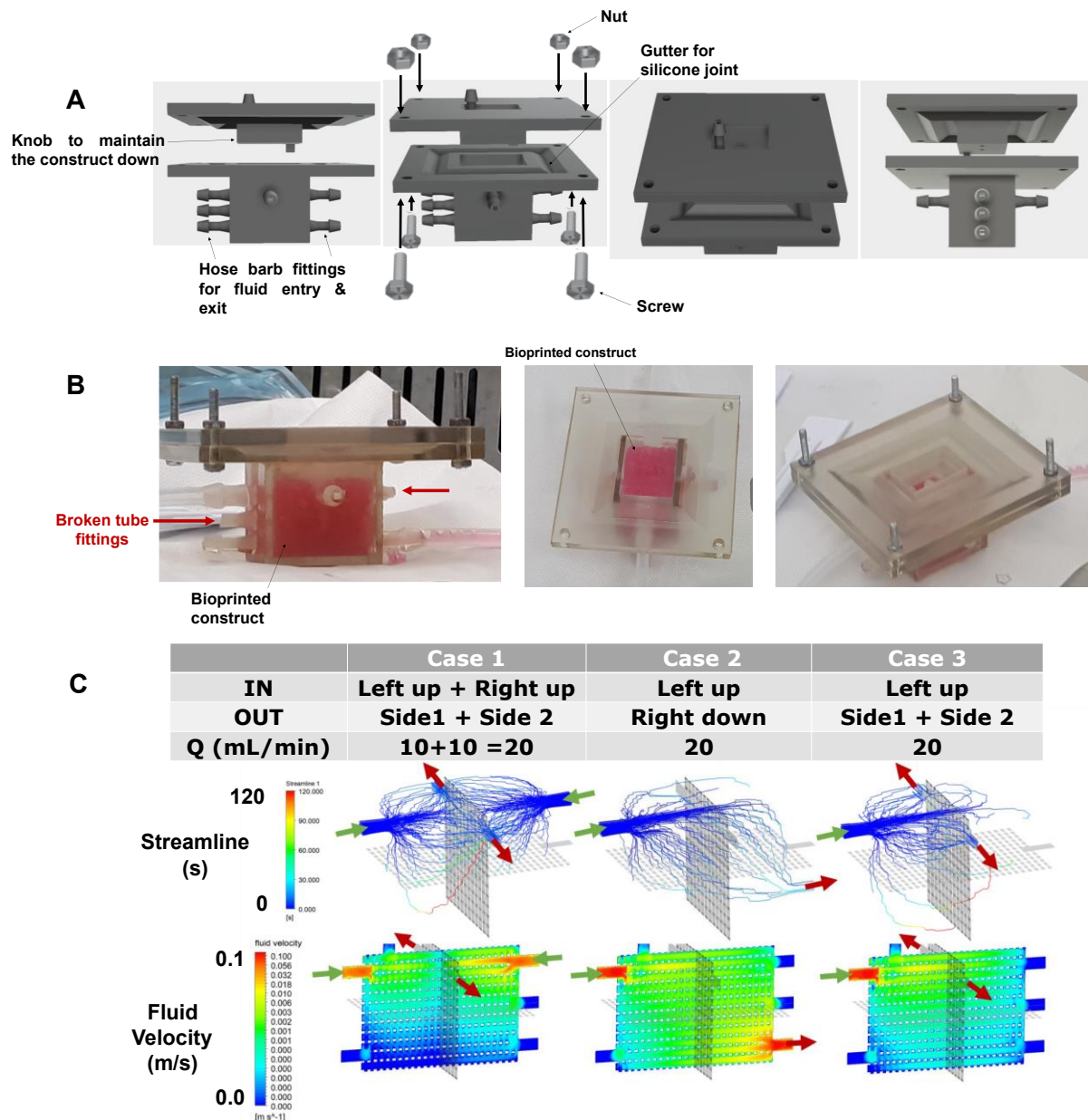


**Figure 5.4: 3D printed culture chamber design and CFD simulations.** (A) CAD representation and (B) picture of the 3D printed culture chamber. (C) Modelling of the liquid path and fluid velocity in bioprinted construct with three different flow configurations leading to homogeneous (case 2) or non-homogeneous (case 1&3) media distribution, with a flow rate of 20 mL/min

### 5.2.2. Characterization of residence time in the "culture chamber"

Simultaneously, we further characterise the media flow in the "culture chamber" by measuring its residence time to validate the CFD models for our bioreactor system. The residence time is a term employed to designate the duration for which a fluid portion (or particle) remains within a control volume. Determining the residence time in the "culture chamber" will determine at which frequency a total media renewal of the "culture chamber" is achieved depending on the flow rate. It can support choices of the optimal flow rate, ensuring proper cell feeding and

preventing starvation or hypoxia. For example, it was reported that 1 – 2 h residence time in cell-retention culture devices resulted in oxygen limitation [621].

Multiple methods exist to determine the residence time in a bioreactor. One of the easiest protocols is to perform a "Pulse experiment", also known as the "Dirac method". This method uses a "pulse" injection of a tracer molecule at the inlet of the bioreactor. The injected volume of the tracer molecule should be minimal, and the injection should be fast to create a short "impulse" of the tracer's concentration. Thus, with an injection duration significantly lower than the residence time, it can be modeled by the Dirac delta function (narrow spike).

For this experiment, the residence time was measured in the 3D printed chamber represented in Figure 5.4\_A, with homogenous flow distribution (case 2 : Figure 5.4\_C). The circuit configuration used for the measure is presented in Chapter 2, Figure 2.5. A rectangle cuboid bioprinted construct of  $2 \times 2 \times 2.7$  cm (x , y , z) with porosity parallel to the Z direction and 12 x 12 pores of square sections of 0.8 mm side (Figures 5.2 & 5.3) was placed in the chamber. A continuous flow of demineralized water was injected through the "culture chamber" with a peristaltic pump. The chamber outlet was harvested in a glass beaker. The liquid in the Becker was pumped out at an identical flow rate to maintain the total volume at 20 mL. A magnetic barrel was used to stir the liquid in the Becker homogeneously, and a conductivity probe was plunged in it. A solution of 0.2 M NaCl was used as the tracer.

The residence time was evaluated at two flow rates, 6 and 10 mL/min, respectively. The different measures are recapitulated in Figure 5.5, and the calculated residence times are shown in Table 5.1.

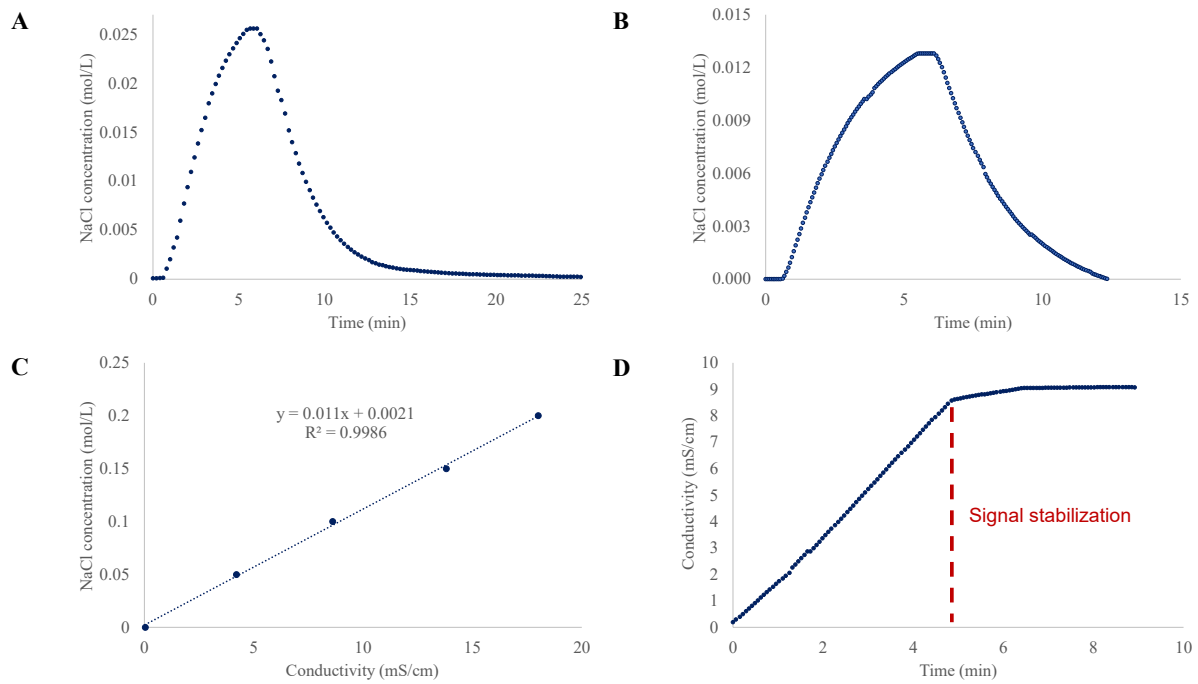


**Figure 5.5: Measure of culture medium residence time in the culture chamber.** Graphs represent (A) The evolution of NaCl concentration measured in the outlet of the chamber after injection of 0.2M NaCl solution with a circulation flow rate of 6 mL/min, (B) The evolution of NaCl concentration measured in the outlet of the chamber after injection of 0.2M NaCl solution with a circulation flow rate of 10 mL/min, (C) The calibration curve of NaCl concentration against measured conductivity and (D) Response time of the conductivity probe plunged in a 0.1M NaCl solution at  $t=0$ .

The residence time (Rt) was estimated with the following equation where  $C(t)$  represents the evolution of NaCl concentration (C) in time (t) and the integral of  $C(t)$  was estimated as the area under the curve (Figure 5.5 A & B) calculated with the trapezoidal rule:

$$Rt = \frac{\int C(t) \cdot t \, dt}{\int C(t) \, dt}$$

The standard deviation ( $\sigma$ ) was calculated as the square root of the variance ( $\sigma^2$ ) with :

$$\sigma^2 = \frac{\int (t - Rt)^2 \cdot C(t) \cdot dt}{\int C(t) \, dt}$$

**Table 5.1: Residence times (Rt) and their standard deviation measured in the culture chambers with homogenous flow configuration for two different flow rates.**

Flow rate (mL/min)		strd deviation (min)
<b>6</b>	6.04	2.33
<b>10</b>	5.65	2.54



No significant difference was noticed between the  $R_t$  measured at the two flow rates tested (Table 5.1). However, the standard deviation was high, representing > 40% of the measured  $R_t$ . This could be explained by an additional experiment qualifying the conductivity probe's Response time. Indeed, while the probe was immersed in a 0.1M NaCl solution, its signal needed about 5 min to stabilize, as shown in Figure 5.5\_D. Therefore, residence time measurements will have to be performed with other probes having a faster response time, as the response time of the probe should be insignificant compared to the residence time. In actual team studies, simulated flow paths and velocities are about to be validated thanks to an advanced analytical approach using MRI (Magnetic Resonance Imaging).

**After the conception and development of the design, the 3D printed chamber was used for sterile bioprinted constructs' culture lasting for 14 to 20 days. During these experiments, we faced several issues, such as leaks from the cap, complex closing procedures, silicone joint manufacturing, and breaking of bioreactor parts. Those challenges prevented the success of long and sterile culture process. Therefore, work was performed to develop a custom culture chamber adapted to the geometry and demand for the construct culture and suitable for sterile culture over 14 days.**

### 5.2.3. *Improvements of the "culture chamber's" designs*

The primary design of our "culture chamber" served as the foundation for the technical evaluation of inserting bioprinted constructs in their chambers and for their connection to the regulation vessel. Such preliminary assays allowed to define specifications for the "culture chamber," focusing on several critical criteria :

- **Increase part's robustness:** resistance to autoclave sterilization, maintain geometry
- **Ease construct's manipulation:** installation of the bioprinted constructs/chamber closure & sealing
- **Efficient chamber water tightness:** caps and ports connected to tubings for perfusion

Multiple changes were operated onto the "culture chamber" design and conception to reach designs that could handle cultivation periods of over 14 days. See below the flowchart for design optimizations in Figure 5.6.

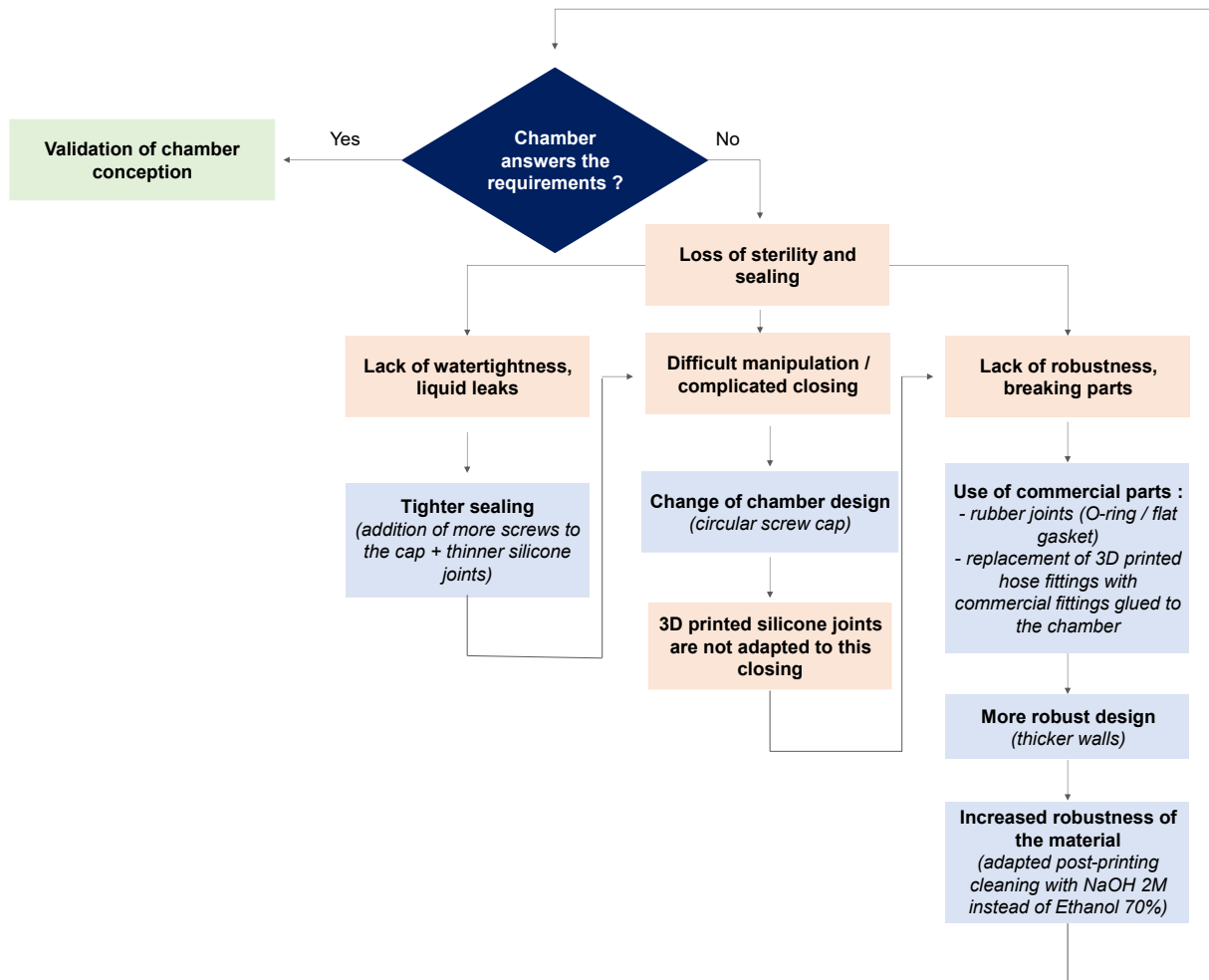


*Figure 5.6: Modifications of the chamber to improve the chamber's robustness, water-tightness and handling*

**Robustness Enhancements:** On the primary design, the entry and exit ports, shaped as hose barb fittings, were fragile and often broke during autoclaving. The post-printing treatment of acrylate materials significantly weakened the material, mainly through autoclave cycles. It led us to implement the following strategies to enhance the devices' robustness (as seen in Figure 5.6):

- Changed the material post-printing cleaning process: We replaced the overnight 70% ethanol wash with a 2M NaOH wash based on the provider's recommendations.
- Redesigned the chamber with at least twice thicker walls to prevent breaking, removing the 3D printed tube fittings and creating inlet/outlet ports with female luer locks glued to the chamber wall (see Figure 5.7).

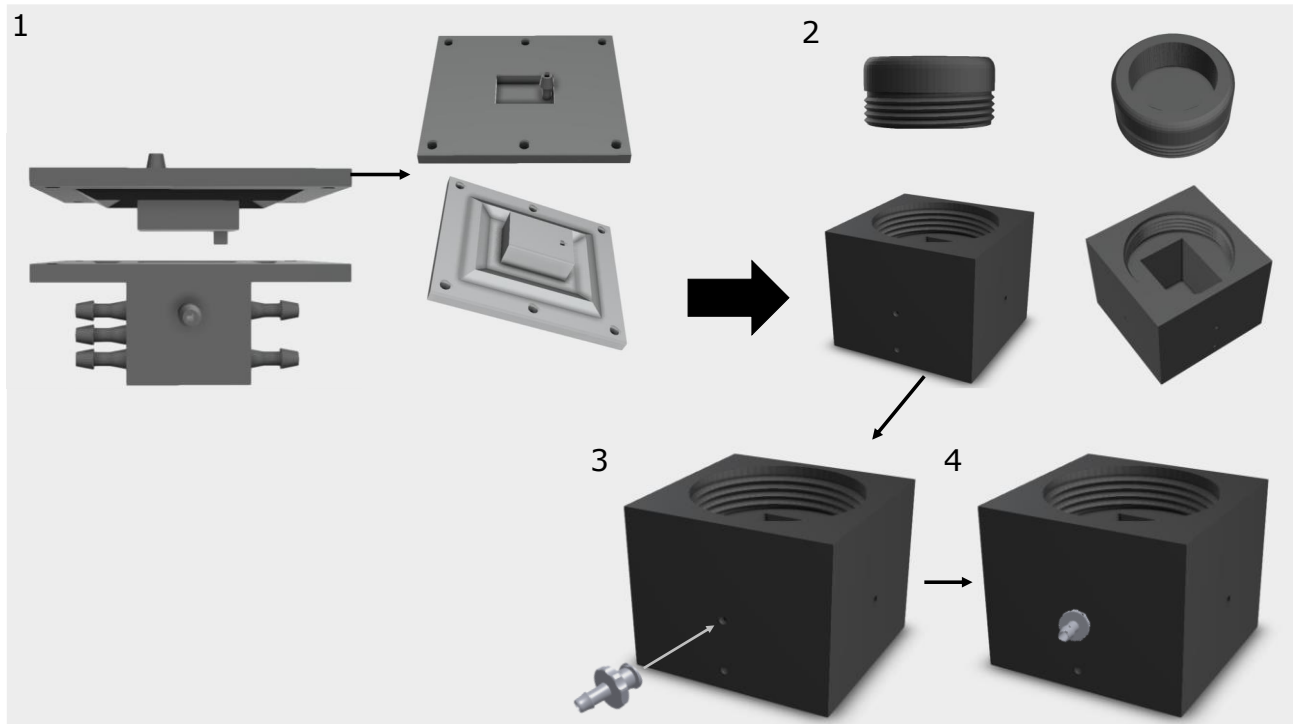


**Figure 5.7: Evolutions of the culture chamber (CAD):** first design (1) was a fully 3D printed "rectangular" bioreactor with cap sealing with four to six bolts. This design was changed for a 3D printed bioreactor with thicker walls and circular screw cap (2), the tube fittings were made by glueing female luer locks to the chamber (3 and 4).

**Ensuring Watertight Sealing:** Watertight sealing of the "culture chamber" was crucial for maintaining long-term cultivation in sterile conditions. The achievement and validation of watertight sealing involved multiple steps including bioprinted construct insertion in the chamber, chamber closure and sealing, proper connection to perfusion tubings. As "culture chambers" are perfused with oxygenated nutritive flow, it could result in air bubbles and overpressure in the culture chamber. Each steps were addressed with the following modifications:

- Cap sealing geometry and joint material adjustments (Figures 5.8 and 5.9).
- Reduction of overpressure: Enlarging tubing's from  $\text{Ø } 2 \text{ mm}$  to  $\text{Ø } 3 \text{ mm}$  to prevent tubing clogging. The exit port from the culture chamber and outlet tubing were enlarged from 2 mm to 4 mm to reduce the fluid velocity (m/s) by 5 resulting in a decrease of the pressure drop from 378 Pa/m for  $\text{Ø } 2 \text{ mm}$  pipes to 24 Pa/m for  $\text{Ø } 4 \text{ mm}$  pipes. The pressure drop was calculated with the Hagen-Poiseuille equation as presented in Chapter 2, section 2.3.2, and correspond to the pressure exerted by the fluid on the pipe wall. Therefore, reducing the pressure drop in the port connecting the outlet pipe to the chamber prevented liquid leaks at the connection point. As a first trial, the peristaltic pump was kept on the inlet side of the culture chamber. Thus, to release overpressure in

the “culture chamber”, an empty-sterile-filtered bottle was connected to the cap of the culture chamber to allow for gas bubble or over-pressured liquid evacuation. Finally, the peristaltic pump was moved from the inlet to the outlet of the culture chamber to force media out instead of pushing it in and to reduce the over-pressure in the chamber.

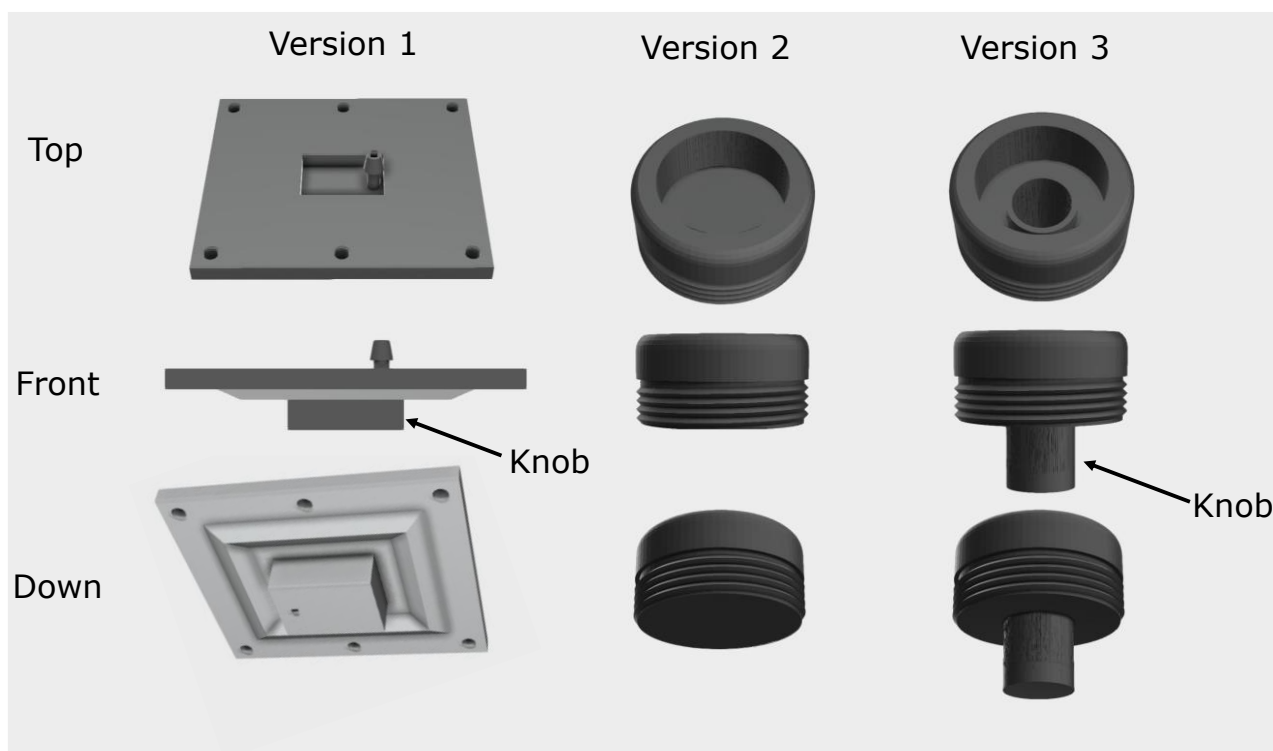


**Figure 5.8: Evolution of the culture chamber's cap:** from a rectangular cap closed with multiple bolts (screws and nuts) to circular screw cap with a knob to maintain the bioprinted construct in place

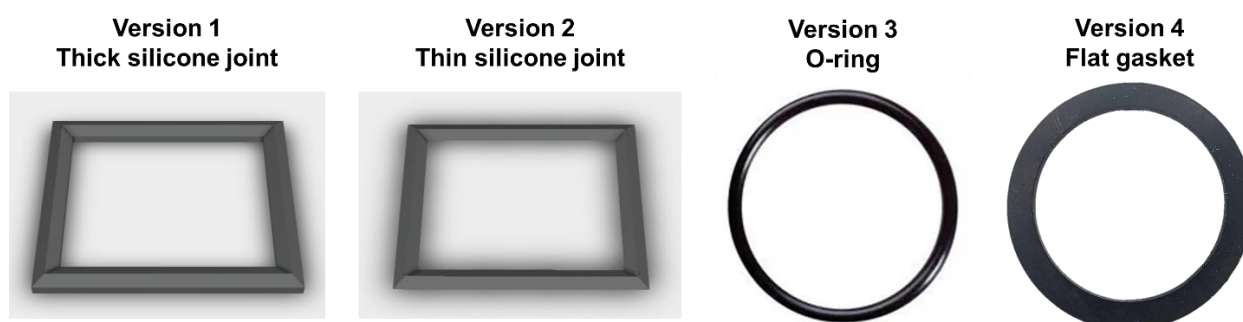


**Figure 5.9: Evolutions of the sealing joints:** from 3D printed silicone joints (rectangular) to commercial rubber seals (circular). Flat- gasket joints provided the best sealing.

As part of these optimizations, we transitioned to a circular screw cap design, replacing the previous rectangular cap. Such change of design allowed the formation of a gaseous headspace within the “culture chamber”. The bioprinted constructs floated at the air/liquid interface due to the presence of trapped air bubbles in the pore channels (see Figure 5.15). In order to maintain

the bioprinted construct in the appropriated location, a small cylindrical knob was added to the cap, enabling the construct to be fully immersed (as shown in Figure 5.8).

**In conclusion, all these optimizations significantly improved the design of the 3D-printed chamber, making it easier to handle without leaks or breaks. In turn, it facilitated a more reproducible process for bio printed construct cultures, allowing them to be conducted over 20 days without leaks or contaminations. These changes also facilitated 3D modeling and printing, reducing the support material required, and enabling the bioreactor to be conveniently placed on a laboratory bench due to its balanced, flat-bottom shape.**

### 5.3. Regulation bioreactor

#### 5.3.1. *Standard cell culture stirred-tank bioreactors adaptations.*

The bioprocessing setup was implemented with two regulated stirred-tank commercial bioreactor devices. The first was a custom reusable system based on a DASbox® stirred-tank (Eppendorf) associated with an Cytosys® controller (Ipratech). Such device was meant to be highly flexible and customizable. On the other hand, the concept was adapted to a commercial system, the Sartorius Ambr®250 HT (demo unit). This system offers less flexibility but provides a more automated and reproducible culture process. The Ambr®250 High Throughput (HT) demo unit (Sartorius) uses single use stirred-tanks with integrated analytics for parameters monitoring (Figure 5.10). In both setups, we can monitor pH, temperature and dO<sub>2</sub> continuously.

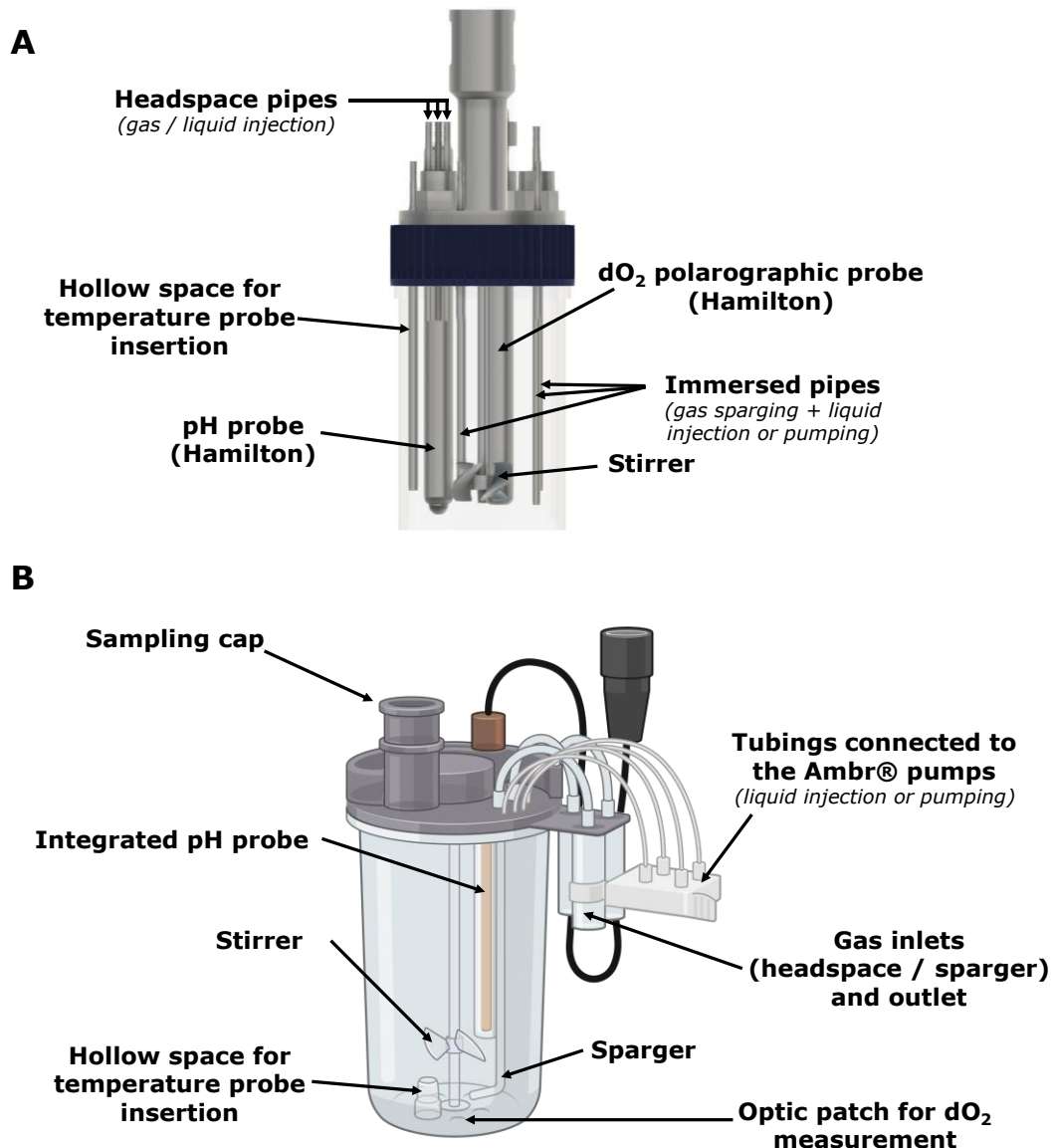


**Figure 5.10:** Comparative representation of the regulated stirred tanks (A) the DASbox® (Eppendorf) represented with CAD, used in the reusable and customized bioreactor setup with Cytosys® (Ipratech) controller and (B) single-use Ambr®250 stirred tank (Illustration from Biorender.com) used with the Ambr®250 HT control system demonstration unit.

The stirred-tank is equipped with probes that are calibrated before the cultures begin. These probes enable the continuous monitoring of the culture medium's temperature, dissolved oxygen partial pressure, and pH. The signals from each probe are transmitted to the bioreactor controller, which uses this feedback for regulation. If any of the measured parameters deviate from the setpoint values, the system automatically adjusts the relevant actuators, as specified in the settings, to correct the deviation and return to the desired setpoint.

To increase the pH, a 0.2 M NaOH solution, labeled as "Base," is employed as a positive actuator. Conversely, CO<sub>2</sub> serves as a negative actuator for pH regulation due to its pH-lowering effect in a culture medium containing a carbonate buffer. For dissolved oxygen (dO<sub>2</sub>)

regulation, positive actuators include air or pure oxygen and adjustments in the stirring speed, while N<sub>2</sub> is used as a negative actuator. Temperature regulation relies solely on the heating jacket. It's worth noting that all these regulation processes are carried out within the stirred tank itself, as illustrated in Figure 5.11. This is due to the current technological limitations that prevent the installation of sensors in the 3D printed culture chamber. However, the culture chamber's temperature is maintained at 37°C by placing the vessel in a bench heating chamber, compensating for heat loss from the media circulating out of the regulated tank. Our future work will dedicate efforts to enabling parameter monitoring and regulation within the culture chamber, which has already been initiated and will continue. However, the details of this work are not presented in this context.

The dynamic fed-batch system was initially developed using our in-house assembled bioreactor system, which consists of the DASbox® stirred tank and the Cytosys® controller. The culture medium volume used in this system ranged from 100 to 200 mL. It's important to note that this setup was maintained in a clean, although not sterile, environment located outside the sterile hood.

To manage the culture chamber within the sterile hood while keeping the stirred tank connected to the controller positioned on the laboratory benchtop, it was necessary to use inlet and outlet tubing for the circulation loop that were at least 130 cm long.

The working volume of the culture chamber was 10.8 mL, with the liquid volume accounting for the remaining space not occupied by the hydrogel. This volume ranged from 2.5 to 6.9 mL, depending on the specific geometry of the bioprinted construct. Consequently, the total volume of media circulating in the system ranged from approximately 21 to 26 mL, while the remaining media in the regulated tank varied from around 74 to 179 mL, depending on the overall media volume used.

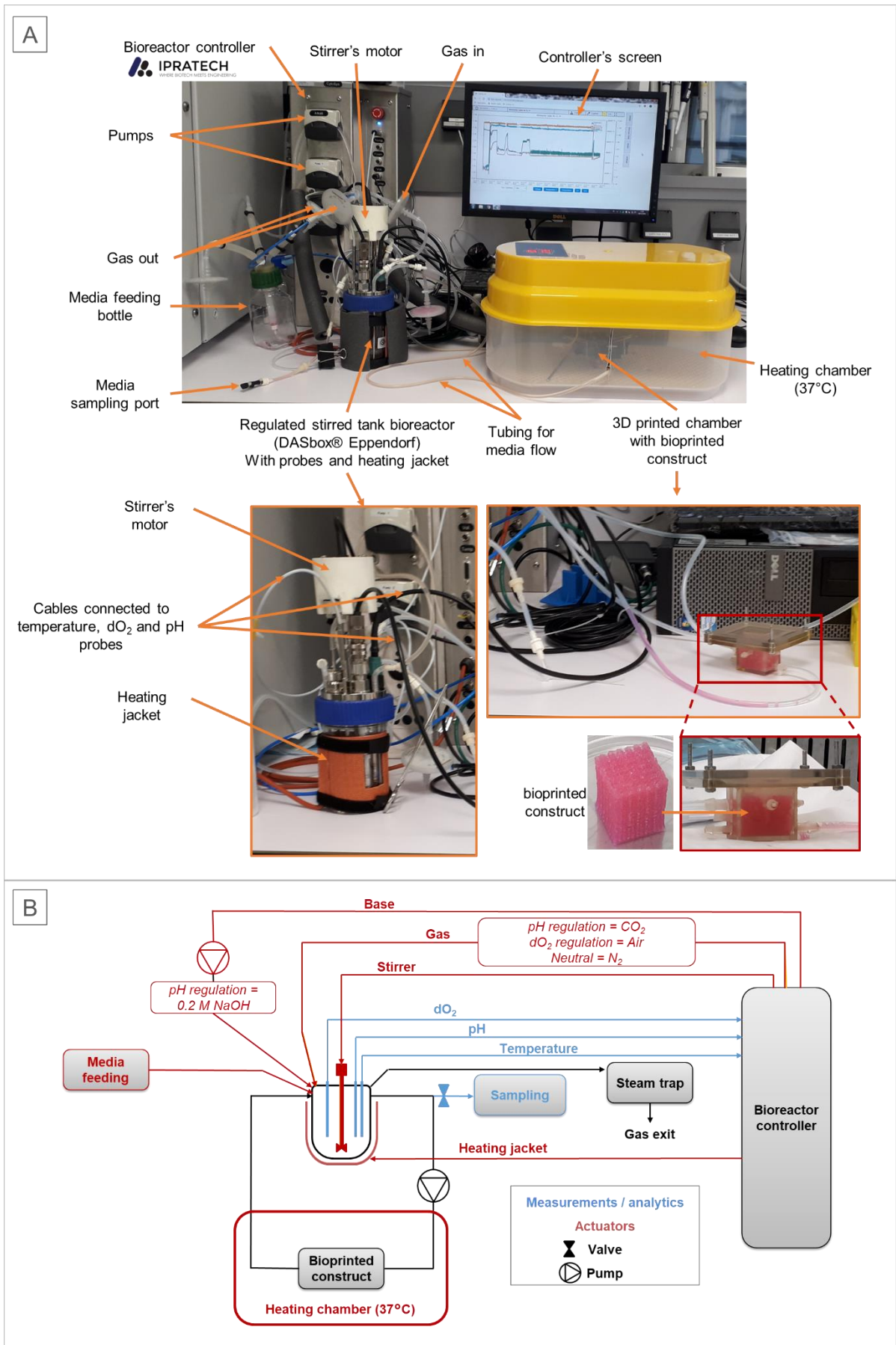


**Figure 5.11: In-house developed bioreactor setup.** The system comprises a Cytosys® (Ipratech) controller and DASbox® (Eppendorf) regulated tank. (A) Pictures of the running setup and (B) detailed Pipe and Instrumentation Diagram (P&ID) of the setup.



The setup was then transferred and adapted to the Ambr®250 system. The total volume of media used was 200 mL. Different setups were implemented with volume of circulating media varying from ~ 13 to 30 mL. To allow for media circulation in Ambr devices, customization would be necessary to implement a circulation loop on such single-use vessels. Ambr®250 device has 4 pumps for media or base feeding to the stirred tank. In this case, one pump was used in reverse mode (negative flow rate) to pump liquid out of the regulation tank and feed the culture chamber. The three other pumps were used for feeding and base injection.

Initially designed for media sampling, a cap on top of the Ambr®250 stirred tank was modified to allow the outlet flow from the culture chamber to return to the Ambr® tank. A primary version of this "Perfusion cap" was made from the existing Ambr® Sampling cap (see Figure 5.12\_A). This version allowed solely the perfusion flow to return to the regulation vessel. A second version was designed entirely and 3D printed in acrylate-based material (Veroclear) to provide two ports for the media inlet and outlet (see Figure 5.12\_B)

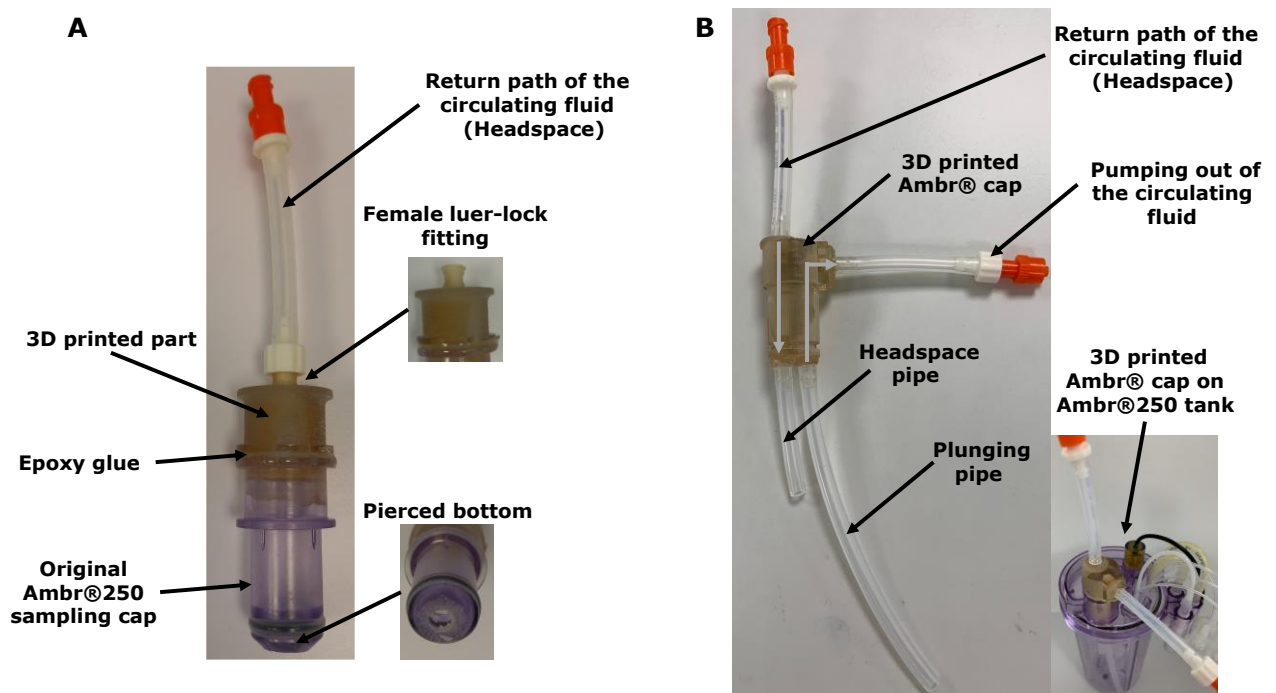


**Figure 5.12: Evolution of the modified Ambr®250 perfusion-cap :** (A) first version with 3D printed part glued on top of the commercial Ambr®250 sampling cap with sawed bottom to allow fluid path. This system allowed circulating fluid to come back to the regulated tank. (B) The final version is entirely 3D printed, allowing circulating fluid to return to the regulated tank and pumping regulated media for injection in the culture chamber.

Standard regulation protocols commonly implemented on cell culture devices were evaluated for maintaining the physiological culture of 3D constructs. **Table 5.2 summarises the different**

**protocols implemented and their effects. The following sections will detail the additional steps to improve culture regulations.**

### 5.3.2. *Optimized regulation of temperature, pH and dO<sub>2</sub> control*

As depicted in Figure 5.13, it became evident that the standard regulation parameters were insufficient for achieving precise control of pH and dissolved oxygen (dO<sub>2</sub>). When applying the regulation settings designed for suspension cell cultures, we observed significant parameter deviations of up to 125% from the setpoint, particularly in the case of dO<sub>2</sub>.

The challenges arose from the use of both air and CO<sub>2</sub> gassing. Air was employed as a positive actuator for dO<sub>2</sub> regulation, while CO<sub>2</sub> was a negative actuator for dO<sub>2</sub> and regulated pH. However, due to the minimal oxygen consumption during the culture, CO<sub>2</sub> was consistently injected, resulting in conflicts regulating dO<sub>2</sub> and pH. This, in turn, led to poor control of both parameters. To address these conflicts and enhance control precision, we introduced nitrogen gas into the system to serve as a neutral gas for down-regulating dO<sub>2</sub>. Consequently, CO<sub>2</sub> was exclusively used for pH regulation, eliminating conflicts between the two control loops. Additionally, adjustments were made to the Proportional-Integral-Derivative (PID) coefficients within the controller's response to better align with the slower metabolic rates of the bioprinted constructs. The PID controller is a feedback mechanism designed to respond to variations in parameters, and it consists of three coefficients:

1. **Proportional (P) coefficient:** Determines the strength of the feedback, responding proportional to the deviation from the setpoint.
2. **Integral (I) coefficient:** Considers the evolution of the deviation over time by integrating the value of the deviation, delivering a response based on the integrated term's growth. It increases the response strength when the deviation is increasing over time or reduces the feedback amplitude when the deviation is decreasing.
3. **Derivative (D) coefficient:** Calculates the derivative of the deviation over time to anticipate its evolution. It influences the speed of the response. A faster response occurs when the deviation's derivation is increasing, preventing oscillations caused by the P coefficient. Conversely, when the deviation's derivation decreases, the response is extended over a longer period of time, counteracting oscillations.

Given the slow cell metabolism within the bioprinted constructs, we adjusted the response strength (P) by decreasing it and increased the derivative value (D) to spread the response over time effectively.

Lastly, to enhance the quality of parameter regulation, we refined the PID coefficients for the first two levels of the  $dO_2$  control loop cascade, specifically for azote/gas mix sparging (negative actuator) and  $O_2$  sparging (positive actuator), which are the primary actuators. Several adjustments were made before identifying the optimal PID settings. These adjustments are summarized in Table 5.2. The adaptability of the regulation settings to different setpoints was tested by changing the setpoint for  $dO_2$  from 40 % to 60% after 8 days of culture. It demonstrated the efficiency of these setting by quickly increasing and stabilizing the  $dO_2$  to the new setpoint value as shown in Figure 5.13\_B.

In the of pH regulation loop, the PID coefficients were not modified but the deadband was increased from 0.01 to 0.2 to minimize value oscillation and reduce excessive base injection, further improving the quality of parameter regulation.

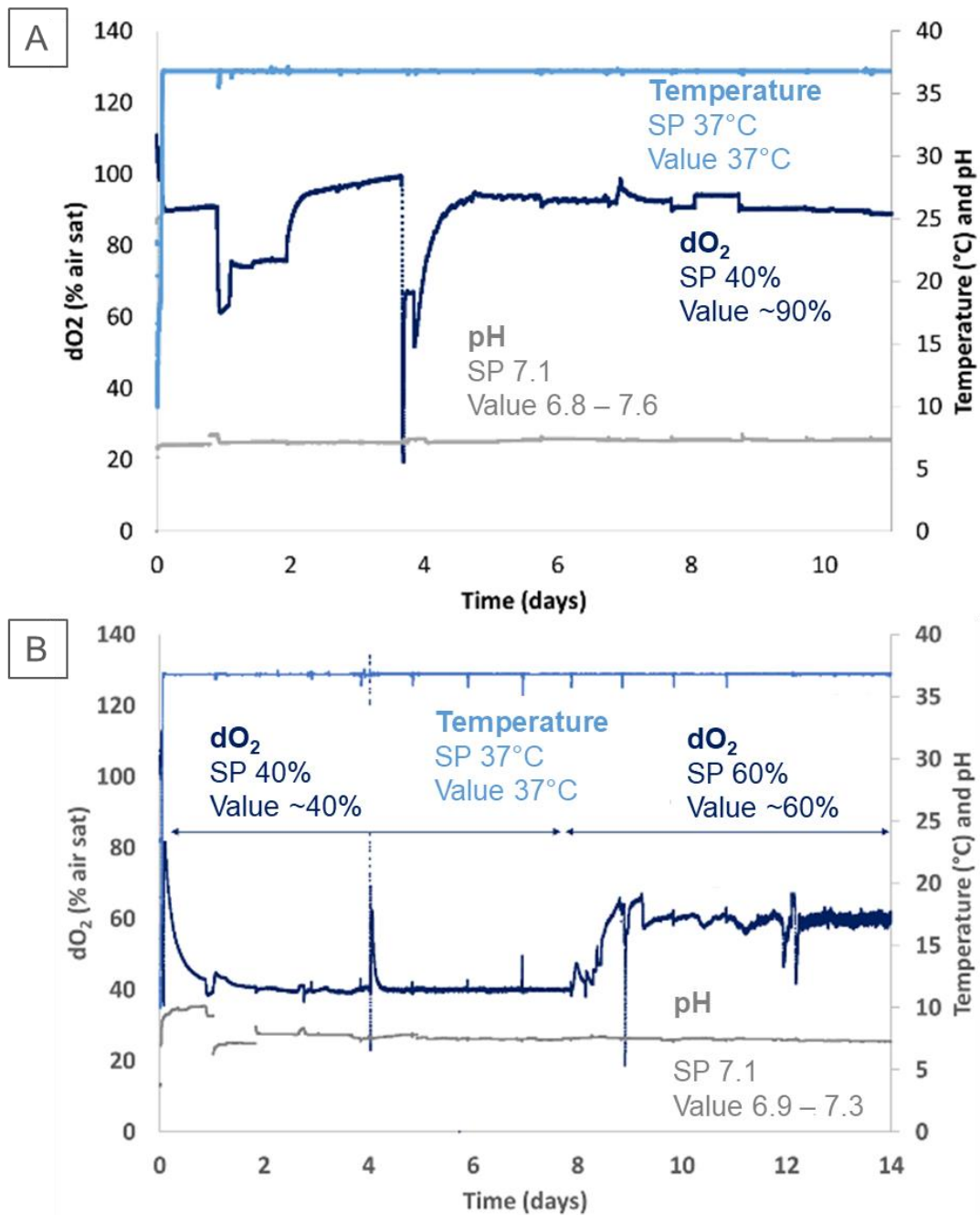


**Figure 5.13 : Regulation of culture parameters for large bioprinted construct containing CHO cells cultured in adapted Ambr®250 setup with (A) Non optimized settings and PID based on those used for suspension CHO cells culture and (B) Optimized settings and PID for bioprinted constructs culture, a change of dO<sub>2</sub> setpoint was performed at day 8 to verify the adaptation of the regulations.**

**Table 5.2: Evolution of the  $dO_2$  control loop PID**

<b>initial <math>dO_2</math> regulation loop</b>	
Level 1	
Output	Gas flow mix ( $N_2$ /mix)
Effect	decreases $dO_2$
Minimum flow rate (mL/min)	0
Maximal flow rate (mL/min)	20
Propotional term (kP)	0.1
Derivative term (kD)	5
Integral term (kI)	100
Level 2	
Output	O2 added flow
Effect	increases $dO_2$
Minimum flow rate (mL/min)	0.1
Maximal flow rate (mL/min)	80
Propotional term (kP)	3.5
Derivative term (kD)	2
Integral term (kI)	250

<b>Optimized <math>dO_2</math> regulation loop</b>	
Level 1	
Output	Gas flow mix ( $N_2$ /mix)
Effect	decreases $dO_2$
Minimum flow rate (mL/min)	0
Maximal flow rate (mL/min)	20
Propotional term (kP)	0.8
Derivative term (kD)	7
Integral term (kI)	99
Level 2	
Output	O2 added flow
Effect	increases $dO_2$
Minimum flow rate (mL/min)	0.01
Maximal flow rate (mL/min)	80
Propotional term (kP)	0.3
Derivative term (kD)	12
Integral term (kI)	249

### 5.3.3. Volume regulation in Ambr® 250ml

In the Ambr®250 system, a unique feature involves regulating the volume tank and recording the flow in and out of the Ambr®250 tank through the system's pumps. However, in our adapted setup, we faced a challenge. The system could record the flow pumped out of the stirred tank by the Ambr® pump but couldn't account for the liquid flow coming back through the new Ambr® perfusion cap (first version shown in Figure 5.12\_A). Consequently, the system would enter a security mode due to a "low volume" alarm, which would cease all regulations. To prevent culture interruption due to this "low volume" alarm, we explored several options listed below:

**Option 1:** Two pumps within the system for media flow circulation, with manual addition of FMB feeding

In this option, one pump of the Ambr®250 was positioned before the culture chamber to transport media from the tank into the chamber, and another was placed after the chamber to move the media from the chamber back into the stirred tank. This arrangement effectively prevented the "low volume" alarm from triggering prematurely. However, a slight delay between the two pumps introduced variability into the recorded volume despite being programmed to operate at the same flow rate. Consequently, it was necessary to manually adjust the recorded volume at least once daily to maintain accuracy. Unfortunately, after 11 days of culture, the delay between the two pumps created an underpressure in the chamber, compromising the seal and allowing air to enter the circuit. Consequently, the culture had to be halted due to the risk of cell drying, starvation, and contamination. Additionally, new leaks occurred at the cap of the 3D printed chamber, even when using the new design with a circular screw cap and O-ring joint. Hence, this configuration required a daily manual edition and resulted in low pressure, leading to a break of sealing and loss of sterility.

**Option 2:** One pump is placed before the chamber to inject inlet media and an empty filtered sterile bottle pumping air in the tank to balance the pumped volume.

In this particular setup, we employed only one Ambr® pump on the chamber's inlet tubing, responsible for transferring the culture medium from the stirred tank to the culture chamber. To maintain a constant volume in the stirred tank, we connected a sterile filtered bottle to the second Ambr® pump. The control system was thereby manipulated to consistently record a stable volume by introducing sterile air from the bottle into the tank at an identical flow rate. However, it's important to note that this configuration had a downside. It resulted in suboptimal regulation of dissolved oxygen (dO<sub>2</sub>) because the continuous introduction of air from the filtered bottle was not integrated into the dO<sub>2</sub> control loop. This oversight led to challenges in effectively regulating dO<sub>2</sub> levels.

**Option 3:** External peristaltic pump with higher flow rates and cap modification (max flow rate achievable with Ambr®250 pumps is 2.5 mL/min or 150 mL/h) + = new leaks

We opted for an external peristaltic pump to address the challenges associated with volume control in the Ambr® system. This approach offered the added benefit of allowing for higher flow rates, reaching up to 14 mL/min, compared to the Ambr® pumps, which were limited to a maximum flow rate of 2.5 mL/min. Modifications were made to the Ambr® perfusion cap to

incorporate external pumps, resulting in the second version depicted in Figure 5.12\_B. This new cap featured the addition of a second tube fitting and an immersed pipe, enabling the pumping of media from the tanks in one direction and the return of media to the tank in the opposite direction. The creation of this modified cap necessitated the design and 3D printing of an entirely new cap. Despite these modifications, some occasional leaks still occurred from the screw cap. To mitigate this issue, adjustments were made to the construct geometry, as described in section 4.1, to facilitate the flow path of fluids through the construct.

Additionally, as detailed in section 5.2.2, the diameter of the outlet tubing was doubled, and an empty sterile-filtered bottle was connected to the cap of the culture chamber. This setup allowed for the evacuation of gas bubbles or over-pressurized liquid. Nonetheless, despite these efforts, some leaks persisted due to inadequate sealing and the potential for pressure buildup in the chamber caused by inefficient media evacuation.

**Option 4:** Displacement of the peristaltic pump from the inlet tubing to the outlet tubing of the culture chamber.

In this option, the filtered bottle connected to the culture chamber cap was removed and the external peristaltic pump was placed on the exit side of the culture chamber to force media out of the chamber and thereby avoid overpressure. This final setup adjustment led to a successful culture for 14 days. During this period, parameters such as pH, oxygen supply, and temperature were precisely regulated, and the culture proceeded without any leaks or contamination. The different setup optimizations presented above are schematized in Figure 5.14.

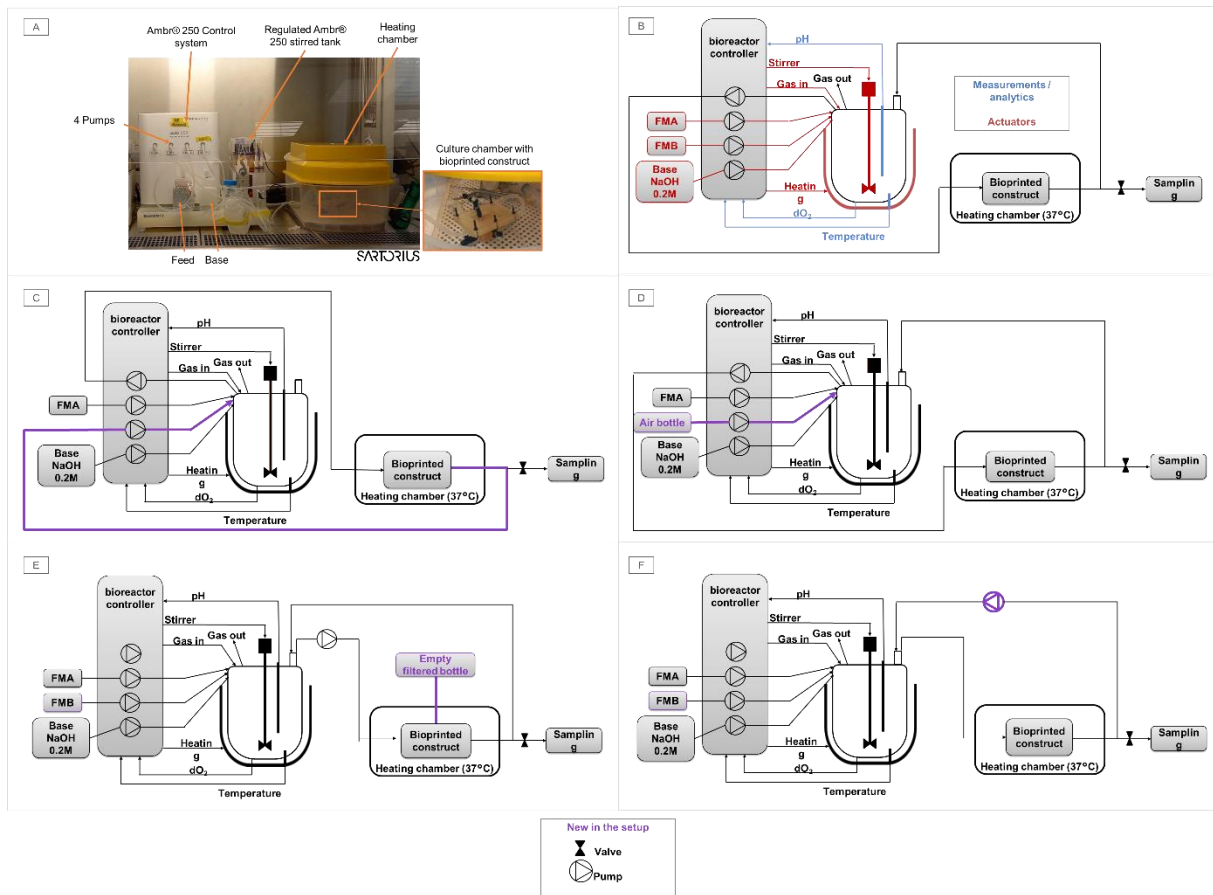


**Figure 5.14: Evolution of bioreactor setup on Ambr®250 system for bioprinted constructs culture with (A) Picture of a bioreactor run on Ambr®250 with large bioprinted construct, (B) Initial bioreactor setup, resulting in "low volume" alarm and arrest of the culture, (C) second setup (Option 1) used two Ambr® pumps for circulation loop, led to culture arrest due to under-pressure which broke the sealing, (D) third setup (Option 2) using one Ambr® pump for circulation loop and one for "air bottle" pumping compensation, (E) fourth setup (Option 3) with external peristaltic pump placed before the chamber and filtered bottle connected to the culture chamber cap, led to culture arrest due to over-pressure and leaks from the chamber cap, (F) fifth setup (Option 4) with external peristaltic pump placed after the chamber was able to prevent over-pressure in the culture chamber and led to successful 14 days culture.**

#### 5.3.4. Integration of new analytics in the bioreactor setup

In 3D culture monitoring, various imaging modalities were evaluated but were still limited in scale and depth of analysis. There, we find standard Fluorescence or Confocal microscopy, Light-sheet-based fluorescence microscopy [622], Tomography (PET—positron emission tomography, OPT—optical projection tomography) [623] or its combination with spectroscopic tools like Raman [624]. All instruments are quite limited in analysis depth, usually  $< 1$  mm [625,626]. Some technologies such as Light Sheet allow the reconstruction of 3D structures from multiple low-depth images, but the largest samples reconstructed with this method were



small organs  $< 1 \text{ cm}^3$  [625,627,628]. Tissue transpiration can reach depths up to  $300\mu\text{m}$  [629,630], but this practice is destructive. Analysed tissue volumes are commonly in the range of  $10 \mu\text{m}^3$  to  $5 \text{ mm}^3$  [624,630]. But again, for larger tissues, it requires sectioning. Thus, we identified a clear challenge in qualifying our large 3D cellularized constructs of  $10 \text{ cm}^3$ , in terms of internal geometry, cellularity, metabolic activity, and their evolution without destructing the samples. Thus, to answer this problem, novel analysis modalities had to be evaluated, allowing for non-destructive observation of our large-scale bioprinted constructs while they were being cultivated in bioreactors.

Consequently, along with my PhD, I evaluated several promising analytical tools to reach such goals. **This work was performed in collaboration with experts of the technologies assessed. I contributed to implementing the culture setups, the cultures and external analysis. This is why, in the following section, I only present the strategy implied in developing such tools but will not discuss the experiment's details and parameter optimizations.**

Additionally, we had to modify the bioreactor setup or "culture chamber" for some of the technologies evaluated. As the in-house developed bioreactor setup (Eppendorf stirred tank with Cytosys® Controller) had more flexibility than commercial AmBr® devices, it is the one with which the developments were performed.

### **Non-destructive offline analytics**

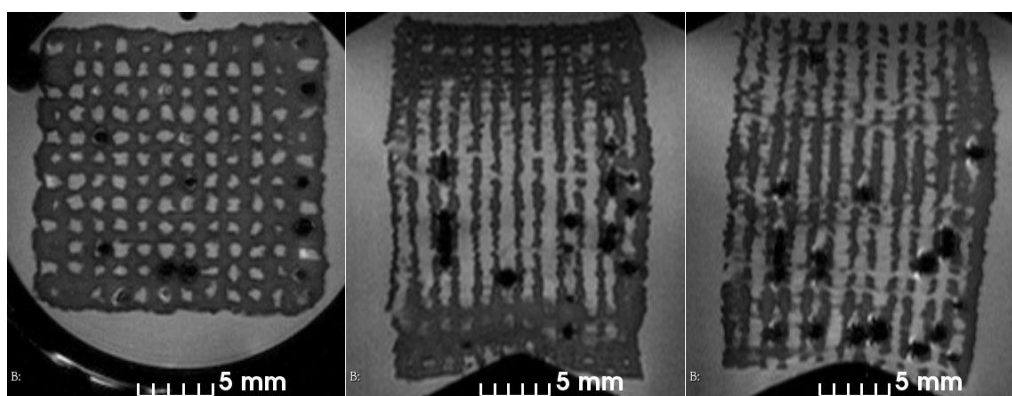
Internal morphological analysis of tissue is commonly performed by histology. This tool was routinely adapted to 3D bioprinted structures by the lab. In the case of our project, large bioprinted structures were sliced into  $5 \mu\text{m}$  sections separated by  $3 \text{ mm}$  between each cut, since it was impossible to cut the whole construct and keep every section. In fact, cutting the whole construct would imply sectioning, staining and imaging approximately 4000 sections for one construct. Thus, this tool cannot fully reconstruct the cellularized hydrogels in routine.

Therefore, to provide non-destructive analytics for observing large 3D constructs, we evaluated tools already applied for *in-vivo* imaging of large organs and tissues. In this field, the Magnetic Resonance Imaging (MRI) is a reference tool for tissue imaging *in vivo* and *in vitro* [631]. Indeed, it stays non-destructive and is the sole imaging tool with X-Ray (Micro-CT) that provides high spatial resolution from  $50\mu\text{m}$  to  $10\text{mm}$  and imaging depth ranging from  $0.1\text{mm}$  to  $1000 \text{ mm}$  [629].

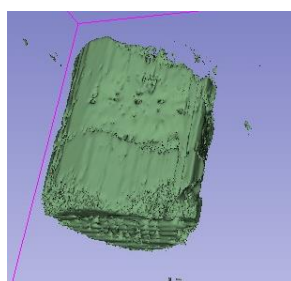
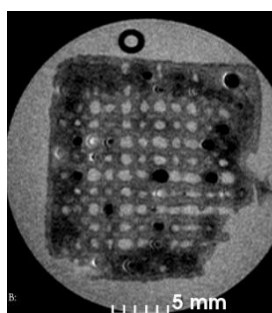
Thus, MRI analyses were performed on our 3D bioprinted objects at the CERMEP (Lyon, France) with a 7T Siemens AvantoFit MRI. We evaluated if this technology can provide insight on :

- The 3D construct geometry and its evolution after the cultivation period
- The 3D construct composition (cellularity or extracellular matrix)

Assays were performed on non-cellularized cultures and HEK bioprinted construct. As demonstrated by the pictures below, MRI determines precisely the internal geometry of the 3D-printed objects. It allows us to identify the morphological evolutions of the object without slicing.



No cells



With cells

3D reconstruction

**Figure 5.15: MRI imaging of bioprinted constructs with or without cells**

As a demonstration of the implementation of such a tool to qualify the 3D structure, Figure 5.15. The MRI imaging of the cell-free construct after 3D printing shows the concordance of the 3D structure with the CAD model, presenting well-defined pores. Dark areas indicate the presence of some air bubbles retained in the porous channels. The MRI of the cellularized Construct after 20 days of culture demonstrates the excellent conservation of the structure and porosity, except for the pores on the periphery, which got crushed due to the construct squeezing into the culture chamber. The dark zone shows that some air bubbles are still present in the structure. If these bubbles were present from the first day, they may have hindered the media

flow and possibly prevented the correct feeding of the cells. The MRI data could be used to reconstruct the whole 3D structure of the construct as shown in Figure 5.15.

Hence, MRI is exciting for studying the real constructs' 3D architecture and evaluating its conformity to the CAD model. It is one of the outputs of this preliminary study for future work. Then, it also provides a non-destructive method to characterize the evolution of the construct structure. Still, such analysis necessitates being performed in high-field MRI, not located at or close to the cultivation site. It stays an offline powerful tool. A proposed evolution is to perform a similar analysis with a low-field MRI, thus remaining close to the cultivation setup and having in-line monitoring of morphological changes.

### **Development of in-line analytics**

As described above, 3D structure cultivation is a very long process (> 14 days) to reach satisfactory cell proliferation, structuration, and metabolic activity. While non-destructive tools are essential to screen and optimize culture conditions, online monitoring providing insight of the construct's evolution over time is also strategic to identify the changes and process phases. This work targeted two read-outs: first, the metabolic activity (lactic acid secretion) as a marker of cell proliferation onset, and second, the cell proliferation itself.

#### *Metabolism monitoring*

Culture sampling allows for the quantification of cell-consumed or secreted molecules. As introduced in Chapter 3 and 4, lactic acid was targeted as a marker of cell proliferation onset and metabolic activity. Thus, we implemented monitoring strategies observed in standard cell culture processes to our 3D bioprinted cultures. Raman spectroscopy acquisition of culture medium has been proven to correctly monitor lactic acid concentration in animal cell cultures [632–634].

In our case, we investigated the technology for monitoring online metabolism of bioprinted construct cultures. The setup is presented in Figure 5.17. The monitoring probe (Rxn-40, Endress-Hauser) was implemented in the regulation stirred tank. Three cultures of 20 days were performed with Raman spectra acquired twice a day during the whole culture duration. Simultaneously, supernatant samples were collected to quantify lactic acid secreted by the cultivated bioprinted construct. To evaluate the robustness of our strategy, two cell models were involved in the experimental plan: HEK cells, which are well known for being high lactic acid producers and dermal fibroblasts being low lactic producers. Thanks to chemiometric analysis, this data set allowed us to build a calibration for lactic acid quantification (sample set = 92) and validate the calibration (sample set = 21). The best model obtained after screening various

spectra pretreatments, spectrum analysis regions, number of PLS components involved provides an error of lactic acid measurement of 0.12g/L (Model parameter:  $R^2=0.96$ ;  $Q^2=0.94$ ;  $RMSEE=0.10$ g/l;  $RMSECV=0.12$ g/l; Number of OPLS component= 1 + 4) as shown in Figure 5.16.

**This work demonstrated that monitoring 3D culture metabolic activity thanks to online tools is also feasible, providing the constitution of appropriate assay calibration and a sufficient sample set. It is the first time this technology was evaluated for this application, and the work presented here takes part in a publication under writing by the team.**

Figure 2 \_ non destructive & on-line tissue metabolism monitoring – Raman spectroscopy

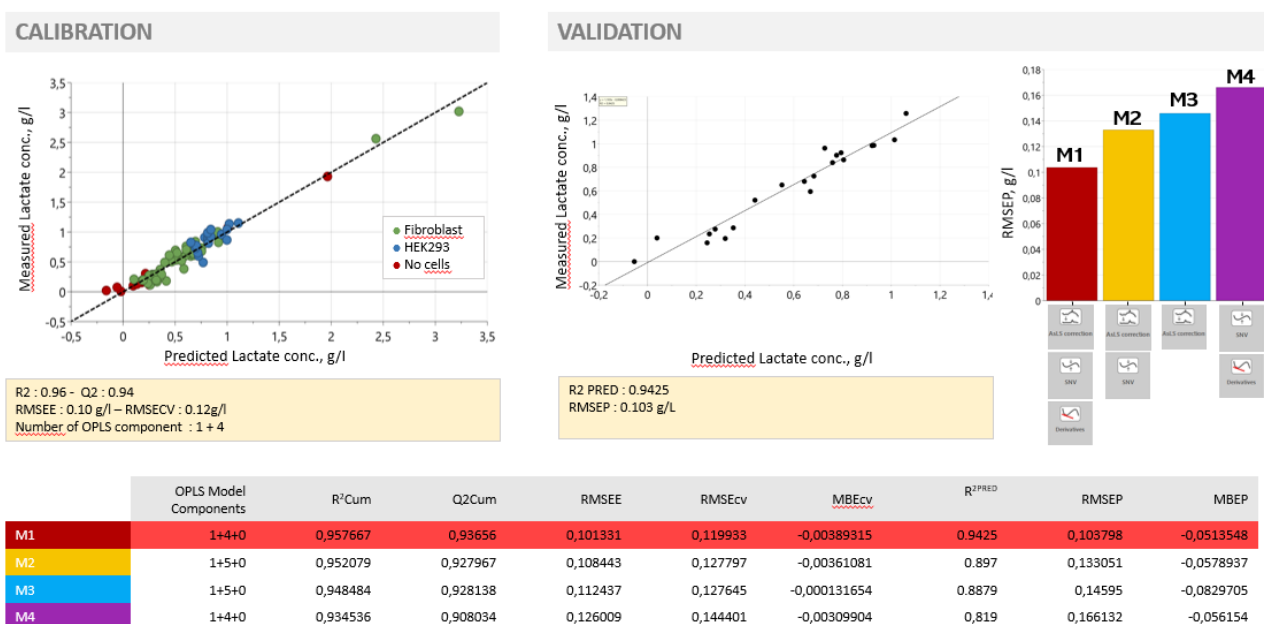


Figure 5.16 : Establishment of a model for lactic acid monitoring with Raman spectrometry

### Bioprinted constructs cellularity monitoring

Raman spectroscopy has also been evaluated for tissue qualification [635–638]. Both the tissue cell content and the extracellular matrix were qualified by Raman spectroscopy.

Thus, to go further, we designed a bioreactor setup to integrate this technology to qualify our 3D cellularized matrix composition., non-destructively and online. In that case, the probe had to be installed onto the "culture chamber" and a contact-free probe was used for solids and semi-solids measurement (Rxn-20 probe from Endress-Hauser).

Moreover, this approach allows for measurements through a low-interfering material, such as borosilicate, which exhibits spectral peaks in lower shifts. These spectral shifts are typically excluded from analysis due to significant noise interference. This feature is particularly

advantageous in a bioreactor setting, where contact-free measurements through a "window" help reduce the risk of contamination or leaks.


To obtain data directly from the bioprinted construct, we designed a new chamber cap that incorporates a transparent borosilicate slide and a hollow cylinder to stabilize and set the probe's height. This design ensures reproducible probe placement (see Figure 5.19).

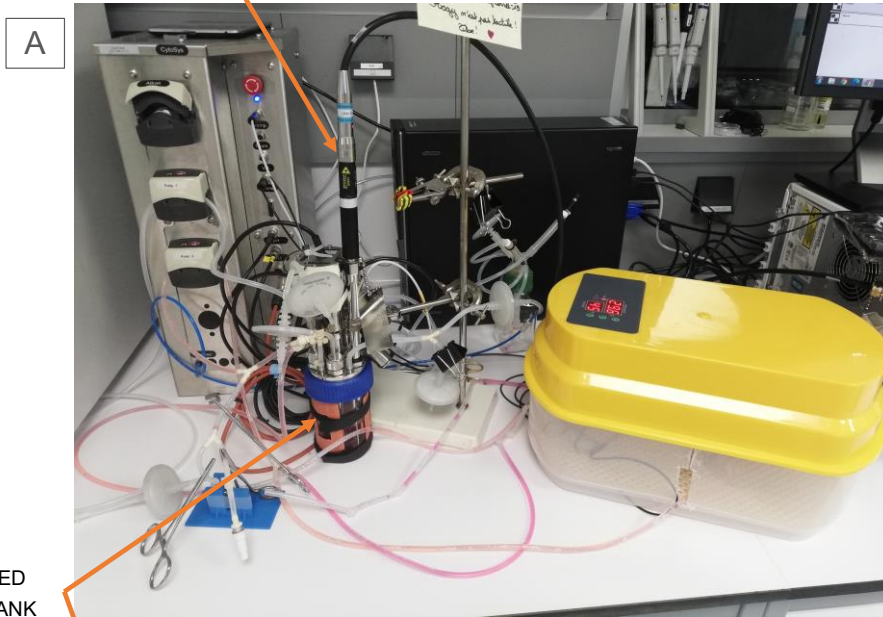
Metabolite analysis was also a part of this setup. In this configuration, media sampling was conducted at the outlet of the bioreactor chamber to measure metabolites in the supernatant immediately after passing through the construct. Since the Raman probe was positioned in the culture chamber and could not fit inside the bench heating chamber, the culture chamber had to be placed outside at room temperature. We placed the inlet and outlet tubing inside the heating chamber to minimise heat loss during fluid circulation, as illustrated in Figure 5.18.

We conducted experiments with two cell types to assess the capability of this technology to measure cell density in a possibly changing hydrogel environment, considering factors like degradation or extracellular matrix (ECM) production. The two cell lines used included a highly proliferative cell line with low to no ECM production (HEK) and a cell line with slower proliferation but high ECM production (Fibroblasts). These cultures were successfully run with this setup, allowing for the continuous acquisition of Raman spectra.

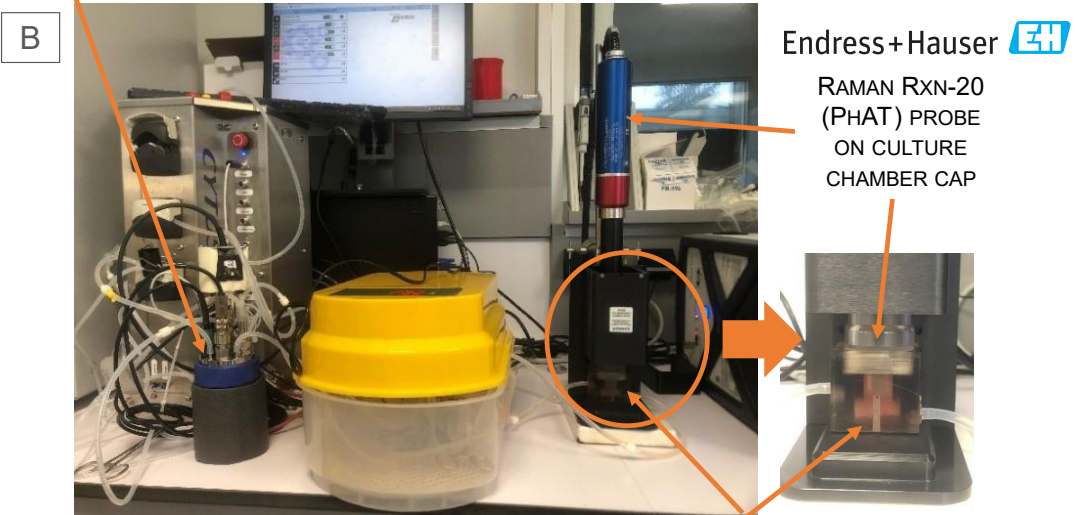
To establish a predictive model of cell concentration from the spectra, we supplemented the data with offline measurements in small-scale bioprinted constructs with varying cell densities. These constructs were measured through the borosilicate window. After each measurement, the small-scale construct was dissociated, and the cells were counted to determine the experimental cell density.


Spectra analysis and the mathematical prediction model were developed by the Raman experts of the team: Emma Petiot, Sarah Pragnère, and Ilyes Bichari. It's important to note that the prediction of cell density was less precise compared to lactate concentration prediction. However, the trends observed indicate the promising potential of this setup. With more data and optimization, this setup could likely offer a much more accurate estimation of cell density within the bioprinted constructs and provide in-line, continuous monitoring of cell proliferation in the bioreactors. They acknowledged that the measurement is localized to a 6 mm diameter spot, and the first 2 mm of the construct is essential. As a result, the measurement may not represent the total cell density inside the construct, and this difference in cell concentration measured with Raman spectroscopy and experimental dissociation may be attributed to the limited measurement area.

RAMAN RXN-40 PROBE  
IMMERSED IN STIRRED TANK  
Endress+Hauser 



REGULATED  
STIRRED TANK



Endress+Hauser 

RAMAN RXN-20  
(PHAT) PROBE  
ON CULTURE  
CHAMBER  
CAP

3D PRINTED CULTURE CHAMBER  
CONTAINING BIOPRINTED TISSUE,  
PERFUSED WITH MEDIA FLOW

**Figure 5.17: Bioreactor setups integrating Raman spectroscopy probes.** (A) Setup with immersion probe (Rxn-40 ; Endress-Hauser) inserted in the regulated tank for lactate monitoring. (B) Setup with contact-free probe (Rxn-20 ; Endress-Hauser) placed on the culture chamber for monitoring of cell density in bioprinted construct.

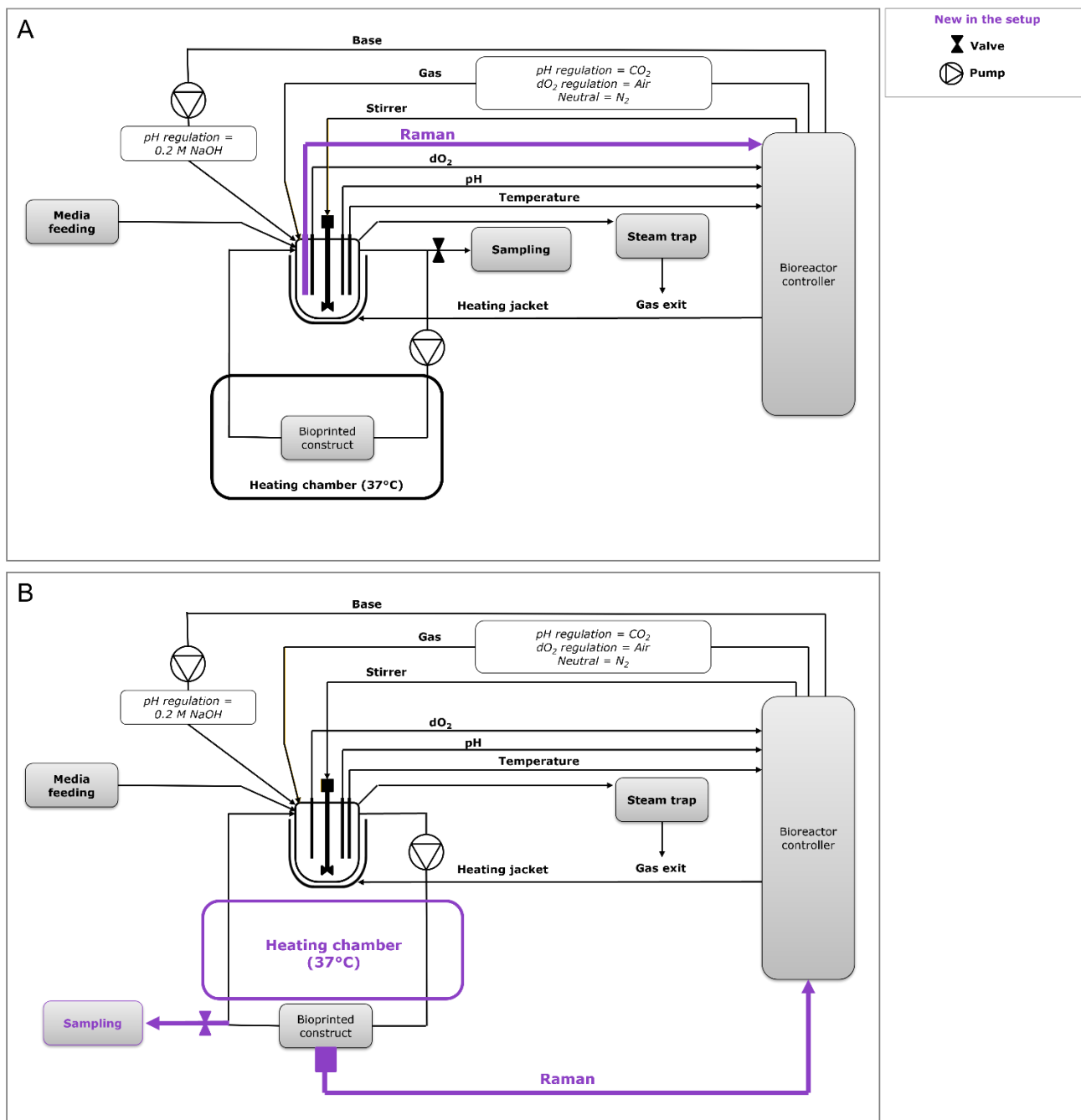


**Figure 5.18 : Detailed Pipe and Instrumentation Diagram of bioreactor setups integrating Raman spectroscopy probes.** Bioreactor setup with Eppendorf DASbox® stirred tank and Ipratech Cytosys® controller integrating (A) A Raman spectroscopy immersion probe for quantification of metabolites in the supernatant and (B) A Raman spectroscopy contact-free probe for estimation of cell density in the construct.

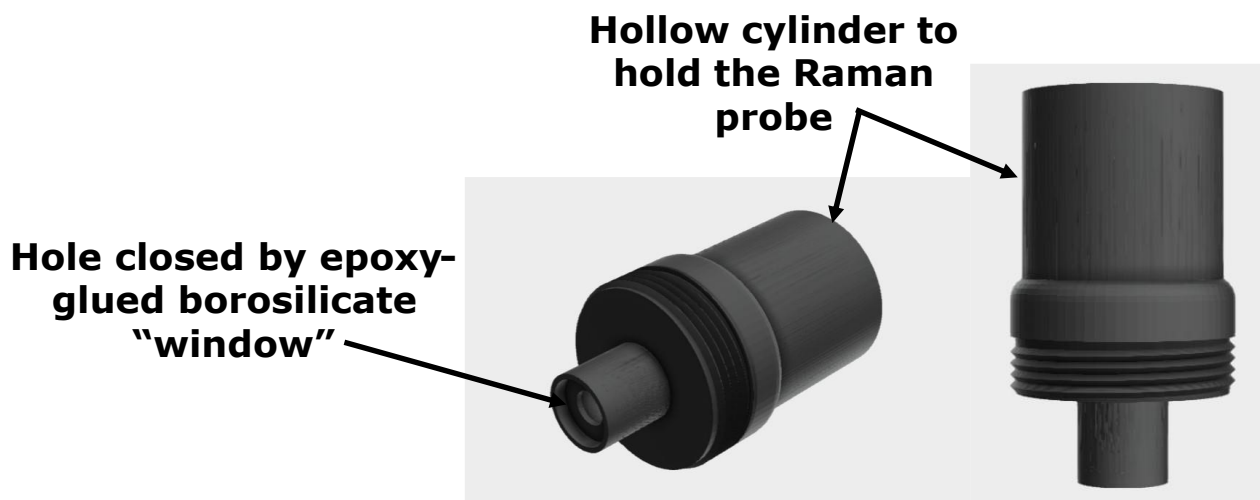


*Figure 5.19: 3D printed chamber cap adapted to the insertion of a Rxn-20 contact-free Raman spectroscopy probe. A borosilicate "window" was glued to the cap with epoxy glue to enable the passage of the red light ray.*

#### 5.4. Conclusion

This chapter presents the development and improvement of several bioreactor setups and analytics adapted for the culture of large bioprinted constructs. These setups have allowed us to carry out cultures over 20 days without contamination. To perform these cultures, multiple improvements had to be made in setup, construct and, chamber design and culture regulation. Further refinement and higher control of the cultures will be achieved by understanding the gas exchange through silicone tubing and selecting the most appropriate material. For example, the tubing was switched to Pharmed pipes in the peristaltic pump region to avoid damage and breakage from pump-generated shear. Thermoplastic elastomer (TPE) material could also be interesting for performing sterile connections or disconnections during the culture using a Biowelder® (Sartorius). For example, multiple chambers could be cultivated in parallel on one bioreactor, and chambers could be sterile-disconnected at different culture times without stopping the whole bioreactor culture. The disconnected construct could either be destroyed for cell count or sterile-analysed by MRI and reconnected to the bioreactor afterwards. The entire setup could even use several tubings of different natures depending on the location and role of the pipe section. Proof-of-concept of multiple new analytics applications to characterise and monitor large bioprinted constructs was performed. Among them, MRI was used as the starting and final point of characterization of constructed 3D architecture. Currently, the evaluation and integration to the setup of a small-scale MRI placed on a laboratory bench is in process in the platform. It will enable the continuous MRI analysis of the construct architecture during the culture. This tool also provides real-time imaging of the liquid flow inside the construct, which helps validate the CFD simulations. If high resolution can be achieved, then MRI could also be



used to detect and study the cells and their spreading in the construct or their action on the matrix composition.

Finally, we evaluated two Raman spectroscopy probes for metabolites and cell density monitoring. The probes were integrated separately in two different bioreactor configurations, and both gave promising results. More data and optimization will be needed to feed the models and improve the estimations. Since the Rxn2 Raman analyser can function with multiple probes working simultaneously, the next step would be integrating both probes in one setup to monitor metabolite concentration and cell density simultaneously, as presented in Figure 5.20. Finding a way to keep the construct's chamber in a 37°C heated atmosphere while the Rxn-20 probe is set would also be advantageous.

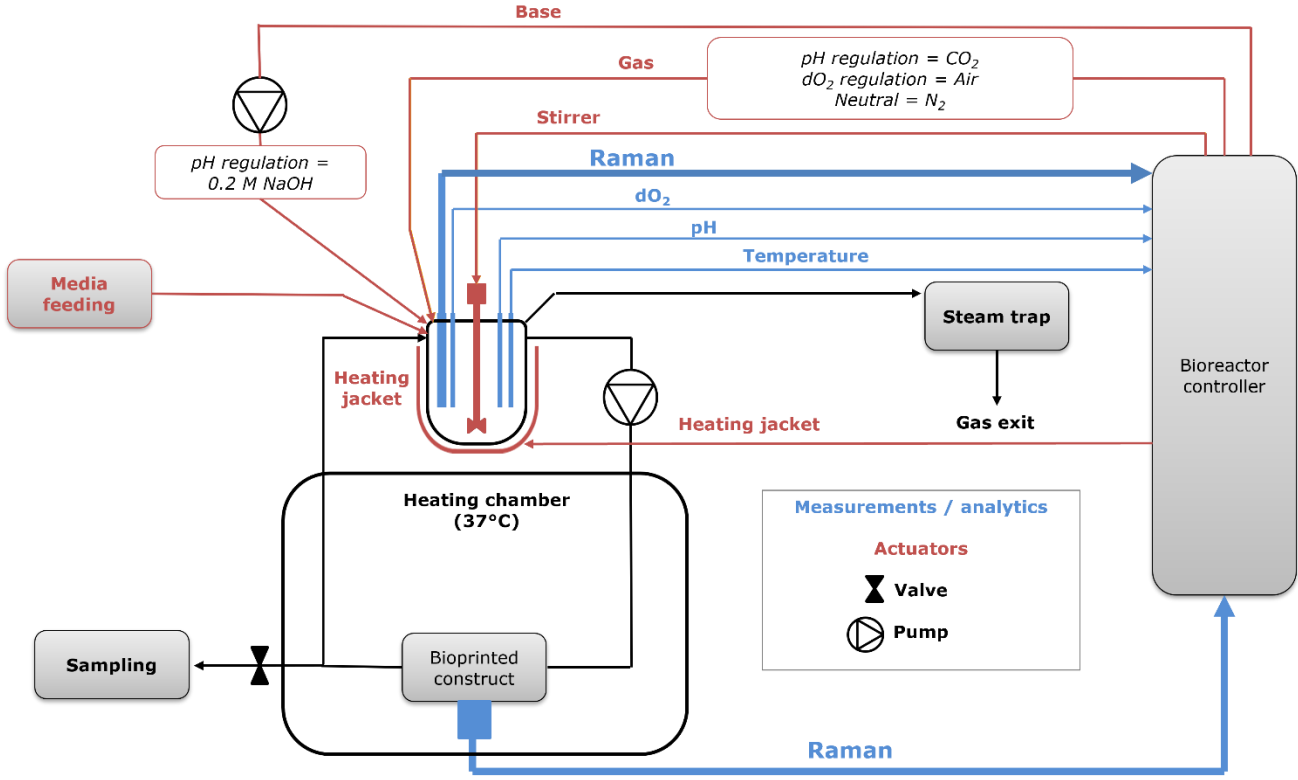


Figure 5.20: Prospects for a proposed future bioreactor setup

## CHAPTER 6. BIOREACTOR CULTURE: A PLATFORM FOR ENHANCED 3D CELL CULTURE AND MONOCLONAL ANTIBODY PRODUCTION

Using bioreactors to cultivate large 3D bioprinted cell constructs presents a promising perspective for the scaling and densification of 3D cell cultures. This study delves into evaluating the feasibility of upscaling and assessing various parameters within the complex bioreactor system. As described in Chapter 5, two bioreactor setups were used. The bioreactor system was validated with the initial setup designed with the Eppendorf DASbox® stirred tank. An Ipratech Cytosys® controller diligently regulated the entire system. The setup was then transferred to the commercial Ambr®250 bioreactor which offers more reproducibility, automation, and scalability for bioproduction applications. Both systems were used for bioprinted cell culture. Bioproduction of monoclonal antibodies was performed with Ambr®250 setup.

### 6.1. Cultivating large bioprinted constructs in bioreactors for densifying 3D cell cultures

In the first part of this study, we evaluated the feasibility of cultivating large-scale bioprinted HEK cells in our bioreactor system and investigated the effect on cell proliferation.

Bioprinting, consolidation and culture conditions were sub-optimal compared to the best options identified in Chapter 4. Still, the bioprinted constructs, designed with a 2 x 2 x 2.7 cm geometry and a 35% infill ratio, are a central focus of this investigation. These constructs were composed of a bioink formulated with final concentrations of 2% w/v Fibrinogen, 2% w/v Alginate, and 5% w/v Gelatin, meticulously seeded with  $3.0 \times 10^6$  HEK cells per mL. The bioprinting process was executed with an 800  $\mu$ m diameter needle and maintained a temperature of 21°C. The hydrogel was further consolidated with 3%<sub>w/v</sub> CaCl<sub>2</sub>, 4%<sub>w/v</sub> transglutaminase, and 10 U/mL Thrombin.

This study deployed two identical constructs, one for the bioreactor experiment and the other as a control, cultured under static conditions in an incubator. The static culture involved immersing the bioprinted construct in a 100 mL culture medium with periodic media changes. In contrast, the construct designated for the bioreactor culture was initially cultivated for 7 days under static conditions, then transitioned into the perfused culture chamber, connected to the circulation loop of the bioreactor setup with a homogeneous flow configuration (as illustrated

in Figure 5.4\_C). The bioreactor culture, extending for 13 days, resulted in a total of 20 days post-printing culture duration, maintained with a media volume of approximately 200 mL.

During the 13 days of bioreactor culture, no bacterial nor fungal contamination was observed, and there were no liquid leaks. On the 11th day, media feeding was performed to compensate for the volume decrease due to sampling.

As illustrated in Figure 6.1\_A, the study successfully maintained the set point regulations. Minor deviations in the dO<sub>2</sub> curve were noted, corresponding to manual interruptions in regulation for interventions on the setup.

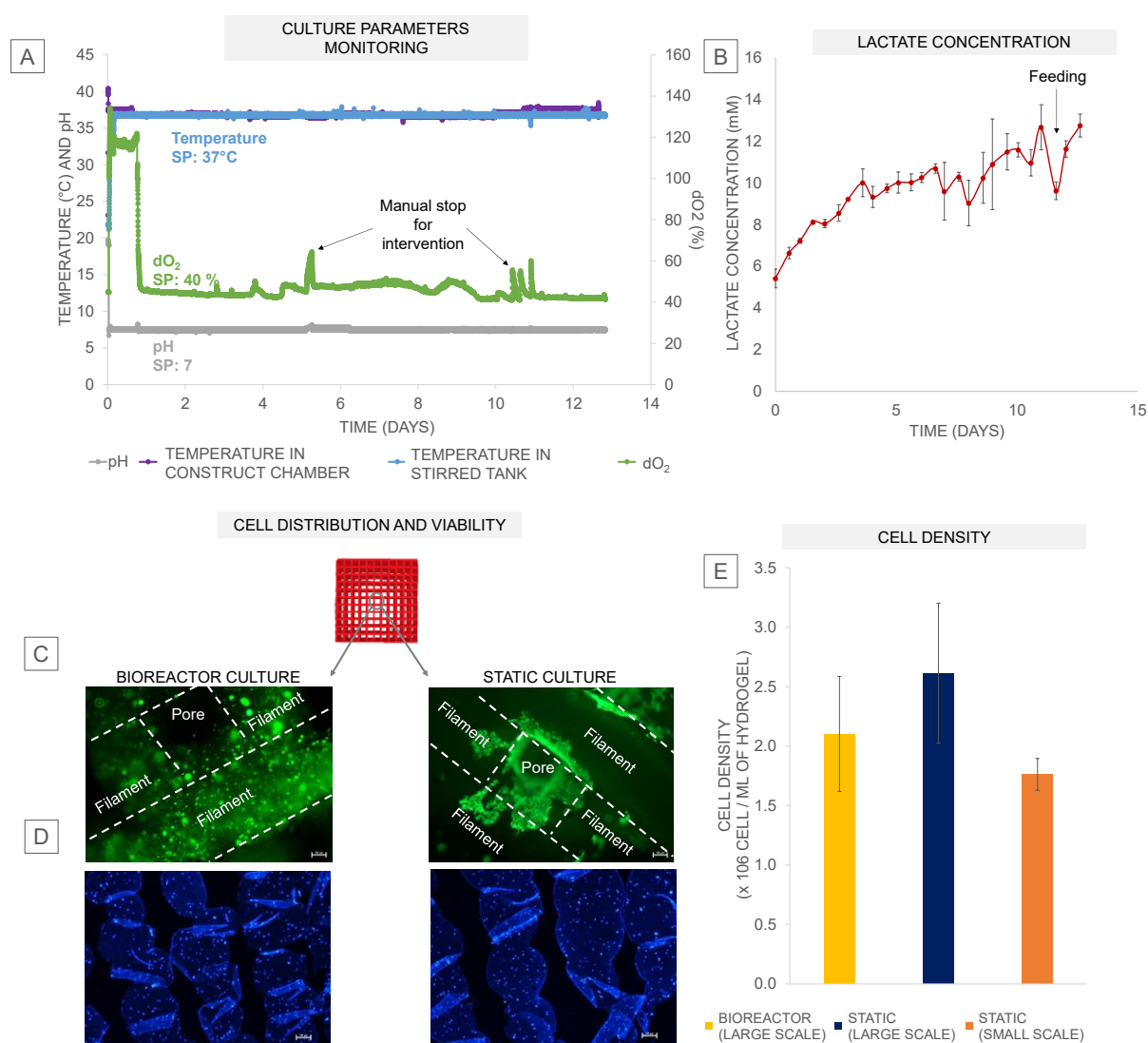


**Figure 6.1: Comparison of HEK-seeded large bioprinted constructs cultured 20 days in either static (incubator) or dynamic conditions (bioreactor).** (A) Continuous monitoring of parameters during the bioreactor culture of bioprinted construct containing HEK cells (7 days pre-culture in static followed by 13 days bioreactor). (B) Evolution of lactate concentration during the bioreactor culture. (C) Live cells were stained with calcein (green) on fresh samples, and (D) cell nuclei were stained on histological sections with DAPI (blue). (E) Cell density in the hydrogel was measured by dissociation and cell counting after 20 days of culture in a large bioprinted

*construct (10.8 cm<sup>3</sup>) compared to a small-scale construct (0.2 cm<sup>3</sup>) grown in static conditions. All the samples were cultivated for 20 days. SP: Setpoint.*

**Cell Distribution and Proliferation:** Bioprinted constructs were retrieved and rinsed with PBS at 20 days of culture. Part of the constructs were sampled for live cell staining with calcein and cell counting after dissociation. The remaining construct was fixed in a paraformaldehyde solution and prepared for histological analysis. Calcein staining revealed the presence of live cells in both control culture and bioreactor culture as depicted in Figure 6.1\_C. However, in the static culture, HEK cells grew mainly on the surface of the hydrogel filaments as monolayers (Figure 6.1\_C). In contrast, the construct were a cultivated phase was performed in the dynamic condition exhibited a more uniform distribution of cells throughout the entire volume of the hydrogel filaments.

Contrary to the live cells' observations with calcein, the distribution of cell nuclei within the hydrogel filaments observed on histological sections was found to be homogeneous in static and dynamic conditions (Figure 6.1\_D). However, the bioreactor-cultivated construct showed increased cell nuclei number relative to the static culture, demonstrated by particle analysis on ImageJ, as presented in Chapter 3, Figure 3.4. This analysis was used to estimate total cell density based on the number of nuclei. Image analysis found that cell concentration in dynamic conditions was almost 1.5 times higher than in the reference static culture. This finding was consistent in Method 1 and Method 2, estimating cell number from the histological slides to be representative of a slice of 5 $\mu$ m or 13  $\mu$ m thickness, respectively, as described in Chapter 3. For example, Method 1 estimated the cell density in a bioreactor-grown construct to be  $\sim 34 \times 10^6$  cell/mL of hydrogel, whereas it was only  $23.5 \times 10^6$  cell/mL of hydrogel in static condition (Chapter 3, Figure 3.4).

The dissociation of the constructs after 20 days of culture allowed for cell recovery and counting. As discussed in Chapter 3, the cell concentration measured after dissociation was notably lower than the concentration estimated through image analysis with only  $2.2 \times 10^6$  cell/mL of hydrogel in bioreactor culture and  $2.7 \times 10^6$  cell/mL of hydrogel in static condition (see Chapter 3, Figure 3.4). Additionally, a culture of non-porous small-scale (0.2 cm<sup>3</sup>) bioprinted constructs, prepared with an identical bioink formulation, consolidation, and cell seeding density, was employed to compare the final cell density after 20 days of culture in a static incubator. As presented in Figure 6.1\_E, the results demonstrate an equivalent final cell density per hydrogel volume in all three cultures.

**Lactate Concentration and cell metabolism:** The lactic acid production was monitored through discrete measurements from supernatant samples, as depicted in Figure 6.1\_B. As expected, the lactate concentration increased during the initial phase of the culture, almost doubling within the first 5 days. Subsequently, the increase in lactate concentration slowed and stabilized within 10 - 12 mM. In Chapter 3, we found that in small-scale bioprinted cultures, the lactate production rate was correlated to the cell proliferative state with reduced lactate production during lag phases (Figure 3.6). Hence, stabilization of lactate production after 5 days could suggest a reduction of cell proliferation rate. However, due to the incapacity to monitor cell proliferation during bioreactor cultures of bioprinted constructs, we cannot verify that the correlation between lactate production and cell proliferation at static small-scale remains true in larger-scale bioreactor cultures.

As a challenge to this hypothesis, a change in cell metabolism within the bioreactor cultures due to the difference in culture scale and regulation of parameters could also be expected.

**In conclusion, using our bioreactor system allowed us to maintain a sterile culture of large bioprinted constructs for 20 days with precise regulation of culture parameters. The settings used in this study did not allow intensification of the culture to reach substantially higher cell density than that measured in static cultures. However, such a dynamic culture system with homogenous media flow through the bioprinted construct favoured a more homogenous cell distribution inside the hydrogel volume.**

## 6.2. Bioproduction of monoclonal antibodies from 3D bioprinted cultures of CHO cells

The work presented in the following section results from a teamwork optimized and finalized through the training and supervision of a master's student, Elliott Cowles.

This part describes the experimental setup and results for Mabs production thanks to 3D bioprinted constructs in a bioreactor. The study begins by conducting a reference run with suspended CHO cells in an Ambr250 bioreactor to serve as a benchmark for evaluating the performance of bioprinted construct cultures.

### 6.2.1. *Establishment of a reference run: CHO cells' suspension in Ambr®250*

A specialized fed-batch technique from SARTORIUS was used to operate a reference run with a suspended CHO cell culture in an Ambr250 bioreactor. It was used as a reference to evaluate

the performance of bioprinted constructs' cultures. The production process with suspension culture was carried out for 14 days in CHO-specific media, including Production Media (PM), Feed Medium A (FMA) and Feed Medium B (FMB). The cell amplification was performed prior to the bioreactor run in Erlenmeyer shake flasks in Stock and Adaptation Media (SAM).

This reference culture was carried out after the optimization of regulation settings presented in Chapter 5, and the culture parameters were successfully monitored and regulated.

The bioreactor culture exhibited typical kinetics, starting with a phase of rapid exponential growth that extended for a week. This phase was followed by a period of slower growth and eventually reached a stationary phase after day 7, as illustrated in Figure 6.2\_A. The data related to glucose consumption and the concentrations of glucose and lactate are presented in Figure 6.2\_B. Glucose consumption continued throughout the culture, and daily adjustments were made from day 4 by adding feed media to maintain the glucose concentration over 1g/L. However, despite adding feed solution, the glucose concentration dropped below 1g/L when the culture reached its maximum density on days 9-10.

In contrast, lactate production peaked during the first week of the culture, specifically on day 6. Subsequently, there was a shift in cell metabolism towards lactate consumption, resulting in a reduction in lactate concentration. This metabolic shift has been extensively documented in previous CHO cell culture studies [135,639,640]. It is consistent with similar profiles of lactate evolution reported in fed-batch cultures of suspended CHO cells [99].

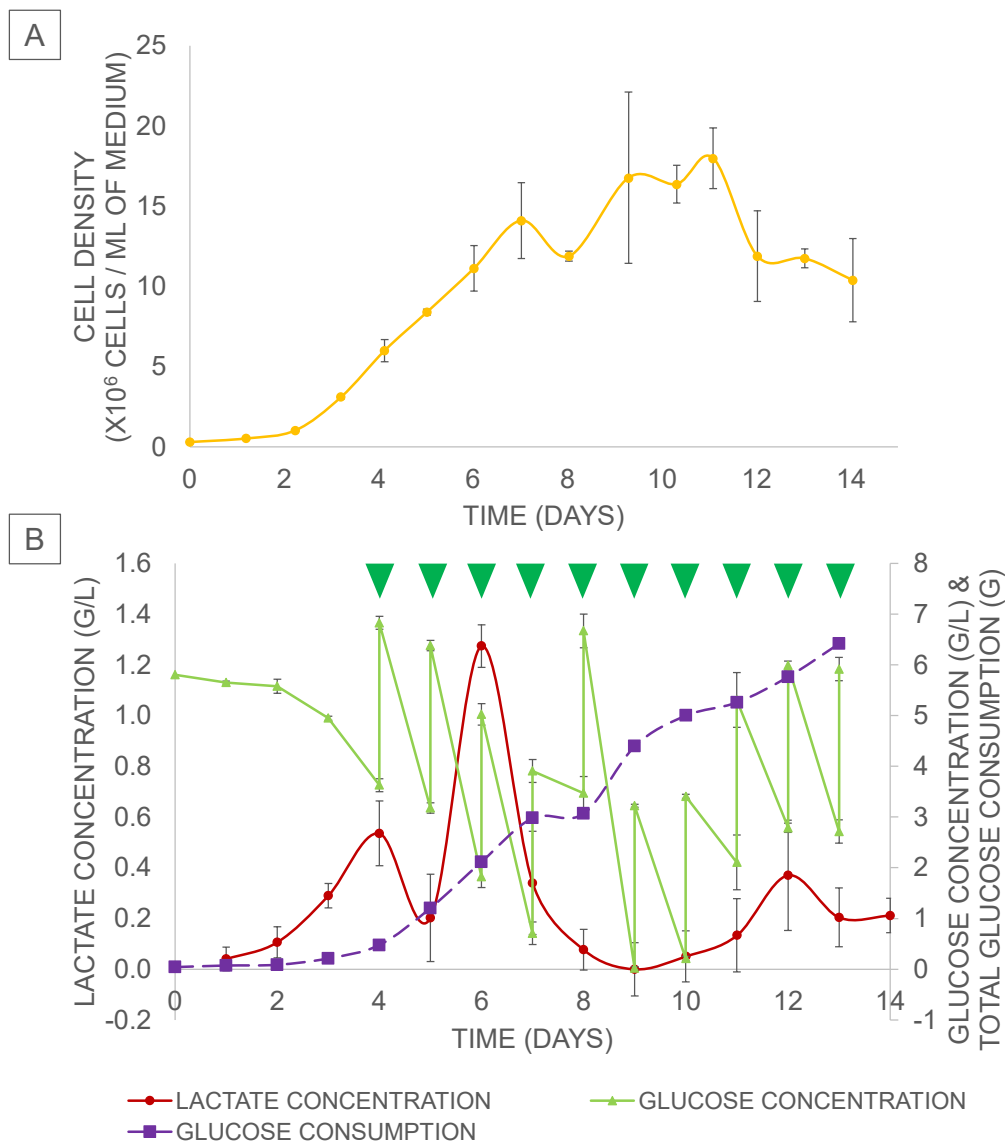


**Figure 6.2: Monitoring of cell proliferation and metabolites of CHO cells grown in suspension in Ambr®250 bioreactor.** (A) Growth curve representing the evolution of suspended cell density. (B) Evolution of lactate and glucose concentrations and total glucose consumption in a 200 mL bioreactor culture. The green triangles indicate the daily feeding with FMA and FMB feed media starting from day 4.

In typical suspension cultures, glucose consumption rates usually fall within a range of 100 to 450 pg/cell/day, increasing to about 700 pg/cell/day in fed-batch production [641,642]. The lactate-specific production rates in suspension cultures commonly range from 90 to 375 pg/cell/day [641,642]. Our reference suspension culture aligned with the range reported for glucose consumption, with displaying a metabolization rate of approximately 500 pg/cell/day (Figure 6.3). On the other hand, the lactate production rate was reduced compared to literature with only ~40 pg/cell/day metabolic rate. In fact, the glucose to lactate molar conversion yield

( $Y_{\text{lact/gluc}}$ ) was inferior to 0.04 which denotes a very low level of lactic fermentation. In fact,  $Y_{\text{lact/gluc}}$  molar ratios under 1 are considered to be representative of oxidative metabolism.

This reference process successfully yielded monoclonal antibodies (mAbs) with a final titer of approximately 1.59 g/L. This titer aligns with the concentrations commonly reported in the literature for industrial fed-batch processes, which typically range from 4 to 10 g/L under optimal conditions [90–92]. While it is acknowledged that optimized suspension fed-batch CHO cell cultures have achieved titers of up to 10 g/L [90–92], it's important to note that the range more commonly reported for this specific cell line in industrial fed-batch processes typically falls within the 2 to 4 g/L range [99,145]. The lower titers observed in this study may be attributed to glucose depletion in the medium around days 9 and 10. The cell-specific mAb productivity of 13 pg/cell/day (Figure 6.3) is slightly reduced compared to the values reported for this cell line commonly reaching 15 - 25 pg/cell/day in similar fed-batch culture without process intensified nor addition of specific enhancer [145].



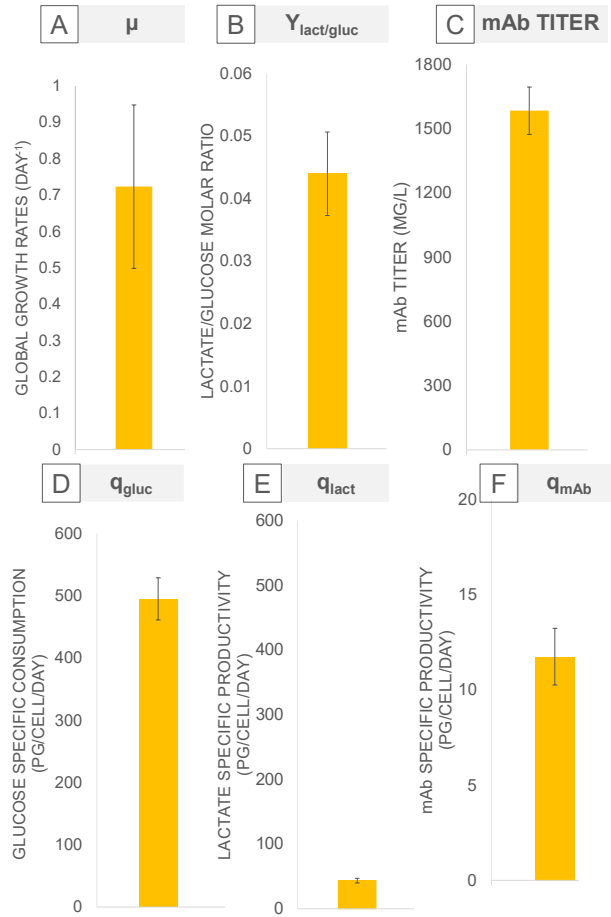


**Figure 6.3: Kinetic parameters regarding cell proliferation, metabolism and mAb production in CHO cell suspension culture in Ambr®250.** (A) Maximal cell-specific growth rate. (B) Glucose to lactate molar conversion yield. (C) Final IgG volumetric titer. (D) Cell-specific rate of glucose consumption. (E) Cell-specific rate of lactate production. (F) Cell-specific rate of mAb production.

### 6.2.2. Small-scale evaluation of SFM impact on cell growth and productivity

After confirming that a bioreactor is an efficient tool for cultivating large 3D bioprinted constructs using HEK cells and establishing a baseline with suspended CHO cells, we investigated the possibility of manufacturing monoclonal antibodies (mAbs) with CHO cells from 3D bioprinted hydrogel structures under conditions resembling an industrial process.

The first stage of this study is transitioning from non-specific, serum-supplemented media (DMEM(+)), commonly employed for tissue culture, to specific, serum-free media designed for suspended CHO cells. These specialized media are formulated to optimize cell growth and mAb production while maintaining product quality and simplifying purification. The evaluation was conducted at a small scale in static cultures within incubators, following the procedures

outlined in Chapters 4 and 2. The various conditions studied are detailed in the accompanying Figure 6.4.

The bioink was seeded in all conditions with  $10 \times 10^6$  cells/mL, a concentration selected to align with the one used for the larger-scale constructs. It ensured an equivalent cell inoculum per medium volume compared to suspension bioreactor runs. The small-scale reference 3D culture was executed using DMEM(+) media under conditions identical to the initial unoptimized cultures outlined in Chapter 4, with consolidation under 3% calcium, 4% transglutaminase and 10U/mL thrombin. Subsequently, two other cultures were carried out, in XtraCHO S.A.M. and PM, chemically defined media designed for industrial CHO cells that secrete mAbs. These cultures followed optimized protocols described in Chapter 3 and 4 with hydrogel consolidation under 1.4 % calcium, 0.4 % transglutaminase and 10U/mL thrombin. In the case of 3D cultures grown in DMEM(+) and PM, media were regularly renewed three times a week, categorizing them as "semi-continuous" cultures (SC). Conversely, the 3D condition involving in situ amplification in SAM followed by the production phase in PM only underwent media changes when glucose concentration fell below 1g/L, thereby classifying it as a "static fed-batch" culture (sFB). The proliferation, metabolism and productivity from small-scale static cultures were compared with the reference run in suspension bioreactor.

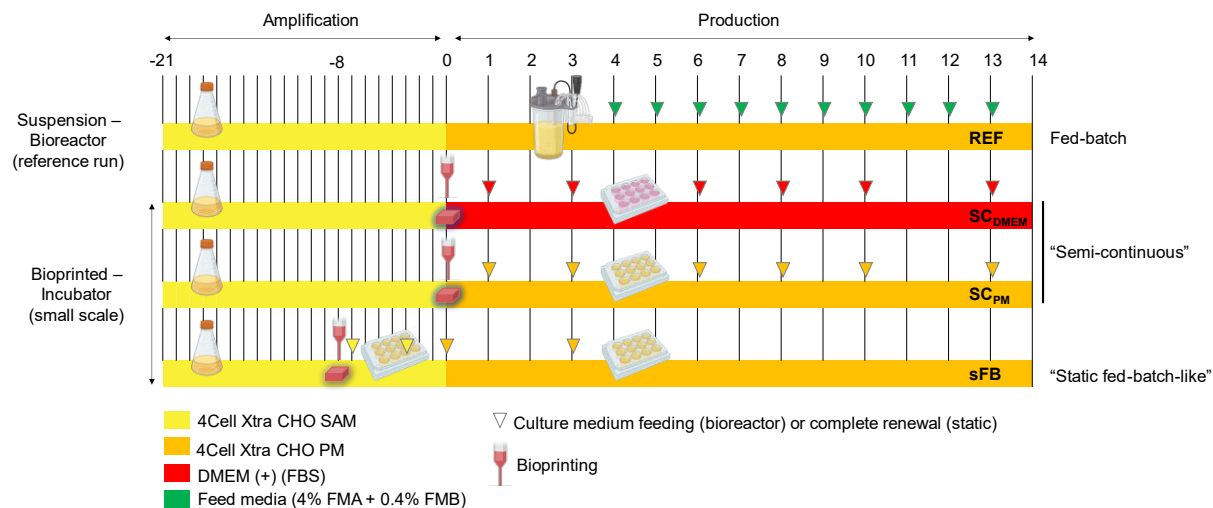


**Figure 6.4: Reference suspension run and static bioprinted conditions evaluated.** The suspension bioreactor culture was used as a reference and designated as REF. The small-scale bioprinted cultures with regular medium change were defined as "semi-continuous". They will be noted SC<sub>DMEM</sub> when cultivated in DMEM(+) medium or SC<sub>PM</sub> when cultivated in PM medium. The small-scale bioprinted culture with amplification phase inside the bioprinted construct with SAM medium was followed by the production phase in the PM medium with media change only when necessary glucose feeding was designated as "static fed-batch-like" and will be noted sFB.

Compared to all the other 3D culture conditions, those carried out in DMEM(+) achieved the highest cell density, reaching  $9 \times 10^6$  cells per mL of hydrogel, equivalent to  $0.9 \times 10^6$  cells per mL of media. It represents a minimum 20% increase compared to the other 3D conditions. As described by the growth kinetics, all 3D printed conditions exhibited slower development than the suspension culture. When assessed on a per-volume basis, the maximum cell concentrations achieved within the hydrogel were approximately half of what was observed in the reference suspension culture. When the cell density in 3D cultures was normalized to the volume of culture medium within the culture wells, these concentrations were approximately 20 times lower than those in the suspension bioreactor.

Consistent with the growth kinetics predictions, all 3D bioprinted conditions displayed a significant, ~ thirteen-fold decrease in the maximum growth rate during the exponential growth phase compared to the suspension culture reference. It aligns with prior findings presented in Chapter 4, indicating reduced proliferation rates in 3D cultures of production cell lines. On the contrary, the reference run (suspension culture) displayed a higher growth rate of 0.72 per day, consistent with the values reported for CHO cells suspension culture in serum-free media, typically ranging from 0.3 to 0.9 per day [193]. When comparing the growth rate of all 3D bioprinted conditions,  $SC_{DMEM}$ ,  $SC_{PM}$  and sFB, we demonstrated that cells grown in CHO-specific media ( $SC_{PM}$  & sFB) proliferated up to 2.5 times faster when compared to cells grown in DMEM(+) ( $SC_{DMEM}$ ).

Live cells were labelled with calcein-AM, and histological sections were stained with hematoxylin-Eosin, to explore the developmental patterns within 3D-printed constructs, as shown in Figure 6.5 Calcein staining confirmed the presence of viable cells in all conditions throughout the culture period.

Despite the increased hydrogel consolidation favouring molecule diffusion in the two 3D conditions grown in CHO-specific media due to enhanced microporosity, histological staining revealed that cell concentration was notably higher near the constructs' surface. Furthermore, 3D cultures of CHO cells grown in CHO-specific media exhibited larger cell aggregates than those grown in DMEM(+), indicating distinct spreading behaviours.

We also observed glucose consumption and lactate production variations among different cell culture conditions. Cells grown in DMEM(+) exhibited the highest glucose consumption, followed by those in PM, while the sFB condition had the lowest glucose consumption. It's worth noting that none of these conditions reduced glucose levels below 2 g/L during the cultures. Among the 3D conditions, the sFB condition closely resembled the suspension

reference regarding metabolic behaviour, with glucose consumption rates falling within the lower range of 100 to 450 pg/cell/day reported in the literature [641,642].

In bioprinted constructs grown in DMEM(+), glucose consumption and lactate production rates significantly increased, up to 2-fold and 3-fold, respectively, compared to cultures in CHO-specific media. In contrast, PM cultures produced very little lactate (<1 g/L) under all scenarios. Both suspension and sFB cultures exhibited values for lactate-specific production rates lower than the 90 to 375 pg/cell/day [641,642] reported in the literature. On the contrary, DMEM(+) cultures surpassed these ranges by 1.5 to 6-fold with specific lactate productivity of almost 580 pg/cell/day (Figure 6.6).

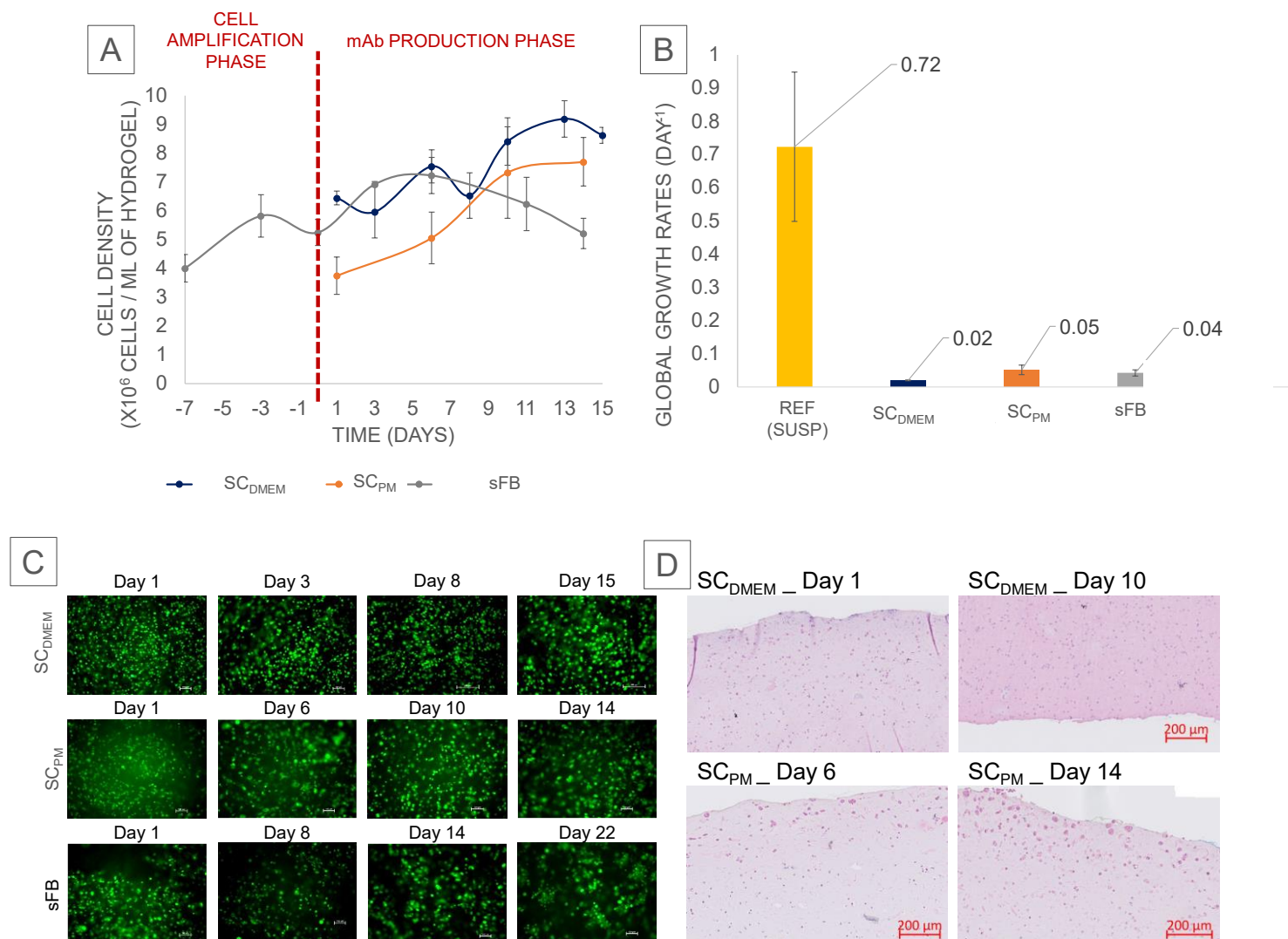


**Figure 6.5: Characterization of HEK cell proliferation in large-scale bioprinted cultures.** (A) Growth curves of the cells in 3D bioprinted culture conditions, (B) Maximal growth rate of CHO cells in the 3D bioprinted conditions compared to suspension reference culture, (C) Live cells staining in 3D constructs with calcein and (D) histological staining with Hematoxylin-Eosin (HE). (n=3)

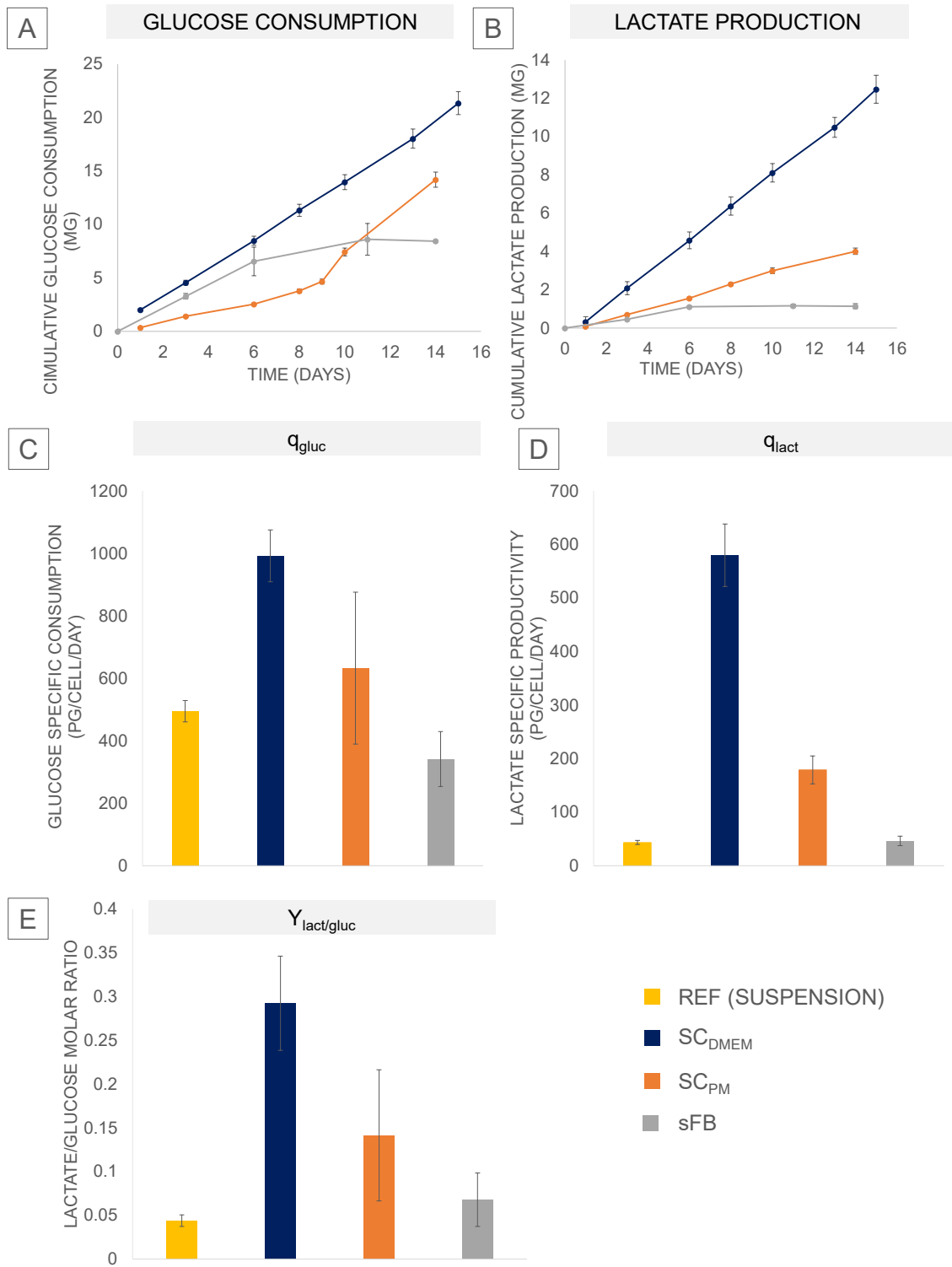


**Figure 6.6: Characterization of CHO cells metabolism in bioprinted constructs.** (A) Cumulated glucose consumption over the culture. (B) Cumulated lactate production. (C) Cell-specific glucose consumption rate. (D) Cell-specific lactate production rate. (E) Glucose to lactate molar conversion yield. (n = 3)

To assess the efficiency of cell metabolism in each condition, we calculated the lactate per glucose ratio ( $Y_{lact/gluc}$ ). In all four conditions (both bioprinted and suspension cultures), the  $Y_{lact/gluc}$  ratios remained low ( $\ll 1$ ), indicating an overall oxidative and efficient metabolism. It's important to note that high lactate concentrations can negatively affect recombinant protein

yields (above 1.8 mg/mL) and impair cell growth (above 3.6 mg/mL). Therefore, lower lactate/glucose ratios are preferable for maintaining high-quality cell cultures.

The results showed a significant increase in this ratio in both SC<sub>DMEM</sub> and SC<sub>PM</sub> bioprinted cultures compared to the suspension and sFB bioprinted cultures. It indicates a higher reliance on lactic fermentation and reduced metabolic efficiency in the SC<sub>DMEM</sub> and SC<sub>PM</sub> conditions.

We then measured IgG levels using an ELISA assay on supernatant samples. When we compared the final IgG recovery in grams and the highest titer achieved in all 3D bioprinted cultures, we found that the sFB culture displayed significantly greater productivity (3.5 fold) than the two SC conditions (see Figure 6.7). However, the productivity in the sFB culture remained substantially lower (11-fold) than that of the reference suspension culture, achieving only 142 mg/L of mAbs (Figure 6.7). The main reason for the variance in the final titer of bioprinted cultures compared to the reference was the considerably reduced cell density in the 3D CHO cultures.

We also investigated whether some of the secreted antibodies were trapped in the hydrogel of bioprinted cultures. To do this, we first qualitatively observed antibody retention in the hydrogel. We used FITC-conjugated anti-human IgG antibodies for immunostaining on histological sections of the constructs and DAPI to stain cell nuclei. The images showed the presence of IgG in the hydrogel, mainly in the vicinity of cells, indicating that some product was retained within the constructs (see Figure 6.8).

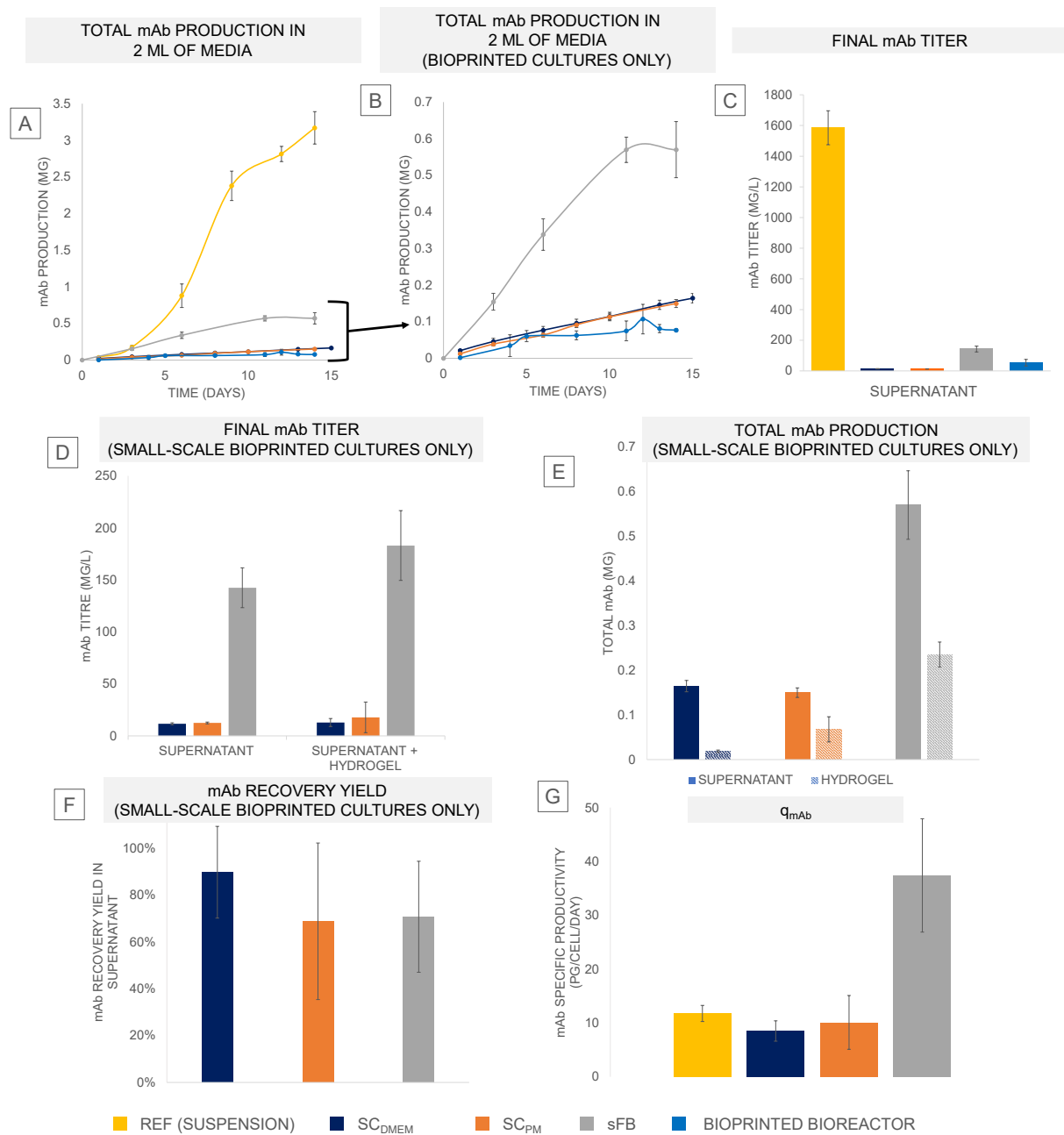


**Figure 6.7: Antibody production from bioprinted cultures of CHO cells.** (A) Evolution of total mAb production per bioprinted culture of  $0.2 \text{ cm}^3$ , (B) Final mAb titer in supernatant of bioprinted cultures vs suspension reference, (C) Final mAb titer in supernatant of bioprinted cultures vs in supernatant + hydrogel of bioprinted cultures, (D) Total amount of mAb recovered in supernatant (dark bars) vs in hydrogel (light bars) at the end of a 14 days culture, (E) Fraction of total mAb quantity recovered in culture supernatant of bioprinted cultures, and (F) IgG specific productivity in bioprinted cultures vs suspension reference. All analysis were performed with  $n=3$ .



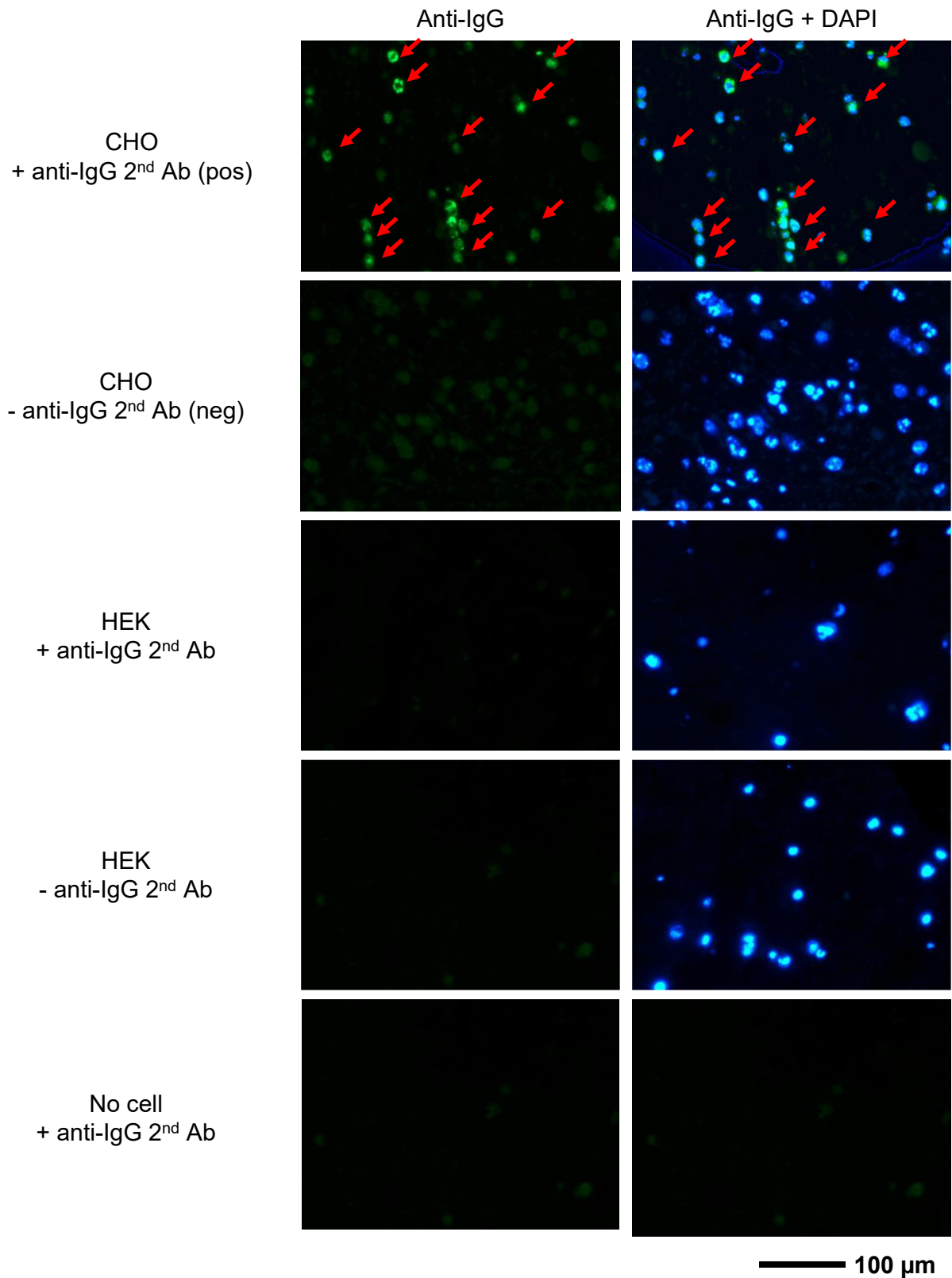


**Figure 6.8: Immunostaining (green) of mAb entrapped in the hydrogel in CHO cells bioprinted construct (first row), cell nuclei were stained with DAPI (blue). A construct containing CHO cells but not stained with the anti-IgG fluorescent antibody was used as a negative control. Constructs containing non-IgG-producing HEK cells and hydrogels without cells were used to validate the absence of fluorescent interference or unspecific binding.**

Then, to quantify the product retained in the hydrogel, we dissociated the bioprinted constructs after a 14-day culture and then centrifuged the mixture to remove the cells. We analyzed the recovered supernatant, including the enzymatic cocktail from the dissociation solution and dissolved hydrogel, using an ELISA assay for mAb quantification. It was estimated that between 10% and 30% of the total IgG production was trapped in the hydrogel, with higher retention observed in cultures with CHO-specific media (see Figure 6.7\_F).

In an attempt to enhance antibody recovery, a strategy was employed involving different washing procedures for the hydrogel slabs. The hydrogels were subjected to cleaning with standard buffers typically used for antibody purification elution, including glycine 0.1M at pH 2.7 and sodium citrate 0.1M at pH 3. The process involved slicing three slabs into smaller pieces and allowing them to soak in each of the respective buffers at room temperature for approximately half an hour. After this soaking step, the liquid above the slabs (supernatant) was carefully transferred to a centrifuge membrane and subjected to centrifugation. Subsequently, the concentrated materials (retentates) were incubated in a phosphate-buffered saline (PBS) solution before luminescence-based ELISA analysis. Unfortunately, neither of the buffers (glycine or sodium citrate) resulted in successful antibody recovery.

The research findings demonstrate that most monoclonal antibodies (mAbs) are released into the culture medium (Figure 6.7\_E&F). Nevertheless, some antibodies are trapped within the hydrogel, prompting further exploration into the factors governing this retention. Our results suggest that the retention of IgG is affected by either the particular culture medium employed or the micro-structural composition of the hydrogel due to the consolidation.

Interestingly, we observed that IgG retention was more pronounced in hydrogels with lighter consolidation. This observation is somewhat counterintuitive, especially considering that these hydrogels were demonstrated to have superior microporosity in Chapter 4. As a result, we speculate that the retention of IgG in the hydrogel may be due to an affinity between the antibody and specific components of the hydrogel. However, it's essential to note that our literature review couldn't validate this hypothesis, as the target of this antibody (kept confidential) is not known to present similarity with compounds of the hydrogel. Furthermore, varying consolidation methods can impact the ultimate composition of the hydrogel, which may affect how antibodies interact with the matrix.

The culture media's composition may also influence Mabs affinity. For instance, the supplementation of DMEM(+) cultures is suspected to alter IgG interaction with the components of the matrix. These changes can manifest through non-destructive interactions

with either the matrix or the IgG, or by modifying the functionality of the IgG itself due to the presence of proteases.

Regarding cell-specific productivity, the reference suspension culture and the SC bioprinted cultures had similar rates, around 10 pg/cell/day, which is relatively low compared to industrial standards. In standard CHO DG44 fed-batch processes, achieving a productivity rate of approximately 15 - 25 pg/cell/day is generally considered a good outcome. Some studies have reported higher specific productivity values, ranging from 20 - 40 pg/cell/day, but these are typically associated with highly intensified processes, including production enhancers or perfusion processes [37,147,643]. It's important to note that specific productivity values exceeding 40 pg/cell/day are rare and challenging to attain [99]. Such remarkable achievements usually require extensive optimization, the implementation of complex bioprocess strategies, and significant genetic engineering of the cells. However, the sFB bioprinted culture outperformed the other conditions, achieving a specific productivity of about 37 pg/cell/day, surpassing the reference suspension culture. It suggests that the bioprinted culture can achieve specific-productivity levels like highly optimized suspension fed-batch cultures even under non-optimal conditions. Such results need to be consolidated by repetition of this set of experiments. Additionally, we should keep in mind that the analytical tools for cell quantification from 3D bioprinted cultures lack precision and reproducibility, as demonstrated in Chapter 3. Therefore, the accuracy of cell quantification can greatly affect the calculated cell-specific rates.

In conclusion, our study demonstrated that 3D bioprinted CHO cell cultures can be sustained in serum-free media suitable for GMP production and achieve impressive cell-specific productivity. However, the productivity remains lower due to limited cell proliferation and low cell density. Optimizing culture parameters is essential to increase specific productivity further, and this is best achieved in bioreactor cultures, which provide precise control, scalability, and compliance with industrial and GMP standards.

### 6.2.3. *Monoclonal antibody production from large bioprinted constructs in bioreactor*

After successfully validating our bioreactor setup for large bioprinted cellularized constructs with HEK cells and establishing a reference run with suspended CHO cells, we aimed to assess

the feasibility of monoclonal antibody (mAb) production with CHO cells from bioprinted hydrogel structures using our bioreactor setup. To enhance reproducibility and scalability, we transitioned from our in-house bioreactor to a commercial system, the Ambr®250.

The transition involved multiple runs to adapt the setup, fine-tune the culture parameters, and identify the optimal settings using Proportional-Integral-Derivative (PID) control for stable regulation (as detailed in Chapter 5). After this preparation, a final run was conducted with a porous bioprinted construct measuring 2 x 2 x 2 cm and containing  $10 \times 10^6$  CHO cells per mL of bioink (eq. to  $\sim 0.2 \times 10^6$  cell/mL of culture media). This run spanned 14 days and maintained sterility and culture parameter regulations. Initially planned as a fed-batch, the culture was a batch-mode operation because the glucose concentration remained consistently above 4 g/L and did not require additional feeding (see Figure 6.9\_B).

No consumption of lactate was observed in this large bioreactor culture and the previous small-scale bioprinted conditions. Both glucose consumption and lactate production were slow, with less than 2 g/L of glucose consumed and lactate concentration remaining below 2g/L over the whole culture process (see Figure 6.9\_B). Unfortunately, due to the inability to non-destructively monitor cell density during the culture, specific consumption or production rates could not be calculated.

The mAb production was measured in the culture supernatant using ELISA assay, and the maximal titer reached approximately 54 mg/L. This titer was equivalent to that achieved in both SC<sub>DMEM</sub> and SC<sub>PM</sub> small-scale cultures but significantly lower than what was obtained in the suspension bioreactor and the sFB small-scale culture as shown in Figure 6.7 (A, B & C) and Figure 6.9 (B & C). The volumetric productivity was decreased compared to the sFB small-scale culture, which is assumed to be less optimal. This decreased productivity can be attributed to two main factors:

1. The starting cell concentration per mL of culture medium was lower in the bioreactor culture (approximately  $0.2 \times 10^6$  cell/mL) compared to the small-scale cultures (about  $1.0 \times 10^6$  cell/mL).
2. The bioreactor culture was conducted directly after bioprinting in Production Media (PM) for 14 days, without an amplification phase in the construct. In contrast, the sFB small-scale culture involved a 7-day amplification in Stock and Adaptation Media (SAM) within the bioprinted construct, followed by 14 days of production in PM. It corresponds to a total of 21 days of continuous culture.

Hence, higher cell seeding density per volume of media and a longer culture time with cell amplification within the construct appear to be beneficial for improving IgG production. To compare large-scale and small-scale cultures, we calculated IgG production per unit of hydrogel volume. The small-scale sFB culture yielded 0.6 mg of IgG per 0.2 cm<sup>3</sup> of hydrogel, resulting in a 3 mg/cm<sup>3</sup> productivity. In the large bioreactor culture, around 54 mg/L of IgG was produced in a 200 mL medium, equating to roughly 2.8 mg/cm<sup>3</sup> in a total hydrogel volume of 3.9 cm<sup>3</sup>. Therefore, the productivity per unit of hydrogel volume was similar between the large CHO construct in the bioreactor culture and the small-scale sFB culture.

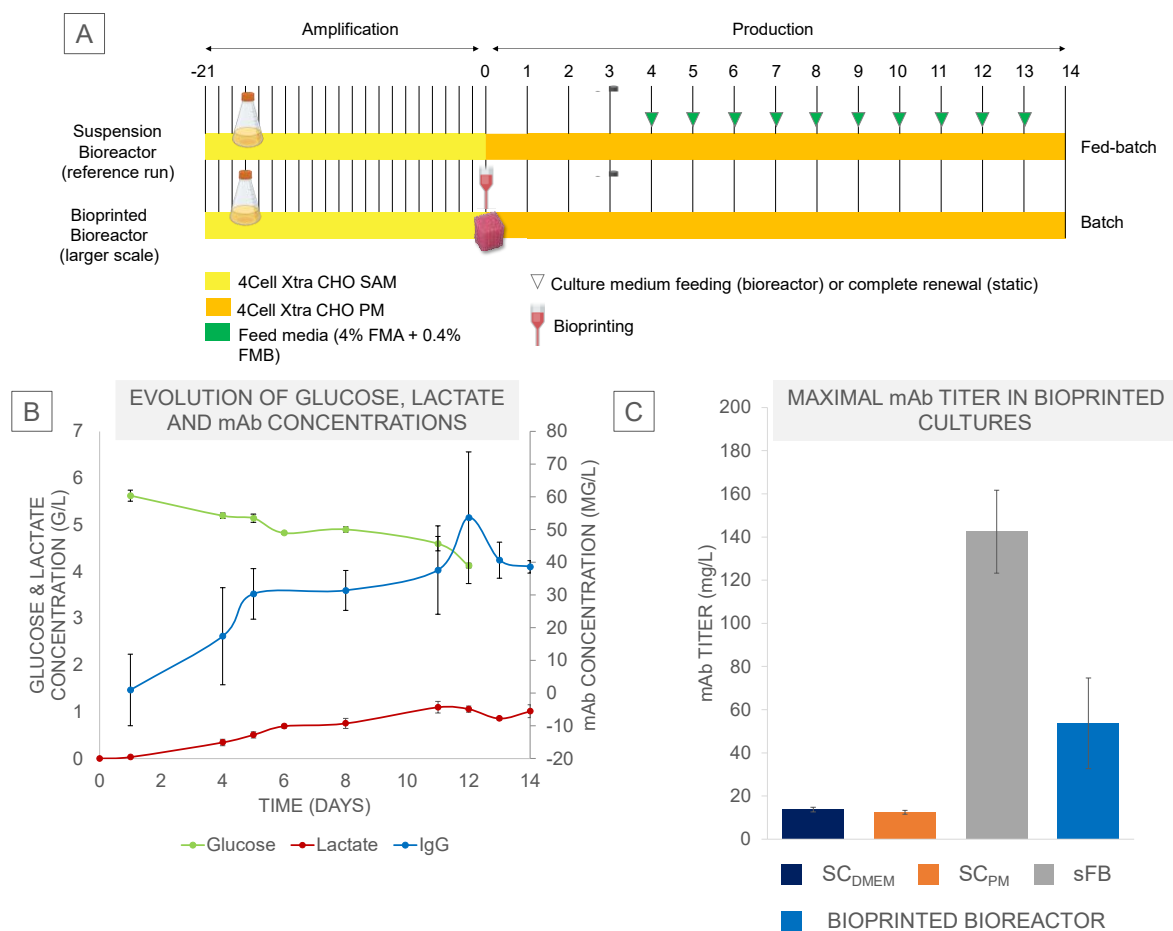


**Figure 6.9: Culture conditions and productivity of large bioprinted CHO cells culture in bioreactor.** (A) Bioreactor culture of reference suspension run and large bioprinted construct in Ambr®250. Evolution of (B) Evolution of glucose, lactate and mAb concentrations and (C) IgG titer in bioprinted cultures of CHO cells in small-scale (incubator) and in large bioprinted construct cultivated in adapted Ambr®250 bioreactor.

### 6.3. Conclusion

In conclusion, this work emphasizes bioreactor culture's potential in advancing large 3D cell culture and monoclonal antibody production. The lack of analytical tools for monitoring cell

density evolution during bioprinted construct culture in a bioreactor prevented the precise evaluation of the cell-specific parameters. However, our discoveries offer essential guidance for improving culture conditions, increasing specific productivity, and leading us toward more efficient and scalable bioproduction processes. These implications go beyond research and hold the potential for significant advancements in industrial and Good Manufacturing Practice (GMP) production of biological products.

## CHAPTER 7. IN SITU TRANSFECTION

In the previous chapters, we presented our work to characterize and optimize cell proliferation in the 3D constructs, scale-up the cultures and develop a 3D-bioprinted-construct-based bioproduction process. We also demonstrated the feasibility of biomolecule production from stably transfected cell lines embedded in 3D bioprinted constructs. Such results make one wonder if bioprinted cell cultures could be suitable for bioproduction based on transiently transfected cells.

Indeed, transiently transfected cells present some advantages for bioproduction, such as the elimination of long and tedious development of stably transfected clones possessing a gene encoding for the protein of interest. Additionally, this technique would enable the use of the same cell line in various production processes to produce different proteins, by mixing the bioink with the desired plasmids without the need for previous development of cell clones. Therefore, we wanted to evaluate the feasibility of transient transfection and gene expression in bioprinted constructs.

To push further our innovative bioproduction model, *in situ* 3D transient cell transfection was evaluated as a potential interesting tool for recombinant protein bioproduction. *In situ* transfection, as described in our literature review in Chapter 1, allows for cell transfection within a 3D matrix. We were most interested in encapsulating the transfecting nucleic acids inside the hydrogels (gene-activated matrices - GAM). Such strategy would allow us to observe a prolonged cell expression, as cells proliferating inside such GAM will get progressively transfected when entering contact with the genetic material [352]. It would ensure progressive and continuous transient transfection of the proliferating cells throughout the culture process.

Therefore, this chapter explored the possibility of on-site cell transfection within our bioprinted constructs. Once more, several dedicated protocols had to be created, including the preparation and optimization of the transforming bioink, the transfectant stability within the bioprinted matrix, and its disponibility and uptake by the growing seeded cells. This investigation allowed to identify several challenges that will need further investigations and alleviate if 3D cellularized structure is transformed in-situ.

### 7.1. Stability of transfecting plasmids in the bioink

In our study, the chosen transforming nucleic acid was a double-stranded DNA plasmid expressing fluorescent marker genes (Green Fluorescent Protein, GFP and mCherry protein). These models were chosen to track their expression in the 3D structures easily.

**Table 7.1: Evaluation of dsDNA stability in bioprinted constructs.** The different conditions evaluated, Sample\_(+) indicate the presence of plasmids in the sample and Sample\_(-) are plasmid free. The “+” and “-“ in the table indicate respectively the presence or absence of observed parameters. Measured and expected plasmid concentration are displayed for the different sampled assayed with Qubit® kit.

Sample	Bioink / hydrogel	Consolidation	Initial plasmid concentration (µg/mL)	Time of culture (days)	3% Collagenase in assayed solution	dilution of sample solution	Plasmid concentration measured with Qubit assay kit (µg/mL)	Expected concentration in the sample volume (ng/µL)
Supernatant	-	-	?	5	-	1	1.58	≤ 0.4
Hydrogel_(+)	+	+	4	7	+	1/5	9.33 ± 0.23	≤ 0.8
Hydrogel_(-)	+	+	0	7	+	1/5	9.64	0
Bioink_(+)	+	-	4	0	-	1/5	1.12	0.8
Bioink_(-)	+	-	0	0	-	1/5	0.642	0
ColA_(+)	-	-	10	0	+	1	16.4	10
ColA_(-)	-	-	0	0	+	1	14	0



First, such plasmids' long-term stability inside the hydrogel had to be evaluated to propose a GAM that would allow cells to transfect as they proliferate inside the hydrogel progressively. Indeed, as described in Chapter 4, our fast cell proliferation commonly started on day 7 to 10 and lasted for up to 13 days. Thus, plasmids must remain inside the material for the whole culture duration. We explored two methods to qualify the stability of our plasmid load over time in consolidated hydrogels.

#### 7.1.1. *DNA quantification on hydrogel consolidated samples*

The first strategy was to use a standard DNA quantification kit, Qubit<sup>®</sup> dsDNA BR Assay Kit, based on detecting fluorescent dyes, specifically tagging double brand DNA. The detection and quantification of fluorescence is performed with a dedicated apparatus, the Qubit fluorometer, in a range of DNA concentration from 0.2  $\mu\text{g/mL}$  to 2000  $\mu\text{g/mL}$ . A standard curve was prepared with 12 points from 0.2  $\mu\text{g/mL}$  to 200  $\mu\text{g/mL}$  of plasmids in  $\text{dH}_2\text{O}$  to confirm the linearity of the measure in the range of concentration of our samples.

Bioink was formulated with GFP-encoding plasmids at a 4 $\mu\text{g/mL}$  concentration to evaluate DNA stability in the bioink. In standard HEK cell transfection in 2D and suspension cultures, plasmid cell ratios are usually reported between 0.1 to 2  $\mu\text{g}$  plasmids per  $10^6$  cells corresponding to plasmids concentrations in supernatant of 0.25 to 2  $\mu\text{g/mL}$  [180,644–648]. In these conditions, the plasmids quickly enter in contact with the cells by deposition by gravity on the anchorage surface in 2D cultures or homogenous mixing in suspended cultures. In bioprinted cultures, the plasmid concentration of 4  $\mu\text{g/mL}$  of bioink was initially chosen to overestimate the plasmid per cell ratio in bio inks seeded with  $1 \times 10^6$  cells to increase the probability of contact between cells and plasmids entrapped in the hydrogel. This choice will be explained in more detail later in paragraph 7.2.1.2.

The experiments to evaluate plasmid stability within the hydrogel were carried out without adding cells to the bioink. Bioprinted constructs of 0.2  $\text{cm}^3$  were consolidated with standard protocols (1h at 37°C with a solution of 3%  $\text{CaCl}_2$ , 4% transglutaminase and 10 U/mL Thrombin) and further incubated at 37°C with 5%  $\text{CO}_2$  for 7 days to simulate culture conditions.

Post-incubation DNA plasmids load was evaluated thanks to sample dissociation in Collagenase A 3% solution, and the dissociation supernatant was recovered for DNA quantification. The DNA plasmid release in the culture media was also estimated thanks to sampling the culture supernatant at day 5.

In the dissociation supernatant, the dissolved hydrogel was diluted to 1/5 in the collagenase solution, corresponding to a theoretical concentration of 0.8  $\mu\text{g}/\text{mL}$  if the totality of the plasmid remained in the hydrogel. Controls were prepared with dissociated hydrogel without plasmid (dilution 1/5 in collagenase A), non-consolidated bioink with 0 or 4  $\mu\text{g}/\text{mL}$  plasmids (dissolved 1/5 in PBS) and 3% Collagenase A solution with 0 or 10  $\mu\text{g}/\text{mL}$  plasmids.

The results showed that such a quantification protocol was not adapted to detecting plasmids in dissociation products nor the culture supernatant (see Table 7.1). A high concentration of Collagenase A present in dissociation supernatant and controls significantly impacted it. In such a case, the DNA concentration measured was over 10-fold higher than expected in the samples and was similar in samples with or without plasmid DNA.

The Collagenase 3%, a dark brown and turbid solution, strongly interfered with or even totally masked the fluorescence. Similarly, the phenol red and other proteins present in DMEM can emit fluorescence from the UV to the orange-red wave lengths and interfere with fluorescence analysis [649]. It may also explain the overestimation of plasmid concentration in the supernatant sample. Consequently, we conclude that the Qubit® dsDNA BR Assay Kit is not suitable for assessing plasmid stability, as it requires hydrogel dissociation with Collagenase, which, in turn, interferes with detecting labelled plasmid fluorescence.

#### 7.1.2. *Optical characterization with fluorescent labelling and microscopy*

To propose an alternative evaluation method, we performed an optical in-situ monitoring of fluorescent-labelled plasmids thanks to microscopy. The plasmids solution (1.5  $\mu\text{g}/\mu\text{L}$ ) was mixed and incubated with an 11 mM DAPI solution or a 2.5 mM Sytox orange solution at a 1 : 1 volume ratio. This step aimed to label the plasmids fluorescently with intercalant reagents. The mixture was then added to the hydrogel at a 1 : 1 volume ratio corresponding to a  $\sim 0.375$   $\mu\text{g}/\mu\text{L}$  plasmid concentration in bioink. Multiple hydrogel consolidations were compared to evaluate their impact on the plasmid stability within the hydrogel (see Figure 7.1). The variation of consolidations was demonstrated to modify the hydrogel mechanical properties and microporosity in Chapter 4. The first consolidation with 3% w/v  $\text{CaCl}_2$ , 4% w/v transglutaminase and 10 U/mL Thrombin corresponded to the strongest consolidation with Young's modulus of  $29 \pm \text{kPa}$  and  $51 \pm 4$  % microporosity. The exact mechanical properties and microporosity of the other hydrogels used in this experiment were not evaluated. Still, they correspond to consolidation without transglutaminase, which is the protocol described by the team as providing the lightest consolidation. They are expected to decrease Young's modulus and increase microporosity. In future studies, these parameters should be qualified for comprehensive analysis.

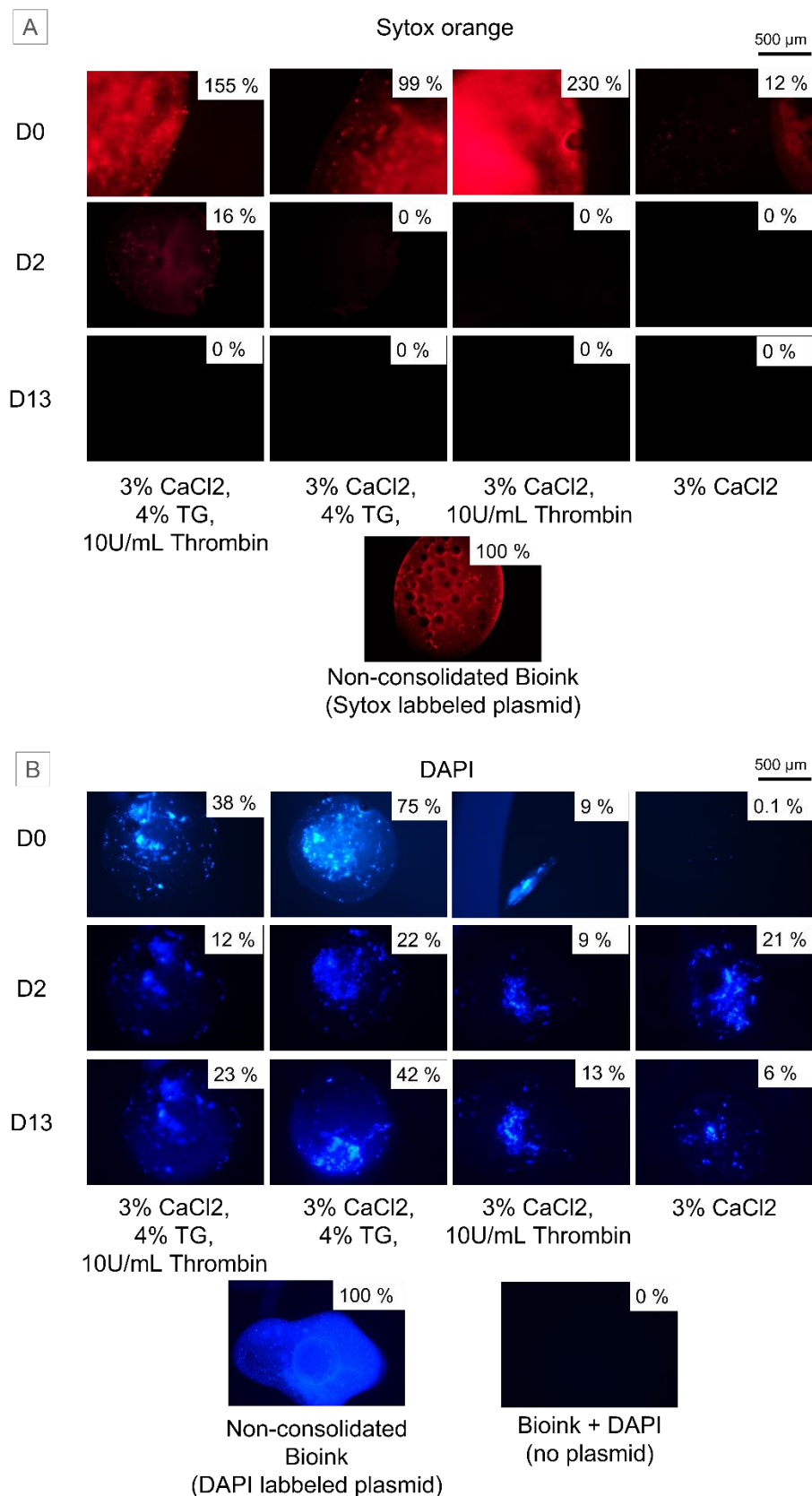


**Figure 7.1: Fluorescent microscopy imaging of labelled pDNA retained in the hydrogel.** Plasmids were labeled with Sytox orange (A) or DAPI (B) before hydrogel incorporation. After consolidation, the hydrogels were consolidated with different solutions, and images were acquired on days 0, 2, and 13. The numerical values indicated on the pictures represent the intensity of fluorescence measured by image analysis, relative to the non-consolidated bioink set as the 100% intensity. TG: transglutaminase.

The constructs were incubated at 37°C in culture media. The fluorescence intensity was observed by fluorescent microscopy at 385nm (DAPI) and 590 nm (Sytox) in the hydrogels at day 0, 1, 2 and 13. The results showed that both dyes could label the plasmids efficiently and were detected in the non-consolidated bioink and consolidated hydrogel at day 0 (see Figure 7.1). After only 2 days of culture, the fluorescence of Sytox dropped to a very low intensity, which amounted to only 0 - 16% of the initial fluorescence intensity in the non-consolidated bioink. Consequently, detecting the Sytox fluorescence exhibited poor stability and rapid bleaching became challenging. The labelling faded over time and became imperceptible within 2 days in the bioink at 37°C, as illustrated in Figure 7.1\_A.

On the contrary, DAPI dye displayed intense fluorescence and was still easily detected in all conditions after 13 days of incubation in culture media at 37°C. Hydrogels consolidated with transglutaminase exhibited higher fluorescence intensity than those consolidated without transglutaminase (see Figure 7.1\_B). The highest intensity was observed in hydrogels consolidated with CaCl<sub>2</sub> and transglutaminase without Thrombin. Hence, it is likely that gelatin polymerization contributes to increased plasmid retention.

Without plasmid, a control mixture with bioink and DAPI solution confirmed that DAPI alone did not remain in the hydrogel and was not detected by fluorescent microscopy from day 0. These results demonstrated that plasmids could persist in the bioink for extended durations. However, the exact percentage of plasmid remaining from the initial concentration is not precisely quantifiable because the measurement of fluorescence intensity is limited to a specific location and cannot be directly correlated with the plasmid concentration using the available data.

An enhancement for this technique could involve constructing a standard curve using bioinks prepared with different, known plasmid concentrations. However, it's important to note that even if fluorescence is measured at day 0, there's no certainty that no plasmids are lost during the consolidation process. Additionally, the distribution of plasmids appears to be uneven, forming aggregates that manifest as intense fluorescent zones in the images (as seen in Figure 7.1). Moreover, the intensity of fluorescence measured may be influenced by variations in construct thickness, which could introduce background fluorescence from the deeper hydrogel layers. Consequently, fluorescence measurements may lack the precision needed to quantify the remaining plasmids in the bioink accurately.

## 7.2. Development and optimization of in-situ transfection methods

### 7.2.1. *In situ transfection methods adapted from 2D protocols*

## Validation of plasmids functionality

In-situ 3D transfection protocols were developed with plasmid models carrying fluorescent reporter genes. This strategy allows us to easily observe the transfection efficiency with microscopic observation of the 3D construct. Here, two plasmids were evaluated in this study; one was the pEGFP-C1 plasmid encoding for the enhanced Green Fluorescent Protein (eGFP or GFP), and the second was encoding for the mCherry (red fluorescent) protein (See Figure 2.6, Chapter 2).

Plasmids production, extraction and qualification (validation of size and purity) were performed as described in Chapter 2 section 2.4.1. Then, their functionality was evaluated in standard 2D transfection protocols.

First, we evaluate the ability of HEK cells to spontaneously incorporate a naked plasmid (not complexed with transfection reagent). 2D transfection protocol was performed with both naked plasmids. The flow cytometry analysis showed no cell transfected, demonstrating the absence of spontaneous uptake of naked plasmids (see Figure 7.2).

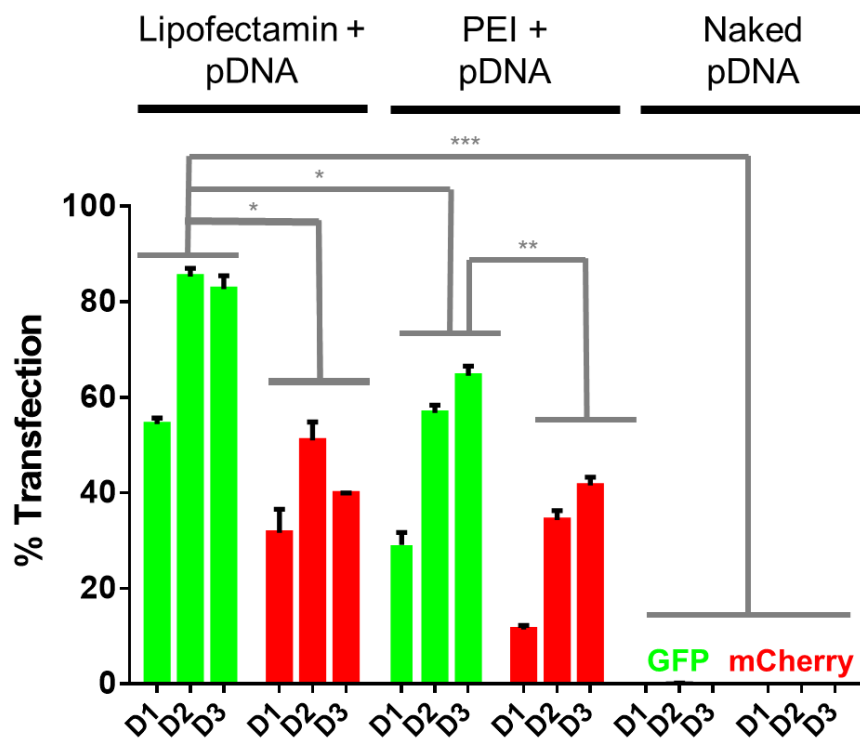


*Figure 7.2: Transfection efficiency in 2D cultures of HEK cells assessed via measurement of transgene expression (GFP or mCherry fluorescent proteins) by flow cytometry.*

Then, the plasmids were complexed with transfection reagents and deposited over 2D cell cultures of HEK cells with ~70% confluency. Two different transfection reagents, Lipofectamine 3000 (ratio 1 : 2 : 2 -  $\mu\text{g}$  ADN :  $\mu\text{L}$  P3000 :  $\mu\text{L}$  Lipofectamine 3000) and PEI

(ratio 1 : 5 -  $\mu\text{g DNA} : \mu\text{g PEI}$ ), were evaluated in 2D cultures. The plasmid to Lipofectamin 3000 ratio was chosen based on the manufacturer's recommendations. The ratio of plasmid-to-PEI was determined based on some literature reports. Some papers reported a high transfection rate of HEK cells with elevated ratios of 1 : 6 to 1 : 10 ( $\mu\text{g pDNA} : \mu\text{g PEI}$ ) [645,650]. However, it's worth noting that other studies have linked cytotoxic effects to PEI at ratios exceeding 1:5 [651,652]. As a result, we opted to establish the maximum value for the ratio at 1:5.

The transfection efficiency was assessed after cell recovery with trypsinization by detecting the percentage of fluorescent cells in the whole population by flow cytometry. The highest transfection level was achieved when cells were transfected with pEGFP-C1 plasmid complexed with Lipofectamin (see Figure 7.2). In this condition, the maximal transfection yield was measured 2-3 days post-transfection, reaching over 80% of cells transfected. PEI demonstrated higher cytotoxicity as microscopic observation of the 2D cell cultures revealed more detached dead cells. This cytotoxicity might be due to the elevated ratio of 1 : 5 ( $\mu\text{g DNA} : \mu\text{g PEI}$ ) which is sometimes reported as the limit for PEI cytotoxicity [651,652].

Both pEGFP-C1 plasmid and pmCherry-C1 have the same size of  $\sim 4.7$  kb. Therefore, the different transfection efficiency measured for both plasmids cannot be attributed to a size hindrance limiting plasmid internalization. It is thus probable that, in HEK cells, the GFP expression is more favourable or efficient than that of mCherry protein. Therefore, for the following experiments, the pEGFP-C1 was selected.

After validating the functionality of the plasmids, we evaluated different *in situ* transfection strategies based on the use of plasmids complexed with commercial reagents (PEI and Lipofectamin) incorporated in the bioink, or plasmids complexed directly with cationic hydrogels. Later, it was necessary to synthesize the cationic materials used to prepare the charged bioink complexed with naked plasmids, designated as Gene-Activated Matrix (GAM). The synthesis of cationic compounds will be detailed in the following paragraphs.

### 7.2.2. *Synthesis and qualification of cationic materials for the preparation of charged bioink as GAM for in-situ transfection*

#### **Synthesis of cationic bioink compounds**

As observed in some literature studies, cationic hydrogels could be an alternative strategy to enhance the transfection in 3D [496,498,548,653,654]. Indeed, such hydrogels possess cationic groups that can act like transfection reagents by retaining the negatively charged nucleic acids

and favour cell membrane penetration. This approach is an elegant strategy to generate a gene-activated bioink while avoiding transfection additives.

Thus, we first developed a protocol to modify gelatin or alginate bioink components into charged hydrogels by covalently binding with positively charged amino groups. The synthesis of cationized gelatin and alginate was adapted from literature [546–548]. The reaction consisted in the activation of carboxylic groups of gelatin and alginate with 1-Ethyl-3-(3-dimethylaminopropyl)carbodiimide (EDC) followed by grafting of 1,6-diaminohexan (see Figure 2.7) .

This amino group provider was chosen since its use for the synthesis of DNA-binding complexes has already been reported [655–657].

The cationized gelatin and alginate were synthesized, dialyzed twice, and lyophilized as described in Chapter 2. The final products were weighted post-lyophilization to assess the recovery yield of synthesis.

The maximal recovery mass was calculated thanks to the equations presented in Chapter 2. In each case, the product mass recovered was twice higher than the theoretical maximal recovery (see Table 7.2).

**Table 7.2: Mass balance of preparation reactions of cationized gelatin and alginate.** Theoretical and measured product mass recovered after synthesis of the cationic compound regarding the initial gelatin or alginate mass. EDC: 1-Ethyl-3-(3-dimethylaminopropyl)carbodiimide ; DH : 1,6-Diaminohexane ; SG : Standard gelatin ; SA : Standard alginate.

	Initial EDC mass (g)	Initial DH mass (g)	Initial SG / SA mass (g)	Theoretical max product mass (g)	Product mass recovery (g)
Gelatin	2.16	13.14	3.9	4.2	8.9
Alginate	2.5	1.5	0.5	0.8	1.9

Such results demonstrate our synthesis product, even after dialysis, was not pure. This is why further characterization was performed to evaluate the fraction and origin of the contaminants before biological testing. Additional dialysis steps could have been replicated to reach higher purity levels.

## **NMR qualification of the synthesized products**

Synthesized cationized gelatin and alginate were analysed thanks to proton NMR. The samples were prepared by dissolution of at least 50 mg/mL in deuterium oxide (D<sub>2</sub>O). Reference NMR spectra were acquired from the cationization reaction, namely pure gelatin, alginate, 1,6-diaminohexane, EDC and MES buffer in the case of cationic alginate.

In the NMR spectrum of synthesized cationic gelatin, the characteristic peaks identified in the standard gelatin spectrum were visible (Figure 7.3). A thin peak at ~2.8 ppm could correspond to the -CH<sub>2</sub> further from the gelatin molecule, corresponding to the peak observed around 2.6 ppm in the spectra of the pure product (peak “a” in Figure 7.3\_A). It would be concordant since the protons far from large complex molecules tend to form more elongated peaks. The shift from 2.6 to 2.8 ppm could be explained by a change in pH due to the grafting reaction with the carboxylic gelatin group. We cannot assert that the peak observed at 2.8 ppm on the cationic gelatin corresponds to grafted diaminohexane. The presence of a triplet at ~1 ppm demonstrated the presence of residual EDC. Nevertheless, the spectra could not confirm the correct grafting of diaminohexane. Therefore, this result shows that the gelatin used for the synthesis was recovered in the end, but it is impossible to validate the correct grafting from these spectra.

In the case of cationic alginate (Figure 7.3\_B), a few peaks of low amplitude corresponding to residual EDC and MES buffer were identified at around 1 ppm, 3.1 ppm, 3.3 ppm, and 3.5 ppm. A peak at 2.8 ppm similar to the one observed in cationic gelatin was also observed in the spectrum of cationic alginate. However, the characteristic peaks in the standard alginate reference spectrum were not discernable in the spectrum of cationic alginate.

Hence, the spectrum acquired from synthesized cationic alginate could not confirm the presence of alginate nor correct grafting of diaminohexane in the recovered product.



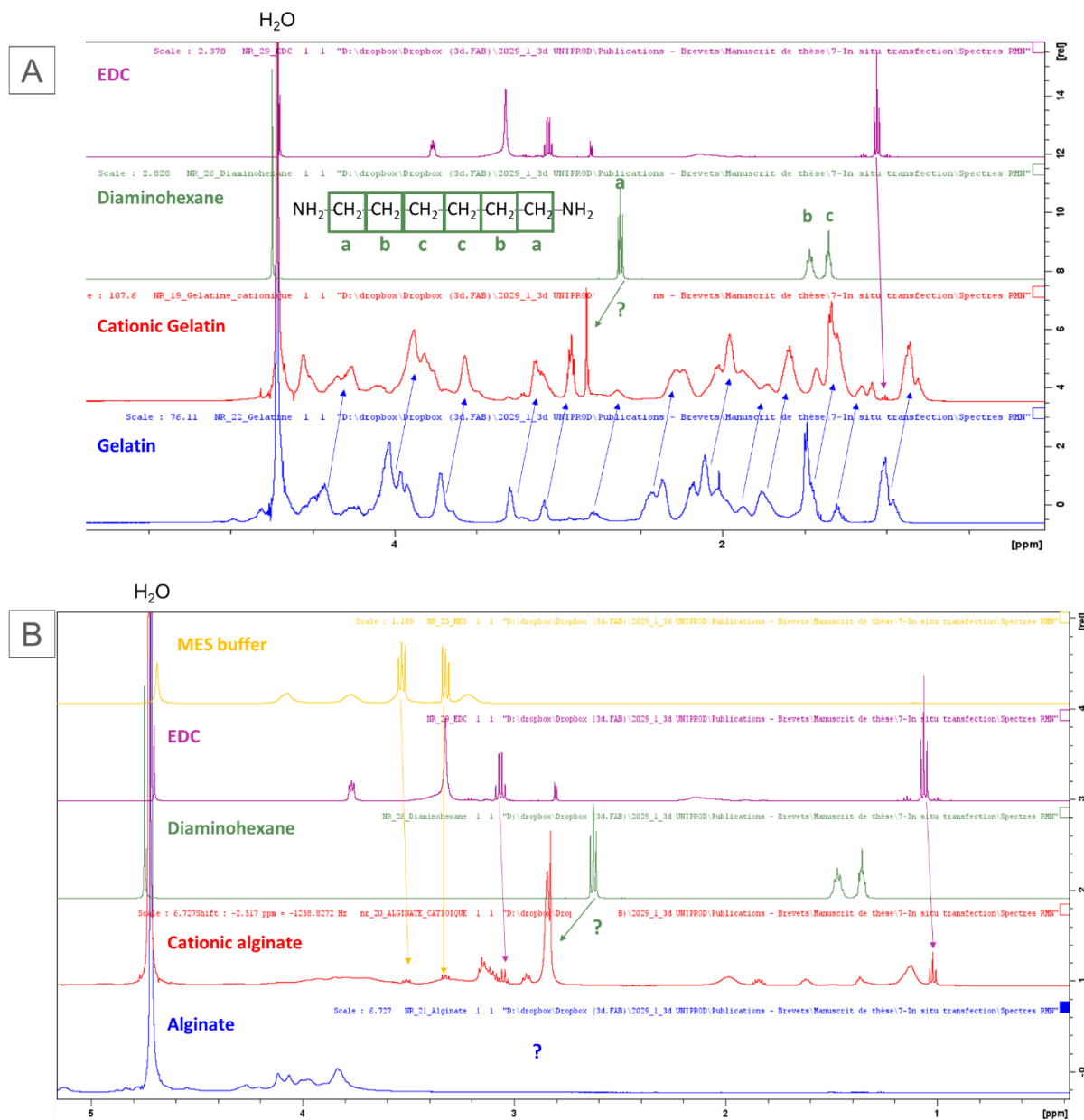


**Figure 7.3: Cationic compounds qualification with  $^1\text{H-NMR}$ .** (A) Comparison of  $^1\text{H-NMR}$  spectra of EDC, diaminohexane, cationic gelatin and standard gelatin. In the spectrum of diaminohexane, the letters over the peaks indicate the corresponding  $-\text{CH}_2$  group of the molecule (B) Comparison of  $^1\text{H-NMR}$  spectra of MES buffer, EDC, diaminohexane, cationic alginate and standard alginate.

$^1\text{H-NMR}$  analysis allowed us to validate the presence of gelatin in synthesized cationic gelatin. The unidentified peak at 2.8 ppm observable in both cationic compound spectra could correspond to a grafted diaminohexane molecule. Still, it cannot be stated with certainty since other contaminants could also be responsible for this peak. Finally, the spectra acquired from cationic alginate did not allow for validating the composition of the synthesized product. Therefore, only the synthesized gelatin was used in the following experiments.

## Formulation and characterization of a cationic bioink

In this step, only the cationic gelatin was used to generate a bioink adapted for in situ transfection, as the quality of synthesized alginate could not be confirmed with NMR. Bioink preparation with cationic gelatin was performed according to the standard formulation protocols. Namely, the cationic gelatin was dissolved at a 20%<sub>w/v</sub> concentration in DMEM(-) with 5X Penicillin-Streptomycin and Amphotericin B and mixed with the two other bioink components to reach a 2%<sub>w/v</sub> Fibrinogen, 2%<sub>w/v</sub> Alginate and 5%<sub>w/v</sub> cationized Gelatin.

Rheological characterization confirmed that this new bioink had appropriated rheology and shear-thinning behaviour to be bioprinted. The rheology was measured with a stress-controlled rotational rheometer (DHR2, TA Instruments, Guyancourt, France) and a 25 mm parallel plate. A comparative analysis of rheological properties was conducted on standard and cationic bioink. Both reveal a shear thinning behaviour where viscosity decreases as the shear rate increases. This characteristic is vital for protecting cells against shear stress during bioprinting [271]. Such a feature is also confirmed by the rate index of both bioinks calculated with the Herschel-Bulkley model (Figure 7.4\_A). The rate index values of 0.62 and 0.94 reported in this study allow to evaluate the flow index (n). This index is calculated as 1- rate index. Values of n less than 1 signify that the material has a shear-thinning behaviour (more fluidic under increasing shear stress). Conversely, n greater than 1 values indicate shear-thickening behavior, wherein the bioink becomes stiffer under increasing shear stress [658]. Therefore, in our case, both bioinks exhibited shear thinning behaviours with n values of 0.38 (standard bioink) and 0.06 (cationic bioink).

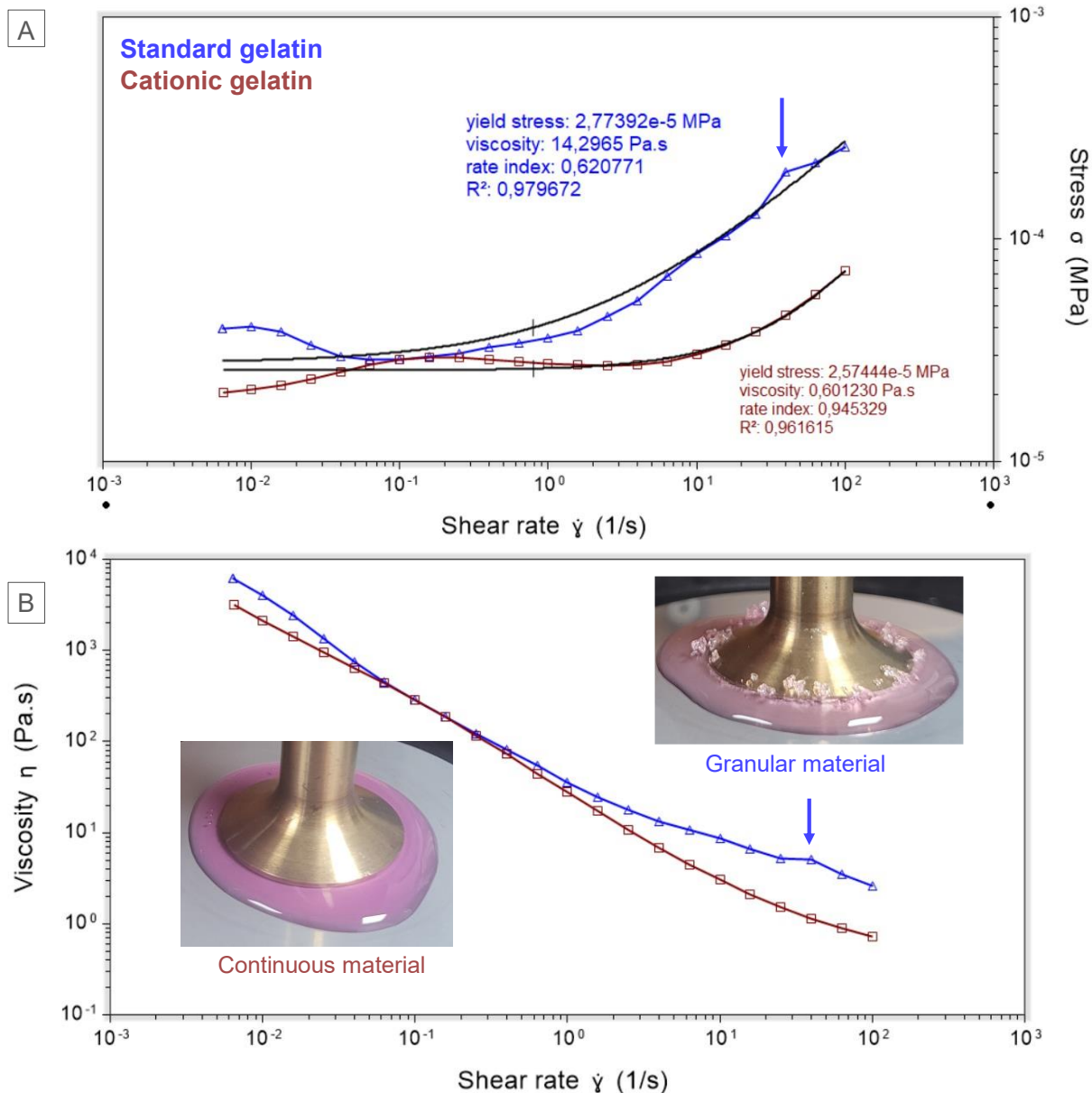


**Figure 7.4: Rheograms of non-consolidated bioinks (2% F, 2% A, 5% G) prepared with standard or cationic gelatin (A) Evolution of shear stress in function of shear rate. (B) Evolution of bioink viscosity in function of shear rate.**

The main difference between both bioinks resides in the minimal viscosity achieved at the highest shear rate of  $10^2 \text{ s}^{-1}$  in both cases. At this elevated shear rate, the viscosity of cationic bioink was decreased by 23-fold compared to the standard formulation with value of 0.6 Pa.s and 14 Pa.s respectively.

At low shear rate, under  $10 \text{ s}^{-1}$ , the shear stress of both bioinks is almost constant. It is characteristic of a solid-like behaviour [271]. The yield stress of the cationic bioink falls within a similar range as that of the standard bioink, measuring approximately 25 and 27 Pa,

respectively. It suggests that both bioinks would necessitate the application of pressure to enable their flow from the printing syringe.

Beyond a  $10 \text{ s}^{-1}$  shear rate, the shear stress increased for both bioinks. In the case of the cationic bioink, the shear stress continuously increased while the viscosity decreased linearly, demonstrating the material's ability to maintain its structural integrity. Conversely, the standard bioink displayed a distinct "break" phenomenon after reaching a shear rate of  $10^1 \text{ s}^{-1}$  as indicated by the blue arrows in Figure 7.4. This behaviour change suggests that the shear stress reached a level capable of irreversibly disrupting the physical network of the bioink, indicative of a viscoplastic material rupture. Following exposure to shear stress, the standard bioink exhibited a granular appearance, while the cationic bioink retained its smooth and continuous nature. Interestingly, when depositing a volume of 0.5 mL of bioink at a temperature of  $21^\circ\text{C}$  in a multiwell plate using a pipet, the standard bioink demonstrated the ability to maintain a three-dimensional structure. In contrast, the cationic bioink flowed and collapsed in a bioink "puddle".

Thus, the current formulation of cationic bioink demonstrates the ability to protect cells during bioprinting. However, its rheological behaviour differs from standard gelatin, preventing the generation of controlled 3D structures through bioprinting. Several hypotheses can be proposed to explain this disparity between the two bioinks.

Firstly, both bioinks were prepared using the same mass-to-volume ratio of stock gelatin or cationic gelatin material. However, the molecular weight of cationic gelatin is different from that of standard gelatin due to the presence of grafted diaminohexane molecules. Additionally, it has been suggested earlier that the cationic gelatin stock powder used may not be pure. Hence, the total concentration of gelatin molecules differs between the two bioinks. This disparity undoubtedly contributed to the distinct rheological behaviour observed. It played a role in the decreased viscosity and the inability to maintain a 3D shape in the cationic bioink.

Furthermore, the grafted-diaminohexane molecule may introduce stereological and charge hindrance effects, potentially modifying the molecular network of the bioink. As a result, the mechanical properties of the bioink may be altered, leading to further differences in rheological behaviour.

In summary, the observed differences in rheological behaviour between the cationic bioink and standard gelatin bioink can be attributed to factors such as variations in gelatin concentration,

impurities in the cationic gelatin stock powder, and potential alterations in the molecular network caused by the grafted-diaminohexane molecule.

### 7.2.3. *Evaluation of the different in situ transfection strategies*

#### **In situ transfection with PEI and Lipofectamine 3000**

The next step consisted of developing novel in situ transfection protocols. The first approach was to transfer protocols from existing 2D transfection protocols. PEI and lipofectamine were evaluated as bioink additives.

Thus, the pEGFP-C1 plasmids were used naked or complexed with PEI or Lipofectamin 3000. The ratios of 1:2 ( $\mu\text{g pDNA}:\mu\text{g PEI}$ ) and 1:1:1 ( $\mu\text{L Lipofectamin}:\mu\text{L P3000}:\mu\text{g pDNA}$ ) were used respectively. They were mixed in the bioink at a concentration of  $4\ \mu\text{g pDNA/mL}$  of bioink and incubated for 15 min at  $37^\circ\text{C}$ . The bioink was seeded with  $1 \times 10^6$  cell/mL of HEK cells. Such a formulation results in a  $4\ \mu\text{g pDNA} / 10^6$  cells. This concentration was initially chosen to increase the likelihood of contact between cells and plasmids embedded in the hydrogel. In fact, in 2D cultures the plasmids come into contact with the cells due to gravity, and in suspended cultures, plasmids are mixed uniformly, allowing them to interact with the cells. On the other hand, in bioprinted cultures, the plasmids are entrapped in the hydrogel, which complicates the contact with cells.

We decided to increase the plasmid-to-cell ratio by 2 to 10 fold compared to the values reported in the literature [644–648]. Still, to ensure that the chance for cells to get in contact with plasmids was close to 100%, we calculated the probability of contact. To do so, we assumed that the cells and plasmids were motionless and homogenously distributed in the hydrogel. In this condition, the likelihood for a plasmid to be in contact with a cell corresponds to the probability of finding a plasmid in a sphere of the same volume as a cell in every point of the hydrogel (see Figure 7.5).

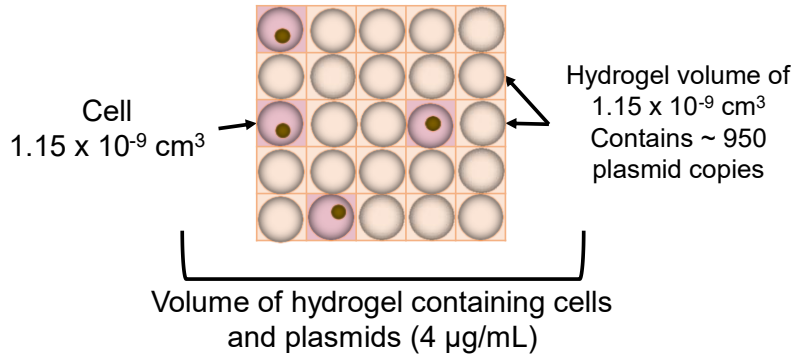


**Figure 7.5: Estimation of the probability of plasmid-cell contact.** The hydrogel volume was fractioned into sub-volumes of  $1.15 \times 10^{-9} \text{ cm}^3$  corresponding to the average volume of an HEK cell. The number of plasmid copies for a sub-volume was calculated as the theoretical number of plasmids in contact with cells.

The volume of a HEK cell was approximated to  $1,15 \times 10^{-9} \text{ cm}^3$  (sphere of  $13 \mu\text{m}$  diameter). The mass of a single pEGFP-C1 plasmid was estimated to  $2 \times 10^{-12} \mu\text{g}$  with the following formula :

$$m_p = MW_p \times C_{DA} \times C_{\mu g}$$

Where,

$m_p$  is the mass of a single pEGFP-C1 plasmid ( $\mu\text{g}$ )

$MW_p$  is the molecular mass of a pEGFP-C1 plasmid = 4731 (pb)

$C_{Da}$  is the pb to Dalton conversion coefficient =  $0.65 \times 10^3 \text{ (Da.pb}^{-1}\text{)}$

$C_{\mu g}$  is the Dalton to  $\mu\text{g}$  conversion coefficient =  $1.66 \times 10^{-18} \text{ (}\mu\text{g.Da}^{-1}\text{)}$

The average number of plasmids in a bioink containing  $4 \mu\text{g/mL}$  of plasmids in a volume of  $1,15 \times 10^{-9} \text{ cm}^3$  would be  $\sim 950$  plasmids. Hence, in this bioink, each cell could theoretically get in contact with  $\sim 950$  plasmids. We considered this value satisfactory since it has been reported that successfully transfected cells usually comprise  $10^2$  to  $5.10^4$  plasmid copies per nucleus [180,659].

The bioprinted constructs were consolidated with  $3 \%_{w/v} \text{ CaCl}_2$ ,  $4 \%_{w/v}$  transglutaminase and  $10 \text{ U/mL}$  thrombin and cultured in DMEM(+) for 15 days. This consolidation was selected from the experiments in paragraph 7.1.2 as hydrogels consolidated with  $3 \% \text{ CaCl}_2$  and  $4 \%$  transglutaminase displayed higher plasmid retention. Thrombin was also used for hydrogel consolidation, as the presence of fibrin is known to be beneficial for cell adhesion and proliferation [273].

The constructs were dissociated at days 2 and 15, and the cells were analyzed for their GFP fluorescence expression by flow cytometry. These culture times were chosen as 2 days corresponds to the highest transgene expression in 2D culture transfection (see Figure 7.2), and 15 days selected as the final point as it was identified in Chapter 4 to correspond to the start of a faster growth phase for HEK cells (Figure 4.1). The results displayed in Figure 7.6 show that none of the conditions presented GFP expression.

Hence, using naked or complexed plasmids with standard transfection reagents did not allow the transfecting of cells inside the hydrogels' 3D structures in the conditions tested. It is important to note that multiple parameters could explain the lack of efficiency of this protocol, including the low cell proliferation and the plasmid concentration. Indeed, although ideal for plasmid retention, the selected hydrogel consolidation was reported in Chapter 4 as not the optimal condition for cell proliferation. Transfection is known to be more efficient in proliferating cells [660]. In the condition presented in this chapter, a long lag phase is expected to be observed up to 15 days, as described in Chapter 4 (Figure 4.1).

Then, we estimated that cells could contact 950 plasmids per cell on average. However, imaging of DAPI labelled plasmids in hydrogel (Figure 7.1) showed that the plasmids seem to aggregate and have a heterogeneous distribution, which might decrease the probability of contact with cells. Additionally, even if cells do get in contact with 950 plasmids, it is not certain that all the plasmids will be internalized in the cell and successfully reach the nucleus. In literature, the plasmid-to-cell ratio reported in 2D or suspension cultures is usually around 0.1 to 2  $\mu\text{g}$  plasmids per  $10^6$  cells [180,644–648] corresponding to approximately  $2 \times 10^4$  to  $4 \times 10^5$  plasmid copy per cell. However, we mentioned earlier that literature reports that the number of plasmid copies per cell nucleus usually ranges from  $10^2$  to  $5 \cdot 10^4$  plasmid [180,659]. Consequently, cells do not internalize and express the entirety of plasmids they are in contact with.

To ensure that cells in bioprinted constructs come into contact with a range of  $2 \times 10^4$  to  $4 \times 10^5$  plasmid copies, the concentration of plasmids in the bioink should be in the range of  $2 \times 10^4$  to  $4 \times 10^5$  plasmids in  $1.15 \times 10^{-9} \text{ cm}^3$ , which corresponds to concentrations of 84  $\mu\text{g/mL}$  to 1700  $\mu\text{g/mL}$ . However, these concentrations are practically and economically unfeasible due to being excessively high.

Therefore, in the next experiments we increased the plasmid concentration to 10  $\mu\text{g/mL}$  of bioink, corresponding to  $\sim 2,000$  plasmid copies per cell. This concentration is comprised in the range of 6.4 to 17  $\mu\text{g/mL}$  commonly reported for the preparation of GAM [437,447,473]. We also identified the consolidation of the bioink as the parameter that should be optimized.

Finally, we investigated other transfecting agents based on cationic materials for bioink formulation.

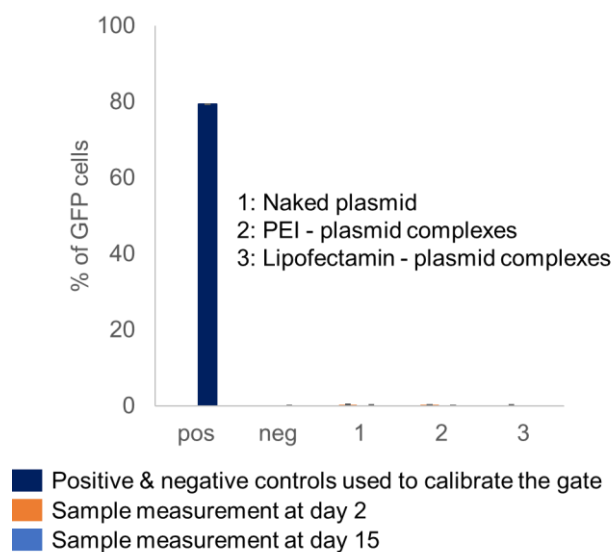


*Figure 7.6: GFP expression measured by flow cytometry of in situ transfected cells recovered by dissociation of the hydrogel.*

### **Biocompatibility and transfection capacity of cationic gelatin and cationic hydrogels**

Finally, the biocompatibility and transfection capacity of the cationic material were evaluated, first by depositing non-consolidated cationic gelatin solution mixed with pEGFP-C1 plasmids in the supernatant of 2D HEK cells cultures at ~70% confluency. Light microscopy observed the cell aspect, and viability was qualified after IP staining and fluorescent microscopy observations. Interestingly, it was observed that cells cultivated with dissolved cationic gelatin tended to detach from the plate's bottom and form cell aggregation (Figure 7.7\_A). Yet, cells stained with IP after 3 days of cultures showed high mortality in all the conditions, including those without cationic gelatin. Hence, cationic gelatin did not present enhanced cytotoxicity compared to standard PEI gelatin after 3 days of culture.

The transfection rate detected in cultures transfected with cationic gelatin was significantly higher than in control cultures transfected with standard gelatin as a reagent or naked plasmid. Yet, the transfection capacity of cationic gelatin was substantially lower than that of PEI (Figure 7.7\_A).



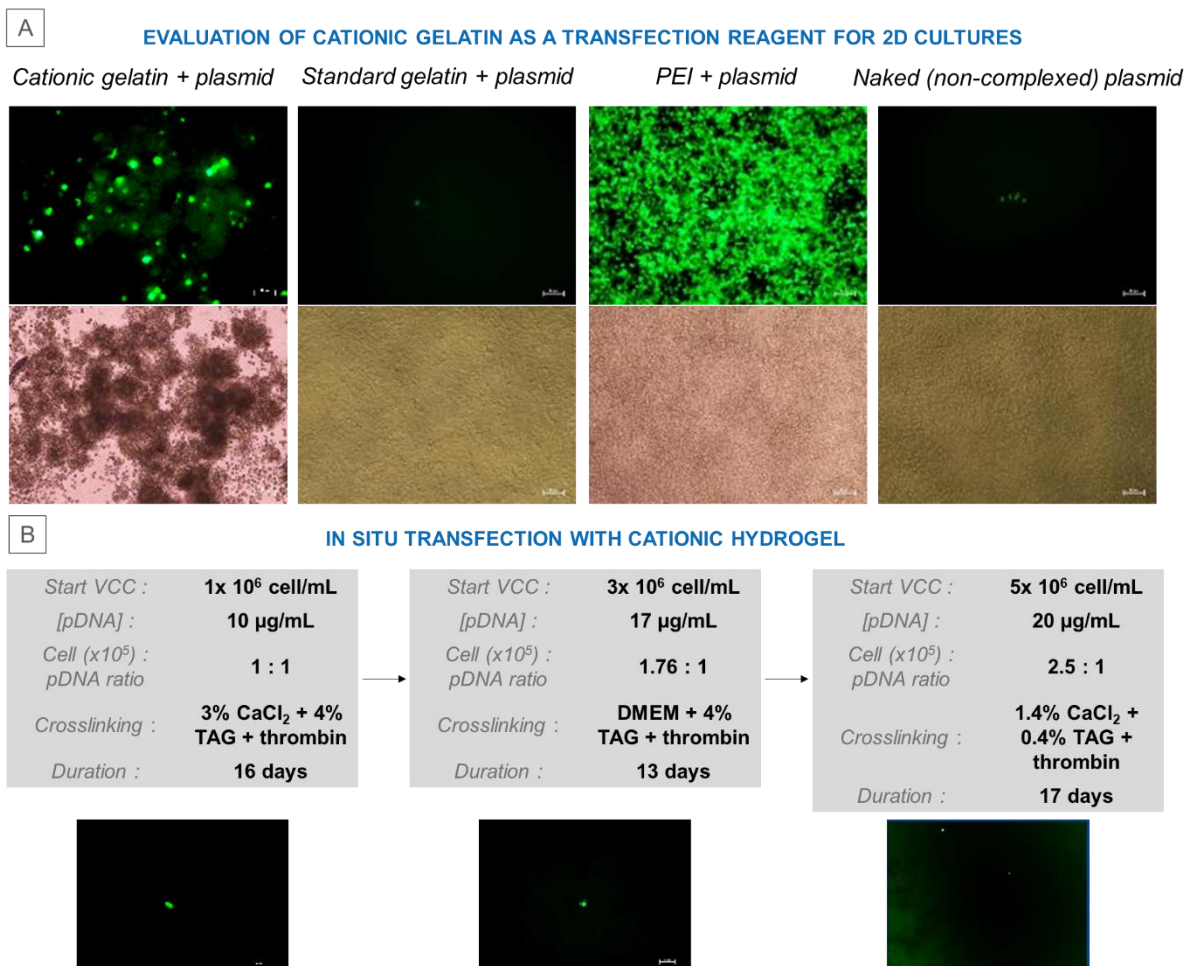


**Figure 7.7: Evaluation of cationized gelatin as a GAM and in-situ transfecting reagent:** (A) Fluorescence and bright field microscopy imaging of HEK cells' 2D cultures transfected with different pDNA-complexing agents: cationic gelatin, standard gelatin, PEI or none. More negative controls (not shown), were prepared with cationic gelatin without plasmid, standard gelatin without plasmid and no reagent & no plasmid to confirm the absence of fluorescent interference. (B) In situ transfection conditions were evaluated in cationic bioink with increasing cell density and plasmid concentration, and pictures were assessed on the last day of culture. TAG: transglutaminase.

Then, a cationic bioink was prepared with cationic gelatin previously mixed with pEGFP-C1 plasmids at 40 µg/mL, resulting in a final concentration of 10 µg/mL plasmids in the bioink. Cells were added to the bioink at 1 x 10<sup>6</sup> cells/mL. The bioink was deposited with a pipet in a 24 well-plate and consolidated with 3 %<sub>w/v</sub> CaCl<sub>2</sub>, 4%<sub>w/v</sub> transglutaminase and 10 U/mL Thrombin to conserve a hydrogel consolidation with good plasmid retention (see Figure 7.1). A reference bioink was prepared in the same conditions, except standard gelatin was used instead of cationic. Controls were prepared with standard and cationic bio-inks without plasmid or cell.

The transfection efficiency was monitored by fluorescent microscopy. The transfection efficiency was estimated to be close to zero in both cationic and standard bio-inks. Less than 5 fluorescent cells were detected by fluorescent microscopy in all triplicates combined.

At this stage, several hypotheses were proposed to explain the generalized low transfection efficiency observed in-situ :

- Lower probability of contact between cells and plasmids compared to 2D conditions due to heterogenous plasmid repartition and immobility of the plasmids in the hydrogel
- Non-growing cells are not transfected

It is why several experiments were tested as exploratory approaches to challenge these hypotheses. First, plasmid and cell concentrations were increased two and five times, respectively, to increase the probability of contact. Increasing the starting cell density was also expected to reduce the lag phase and favour earlier cell growth, as demonstrated in Chapter 4. As seen in Figure 7.7\_B, this strategy did not improve the transfection rate significantly as there were still less than 5 fluorescent cells detected by fluorescent microscopy in all triplicates combined. Various consolidation solutions were also evaluated to modulate hydrogel stiffness and microporosity, as it was demonstrated in Chapter 4 and Paragraph 7.1.2. that hydrogel consolidation affects both cell proliferation rate and plasmid retention in the hydrogel.

We conserved Fibrinogen crosslinking with Thrombin in all conditions tested to favour cell adhesion. At first, we conserved the 4% transglutaminase as we demonstrated that it was favourable to plasmid retention. We replaced the 3% CaCl<sub>2</sub> solution with DMEM(+) medium already containing 0.026% calcium. As it did not allow the detection of more than 3 fluorescent cells after 13 days of culture, we evaluated another consolidation selected in Chapter 4 as one of the most optimal for cell proliferation, with a 10-fold reduction of transglutaminase concentration and decreased calcium content to 1.4%.

Hence, increasing plasmid concentration from 4 µg/mL to 20 µg/mL, changing the transfection strategy by using cationic bioink and modifying the hydrogel consolidation did not allow to rise the transfection efficiency.

### 7.3.Conclusion

In this chapter, we studied the feasibility of transfecting cells directly inside the hydrogel structures by encapsulating plasmids in the bioink. Two strategies were evaluated: the addition of commercial transfection reagents into the encapsulating hydrogel and the hydrogel modification into cationic hydrogels.

The cationic hydrogels were formulated from modified gelatin or alginate. They were synthesized by forming an amide bond between the carboxylic groups of gelatin or alginate and

an amine group of 1,6 – diaminohexane. H-NMR could not validate the success of the grafting, yet the presence of gelatin molecules in cationic gelatin was confirmed. On the contrary, In the case of cationic alginate, the recovered product displayed an NMR profile with a low resemblance to the standard alginate, suggesting that it might be highly contaminated with the reaction substrates and by-products, and the presence of alginate molecules could not be established. In both cases, the synthesis of cationic compounds resulted in a product lacking purity with the presence of residual by-products. This cationic product could be further purified with extended dialysis or more stringent strategies such as ion-exchange HPLC.

The bioink prepared from the cationic gelatin was not able to produce 3D structures, yet its shear-thinning properties would allow the protection of cells subjected to shear stress during bioprinting [271]. Thus, to produce 3D architectures with charged material, this cationic gelatin could be used as an additive for a bioink containing a proportion of the standard gelatin. The capacity of cationized bioink prepared with synthesized gelatin to support transfection was pursued.

Neither commercial transfection reagents nor cationic hydrogel enabled cell transfection *in situ* with satisfactory yields. Even though cationic gelatin was behaving as a suitable transfection reagent in 2D cultures, very few cells were transfected in 3D.

In the experiments presented above, the hydrogel consolidation and the plasmids and cell concentrations tested did not allow to overcome the limitation in transfection efficiency. Yet, even though the plasmid volumic concentrations (4 – 20  $\mu\text{g}/\text{mL}$ ) were higher than the standard values used for 2D transfection protocols and included the usual values of 6.4 to 17  $\mu\text{g}/\text{mL}$  reported in the literature for GAM preparation [437,447,473], it should be noted that, contrarily to 2D cultures, the plasmids are immobilized and theoretically unable to diffuse in the hydrogel which strongly reduces the probability of plasmid-cell contact. Hence, even though in our 3D experiments, cells could theoretically get in contact with 950 to 4000 plasmid copies per cell, this value is low compared to the plasmid-to-cell ratios usually employed in 2D or suspension cultures comprised in a range of 0.1 to 2  $\mu\text{g}$  plasmids per  $10^6$  cells [180,644–648], corresponding to  $\sim 2 \times 10^4$  to  $4 \times 10^5$  plasmid copy per cell in the media supernatant. Additionally, our 2D transfection experiments reached successful cell transfection with plasmid concentrations corresponding to  $10^5$  -  $10^6$  plasmid copies per cell added to the culture medium. Hence, the plasmid to cell concentrations used in our 3D experiments remained lower than those reported in the literature or validated experimentally for transfection of 2D cell cultures.

In addition, the in situ transfection experiments were performed in serum-containing media, which might decrease the transfection efficiency, even though it has been reported that 3D transfection could be performed in the presence of serum [352,447].

HEK cells are gelatinase-secreting cells; this ability could be favourable to accessing the entrapped plasmids even in substantial hydrogel consolidation [302]. We showed in Figure 7.1 that plasmids are better retained in hydrogel after heavy consolidation. Yet, strong hydrogel consolidation was demonstrated in Chapter 4 to affect cell proliferation negatively. However, cell proliferation is essential to an efficient transfection process as it facilitates the insertion of plasmids in cell nuclei. Additionally, in 3D, cells would need to proliferate to come into contact with the plasmids entrapped in the hydrogel. The limited cell proliferation in 3D hydrogel cultures can provide another explanation for the absence of transfection in 3D cultures.

In the case of transfection performed in cationic hydrogels, the 1,6-diaminohexane used to prepare the cationic gelatin was chosen due to its reported use to form DNA-binding molecules [655–657]. However, we came across some literature reporting cytotoxic effects caused by this molecule [656,661,662]. Even though no evident cytotoxic effect of diaminohexane-grafted compounds was detected in our work, its impact on cell proliferation and interaction with the matrix should be evaluated in the future. It might not be the most suitable source of amino groups for cationized gelatin synthesis. Other molecules such as ethylenediamine [448,496–498], putrescine, spermidine or spermine [498] have already been used to generate cationic hydrogels. Some amino acids, such as Arginine, are also known to favour transfection and are used to produce cell-penetration peptides [482]. Such molecules should be evaluated as they could be better candidates.

The zeta potential of cationic hydrogels should also be studied, as it is known that under 10 mV or over 17 mV can reduce cell adhesion and cause cytotoxicity [453,501,503]. On the contrary, increased cationic amino group content on the anchorage surface offered better cell adhesion and increased proliferation and stabilization of naked plasmids by electrostatic interactions [500–504].

Finally, the exact mechanism occurring during in situ transfection with cationic hydrogel has not been described in the literature. It is unknown if the hydrogel's cationic groups enable cell membrane crossing by destabilising its negative charge or if it enters the cells as a plasmid-cationic complex. In the first scenario, the naked plasmids can enter the cells but do not reach the nucleus or cross its membrane, resulting in no transgene expression. Future work could investigate this hypothesis by performing in situ transfection with mRNA instead of plasmids.

mRNA would allow transgene expression upon internalization in cell cytoplasm without reaching the nucleus safely.

## CHAPTER 8. GENERAL DISCUSSION

**The present study originated from the convergence of two distinct scientific domains: bioprocessing and bioprinting.**

Our primary objective was to assess a novel therapeutic bioproduction strategy leveraging bioprinting as a manufacturing tool. Our initial undertaking involved the development of tools specifically designed to characterize cell proliferation within 3D hydrogel structures, as no tailored methodologies were available at the time. This research is detailed in Chapter 3. We successfully formulated and refined a dissociation protocol for retrieving entrapped cells while minimizing process duration and cell loss. We also explored alternative methods, such as cell counting through image analysis of histological sections and live cell staining within intact constructs. Ultimately, the cell numbers were attempted to be estimated by correlating cell proliferation and lactate metabolism. Our findings revealed significant variations in cell density as assessed by each of these methods, attributed to multiple factors:

- **Sample variability:** Even slight disparities in initial cell concentration, hydrogel consolidation, or construct geometry (over/under-extrusion) could lead to substantial differences in cell density after several days of culture, particularly during rapid cell proliferation phases.
- **Technical reproducibility and precision of analytical procedures:** Each method we examined had inherent sources of error and lacked accuracy.
- **Operator errors:** Some variability could be attributed to operator handling. Each sample was measured at least in triplicate following a strict protocol to mitigate this.

Out of the three methods evaluated, dissociation was deemed the most representative of cell behaviour within the constructs. It was the sole approach to directly estimating total cell numbers within a hydrogel volume. However, it is essential to note that while we made substantial efforts to optimize this technique, the precision and calibration of hydrogel dissociation remain limited. It is due to the inability to assess total cell loss and mortality during the dissociation process, as no reference method exists for such evaluations. Our protocol was inspired and adapted from native tissue dissociation techniques, typically used to recover and isolate specific cell types. Our optimized dissociation protocol have recently been patented [549]. In literature, dissociation is used to recover cell from tissue biopsies for experimental

[663] or clinical [664] purposes. The main techniques are based on enzymatic digestion, principally conducted with Collagenase. This enzyme is commonly used for dissociating tissues such as dermis [203], fat [665], pancreas [666] or liver [667] allowing for the recovery of cells with high viability [664] and structural integrity [663,668]. Pepsin is another enzyme used for digesting extracellular matrix or deparaffined tissues, but it is not recommended for cell recovery with high viability purposes due to its strong acidic conditions [669]. Dispase is a gentler alternative to trypsin for cell detachment [670] and is used for separating epidermal sheets from dermis or tissue dissociation [671]. Mechanical methods like GentleMACS can also be used for mechanical tissue dissociation [672]. Alginate lyase has also been used to dissociate micro-beads made of alginate [673] and alginate-poly-l-lysine-alginate [674]. In the last, cells were recovered with an 83% viability. Overall, different enzymes and methods are employed depending on the specific purpose and requirements of the cell recovery process.

In those applications, there is no need for a comprehensive assessment of total cell recovery or estimation of cell mortality before or during the process. Thus, while dissociation appears to be the most suitable method for cell retrieval and assessment of cell density in 3D hydrogel cell culture, further work is necessary to optimize and calibrate this method or to identify more suitable analytical tools. As an example, our team has worked on the development of automated microscopy techniques with Incucyte® (Sartorius) coupled to Artificial Intelligence-based image analysis to have automated culture imaging and analysis in the incubator (Patent EP22306652.3 - PCT – 2023). The use of MTT assays [214] or measurement of LDH activity [193] used in standard cell cultures could also be implemented in our 3D constructs.

Following establishing a protocol for evaluating cell numbers in hydrogel, Chapter 4 focused on characterizing the behaviour of four bioproduction cell lines within bioprinted constructs in small-scale, static cultures. Our bioink favored the survival and proliferation of all the tested mammalian cell lines. Our findings indicated that bioproduction cell lines cultured in bioprinted constructs exhibited altered metabolic and proliferative kinetics compared to 2D culture conditions. All four cell lines displayed a significant reduction in cell proliferation, with CHO, HEK, and MDCK also showing notably increased metabolic rates. These three cell lines could proliferate within the hydrogel, displaying cell- and tissue-specific morphologies, 3D organization, and structural features. This proliferative capability within the hydrogel may be attributed to these cell lines' ability to secrete MMP 2 and 9, enzymes capable of degrading gelatin in the hydrogels [302,304,305,598]. In contrast, Vero epithelial cells, that do not secrete MMP under normal conditions [305], could not proliferate within the hydrogel. Instead, they formed cell layers on the surface, consistent with their epithelial nature.

Our results demonstrated that production cell lines could exhibit cellular behaviours more closely aligned with in vivo cell physiology, characterized by reduced growth rates and increased metabolism. These cells also displayed tissue-specific morphologies and organizations. We could observe cyst formation for MDCK cell 3D culture, as already identified in the literature. Further characterization is warranted to identify tissue-specific markers and functions to validate these findings. For instance, work is currently underway to develop histological staining protocols targeting GP135, a membrane protein of MDCK located in the apical membrane of fully polarized cells [229,233], and collagen IV, which is expected to be expressed by Vero cells in the epithelium's basal matrix [305]. Electron microscopy analysis on thin sections of our hydrogels was also explored to identify cells and hydrogel ultrastructures. Hydrogel characterization was furthered with mechanical analysis. Being costly and labour-intensive, such analysis were only performed on optimized HEK samples. Nevertheless, they should now be transferred to the other cell lines as it is known that cell behaviour is also affected by the 3D support nature [208–210], porosity and micro-pattern [211] and mechanical properties [19,212].

As a second phase of the 3D growth capabilities of these cell lines, we explored the possibility of densifying our 3D cultures. Here, we employ a Design Of Experiment approach to identify parameters affecting hydrogel properties, cell proliferation, and metabolism. We concluded that cell density and growth rate were primarily influenced by hydrogel microporosity and parameters related to bioink consolidation. Therefore, enhancing hydrogel microporosity could increase the maximum achievable cell density within 3D bioprinted constructs. However, the cell concentrations achieved in our study remained lower than those reported in industrial processes with suspension or microcarrier cultures. Further investigations should be conducted to evaluate those hydrogel parameters further and gain deeper insights into how hydrogel microporosity affects cell proliferation. Targeted topics would be :

- Studying the gelatin/alginate/fibrinogen ratios and their impact on the consolidation strength and culture duration.
- Describing the molecule/oxygen diffusion kinetics within the hydrogels.
- Evaluating the hydrogel micro/nano-patterning effect

Our laboratory recently developed a gelatin quantification protocol based on a collagen assay kit to address the first point. This protocol can be implemented in future work to quantify the gelatin content of different hydrogels and/or the amount of gelatin released in culture



supernatants post-consolidation. Understanding the hydrogels' precise composition and gelatin content along the culture is crucial for evaluating the abundance of RGD motifs for cell adhesion [273]. Quantifying fibrin content would also be valuable for comparing the abundance of adhesion motifs in various hydrogels [265].

The second point is a valuable addition to our estimation of microporosity percentage. Estimating the global microporosity of hydrogels is insufficient for predicting the diffusion kinetics of various biomolecules within the hydrogels. Multiple methods could be employed to evaluate the diffusion rate within the hydrogel. For instance, probes exist for measuring oxygen levels in vivo [675,676]. They could be inserted at various sites within a bioprinted construct to calculate the gradient of the target molecule. Other works report the use of biocompatible oxygen-reactive molecules directly incorporated to the hydrogels to monitor oxygen diffusion [677]. Additionally, we are exploring an alternative approach involving live imaging of a fluorescent molecule deposited in the centre of a cylinder-shaped hydrogel construct. This allows us to estimate the molecule's diffusion rate and identify diffusion mechanisms and potential retention phenomena, as described in the "drunken sailor" analogy [678,679].

Furthermore, while TEM imaging provided 2D images of hydrogel sections and information about microporosity, it did not enable the precise determination of the 3D micro-pattern of the anchorage molecule network. On the other hand, Scanning Electron Microscopy (SEM) has previously been employed to observe the microstructure of gelatin and alginate-based hydrogels [680–683]. Such imaging techniques could offer additional insights into the characterization of hydrogels, including the micro-pattern [204] and topography [684] of the anchorage surface. Atomic Force Microscopy (AFM) is another technique that could provide information about hydrogel topography [683].

Following the confirmation of four production cell lines' ability to proliferate within 3D bioprinted constructs and the characterization of their behaviour in 3D conditions, we deployed a scale-up strategy of the cultures by producing larger 3D constructs.

To achieve this, we developed **the first and unique bioreactor setup suitable for cultivating large bioprinted constructs** exceeding 10 cm<sup>3</sup>. The technical aspects of this setup are detailed in Chapter 5. Our work established a "dynamic fed-batch" system based on a regulated stirred tank as a media reservoir, supplying a perfused "construct culture chamber." The culture chamber received a continuous media supply from a circulation loop connected to the stirred tank. Additional studies were conducted on the setup to incorporate online analytics, such as a Raman spectroscopy probe. This system was used to successfully cultivate HEK and CHO cells for 14 to 20 days, as presented in Chapter 6. As described in Chapter 5 and 6, implementing

such a bioprocess culture protocol for cultivating 3D bioprinted structure was not trivial. It relied on consideration and expertise of several scientific fields (Material science, Chemical engineering and Bioprocess, Cellular biology and Bioproduction).

Results demonstrated that dynamic bioreactor cultures of 10.8 cm<sup>3</sup> constructs led to a more uniform colonization of the hydrogel volume than static conditions, where cells were predominantly located on the hydrogel's surface. Cell proliferation appeared to be slower in dynamic conditions compared to static cultures. Nevertheless, again as described earlier, the absence of suitable non-destructive cell number monitoring tools during culture hindered the assessment of cell density evolution or the identification of potential cell concentration peaks during the culture. We proposed Raman spectroscopy to continuously and non-destructively monitor cell metabolism and cell proliferation within the hydrogel to address this issue. This is the first time that a bioreactor system with such level of monitoring and control has been reported for 3D bioprinted constructs culture and could offer interesting perspectives in other applications such as tissue engineering. Indeed, the bioreactor setup and technologies developed during this Ph.D project have then been successfully transferred to other applications such as the culture of bioprinted fibroblasts culture for the reconstitution of connective tissue.

To assess the potential of this technology for biopharmaceutical production, we investigated the secretion of recombinant monoclonal antibodies (mAbs) from bioprinted constructs cellularized with IgG1-producing CHO cells. This research began with small-scale cultures in an incubator. We demonstrated that cell-specific IgG productivity could be enhanced in small-scale bioprinted CHO cell cultures when cultivated in CHO-specific media using a fed-batch mode with an amplification phase post-bioprinting followed by a production phase. In these non-optimized conditions, the specific productivity matched those reported in the literature for optimized suspension fed-batch cultures, exceeding 30 pg/cell/day. We also established that scaled-up bioprinted constructs cultivated in our bioreactor setup produced mAbs with reduced media consumption. However, due to reduced cell density, the final volumetric productivity was significantly lower compared to suspension cultures. We estimated that bioprinted constructs of approximately 120 cm<sup>3</sup> would be required to achieve a final titer equivalent to the suspension reference run of 250 ml. Such bioprinted structure scale were already achieved within the team for MDCK cellularized porous structures.

As for Mabs product qualification, none of the traditional product quality characterization were performed as part of this work. We now envisage to perform host cell protein (HCP) and IgG glycosylation assay to assess the potential of our novel bioproduction strategy.

In the final chapter of this project, we explored the possibility of transfecting cells within the hydrogel constructs to enable more flexible and personalized production using a single technology. In this chapter, we demonstrated the stability of plasmid DNA within hydrogels over 13 days. We developed a cationic bioink to facilitate in situ transfection without commercial reagents. However, neither commercial reagents nor cationic hydrogels resulted in successful in situ transfection. The inefficiency of the protocols could not be conclusively explained due to a lack of understanding of the internalization mechanisms that occur during in situ transfection. Nonetheless, we provide multiple hypotheses and suggestions for potential improvements.

## CONCLUSION

In summary, this project has led to the development of a novel therapeutic biomanufacturing technology based on 3D bioprinted cultures of production cells. Our work has provided a deeper understanding of the global changes in cellular kinetics within 3D cultures and has described both the advantages and limitations of this culture method for bioproduction (see Table 8.1). We demonstrated that mAb-producing cell lines cultivated in such 3D bioprinted constructs, even in non-optimal static culture conditions in an incubator, exhibited higher specific productivity than the suspended bioreactor reference and equivalent specific productivity compared to values reported in the literature for optimized cultures in standard fed-batch suspension. Thus, we have demonstrated the potential of this technology to increase cell-specific productivity ( $q_p$ ) and raise questions about the potential of this new bioproduction model to surpass the current maximum cell-specific productivity of 90 pg/cell/day. The 3D culture of these cell lines can be scaled up and cultivated in a custom bioreactor system with full control over key culture parameters. However, the inability of 3D cell culture to reach the high cell densities achieved in standard culture processes results in low volumetric productivity that cannot compete with current industrial bioprocesses. Our work has demonstrated that optimizing bioprinting parameters and hydrogel properties could enhance cell proliferation and increase the maximum cell density achievable. Nonetheless, while it is theoretically possible for cells to grow at very high cell density by colonizing 100% of the construct volume, it remains uncertain whether such a phenomenon is practically achievable. In fact, the greater resemblance of 3D cell culture to the *in vivo* environment may also trigger *in vivo*-like responses, such as cell-contact-induced apoptosis. Our research has indicated the presence of successive growth phases interspersed with stationary phases or even a reduction in cell density for some cell lines, which aligns with the growth-apoptosis cycles observed in tissues [685,686].

Furthermore, existing *in situ* transfection tools have not yet achieved efficiencies equivalent to those reported in monolayer or suspension cultures. Our work has not been able to overcome this obstacle, but we have proposed suggestions for improving *in situ* transfection efficiency.

To date, the size of such 3D cultures would be limited to a few hundred cubic centimeters, which is the maximum size that our team can print and exceeds the size of any bioprinted construct reported in the literature. Consequently, we have concluded that with current technical capabilities, this technology does not present a compelling alternative to standard industrial bioproduction processes for recombinant proteins. Nevertheless, its similarity to the *in vivo* environment, increased specific productivity, and the cell-protective effects of the hydrogel matrix against hydrodynamic stresses present intriguing potential for personalized or niche

therapies, such as stem cell-based treatments or extracellular vesicle production. Additionally, the high potential of this technology for in situ infection, which was not explored in this work, offers interesting prospects for biomanufacturing viral products.

Table 8.1: Main advantages and limitations of the technology developed in the present work



# VALORIZATION

## Publications

Chastagnier, L., El-Kholti, N., Essayan, L., Thomann, C., Courtial, E.-J., Marquette, C., & Petiot, E. (2023). Deciphering dermal fibroblast behavior in 3D bioprinted dermis constructs. *Bioprinting*, 32(April), 2023.03.07.531460. <https://doi.org/10.1016/j.bprint.2023.e00275>

Chastagnier, L., Marquette, C., & Petiot, E. (2023). In situ transient transfection of 3D cell cultures and tissues, a promising tool for tissue engineering and gene therapy. *Biotechnology Advances*, 68(July), 108211. <https://doi.org/10.1016/j.biotechadv.2023.108211>

(Submitted to *Biofabrication*, september 2023) Laura Chastagnier, Lucie Essayan, Celine Thomann, Julia Niemann, Elisabeth Errazuriz-Cerda, Manon Laithier, Anne Baudouin, Christophe Marquette, Emma Petiot, Production cell lines 3D bioprinting : Evaluation of a novel bioproduction support.

## Patents

Petiot, E., Chastagnier, L., Courtial, E.-J., & Marquette, C. (2023). Production of cellular products from cells integrated in a matrix ; Patent No. EP4141095A1; WO2023025804A1 (Patent EP4141095A1; WO2023025804A1). In *European Patent Office (EPO)*; Patent No. EP4141095A1; WO2023025804A1 (EP4141095A1; WO2023025804A1).

Petiot, E., & Chastagnier, L. (2023). Methods for production of engineered cells ; Patent No. EP4141096A1; WO2023025812A1. *European Patent Office (EPO)*, Patent No. EP4141096A1; WO2023025812A1.

Marquette, C., Petiot, E., Chastagnier, L., Cherblanc, A., Dos Santos, M., Thepot, A., & Godet, B. (n.d.). *Implants corporels tridimensionnels*, Patent number: WO2022269215A1 (Patent WO2022269215A1).

Marquette, C., Petiot, E., Chastagnier, L., Cherblanc, A., Dos Santos, M., Thepot, A., & Godet, B. (2022). *Procédé de consolidation d'un hydrogel alginate/gelatine*; Patent Number WO2022269214A1 (Patent WO2022269214A1). <https://doi.org/WO2022269214A1>

## References

- [1] Langer E and Rader R 2015 Biopharmaceutical Manufacturing: Historical and Future Trends in Titters, Yields, and Efficiency in Commercial-Scale Bioprocessing *BioProcessing Journal* **13** 47–54
- [2] Walsh G and Walsh E 2022 Biopharmaceutical benchmarks 2022 *Nat Biotechnol* **40** 1722–60
- [3] Tian Y, Hu D, Li Y and Yang L 2022 Development of therapeutic vaccines for the treatment of diseases *Molecular Biomedicine* **3** 1–30
- [4] Li F, Vijayasankaran N, Shen A, Kiss R and Amanullah A 2010 Cell culture processes for monoclonal antibody production *MAbs* **2** 466–79
- [5] Tripathi N K and Shrivastava A 2019 Recent Developments in Bioprocessing of Recombinant Proteins: Expression Hosts and Process Development *Front Bioeng Biotechnol* **7**
- [6] Butler M 2005 Animal cell cultures: Recent achievements and perspectives in the production of biopharmaceuticals *Appl Microbiol Biotechnol* **68** 283–91
- [7] Park S Y, Kim J Y, Ryu K H, Kim A Y, Kim J M, Ko Y J and Lee E G 2021 Production of a foot-and-mouth disease vaccine antigen using suspension-adapted BHK-21 cells in a bioreactor *Vaccines (Basel)* **9** 1–13
- [8] Telling R C and Elsworth R 1965 Submerged culture of hamster kidney cells in a stainless steel vessel *Biotechnol Bioeng* **7** 417–34
- [9] Chen J R, Liu Y M, Tseng Y C and Ma C 2020 Better influenza vaccines: An industry perspective *J Biomed Sci* **27** 1–11
- [10] Pérez-Rubio A, Ancochea J and Eiros Bouza J M 2020 Quadrivalent cell culture influenza virus vaccine. Comparison to egg-derived vaccine *Hum Vaccin Immunother* **16** 1746–52
- [11] Noh S M, Sathyamurthy M and Lee G M 2013 Development of recombinant Chinese hamster ovary cell lines for therapeutic protein production *Curr Opin Chem Eng* **2** 391–7
- [12] Zhu M M, Mollet M, Hubert R S, Kyung Y S and Zhang G G 2017 *Handbook of Industrial Chemistry and Biotechnology*
- [13] Wurm F M 2004 Production of recombinant protein therapeutics in cultivated mammalian cells *Nat Biotechnol* **22** 1393–8
- [14] Horie M, Yamano-Adachi N, Kawabe Y, Kaneoka H, Fujita H, Nagamori E, Iwai R, Sato Y, Kanie K, Ohta S, Somiya M and Ino K 2022 Recent advances in animal cell technologies for industrial and medical applications *J Biosci Bioeng* **133** 509–14

- [15] Tatar M, Shoorekchali J M, Faraji M R, Seyyedkolae M A, Pagán J A and Wilson F A 2022 COVID-19 vaccine inequality: A global perspective *J Glob Health* **12** 10–3
- [16] Ahmadiani S and Nikfar S 2016 Challenges of access to medicine and the responsibility of pharmaceutical companies: A legal perspective *DARU, Journal of Pharmaceutical Sciences* **24** 1–7
- [17] Thiel K A 2004 Biomanufacturing , from bust to boom ... to bubble ? **22** 1365–72
- [18] Merten O W 2006 Introduction to animal cell culture technology - Past, present and future *Cytotechnology* **50** 1–7
- [19] Martinac B, Nikolaev Y A, Silvani G, Bavi N, Romanov V, Nakayama Y, Martinac A D, Rohde P, Bavi O and Cox C D 2020 *Cell membrane mechanics and mechanosensory transduction* vol 86 (Elsevier Inc.)
- [20] Nienow A W 2006 Reactor engineering in large scale animal cell culture *Cytotechnology* **50** 9–33
- [21] Griffiths B and Wurm F 2003 Mammalian Cell Culture *Encyclopedia of Physical Science and Technology (Third Edition)* ed R A Meyers (New York: Academic Press) pp 31–47
- [22] Wang D, Liu W, Han B and Xu R 2005 The Bioreactor: A Powerful Tool for Large-Scale Culture of Animal Cells *Curr Pharm Biotechnol* **6** 397–403
- [23] Pörtner R, Platas O B B, Fassnacht D, Nehring D, Czermak P, Märkl H, Portner R, Platas O B B, Fassnacht D, Nehring D, Czermak P and Markl H 2007 Fixed Bed Reactors for the Cultivation of Mammalian Cells: Design, Performance and Scale-Up *Open Biotechnol J* **1** 41–6
- [24] Powers A D, Piras B A, Clark R K, Lockey T D and Meagher M M 2016 Development and Optimization of AAV hFIX Particles by Transient Transfection in an iCELLis ® Fixed-Bed Bioreactor *Hum Gene Ther Methods* **27** 112–21
- [25] Berrie D M, Waters R C, Montoya C, Chatel A and Vela E M 2020 Development of a high-yield live-virus vaccine production platform using a novel fixed-bed bioreactor *Vaccine* **38** 3639–45
- [26] Leinonen H M, Lepola S, Lipponen E M, Heikura T, Koponen T, Parker N, Ylä-Herttuala S and Lesch H P 2020 Benchmarking of Scale-X Bioreactor System in Lentiviral and Adenoviral Vector Production *Hum Gene Ther* **31** 376–84
- [27] Lesch H P, Valonen P and Karhinen M 2021 Evaluation of the Single-Use Fixed-Bed Bioreactors in Scalable Virus Production *Biotechnol J* **16**
- [28] Gelbgras V, Wylock C E, Drugmand J-C and Haut B 2011 Segregated Model of Adherent Cell Culture in a Fixed-Bed Bioreactor *Chemical Product and Process Modeling* **6**



- [29] Chisti Y and Moo-Young M 2003 Bioreactors *Encyclopedia of Physical Science and Technology (Third Edition)* ed R A Meyers (New York: Academic Press) pp 247–71
- [30] Ho C S, Wang D I and Erdugo C L B 1991 Animal cell bioreactors. ed C S Ho and D I Wang *Biotechnology* **17** 3–478
- [31] Aijaz A, Trawinski D, McKirgan S and Parekkadan B 2019 Non-invasive cell counting of adherent, suspended and encapsulated mammalian cells using optical density *Biotechniques* **68** 35–40
- [32] Wu P, Ozturk S S, Blackie J D, Thrift J C, Figueroa C and Naveh D 1995 Evaluation and applications of optical cell density probes in mammalian cell bioreactors *Biotechnol Bioeng* **45** 495–502
- [33] Petiot E, Ansorge S, Rosa-Calatrava M and Kamen A 2017 Critical phases of viral production processes monitored by capacitance *J Biotechnol* **242** 19–29
- [34] Lu F, Toh P C, Burnett I, Li F, Hudson T, Amanullah A and Li J 2013 Automated dynamic fed-batch process and media optimization for high productivity cell culture process development *Biotechnol Bioeng* **110** 191–205
- [35] Esmonde-White K A, Cuellar M and Lewis I R 2022 The role of Raman spectroscopy in biopharmaceuticals from development to manufacturing *Anal Bioanal Chem* **414** 969–91
- [36] Araujo-Andrade C, Pichardo-Molina J L, Barbosa-Sabanero G and Frausto-Reyes C 2008 Identification of antibody isotypes in biological fluids by means of micro-Raman spectroscopy and chemometric methods *Optical Diagnostics and Sensing VIII* **6863** 68630P
- [37] Schwarz H, Mäkinen M E, Castan A and Chotteau V 2022 Monitoring of amino acids and antibody N-glycosylation in high cell density perfusion culture based on Raman spectroscopy *Biochem Eng J* **182**
- [38] Mosca S, Conti C, Stone N and Matousek P 2021 Spatially offset Raman spectroscopy *Nature Reviews Methods Primers* **1**
- [39] Cialla-May D, Schmitt M and Popp J 2019 Theoretical principles of Raman spectroscopy *Physical Sciences Reviews* **4** 1–9
- [40] Löffelholz C, Kaiser S C, Kraume M, Eibl R and Eibl D 2013 Dynamic Single-Use Bioreactors Used in Modern Liter- and m3- Scale Biotechnological Processes: Engineering Characteristics and Scaling Up *Advances in biochemical engineering/biotechnology* vol 123 pp 1–44
- [41] Singh V 1999 Disposable bioreactor for cell culture using wave-induced agitation *Cytotechnology* **30** 149–58

- [42] Eibl R and Eibl D 2019 *Single-Use Technology in Biopharmaceutical Manufacture* ed R Eibl and D Eibl (Wiley)
- [43] Jossen V, Eibl R and Eibl D 2019 Single-Use Bioreactors – An Overview *Single-Use Technology in Biopharmaceutical Manufacture* (Wiley) pp 37–52
- [44] Shukla A A and Gottschalk U 2013 Single-use disposable technologies for biopharmaceutical manufacturing *Trends Biotechnol* **31** 147–54
- [45] Okonkowski J, Balasubramanian U, Seamans C, Fries S, Zhang J, Salmon P, Robinson D and Chartrain M 2007 Cholesterol delivery to NS0 cells: Challenges and solutions in disposable linear low-density polyethylene-based bioreactors *J Biosci Bioeng* **103** 50–9
- [46] Walter J K and Gottschalk U 2010 Concepts for Disposables in Biopharmaceutical Manufacture *Current Trends in Monoclonal Antibody Development and Manufacturing* (New York, NY: Springer New York) pp 87–99
- [47] Jacquemart R, Vandersluis M, Zhao M, Sukhija K, Sidhu N and Stout J 2016 A Single-use Strategy to Enable Manufacturing of Affordable Biologics *Comput Struct Biotechnol J* **14** 309–18
- [48] Nienow A W, Langheinrich C, Stevenson N C, Nicholas Emery A, Clayton T M and Slater N K H 1996 Homogenisation and oxygen transfer rates in large agitated and sparged animal cell bioreactors: Some implications for growth and production *Cytotechnology* **22** 87–94
- [49] Langheinrich C, Nienow A W, Eddleston T, Stevenson N C, Emery A N, Clayton T M and Slater N K H 1998 Liquid homogenization studies in animal cell bioreactors of up to 8 m<sup>3</sup> in volume *Food and Bioproducts Processing: Transactions of the Institution of Chemical Engineers, Part C* **76** 107–16
- [50] Varley J and Birch J 1999 Reactor design for large scale suspension animal cell culture *Cytotechnology* **29** 177–205
- [51] Chisti Y 1993 Animal cell culture in stirred bioreactors: observations on scale-up *Process Biochemistry* **28** 511–7
- [52] Murhammer D W and Goochee C F 1990 Sparged Animal Cell Bioreactors: Mechanism of Cell Damage and Pluronic F-68 Protection *Biotechnol Prog* **6** 391–7
- [53] Al-Rubeai M, Singh R P, Emery A N and Zhang Z 1995 Cell cycle and cell size dependence of susceptibility to hydrodynamic forces *Biotechnol Bioeng* **46** 88–92
- [54] Delafosse A, Collignon M-L, Marc A, Toye D and Olmos E 2015 Revisiting the determination of hydromechanical stresses encountered by microcarriers in stem cell culture bioreactors *BMC Proc* **9** 9–11

- [55] Cherry R S and Papoutsakis E T 1988 Physical mechanisms of cell damage in microcarrier cell culture bioreactors *Biotechnol Bioeng* **32** 1001–14
- [56] Cherry R S and Papoutsakis E T 1986 Hydrodynamic effects on cells in agitated tissue culture reactors *Bioprocess Engineering* **1** 29–41
- [57] Maul T M, Chew D W, Nieponice A and Vorp D A 2011 Mechanical stimuli differentially control stem cell behavior: Morphology, proliferation, and differentiation *Biomech Model Mechanobiol* **10** 939–53
- [58] Sieck J B, Cordes T, Budach W E, Rhiel M H, Suemeghy Z, Leist C, Villiger T K, Morbidelli M and Soos M 2013 Development of a Scale-Down Model of hydrodynamic stress to study the performance of an industrial CHO cell line under simulated production scale bioreactor conditions *J Biotechnol* **164** 41–9
- [59] Zhu H, Nienow A W, Bujalski W and Simmons M J H 2009 Mixing studies in a model aerated bioreactor equipped with an up- or a down-pumping “Elephant Ear” agitator: Power, hold-up and aerated flow field measurements *Chemical Engineering Research and Design* **87** 307–17
- [60] Collignon M L, Delafosse A, Calvo S, Martin C, Marc A, Toye D and Olmos E 2016 Large-Eddy Simulations of microcarrier exposure to potentially damaging eddies inside mini-bioreactors *Biochem Eng J* **108** 30–43
- [61] Olmos E, Fischbach N and Marc A 2007 Computational Fluid Dynamics Applied to Laboratory Scale Cell Culture Reactors for the Prediction of Hydrodynamic Stress *Cell Technology for Cell Products* (Dordrecht: Springer Netherlands) pp 587–90
- [62] Borys B S, Roberts E L, Le A and Kallos M S 2018 Scale-up of embryonic stem cell aggregate stirred suspension bioreactor culture enabled by computational fluid dynamics modeling *Biochem Eng J* **133** 157–67
- [63] Marc A and Olmos É 2010 Procédés de culture en masse de cellules animales 22
- [64] Michaels J D, Nowak J E, Mallik A K, Koczko K, Wasan D T and Papoutsakis E T 1995 Interfacial properties of cell culture media with cell-protecting additives *Biotechnol Bioeng* **47** 420–30
- [65] Tharmalingam T, Ghebeh H, Wuerz T and Butler M 2008 Pluronic Enhances the Robustness and Reduces the Cell Attachment of Mammalian Cells *Mol Biotechnol* **39** 167–77
- [66] Dyson M R 2016 Fundamentals of expression in mammalian cells *Adv Exp Med Biol* **896** 217–24
- [67] Thompson C M, Petiot E, Mullick A, Aucoin M G, Henry O and Kamen A A 2015 Critical assessment of influenza VLP production in Sf9 and HEK293 expression systems *BMC Biotechnol* **15** 31

- [68] Genzel Y 2015 Designing cell lines for viral vaccine production: Where do we stand? *Biotechnol J* **10** 728–40
- [69] Tan E, Chin C S H, Lim Z F S and Ng S K 2021 HEK293 Cell Line as a Platform to Produce Recombinant Proteins and Viral Vectors *Front Bioeng Biotechnol* **9** 1–9
- [70] Butler M and Spearman M 2014 The choice of mammalian cell host and possibilities for glycosylation engineering *Curr Opin Biotechnol* **30** 107–12
- [71] Urlaub G, Käs E, Carothers A M and Chasin L A 1983 Deletion of the diploid dihydrofolate reductase locus from cultured mammalian cells *Cell* **33** 405–12
- [72] Urlaub G and Chasin L A 1980 Isolation of Chinese hamster cell mutants deficient in dihydrofolate reductase activity *Proc Natl Acad Sci U S A* **77** 4216–20
- [73] Tree J A, Richardson C, Fooks A R, Clegg J C and Looby D 2001 Comparison of large-scale mammalian cell culture systems with egg culture for the production of influenza virus A vaccine strains *Vaccine* **19** 3444–50
- [74] Kistner O, Barrett P N, Mundt W, Reiter M, Schober-Bendixen S and Dorner F 1998 Development of a mammalian cell (Vero) derived candidate influenza virus vaccine *Vaccine* **16** 960–8
- [75] Pau M G, Ophorst C, Koldijk M H, Schouten G, Mehtali M and Uytdehaag F 2001 The human cell line PER.C6 provides a new manufacturing system for the production of influenza vaccines *Vaccine* **19** 2716–21
- [76] Tomita M and Tsumoto K 2011 Hybridoma technologies for antibody production *Immunotherapy* **3** 371–80
- [77] Kong B W, Lee J Y, Bottje W G, Lassiter K, Lee J and Foster D N 2011 Genome-wide differential gene expression in immortalized DF-1 chicken embryo fibroblast cell line *BMC Genomics* **12** 1–19
- [78] Thomas P and Smart T G 2005 HEK293 cell line: A vehicle for the expression of recombinant proteins *J Pharmacol Toxicol Methods* **51** 187–200
- [79] Maurisse R, De Semir D, Enamekhoo H, Bedayat B, Abdolmohammadi A, Parsi H and Gruenert D C 2010 Comparative transfection of DNA into primary and transformed mammalian cells from different lineages *BMC Biotechnol* **10** 1–9
- [80] Yuan J, Xu W W, Jiang S, Yu H and Poon H F 2018 The scattered twelve tribes of HEK293 *Biomedical and Pharmacology Journal* **11** 621–3
- [81] Lin Y C, Boone M, Meuris L, Lemmens I, Van Roy N, Soete A, Reumers J, Moisse M, Plaisance S, Drmanac R, Chen J, Speleman F, Lambrechts D, Van De Peer Y, Tavernier J and Callewaert

- N 2014 Genome dynamics of the human embryonic kidney 293 lineage in response to cell biology manipulations *Nat Commun* **5**
- [82] Wei F, Wang H, Chen X, Li C and Huang Q 2014 Dissecting the roles of E1A and E1B in adenoviral replication and RCAd-enhanced RDAd transduction efficacy on tumor cells *Cancer Biol Ther* **15** 1358–66
- [83] Inada M, Izawa G, Kobayashi W and Ozawa M 2016 293 Cells Express Both Epithelial As Well As Mesenchymal Cell Adhesion Molecules *Int J Mol Med* **37** 1521–7
- [84] Stepanenko A A and Dmitrenko V V. 2015 HEK293 in cell biology and cancer research: Phenotype, karyotype, tumorigenicity, and stress-induced genome-phenotype evolution *Gene* **569** 182–90
- [85] Shaw G, Morse S, Ararat M and Graham F L 2002 Preferential transformation of human neuronal cells by human adenoviruses and the origin of HEK 293 cells. *The FASEB journal : official publication of the Federation of American Societies for Experimental Biology* **16** 869–71
- [86] Debeb B G, Zhang X, Krishnamurthy S, Gao H, Cohen E, Li L, Rodriguez A A, Landis M D, Lucci A, Ueno N T, Robertson F, Xu W, Lacerda L, Buchholz T A, Cristofanilli M, Reuben J M, Lewis M T and Woodward W A 2010 Characterizing cancer cells with cancer stem cell-like features in 293T human embryonic kidney cells *Mol Cancer* **9** 1–12
- [87] Ferreira R G, Gordon N F, Stock R and Petrides D 2021 Adenoviral vector covid-19 vaccines: Process and cost analysis *Processes* **9**
- [88] Yang J, Guertin P, Jia G, Lv Z, Yang H and Ju D 2019 Large-scale microcarrier culture of HEK293T cells and Vero cells in single-use bioreactors *AMB Express* **9**
- [89] Butler M and Spearman M 2014 The choice of mammalian cell host and possibilities for glycosylation engineering *Curr Opin Biotechnol* **30** 107–12
- [90] Abaandou L, Quan D and Shiloach J 2021 Affecting hek293 cell growth and production performance by modifying the expression of specific genes *Cells* **10** 1–21
- [91] Backliwal G, Hildinger M, Chenuet S, Wulhfard S, De Jesus M and Wurm F M 2008 Rational vector design and multi-pathway modulation of HEK 293E cells yield recombinant antibody titers exceeding 1 g/l by transient transfection under serum-free conditions *Nucleic Acids Res* **36**
- [92] Handlogten M W, Lee-O'Brien A, Roy G, Levitskaya S V., Venkat R, Singh S and Ahuja S 2018 Intracellular response to process optimization and impact on productivity and product aggregates for a high-titer CHO cell process *Biotechnol Bioeng* **115** 126–38

- [93] Stepanenko A A and Dmitrenko V V. 2015 HEK293 in cell biology and cancer research: Phenotype, karyotype, tumorigenicity, and stress-induced genome-phenotype evolution *Gene* **569** 182–90
- [94] Binz R L, Tian E, Sadhukhan R, Zhou D, Hauer-Jensen M and Pathak R 2019 Identification of novel breakpoints for locus- and region-specific translocations in 293 cells by molecular cytogenetics before and after irradiation *Sci Rep* **9** 1–10
- [95] Tjio J H and Puck T T 1958 GENETICS OF SOMATIC MAMMALIAN CELLS *J Exp Med* **108** 259–68
- [96] Ng S K 2012 Generation of high-expressing cells by methotrexate amplification of destabilized dihydrofolate reductase selection marker *Methods in Molecular Biology* **801** 161–72
- [97] No Soo Kim, Tae Ho Byun and Gyun Min Lee 2001 Key determinants in the occurrence of clonal variation in humanized antibody expression of cho cells during dihydrofolate reductase mediated gene amplification *Biotechnol Prog* **17** 69–75
- [98] Heffner K, Hizal D B, Majewska N I, Kumar S, Dhara V G, Zhu J, Bowen M, Hatton D, Yerganian G, Yerganian A, O’Meally R, Cole R and Betenbaugh M 2020 Expanded Chinese hamster organ and cell line proteomics profiling reveals tissue-specific functionalities *Sci Rep* **10** 1–12
- [99] Schulze M, Niemann J, Wijffels R H, Matuszczyk J and Martens D E 2021 Rapid intensification of an established CHO cell fed-batch process *Biotechnol Prog* 1–15
- [100] Derouazi M, Martinet D, Besuchet Schmutz N, Flaction R, Wicht M, Bertschinger M, Hacker D L, Beckmann J S and Wurm F M 2006 Genetic characterization of CHO production host DG44 and derivative recombinant cell lines *Biochem Biophys Res Commun* **340** 1069–77
- [101] Gaush C R, Hard W L, Smith T F and Read W O 1966 Characterization of an Established Line of Canine Kidney Cells (MDCK) *Proceedings of the Society for Experimental Biology and Medicine* **122** 931–5
- [102] Stulberg C S, Coriell L L, Kniazeff A J and Shannon J E 1970 The animal cell culture collection *In Vitro* **5** 1–16
- [103] Cassio D 2013 Long term culture of MDCK strains alters chromosome content *BMC Res Notes* **6**
- [104] Leighton J, Estes L W, Mansukhani S and Brada Z 1970 A cell line derived from normal dog kidney (mdck) exhibiting qualities of papillary adenocarcinoma and of renal tubular epithelium *Cancer* 1022–8
- [105] Herzlinger D A, Easton T G and Ojakian G K 1982 The MDCK epithelial cell line expresses a cell surface antigen of the kidney distal tubule *Journal of Cell Biology* **93** 269–77

- [106] McAteer J A, Evan A P and Gardner K D 1987 Morphogenetic clonal growth of kidney epithelial cell line MDCK *Anat Rec* **217** 229–39
- [107] Wohlgemuth N, Lane A P and Pekosz A 2018 Influenza A Virus M2 Protein Apical Targeting Is Required for Efficient Virus Replication *J Virol* **92** 1–17
- [108] Suderman M, Moniwa M, Alkie T N, Ojkic D, Broes A, Pople N and Berhane Y 2021 Comparative susceptibility of madin–darby canine kidney (Mdck) derived cell lines for isolation of swine origin influenza a viruses from different clinical specimens *Viruses* **13**
- [109] Marozin S, Prank U and Sodeik B 2004 Herpes simplex virus type 1 infection of polarized epithelial cells requires microtubules and access to receptors present at cell-cell contact sites *Journal of General Virology* **85** 775–86
- [110] Sears A E, McGwire B S and Roizman B 1991 Infection of polarized MDCK cells with herpes simplex virus 1: Two asymmetrically distributed cell receptors interact with different viral proteins *Proc Natl Acad Sci U S A* **88** 5087–91
- [111] Fuller S, von Bonsdorff C H and Simons K 1984 Vesicular stomatitis virus infects and matures only through the basolateral surface of the polarized epithelial cell line, MDCK *Cell* **38** 65–77
- [112] Kristensson K, Lundh B, Norrby E, Payne L and Örvell C 1984 Asymmetric Budding of Viruses in Ependymal and Choroid Plexus Epithelial Cells *Neuropathol Appl Neurobiol* **10** 209–19
- [113] Blank C A, Anderson D A, Beard M and Lemon S M 2000 Infection of Polarized Cultures of Human Intestinal Epithelial Cells with Hepatitis A Virus: Vectorial Release of Progeny Virions through Apical Cellular Membranes *J Virol* **74** 6476–84
- [114] Ciarlet M, Crawford S E and Estes M K 2001 Differential Infection of Polarized Epithelial Cell Lines by Sialic Acid-Dependent and Sialic Acid-Independent Rotavirus Strains *J Virol* **75** 11834–50
- [115] Ulloa F and Real F X 2001 Differential distribution of sialic acid in  $\alpha$ 2,3 and  $\alpha$ 2,6 linkages in the apical membrane of cultured epithelial cells and tissues *Journal of Histochemistry and Cytochemistry* **49** 501–9
- [116] Kovbasnjuk O N and Spring K R 2000 The Apical Membrane Glycocalyx of MDCK Cells *J Membr Biol* **176** 19–29
- [117] Hegde N R 2015 Cell culture-based influenza vaccines: A necessary and indispensable investment for the future *Hum Vaccin Immunother* **11** 1223–34
- [118] Onions D, Egan W, Jarrett R, Novicki D and Gregersen J P 2010 Validation of the safety of MDCK cells as a substrate for the production of a cell-derived influenza vaccine *Biologicals* **38** 544–51

- [119] Dukes J D, Whitley P and Chalmers A D 2011 The MDCK variety pack: Choosing the right strain *BMC Cell Biol* **12** 2–5
- [120] Matrosovich M, Matrosovich T, Carr J, Roberts N A and Klenk H-D 2003 Overexpression of the  $\alpha$ -2,6-Sialyltransferase in MDCK Cells Increases Influenza Virus Sensitivity to Neuraminidase Inhibitors *J Virol* **77** 8418–25
- [121] Tsai H C, Lehman C W, Lin C C, Tsai S W and Chen C M 2019 Functional evaluation for adequacy of MDCK-lineage cells in influenza research *BMC Res Notes* **12** 4–9
- [122] Huang D, Peng W J, Ye Q, Liu X P, Zhao L, Fan L, Xia-Hou K, Jia H J, Luo J, Zhou L T, Li B B, Wang S L, Xu W T, Chen Z and Tan W S 2015 Serum-free suspension culture of MDCK cells for production of influenza H1N1 Vaccines *PLoS One* **10** 1–11
- [123] Abdoli A, Soleimanjahi H, Jamali A, Mehrbod P, Gholami S, Kianmehr Z, Feizi N, Saleh M, Bahrami F, Mokhtari-Azad T, Abdoli M and Kheiri M T 2016 Comparison between MDCK and MDCK-SIAT1 cell lines as preferred host for cell culture-based influenza vaccine production *Biotechnol Lett* **38** 941–8
- [124] Chu C, Lugovtsev V, Golding H, Betenbaugh M and Shiloach J 2009 Conversion of MDCK cell line to suspension culture by transfecting with human *siat7e* gene and its application for influenza virus production *Proc Natl Acad Sci U S A* **106** 14802–7
- [125] Bock A, Sann H, Schulze-Horsel J, Genzel Y, Reichl U and Möhler L 2009 Growth behavior of number distributed adherent MDCK cells for optimization in microcarrier cultures *Biotechnol Prog* **25** 1717–31
- [126] Hu A Y C, Weng T C, Tseng Y F, Chen Y S, Wu C H, Hsiao S, Chou A H, Chao H J, Gu A, Wu S C, Chong P and Lee M S 2008 Microcarrier-based MDCK cell culture system for the production of influenza H5N1 vaccines *Vaccine* **26** 5736–40
- [127] Genzel Y, Behrendt I, König S, Sann H and Reichl U 2004 Metabolism of MDCK cells during cell growth and influenza virus production in large-scale microcarrier culture *Vaccine* **22** 2202–8
- [128] Genzel Y, Dietzsch C, Rapp E, Schwarzer J and Reichl U 2010 MDCK and Vero cells for influenza virus vaccine production: A one-to-one comparison up to lab-scale bioreactor cultivation *Appl Microbiol Biotechnol* **88** 461–75
- [129] Gallo-Ramírez L E, Nikolay A, Genzel Y and Reichl U 2015 Bioreactor concepts for cell culture-based viral vaccine production *Expert Rev Vaccines* **14** 1181–95
- [130] Ammerman N C, Beier-Sexton M and Azad A F 2008 Growth and maintenance of vero cell lines *Curr Protoc Microbiol* 1–7



- [131] Naoki O, Arihiro K, Toshiyuki Y, Noriko H, Fumio K, Suyoshi S, Makoto K, Kentaro H and Hattori M 2014 The genome landscape of the African Green Monkey kidney-derived vero cell line *DNA Research* **21** 673–83
- [132] Murira A and Lamarre A 2016 Type-I interferon responses: From friend to foe in the battle against chronic viral infection *Front Immunol* **7** 1–8
- [133] McNab F, Mayer-Barber K, Sher A, Wack A and O’Garra A 2015 Type I interferons in infectious disease *Nat Rev Immunol* **15** 87–103
- [134] Harcourt J, Tamin A, Lu X, Kamili S, Sakthivel S K, Murray J, Queen K, Tao Y, Paden C R, Zhang J, Li Y, Uehara A, Wang H, Goldsmith C, Bullock H A, Wang L, Whitaker B, Lynch B, Gautam R, Schindewolf C, Lokugamage K G, Scharton D, Plante J A, Mirchandani D, Widen S G, Narayanan K, Makino S, Ksiazek T G, Plante K S, Weaver S C, Lindstrom S, Tong S, Menachery V D and Thornburg N J 2020 Severe acute respiratory syndrome coronavirus 2 from patient with coronavirus disease, United States *Emerg Infect Dis* **26** 1266–73
- [135] Rish A J, Drennen J K and Anderson C A 2022 Metabolic trends of Chinese hamster ovary cells in biopharmaceutical production under batch and fed-batch conditions *Biotechnol Prog* **38**
- [136] Buchsteiner M, Quek L E, Gray P and Nielsen L K 2018 Improving culture performance and antibody production in CHO cell culture processes by reducing the Warburg effect *Biotechnol Bioeng* **115** 2315–27
- [137] Siddiqui F A, Prakasam G, Chattopadhyay S, Rehman A U, Padder R A, Ansari M A, Irshad R, Mangalhari K, Bamezai R N K, Husain M, Ali S M and Iqbal M A 2018 Curcumin decreases Warburg effect in cancer cells by down-regulating pyruvate kinase M2 via mTOR-HIF1 $\alpha$  inhibition *Sci Rep* **8** 2–10
- [138] Martínez-Monge I, Albiol J, Lecina M, Liste-Calleja L, Miret J, Solà C and Cairó J J 2019 Metabolic flux balance analysis during lactate and glucose concomitant consumption in HEK293 cell cultures *Biotechnol Bioeng* **116** 388–404
- [139] Wahl A, Sidorenko Y, Dauner M, Genzel Y and Reichl U 2008 Metabolic flux model for an anchorage-dependent MDCK cell line: Characteristic growth phases and minimum substrate consumption flux distribution *Biotechnol Bioeng* **101** 135–52
- [140] Carinhas N, Pais D A M, Koshkin A, Fernandes P, Coroadinha A S, Carrondo M J T, Alves P M and Teixeira A P 2016 Metabolic flux profiling of MDCK cells during growth and canine adenovirus vector production *Sci Rep* **6** 1–11
- [141] Petiot E, Guedon E, Blanchard F, Gény C, Pinton H and Marc A 2010 Kinetic characterization of vero cell metabolism in a serum-free batch culture process *Biotechnol Bioeng* **107** 143–53

- [142] Young J D 2013 Metabolic flux rewiring in mammalian cell cultures *Curr Opin Biotechnol* **24** 1108–15
- [143] Sébastien Quesney, Annie Marc, Catherine Gerdil, Cyrille Gimenez, Jacqueline Marvel, Yves Richard and Bernard Meignier 2003 Kinetics and metabolic specificities of Vero cells in bioreactor cultures with serum-free medium *Cytotechnology* **42** 1–11
- [144] Kober L, Zehe C and Bode J 2013 Optimized signal peptides for the development of high expressing CHO cell lines *Biotechnol Bioeng* **110** 1164–73
- [145] Ruhl S, de Almeida N, Carpio M, Rupprecht J, Greller G and Matuszczyk J-C 2020 A Rapid, Low-Risk Approach for Process Transfer of Biologics from Development to Manufacturing Scale *Bioprocess Int* **19** 44–51
- [146] Reinhart D, Damjanovic L, Kaisermayer C, Sommeregger W, Gili A, Gasselhuber B, Castan A, Mayrhofer P, Grünwald-Gruber C and Kunert R 2019 Bioprocessing of Recombinant CHO-K1, CHO-DG44, and CHO-S: CHO Expression Hosts Favor Either mAb Production or Biomass Synthesis *Biotechnol J* **14** 1–11
- [147] Clincke M F, Mölleryd C, Zhang Y, Lindskog E, Walsh K and Chotteau V 2013 Very high density of CHO cells in perfusion by ATF or TFF in WAVE bioreactor<sup>TM</sup>: Part I: Effect of the cell density on the process *Biotechnol Prog* **29** 754–67
- [148] Clarke C, Henry M, Doolan P, Kelly S, Aherne S, Sanchez N, Kelly P, Kinsella P, Breen L, Madden S F, Zhang L, Leonard M, Clynes M, Meleady P and Barron N 2012 Integrated miRNA , mRNA and protein expression analysis reveals the role of post-transcriptional regulation in controlling CHO cell growth rate 1–14
- [149] Mahé A, Martiné A, Fagète S and Girod P A 2022 Exploring the limits of conventional small-scale CHO fed-batch for accelerated on demand monoclonal antibody production *Bioprocess Biosyst Eng* **45** 297–307
- [150] Cervera L, Gutiérrez S, Gòdia F and Segura M M 2011 Optimization of HEK 293 cell growth by addition of non-animal derived components using design of experiments *BMC Proc* **5** P126
- [151] Chin C L, Goh J B, Srinivasan H, Liu K I, Gowher A, Shanmugam R, Lim H L, Choo M, Tang W Q, Tan A H-M, Nguyen-Khuong T, Tan M H and Ng S K 2019 A human expression system based on HEK293 for the stable production of recombinant erythropoietin *Sci Rep* **9** 16768
- [152] Liu X M, Liu H, Wu B C, Li S C, Ye L L, Wang Q W, Huang P T and Chen Z L 2006 Suspended aggregates as an immobilization mode for high-density perfusion culture of HEK 293 cells in a stirred tank bioreactor *Appl Microbiol Biotechnol* **72** 1144–51

- [153] Liu H, Liu X M, Li S C, Wu B C, Ye L L, Wang Q W and Chen Z L 2009 A high-yield and scaleable adenovirus vector production process based on high density perfusion culture of HEK 293 cells as suspended aggregates *J Biosci Bioeng* **107** 524–9
- [154] Butler M and Thilly W G 1982 MDCK microcarrier cultures: Seeding density effects and amino acid utilization *In Vitro* **18** 213–9
- [155] Wu Y, Bissinger T, Genzel Y, Liu X, Reichl U and Tan W S 2021 High cell density perfusion process for high yield of influenza A virus production using MDCK suspension cells *Appl Microbiol Biotechnol* **105** 1421–34
- [156] Bock A, Schulze-Horsel J, Schwarzer J, Rapp E, Genzel Y and Reichl U 2011 High-density microcarrier cell cultures for influenza virus production *Biotechnol Prog* **27** 241–50
- [157] Rehberg M, Ritter J B, Genzel Y, Flockerzi D and Reichl U 2013 The relation between growth phases, cell volume changes and metabolism of adherent cells during cultivation *J Biotechnol* **164** 489–99
- [158] Kistner O, Howard K, Spruth M, Wodal W, Brühl P, Crowe B A, Savidis-dacho H, Livey I, Reiter M, Tauer C, Grillberger L, Mundt W and Falkner F G 2008 Cell culture (Vero) derived whole virus (H5N1) vaccine based on wild-type virus strain induces cross-protective immune responses **25** 6028–36
- [159] Barrett P N, Mundt W, Kistner O and Howard M K 2009 Vero cell platform in vaccine production: Moving towards cell culture-based viral vaccines *Expert Rev Vaccines* **8** 607–18
- [160] Han X, Schwinde J and Sha M 2018 High-density Vero cell perfusion culture in BioBLU 5p single-use vessels *N Biotechnol* **44** S130
- [161] Choi S K, Chang H N, Lee G M, Kim I H and Oh D J 1995 High cell density perfusion cultures of anchorage-dependent Vero cells in a depth filter perfusion system *Cytotechnology* **17** 173–83
- [162] Mendonça R Z and Pereira C A 1998 Cell metabolism and medium perfusion in VERO cell cultures on microcarriers in a bioreactor *Bioprocess Engineering* **18** 213–8
- [163] Arifin M A, Mel M, Abdul Karim M I and Ideris A 2010 Production of newcastle disease virus by vero cells grown on cytodex 1 microcarriers in a 2-litre stirred tank bioreactor *J Biomed Biotechnol* **2010**
- [164] Petiot E, Guedon E, Blanchard F, Gény C, Pinton H and Marc A 2010 Kinetic characterization of vero cell metabolism in a serum-free batch culture process *Biotechnol Bioeng* **107** 143–53
- [165] Tseng Y F, Hu A Y C, Huang M L, Yeh W Z, Weng T C, Chen Y S, Chong P and Lee M S 2011 Adaptation of high-growth influenza H5N1 vaccine virus in Vero cells: Implications for pandemic preparedness *PLoS One* **6** 3–7

- [166] Nold V, Junghans L, Bisgen L, Drerup R, Presser B, Gorr I, Schwab T, Knapp B and Wieschalka S 2022 Applying intensified design of experiments to mammalian cell culture processes *Eng Life Sci* **22** 784–95
- [167] Kumar V, Bhalla A and Rathore A S 2014 Design of experiments applications in bioprocessing: Concepts and approach *Biotechnol Prog* **30** 86–99
- [168] Mandenius C-F and Brundin A 2008 Bioprocess optimization using design-of-experiments methodology *Biotechnol Prog* **24** 1191–203
- [169] Whitford W G, Lundgren M and Fairbank A 2018 *Cell Culture Media in Bioprocessing* (Elsevier Ltd.)
- [170] Cervera L, Gutiérrez S, Gòdia F and Segura M M 2011 Optimization of HEK 293 cell growth by addition of non-animal derived components using design of experiments *BMC Proc* **5** P126
- [171] Yao T and Asayama Y 2017 Animal-cell culture media: History, characteristics, and current issues *Reprod Med Biol* **16** 99–117
- [172] Backliwal G, Hildinger M, Chenuet S, DeJesus M and Wurm F M 2008 Coexpression of acidic fibroblast growth factor enhances specific productivity and antibody titers in transiently transfected HEK293 cells *N Biotechnol* **25** 162–6
- [173] Mosser M, Chevalot I, Olmos E, Blanchard F, Kapel R, Oriol E, Marc I and Marc A 2013 Combination of yeast hydrolysates to improve CHO cell growth and IgG production *Cytotechnology* **65** 629–41
- [174] No W P 2021 Vero Cell-based Vaccine Production : Cell lines , Media and Bioreactor Options 1–9
- [175] Liste-Calleja L, Lecina M and Cairó J J 2013 HEK293 cell culture media study: increasing cell density for different bioprocess applications *BMC Proc* **7** 16–8
- [176] Schwarz H, Zhang Y, Zhan C, Malm M, Field R, Turner R, Sellick C, Varley P, Rockberg J and Chotteau V 2020 Small-scale bioreactor supports high density HEK293 cell perfusion culture for the production of recombinant Erythropoietin *J Biotechnol* **309** 44–52
- [177] Särnlund S, Jiang Y and Chotteau V 2021 Process intensification to produce a difficult-to-express therapeutic enzyme by high cell density perfusion or enhanced fed-batch *Biotechnol Bioeng* **118** 3533–44
- [178] MacDonald M A, Nöbel M, Roche Recinos D, Martínez V S, Schulz B L, Howard C B, Baker K, Shave E, Lee Y Y, Marcellin E, Mahler S, Nielsen L K and Munro T 2022 Perfusion culture of Chinese Hamster Ovary cells for bioprocessing applications *Crit Rev Biotechnol* **42** 1099–115

- [179] Reger L N, Saballus M, Kappes A, Kampmann M, Wijffels R H, Martens D E and Niemann J 2023 A novel hybrid bioprocess strategy addressing key challenges of advanced biomanufacturing *Front Bioeng Biotechnol* **11** 1–13
- [180] Lavado-García J, Pérez-Rubio P, Cervera L and Gòdia F 2022 The cell density effect in animal cell-based bioprocessing: Questions, insights and perspectives *Biotechnol Adv* **60**
- [181] Robinson D K and Memmert K W 1991 Kinetics of recombinant immunoglobulin production by mammalian cells in continuous culture *Biotechnol Bioeng* **38** 972–6
- [182] Bryan L, Henry M, Kelly R M, Lloyd M, Frye C C, Osborne M D, Clynes M and Meleady P 2021 Global phosphoproteomic study of high/low specific productivity industrially relevant mAb producing recombinant CHO cell lines *Curr Res Biotechnol* **3** 49–56
- [183] Nasser S S, Ghaffari N, Braasch K, Jardon M A, Butler M, Kennard M, Gopaluni B and Piret J M 2014 Increased CHO cell fed-batch monoclonal antibody production using the autophagy inhibitor 3-MA or gradually increasing osmolality *Biochem Eng J* **91** 37–45
- [184] Aki Y, Katsumata Y, Kakihara H, Nonaka K and Fujiwara K 2021 4-(2,5-Dimethyl-1H-pyrrol-1-yl)-N-(2,5-dioxopyrrolidin-1-yl) benzamide improves monoclonal antibody production in a Chinese hamster ovary cell culture *PLoS One* **16** 1–20
- [185] Kim M S, Kim N S, Sung Y H and Lee G M 2002 Biphasic culture strategy based on hyperosmotic pressure for improved humanized antibody production in Chinese hamster ovary cell culture *In Vitro Cell Dev Biol Anim* **38** 314–9
- [186] Hogiri T, Tamashima H, Nishizawa A and Okamoto M 2018 Optimization of a pH-shift control strategy for producing monoclonal antibodies in Chinese hamster ovary cell cultures using a pH-dependent dynamic model *J Biosci Bioeng* **125** 245–50
- [187] Kim S H, Baek M, Park S, Shin S, Lee J S and Lee G M 2022 Improving the secretory capacity of CHO producer cells: The effect of controlled Blimp1 expression, a master transcription factor for plasma cells *Metab Eng* **69** 73–86
- [188] Zhou M, Crawford Y, Ng D, Tung J, Pynn A F J, Meier A, Yuk I H, Vijayasankaran N, Leach K, Joly J, Snedecor B and Shen A 2011 Decreasing lactate level and increasing antibody production in Chinese Hamster Ovary cells (CHO) by reducing the expression of lactate dehydrogenase and pyruvate dehydrogenase kinases *J Biotechnol* **153** 27–34
- [189] Nishijima K, Fujiki T, Kojima H and Iijima S 2000 The effects of cell adhesion on the growth and protein productivity of animal cells 147–55
- [190] Peschel B, Frentzel S, Laske T, Genzel Y and Reichl U 2013 Comparison of influenza virus yields and apoptosis-induction in an adherent and a suspension MDCK cell line *Vaccine* **31** 5693–9

- [191] Gigout A, Levasseur S, Girard-Lauriault P L, Buschmann M D, Wertheimer M R and Jolicoeur M 2009 CHO cells adhering to nitrogen-rich plasma-polymerised ethylene exhibit high production of a specific recombinant protein *Macromol Biosci* **9** 979–88
- [192] Takagi M, Hayashi H and Yoshida T 2000 The effect of osmolarity on metabolism and morphology in adhesion and suspension chinese hamster ovary cells producing tissue plasminogen activator *Cytotechnology* **32** 171–9
- [193] Chevalot I, Visvikis A, Nabet P, Engasser J M and Marc A 1994 Production of a membrane-bound proteins, the human gamma-glutamyl transferase, by CHO cells cultivated on microcarriers, in aggregates and in suspension *Cytotechnology* **16** 121–9
- [194] Hutchinson L and Kirk R 2011 High drug attrition rates - Where are we going wrong? *Nat Rev Clin Oncol* **8** 189–90
- [195] Anton D, Burckel H, Josset E and Noel G 2015 Three-dimensional cell culture: A breakthrough in vivo *Int J Mol Sci* **16** 5517–27
- [196] Souza A G, Silva I B B, Campos-Fernandez E, Barcelos L S, Souza J B, Marangoni K, Goulart L R and Alonso-Goulart V 2018 Comparative Assay of 2D and 3D Cell Culture Models: Proliferation, Gene Expression and Anticancer Drug Response *Curr Pharm Des* **24** 1689–94
- [197] Edmondson R, Broglie J J, Adcock A F and Yang L 2014 Three-dimensional cell culture systems and their applications in drug discovery and cell-based biosensors *Assay Drug Dev Technol* **12** 207–18
- [198] Abugomaa A, Elbadawy M, Yamanaka M, Goto Y, Hayashi K, Mori T, Uchide T, Azakami D, Fukushima R, Yoshida T, Shibutani M, Yamashita R, Kobayashi M, Yamawaki H, Shinohara Y, Kaneda M, Usui T and Sasaki K 2020 Establishment of 2.5D organoid culture model using 3D bladder cancer organoid culture *Sci Rep* **10** 3–5
- [199] De La Zerda A, Kratochvil M J, Suhar N A and Heilshorn S C 2018 Review: Bioengineering strategies to probe T cell mechanobiology *APL Bioeng* **2** 1–27
- [200] Diering, Maxson & Mitchell and Freeman 2018 Bridging the gap: from 2D cell culture to 3D microengineered extracellular *Physiol Behav* **176** 139–48
- [201] Ravi M, Paramesh V, Kaviya S R, Anuradha E and Paul Solomon F D 2015 3D cell culture systems: Advantages and applications *J Cell Physiol* **230** 16–26
- [202] Pourchet L J, Thepot A, Albouy M, Courtial E J, Boher A, Blum L J and Marquette C A 2017 Human Skin 3D Bioprinting Using Scaffold-Free Approach *Adv Healthc Mater* **6** 1601101
- [203] Chastagnier L, El-Kholti N, Essayan L, Thomann C, Courtial E-J, Marquette C and Petiot E 2023 Deciphering dermal fibroblast behavior in 3D bioprinted dermis constructs *Bioprinting* **32** 2023.03.07.531460

- [204] Moussa H I, Logan M, Chan W Y, Wong K, Rao Z, Aucoin M G and Tsui T Y 2018 Pattern-dependent mammalian cell (Vero) morphology on tantalum/silicon oxide 3D nanocomposites *Materials* **11** 17–20
- [205] Mastro A M and Vogler E A 2009 A three-dimensional osteogenic tissue model for the study of metastatic tumor cell interactions with bone *Cancer Res* **69** 4097–100
- [206] Hynes R O 2002 Integrins: Bidirectional, Allosteric Signaling Machines *Cell Press* **110** 673–87
- [207] Klezovitch O and Vasioukhin V 2015 Cadherin signaling: Keeping cells in touch *FI000Res* **4**
- [208] Kawaue T, Yow I, Pan Y, Le A P, Lou Y, Loberas M, Shagirov M, Teng X, Prost J, Hiraiwa T, Ladoux B and Toyama Y 2023 Inhomogeneous mechanotransduction defines the spatial pattern of apoptosis-induced compensatory proliferation *Dev Cell* **58** 267-277.e5
- [209] Chagnon-Lessard S, Jean-Ruel H, Godin M and Pelling A E 2021 Mechanotransduction of Strain Regulates an Invasive Phenotype in Newly Transformed Epithelial Cells *Front Phys* **9** 1–11
- [210] Guo J, Wang Y, Sachs F and Meng F 2014 Actin stress in cell reprogramming *Proc Natl Acad Sci U S A* **111** E5252–61
- [211] Moussa H I, Logan M, Chan W Y, Wong K, Rao Z, Aucoin M G and Tsui T Y 2018 Pattern-dependent mammalian cell (Vero) morphology on tantalum/silicon oxide 3D nanocomposites *Materials* **11** 17–20
- [212] Mih J D, Marinkovic A, Liu F, Sharif A S and Tschumperlin D J 2012 Matrix stiffness reverses the effect of actomyosin tension on cell proliferation *J Cell Sci* **125** 5974–83
- [213] Chignola R, Schenetti A, Andrighetto G, Chiesa E, Foroni R, Sartoris S, Tridente G and Liberati D 2000 Forecasting the growth of multicell tumour spheroids: Implications for the dynamic growth of solid tumours *Cell Prolif* **33** 219–29
- [214] Adcock A F 2015 Three-Dimensional (3D) Cell Cultures in Cell-based Assays for in-vitro Evaluation of Anticancer Drugs *J Anal Bioanal Tech* **06**
- [215] Ikari R, Mukaisho K I, Kageyama S, Nagasawa M, Kubota S, Nakayama T, Murakami S, Taniura N, Tanaka H, Kushima R and Kawauchi A 2021 Differences in the central energy metabolism of cancer cells between conventional 2d and novel 3d culture systems *Int J Mol Sci* **22** 1–13
- [216] Shafiee A, Norotte C and Ghadiri E 2017 Cellular bioink surface tension: A tunable biophysical parameter for faster maturation of bioprinted tissue *Bioprinting* **8** 13–21
- [217] Mironov V, Prestwich G and Forgacs G 2007 Bioprinting living structures *J Mater Chem* **17** 2054–60

- [218] Jakab K, Damon B, Neagu A, Kachurin A and Forgacs G 2006 Three-dimensional tissue constructs built by bioprinting *Biorheology* **43** 509–13
- [219] Jakab K, Norotte C, Marga F, Murphy K, Vunjak-Novakovic G and Forgacs G 2010 Tissue engineering by self-assembly and bio-printing of living cells *Biofabrication* **2**
- [220] Zheng J, Liu Y, Hou C, Li Z, Yang S, Liang X, Zhou L, Guo J, Zhang J and Huang X 2022 Ovary-derived Decellularized Extracellular Matrix-based Bioink for Fabricating 3D Primary Ovarian Cells-laden Structures for Mouse Ovarian Failure Correction *Int J Bioprint* **8** 269–82
- [221] Laronda M M, Rutz A L, Xiao S, Whelan K A, Duncan F E, Roth E W, Woodruff T K and Shah R N 2017 A bioprosthesis ovary created using 3D printed microporous scaffolds restores ovarian function in sterilized mice *Nat Commun* **8** 1–10
- [222] Wu T, Gao Y Y, Su J, Tang X N, Chen Q, Ma L W, Zhang J J, Wu J M and Wang S X 2022 Three-dimensional bioprinting of artificial ovaries by an extrusion-based method using gelatin-methacryloyl bioink *Climacteric* **25** 170–8
- [223] Torban E and Goodyer P R 1998 Effects of PAX2 expression in a human fetal kidney (HEK293) cell line *Biochim Biophys Acta Mol Cell Res* **1401** 53–62
- [224] Su G, Zhao Y, Wei J, Han J, Chen L, Xiao Z, Chen B and Dai J 2013 The effect of forced growth of cells into 3D spheres using low attachment surfaces on the acquisition of stemness properties *Biomaterials* **34** 3215–22
- [225] Wong H L, Wang M X, Cheung P T, Yao K M and Chan B P 2007 A 3D collagen microsphere culture system for GDNF-secreting HEK293 cells with enhanced protein productivity *Biomaterials* **28** 5369–80
- [226] Ouyang L, Yao R, Chen X, Na J and Sun W 2015 3D printing of HEK 293FT cell-laden hydrogel into macroporous constructs with high cell viability and normal biological functions *Biofabrication* **7**
- [227] Ioannidis K, Danalatos R I, Champeris Tsaniras S, Kaplani K, Lokka G, Kanellou A, Papachristou D J, Bokias G, Lygerou Z and Taraviras S 2020 A Custom Ultra-Low-Cost 3D Bioprinter Supports Cell Growth and Differentiation *Front Bioeng Biotechnol* **8** 1–13
- [228] Hall H G, Farson D A and Bissell M J 1982 Lumen formation by epithelial cell lines in response to collagen overlay: a morphogenetic model in culture. *Proc Natl Acad Sci U S A* **79** 4672–6
- [229] Bryant D M and Mostov K E 2008 From cells to organs: Building polarized tissue *Nat Rev Mol Cell Biol* **9** 887–901
- [230] O'Brien L E, Zegers M M P and Mostov K E 2002 Building epithelial architecture: Insights from three-dimensional culture models *Nat Rev Mol Cell Biol* **3** 531–7



- [231] Brien L E O, Zegers M M P and Mostov K E 2002 Culture Models *Group (New York)* **3** 1–7
- [232] Zegers M M P, O'Brien L E, Yu W, Datta A and Mostov K E 2003 Epithelial polarity and tubulogenesis in vitro *Trends Cell Biol* **13** 169–76
- [233] Meder D, Shevchenko A, Simons K and Füllekrug J 2005 Gp135/podocalyxin and NHERF-2 participate in the formation of a preapical domain during polarization of MDCK cells *Journal of Cell Biology* **168** 303–13
- [234] O'Brien L E, Tang K, Kats E S, Schutz-Geschwender A, Lipschutz J H and Mostov K E 2004 ERK and MMPs sequentially regulate distinct stages of epithelial tubule development *Dev Cell* **7** 21–32
- [235] Hunter M P and Zegers M M 2010 Pak1 regulates branching morphogenesis in 3D MDCK cell culture by a PIX and  $\beta$ 1-integrin-dependent mechanism *Am J Physiol Cell Physiol* **299**
- [236] Gierke S and Wittmann T 2012 EB1-recruited microtubule +TIP complexes coordinate protrusion dynamics during 3D epithelial remodeling *Current Biology* **22** 753–62
- [237] Nakamura T and Mizuno S 2010 The discovery of Hepatocyte Growth Factor (HGF) and its significance for cell biology, life sciences and clinical medicine *Proc Jpn Acad Ser B Phys Biol Sci* **86** 588–610
- [238] Montesano R, Schaller G and Orci L 1991 *Induction of Epithelial Tubular Morphogenesis In Vitro by Fibroblast-Derived Soluble Factors* vol 66
- [239] Jiang S T, Chiu S J, Chen H C, Chuang W J and Tang M J 2001 Role of  $\alpha$ 3 $\beta$ 1 integrin in tubulogenesis of Madin-Darby canine kidney cells *Kidney Int* **59** 1770–8
- [240] Koban R, Lam T, Schwarz F, Kloke L, Bürge S, Ellerbrok H and Neumann M 2020 Simplified bioprinting-based 3d cell culture infection models for virus detection *Viruses* **12**
- [241] To C Z and Bhunia A K 2019 Three dimensional vero cell-platform for rapid and sensitive screening of Shiga-toxin producing Escherichia coli *Front Microbiol* **10** 1–15
- [242] Danielson J J, Perez N, Romano J D and Coppens I 2018 Modelling Toxoplasma gondii infection in a 3D cell culture system In Vitro: Comparison with infection in 2D cell monolayers *PLoS One* **13** 1–13
- [243] Nocera A D, Comín R, Salvatierra N A and Cid M P 2018 Development of 3D printed fibrillar collagen scaffold for tissue engineering *Biomed Microdevices* **20** 1–13
- [244] Naing M W and Williams D J 2011 Three-dimensional culture and bioreactors for cellular therapies *Cytotherapy* **13** 391–9
- [245] Cukierman E, Pankov R, Stevens D R and Yamada K M 2001 Taking Cell-Matrix Adhesions to the Third Dimension *Science, New Series* **294** 1708–12

- [246] Jacks T and Weinberg R A 2002 Taking the Study of Cancer Cell Survival to a New Dimension *Cell* **111** 923–5
- [247] Vig K, Chaudhari A, Tripathi S, Dixit S, Sahu R, Pillai S, Dennis V and Singh S 2017 Advances in Skin Regeneration Using Tissue Engineering *Int J Mol Sci* **18** 789
- [248] Demirtaş T T, Irmak G and Gümüşderelioğlu M 2017 A bioprintable form of chitosan hydrogel for bone tissue engineering *Biofabrication* **9**
- [249] Moncal K K, Aydin R S T, Abu-Laban M, Heo D N, Rizk E, Tucker S M, Lewis G S, Hayes D and Ozbolat I T 2019 Collagen-infilled 3D printed scaffolds loaded with miR-148b-transfected bone marrow stem cells improve calvarial bone regeneration in rats *Materials Science and Engineering C* **105** 110128
- [250] Pragnere S, El Kholti N, Gudimard L, Essayan L, Marquette C, Petiot E and Paillet-Mattei C 2022 Quantification of cell contractile behavior based on non-destructive macroscopic measurement of tension forces on bioprinted hydrogel *J Mech Behav Biomed Mater* **134** 105365
- [251] Baharvand H, Hashemi S M, Ashtiani S K and Farrokhi A 2006 Differentiation of human embryonic stem cells into hepatocytes in 2D and 3D culture systems in vitro *International Journal of Developmental Biology* **50** 645–52
- [252] Majety M, Pradel L P, Gies M and Ries C H 2015 Fibroblasts influence survival and therapeutic response in a 3D co-culture model *PLoS One* **10** 1–18
- [253] Rebelo S P, Costa R, Silva M M, Marcelino P, Brito C and Alves P M 2017 Three-dimensional co-culture of human hepatocytes and mesenchymal stem cells: improved functionality in long-term bioreactor cultures: 3D co-cultures of human hepatocytes and MSCs in bioreactors *J Tissue Eng Regen Med* **11** 2034–45
- [254] Mastro A M and Vogler E A 2009 A three-dimensional osteogenic tissue model for the study of metastatic tumor cell interactions with bone *Cancer Res* **69** 4097–100
- [255] Lawko N, Plaskasovitis C, Stokes C, Abelseth L, Fraser I, Sharma R, Kirsch R, Hasan M, Abelseth E and Willerth S M 2021 3D Tissue Models as an Effective Tool for Studying Viruses and Vaccine Development *Front Mater* **8** 1–17
- [256] Calejo I, Labrador-Rached C J, Gomez-Florit M, Docheva D, Reis R L, Domingues R M A and Gomes M E 2022 Bioengineered 3D Living Fibers as In Vitro Human Tissue Models of Tendon Physiology and Pathology *Adv Healthc Mater* **11** 1–14
- [257] Liverani C, De Vita A, Minardi S, Kang Y, Mercatali L, Amadori D, Bongiovanni A, La Manna F, Ibrahim T and Tasciotti E 2019 A biomimetic 3D model of hypoxia-driven cancer progression *Sci Rep* **9** 1–13

- [258] Candini O, Grisendi G, Foppiani E M, Brogli M, Aramini B, Masciale V, Spano C, Petrachi T, Veronesi E, Conte P, Mari G and Dominici M 2019 A Novel 3D In Vitro Platform for Pre-Clinical Investigations in Drug Testing, Gene Therapy, and Immuno-oncology *Sci Rep* **9** 1–12
- [259] Alluri R, Jakus A, Bougioukli S, Pannell W, Sugiyama O, Tang A, Shah R and Lieberman J R 2018 3D printed hyperelastic “bone” scaffolds and regional gene therapy: A novel approach to bone healing *J Biomed Mater Res A* **106** 1104–10
- [260] Rodrigues M E, Costa A R, Fernandes P, Henriques M, Cunnah P, Melton D W, Azeredo J and Oliveira R 2013 Evaluation of macroporous and microporous carriers for CHO-K1 cell growth and monoclonal antibody production *J Microbiol Biotechnol* **23** 1308–21
- [261] Ozbolat I T, Peng W and Ozbolat V 2016 Application areas of 3D bioprinting *Drug Discov Today* **21** 1257–71
- [262] Chimene D, Lennox K K, Kaunas R R and Gaharwar A K 2016 Advanced Bioinks for 3D Printing: A Materials Science Perspective *Ann Biomed Eng* **44** 2090–102
- [263] Liang W, Kienitz B L, Penick K J, Welter J F, Zawodzinski T A and Baskaran H 2010 Concentrated collagen-chondroitin sulfate scaffolds for tissue engineering applications *J Biomed Mater Res A* **94A** 1050–60
- [264] Tierney C M, Haugh M G, Liedl J, Mulcahy F, Hayes B and O’Brien F J 2009 The effects of collagen concentration and crosslink density on the biological, structural and mechanical properties of collagen-GAG scaffolds for bone tissue engineering *J Mech Behav Biomed Mater* **2** 202–9
- [265] de Melo B A G, Jodat Y A, Cruz E M, Benincasa J C, Shin S R and Porcionatto M A 2020 Strategies to use fibrinogen as bioink for 3D bioprinting fibrin-based soft and hard tissues *Acta Biomater* **117** 60–76
- [266] Fay C D 2020 Computer-Aided Design and Manufacturing (CAD/CAM) for Bioprinting *Methods in Molecular Biology* vol 2140 pp 27–41
- [267] Dufaud M, Solé L, Maumus M, Simon M, Perrier-Groult E, Subra G, Jorgensen C and Noël D 2022 3D bioprinting of articular cartilage: Recent advances and perspectives *Bioprinting* **28**
- [268] Persaud A, Maus A, Strait L and Zhu D 2022 3D Bioprinting with Live Cells *Engineered Regeneration* **3** 292–309
- [269] Murphy S V. and Atala A 2014 3D bioprinting of tissues and organs *Nat Biotechnol* **32** 773–85
- [270] Li X, Zheng F, Wang X, Geng X, Zhao S, Liu H, Dou D, Leng Y, Wang L and Fan Y 2022 Biomaterial inks for extrusion-based 3D bioprinting: Property, classification, modification, and selection *Int J Bioprint* **9** 649

- [271] Lemarié L, Anandan A, Petiot E, Marquette C and Courtial E-J 2021 Rheology, simulation and data analysis toward bioprinting cell viability awareness *Bioprinting* **21**
- [272] Schwab A, Levato R, Este M D, Piluso S, Eglin D, Malda J, D'Este M, Piluso S, Eglin D and Malda J 2020 Printability and Shape Fidelity of Bioinks in 3D Bioprinting *Chem Rev* **120** 11028–55
- [273] Hospodiuk M, Dey M, Sosnoski D and Ozbolat I T 2017 The bioink: A comprehensive review on bioprintable materials *Biotechnol Adv* **35** 217–39
- [274] Mouser V H M, Melchels F P W, Visser J, Dhert W J A, Gawlitta D and Malda J 2016 Yield stress determines bioprintability of hydrogels based on gelatin-methacryloyl and gellan gum for cartilage bioprinting *Biofabrication* **8** 1–24
- [275] Nogueira L F B, Maniglia B C, Buchet R, Millán J L, Ciancaglini P, Bottini M and Ramos A P 2022 Three-dimensional cell-laden collagen scaffolds: From biochemistry to bone bioengineering *J Biomed Mater Res B Appl Biomater* **110** 967–83
- [276] Osidak E O, Kozhukhov V I, Osidak M S and Domogatsky S P 2020 Collagen as bioink for bioprinting: A comprehensive review *Int J Bioprint* **6** 1–10
- [277] Yang X, Lu Z, Wu H, Li W, Zheng L and Zhao J 2018 Collagen-alginate as bioink for three-dimensional (3D) cell printing based cartilage tissue engineering *Materials Science and Engineering C* **83** 195–201
- [278] Shi Y, Xing T L, Zhang H B, Yin R X, Yang S M, Wei J and Zhang W J 2018 Tyrosinase-doped bioink for 3D bioprinting of living skin constructs *Biomedical Materials (Bristol)* **13**
- [279] Pourchet L, Petiot E, Loubière C, Olmos E, Dos Santos M, Thépot A, Loïc B J and Marquette C A 2019 Large 3D bioprinted tissue: Heterogeneous perfusion and vascularization *Bioprinting* **13** e00039
- [280] Marquette C A, Pourchet L, Thepot A and Dos Santos M 2016 Method for manufacturing body substitutes by additive deposition
- [281] Ricard-Blum S 2011 The Collagen Family *Cold Spring Harb Perspect Biol* **3** a004978–a004978
- [282] Poppe J 1992 Gelatin *Thickening and Gelling Agents for Food* (Boston, MA: Springer US) pp 98–123
- [283] Naomi R, Ridzuan P M and Bahari H 2021 Current insights into collagen type I *Polymers (Basel)* **13** 1–19
- [284] Sarika P R, James N R, Anil kumar P R and Raj D K 2016 Preparation, characterization and biological evaluation of curcumin loaded alginate aldehyde–gelatin nanogels *Materials Science and Engineering C* **68** 251–7

- [285] Desanlis A, Albouy M, Rousselle P, Thépot A, Santos M Dos, Auxenfans C and Marquette C 2021 Validation of an implantable bioink using mechanical extraction of human skin cells: First steps to a 3D bioprinting treatment of deep second degree burn *J Tissue Eng Regen Med* **15** 37–48
- [286] Yue K, Trujillo-de Santiago G, Alvarez M M, Tamayol A, Annabi N and Khademhosseini A 2015 Synthesis, properties, and biomedical applications of gelatin methacryloyl (GelMA) hydrogels *Biomaterials* **73** 254–71
- [287] Van Den Bulcke A I, Bogdanov B, De Rooze N, Schacht E H, Cornelissen M and Berghmans H 2000 Structural and rheological properties of methacrylamide modified gelatin hydrogels *Biomacromolecules* **1** 31–8
- [288] Xiang L and Cui W 2021 Biomedical application of photo-crosslinked gelatin hydrogels *Journal of Leather Science and Engineering* **3**
- [289] Han Y, Yang J, Zhao W, Wang H, Sun Y, Chen Y, Luo J, Deng L, Xu X, Cui W and Zhang H 2021 Biomimetic injectable hydrogel microspheres with enhanced lubrication and controllable drug release for the treatment of osteoarthritis *Bioact Mater* **6** 3596–607
- [290] Lv B, Lu L, Hu L, Cheng P, Hu Y, Xie X, Dai G, Mi B, Liu X and Liu G 2023 Recent advances in GelMA hydrogel transplantation for musculoskeletal disorders and related disease treatment *Theranostics* **13** 2015–39
- [291] Kilic Bektas C and Hasirci V 2020 Cell loaded 3D bioprinted GelMA hydrogels for corneal stroma engineering *Biomater Sci* **8** 438–49
- [292] Nguyen A K, Goering P L, Reipa V and Narayan R J 2019 Toxicity and photosensitizing assessment of gelatin methacryloyl-based hydrogels photoinitiated with lithium phenyl-2,4,6-trimethylbenzoylphosphinate in human primary renal proximal tubule epithelial cells *Biointerphases* **14** 1–8
- [293] Bertoni F, Barbani N, Giusti P and Ciardelli G 2006 Transglutaminase reactivity with gelatine: Perspective applications in tissue engineering *Biotechnol Lett* **28** 697–702
- [294] Pragnere S, El Kholti N, Gudimard L, Essayan L, Marquette C, Petiot E and Pailier-Mattei C 2022 Quantification of cell contractile behavior based on non-destructive macroscopic measurement of tension forces on bioprinted hydrogel *J Mech Behav Biomed Mater* **134** 105365
- [295] Marquette C, Petiot E, Chastagnier L, Cherblanc A, Dos Santos M, Thepot A and Godet B 2022 Procédé de consolidation d'un hydrogel alginate/gelatine; Patent Number WO2022269214A1
- [296] Hoang Thi T T, Lee Y, Le Thi P and Park K D 2019 Engineered horseradish peroxidase-catalyzed hydrogels with high tissue adhesiveness for biomedical applications *Journal of Industrial and Engineering Chemistry* **78** 34–52

- [297] Asim S, Tabish T A, Liaqat U, Ozbolat I T and Rizwan M 2023 Advances in Gelatin Bioinks to Optimize Bioprinted Cell Functions *Adv Healthc Mater* **2203148** 1–23
- [298] Heino J 2007 The collagen family members as cell adhesion proteins *BioEssays* **29** 1001–10
- [299] Taubenberger A, Cisneros D A, Friedrichs J, Puech P H, Muller D J and Franz C M 2007 Revealing early steps of  $\alpha 2\beta 1$  integrin-mediated adhesion to collagen type I by using single-cell force spectroscopy *Mol Biol Cell* **18**
- [300] Ma Y, De Castro Brás L E, Toba H, Iyer R P, Hall M E, Winniford M D, Lange R A, Tyagi S C and Lindsey M L 2014 Myofibroblasts and the extracellular matrix network in post-myocardial infarction cardiac remodeling *Pflugers Arch* **466** 1113–27
- [301] Yabluchanskiy A, Ma Y, Iyer R P, Hall M E and Lindsey M L 2013 Matrix metalloproteinase-9: Many shades of function in cardiovascular disease *Physiology* **28** 391–403
- [302] Liu C H and Wu P S 2006 Characterization of matrix metalloproteinase expressed by human embryonic kidney cells *Biotechnol Lett* **28** 1725–30
- [303] Elliott P, Hohmann A and Spanos J 2003 Protease expression in the supernatant of Chinese Hamster Ovary cells grown in serum-free culture *Biotechnol Lett* **25** 1949–52
- [304] Jordà M, Olmeda D, Vinyals A, Valero E, Cubillo E, Llorens A, Cano A and Fabra À 2005 Upregulation of MMP-9 in MDCK epithelial cell line in response to expression of the Snail transcription factor *J Cell Sci* **118** 3371–85
- [305] Yeo S J, Kim S J, Kim J H, Lee H J and Kook Y H 1999 Influenza A virus infection modulates the expression of type IV collagenase in epithelial cells *Arch Virol* **144** 1361–70
- [306] Kokol V, Pottathara Y B, Mihelčič M and Perše L S 2021 Rheological properties of gelatine hydrogels affected by flow- and horizontally-induced cooling rates during 3D cryo-printing *Colloids Surf A Physicochem Eng Asp* **616**
- [307] Liu W, Heinrich M A, Zhou Y, Akpek A, Hu N, Liu X, Guan X, Zhong Z, Jin X, Khademhosseini A and Zhang Y S 2017 Extrusion Bioprinting of Shear-Thinning Gelatin Methacryloyl Bioinks *Adv Healthc Mater* **6** 1–11
- [308] Lee K Y and Mooney D J 2012 Alginate: Properties and biomedical applications *Progress in Polymer Science (Oxford)* **37** 106–26
- [309] Ertesvåg H 2015 Alginate-modifying enzymes: Biological roles and biotechnological uses *Front Microbiol* **6** 1–10
- [310] Hassan R M 1993 Alginate polyelectrolyte Ionotropic gels. XIII geometrical aspects for chelation in metal alginate complexes related to their physico-chemical properties *Polym Int* **31** 81–6

- [311] LeRoux M A, Guilak F and Setton L A 1999 Compressive and shear properties of alginate gel: Effects of sodium ions and alginate concentration *J Biomed Mater Res* **47** 46–53
- [312] Iskandar L, Rojo L, Di Silvio L and Deb S 2019 The effect of chelation of sodium alginate with osteogenic ions, calcium, zinc, and strontium *J Biomater Appl* **34** 573–84
- [313] Zhang X, Wang X, Fan W, Liu Y, Wang Q and Weng L 2022 Fabrication, Property and Application of Calcium Alginate Fiber: A Review *Polymers (Basel)* **14**
- [314] Jiang T, Munguia-Lopez J G, Flores-Torres S, Grant J, Vijayakumar S, Leon-Rodriguez A De and Kinsella J M 2017 Directing the Self-Assembly of Tumour Spheroids by Bioprinting Cellular Heterogeneous Models within Alginate/Gelatin Hydrogels *Sci Rep* **7** 1–9
- [315] Sakai S and Kawakami K 2007 Synthesis and characterization of both ionically and enzymatically cross-linkable alginate *Acta Biomater* **3** 495–501
- [316] Thakur A, Sengupta R, Matsui H, Lillicrap D, Jones K and Hortelano G 2010 Characterization of viability and proliferation of alginate-poly-L-lysine- alginate encapsulated myoblasts using flow cytometry *J Biomed Mater Res B Appl Biomater* **94** 296–304
- [317] Nemati S, Alizadeh Sardroud H, Baradar Khoshfetrat A, Khaksar M, Ahmadi M, Amini H, Saberianpour S, Delkhosh A, Akbar Movassaghpour A and Rahbarghazi R 2019 The effect of alginate–gelatin encapsulation on the maturation of human myelomonocytic cell line U937 *J Tissue Eng Regen Med* **13** 25–35
- [318] Gonzalez-Pujana A, Rementeria A, Blanco F J, Igartua M, Pedraz J L, Santos-Vizcaino E and Hernandez R M 2017 The role of osmolarity adjusting agents in the regulation of encapsulated cell behavior to provide a safer and more predictable delivery of therapeutics *Drug Deliv* **24** 1654
- [319] Attia N, Santos E, Abdelmouty H, Arafa S, Zohdy N, Hernández R M, Orive G and Pedraz J L 2014 Behaviour and ultrastructure of human bone marrow-derived mesenchymal stem cells immobilised in alginate-poly-l-lysine-alginate microcapsules *J Microencapsul* **31** 579–89
- [320] Thiang Yian Wong, Preston L A and Schiller N L 2000 Alginate lyase: Review of major sources and enzyme characteristics, structure-function analysis, biological roles, and applications *Annu Rev Microbiol* **54** 289–340
- [321] Kattula S, JR B and Wolberg AS 2017 Fibrinogen and fibrin in hemostasis and thrombosis *Arterioscler Thromb Vasc Biol* **37** e13–21
- [322] Melo B A G De, Jodat Y A, Mehrotra S, Calabrese M A, Kamperman T, Mandal B B, Santana M H A, Alsberg E and Leijten J 2019 3D Printed Cartilage-Like Tissue Constructs with Spatially Controlled Mechanical Properties **1906330** 1–13

- [323] Poole L G, Kopec A K, Flick M J and Luyendyk J P 2022 Cross-linking by tissue transglutaminase-2 alters fibrinogen-directed macrophage proinflammatory activity *Journal of Thrombosis and Haemostasis* **20** 1182–92
- [324] Midwood K S and Schwarzbauer J E 2002 Tenascin-C modulates matrix contraction via focal adhesion kinase- and Rho-mediated signaling pathways. *Mol Biol Cell* **13** 3601–13
- [325] Kular J K, Basu S and Sharma R I 2014 The extracellular matrix: Structure, composition, age-related differences, tools for analysis and applications for tissue engineering *J Tissue Eng* **5**
- [326] Ahmed T A E, Griffith M and Hincke M 2007 Characterization and Inhibition of Fibrin Hydrogel–Degrading Enzymes During Development of Tissue Engineering Scaffolds *Tissue Eng* **13** 1469–77
- [327] Li Y, Meng H, Liu Y and Lee B P 2015 Fibrin Gel as an Injectable Biodegradable Scaffold and Cell Carrier for Tissue Engineering **2015**
- [328] Hotary K B, Yana I, Sabeh F, Li X, Holmbeck K, Birkedal-hansen H, Allen E D, Hiraoka N and Weiss S J 2002 Matrix Metalloproteinases ( MMPs ) Regulate Fibrin-invasive Activity via MT1-MMP – dependent and – independent Processes **195**
- [329] Yuet M K, Zhang J, Zhou S, Cheung C, Doberstein K, Samper V, Yu H, Khong Y M, Zhang J, Zhou S, Cheung C, Doberstein K, Samper V and Yu H 2007 Novel Intra-Tissue Perfusion System for Culturing Thick Liver Tissue *Tissue Eng* **13** 2345–56
- [330] Mazio C, Casale C, Imperato G, Urciuolo F, Attanasio C, De Gregorio M, Rescigno F and Netti P A 2019 Pre-vascularized dermis model for fast and functional anastomosis with host vasculature *Biomaterials* **192** 159–70
- [331] Chen H C and Hu Y C 2006 Bioreactors for tissue engineering *Biotechnol Lett* **28** 1415–23
- [332] Plunkett N and O’Brien F J 2011 Bioreactors in tissue engineering *Technology and Health Care* **19** 55–69
- [333] Dermenoudis S and Missirlis Y F 2010 Bioreactors in tissue engineering *Adv Eng Mater* **12**
- [334] Concaro S, Gustavson F and Gatenholm P 2008 Bioreactors for Tissue Engineering of Cartilage *Bioreactor Systems for Tissue Engineering II*
- [335] Margolis L, Hatfill S, Chuaqui R, Vocke C, Emmert-Buck M, Lineman W M and Duray P H 1999 Long term organ culture of human prostate tissue in a NASA-designed rotating wall bioreactor *Journal of Urology* **161** 290–7
- [336] Asnaghi M A, Jungebluth P, Raimondi M T, Dickinson S C, Rees L E N, Go T, Cogan T A, Dodson A, Parnigotto P P, Hollander A P, Birchall M A, Conconi M T, Macchiarini P and



- Mantero S 2009 A double-chamber rotating bioreactor for the development of tissue-engineered hollow organs: From concept to clinical trial *Biomaterials* **30** 5260–9
- [337] Lin C H, Hsu S hui, Huang C E, Cheng W T and Su J M 2009 A scaffold-bioreactor system for a tissue-engineered trachea *Biomaterials* **30** 4117–26
- [338] Navarro J, Santoro M, Swayambunathan J, Mikos A G, Janes M E and Fisher J P 2019 Dual - chambered membrane bioreactor for coculture of stratified cell populations
- [339] Zohar B, Blinder Y, Mooney D J and Levenberg S 2018 Flow-Induced Vascular Network Formation and Maturation in Three-Dimensional Engineered Tissue *ACS Biomater Sci Eng* **4** 1265–71
- [340] Heng J, Mozhi A, Davoodi P, Ramasamy S, Fuh J Y H, Liou Y and Wang C 2019 Investigation of the application of a Taylor-Couette bioreactor in the post- processing of bioprinted human dermal tissue *Biochem Eng J* **151** 107317
- [341] Salerno S, Curcio E, Bader A, Giorno L, Drioli E and De Bartolo L 2018 Gas permeable membrane bioreactor for the co-culture of human skin derived mesenchymal stem cells with hepatocytes and endothelial cells *J Memb Sci* **563** 694–707
- [342] Lovett M, Rockwood D, Baryshyan A and Kaplan D L 2010 Simple modular bioreactors for tissue engineering: A system for characterization of oxygen gradients, human mesenchymal stem cell differentiation, and prevascularization *Tissue Eng Part C Methods* **16** 1565–73
- [343] Weyand B, Israelowitz M, Schroeder H P and Vogt P M 2008 Fluid Dynamics in Bioreactor Design: Considerations for the Theoretical and Practical Approach *Advances in biochemical engineering/biotechnology* vol 123 pp 127–41
- [344] Pu F, Rhodes N P, Bayon Y, Chen R, Brans G, Benne R and Hunt J A 2010 The use of flow perfusion culture and subcutaneous implantation with fibroblast-seeded PLLA-collagen 3D scaffolds for abdominal wall repair *Biomaterials* **31** 4330–40
- [345] Gugerell A, Neumann A, Kober J, Tammaro L, Hoch E, Schnabelrauch M, Kamolz L, Kasper C and Keck M 2015 Adipose-derived stem cells cultivated on electrospun l-lactide/glycolide copolymer fleece and gelatin hydrogels under flow conditions - Aiming physiological reality in hypodermis tissue engineering *Burns* **41** 163–71
- [346] Raredon M S B, Rocco K A, Gheorghe C P, Sivarapatna A, Ghaedi M, Balestrini J L, Raredon T L, Calle E A and Niklason L E 2016 Biomimetic Culture Reactor for Whole-Lung Engineering *Biores Open Access* **5** 72–83
- [347] Zhao F and Ma T 2005 Perfusion bioreactor system for human mesenchymal stem cell tissue engineering: Dynamic cell seeding and construct development *Biotechnol Bioeng* **91** 482–93

- [348] Gauvin R, Parenteau-Bareil R, Larouche D, Marcoux H, Bisson F, Bonnet A, Auger F A, Bolduc S and Germain L 2011 Dynamic mechanical stimulations induce anisotropy and improve the tensile properties of engineered tissues produced without exogenous scaffolding *Acta Biomater* **7** 3294–301
- [349] Wolchok J C, Brokopp C, Underwood C J and Tresco P A 2009 The effect of bioreactor induced vibrational stimulation on extracellular matrix production from human derived fibroblasts *Biomaterials* **30** 327–35
- [350] Schmelzer E, Triolo F, Turner M E, Thompson R L, Zeilinger K, Reid L M, Gridelli B and Gerlach J C 2010 Three-Dimensional Perfusion Bioreactor Culture Supports Differentiation of Human Fetal Liver Cells *Tissue Eng Part A* **16** 2007–16
- [351] Pazzano D, Mercier K A, Moran J M, Fong S S, DiBiasio D D, Rulfs J X, Kohles S S and Bonassar L J 2000 Comparison of Chondrogenesis in Static and Perfused Bioreactor Culture *Biotechnol Prog* **16** 893–6
- [352] Chastagnier L, Marquette C and Petiot E 2023 In situ transient transfection of 3D cell cultures and tissues, a promising tool for tissue engineering and gene therapy *Biotechnol Adv* **68** 108211
- [353] Kim D H, Saetrom P, Snøve O and Rossi J J 2008 MicroRNA-directed transcriptional gene silencing in mammalian cells
- [354] Liu J, Schuff-Werner P and Steiner M 2004 Double transfection improves small interfering RNA-induced thrombin receptor (PAR-1) gene silencing in DU 145 prostate cancer cells *FEBS Lett* **577** 175–80
- [355] Kang M A, Young K, Ji K, Seol Y, Chan K, Myeong K, Nam J and Nam M J 2000 The growth inhibition of hepatoma by gene transfer of antisense vascular endothelial growth factor
- [356] Jaenisch R and Mintz B 1974 Simian virus 40 DNA sequences in DNA of healthy adult mice derived from preimplantation blastocysts injected with viral DNA *Proc Natl Acad Sci U S A* **71** 1250–4
- [357] Gordon J W, Scangos G A, Plotkin D J, Barbosa J A and Ruddle F H 1980 Genetic transformation of mouse embryos by microinjection of purified DNA *Proc Natl Acad Sci U S A* **77** 7380–4
- [358] Raes L, De Smedt S C, Raemdonck K and Braeckmans K 2021 Non-viral transfection technologies for next-generation therapeutic T cell engineering *Biotechnol Adv* **49** 107760
- [359] Rita Costa A, Elisa Rodrigues M, Henriques M, Azeredo J and Oliveira R 2010 Guidelines to cell engineering for monoclonal antibody production *European Journal of Pharmaceutics and Biopharmaceutics* **74** 127–38

- [360] Miyake M, Yoshikawa T, Fujita S and Miyake J 2009 Transfection microarray<sup>TM</sup> and the applications *Mol Biosyst* **5** 444–9
- [361] Okita K, Nakagawa M, Hyenjong H, Ichisaka T and Yamanaka S 2008 Generation of mouse induced pluripotent stem cells without viral vectors *Science (1979)* **322** 949–53
- [362] Yang F, Cho S W, Son S M, Bogatyrev S R, Singh D, Green J J, Mei Y, Park S, Bhang S H, Kim B S, Langer R and Anderson D G 2010 Genetic engineering of human stem cells for enhanced angiogenesis using biodegradable polymeric nanoparticles *Proc Natl Acad Sci U S A* **107** 3317–22
- [363] Cross, Sarah J. Linker, Kay E. Leslie F M 2016 Pkm2 regulates cardiomyocyte cell cycle and promotes cardiac regeneration *Physiol Behav* **176** 100–106
- [364] SZYBALSKA E H and SZYBALSKI W 1962 Genetics of human cress line. IV. DNA-mediated heritable transformation of a biochemical trait. *Proc Natl Acad Sci U S A* **48** 2026–34
- [365] Szybalski W 2013 The 50th anniversary of gene therapy: Beginnings and present realities *Gene* **525** 151–4
- [366] Jackson D a, H. R and Berg P 1972 Biochemical Method for Inserting New Genetic Information into DNA of *Nature* **69** 2904–9
- [367] Cohen S N, Chang A C Y, Boyer H W and Helling R B 1973 Construction of biologically functional bacterial plasmids in vitro *Proc Natl Acad Sci U S A* **70** 3240–4
- [368] Capecchi M R 1980 High efficiency transformation by direct microinjection of DNA into cultured mammalian cells *Cell* **22** 479–88
- [369] Mellott A J, Forrest M L and Detamore M S 2013 Physical non-viral gene delivery methods for tissue engineering *Ann Biomed Eng* **41** 446–68
- [370] Narayanan R, Jastreboff M M, Chiu C F and Bertino J R 1986 In vivo expression of a nonselected gene transferred into murine hematopoietic stem cells by electroporation *Biochem Biophys Res Commun* **141** 1018–24
- [371] Kurata S I, Tsukakoshi M, Kasuya T and Ikawa Y 1986 The laser method for efficient introduction of foreign DNA into cultured cells *Exp Cell Res* **162** 372–8
- [372] Tao W, Wilkinson J, Stanbridge E J and Berns M W 1987 Direct gene transfer into human cultured cells facilitated by laser micropuncture of the cell membrane *Proc Natl Acad Sci U S A* **84** 4180–4
- [373] Ramamoorth M and Narvekar A 2015 Non viral vectors in gene therapy - An overview *Journal of Clinical and Diagnostic Research* **9** GE01–6

- [374] Wang W, Li W, Ma N and Steinhoff G 2013 Non-Viral Gene Delivery Methods *Curr Pharm Biotechnol* **14** 46–60
- [375] Medina-Kauwe L K, Xie J and Hamm-Alvarez S 2005 Intracellular trafficking of nonviral vectors *Gene Ther* **12** 1734–51
- [376] Bus T, Traeger A and Schubert U S 2018 The great escape: How cationic polyplexes overcome the endosomal barrier *J Mater Chem B* **6** 6904–18
- [377] Tsoncheva V L, Todorova K A, Ivanov I G and Maximova V A 2005 Spontaneous transfection of mammalian cells with plasmid DNA *Zeitschrift fur Naturforschung - Section C Journal of Biosciences* **60** 644–8
- [378] Middaugh C R and Ramsey J B 2007 Analysis of cationic-lipid-plasmid-DNA complexes *Anal Chem* **79** 7240–8
- [379] Chen C and Okayama H 1987 High-efficiency transformation of mammalian cells by plasmid DNA *Mol Cell Biol* **7** 2745–52
- [380] Orrantia E and Chang P L 1990 Intracellular distribution of DNA internalized through calcium phosphate precipitation *Exp Cell Res* **190** 170–4
- [381] Milman G and Herzberg M 1982 Efficient DNA transfection and rapid assay for thymidine kinase activity and viral antigenic determinants *Somatic Cell Genet* **7** 161–70
- [382] Chaney W G, Howard D R, Pollard J W, Sallustio S and Stanley P 1986 High-frequency transfection of CHO cells using polybrene *Somat Cell Mol Genet* **12** 237–44
- [383] Schaefer-Ridder M, Wang Y and Hofschneider P H 1982 Liposomes as gene carriers: Efficient transformation of mouse L cells by thymidine kinase gene *Science (1979)* **215** 166–8
- [384] Hunt M A, Currie M J, Robinson B A and Dachs G U 2010 Optimizing transfection of primary human umbilical vein endothelial cells using commercially available chemical transfection reagents *Journal of Biomolecular Techniques* **21** 66–72
- [385] Rejman J, Bragonzi A and Conese M 2005 Role of clathrin- and caveolae-mediated endocytosis in gene transfer mediated by lipo- and polyplexes *Molecular Therapy* **12** 468–74
- [386] Van Der Aa M A E M, Huth U S, Häfele S Y, Schubert R, Oosting R S, Mastrobattista E, Hennink W E, Peschka-Süss R, Koning G A and Crommelin D J A 2007 Cellular uptake of cationic polymer-DNA complexes via caveolae plays a pivotal role in gene transfection in COS-7 cells *Pharm Res* **24** 1590–8
- [387] Boussif O, Lezoual C H F, Zanta M A, Mergny M D, Scherman D, Demeneix B and Behr J P 1995 A versatile vector for gene and oligonucleotide transfer into cells in culture and in vivo: Polyethylenimine *Proc Natl Acad Sci U S A* **92** 7297–301

- [388] Douglas K L, Piccirillo C A and Tabrizian M 2008 Cell line-dependent internalization pathways and intracellular trafficking determine transfection efficiency of nanoparticle vectors *European Journal of Pharmaceutics and Biopharmaceutics* **68** 676–87
- [389] Joshee N, Bastola D R and Cheng P W 2002 Transferrin-facilitated lipofection gene delivery strategy: Characterization of the transfection complexes and intracellular trafficking *Hum Gene Ther* **13** 1991–2004
- [390] O’Neill M J, Guo J, Byrne C, Darcy R and O’Driscoll C M 2011 Mechanistic studies on the uptake and intracellular trafficking of novel cyclodextrin transfection complexes by intestinal epithelial cells *Int J Pharm* **413** 174–83
- [391] Gillard M, Jia Z, Hou J J C, Song M, Gray P P, Munro T P and Monteiro M J 2014 Intracellular trafficking pathways for nuclear delivery of plasmid DNA complexed with highly efficient endosome escape polymers *Biomacromolecules* **15** 3569–76
- [392] Hoffmann M, Hersch N, Gerlach S, Dreissen G, Springer R, Merkel R, Csiszár A and Hoffmann B 2020 Complex size and surface charge determine nucleic acid transfer by fusogenic liposomes *Int J Mol Sci* **21**
- [393] Elouahabi A, Thiry M, Pector V, Ruyschaert J M and Vandenbranden M 2003 Calorimetry of cationic liposome-DNA complex and intracellular visualization of the complexes *Methods Enzymol* **373** 313–32
- [394] Zhou X and Huang L 1994 DNA transfection mediated by cationic liposomes containing lipopolylysine: characterization and mechanism of action *Biochim Biophys Acta* **1189** 195–203
- [395] Elouahabi A and Ruyschaert J M 2005 Formation and intracellular trafficking of lipoplexes and polyplexes *Molecular Therapy* **11** 336–47
- [396] Bus T, Englert C, Reifarth M, Borchers P, Hartlieb M, Vollrath A, Hoepfener S, Traeger A and Schubert U S 2017 3Rd Generation Poly(Ethylene Imine)S for Gene Delivery *J Mater Chem B* **5** 1258–74
- [397] Bao S, Thrall B D and Miller D L 1997 Transfection of a reporter plasmid into cultured cells by sonoporation in vitro *Ultrasound Med Biol* **23** 953–9
- [398] Matsuno Y, Iwata H, Umeda Y, Takagi H, Mori Y, Miyazaki J I, Kosugi A and Hirose H 2003 Nonviral Gene Gun Mediated Transfer into the Beating Heart *ASAIO Journal* **49** 641–4
- [399] Potter H, Weir L and Leder P 1984 Enhancer-dependent expression of human  $\kappa$  immunoglobulin genes introduced into mouse pre-B lymphocytes by electroporation *Proc Natl Acad Sci U S A* **81** 7161–5
- [400] Huber P E and Pfisterer P 2000 In vitro and in vivo transfection of plasmid DNA in the Dunning prostate tumor R3327-AT1 is enhanced by focused ultrasound *Gene Ther* **7** 1516–25

- [401] Zhu Q, Hamilton M, Vasquez B and He M 2019 3D-printing enabled micro-assembly of a microfluidic electroporation system for 3D tissue engineering *Lab Chip* **19** 2362–72
- [402] Cui X, Dean D, Ruggeri Z M and Boland T 2010 Cell damage evaluation of thermal inkjet printed chinese hamster ovary cells *Biotechnol Bioeng* **106** 963–9
- [403] Yamashita Y I, Shimada M, Tachibana K, Harimoto N, Tsujita E, Shirabe K, Miyazaki J I and Sugimachi K 2002 In vivo gene transfer into muscle via electro-sonoporation *Hum Gene Ther* **13** 2079–84
- [404] Reilly M J, Larsen J D and Sullivan M O 2012 Polyplexes traffic through caveolae to the Golgi and endoplasmic reticulum en route to the nucleus *Mol Pharm* **9** 1280–90
- [405] Vaughan E E and Dean D A 2006 Intracellular trafficking of plasmids during transfection is mediated by microtubules *Molecular Therapy* **13** 422–8
- [406] Pelkmans L, Bü T, Zerial M and Helenius A 2004 Caveolin-Stabilized Membrane Domains as Multifunctional Transport and Sorting Devices in Endocytic Membrane Traffic Other Rab GTPases of early and recycling endosomes are segregated into distinct membrane domains that display different biochemical composition *Cell* **118** 767–80
- [407] Parton R G 2004 Caveolae meet endosomes: A stable relationship? *Dev Cell* **7** 458–60
- [408] DiCiccio J E and Steinberg B E 2011 Lysosomal pH and analysis of the counter ion pathways that support acidification *Journal of General Physiology* **137** 385–90
- [409] Farhood H, Serbina N and Huang L 1995 The role of dioleoyl phosphatidylethanolamine in cationic liposome mediated gene transfer *BBA - Biomembranes* **1235** 289–95
- [410] Avital Y Y, Grønbech-Jensen N and Farago O 2016 The thermodynamics of endosomal escape and DNA release from lipoplexes *Physical Chemistry Chemical Physics* **18** 2591–6
- [411] Caracciolo G, Caminiti R, Digman M A, Gratton E and Sanchez S 2009 Efficient escape from endosomes determines the superior efficiency of multicomponent lipoplexes *Journal of Physical Chemistry B* **113** 4995–7
- [412] Pollard H, Toumaniantz G, Amos J L, Avet-Loiseau H, Guihard G, Behr J P and Escande D 2001 Ca<sup>2+</sup>-sensitive cytosolic nucleases prevent efficient delivery to the nucleus of injected plasmids *Journal of Gene Medicine* **3** 153–64
- [413] Lechardeur D, Sohn K J, Haardt M, Joshi P B, Monck M, Graham R W, Beatty B, Squire J, O’Brodvich H and Lukacs G L 1999 Metabolic instability of plasmid DNA in the cytosol: A potential barrier to gene transfer *Gene Ther* **6** 482–97

- [414] Lukacs G L, Haggie P, Seksek O, Lechardeur D, Freedman N and Verkman A S 2000 Size-dependent DNA mobility in cytoplasm and nucleus *Journal of Biological Chemistry* **275** 1625–9
- [415] Dauty E and Verkman A S 2005 Actin cytoskeleton as the principal determinant of size-dependent DNA mobility in cytoplasm: A new barrier for non-viral gene delivery *Journal of Biological Chemistry* **280** 7823–8
- [416] Vaughan E, DeGiulio J and Dean D 2006 Intracellular Trafficking of Plasmids for Gene Therapy: Mechanisms of Cytoplasmic Movement and Nuclear Import *Curr Gene Ther* **6** 671–81
- [417] Collot M, Louvard D and Singer S J 1984 Lysosomes are associated with microtubules and not with intermediate filaments in cultured fibroblasts *Proc Natl Acad Sci U S A* **81** 788–92
- [418] Matteoni R and Kreis T E 1987 Translocation and clustering of endosomes and lysosomes depends on microtubules *Journal of Cell Biology* **105** 1253–65
- [419] Granger E, McNee G, Allan V and Woodman P 2014 The role of the cytoskeleton and molecular motors in endosomal dynamics *Semin Cell Dev Biol* **31** 20–9
- [420] Cardarelli F, Digiacomio L, Marchini C, Amici A, Salomone F, Fiume G, Rossetta A, Gratton E, Pozzi D and Caracciolo G 2016 The intracellular trafficking mechanism of Lipofectamine-based transfection reagents and its implication for gene delivery *Sci Rep* **6** 1–8
- [421] Lechardeur D, Verkman A S and Lukacs G L 2005 Intracellular routing of plasmid DNA during non-viral gene transfer *Adv Drug Deliv Rev* **57** 755–67
- [422] Maurisse R, De Semir D, Enamekhoo H, Bedayat B, Abdolmohammadi A, Parsi H and Gruenert D C 2010 Comparative transfection of DNA into primary and transformed mammalian cells from different lineages *BMC Biotechnol* **10** 1–9
- [423] Escriou V, Ciolina C, Lacroix F, Byk G, Scherman D and Wils P 1998 Cationic lipid-mediated gene transfer: Effect of serum on cellular uptake and intracellular fate of lipopolyamine/DNA complexes *Biochim Biophys Acta Biomembr* **1368** 276–88
- [424] Misra S K, Biswas J, Kondaiah P and Bhattacharya S 2013 Gene Transfection in High Serum Levels: Case Studies with New Cholesterol Based Cationic Gemini Lipids *PLoS One* **8**
- [425] Blagoev B and Pandey A 2001 Microarrays go live - New prospects for proteomics *Trends Biochem Sci* **26** 639–41
- [426] Mousses S, Kallioniemi A, Kauraniemi P, Elkahloun A and Kallioniemi O P 2002 Clinical and functional target validation using tissue and cell microarrays *Curr Opin Chem Biol* **6** 97–101

- [427] Ziauddin J and Sabatini D M 2001 Microarrays of cells expressing defined cDNAs. *Nature* **411** 107
- [428] Reinisalo M, Urtti A and Honkakoski P 2006 Freeze-drying of cationic polymer DNA complexes enables their long-term storage and reverse transfection of post-mitotic cells *Journal of Controlled Release* **110** 437–43
- [429] Okazaki A, Jo J I and Tabata Y 2007 A reverse transfection technology to genetically engineer adult stem cells *Tissue Eng* **13** 245–51
- [430] Bengali Z, Pannier A K, Segura T, Anderson B C, Jang J H, Mustoe T A and Shea L D 2005 Gene delivery through cell culture substrate adsorbed DNA complexes *Biotechnol Bioeng* **90** 290–302
- [431] Wu R Z, Bailey S N, Sabatini D M, Bailey S N and Sabatini D M 2002 Cell-biological applications of transfected-cell microarrays **12** 485–8
- [432] Uchimura E, Yamada S, Uebersax L, Yoshikawa T, Matsumoto K, Kishi M, Funeriu D P, Miyake M and Miyake J 2005 On-chip transfection of PC12 cells based on the rational understanding of the role of ECM molecules : efficient , non-viral transfection of PC12 cells using collagen IV **378** 40–3
- [433] Paidikondala M, Kadekar S and Varghese O P 2019 Innovative strategy for 3D transfection of primary human stem cells with BMP-2 expressing plasmid DNA: A clinically translatable strategy for ex vivo gene therapy *Int J Mol Sci* **20**
- [434] Yoo J J and Atala A 1997 A novel gene delivery system using urothelial tissue engineered neo-organs *Journal of Urology* **158** 1066–70
- [435] Xie Y, Yang S T and Kniss D A 2001 Three-dimensional cell-scaffold constructs promote efficient gene transfection: Implications for cell-based gene therapy *Tissue Eng* **7** 585–98
- [436] Loozen L D, Wegman F, Öner F C, Dhert W J A and Alblas J 2013 Porous bioprinted constructs in BMP-2 non-viral gene therapy for bone tissue engineering *J Mater Chem B* **1** 6619–26
- [437] Raftery R M, Mencía Castaño I, Chen G, Cavanagh B, Quinn B, Curtin C M, Cryan S A and O'Brien F J 2017 Translating the role of osteogenic-angiogenic coupling in bone formation: Highly efficient chitosan-pDNA activated scaffolds can accelerate bone regeneration in critical-sized bone defects *Biomaterials* **149** 116–27
- [438] Takahashi K and Yamanaka S 2006 Induction of Pluripotent Stem Cells from Mouse Embryonic and Adult Fibroblast Cultures by Defined Factors *Cell* **126** 663–76
- [439] Matsui A, Uchida S, Hayashi A, Kataoka K and Itaka K 2018 Prolonged engraftment of transplanted hepatocytes in the liver by transient pro-survival factor supplementation using ex vivo mRNA transfection *Journal of Controlled Release* **285** 1–11



- [440] Hosseinkhani H, Hosseinkhani M, Gabrielson N P, Pack D W, Khademhosseini A and Kobayashi H 2008 DNA nanoparticles encapsulated in 3D tissue-engineered scaffolds enhance osteogenic differentiation of mesenchymal stem cells *J Biomed Mater Res A* **85** 47–60
- [441] Yang R, Chen F, Guo J, Zhou D and Luan S 2020 Recent advances in polymeric biomaterials-based gene delivery for cartilage repair *Bioact Mater* **5** 990–1003
- [442] Giacca M and Zacchigna S 2012 VEGF gene therapy: Therapeutic angiogenesis in the clinic and beyond *Gene Ther* **19** 622–9
- [443] Isner J M, Pieczek A, Schainfeld R, Blair R, Haley L, Asahara T, Rosenfield K, Razvi S, Walsh K and Symes J F 1996 Clinical evidence of angiogenesis after arterial gene transfer of phVEGF165 in patient with ischaemic limb *Lancet* **348** 370–4
- [444] Raftery R M, Mencía-Castaño I, Sperger S, Chen G, Cavanagh B, Feichtinger G A, Redl H, Hacopian A and O'Brien F J 2018 Delivery of the improved BMP-2-Advanced plasmid DNA within a gene-activated scaffold accelerates mesenchymal stem cell osteogenesis and critical size defect repair *Journal of Controlled Release* **283** 20–31
- [445] Yeh H C D and Kuo M H C 2006 Co-transfection with the osteogenic protein (OP)-1 gene and the insulin-like growth factor (IGF)-I gene enhanced osteoblastic cell differentiation *International Journal of Learning and Intellectual Capital* **3** 57–73
- [446] Chopinet L, Wasungu L and Rols M P 2012 First explanations for differences in electrotransfection efficiency in vitro and in vivo using spheroid model *Int J Pharm* **423** 7–15
- [447] He C-X, Li N, Hu Y-L, Zhu X-M, Li H-J, Han M, Miao P-H, Hu Z-J, Wang G, Liang W-Q, Tabata Y and Gao J-Q 2011 Effective Gene Delivery to Mesenchymal Stem Cells Based on the Reverse Transfection and Three-Dimensional Cell Culture System *Pharm Res* **28** 1577–90
- [448] Fukunaka Y, Iwanaga K, Morimoto K, Kakemi M and Tabata Y 2002 Controlled release of plasmid DNA from cationized gelatin hydrogels based on hydrogel degradation *Journal of Controlled Release* **80** 333–43
- [449] Husteden C, Doberenz F, Goergen N, Pinnapireddy S R, Janich C, Langner A, Syrowatka F, Repanas A, Erdmann F, Jedelská, J J, Bakowsky U, Groth T, Wö C, Jedelská J, Bakowsky U, Groth T and Wölk C 2020 Contact-Triggered Lipofection from Multilayer Films Designed as Surfaces for in Situ Transfection Strategies in Tissue Engineering *ACS Appl Mater Interfaces* **12** 8963–77
- [450] Gao J Q, Zhao Q Q, Lv T F, Shuai W P, Zhou J, Tang G P, Liang W Q, Tabata Y and Hu Y L 2010 Gene-carried chitosan-linked-PEI induced high gene transfection efficiency with low toxicity and significant tumor-suppressive activity *Int J Pharm* **387** 286–94

- [451] Shi B, Zhang H, Shen Z, Bi J and Dai S 2013 Developing a chitosan supported imidazole Schiff-base for high-efficiency gene delivery *Polym Chem* **4** 840–50
- [452] Corsi K, Chellat F, Yahia L and Fernandes J C 2003 Mesenchymal stem cells, MG63 and HEK293 transfection using chitosan-DNA nanoparticles *Biomaterials* **24** 1255–64
- [453] Huang M, Khor E and Lim L Y 2004 Uptake and Cytotoxicity of Chitosan Molecules and Nanoparticles: Effects of Molecular Weight and Degree of Deacetylation *Pharm Res* **21** 344–53
- [454] He W, Guo Z, Wen Y, Wang Q, Xie B, Zhu S and Wang Q 2012 Alginate-graft-PEI as a gene delivery vector with high efficiency and low cytotoxicity *J Biomater Sci Polym Ed* **23** 315–31
- [455] Padmanabhan K and Smith T J 2002 A Preliminary Investigation of Modified Alginates as a Matrix for Gene Transfection in a HeLa Cell Model *Pharm Dev Technol* **7** 97–101
- [456] Walsh D P, Heise A, O'Brien F J and Cryan S A 2017 An efficient, non-viral dendritic vector for gene delivery in tissue engineering *Gene Ther* **24** 681–91
- [457] Menciá Castanõ I, Curtin C M, Duffy G P and O'Brien F J 2016 Next generation bone tissue engineering: Non-viral miR-133a inhibition using collagen-nanohydroxyapatite scaffolds rapidly enhances osteogenesis *Sci Rep* **6** 1–10
- [458] Yan L P, Castaño I M, Sridharan R, Kelly D, Lemoine M, Cavanagh B L, Dunne N J, McCarthy H O and O'Brien F J 2020 Collagen/GAG scaffolds activated by RALA-siMMP-9 complexes with potential for improved diabetic foot ulcer healing *Materials Science and Engineering C* **114** 111022
- [459] De Laporte L, Lei Yan A and Shea L D 2009 Local gene delivery from ECM-coated poly(lactide-co-glycolide) multiple channel bridges after spinal cord injury *Biomaterials* **30** 2361–8
- [460] Dhaliwal A, Maldonado M, Han Z and Segura T 2010 Differential uptake of DNA-poly(ethylenimine) polyplexes in cells cultured on collagen and fibronectin surfaces *Acta Biomater* **6** 3436–47
- [461] Tierney E G, McSorley K, Hastings C L, Cryan S A, O'Brien T, Murphy M J, Barry F P, O'Brien F J and Duffy G P 2013 High levels of ephrinB2 over-expression increases the osteogenic differentiation of human mesenchymal stem cells and promotes enhanced cell mediated mineralisation in a polyethyleneimine-ephrinB2 gene-activated matrix *Journal of Controlled Release* **165** 173–82
- [462] Hosseinkhani H, Azzam T, Kobayashi H, Hiraoka Y, Shimokawa H, Domb A J and Tabata Y 2006 Combination of 3D tissue engineered scaffold and non-viral gene carrier enhance in vitro DNA expression of mesenchymal stem cells *Biomaterials* **27** 4269–78

- [463] Fitzgerald K A, Guo J, Tierney E G, Curtin C M, Malhotra M, Darcy R, O'Brien F J and O'Driscoll C M 2015 The use of collagen-based scaffolds to simulate prostate cancer bone metastases with potential for evaluating delivery of nanoparticulate gene therapeutics *Biomaterials* **66** 53–66
- [464] Keeney M, van den Beucken J J J P, van der Kraan P M, Jansen J A and Pandit A 2010 The ability of a collagen/calcium phosphate scaffold to act as its own vector for gene delivery and to promote bone formation via transfection with VEGF165 *Biomaterials* **31** 2893–902
- [465] Hosseinkhani H, Yamamoto M, Inatsugu Y, Hiraoka Y, Inoue S, Shimokawa H and Tabata Y 2006 Enhanced ectopic bone formation using a combination of plasmid DNA impregnation into 3-D scaffold and bioreactor perfusion culture *Biomaterials* **27** 1387–98
- [466] Raftery R M, Tierney E G, Curtin C M, Cryan S A and O'Brien F J 2015 Development of a gene-activated scaffold platform for tissue engineering applications using chitosan-pDNA nanoparticles on collagen-based scaffolds *Journal of Controlled Release* **210** 84–94
- [467] Raftery R, O'Brien F J and Cryan S A 2013 Chitosan for gene delivery and orthopedic tissue engineering applications *Molecules* **18** 5611–47
- [468] Lee M, Nah J W, Kwon Y, Koh J J, Ko K S and Kim S W 2001 Water-soluble and low molecular weight chitosan-based plasmid DNA delivery *Pharm Res* **18** 427–31
- [469] Chollakup R, Uttayarat P, Chworos A and Smitthipong W 2020 Noncovalent Sericin-Chitosan Scaffold : Physical Properties and Low Cytotoxicity Effect *Int J Mol Sci*
- [470] MacLaughlin F C, Mumper R J, Wang J, Tagliaferri J M, Gill I, Hinchcliffe M and Rolland A P 1998 Chitosan and depolymerized chitosan oligomers as condensing carriers for in vivo plasmid delivery *Journal of Controlled Release* **56** 259–72
- [471] Köping-Höggård M, Vårum K M, Issa M, Danielsen S, Christensen B E, Stokke B T and Artursson P 2004 Improved chitosan-mediated gene delivery based on easily dissociated chitosan polyplexes of highly defined chitosan oligomers *Gene Therapy* **2004 11:19** **11** 1441–52
- [472] Tierney E G, Duffy G P, Hibbitts A J, Cryan S A and O'Brien F J 2012 The development of non-viral gene-activated matrices for bone regeneration using polyethyleneimine (PEI) and collagen-based scaffolds *Journal of Controlled Release* **158** 304–11
- [473] Curtin C M, Cunniffe G M, Lyons F G, Bessho K, Dickson G R, Duffy G P and O'Brien F J 2012 Innovative collagen nano-hydroxyapatite scaffolds offer a highly efficient non-viral gene delivery platform for stem cell-mediated bone formation *Advanced Materials* **24** 749–54

- [474] Castaño I M, Raftery R M, Chen G, Cavanagh B, Quinn B, Duffy G P, O'Brien F J and Curtin C M 2020 Rapid bone repair with the recruitment of CD206+M2-like macrophages using non-viral scaffold-mediated miR-133a inhibition of host cells *Acta Biomater* **109** 267–79
- [475] Costard L S, Kelly D C, Power R N, Hobbs C, Jaskaniec S, Nicolosi V, Cavanagh B L, Curtin C M and O'Brien F J 2020 Layered double hydroxide as a potent non-viral vector for nucleic acid delivery using gene-activated scaffolds for tissue regeneration applications *Pharmaceutics* **12** 1–24
- [476] Bakan F, Kara G, Cokol Cakmak M, Cokol M and Denkbas E B 2017 Synthesis and characterization of amino acid-functionalized calcium phosphate nanoparticles for siRNA delivery *Colloids Surf B Biointerfaces* **158** 175–81
- [477] Curtin C M, Tierney E G, Mcsorley K, Cryan S A, Duffy G P and O'Brien F J 2015 Combinatorial gene therapy accelerates bone regeneration: Non-viral dual delivery of VEGF and BMP2 in a collagen-nanohydroxyapatite scaffold *Adv Healthc Mater* **4** 223–7
- [478] Castaño I M, Curtin C M, Shaw G, Mary Murphy J, Duffy G P and O'Brien F J 2015 A novel collagen-nanohydroxyapatite microRNA-activated scaffold for tissue engineering applications capable of efficient delivery of both miR-mimics and antagomiRs to human mesenchymal stem cells *Journal of Controlled Release* **200** 42–51
- [479] Zhang H, Qing F, Zhao H, Fan H, Liu M and Zhang X 2017 Cellular internalization of rod-like nano hydroxyapatite particles and their size and dose-dependent effects on pre-osteoblasts *J Mater Chem B* **5** 1205–17
- [480] Sapet C, Formosa C, Sicard F, Bertosio E, Zelphati O and Laurent N 2013 3D-fection: Cell transfection within 3D scaffolds and hydrogels *Ther Deliv* **4** 673–85
- [481] Gonzalez-Fernandez T, Rathan S, Hobbs C, Pitacco P, Freeman F E, Cunniffe G M, Dunne N J, McCarthy H O, Nicolosi V, O'Brien F J and Kelly D J 2019 Pore-forming bioinks to enable spatio-temporally defined gene delivery in bioprinted tissues *Journal of Controlled Release* **301** 13–27
- [482] Raftery R M, Walsh D P, Blokpoel Ferreras L, Mencía Castaño I, Chen G, LeMoine M, Osman G, Shakesheff K M, Dixon J E and O'Brien F J 2019 Highly versatile cell-penetrating peptide loaded scaffold for efficient and localised gene delivery to multiple cell types: From development to application in tissue engineering *Biomaterials* **216**
- [483] Heitz F, Morris M C and Divita G 2009 Twenty years of cell-penetrating peptides: from molecular mechanisms to therapeutics *Br J Pharmacol* **157** 195–206

- [484] Nakase I, Takeuchi T, Tanaka G and Futaki S 2008 Methodological and cellular aspects that govern the internalization mechanisms of arginine-rich cell-penetrating peptides *Adv Drug Deliv Rev* **60** 598–607
- [485] Futaki S, Nakase I, Tadokoro A, Takeuchi T and Jones A T 2007 Arginine-rich peptides and their internalization mechanisms *Biochem Soc Trans* **35** 784–7
- [486] Zorko M and Langel Ü 2005 Cell-penetrating peptides: Mechanism and kinetics of cargo delivery *Adv Drug Deliv Rev* **57** 529–45
- [487] Kalafatovic D and Giralt E 2017 Cell-Penetrating Peptides: Design Strategies beyond Primary Structure and Amphipathicity *Molecules : A Journal of Synthetic Chemistry and Natural Product Chemistry* **22**
- [488] Walsh D P, Raftery R M, Castaño I M, Murphy R, Cavanagh B, Heise A, O'Brien F J and Cryan S A 2019 Transfection of autologous host cells in vivo using gene activated collagen scaffolds incorporating star-polypeptides *Journal of Controlled Release* **304** 191–203
- [489] Power R N, Cavanagh B L, Dixon J E, Curtin C M and O'Brien F J 2022 Development of a Gene-Activated Scaffold Incorporating Multifunctional Cell-Penetrating Peptides for pSDF-1 $\alpha$  Delivery for Enhanced Angiogenesis in Tissue Engineering Applications *Int J Mol Sci* **23**
- [490] Miura N, Akita H, Tateshita N, Nakamura T and Harashima H 2017 Modifying Antigen-Encapsulating Liposomes with KALA Facilitates MHC Class I Antigen Presentation and Enhances Anti-tumor Effects *Molecular Therapy* **25** 1003–13
- [491] Liu Y, Wan H-H, Tian D-M, Xu X-J, Bi C-L, Zhan X-Y, Huang B-H, Xu Y-S, Yan L-P, Liu Y ;, Wan H-H ;, Tian D-M ;, Xu X-J ;, Bi C-L ;, Zhan X-Y ;, Huang B-H ;, Xu Y-S ; and Yan L-P 2021 Development and Characterization of High Efficacy Cell-Penetrating Peptide via Modulation of the Histidine and Arginine Ratio for Gene Therapy *Materials 2021, Vol. 14, Page 4674* **14** 4674
- [492] McErlean E M, McCrudden C M, McBride J W, Cole G, Kett V L, Robson T, Dunne N J and McCarthy H O 2021 Rational design and characterisation of an amphipathic cell penetrating peptide for non-viral gene delivery *Int J Pharm* **596** 120223
- [493] Fang J, Zhu Y Y, Smiley E, Bonadio J, Rouleau J P, Goldstein S A, Mccauley L K, Davidson B L and Roessler B J 1996 Stimulation of new bone formation by direct transfer of osteogenic plasmid genes *Proc Natl Acad Sci U S A* **93** 5753–8
- [494] Bonadio J, Smiley E, Patil P and Goldstein S 1999 Localized, direct plasmid gene delivery in vivo: Prolonged therapy results in reproducible tissue regeneration *Nat Med* **5** 753–9

- [495] Bengali Z, Rea J C and Shea L D 2007 Gene expression and internalization following vector adsorption to immobilized proteins: dependence on protein identity and density *J Gene Med* **9** 668–78
- [496] Thakor D, Spigelman I, Tabata Y and Nishimura I 2007 Subcutaneous peripheral injection of cationized Gelatin/DNA polyplexes as a platform for non-viral gene transfer to sensory neurons *Molecular Therapy* **15** 2124–31
- [497] Chen J P and Su C H 2011 Surface modification of electrospun PLLA nanofibers by plasma treatment and cationized gelatin immobilization for cartilage tissue engineering *Acta Biomater* **7** 234–43
- [498] Kushibiki T, Nagata-nakajima N, Sugai M and Shimizu A 2006 Enhanced anti-fibrotic activity of plasmid DNA expressing small interference RNA for TGF- $\beta$  type II receptor for a mouse model of obstructive nephropathy by cationized gelatin prepared from different amine compounds **110** 610–7
- [499] Hu W-W W and Ting J-C C 2019 Gene immobilization on alginate/polycaprolactone fibers through electrophoretic deposition to promote in situ transfection efficiency and biocompatibility *Int J Biol Macromol* **121** 1337–45
- [500] Dekker A and Beugeling T 1991 *3. Protein adsorption and the interaction of human endothelial cells with polymer surfaces*
- [501] Altankov G, Richau K and Groth T 2003 The role of surface zeta potential and substratum chemistry for regulation of dermal fibroblasts interaction *Materwiss Werksttech* **34** 1120–8
- [502] Lee J H, Jung H W, Kang I K and Lee H B 1994 Cell behaviour on polymer surfaces with different functional groups *Biomaterials* **15** 705–11
- [503] Kishida A, Iwata H, Tamada Y and Ikada Y 1990 *Cell behaviour on polymer surfaces grafted with non-ionic and ionic monomers*
- [504] Chen Q, Zhang D, Zhang W, Zhang H, Zou J, Chen M, Li J, Yuan Y and Liu R 2021 Dual mechanism  $\beta$ -amino acid polymers promoting cell adhesion *Nat Commun*
- [505] Petersen A, Joly P, Bergmann C, Korus G and Duda G N 2012 The impact of substrate stiffness and mechanical loading on fibroblast-induced scaffold remodeling *Tissue Eng Part A* **18** 1804–17
- [506] Wang F, Zhang L J, Wang Y and Liang S Z 2015 Feeder-culture bioreactors inducing osteogenic and chondrogenic differentiation of human mesenchymal stem cells on polylactic glycolic acid/tricalcium phosphate (PLGA/TCP) scaffolds *J Biomater Tissue Eng* **5** 557–64
- [507] Fajrial A K, He Q Q, Wirusanti N I, Slansky J E and Ding X 2020 A review of emerging physical transfection methods for CRISPR/Cas9-mediated gene editing *Theranostics* **10** 5532–49

- [508] Hartikka J, Sukhu L, Buchner C, Hazard D, Bozoukova V, Margalith M, Nishioka W K, Wheeler C J, Manthorp M and Sawdey M 2001 Electroporation-facilitated delivery of plasmid DNA in skeletal muscle: Plasmid dependence of muscle damage and effect of poloxamer 188 *Molecular Therapy* **4** 407–15
- [509] Miller D L, Bao S, Gies R A and Thrall B D 1999 Ultrasonic enhancement of gene transfection in murine melanoma tumors *Ultrasound Med Biol* **25** 1425–30
- [510] Sakamoto K, Nakamura H, Takagi M, Takeda S and Katsube K ichi 1998 Ectopic expression of lunatic Fringe leads to downregulation of Serrate- 1 in the developing chick neural tube; analysis using in ovo electroporation transfection technique *FEBS Lett* **426** 337–41
- [511] Suzuki T, Shin B C, Fujikura K, Matsuzaki T and Takata K 1998 Direct gene transfer into rat liver cells by in vivo electroporation *FEBS Lett* **425** 436–40
- [512] Vanbever R, Langers G, Montmayeur S and Pr eat V 1998 Transdermal delivery of fentanyl: Rapid onset of analgesia using skin electroporation *Journal of Controlled Release* **50** 225–35
- [513] Marrero B and Heller R 2012 The use of an in vitro 3D melanoma model to predict in vivo plasmid transfection using electroporation *Biomaterials* **33** 3036–46
- [514] Wasungu L, Escoffre J M, Valette A, Teissie J and Rols M P 2009 A 3D in vitro spheroid model as a way to study the mechanisms of electroporation *Int J Pharm* **379** 278–84
- [515] Rols M P 2008 Mechanism by which electroporation mediates DNA migration and entry into cells and targeted tissues. *Methods Mol Biol* **423** 19–33
- [516] Pavlin M and Kandu er M 2015 New Insights into the Mechanisms of Gene Electrotransfer - Experimental and Theoretical Analysis *Sci Rep* **5** 1–11
- [517] Bouakaz A, Zeghimi A and Doinikov A A 2016 Sonoporation: Concept and Mechanisms *Therapeutic Ultrasound. Advances in Experimental Medicine and Biology* **880** 293–308
- [518] Yang Y, Li Q, Guo X, Tu J and Zhang D 2020 Mechanisms underlying sonoporation: Interaction between microbubbles and cells *Ultrason Sonochem* **67** 105096
- [519] Longsine-Parker W, Wang H, Koo C, Kim J, Kim B, Jayaraman A and Han A 2013 Microfluidic electro-sonoporation: A multi-modal cell poration methodology through simultaneous application of electric field and ultrasonic wave *Lab Chip* **13** 2144–52
- [520] Sheyn D, Pelled G, Zilberman Y, Gazit Z and Gazit D 2006 753. Ectopic Bone Formation In Vivo Induced by Sonoporation: Ultrasound-Based Non Viral Gene Delivery System *Molecular Therapy* **13** S291
- [521] Bulysheva A, Heller L, Francis M, Varghese F, Boye C and Heller R 2021 Monopolar gene electrotransfer enhances plasmid DNA delivery to skin *Bioelectrochemistry* **140** 107814

- [522] Borrell V 2010 In vivo gene delivery to the postnatal ferret cerebral cortex by DNA electroporation *J Neurosci Methods* **186** 186–95
- [523] Terada Y, Tanaka H, Okado T, Inoshita S, Kuwahara M, Akiba T, Sasaki S and Marumo F 2001 Efficient and ligand-dependent regulated erythropoietin production by naked DNA injection and in vivo electroporation *American Journal of Kidney Diseases* **38** 50–3
- [524] Nishimura K, Yonezawa K, Fumoto S, Miura Y, Hagimori M, Nishida K and Kawakami S 2019 Application of direct sonoporation from a defined surface area of the peritoneum: Evaluation of transfection characteristics in mice *Pharmaceutics* **11**
- [525] Brun P, Dettin M, Campana L G, Dughiero F, Sgarbossa P, Bernardello C, Tosi A L, Zamuner A and Sieni E 2019 Cell-seeded 3D scaffolds as in vitro models for electroporation *Bioelectrochemistry* **125** 15–24
- [526] Sieni E, Bazzolo B, Pieretti F, Zamuner A, Tasso A, Dettin M and Conconi M T 2020 Breast cancer cells grown on hyaluronic acid-based scaffolds as 3D in vitro model for electroporation *Bioelectrochemistry* **136** 107626
- [527] Haberl S and Pavlin M 2010 Use of collagen gel as a three-dimensional in vitro model to study electroporation and gene electrotransfer *Journal of Membrane Biology* **236** 87–95
- [528] Tsuchiya S, Chiba M, Kishimoto K N, Nakamura H, Tsuchiya M and Hayashi H 2017 Transfer of the bone morphogenetic protein 4 gene into rat periodontal ligament by in vivo electroporation *Arch Oral Biol* **74** 123–32
- [529] Heller E, Garcia-Sanchez T, Moshkovits Y, Rabinovici R, Grynberg D, Segev A, Asirvatham S J, Ivorra A and Maor E 2021 Comparing High-Frequency With Monophasic Electroporation Protocols in an In Vivo Beating Heart Model *JACC Clin Electrophysiol* **7** 959–64
- [530] Lee K, Kim J D, Lee C Y, Her S and Jung H 2011 A high-capacity, hybrid electro-microneedle for in-situ cutaneous gene transfer *Biomaterials* **32** 7705–10
- [531] Cencen V 2016 A Microfluidic Device for Transfection of Mammalian Cells Using Adjustable Shear Stress
- [532] Xu T, Rohozinski J, Zhao W, Moorefield E C, Atala A and Yoo J J 2009 Inkjet-mediated gene transfection into living cells combined with targeted delivery *Tissue Eng Part A* **15** 95–101
- [533] Ho L and Hsu S hui 2018 Cell reprogramming by 3D bioprinting of human fibroblasts in polyurethane hydrogel for fabrication of neural-like constructs *Acta Biomater* **70** 57–70
- [534] Miyazaki H, Ogura M, Sakaguchi Y, Hasegawa T, Atobe S and Terai K 2021 Mechanism of jet injector-induced plasmid DNA uptake: Contribution of shear stress and endocytosis *Int J Pharm* **609** 121200



- [535] Lucas L, Aravind A, Emma P, Christophe M and Edwin-Joffrey C 2021 Rheology, simulation and data analysis toward bioprinting cell viability awareness *Bioprinting* **21**
- [536] Huang N-C C, Lee C-M M and Hsu S-H hui 2020 Effective naked plasmid DNA delivery into stem cells by microextrusion-based transient-transfection system for in situ cardiac repair *Cytotherapy* **22** 70–81
- [537] Heinz F X and Stiasny K 2021 Distinguishing features of current COVID-19 vaccines: knowns and unknowns of antigen presentation and modes of action *NPJ Vaccines* **6**
- [538] Romani B, Kavyanifard A and Allahbakhshi E 2017 Antibody production by in vivo RNA transfection *Sci Rep* **7** 1–8
- [539] Roesler E, Weiss R, Weinberger E E, Fruehwirth A, Stoecklinger A, Mostböck S, Ferreira F, Thalhamer J and Scheiblhofer S 2009 Immunize and disappear-Safety-optimized mRNA vaccination with a panel of 29 allergens *Journal of Allergy and Clinical Immunology* **124**
- [540] Pardi N, Tuyishime S, Muramatsu H, Kariko K, Mui B L, Tam Y K, Madden T D, Hope M J and Weissman D 2015 Expression kinetics of nucleoside-modified mRNA delivered in lipid nanoparticles to mice by various routes *Journal of Controlled Release* **217** 345–51
- [541] Andrews C D, Luo Y, Sun M, Yu J, Goff A J, Glass P J, Padte N N, Huang Y and Ho D D 2017 In Vivo Production of Monoclonal Antibodies by Gene Transfer via Electroporation Protects against Lethal Influenza and Ebola Infections *Mol Ther Methods Clin Dev* **7** 74–82
- [542] Yamano N, Takahashi M, Ali Haghparast S M, Onitsuka M, Kumamoto T, Frank J and Omasa T 2016 Increased recombinant protein production owing to expanded opportunities for vector integration in high chromosome number Chinese hamster ovary cells *J Biosci Bioeng* **122** 226–31
- [543] Satorius Stedim Data Analytics AB 2017 MODDE 12 users guide
- [544] Lamas C P, Vega C and Noya E G 2022 Freezing point depression of salt aqueous solutions using the Madrid-2019 model *Journal of Chemical Physics* **156**
- [545] Uggeri J, Gatti R, Belletti S, Scandroglio R, Corradini R, Rotoli B M and Orlandini G 2000 Calcein-AM is a detector of intracellular oxidative activity *Histochem Cell Biol* **122** 499–505
- [546] Likitdecharoj P and Ratanavaraporn J 2016 Preparation and characterization of anionized and cationized gelatin derivatives and their microspheres for drug delivery system *2016 9th Biomedical Engineering International Conference (BMEiCON) (IEEE)* pp 1–5
- [547] Ofner C M and Bubnis W A 1996 Chemical and swelling evaluations of amino group crosslinking in gelatin and modified gelatin matrices *Pharm Res* **13** 1821–7

- [548] Padmanabhan K and Smith T J 2002 A Preliminary Investigation of Modified Alginates as a Matrix for Gene Transfection in a HeLa Cell Model *Pharm Dev Technol* **7** 97–101
- [549] Petiot E, Chastagnier L, Courtial E-J and Marquette C 2023 Production of cellular products from cells integrated in a matrix *European Patent Office (EPO); Patent No. EP4141095A1; WO2023025804A1*
- [550] Stenn K S, Link R, Moellmann G, Madri J and Kuklinska E 1989 Dispase, a Neutral Protease From *Bacillus Polymyxa*, Is a Powerful Fibronectinase and Type IV Collagenase *Journal of Investigative Dermatology* **93** 287–90
- [551] Chomarat N, Robert L, Seris J L and Kern P 1994 Comparative efficiency of pepsin and proctase for the preparation of bovine skin gelatin *Enzyme Microb Technol* **16** 756–60
- [552] Nestler L, Evege E, Mclaughlin J, Munroe D, Tan T, Wagner K and Stiles B 2004 TrypLE™ Express: A Temperature Stable Replacement for Animal Trypsin in Cell Dissociation Applications *Quest* **1** 42–7
- [553] Liang T W, Demarco R A, Mrsny R J, Gurney A, Gray A, Hooley J, Aaron H L, Huang A, Klassen T, Tumas D B and Fong S 2000 Characterization of huJAM: Evidence for involvement in cell-cell contact and tight junction regulation *Am J Physiol Cell Physiol* **279** 1733–43
- [554] Hsu L W, Lee P L, Chen C T, Mi F L, Juang J H, Hwang S M, Ho Y C and Sung H W 2012 Elucidating the signaling mechanism of an epithelial tight-junction opening induced by chitosan *Biomaterials* **33** 6254–63
- [555] Zhu B, Chen M, Yin H, Du Y and Ning L 2016 Enzymatic hydrolysis of alginate to produce oligosaccharides by a new purified endo-type alginate lyase *Mar Drugs* **14**
- [556] Qin H M, Miyakawa T, Inoue A, Nishiyama R, Nakamura A, Asano A, Ojima T and Tanokura M 2018 Structural basis for controlling the enzymatic properties of polymannuronate preferred alginate lyase FlAlY A from the PL-7 family *Chemical Communications* **54** 555–8
- [557] Cohen J, Zaleski K L, Nourissat G, Julien T P, Randolph M A and Yaremchuk M J 2011 Survival of porcine mesenchymal stem cells over the alginate recovered cellular method *J Biomed Mater Res A* **96 A** 93–9
- [558] Oeller M, Laner-plamberger S, Krisch L, Rohde E, Strunk D and Schallmoser K 2021 Human platelet lysate for good manufacturing practice-compliant cell production *Int J Mol Sci* **22**
- [559] Wrzyszczyk A and Wozniak M 2012 On the origin of matrix metalloproteinase-2 and -9 in blood platelets *Platelets* **23** 467–74
- [560] Adhikari N, Amin S A and Jha T 2020 *Collagenases and gelatinases and their inhibitors as anticancer agents* (Elsevier Inc.)

- [561] Dmitrieva N I, Michea L F, Rocha G M and Burg M B 2001 Cell cycle delay and apoptosis in response to osmotic stress *Comparative Biochemistry and Physiology - A Molecular and Integrative Physiology* **130** 411–20
- [562] Wang L, Liu Y, Wang H, Liu X, Chen J, Wang M H, Wang J and Huang H 2014 Epoxyeicosatrienoic acids attenuating hypotonic-induced apoptosis of IMCD cells via  $\gamma$ -ENaC inhibition *PLoS One* **9** 2–8
- [563] Selzner N, Selzner M, Graf R, Ungethuem U, Fitz J G and Clavien P A 2004 Water induces autocrine stimulation of tumor cell killing through ATP release and P2 receptor binding *Cell Death Differ* **11** S172–80
- [564] Kuystermans D and Al-Rubeai M 2015 *Biopharmaceutical Products from Animal Cell Culture*
- [565] Horie M, Yamano-Adachi N, Kawabe Y, Kaneoka H, Fujita H, Nagamori E, Iwai R, Sato Y, Kanie K, Ohta S, Somiya M and Ino K 2022 Recent advances in animal cell technologies for industrial and medical applications *J Biosci Bioeng* **133** 509–14
- [566] Zamorano F, Wouwer A Vande and Bastin G 2010 Metabolic flux analysis of CHO-320 cells: Undetermined network and effect of measurement errors *IFAC Proceedings Volumes (IFAC-PapersOnline)* **43** 437–42
- [567] Martínez-Monge I, Albiol J, Lecina M, Liste-Calleja L, Miret J, Solà C and Cairó J J 2019 Metabolic flux balance analysis during lactate and glucose concomitant consumption in HEK293 cell cultures *Biotechnol Bioeng* **116** 388–404
- [568] Martínez V S, Dietmair S, Quek L E, Hodson M P, Gray P and Nielsen L K 2013 Flux balance analysis of CHO cells before and after a metabolic switch from lactate production to consumption *Biotechnol Bioeng* **110** 660–6
- [569] Bastin G, Chotteau V and Vande Wouwer A 2021 Metabolic flux analysis of VERO cells under various culture conditions *Processes* **9** 1–20
- [570] Tapia F, Vázquez-Ramírez D, Genzel Y and Reichl U 2016 Bioreactors for high cell density and continuous multi-stage cultivations: options for process intensification in cell culture-based viral vaccine production *Appl Microbiol Biotechnol* **100** 2121–32
- [571] Barrett P N, Mundt W, Kistner O and Howard M K 2009 Vero cell platform in vaccine production: Moving towards cell culture-based viral vaccines *Expert Rev Vaccines* **8** 607–18
- [572] Voisard D, Meuwly F, Ruffieux P A, Baer G and Kadouri A 2003 Potential of cell retention techniques for large-scale high-density perfusion culture of suspended mammalian cells *Biotechnol Bioeng* **82** 751–65

- [573] Lomba A L O, Tirapelle M C, Biaggio R T, Abreu-Neto M S, Covas D T, Picanço-Castro V, Swiech K and Mizukami A 2021 Serum-Free Suspension Adaptation of HEK-293T Cells: Basis for Large-Scale Biopharmaceutical Production *Brazilian Archives of Biology and Technology* **64**
- [574] Lavado-García J, Pérez-Rubio P, Cervera L and Gòdia F 2022 The cell density effect in animal cell-based bioprocessing: Questions, insights and perspectives *Biotechnol Adv* **60**
- [575] Cervera L, Gutiérrez-Granados S, Martínez M, Blanco J, Gòdia F and Segura M M 2013 Generation of HIV-1 Gag VLPs by transient transfection of HEK 293 suspension cell cultures using an optimized animal-derived component free medium *J Biotechnol* **166** 152–65
- [576] Huynh H T, Tran T T B, Chan L C L, Nielsen L K and Reid S 2015 Effect of the peak cell density of recombinant AcMNPV-infected Hi5 cells on baculovirus yields *Appl Microbiol Biotechnol* **99** 1687–700
- [577] Le Ru A, Jacob D, Transfiguracion J, Ansoerge S, Henry O and Kamen A A 2010 Scalable production of influenza virus in HEK-293 cells for efficient vaccine manufacturing *Vaccine* **28** 3661–71
- [578] Rosellini A, Freer G, Quaranta P, Dovere V, Menichini M, Maggi F, Mazzetti P and Pistello M 2019 Enhanced in vitro virus expression using 3-dimensional cell culture spheroids for infection *J Virol Methods* **265** 99–104
- [579] Wong H L, Wang M X, Cheung P T, Yao K M and Chan B P 2007 A 3D collagen microsphere culture system for GDNF-secreting HEK293 cells with enhanced protein productivity *Biomaterials* **28** 5369–80
- [580] Agarwal S, Saha S, Balla V K, Pal A, Barui A and Bodhak S 2020 Current Developments in 3D Bioprinting for Tissue and Organ Regeneration—A Review *Front Mech Eng* **6**
- [581] Matai I, Kaur G, Seyedsalehi A, McClinton A and Laurencin C T 2020 Progress in 3D bioprinting technology for tissue/organ regenerative engineering *Biomaterials* **226** 119536
- [582] Bock A, Sann H, Schulze-Horsel J, Genzel Y, Reichl U and Möhler L 2009 Growth behavior of number distributed adherent MDCK cells for optimization in microcarrier cultures *Biotechnol Prog* **25** 1717–31
- [583] Henry O, Jolicoeur M and Kamen A 2011 Unraveling the metabolism of HEK-293 cells using lactate isotopomer analysis *Bioprocess Biosyst Eng* **34** 263–73
- [584] Lee Y Y, Wong K T K, Nissom P M, Wong D C F and Yap M G S 2007 Transcriptional profiling of batch and fed-batch protein-free 293-HEK cultures *Metab Eng* **9** 52–67
- [585] Ahn W S and Antoniewicz M R 2011 Metabolic flux analysis of CHO cells at growth and non-growth phases using isotopic tracers and mass spectrometry *Metab Eng* **13** 598–609

- [586] Crabtree H G 1929 Observations on the carbohydrate metabolism of tumours *Biochemical Journal* **23** 536–45
- [587] Warburg O 1956 On the Origin of Cancer Cells *Science (1979)* **123** 309–14
- [588] Certo M, Tsai C H, Pucino V, Ho P C and Mauro C 2021 Lactate modulation of immune responses in inflammatory versus tumour microenvironments *Nat Rev Immunol* **21** 151–61
- [589] Li X, Yang Y, Zhang B, Lin X, Fu X, An Y, Zou Y, Wang J X, Wang Z and Yu T 2022 Lactate metabolism in human health and disease *Signal Transduct Target Ther* **7**
- [590] Rybkowska P, Radoszkiewicz K, Kawalec M, Dymkowska D, Zabłocka B, Zabłocki K and Sarnowska A 2023 The Metabolic Changes between Monolayer (2D) and Three-Dimensional (3D) Culture Conditions in Human Mesenchymal Stem/Stromal Cells Derived from Adipose Tissue *Cells* **12**
- [591] Wurm F M 2013 CHO quasispecies-Implications for manufacturing processes *Processes* **1** 296–311
- [592] Shen C, Gu M, Song C, Miao L, Hu L, Liang D and Zheng C 2008 The tumorigenicity diversification in human embryonic kidney 293 cell line cultured in vitro *Biologicals* **36** 263–8
- [593] Yang L, Gu X, Yu J, Ge S and Fan X 2021 Oncolytic Virotherapy: From Bench to Bedside *Front Cell Dev Biol* **9** 1–18
- [594] Singh P K, Doley J, Ravi Kumar G, Sahoo A P and Tiwari A K 2012 Oncolytic viruses & their specific targeting to tumour cells *Indian Journal of Medical Research* **136** 571–84
- [595] Herzlinger D A, Easton T G and Ojakian G K 1982 The MDCK epithelial cell line expresses a cell surface antigen of the kidney distal tubule *Journal of Cell Biology* **93** 269–77
- [596] Bryant D M, Roignot J, Datta A, Overeem A W, Kim M, Yu W, Peng X, Eastburn D J, Ewald A J, Werb Z and Mostov K E 2014 A molecular switch for the orientation of epithelial cell polarization *Dev Cell* **31** 171–87
- [597] Liu S, Netzel-Arnett S, Birkedal-Hansen H and Leppla S H 2000 Tumor cell-selective cytotoxicity of matrix metalloproteinase-activated anthrax toxin *Cancer Res* **60** 6061–7
- [598] Schauer N, Dinc M, Raabe B, Hummel T, Müller M, Sobek H and Mizaikoff B 2018 Selective binding of matrix metalloproteases MMP-9 and MMP-12 to inhibitor-assisted thermolysin-imprinted beads *RSC Adv* **8** 32387–94
- [599] Chaudhary A K, Pandya S, Ghosh K and Nadkarni A 2013 Matrix metalloproteinase and its drug targets therapy in solid and hematological malignancies: An overview *Mutat Res Rev Mutat Res* **753** 7–23

- [600] Kandhwal M, Behl T, Singh S, Sharma N, Arora S, Bhatia S, Al-Harrasi A, Sachdeva M and Bungau S 2022 Role of matrix metalloproteinase in wound healing *Am J Transl Res* **14** 4391–405
- [601] Liu C J, Chang K W, Lin S C and Cheng H W 2009 Presurgical serum levels of matrix metalloproteinase-9 and vascular endothelial growth factor in oral squamous cell carcinoma *Oral Oncol* **45** 920–5
- [602] Quintero-Fabián S, Arreola R, Becerril-Villanueva E, Torres-Romero J C, Arana-Argáez V, Lara-Riegos J, Ramírez-Camacho M A and Alvarez-Sánchez M E 2019 Role of Matrix Metalloproteinases in Angiogenesis and Cancer *Front Oncol* **9** 1–21
- [603] Alchalabi A S H, Rahim H, Aklilu E, Al-Sultan I I, Aziz A R, Malek M F, Ronald S H and Khan M A 2016 Histopathological changes associated with oxidative stress induced by electromagnetic waves in rats' ovarian and uterine tissues *Asian Pacific Journal of Reproduction* **5** 301–10
- [604] Ernst L M and Ruchelli E D 2019 *Color Atlas of Human Fetal and Neonatal Histology Second Edition*
- [605] Seely J C, Hard G C and Blankenship B 2017 *Kidney* (Elsevier Inc.)
- [606] He X, Yang Y, Han Y, Cao C, Zhang Z, Li L, Xiao C, Guo H, Wang L, Han L, Qu Z, Liu N, Han S and Xu F 2023 Extracellular matrix physical properties govern the diffusion of nanoparticles in tumor microenvironment. *Proc Natl Acad Sci U S A* **120** e2209260120
- [607] Zagari F, Jordan M, Stettler M, Broly H and Wurm F M 2013 Lactate metabolism shift in CHO cell culture: The role of mitochondrial oxidative activity *N Biotechnol* **30** 238–45
- [608] Ozturk S S and Palsson B 1990 Effect of initial cell density on hybridoma growth, metabolism, and monoclonal antibody production *J Biotechnol* **16** 259–78
- [609] Rodriguez E N, Perez M, Casanova P and Martinez L 2001 Effect of Seed Cell Density on Specific Growth Rate Using CHO Cells as Model *Animal Cell Technology: From Target to Market* **2** 434–7
- [610] Marteiijn R C L, Oude-Elferink M M A, Martens D E, De Gooijer C D and Tramper J 2000 Effect of low inoculation density in the scale-up of insect cell cultures *Biotechnol Prog* **16** 795–9
- [611] Baker B M and Chen C S 2012 Deconstructing the third dimension-how 3D culture microenvironments alter cellular cues *J Cell Sci* **125** 3015–24
- [612] Colom A, Galgoczy R, Almendros I, Xaubet A, Farré R and Alcaraz J 2014 Oxygen diffusion and consumption in extracellular matrix gels: Implications for designing three-dimensional cultures *J Biomed Mater Res A* **102** 2776–84

- [613] McMurtrey R J 2016 Analytic models of oxygen and nutrient diffusion, metabolism dynamics, and architecture optimization in three-dimensional tissue constructs with applications and insights in cerebral organoids *Tissue Eng Part C Methods* **22** 221–49
- [614] Shi Y G, Qian L, Zhang N, Han C R, Liu Y, Zhang Y F and Ma Y Q 2011 Changes in morphology and activity of transglutaminase following cross-linking and immobilization on a polypropylene microporous membrane *Molecules* **16** 10046–58
- [615] Lagies S, Schlimpert M, Neumann S, Wäldin A, Kammerer B, Borner C and Peintner L 2020 Cells grown in three-dimensional spheroids mirror in vivo metabolic response of epithelial cells *Commun Biol* **3**
- [616] Souza A G, Silva I B B, Campos-Fernandez E, Barcelos L S, Souza J B, Marangoni K, Goulart L R and Alonso-Goulart V 2018 Comparative Assay of 2D and 3D Cell Culture Models: Proliferation, Gene Expression and Anticancer Drug Response *Curr Pharm Des* **24** 1689–94
- [617] Colom A, Galgoczy R, Almendros I, Xaubet A, Farré R and Alcaraz J 2014 Oxygen diffusion and consumption in extracellular matrix gels: Implications for designing three-dimensional cultures *J Biomed Mater Res A* **102** 2776–84
- [618] Zhang Y, Wang W, Xie Y, Yu W, Teng H, Liu X, Zhang X, Guo X, Fei J and Ma X 2007 In vivo culture of encapsulated endostatin-secreting Chinese hamster ovary cells for systemic tumor inhibition *Hum Gene Ther* **18** 474–81
- [619] Martin I, Wendt D and Heberer M 2004 The role of bioreactors in tissue engineering *Trends Biotechnol* **22** 80–6
- [620] Oosterhuis N M G 2017 Single-Use Bioreactors for Continuous Bioprocessing: Challenges and Outlook *Continuous Biomanufacturing - Innovative Technologies and Methods* (Wiley) pp 131–48
- [621] Pörtner R 2015 Bioreactors for Mammalian Cells pp 89–135
- [622] Reynaud E G, Kržič U, Greger K and Stelzer E H K 2008 Light sheet-based fluorescence microscopy: More dimensions, more photons, and less photodamage *HFSP J* **2** 266–75
- [623] Gil C J, Evans C J, Li L, Allphin A J, Tomov M L, Jin L, Vargas M, Hwang B, Wang J, Putaturo V, Kabboul G, Alam A S, Nandwani R K, Wu Y, Sushmit A, Fulton T, Shen M, Kaiser J M, Ning L, Veneziano R, Willet N, Wang G, Drissi H, Weeks E R, Bauser-Heaton H D, Badea C T, Roeder R K and Serpooshan V 2023 Leveraging 3d Bioprinting And Photon-Counting Computed Tomography to Enable Noninvasive Quantitative Tracking of Multifunctional Tissue Engineered Constructs *Adv Healthc Mater*

- [624] Wang N, Wang X, Yan T, Xie H, Wang L, Ren F, Chen D, Zhang D, Zeng Q, Zhu S and Chen X 2023 Label-free structural and functional volumetric imaging by dual-modality optical-Raman projection tomography *Sci Adv* **9**
- [625] Luna-Palacios Y Y, Licea-Rodriguez J, Camacho-Lopez M D, Teichert I, Riquelme M and Rocha-Mendoza I 2022 Multicolor light-sheet microscopy for a large field of view imaging: A comparative study between Bessel and Gaussian light-sheets configurations *J Biophotonics* **15** 1–15
- [626] Reihani S N S and Oddershede L B 2009 Confocal microscopy of thick specimens *J Biomed Opt* **14** 030513
- [627] Kim J S, Min J, Recknagel A K, Riccio M and Butcher J T 2011 Quantitative Three-Dimensional Analysis of Embryonic Chick Morphogenesis Via Microcomputed Tomography *Anatomical Record* **294** 1–10
- [628] Xu N, LaGrow T J, Anumba N, Lee A, Zhang X, Yousefi B, Bassil Y, Clavijo G P, Khalilzad Sharghi V, Maltbie E, Meyer-Baese L, Nezafati M, Pan W J and Keilholz S 2022 Functional Connectivity of the Brain Across Rodents and Humans *Front Neurosci* **16** 1–27
- [629] Leferink A M, Van Blitterswijk C A and Moroni L 2016 Methods of Monitoring Cell Fate and Tissue Growth in Three-Dimensional Scaffold-Based Strategies for in Vitro Tissue Engineering *Tissue Eng Part B Rev* **22** 265–83
- [630] Kiemen A L, Damanakis A I, Braxton A M, He J, Laheru D, Fishman E K, Chames P, Pérez C A, Wu P H, Wirtz D, Wood L D and Hruban R H 2023 Tissue clearing and 3D reconstruction of digitized, serially sectioned slides provide novel insights into pancreatic cancer *Med* **4** 75–91
- [631] Chau A C M, Hua J and Taylor D B 2016 Analysing breast tissue composition with MRI using currently available short, simple sequences *Clin Radiol* **71** 287–92
- [632] Moretto J 2011 Process Raman Spectroscopy for In-Line CHO Cell Culture Monitoring Experimental
- [633] Abu-Absi N R, Kenty B M, Cuellar M E, Borys M C, Sakhamuri S, Strachan D J, Hausladen M C and Li Z J 2011 Real time monitoring of multiple parameters in mammalian cell culture bioreactors using an in-line Raman spectroscopy probe. *Biotechnol Bioeng* **108** 1215–21
- [634] Li M, Ebel B, Chauchard F, Guédon E and Marc A 2018 Parallel comparison of in situ Raman and NIR spectroscopies to simultaneously measure multiple variables toward real-time monitoring of CHO cell bioreactor cultures *Biochem Eng J* **137** 205–13
- [635] Koljenović S, Bakker Schut T C, Wolthuis R, de Jong B, Santos L, Caspers P J, Kros J M and Puppels G J 2005 Tissue characterization using high wave number Raman spectroscopy *J Biomed Opt* **10** 31116



- [636] Rau J V, Fosca M, Graziani V, Taffon C, Rocchia M, Caricato M, Pozzilli P, Onetti Muda A and Crescenzi A 2017 Proof-of-concept Raman spectroscopy study aimed to differentiate thyroid follicular patterned lesions *Sci Rep* **7** 1–11
- [637] Desroches J, Jermyn M, Pinto M, Picot F, Tremblay M A, Obaid S, Marple E, Urmey K, Trudel D, Soulez G, Guiot M C, Wilson B C, Petrecca K and Leblond F 2018 A new method using Raman spectroscopy for in vivo targeted brain cancer tissue biopsy *Sci Rep* **8** 1–10
- [638] Meksiarun P, Andriana B B, Matsuyoshi H and Sato H 2016 Non-invasive Quantitative Analysis of Specific Fat Accumulation in Subcutaneous Adipose Tissues using Raman Spectroscopy *Sci Rep* **6** 1–8
- [639] Martínez-Monge I, Comas P, Triquell J, Casablancas A, Lecina M, Paredes C J and Cairó J J 2019 Concomitant consumption of glucose and lactate: A novel batch production process for CHO cells *Biochem Eng J* **151** 107358
- [640] Altamirano C, Illanes A, Becerra S, Cairó J J and Gòdia F 2006 Considerations on the lactate consumption by CHO cells in the presence of galactose *J Biotechnol* **125** 547–56
- [641] Pan X, Dalm C, Wijffels R H and Martens D E 2017 Metabolic characterization of a CHO cell size increase phase in fed-batch cultures *Appl Microbiol Biotechnol* **101** 8101–13
- [642] López-Meza J, Araíz-Hernández D, Carrillo-Cocom L M, López-Pacheco F, Rocha-Pizaña M del R and Alvarez M M 2016 Using simple models to describe the kinetics of growth, glucose consumption, and monoclonal antibody formation in naive and infliximab producer CHO cells *Cytotechnology* **68** 1287–300
- [643] Jiang Z and Sharfstein S T 2008 Sodium butyrate stimulates monoclonal antibody over-expression in CHO cells by improving gene accessibility *Biotechnol Bioeng* **100** 189–94
- [644] De Los Milagros Bassani Molinas M, Beer C, Hesse F, Wirth M and Wagner R 2014 Optimizing the transient transfection process of HEK-293 suspension cells for protein production by nucleotide ratio monitoring *Cytotechnology* **66** 493–514
- [645] Dekevic G, Tasto L, Czermak P and Salzig D 2022 Statistical experimental designs to optimize the transient transfection of HEK 293T cells and determine a transfer criterion from adherent cells to larger-scale cell suspension cultures *J Biotechnol* **346** 23–34
- [646] Swiech K, Kamen A, Ansorge S, Durocher Y, Picanço-Castro V, Russo-Carbolante E M S, Neto M S A and Covas D T 2011 Transient transfection of serum-free suspension HEK 293 cell culture for efficient production of human rFVIII *BMC Biotechnol* **11** 114
- [647] Nettleship J E, Watson P J, Rahman-Huq N, Fairall L, Posner M G, Upadhyay A, Reddivari Y, Chamberlain J M G, Kolstoe S E, Bagby S, Schwabe J W R and Owens R J 2015 Transient Expression in HEK 293 Cells: An Alternative to E. coli for the Production of Secreted and

Intracellular Mammalian Proteins *Festivals 2.0: Consuming, Producing and Participating in the Extended Festival Experience*. vol 26 pp 209–22

- [648] Heng Z S L, Yeo J Y, Koh D W S, Gan S K E and Ling W L 2022 Augmenting recombinant antibody production in HEK293E cells: Optimizing transfection and culture parameters *Antib Ther* **5** 30–41
- [649] Stadtfeld M, Varas F and Graf T 2005 Fluorescent protein-cell labeling and its application in time-lapse analysis of hematopoietic differentiation *Methods Mol Med* **105** 395–412
- [650] Fliedl L and Kaisermayer C 2011 Transient gene expression in HEK293 and vero cells immobilised on microcarriers *J Biotechnol* **153** 15–21
- [651] Longo P A, Kavran J M, Kim M S and Leahy D J 2013 *Transient mammalian cell transfection with polyethylenimine (PEI)* vol 529 (Elsevier Inc.)
- [652] Ehrhardt C, Schmolke M, Matzke A, Knoblauch A, Will C, Wixler V and Ludwig S 2006 Polyethylenimine, a cost-effective transfection reagent *Signal Transduct* **6** 179–84
- [653] Fukunaka Y, Iwanaga K, Morimoto K, Kakemi M and Tabata Y 2002 Controlled release of plasmid DNA from cationized gelatin hydrogels based on hydrogel degradation *Journal of Controlled Release* **80** 333–43
- [654] Matsumoto G, Kushibiki T, Kinoshita Y, Lee U, Omi Y, Kubota E and Tabata Y 2006 Cationized gelatin delivery of a plasmid DNA expressing small interference RNA for VEGF inhibits murine squamous cell carcinoma *Cancer Sci* **97** 313–21
- [655] Jain N, Mittal R, Srivastava T S, Satyamoorthy K and Chitnis M P 1994 Synthesis, Characterization, DNA Binding, and Cytotoxic Studies of Dinuclear Complexes of Palladium ( II ) and Platinum ( II ) with 2 , 2 - Bipyridine and Diaminoalkane-N,N'-Diacetic Acid 79–94
- [656] Kim S 2018 Recent Development of Bio-Reducible Polymers for Efficient Gene Delivery System *J Cancer Treatment Diagn* **2** 17–23
- [657] Chis A A, Dobrea C M, Rus L L, Frum A, Morgovan C, Butuca A, Totan M, Juncan A M, Gligor F G and Arseniu A M 2021 Dendrimers as non-viral vectors in gene-directed enzyme prodrug therapy *Molecules* **26**
- [658] Vajravelu K, Sreenadh S, Devaki P and Prasad K V. 2011 Mathematical model for a Herschel-Bulkley fluid flow in an elastic tube *Central European Journal of Physics* **9** 1357–65
- [659] Cohen R N, van der Aa M A E M, Macaraeg N, Lee A P and Szoka F C 2009 Quantification of plasmid DNA copies in the nucleus after lipoplex and polyplex transfection *Journal of Controlled Release* **135** 166–74

- [660] Riddle K W, Kong H J, Leach J K, Fischbach C, Cheung C, Anseth K S and Mooney D J 2007 Modifying the proliferative state of target Cells to control DNA expression and identifying cell types transfected in vivo *Molecular Therapy* **15** 361–8
- [661] Kim S T, Saha K, Kim C and Rotello V M 2013 The role of surface functionality in determining nanoparticle cytotoxicity *Acc Chem Res* **46** 681–91
- [662] Huang Y, Wu C X, Song Y, Huang M, Tian D N, Yang X Bin and Fan Y R 2018 Synthesis, DNA binding, and anticancer properties of bis-naphthalimide derivatives with lysine-modified polyamine linkers *Molecules* **23**
- [663] Wolters G H J, Vos -Scheperkeuter G H, van Deijnen J H M and van Schilfgaarde R 1992 An analysis of the role of collagenase and protease in the enzymatic dissociation of the rat pancreas for islet isolation *Diabetologia* **35** 735–42
- [664] Moscatello D K, Schiavi J, Marquart J D and Lawrence N 2008 Collagenase-assisted fat dissociation for autologous fat transfer *Dermatologic Surgery* **34** 1314–22
- [665] Moscatello D K, Schiavi J, Marquart J D and Lawrence N 2008 Collagenase-assisted fat dissociation for autologous fat transfer *Dermatologic Surgery* **34** 1314–22
- [666] Wolters G H J, Vos -Scheperkeuter G H, van Deijnen J H M and van Schilfgaarde R 1992 An analysis of the role of collagenase and protease in the enzymatic dissociation of the rat pancreas for islet isolation *Diabetologia* **35** 735–42
- [667] Howard R B, Christensen A K, Gibbs F A and Pesch L A 1967 The enzymatic preparation of isolated intact parenchymal cells from rat liver. *J Cell Biol* **35** 675–84
- [668] Howard R B, Christensen A K, Gibbs F A and Pesch L A 1967 The enzymatic preparation of isolated intact parenchymal cells from rat liver. *J Cell Biol* **35** 675–84
- [669] Pouliot R A, Young B M, Link P A, Park H E, Kahn A R, Shankar K, Schneck M B, Weiss D J and Heise R L Porcine Lung-Derived Extracellular Matrix Hydrogel Properties Are Dependent on Pepsin Digestion Time
- [670] Cassiman' J J, Brugmans M and Van Den Berghe H 1981 *GROWTH AND SURFACE PROPERTIES OF DISPASE DISSOCIATED HUMAN FIBROBLASTS* vol 5
- [671] KITANO Y and OKADA N 1983 Separation of the epidermal sheet by dispase *British Journal of Dermatology* **108** 555–60
- [672] Jungblut M, Oeltze K, Zehnter I, Hasselmann D and Bosio A 2008 Preparation of single-cell suspensions from mouse spleen with the gentleMACS Dissociator *Journal of Visualized Experiments* 1–2

- [673] Gonzalez-Pujana A, Rementeria A, Blanco F J, Igartua M, Pedraz J L, Santos-Vizcaino E and Hernandez R M 2017 The role of osmolarity adjusting agents in the regulation of encapsulated cell behavior to provide a safer and more predictable delivery of therapeutics *Drug Deliv* **24** 1654
- [674] Attia N, Santos E, Abdelmouty H, Arafa S, Zohdy N, Hernández R M, Orive G and Pedraz J L 2014 Behaviour and ultrastructure of human bone marrow-derived mesenchymal stem cells immobilised in alginate-poly-l-lysine-alginate microcapsules *J Microencapsul* **31** 579–89
- [675] Zhou L, Hou H, Wei H, Yao L, Sun L, Yu P, Su B and Mao L 2019 In Vivo Monitoring of Oxygen in Rat Brain by Carbon Fiber Microelectrode Modified with Antifouling Nanoporous Membrane *Anal Chem* **91** 3645–51
- [676] Rivas L, Dulay S, Miserere S, Pla L, Marin S B, Parra J, Eixarch E, Gratacós E, Illa M, Mir M and Samitier J 2020 Micro-needle implantable electrochemical oxygen sensor: ex-vivo and in-vivo studies *Biosens Bioelectron* **153**
- [677] Wilson R L, Connell J P and Grande-Allen K J 2019 Monitoring Oxygen Levels within Large, Tissue-Engineered Constructs Using Porphyrin-Hydrogel Microparticles *ACS Biomater Sci Eng* **5** 4522–30
- [678] Chinnery H R and Keller K E 2020 Tunneling Nanotubes and the Eye: Intercellular Communication and Implications for Ocular Health and Disease *Biomed Res Int* **2020** 24–9
- [679] Müller P, Rogers K W, Yu S R, Brand M and Schier A F 2013 Morphogen transport *Development (Cambridge)* **140** 1621–38
- [680] Chen Q, Tian X, Fan J, Tong H, Ao Q and Wang X 2020 An Interpenetrating Alginate/Gelatin Network for Three-Dimensional (3D) Cell Cultures and Organ Bioprinting *Molecules* **25** 756
- [681] Liu Y, Weng R, Wang W, Wei X, Li J, Chen X, Liu Y, Lu F and Li Y 2020 Tunable physical and mechanical properties of gelatin hydrogel after transglutaminase crosslinking on two gelatin types *Int J Biol Macromol* **162** 405–13
- [682] Rahali K, Ben Messaoud G, Kahn C J F, Sanchez-Gonzalez L, Kaci M, Cleymand F, Fleutot S, Linder M, Desobry S and Arab-Tehrany E 2017 Synthesis and characterization of nanofunctionalized gelatin methacrylate hydrogels *Int J Mol Sci* **18**
- [683] Martinez-Garcia F D, Fischer T, Hayn A, Mierke C T, Burgess J K and Harmsen M C 2022 A Beginner's Guide to the Characterization of Hydrogel Microarchitecture for Cellular Applications *Gels* **8** 1–20
- [684] Tudoreanu R, Handrea-Dragan I M, Boca S and Botiz I 2022 Insight and Recent Advances into the Role of Topography on the Cell Differentiation and Proliferation on Biopolymeric Surfaces *Int J Mol Sci* **23**
- [685] Greco V 2013 The death and growth connection *Nat Rev Mol Cell Biol* **14** 6

[686] Loftus L V., Amend S R and Pienta K J 2022 Interplay between Cell Death and Cell Proliferation Reveals New Strategies for Cancer Therapy *Int J Mol Sci* **23**